

Advances in
Quantum Chemistry

Volume 51



ADVANCES IN
QUANTUM CHEMISTRY

VOLUME 51

EDITORIAL BOARD

David M. Bishop (Ottawa, Canada)
Guillermina Estiú (University Park, PA, USA)
Frank Jensen (Odense, Denmark)
Mel Levy (Greensboro, NC, USA)
Jan Linderberg (Aarhus, Denmark)
William H. Miller (Berkeley, CA, USA)
John Mintmire (Stillwater, OK, USA)
Manoj Mishra (Mumbai, India)
Jens Oddershede (Odense, Denmark)
Josef Paldus (Waterloo, Canada)
Pekka Pyykkö (Helsinki, Finland)
Mark Ratner (Evanston, IL, USA)
Adrian Roitberg (Gainesville, FL, USA)
Dennis Salahub (Calgary, Canada)
Henry F. Schaefer III (Athens, GA, USA)
Per Siegbahn (Stockholm, Sweden)
John Stanton (Austin, TX, USA)
Harel Weinstein (New York, NY, USA)

ADVANCES IN QUANTUM CHEMISTRY

EDITORS

JOHN R. SABIN

QUANTUM THEORY PROJECT
UNIVERSITY OF FLORIDA
GAINESVILLE, FLORIDA

ERKKI BRÄNDAS

DEPARTMENT OF QUANTUM CHEMISTRY
UPPSALA UNIVERSITY
UPPSALA, SWEDEN

FOUNDING EDITOR

PER-OLOV LÖWDIN

1916–2000

VOLUME 51



ELSEVIER

AMSTERDAM • BOSTON • HEIDELBERG • LONDON • NEW YORK • OXFORD
PARIS • SAN DIEGO • SAN FRANCISCO • SINGAPORE • SYDNEY • TOKYO

Academic Press is an imprint of Elsevier



Academic Press is an imprint of Elsevier
84 Theobald's Road, London WC1X 8RR, UK
Radarweg 29, PO Box 211, 1000 AE Amsterdam, The Netherlands
525 B Street, Suite 1900, San Diego, CA 92101-4495, USA
30 Corporate Drive, Suite 400, Burlington, MA 01803, USA

First edition 2006

Copyright © 2006, Elsevier Inc. All rights reserved

No part of this publication may be reproduced, stored in a retrieval system or transmitted in any form or by any means electronic, mechanical, photocopying, recording or otherwise without the prior written permission of the publisher

Permissions may be sought directly from Elsevier's Science & Technology Rights Department in Oxford, UK: phone (+44) (0) 1865 843830; fax (+44) (0) 1865 853333; email: permissions@elsevier.com. Alternatively you can submit your request online by visiting the Elsevier web site at <http://elsevier.com/locate/permissions>, and selecting: *Obtaining permission to use Elsevier material*

Notice

No responsibility is assumed by the publisher for any injury and/or damage to persons or property as a matter of products liability, negligence or otherwise, or from any use or operation of any methods, products, instructions or ideas contained in the material herein. Because of rapid advances in the medical sciences, in particular, independent verification of diagnoses and drug dosages should be made

ISBN-13: 978-0-12-034851-0

ISBN-10: 0-12-034851-9

ISSN: 0065-3276

For information on all Academic Press publications visit our web site at http://books.elsevier.com

Printed and bound in USA

06 07 08 09 10 10 9 8 7 6 5 4 3 2 1

Working together to grow
libraries in developing countries

www.elsevier.com | www.bookaid.org | www.sabre.org

ELSEVIER

BOOK AID
International

Sabre Foundation

Contents

<i>Contributors</i>	vii
<i>Preface</i>	ix
The Usefulness of Exponential Wave Function Expansions Employing One- and Two-Body Cluster Operators in Electronic Structure Theory: The Extended and Generalized Coupled-Cluster Methods	1
Peng-Dong Fan and Piotr Piecuch	
1. Introduction	2
2. Practical ways of improving coupled-cluster methods employing singly and doubly excited clusters via extended coupled-cluster theory	4
3. Non-iterative corrections to extended coupled-cluster energies: Generalized method of moments of coupled-cluster equations	26
4. Virtual exactness of exponential wave function expansions employing generalized one- and two-body cluster operators in electronic structure theory	43
Acknowledgements	54
References	54
Angular Momentum Diagrams	59
Paul E.S. Wormer and Josef Paldus	
1. Introduction	60
2. The essentials of SU(2)	62
3. Diagrams	74
4. Basic rules for angular momentum diagrams	89
5. Irreducible closed diagrams	101
6. Concluding remarks	113
Acknowledgement	115
Appendix: Summary of the graphical rules	115
References	121
Chemical Graph Theory—The Mathematical Connection	125
Ivan Gutman	
1. Prologue	125
2. Introduction	126
3. The first case study: Graph energy	127
4. The second case study: Connectivity (Randić) index	130
5. More examples	132

6. Concluding remarks	133
Acknowledgement	134
References	134
Atomic Charges <i>via</i> Electronegativity Equalization: Generalizations and Perspectives	139
Alexander A. Oliferenko, Sergei A. Pisarev, Vladimir A. Palyulin and Nikolai S. Zefirov	
1. Introduction	140
2. Two approaches to electronegativity redistribution	141
3. Principle of electronegativity relaxation	149
4. Numerical examples	152
5. Chemical applications of atomic charges	153
6. Conclusions	153
References	154
Fast Padé Transform for Exact Quantification of Time Signals in Magnetic Resonance Spectroscopy	157
Dževad Belkić	
1. Introduction	158
2. Challenges with quantification of time signals from MRS	161
3. The quantum-mechanical concept of resonances in scattering and spectroscopy	168
4. Resonance profiles	171
5. The role of quantum mechanics in signal processing	172
6. Suitability of the fast Padé transform for signal processing	174
7. Fast Padé transforms inside and outside the unit circle	175
8. Results	184
9. Discussion	222
10. Conclusion	228
Acknowledgements	232
References	232
Probing the Interplay between Electronic and Geometric Degrees-of-Freedom in Molecules and Reactive Systems	235
Roman F. Nalewajski	
1. Introduction	236
2. Summary of basic relations	241
3. Electronic and nuclear sensitivities in geometric representations	256
4. Minimum-energy coordinates in compliance formalism	263
5. Compliant indices of atoms-in-molecules	265
6. Atomic resolution—A reappraisal	271
7. Collective charge displacements and mapping relations	276
8. Concepts for reacting molecules	282
9. Conclusion	299
References	301
<i>Subject Index</i>	307

Contributors

Numbers in parentheses indicate the pages where the authors' contributions can be found.

Dževad Belkić, Karolinska Institute, PO Box 260, S-171 76 Stockholm, Sweden, dzevad.belkic@ki.se

Peng-Dong Fan, Department of Chemistry, Michigan State University, East Lansing, MI 48824, USA and Quantum Theory Project, Department of Chemistry, University of Florida, PO Box 118435 Gainesville, FL 32611, USA

Ivan Gutman, Faculty of Science, University of Kragujevac, 34000 Kragujevac, Serbia, gutman@kg.ac.yu

Roman F. Nalewajski, Department of Theoretical Chemistry, Jagiellonian University, R. Ingardena 3, 30-060 Cracow, Poland

Alexander A. Oliferenko, Pacific Northwest National Laboratory, Richland, WA 99352, USA and Department of Chemistry, Moscow State University, Moscow 119992, Russia, aleksandr.oliferenko@pnl.gov.

Josef Paldus, Department of Applied Mathematics, Department of Chemistry, and Guelph-Waterloo Center for Graduate Work in Chemistry—Waterloo Campus, University of Waterloo, Waterloo, Ontario, Canada, N2L 3G1, paldus@scienide.uwaterloo.ca

Vladimir A. Palyulin, Department of Chemistry, Moscow State University, Moscow 119992, Russia

Piotr Piecuch, Department of Chemistry, Michigan State University, East Lansing, MI 48824, USA and Department of Physics and Astronomy, Michigan State University, East Lansing, MI 48824, USA, piecuch@cem.msu.edu

Sergei A. Pisarev, Department of Chemistry, Moscow State University, Moscow 119992, Russia

Paul E.S. Wormer, Theoretical Chemistry, Institute for Molecules and Materials, Radboud University Nijmegen, Toernooiveld, 6525 ED Nijmegen, The Netherlands, pwormer@teochem.ru.nl

Nikolai S. Zefirov, Department of Chemistry, Moscow State University, Moscow 119992, Russia

This page intentionally left blank

Preface

Volume 51 of *Advances in Quantum Chemistry* deals with various aspects of mathematical versus chemical applications. Some parts belong to established scientific domains, where technical progress has been crucial for the development of modern quantum chemistry as well as the quantification problem in spectral resonance analysis. Other advances, though remarkably useful, have attracted controversial comments as, e.g., being too simple in execution to be correct. All told, should not the possible interconnections between mathematics and natural sciences in general and in chemistry in particular lead to more interesting and useful interpretations? As is usual, the editors leave the decision to the readers.

The first article in the volume, by Peng-Dong Fan and Piotr Piecuch, concerns the calculation of molecular electronic structure to high accuracy, using a variety of one- and two-body schemes in the coupled cluster (CC) family of methods. Questions involving accurate calculation of potential surfaces, including regions representing bond breaking are addressed, and the use of *a posteriori* corrections leading to increased accuracy are taken up. Perhaps the most controversial question addressed in this chapter deals with the possibility of obtaining a “virtually exact” many-electron wavefunction using no more than two-body operators in a cluster expansion.

Chapter 2 is devoted to “Angular Momentum Diagrams”, written by Paul Wormer and Josef Paldus. It represents a shorter version of what could have been a book on the Unitary Group Approach, UGA. It takes the reader from the purely mathematical work on invariant theory by Clebsch and Gordan, via Jucys and Bandzaitis to current versions of modern many-body theories applied to realistic quantum chemical systems, including recent developments by the authors and Piotr Piecuch, an author of the previous chapter.

In Chapters 3 and 4, Ivan Gutman and Alexander Oliferenko respectively, portray Chemical Graph Theory (CGT). Chemical graphs deal with mathematical aspects of classical chemical structure theory building from, but not limited to, the classical concepts. It is argued that a clear symbiosis between CGT and several other modern areas of chemical theory including for the most part quantum chemistry should be expected. In Chapter 3 Gutman examines the impact that research done in CGT may have on mathematics advocating with two explicit case studies that the influence is not insignificant. Oliferenko *et al.*, in the following chapter, rationalizes electrostatics and molecular descriptors in terms of CGT displaying interesting formulations where CGT meets mathematical physics.

Dževad Belkić advances quantum mechanical signal processing through the fast Padé transform (FPT) in Chapter 5. Here, it is shown that the FPT can analytically continue general functions outside their domain, and is an effective solver of generalized eigenproblems. The analogy between the spectral characteristics of synthesized time signals and Magnetic Resonance Spectroscopy (MRS) is employed to carry out reliable quantifications

of one of the most promising non-invasive diagnostic tools in medicine. Belkić supports the theory with numerous tables and figures, displaying the mathematical problems (ill-conditioned) of initial MRS data and the remarkable reliability of the fast Padé transform to quantify spectral structures from isolated resonances to tightly overlapped and nearly confluent ones.

The concluding chapter, by Roman Nalewajski, gives a mathematical view of molecular equilibria using a Density-Functional Theory (DFT) description. Both the externally *closed* (N -controlled) and *open* (μ -controlled) systems are explored within the Born–Oppenheimer approximation. The complementary *Electron Following* (EF) and *Electron Preceding* (EP) perspectives on molecular processes are examined, in which the external potential due to nuclei and the system electron density, respectively, provide the local state-variable of the molecular ground-state.

We offer this volume of *Advances in Quantum Chemistry* to you with the confidence that it will be an interesting and informative read.

Erkki J. Brändas and John R. Sabin
Editors

The Usefulness of Exponential Wave Function Expansions Employing One- and Two-Body Cluster Operators in Electronic Structure Theory: The Extended and Generalized Coupled-Cluster Methods

Peng-Dong Fan^{1,*} and Piotr Piecuch^{1,2}

¹*Department of Chemistry, Michigan State University, East Lansing, MI 48824, USA*

²*Department of Physics and Astronomy, Michigan State University, East Lansing, MI 48824, USA*

E-mail: piecuch@cem.msu.edu

Abstract

In this paper, the applicability of exponential cluster expansions involving one- and two-body operators in high accuracy *ab initio* electronic structure calculations is examined. First, the extended coupled-cluster method with singles and doubles (ECCSD) is tested in the demanding studies of systems with strong quasi-degeneracies, including potential energy surfaces involving multiple bond breaking. The numerical results show that the single-reference ECCSD method is capable of providing a qualitatively correct description of quasi-degenerate electronic states and potential energy surfaces involving bond breaking, eliminating, in particular, the failures and the unphysical behavior of standard coupled-cluster methods in similar cases. It is also demonstrated that one can obtain entire potential energy surfaces with millihartree accuracies by combining the ECCSD theory with the non-iterative *a posteriori* corrections obtained by using the generalized variant of the method of moments of coupled-cluster equations. This is one of the first instances where the relatively simple single-reference formalism, employing only one- and two-body clusters in the design of the relevant energy expressions, provides a highly accurate description of the dynamic and significant non-dynamic correlation effects characterizing quasi-degenerate and multiply bonded systems. Second, an evidence is presented that one may be able to represent the virtually exact ground- and excited-state wave functions of many-electron systems by exponential cluster expansions employing general two-body or one- and two-body operators. Calculations for small many-electron model systems indicate the existence of finite two-body parameters that produce the numerically exact wave functions for ground and excited states. This finding may have a significant impact on future quantum calculations for many-electron systems, since normally one needs triply excited, quadruply excited, and other higher-than-doubly excited Slater determinants, in addition to all singly and doubly excited determinants, to obtain the exact or virtually exact wave functions.

Contents

1. Introduction	2
2. Practical ways of improving coupled-cluster methods employing singly and doubly excited clusters via extended coupled-cluster theory	4
2.1. Extended coupled-cluster theory: A brief overview of the general formalism	4
2.2. Extended coupled-cluster methods with singles and doubles	7
2.2.1. The Piecuch–Bartlett ECCSD approach	8
2.2.2. The Arponen–Bishop ECCSD approach	9

* Present address: Quantum Theory Project, Department of Chemistry, University of Florida, PO Box 118435, Gainesville, FL 32611, USA.

2.3. Numerical results for multiple bond breaking	13
2.3.1. The Piecuch–Bartlett ECCSD approach	13
2.3.2. The Arponen–Bishop ECCSD approach	22
2.4. Conclusion	24
3. Non-iterative corrections to extended coupled-cluster energies: Generalized method of moments of coupled-cluster equations	26
3.1. The method of moments of coupled-cluster equations	26
3.2. The generalized MMCC formalism	31
3.3. The ECCSD(T), ECCSD(TQ), QECCSD(T), and QECCSD(TQ) methods and their performance in calculations for triple bond breaking in N ₂	34
3.4. Summary	42
4. Virtual exactness of exponential wave function expansions employing generalized one- and two-body cluster operators in electronic structure theory	43
4.1. Theory	43
4.1.1. The $\exp(X)$ conjecture	44
4.1.2. Formal arguments in favor of the $\exp(X)$ conjecture (ground states)	46
4.1.3. Extension of the $\exp(X)$ conjecture to excited states	49
4.2. Numerical results	50
4.3. Summary	54
Acknowledgements	54
References	54

1. INTRODUCTION

Great advances have been made in *ab initio* quantum chemistry. Highly accurate calculations for closed-shell and simple open-shell molecular systems involving a few atoms are nowadays routine. This, in particular, applies to coupled-cluster (CC) theory [1–5], which has become the *de facto* standard for high accuracy calculations for atomic and molecular systems [6–13]. The basic single-reference CC methods, such as CCSD (CC approach with singles and doubles) [14] and the non-iterative CCSD + T(CCSD) = CCSD[T] [15] and CCSD(T) [16] approaches that account for the effect of tri-excited clusters by using arguments based on the many-body perturbation theory (MBPT), in either the spin-orbital [14–16] and spin-free [17–19] or orthogonally spin-adapted [20–22] forms, are nowadays routinely used in accurate electronic structure calculations. The idea of adding the *a posteriori* corrections due to higher-than-doubly excited clusters to CCSD energies, on which the CCSD[T] and CCSD(T) approaches and their higher-order analogs, such as CCSD(TQ_f) (CC method with singles, doubles, and non-iterative triples and quadruples) [23], are based, is particularly attractive, since it leads to methods that offer an excellent compromise between high accuracy and relatively low computer cost, as has been demonstrated over and over in numerous atomic and molecular applications [7–10,12,13].

There are, however, open problems in CC theory. First and foremost is the pervasive failing of the standard single-reference CC methods, such as CCSD, CCSD[T], CCSD(T), and CCSD(TQ_f), at larger internuclear separations, when the spin-adapted restricted Hartree–Fock (RHF) configuration is used as a reference, which limits the applicability of the standard CC approaches to molecules near their equilibrium geometries. Second is the large computer effort associated with the need for using higher-than-doubly excited clusters in calculations involving quasi-degenerate electronic states and bond breaking, particularly when larger many-electron systems are examined. Undoubtedly, it would be very useful to extend the applicability of the standard single-reference CC methods to entire molecular

potential energy surfaces (PESs) involving bond breaking, and quasi-degenerate electronic states in general, without invoking complicated and often time-consuming steps associated with the more traditional multi-reference approaches, in which one has to choose active orbitals and multi-dimensional reference spaces on an *ad hoc* molecule-by-molecule basis. Ideally, one would like to develop a straightforward theory which could provide a virtually exact description of many-electron wave functions with the exponential, CC-like, expansions involving one- and two-body operators only, since the molecular electronic Hamiltonian does not include higher-than-two-body interactions.

There are several specific challenges in all those areas. First of all, the RHF-based CCSD method, on which the non-iterative CCSD[T], CCSD(T), and CCSD(TQ_f) approaches are based, is inadequate for the description of bond breaking and quasi-degenerate states, since it neglects all higher-than-doubly excited clusters, including, for example, the important triply and quadruply excited T_3 and T_4 components. Second, the non-iterative triples and quadruples corrections defining the CCSD[T], CCSD(T), and CCSD(TQ_f) methods aggravate the situation even further, since the usual arguments originating from MBPT, on which these non-iterative CC approximations are based, fail due to the divergent behavior of the MBPT series at larger internuclear separations (or when the strong configurational quasi-degeneracy and large non-dynamic correlation effects set in). In consequence, the ground-state PESs obtained with the CCSD[T], CCSD(T), CCSD(TQ_f), and other standard non-iterative CC approaches are completely pathological when the RHF configuration is used as a reference (*cf.*, *e.g.*, Refs. [9,11–13,24–37] and references therein). The iterative extensions of the CCSD[T], CCSD(T), and CCSD(TQ_f) methods, including, among many others, the CCSDT- n [21,38–41] and CCSDTQ-1 [42] approaches, and the non-iterative CCSDT + Q(CCSDT) = CCSDT[Q] [42] and CCSDT(Q_f) [23] methods, in which the *a posteriori* corrections due to T_4 cluster components are added to the full CCSDT (CC singles, doubles, and triples) [43,44] energies, improve the description of PES in the bond breaking region, but ultimately all of these approaches break down at larger internuclear distances (see, *e.g.*, Refs. [28,29,34]). One might try to resolve the failures of the standard single-reference CC approaches in the bond breaking region and for quasi-degenerate electronic states in more of a brute-force manner by including the triply excited, quadruply excited, pentuply excited, *etc.* clusters fully and in a completely iterative fashion, but, unfortunately, the resulting CCSDTQ (CC singles, doubles, triples, and quadruples) [45–48], CCSDTQP (CC singles, doubles, triples, quadruples, and pentuples) [49], *etc.* approaches are far too expensive for routine molecular applications. For example, the full CCSDTQ method requires iterative steps that scale as $n_o^4 n_u^6$ (n_o (n_u) is the number of occupied (unoccupied) orbitals in the molecular orbital basis). This \mathcal{N}^{10} scaling of the CPU operation count with the system size (\mathcal{N}) characterizing the CCSDTQ approach, combined with the enormous $n_o^4 n_u^4$ storage requirements for quadruply excited cluster amplitudes, restricts the applicability of the CCSDTQ method to very small systems, consisting of ~ 2 – 3 light atoms described by small basis sets. For comparison, CCSD(T) is an $n_o^2 n_u^4$ (or \mathcal{N}^6) procedure in the iterative CCSD steps and an $n_o^3 n_u^4$ (or \mathcal{N}^7) procedure in the non-iterative part related to the calculation of the triples (T) correction, and the storage requirements for cluster amplitudes characterizing the CCSD(T) calculations are very small ($n_o n_u$ for singles and $n_o^2 n_u^2$ for doubles). In consequence, it is nowadays possible to perform the fairly routine CCSD(T) calculations for systems with up to 20–30 light atoms and a few heavier (transition metal) atoms. This indicates that in searching for new methods that would help to overcome the failures of the standard CC approaches in the bond breaking region and

other cases of electronic quasi-degeneracies, one should focus on the idea of improving the results of the low-order CC calculations, such as CCSD, with the non-iterative corrections of the CCSD(T) type, since such methods have a chance to be applied to larger molecular systems in the not-too-distant future.

In view of the above discussion, the question: *Can one improve the quality of standard CC wave functions in the bond breaking region at the basic CCSD level of the single-reference CC theory?* seems to be particularly important. In this paper, we review the results of our recent studies which clearly show that this can be accomplished by exploring the extended coupled-cluster (ECC) theory. The basic ECCSD results, particularly when multiple bonds are stretched or broken, are qualitatively much better than the corresponding standard CCSD results. However, they are not yet fully quantitative. This prompts another question: *Can one improve the quality of the ECCSD results by adding a simple a posteriori correction to the ECCSD energy which is obtained by using the singly and doubly excited cluster amplitudes obtained with the ECCSD approach?* In this paper, we demonstrate that the answer to this question may also be affirmative if we use, for example, the generalized method of moments of coupled-cluster equations (GMMCC). Eventually, of course, one would prefer to use only one- and two-body clusters to obtain an exact or virtually exact description of many-electron systems, since, as we have already mentioned, the Hamiltonians used in quantum chemistry do not contain higher-than-pairwise interactions. This prompts the third and the final question examined in this work: *Can one obtain the exact or virtually exact many-electron wave functions by using exponential expansions involving at most two-body cluster operators?*

2. PRACTICAL WAYS OF IMPROVING COUPLED-CLUSTER METHODS EMPLOYING SINGLY AND DOUBLY EXCITED CLUSTERS VIA EXTENDED COUPLED-CLUSTER THEORY

2.1. Extended coupled-cluster theory: A brief overview of the general formalism

The extended coupled-cluster (ECC) theory is based on the asymmetric, doubly connected energy functional [50–60],

$$E_0^{(\text{ECC})} = \langle \Phi | \bar{\bar{H}} | \Phi \rangle, \quad (1)$$

where $|\Phi\rangle$ is the independent-particle-model reference configuration (e.g., the Hartree–Fock determinant) and

$$\bar{\bar{H}} = e^{\Sigma^\dagger} (e^{-T} H e^T) e^{-\Sigma^\dagger} = e^{\Sigma^\dagger} \bar{H} e^{-\Sigma^\dagger} = (e^{\Sigma^\dagger} \bar{H})_C = [e^{\Sigma^\dagger} (H e^T)_C]_C \quad (2)$$

is the doubly transformed Hamiltonian, obtained by transforming the similarity-transformed Hamiltonian \bar{H} used in the standard CC theory,

$$\bar{H} = e^{-T} H e^T = (H e^T)_C, \quad (3)$$

where H is the Hamiltonian and C stands for the connected part of the corresponding operator expression, with the exponential operator $e^{-\Sigma^\dagger}$. T is the usual cluster operator, which is a particle–hole excitation operator generating the connected components of the

many-electron ground-state wave function

$$|\Psi_0\rangle = e^T |\Phi\rangle, \quad (4)$$

and Σ^\dagger is the auxiliary hole-particle deexcitation operator. In the exact theory, T is a sum of all many-body components T_n with $n = 1, \dots, N$,

$$T = \sum_{n=1}^N T_n, \quad (5)$$

where N is the number of electrons and T_n is defined as

$$T_n = \sum_{i_1 < \dots < i_n, a_1 < \dots < a_n} t_{a_1 \dots a_n}^{i_1 \dots i_n} E_{i_1 \dots i_n}^{a_1 \dots a_n}, \quad (6)$$

with

$$E_{i_1 \dots i_n}^{a_1 \dots a_n} = \prod_{\kappa=1}^n c^{a_\kappa} c_{i_\kappa} \quad (7)$$

representing the excitation operators and $t_{a_1 \dots a_n}^{i_1 \dots i_n}$ designating the corresponding cluster amplitudes. We use a notation in which c^p (c_p) are the usual creation (annihilation) operators ($c^p = c_p^\dagger$) associated with a given orthonormal spin-orbital basis set $\{p\}$. Letters i_1, \dots, i_n represent the occupied spin-orbitals in $|\Phi\rangle$ and a_1, \dots, a_n designate the unoccupied spin-orbitals. The auxiliary operator Σ^\dagger is defined as

$$\Sigma^\dagger = \sum_{n=1}^N \Sigma_n^\dagger, \quad (8)$$

where

$$\Sigma_n^\dagger = \sum_{i_1 < \dots < i_n, a_1 < \dots < a_n} \sigma_{i_1 \dots i_n}^{a_1 \dots a_n} E_{a_1 \dots a_n}^{i_1 \dots i_n}. \quad (9)$$

The operators

$$E_{a_1 \dots a_n}^{i_1 \dots i_n} = \prod_{\kappa=1}^n c^{i_\kappa} c_{a_\kappa} \quad (10)$$

and the coefficients $\sigma_{i_1 \dots i_n}^{a_1 \dots a_n}$ are the corresponding deexcitation operators and amplitudes, respectively.

The operators T and Σ^\dagger (or the corresponding amplitudes $t_{a_1 \dots a_n}^{i_1 \dots i_n}$ and $\sigma_{i_1 \dots i_n}^{a_1 \dots a_n}$) defining the wave function $|\Psi_0\rangle$ through equation (4) and the energy $E_0^{(\text{ECC})}$ through equation (1) can be determined in various ways. For example, in the simple variant of the ECC theory proposed by Piecuch and Bartlett [60], which can be applied to both ground and excited states, the T and Σ^\dagger operators are determined by considering the doubly transformed form of the electronic Schrödinger equation, *i.e.*,

$$\bar{\bar{H}}|\Phi\rangle = E_0|\Phi\rangle, \quad (11)$$

and its left-hand analog,

$$\langle \tilde{\Phi} | \bar{\bar{H}} = E_0 \langle \tilde{\Phi} |, \quad (12)$$

where $\langle \tilde{\Phi} |$ is the left eigenstate of $\bar{\bar{H}}$ corresponding to the right reference eigenstate $|\Phi\rangle$. We obtain equation (11) by inserting the formula for the CC wave function, equation (4), into the Schrödinger equation,

$$H|\Psi_0\rangle = E_0|\Psi_0\rangle, \quad (13)$$

and by premultiplying the resulting equation by $e^{\Sigma^\dagger} e^{-T}$, while utilizing the fact that $|\Psi_0\rangle = e^T |\Phi\rangle = e^T e^{-\Sigma^\dagger} |\Phi\rangle$ (Σ^\dagger is a deexcitation operator, so that $(\Sigma^\dagger)^k |\Phi\rangle = 0$ for $k > 0$). In general, the $\langle \tilde{\Phi} |$ dual state entering equation (12) depends on the values of T and Σ^\dagger defining $\bar{\bar{H}}$. In the ECC theory of Piecuch and Bartlett, we simply require that T and Σ^\dagger are such that $\langle \tilde{\Phi} | = \langle \Phi |$. Thus, the final system of equations used to determine the two different cluster operators T and Σ^\dagger consists of equation (11) and

$$\langle \Phi | \bar{\bar{H}} = \langle \Phi | E_0, \quad (14)$$

which is the left-hand counterpart of equation (11). It is worth mentioning that equation (14) can also be obtained by considering the bra counterpart of the connected cluster form of the electronic Schrödinger equation,

$$\bar{H}|\Phi\rangle = E_0|\Phi\rangle, \quad (15)$$

where \bar{H} is defined by equation (3), *i.e.*,

$$\langle \Phi | (1 + \Lambda) \bar{H} = E_0 \langle \Phi | (1 + \Lambda), \quad (16)$$

where Λ is the well-known “lambda” deexcitation operator of the analytic gradient CC theory of Bartlett and co-workers [61,62], and by identifying the left-hand ground eigenstate of \bar{H} , $\langle \Phi | (1 + \Lambda)$, with $\langle \Phi | e^{\Sigma^\dagger}$. An alternative reasoning that leads to equation (14) is based on considering the adjoint form of the electronic Schrödinger equation, *i.e.*,

$$\langle \tilde{\Psi}_0 | H = E_0 \langle \tilde{\Psi}_0 |, \quad (17)$$

where the dual state $\langle \tilde{\Psi}_0 |$, satisfying the condition $\langle \tilde{\Psi}_0 | \Psi_0 \rangle = 1$, is the CC bra ground state [60,63,64],

$$\langle \tilde{\Psi}_0 | = \langle \Phi | (1 + \Lambda) e^{-T}. \quad (18)$$

Clearly, in the exact, full CI or full CC, limit, there exists a deexcitation operator Σ^\dagger , such that $(1 + \Lambda) = e^{\Sigma^\dagger}$, so that one can always give the dual CC state $\langle \tilde{\Psi}_0 |$ a completely bi-exponential form,

$$\langle \tilde{\Psi}_0 | = \langle \Phi | e^{\Sigma^\dagger} e^{-T}. \quad (19)$$

By inserting equation (19) into equation (17) and by multiplying the resulting equation on the right by $e^T e^{-\Sigma^\dagger}$, we obtain the desired equation (14).

In the original work by Arponen and Bishop [50–59], the operators T and Σ^\dagger of the ECC formalism are determined by imposing the stationary conditions on the energy functional $E_0^{(\text{ECC})}$, equation (1), with respect to operators T and Σ^\dagger ,

$$\frac{\delta E_0^{(\text{ECC})}}{\delta T} = 0, \quad \frac{\delta E_0^{(\text{ECC})}}{\delta \Sigma^\dagger} = 0. \quad (20)$$

The bi-variational character of the ECC theory of Arponen and Bishop is particularly useful in calculations of molecular properties other than energy, since one can apply the Hellmann–Feynmann theorem in such calculations [65–73]. The question addressed in this paper is how the bi-variational ECC theory of Arponen and Bishop and the ECC theory of Piecuch and Bartlett, which uses equations (11) and (14) rather than equation (20) to determine T and Σ^\dagger , work when molecular PESs along bond breaking coordinates and cases of severe quasi-degeneracy are examined.

2.2. Extended coupled-cluster methods with singles and doubles

The approximate ECC methods, such as the ECCSD approaches examined in this paper and developed in Refs. [74–77], are obtained as follows: First, as in all standard CC approximations, we truncate the many-body expansions of T and Σ^\dagger , equations (5) and (8), respectively, at some excitation level $m_A < N$, so that T is replaced by $T^{(A)}$,

$$T^{(A)} = \sum_{n=1}^{m_A} T_n, \quad (21)$$

and Σ^\dagger is replaced by

$$(\Sigma^{(A)})^\dagger = \sum_{n=1}^{m_A} \Sigma_n^\dagger. \quad (22)$$

Next, we use either the Piecuch–Bartlett approach (equations (11) and (14)) or the Arponen–Bishop approach (equation (20)) to obtain a system of equations for the unknown cluster amplitudes $t_{a_1 \dots a_n}^{i_1 \dots i_n}$ and $\sigma_{i_1 \dots i_n}^{a_1 \dots a_n}$, $n = 1, \dots, m_A$. Once $t_{a_1 \dots a_n}^{i_1 \dots i_n}$ and $\sigma_{i_1 \dots i_n}^{a_1 \dots a_n}$ are determined, we use the approximate form of the energy functional (1),

$$E_0^{(A)} = \langle \Phi | \bar{H}^{(A)} | \Phi \rangle, \quad (23)$$

where

$$\bar{H}^{(A)} = e^{(\Sigma^{(A)})^\dagger} (e^{-T^{(A)}} H e^{T^{(A)}}) e^{-(\Sigma^{(A)})^\dagger}, \quad (24)$$

to calculate the ground-state energy.

In the specific case of the ECCSD approach, T is approximated by the sum of one- and two-body components, T_1 and T_2 , respectively,

$$T \approx T^{(\text{ECCSD})} = T_1 + T_2, \quad (25)$$

where

$$T_1 = \sum_{i,a} t_a^i E_i^a \quad (26)$$

and

$$T_2 = \sum_{i < j, a < b} t_{ab}^{ij} E_{ij}^{ab}, \quad (27)$$

with

$$E_i^a = c^a c_i \quad (28)$$

and

$$E_{ij}^{ab} = c^a c_i c^b c_j \quad (29)$$

representing the elementary single and double excitation operators, and t_a^i and t_{ab}^{ij} designating the corresponding singly and doubly excited cluster amplitudes. A similar truncation scheme is applied to operator Σ^\dagger , *i.e.*,

$$\Sigma^\dagger \approx (\Sigma^{\text{(ECCSD)}})^\dagger = \Sigma_1^\dagger + \Sigma_2^\dagger, \quad (30)$$

where

$$\Sigma_1^\dagger = \sum_{i,a} \sigma_i^a E_a^i \quad (31)$$

and

$$\Sigma_2^\dagger = \sum_{i < j, a < b} \sigma_{ij}^{ab} E_{ab}^{ij}, \quad (32)$$

with E_a^i and E_{ab}^{ij} designating the one- and two-body elementary deexcitation operators, $E_a^i = (E_i^a)^\dagger$ and $E_{ab}^{ij} = (E_{ij}^{ab})^\dagger$, respectively, and σ_i^a and σ_{ij}^{ab} representing the corresponding deexcitation amplitudes.

2.2.1. The Piecuch–Bartlett ECCSD approach

In the ECCSD method of Piecuch and Bartlett [60], we obtain the equations for the cluster amplitudes t_a^i , t_{ab}^{ij} , σ_i^a , and σ_{ij}^{ab} , defining T_1 , T_2 , Σ_1^\dagger , and Σ_2^\dagger , respectively, by left- and right-projecting equations (11) and (14), where T is given by equation (25) and Σ^\dagger is given by equation (30), on the singly and doubly excited determinants $|\Phi_i^a\rangle = E_i^a|\Phi\rangle$ and $|\Phi_{ij}^{ab}\rangle = E_{ij}^{ab}|\Phi\rangle$. We obtain

$$\langle \Phi_i^a | \bar{H}^{\text{(ECCSD)}} | \Phi \rangle = 0, \quad (33)$$

$$\langle \Phi_{ij}^{ab} | \bar{H}^{\text{(ECCSD)}} | \Phi \rangle = 0, \quad i < j, a < b, \quad (34)$$

$$\langle \Phi | \bar{H}^{\text{(ECCSD)}} | \Phi_i^a \rangle = 0, \quad (35)$$

$$\langle \Phi | \bar{H}^{\text{(ECCSD)}} | \Phi_{ij}^{ab} \rangle = 0, \quad i < j, a < b, \quad (36)$$

where

$$\bar{H}^{\text{(ECCSD)}} = e^{\Sigma_1^\dagger + \Sigma_2^\dagger} (e^{-T_1 - T_2} H e^{T_1 + T_2}) e^{-\Sigma_1^\dagger - \Sigma_2^\dagger} = e^{\Sigma_1^\dagger + \Sigma_2^\dagger} \bar{H}^{\text{(CCSD)}} e^{-\Sigma_1^\dagger - \Sigma_2^\dagger} \quad (37)$$

is the doubly transformed Hamiltonian of the ECCSD method, with

$$\bar{H}^{\text{(CCSD)}} = e^{-T_1 - T_2} H e^{T_1 + T_2} = (H e^{T_1 + T_2})_C \quad (38)$$

representing the similarity transformed Hamiltonian of the CCSD approximation. Once equations (33)–(36) are solved for operators T_1 , T_2 , Σ_1^\dagger , and Σ_2^\dagger , the ground-state energy

$E_0^{(\text{ECCSD})}$ is calculated as follows:

$$\begin{aligned} E_0^{(\text{ECCSD})} &= \langle \Phi | \bar{\bar{H}}^{(\text{ECCSD})} | \Phi \rangle \\ &= \langle \Phi | e^{\Sigma_1^\dagger + \Sigma_2^\dagger} (e^{-T_1 - T_2} H e^{T_1 + T_2}) e^{-\Sigma_1^\dagger - \Sigma_2^\dagger} | \Phi \rangle \\ &= \langle \Phi | e^{\Sigma_1^\dagger + \Sigma_2^\dagger} (e^{-T_1 - T_2} H e^{T_1 + T_2}) | \Phi \rangle, \end{aligned} \quad (39)$$

where we used the fact that $e^{-\Sigma^\dagger} |\Phi\rangle = |\Phi\rangle$.

Since the full ECCSD formalism defined by equations (33)–(39) is rather complex, in this paper, in addition to the full ECCSD method, we consider the sequence of the linear (LECCSD), bi-linear (BECCSD), and quadratic (QECCSD) approaches, which represent approximations to full ECCSD. The LECCSD, BECCSD, and QECCSD methods are obtained by replacing the doubly transformed Hamiltonian $\bar{\bar{H}}^{(\text{ECCSD})}$, equation (37), in equations (33)–(36) and (39) by

$$\bar{\bar{H}}^{(\text{LECCSD})} = (1 + \Sigma_1^\dagger + \Sigma_2^\dagger) \bar{H}^{(\text{CCSD})} (1 - \Sigma_1^\dagger - \Sigma_2^\dagger), \quad (40)$$

in the LECCSD case,

$$\begin{aligned} \bar{\bar{H}}^{(\text{BECCSD})} &= (1 + \Sigma_1^\dagger + \Sigma_2^\dagger) \bar{H}^{(\text{CCSD})} (1 - \Sigma_1^\dagger - \Sigma_2^\dagger) \\ &\quad + \frac{1}{2} (\Sigma_1^\dagger + \Sigma_2^\dagger)^2 \bar{H}^{(\text{CCSD})} + \frac{1}{2} \bar{H}^{(\text{CCSD})} (\Sigma_1^\dagger + \Sigma_2^\dagger)^2, \end{aligned} \quad (41)$$

in the BECCSD case, and

$$\begin{aligned} \bar{\bar{H}}^{(\text{QECCSD})} &= \left[1 + \Sigma_1^\dagger + \Sigma_2^\dagger + \frac{1}{2} (\Sigma_1^\dagger + \Sigma_2^\dagger)^2 \right] \bar{H}^{(\text{CCSD})} \\ &\quad \times \left[1 - \Sigma_1^\dagger - \Sigma_2^\dagger + \frac{1}{2} (\Sigma_1^\dagger + \Sigma_2^\dagger)^2 \right], \end{aligned} \quad (42)$$

in the QECCSD case.

2.2.2. The Arponen–Bishop ECCSD approach

In the case of the bi-variational ECCSD method of Arponen and Bishop [50–59], we obtain the system of equations for the singly and doubly excited cluster amplitudes t_a^i and t_{ab}^{ij} defining T_1 and T_2 and the deexcitation amplitudes σ_i^a and σ_{ij}^{ab} defining Σ_1^\dagger and Σ_2^\dagger from the stationary condition represented by equation (20). The resulting equations can be given the following form:

$$\frac{\partial E_0^{(\text{ECCSD})}}{\partial \sigma_i^a} = \langle \Phi_i^a | e^{\Sigma_1^\dagger + \Sigma_2^\dagger} \bar{H}^{(\text{CCSD})} | \Phi \rangle = 0, \quad (43)$$

$$\frac{\partial E_0^{(\text{ECCSD})}}{\partial \sigma_{ij}^{ab}} = \langle \Phi_{ij}^{ab} | e^{\Sigma_1^\dagger + \Sigma_2^\dagger} \bar{H}^{(\text{CCSD})} | \Phi \rangle = 0, \quad i < j, a < b, \quad (44)$$

$$\begin{aligned} \frac{\partial E_0^{(\text{ECCSD})}}{\partial t_a^i} &= \langle \Phi | e^{\Sigma_1^\dagger + \Sigma_2^\dagger} [\bar{H}^{(\text{CCSD})}, E_i^a] | \Phi \rangle \\ &= \langle \Phi | e^{\Sigma_1^\dagger + \Sigma_2^\dagger} (\bar{H}^{(\text{CCSD})} E_i^a)_C | \Phi \rangle = 0, \end{aligned} \quad (45)$$

$$\begin{aligned}
\frac{\partial E_0^{(\text{ECCSD})}}{\partial t_{ab}^{ij}} &= \langle \Phi | e^{\Sigma_1^\dagger + \Sigma_2^\dagger} [\bar{H}^{(\text{CCSD})}, E_{ij}^{ab}] | \Phi \rangle \\
&= \langle \Phi | e^{\Sigma_1^\dagger + \Sigma_2^\dagger} (\bar{H}^{(\text{CCSD})} E_{ij}^{ab})_C | \Phi \rangle = 0, \quad i < j, a < b,
\end{aligned} \tag{46}$$

where $E_0^{(\text{ECCSD})}$ is the ECCSD energy functional, equation (39), and $\bar{H}^{(\text{CCSD})}$ is the similarity-transformed Hamiltonian defined by equation (38).

It can be shown that the full ECCSD method, defined by equations (43)–(46), leads to computational steps that scale as \mathcal{N}^{10} with the system size. This is a lot more than the \mathcal{N}^6 steps of the standard CCSD approach. In order to reduce the computer costs of the full ECCSD calculations, we must truncate the power series expansion for $e^{\Sigma_1^\dagger + \Sigma_2^\dagger}$ in the ECCSD energy functional $E_0^{(\text{ECCSD})}$, equation (39), at the low power of $(\Sigma_1^\dagger + \Sigma_2^\dagger)$. The simplest approximation of this type that one might suggest is the linearized ECCSD (LECCSD) formalism, in which we replace the energy functional $E_0^{(\text{ECCSD})}$, equation (39), by the expression linear in Σ_1^\dagger and Σ_2^\dagger ,

$$\begin{aligned}
E_0^{(\text{LECCSD})} &= \langle \Phi | (1 + \Sigma_1^\dagger + \Sigma_2^\dagger) \bar{H}^{(\text{CCSD})} | \Phi \rangle \\
&= \langle \Phi | \bar{H}^{(\text{CCSD})} | \Phi \rangle + \langle \Phi | \Sigma_1^\dagger \bar{H}^{(\text{CCSD})} | \Phi \rangle + \langle \Phi | \Sigma_2^\dagger \bar{H}^{(\text{CCSD})} | \Phi \rangle \\
&= \langle \Phi | \bar{H}^{(\text{CCSD})} | \Phi \rangle + \sum_{i,a} \sigma_i^a \langle \Phi_i^a | \bar{H}^{(\text{CCSD})} | \Phi \rangle \\
&\quad + \sum_{i < j, a < b} \sigma_{ij}^{ab} \langle \Phi_{ij}^{ab} | \bar{H}^{(\text{CCSD})} | \Phi \rangle.
\end{aligned} \tag{47}$$

The most expensive steps of the LECCSD method, as defined by equation (47), scale as $n_o^2 n_u^4$ (or \mathcal{N}^6 with the system size), but, unfortunately, the LECCSD method based on the Arponen–Bishop theory does not improve the CCSD results at all, since once we impose the stationary conditions on the energy functional $E_0^{(\text{LECCSD})}$, equation (47), with respect to operators T_1 , T_2 , Σ_1^\dagger , and Σ_2^\dagger , we obtain the following equations:

$$\frac{\partial E_0^{(\text{LECCSD})}}{\partial \sigma_i^a} = \langle \Phi_i^a | \bar{H}^{(\text{CCSD})} | \Phi \rangle = 0, \tag{48}$$

$$\frac{\partial E_0^{(\text{LECCSD})}}{\partial \sigma_{ij}^{ab}} = \langle \Phi_{ij}^{ab} | \bar{H}^{(\text{CCSD})} | \Phi \rangle = 0, \quad i < j, a < b, \tag{49}$$

which are the usual CCSD equations for T_1 and T_2 , and

$$\frac{\partial E_0^{(\text{LECCSD})}}{\partial t_a^i} = \langle \Phi | (1 + \Sigma_1^\dagger + \Sigma_2^\dagger) (\bar{H}^{(\text{CCSD})} E_i^a)_C | \Phi \rangle = 0, \tag{50}$$

$$\frac{\partial E_0^{(\text{LECCSD})}}{\partial t_{ab}^{ij}} = \langle \Phi | (1 + \Sigma_1^\dagger + \Sigma_2^\dagger) (\bar{H}^{(\text{CCSD})} E_{ij}^{ab})_C | \Phi \rangle = 0, \quad i < j, a < b, \tag{51}$$

which are the Σ^\dagger equations that are completely decoupled from the CCSD system, equations (48) and (49), and solved only after the T_1 and T_2 cluster are determined. In other words, the LECCSD approximation does not provide for the coupling between the

T and Σ^\dagger equations, which is essential for improving the quality of T_1 and T_2 clusters in the bond breaking region.

The above analysis indicates that in order to obtain the T_1 and T_2 clusters, which are better than those provided by the LECCSD = CCSD approximation, we must introduce non-linear terms in Σ_1^\dagger and Σ_2^\dagger into the LECCSD energy functional that couple the T and Σ^\dagger equations. The lowest-order approximation of this type is obtained by truncating the ECCSD energy functional, equation (39), at terms quadratic in $(\Sigma_1^\dagger + \Sigma_2^\dagger)$. We call it the QECCSD approximation. The formula for the QECCSD energy functional used in the Arponen–Bishop version of the QECCSD theory is

$$\begin{aligned}
 E_0^{(\text{QECCSD})} &= \langle \Phi | \left[1 + (\Sigma_1^\dagger + \Sigma_2^\dagger) + \frac{1}{2}(\Sigma_1^\dagger + \Sigma_2^\dagger)^2 \right] \bar{H}^{(\text{CCSD})} | \Phi \rangle \\
 &= \langle \Phi | \bar{H}^{(\text{CCSD})} | \Phi \rangle + \langle \Phi | \Sigma_1^\dagger \bar{H}^{(\text{CCSD})} | \Phi \rangle \\
 &\quad + \langle \Phi | \left[\Sigma_2^\dagger + \frac{1}{2}(\Sigma_1^\dagger)^2 \right] \bar{H}^{(\text{CCSD})} | \Phi \rangle \\
 &\quad + \langle \Phi | \Sigma_1^\dagger \Sigma_2^\dagger \bar{H}^{(\text{CCSD})} | \Phi \rangle + \frac{1}{2} \langle \Phi | (\Sigma_2^\dagger)^2 \bar{H}^{(\text{CCSD})} | \Phi \rangle
 \end{aligned} \tag{52}$$

or, somewhat more explicitly,

$$\begin{aligned}
 E_0^{(\text{QECCSD})} &= \langle \Phi | \bar{H}^{(\text{CCSD})} | \Phi \rangle + \sum_{i,a} \sigma_i^a \langle \Phi_i^a | \bar{H}^{(\text{CCSD})} | \Phi \rangle \\
 &\quad + \sum_{i < j, a < b} (\sigma_{ij}^{ab} + \mathcal{A}_{ij} \sigma_i^a \sigma_j^b) \langle \Phi_{ij}^{ab} | \bar{H}^{(\text{CCSD})} | \Phi \rangle \\
 &\quad + \sum_{i < j < k, a < b < c} \mathcal{A}_{i/jk} \mathcal{A}_{a/bc} \sigma_i^a \sigma_{jk}^{bc} \langle \Phi_{ijk}^{abc} | \bar{H}^{(\text{CCSD})} | \Phi \rangle \\
 &\quad + \sum_{i < j < k < l, a < b < c < d} \mathcal{A}_{ij/kl} \mathcal{A}_{b/cd} \sigma_{ij}^{ab} \sigma_{kl}^{cd} \langle \Phi_{ijkl}^{abcd} | \bar{H}^{(\text{CCSD})} | \Phi \rangle,
 \end{aligned} \tag{53}$$

where $\mathcal{A}_{ij} = 1 - (ij)$, $\mathcal{A}_{i/jk} = 1 - (ij) - (ik)$, $\mathcal{A}_{a/bc} = 1 - (ab) - (ac)$, and $\mathcal{A}_{ij/kl} = 1 - (ik) - (il) - (jk) - (jl) + (ik)(jl)$ are the suitable index antisymmetrizers ((ij) and (ab) are index interchanges). The stationary conditions of the type of equations (43)–(46), written for the QECCSD energy functional $E_0^{(\text{QECCSD})}$, equation (52) or (53), are

$$\begin{aligned}
 \frac{\partial E_0^{(\text{QECCSD})}}{\partial \sigma_i^a} &= \langle \Phi_i^a | \bar{H}^{(\text{CCSD})} | \Phi \rangle + \sum_{j,b} \sigma_j^b \langle \Phi_{ij}^{ab} | \bar{H}^{(\text{CCSD})} | \Phi \rangle \\
 &\quad + \sum_{j < k, b < c} \sigma_{jk}^{bc} \langle \Phi_{ijk}^{abc} | \bar{H}^{(\text{CCSD})} | \Phi \rangle \\
 &= 0,
 \end{aligned} \tag{54}$$

$$\begin{aligned}
 \frac{\partial E_0^{(\text{QECCSD})}}{\partial \sigma_{ij}^{ab}} &= \langle \Phi_{ij}^{ab} | \bar{H}^{(\text{CCSD})} | \Phi \rangle + \sum_{k,c} \sigma_k^c \langle \Phi_{ijk}^{abc} | \bar{H}^{(\text{CCSD})} | \Phi \rangle \\
 &\quad + \sum_{k < l, c < d} \sigma_{kl}^{cd} \langle \Phi_{ijkl}^{abcd} | \bar{H}^{(\text{CCSD})} | \Phi \rangle \\
 &= 0,
 \end{aligned} \tag{55}$$

$$\begin{aligned}
\frac{\partial E_0^{(\text{QECCSD})}}{\partial t_a^i} &= \langle \Phi | \left[1 + (\Sigma_1^\dagger + \Sigma_2^\dagger) + \frac{1}{2}(\Sigma_1^\dagger + \Sigma_2^\dagger)^2 \right] (\bar{H}^{(\text{CCSD})} E_i^a)_C | \Phi \rangle \\
&= \langle \Phi | (\bar{H}^{(\text{CCSD})} E_i^a)_C | \Phi \rangle + \sum_{j,b} \sigma_j^b \langle \Phi_j^b | (\bar{H}^{(\text{CCSD})} E_i^a)_C | \Phi \rangle \\
&\quad + \sum_{j < k, b < c} (\sigma_{jk}^{bc} + \mathcal{A}_{jk} \sigma_j^b \sigma_k^c) \langle \Phi_{jk}^{bc} | (\bar{H}^{(\text{CCSD})} E_i^a)_C | \Phi \rangle \\
&\quad + \sum_{j < k < l, b < c < d} \mathcal{A}_{j/kl} \mathcal{A}_{b/cd} \sigma_j^b \sigma_{kl}^{cd} \langle \Phi_{jkl}^{bcd} | (\bar{H}^{(\text{CCSD})} E_i^a)_C | \Phi \rangle \\
&\quad + \sum_{j < k < l < m, b < c < d < e} \mathcal{A}_{jk/lm} \mathcal{A}_{c/de} \sigma_{jk}^{bc} \sigma_{lm}^{de} \langle \Phi_{jklm}^{bcde} | (\bar{H}^{(\text{CCSD})} E_i^a)_C | \Phi \rangle \\
&= 0,
\end{aligned} \tag{56}$$

$$\begin{aligned}
\frac{\partial E_0^{(\text{QECCSD})}}{\partial t_{ab}^{ij}} &= \langle \Phi | \left[1 + (\Sigma_1^\dagger + \Sigma_2^\dagger) + \frac{1}{2}(\Sigma_1^\dagger + \Sigma_2^\dagger)^2 \right] (\bar{H}^{(\text{CCSD})} E_{ij}^{ab})_C | \Phi \rangle \\
&= \langle \Phi | (\bar{H}^{(\text{CCSD})} E_{ij}^{ab})_C | \Phi \rangle + \sum_{k,c} \sigma_k^c \langle \Phi_k^c | (\bar{H}^{(\text{CCSD})} E_{ij}^{ab})_C | \Phi \rangle \\
&\quad + \sum_{k < l, c < d} (\sigma_{kl}^{cd} + \mathcal{A}_{kl} \sigma_k^c \sigma_l^d) \langle \Phi_{kl}^{cd} | (\bar{H}^{(\text{CCSD})} E_{ij}^{ab})_C | \Phi \rangle \\
&\quad + \sum_{k < l < m, c < d < e} \mathcal{A}_{k/lm} \mathcal{A}_{c/de} \sigma_k^c \sigma_{lm}^{de} \langle \Phi_{klm}^{cde} | (\bar{H}^{(\text{CCSD})} E_{ij}^{ab})_C | \Phi \rangle \\
&\quad + \sum_{k < l < m < n, c < d < e < f} \mathcal{A}_{kl/mn} \mathcal{A}_{d/ef} \sigma_{kl}^{cd} \sigma_{mn}^{ef} \\
&\quad \times \langle \Phi_{klmn}^{cdef} | (\bar{H}^{(\text{CCSD})} E_{ij}^{ab})_C | \Phi \rangle \\
&= 0.
\end{aligned} \tag{57}$$

As one can see, the QECCSD equations for the t_a^i and t_{ab}^{ij} amplitudes, equations (54) and (55), respectively, are strongly and nontrivially coupled with the equations for the σ_i^a and σ_{ij}^{ab} amplitudes, equations (56) and (57), respectively, so that unlike in the standard CCSD approach, the T_1 and T_2 clusters are no longer calculated independent of the Σ_1^\dagger and Σ_2^\dagger clusters. A similarly strong coupling is present in the QECCSD, BECCSD, and ECCSD methods based on the Piecuch–Bartlett ECC theory described in Section 2.2.1. As shown below, the non-trivial coupling between T and Σ^\dagger equations has a positive effect on improving the quality of the T_1 and T_2 clusters resulting from the QECCSD and similar calculations. At the same time, the most expensive steps of the QECCSD approach based on equations (54)–(57) scale as n_u^6 (\mathcal{N}^6 with the system size). Similar remarks apply to the QECCSD and BECCSD methods based on the Piecuch–Bartlett approach discussed in Section 2.2.1.

2.3. Numerical results for multiple bond breaking

2.3.1. The Piecuch–Bartlett ECCSD approach

In this subsection, we discuss the results of the full and approximate ECCSD calculations for the minimum basis set (MBS) S4 model [78–80] and the STO-3G [81] model of N_2 employing the ECC theory of Piecuch and Bartlett. All ECCSD, LECCSD, BECCSD, and QECCSD calculations described here were performed using the pilot computer codes, in which the relevant cluster amplitudes t_a^i , t_{ab}^{ij} , σ_i^a , and σ_{ij}^{ab} are determined by minimizing the sum of the squares of the equations constituting the ECCSD system, equations (33)–(36), with the downhill simplex method [82]. This algorithm is based on an obvious fact that the global minimum being sought is zero. For smaller values of the parameter α describing the S4 model ($\alpha \approx 2.0$ bohr) and in the vicinity of the equilibrium geometry of N_2 (the N–N separation $R \approx 2.0$ bohr), where the standard CCSD approach provides a reasonable description of the ground-state wave function, the initial guesses for cluster amplitudes t_a^i , t_{ab}^{ij} , σ_i^a , and σ_{ij}^{ab} were obtained by using the CCSD values for t_a^i and t_{ab}^{ij} and by assuming that the initial values of σ_i^a and σ_{ij}^{ab} satisfy the conditions $\sigma_i^a = t_a^i$ and $\sigma_{ij}^{ab} = t_{ab}^{ij}$ (one can show that the first-order MBPT estimates of the cluster operator T and the auxiliary operator Σ are identical; *cf.*, *e.g.*, Refs. [83,84]). For larger values of α and R , where T and Σ significantly differ, we used the previously converged t_a^i , t_{ab}^{ij} , σ_i^a , and σ_{ij}^{ab} amplitudes, obtained for smaller values of α and R , to initiate the numerical procedures used to determine T and Σ .

We begin the discussion of our ECCSD test calculations with the MBS S4 model, which consists of four hydrogen atoms arranged in a square configuration, described by a small basis set consisting of only one s orbital centered on each hydrogen atom [78–80]. The geometry of the S4 model is determined by a single parameter α , which is defined as a distance between the nearest-neighbor hydrogen atoms. The small number of electrons and the fact that the molecular orbital basis set consists in this case of only four orbitals that are fully determined by the high spatial symmetry of the S4 model cause that there are only eight spin- and symmetry-adapted configuration state functions (CSFs) that are relevant to the ground-state full CI problem. In addition to the RHF determinant, which we use as a reference, we only need six doubly excited CSFs and one quadruply excited CSF to describe the exact, full CI, ground state of the MBS S4 model. There are no single and triple excitations in the full CI expansion of the ground-state wave function, so that $T_1 = T_3 = 0$ and the CCD (CC doubles), CCSD, and CCSDT approximations become completely equivalent. Similarly, the one- and three-body components of the deexcitation operator Σ^\dagger vanish, so that the ECCD and ECCSD methods give identical results. Because of the presence of only four electrons in the MBS S4 model, there is no difference between the BECCSD = BECCD, QECCSD = QECCD, and full ECCSD = ECCD approximations in this case. Thus, we only report the results of the full ECCD calculations, which we compare with the standard CCD and exact full CI results.

The MBS S4 configurations with larger values of α create a serious challenge for the standard single-reference CC methods (even the powerful genuine MRCC approaches may have a difficulty in describing the region of larger α values [78,80]). This is related to the fact that larger α values correspond to a dissociation of the S4 model into four hydrogen atoms. This process is very difficult to describe by the RHF-based single-reference methods, particularly in the region of the intermediate α values where the ground-state wave

Table 1. Ground-state energies of the MBS S4 model system as functions of the parameter α^a

α	Full CI	CCD ^b	ECCD ^c	$\langle \text{CCD} \rangle^d$	$\langle \text{ECCD} \rangle^d$
0.5	3.952114	−0.093	0.015	0.032	0.015
1.0	−0.668783	−0.424	0.110	0.236	0.110
1.5	−1.694327	−1.235	0.376	0.862	0.376
2.0	−1.975862	−2.834	0.871	2.188	0.871
2.5	−2.043797	−5.674	1.609	4.447	1.609
3.0	−2.044850	−9.568	2.373	6.895	2.373
3.5	−2.028186	−13.083	2.754	7.698	2.754
4.0	−2.011713	−14.385	2.496	6.218	2.496
4.5	−2.000438	−13.094	1.812	3.896	1.812
5.0	−1.994021	−10.292	1.107	2.054	1.107
6.0	−1.989199	−4.748	0.297	0.431	0.296
7.0	−1.988164	−1.743	0.062	0.076	0.061

^a The full CI total energies are in hartree. The CCD and ECCD energies are in millihartree relative to the corresponding full CI energy values. The parameter α is in bohr.

^b For the MBS S4 model, CCD = CCSD.

^c The ECCD method of Piecuch and Bartlett. For the MBS S4 model, ECCD = ECCSD = BECCSD = QECCSD.

^d $\langle X \rangle$ ($X = \text{CCD}, \text{ECCD}$) is the expectation value of the Hamiltonian with the normalized $e^{T_2}|\Phi\rangle$ wave function, where T_2 is obtained with method X (see equation (58)).

function of the S4 system undergoes a significant rearrangement of its structure. As shown in Table 1 and Fig. 1, the CCD = CCSD approximation breaks down at larger values of α . For $\alpha \leq 2.0$ bohr, the unsigned errors in the CCD results, relative to full CI, do not exceed 2.834 millihartree. However, for $3.5 \text{ bohr} \leq \alpha \leq 4.5 \text{ bohr}$, the unsigned errors in the CCD results increase to 13–14 millihartree and the CCD potential energy curve corresponding to the dissociation of the S4 model into four hydrogen atoms goes significantly below the exact, full CI, potential curve (see Fig. 1). For $\alpha \leq 2.0$ bohr, the ground-state wave function of the MBS S4 model is dominated by two CSFs: the RHF determinant and the doubly excited determinant corresponding to the HOMO \rightarrow LUMO bi-excitation [78–80]. For larger values of α , essentially all electron configurations present in the full CI expansion become very important, creating a strongly quasi-degenerate situation, and the role of the T_4 cluster component becomes significant in the intermediate $2.5 \text{ bohr} \leq \alpha \leq 6.0 \text{ bohr}$ region. This leads to the failure of the CCD approximation observed in Table 1 and Fig. 1.

The results in Table 1 and Fig. 1 show that the ECCD theory provides substantial improvements in the poor description of the dissociation of the S4 model into four hydrogen atoms by the CCD method. The 13–14 millihartree unsigned errors in the CCD energies in the $3.5 \text{ bohr} \leq \alpha \leq 4.5 \text{ bohr}$ region reduce to 2–3 millihartree, when the ECCD approach is employed. The considerable reduction of errors in the CCD results is observed at all values of α , even in the $\alpha \leq 2.0$ bohr region, where the maximum unsigned error in the ECCD results is 0.871 millihartree, as opposed to 2.834 millihartree obtained with the CCD approach (see Table 1). Unlike the CCD potential energy curve shown in Fig. 1, which is located significantly below the full CI curve, the ECCD potential energy curve

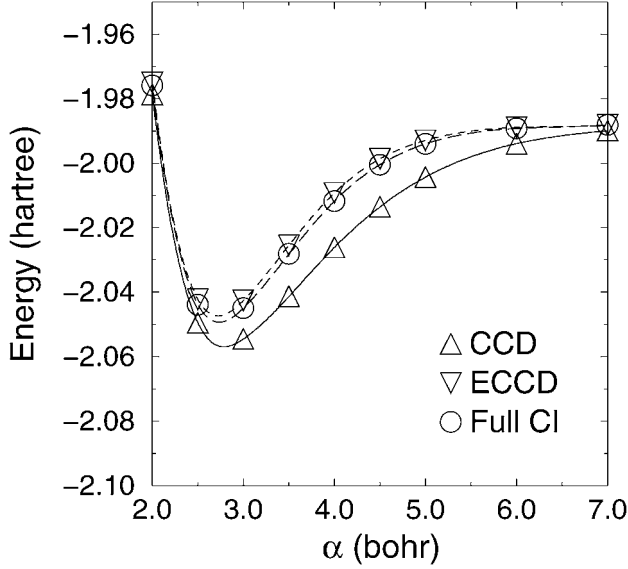


Fig. 1. Potential energy curves for the MBS S4 system. ECCD represents the Piecuch–Bartlett variant of the ECCD approach (in this case, the ECCD and ECCSD approaches are equivalent).

describing the dissociation of the S4 system into four H atoms is located slightly above the full CI curve. Thus, in spite of its formally non-variational character, the ECCD approach based on the ECC theory of Piecuch and Bartlett [60] provides a highly accurate and effectively variational description of the simultaneous breaking of all four H–H bonds in the S4 system.

The substantial improvement in the description of the S4 model system offered by the ECCD approach suggests that the T_2 clusters resulting from the ECCD calculations are considerably better than the CCD T_2 values. This can be seen by calculating the expectation values of the Hamiltonian, designated by $\langle X \rangle$, where $X = \text{CCD}$ or ECCD , with the normalized CCD-like wave functions

$$|\Psi_0^{(X)}\rangle = N^{(X)} e^{T_2^{(X)}} |\Phi\rangle, \quad X = \text{CCD}, \text{ECCD}, \quad (58)$$

where $T_2^{(X)}$ ($X = \text{CCD}, \text{ECCD}$) are the T_2 cluster components obtained with the CCD and ECCD methods, respectively, and $N^{(X)} = \langle \Phi | e^{(T_2^{(X)})^\dagger} e^{T_2^{(X)}} | \Phi \rangle^{-1/2}$ are the appropriate normalization factors. Clearly, the $\langle \text{CCD} \rangle$ and $\langle \text{ECCD} \rangle$ values provide the upper bounds to the exact, full CI, energies. However, as demonstrated in Table 1, the $\langle \text{CCD} \rangle$ energies remain poor in the $3.5 \text{ bohr} \leq \alpha \leq 4.5 \text{ bohr}$ region, whereas the expectation values of the Hamiltonian calculated with the ECCD wave function $|\Psi_0^{(\text{ECCD})}\rangle$, equation (58), are very close to the corresponding full CI energies.

The MBS S4 model is so simple that we can clearly understand the reasons of the excellent performance of the ECCSD = ECCD theory at larger α values. The MBS S4 system has only four electrons and the T_1 and T_3 components vanish due to the high symmetry of the Hamiltonian. Thus, in order to obtain a highly accurate description of the ground

electronic state of the MBS S4 system, we must use a method which is capable of providing an accurate description of the effects due to connected quadruply excited (T_4) cluster components, which are missing in the CCSD calculations. It turns out that at least some of the T_4 effects are brought into the ECC formalism as products of the low-order many-body components of Σ^\dagger and T . Indeed, as shown, for example, in Ref. [23], the leading, fifth-order, contribution to the energy due to T_4 clusters can be estimated by adding the $E_{\text{QQ}}^{[5]}$ term, defined as

$$E_{\text{QQ}}^{[5]} = \frac{1}{4} \langle \Phi | (T_2^\dagger)^2 (V_N T_2^2)_C | \Phi \rangle, \quad (59)$$

to

$$E_{\text{QT}}^{[5]} = \frac{1}{2} \langle \Phi | (T_2^\dagger)^2 (V_N T_3^{[2]})_C | \Phi \rangle, \quad (60)$$

where the approximate T_3 cluster operator is evaluated as

$$T_3^{[2]} = R_0^{(3)} (V_N T_2)_C. \quad (61)$$

In the above expression, $R_0^{(3)}$ designates the three-body part of the MBPT reduced resolvent and V_N represents the two-body part of the Hamiltonian in the normal-ordered form, $H_N = H - \langle \Phi | H | \Phi \rangle$. For the MBS S4 model, the $E_{\text{QT}}^{[5]}$ energy component, equation (60), vanishes, since $T_3^{[2]} = 0$. Thus, the entire fifth-order effect due to T_4 can be estimated in this case by the $E_{\text{QQ}}^{[5]}$ contribution, equation (59), which appears in the ECCD energy as the $\frac{1}{4} \langle \Phi | (\Sigma_2^\dagger)^2 (V_N T_2^2)_C | \Phi \rangle$ term, since T_2 and Σ_2 are similar when the MBPT series converges. This means that the ECCD energy for the MBS S4 model contains a great deal of information about the leading effects due to T_4 and these are sufficient to provide the excellent results at all values of the parameter α observed in Fig. 1 and Table 1.

The MBS S4 model allows us to obtain useful insights into the performance of the ECC approximations in the calculations for quasi-degenerate electronic states, but we cannot use it to test all important aspects of the ECC theory. For example, the MBS S4 system is too simple to analyze the importance of the T_1 and Σ_1^\dagger components and it does not allow us to understand the significance of terms that distinguish the LECCSD, BECCSD, QECCSD, and full ECCSD approximations defined in Section 2.2.1. Moreover, multiple bond breaking in real molecules can be sometimes considerably more complicated than the dissociation of the H_4 cluster represented by the S4 system into four hydrogen atoms. A good example of the very challenging situation, which in many respects is substantially more complex than the situation created by the S4 model, is provided by the triple bond breaking in N_2 , where the standard CCSD approach displays a colossal failure (see Table 2 and Fig. 2). We tested the ECCSD, LECCSD, BECCSD, and QECCSD methods, based on equations (33)–(42), using the minimum basis set STO-3G [81] model of N_2 . In all correlated calculations for N_2 discussed below, the lowest two core orbitals were kept frozen.

The results in Table 2 and Fig. 2 clearly demonstrate that the complete ECCSD formalism of Piecuch and Bartlett [60], in which all non-linear terms in $(\Sigma_1^\dagger + \Sigma_2^\dagger)$ and $(T_1 + T_2)$ are included, and its bi-linear and quadratic variants, BECCSD and QECCSD, respectively, defined by the truncated Hamiltonians $\bar{H}^{(\text{BECCSD})}$ and $\bar{H}^{(\text{QECCSD})}$, equations (41) and (42), respectively, provide remarkable improvements in the very poor description of the potential energy curve of N_2 by the standard CCSD method. The huge negative errors in the

Table 2. Ground-state energies of the N_2 molecule, as described by the STO-3G basis set^a

R^b	Full CI	CCSD	BECCSD ^c	QECCSD ^c	ECCSD ^c
1.0	−101.791600	0.319	0.298	0.298	0.298
1.5	−106.720117	1.102	0.885	0.885	0.885
2.0	−107.623240	3.295	1.897	1.897	1.897
2.5	−107.651880	9.220	3.442	3.442	3.428
3.0	−107.546614	13.176	3.919	3.908	3.758
3.5	−107.473442	−38.645	5.280	5.322	4.746
4.0	−107.447822	−140.376	15.580	15.968	14.122
4.5	−107.441504	−184.984	26.795	27.769	24.039
5.0	−107.439549	−200.958	34.134	35.732	30.390
5.5	−107.438665	−206.974	38.368	40.491	33.867
6.0	−107.438265	−209.538	40.730	43.227	35.746
7.0	−107.438054	−211.915	42.754	45.595	37.306
8.0	−107.438029	−213.431	43.405	46.320	37.799

^a The full CI total energies are in hartree. The CC and ECC energies are in millihartree relative to the corresponding full CI energy values. The lowest two occupied orbitals were frozen in the correlated calculations.

^b The N–N separation in bohr. The equilibrium value of R is 2.068 bohr.

^c The BECCSD, QECCSD, and full ECCSD methods based on the Piecuch–Bartlett variant of the ECC theory.

CCSD results at larger N–N separations, $R \geq 4.5$ bohr, of about −200 millihartree, reduce to much smaller positive errors when the ECC methods are employed (24–38 millihartree in the full ECCSD case, 27–43 millihartree in the BECCSD case, and 28–46 millihartree in the QECCSD case). We also observe a considerable reduction of errors for smaller values of R , including the equilibrium, $R \approx 2.0$ bohr, region (see Table 2). As shown in Table 2 and Fig. 2, the BECCSD, QECCSD, and full ECCSD approaches eliminate the pathological behavior of the CCSD method at larger N–N distances. As in the MBS S4 case, the BECCSD, QECCSD, and full ECCSD approaches restore the effectively variational description of the potential energy curve of N_2 at all internuclear separations.

Our results for N_2 show that it is not necessary to insist on the bi-variational determination of the Σ^\dagger and T operators, exploited in the Arponen–Bishop ECC formalism, in order to obtain significant improvements in the description of multiple bond breaking by the ECC theory. The fact that the ECC theory of Piecuch and Bartlett is not rigorously bi-variational seems to be of lesser significance, since our BECCSD, QECCSD, and ECCSD results obtained with this theory are of the same quality as the strictly bi-variational QECCSD results for N_2 reported in Section 2.3.2. The presence of quadratic terms in Σ^\dagger in $\bar{\bar{H}}^{(\text{ECCSD})}$, $\bar{\bar{H}}^{(\text{BECCSD})}$, and $\bar{\bar{H}}^{(\text{QECCSD})}$, equations (37), (41), and (42), respectively, and the use of two independent cluster operators, T and Σ , in the ECC formalism, which are optimized by solving a coupled system of equations, seem to be far more important for improving the results in the strongly quasi-degenerate bond breaking region than the particular way of obtaining the t_a^i , t_{ab}^{ij} , σ_i^a , and σ_{ij}^{ab} amplitudes that defines the ECCSD formalism of Piecuch and Bartlett.

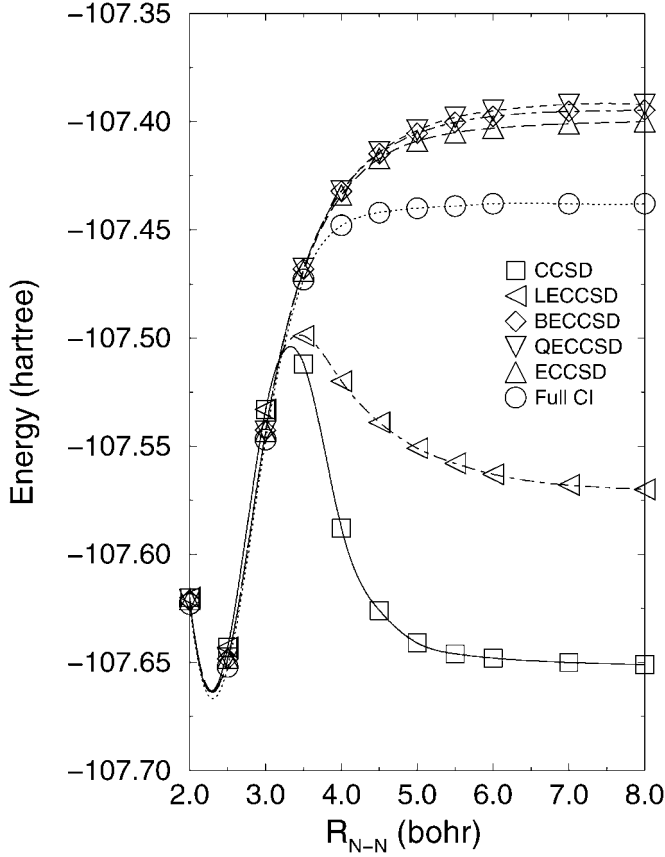


Fig. 2. Potential energy curves for the N_2 molecule, as described by the STO-3G basis set. The LECCSD, BECCSD, QECCSD, and ECCSD methods are based on the Piecuch–Bartlett variant of the ECC theory.

The importance of the quadratic terms in $(\Sigma_1^\dagger + \Sigma_2^\dagger)$, such as $\frac{1}{2}(\Sigma_1^\dagger + \Sigma_2^\dagger)^2 \bar{H}^{(\text{CCSD})}$ and $\frac{1}{2} \bar{H}^{(\text{CCSD})} (\Sigma_1^\dagger + \Sigma_2^\dagger)^2$, in the ECCSD equations becomes apparent when we compare the BECCSD or QECCSD results with the results of the LECCSD calculations. These quadratic terms are ignored in the LECCSD method (see equation (40)) and, in consequence, the LECCSD potential energy curve for N_2 has the same type of hump for the intermediate values of R as the CCSD curve (see Fig. 2). It is interesting to observe, though, a reduction of errors in the CCSD results at larger N–N separations, when the LECCSD approach is employed. This corroborates our earlier statements that the use of two independent cluster operators, T and Σ^\dagger , in the ECC theory is more important for improving the poor CCSD results at larger R values than the specific procedure used to determine T and Σ^\dagger . It is also worth noticing that we can safely neglect the higher-order non-linear terms, such as $\frac{1}{2}(\Sigma_1^\dagger + \Sigma_2^\dagger)^2 \bar{H}^{(\text{CCSD})} (\Sigma_1^\dagger + \Sigma_2^\dagger)$, $\frac{1}{2}(\Sigma_1^\dagger + \Sigma_2^\dagger) \bar{H}^{(\text{CCSD})} (\Sigma_1^\dagger + \Sigma_2^\dagger)^2$, and $\frac{1}{4}(\Sigma_1^\dagger + \Sigma_2^\dagger)^2 \bar{H}^{(\text{CCSD})} (\Sigma_1^\dagger + \Sigma_2^\dagger)^2$, which are present in the QECCSD and full ECCSD methods (*cf.* equations (42) and (37), respectively) and absent in the BECCSD approach

(see equation (41)). The BECCSD results are of the same quality as the QECCSD and full ECCSD results (see Fig. 2 and Table 2). The BECCSD approximation represents the lowest-order ECC approach among various ECC methods examined in this work capable of providing the qualitatively correct description of triple bond breaking in N_2 .

Finally, before describing the calculations employing the Arponen–Bishop ECC theory, let us discuss the quality of the T_1 and T_2 clusters resulting from various types of the ECCSD calculations for N_2 . The remarkable improvements in the description of triple bond breaking in N_2 , offered by the BECCSD, QECCSD, and full ECCSD methods, imply that the T_1 and T_2 clusters resulting from the bi-linear, quadratic, and full ECCSD calculations are much more accurate than the T_1 and T_2 operators obtained with the standard CCSD approach. As in the case of the MBS S4 model, we examined the quality of the T_1 and T_2 clusters obtained in the CCSD and various ECC calculations for N_2 by computing the expectation values of the Hamiltonian, designated by $\langle X \rangle$, where $X = \text{CCSD, BECCSD, QECCSD, ECCSD}$, with the normalized CCSD-like wave functions

$$|\Psi_0^{(X)}\rangle = N^{(X)} e^{T_1^{(X)} + T_2^{(X)}} |\Phi\rangle, \quad X = \text{CCSD, BECCSD, QECCSD, ECCSD}, \quad (62)$$

where $T_1^{(X)}$ and $T_2^{(X)}$ ($X = \text{CCSD, BECCSD, QECCSD, ECCSD}$) are the T_1 and T_2 cluster components obtained with the CCSD, BECCSD, QECCSD, and complete ECCSD methods, respectively, and $N^{(X)} = \langle \Phi | e^{(T_1^{(X)})^\dagger + (T_2^{(X)})^\dagger} e^{T_1^{(X)} + T_2^{(X)}} | \Phi \rangle^{-1/2}$ are the corresponding normalization factors (see Table 3). As demonstrated in Table 3, the expectation values of the Hamiltonian obtained with the CCSD wave function are extremely poor at larger N–N separations, whereas the expectation values of the Hamiltonian calculated with the

Table 3. Ground-state energies of the N_2 molecule, as described by the STO-3G basis set^a

R^b	Full CI	$\langle \text{CCSD} \rangle^c$	$\langle \text{BECCSD} \rangle^c$	$\langle \text{QECCSD} \rangle^c$	$\langle \text{ECCSD} \rangle^c$
1.0	−101.791600	0.298	0.298	0.298	0.298
1.5	−106.720117	0.890	0.888	0.888	0.888
2.0	−107.623240	2.004	1.946	1.946	1.946
2.5	−107.651880	4.316	3.775	3.775	3.775
3.0	−107.546614	5.288	4.160	4.160	4.161
3.5	−107.473442	16.755	3.378	3.387	3.388
4.0	−107.447822	80.696	6.922	7.206	7.145
4.5	−107.441504	95.003	10.603	11.506	11.277
5.0	−107.439549	91.561	12.391	13.877	13.327
5.5	−107.438665	86.652	13.056	14.931	14.224
6.0	−107.438265	83.037	13.276	15.356	14.553
7.0	−107.438054	79.607	13.393	15.571	14.724
8.0	−107.438029	78.563	13.451	15.578	14.758

^a The full CI total energies are in hartree. The remaining energies are in millihartree relative to the corresponding full CI energy values. The lowest two occupied orbitals were frozen in the correlated calculations.

^b The N–N separation in bohr. The equilibrium value of R is 2.068 bohr.

^c $\langle X \rangle$ ($X = \text{CCSD, BECCSD, QECCSD, ECCSD}$) is the expectation value of the Hamiltonian with the normalized $e^{T_1 + T_2} |\Phi\rangle$ wave function, where T_1 and T_2 are obtained with method X (cf. equation (62)).

BECCSD, QECCSD, and full ECCSD wave functions, $|\Psi_0^{(\text{BECCSD})}\rangle$, $|\Psi_0^{(\text{QECCSD})}\rangle$, and $|\Psi_0^{(\text{ECCSD})}\rangle$, respectively, as defined by equation (62), are very close to the corresponding full CI energies at all values of R . The fact that we observe a fairly substantial (2–3-fold) reduction of unsigned errors, when the standard CCSD energy expression, $E_0^{(\text{CCSD})} = \langle \Phi | \bar{H}^{(\text{CCSD})} | \Phi \rangle$, is replaced by the expectation value of the Hamiltonian with the CCSD wave function, does not help the CCSD theory too much, since the $\langle \text{CCSD} \rangle$ energies are characterized by the very large, 79–95 millihartree, errors in the $R \geq 4.0$ bohr region. When the BECCSD, QECCSD, and ECCSD energy expressions, based on equation (39), are replaced by the expectation values of the Hamiltonian with the BECCSD, QECCSD, and ECCSD wave functions defined by equation (62), the 24–46 millihartree errors in the BECCSD, QECCSD, and ECCSD energies in the $R \geq 4.5$ bohr region reduce to 11–13 millihartree in the BECCSD case, 12–16 millihartree in the QECCSD case, and 11–15 millihartree in the full ECCSD case (see Table 3). The fact that we can improve the description of the potential energy curve of N_2 by simply replacing the BECCSD, QECCSD, and ECCSD energy expressions, based on equation (39), by the expectation values of the Hamiltonian calculated with the BECCSD, QECCSD, and ECCSD wave functions, $|\Psi_0^{(\text{BECCSD})}\rangle$, $|\Psi_0^{(\text{QECCSD})}\rangle$, and $|\Psi_0^{(\text{ECCSD})}\rangle$, respectively, is interesting in its own right and worth further exploration.

The relatively high quality of the T_1 and T_2 clusters resulting from the BECCSD, QECCSD, and full ECCSD calculations and the poor quality of the T_1 and T_2 clusters obtained with the standard CCSD approach can also be seen by examining the overlaps of the normalized CCSD, BECCSD, QECCSD, and ECCSD wave functions, $|\Psi_0^{(\text{CCSD})}\rangle$, $|\Psi_0^{(\text{BECCSD})}\rangle$, $|\Psi_0^{(\text{QECCSD})}\rangle$, and $|\Psi_0^{(\text{ECCSD})}\rangle$, respectively, equation (62), with the normalized full CI wave function $|\Psi_0^{(\text{Full CI})}\rangle$, as functions of the N–N separation R (see Fig. 3(a)). As demonstrated in Fig. 3(a), the overlaps between the normalized BECCSD, QECCSD, or ECCSD wave functions and $|\Psi_0^{(\text{Full CI})}\rangle$ vary between 0.98 and 1.0 in the entire R region. For comparison, the overlap of the normalized CCSD and full CI wave functions, which is close to 1.0 in the vicinity of the equilibrium geometry ($R \approx 2.0$ bohr), decreases to ~ 0.93 at larger N–N separations.

The substantial differences between the T_1 and T_2 cluster components resulting from the standard CCSD calculations and their analogs obtained in the BECCSD, QECCSD, and ECCSD calculations at larger N–N distances that lead to the big differences between the behavior of the CCSD and BECCSD/QECCSD/ECCSD approaches in the bond breaking region are shown in Fig. 3(b). Suppose Y and Z are two excitation operators, defined by the amplitudes y_J and z_J , respectively (t_a^i and t_{ab}^{ij} for the cluster operator T and $\sigma_a^i = \sigma_i^a$ and $\sigma_{ab}^{ij} = \sigma_{ij}^{ab}$ for the cluster operator Σ). The following quantity provides us with an accurate measure of how different or how similar the two operators Y and Z are

$$d(Y, Z) = \sqrt{\sum_J (y_J - z_J)^2}. \quad (63)$$

When $Y = Z$, we obtain $d(Y, Z) = 0$. When the cluster amplitudes y_J and z_J defining operators Y and Z , respectively, have similar values, $d(Y, Z)$ is close to 0. Otherwise, the value of $d(Y, Z)$ is significantly greater than 0. As shown in Fig. 3(b), the cluster operators T resulting from the CCSD and BECCSD/QECCSD/ECCSD calculations are almost identical when R is small or when R is close to the equilibrium bond

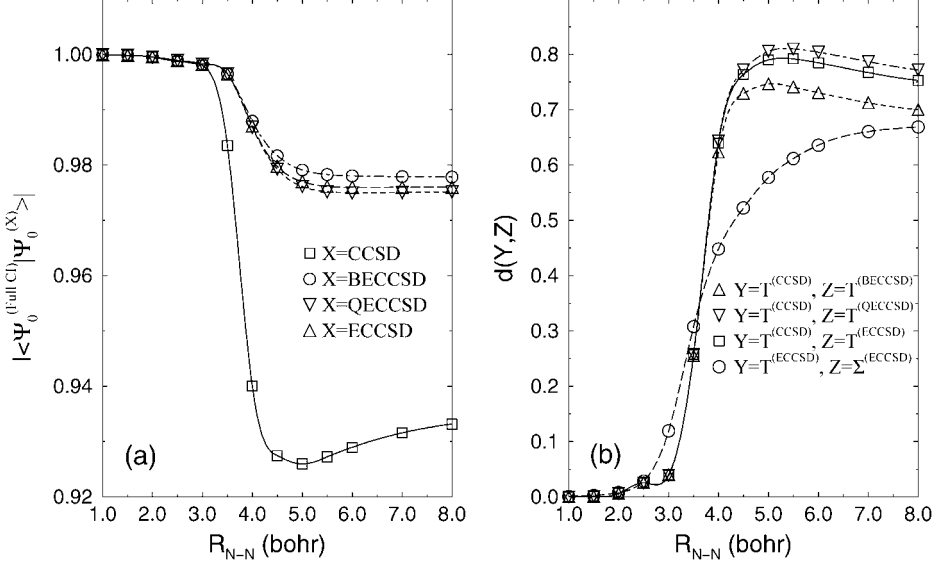


Fig. 3. (a) The overlaps of the normalized CCSD, BECCSD, QECCSD, and ECCSD wave functions, equation (62), with the normalized full CI wave function for the STO-3G N₂ molecule, as functions of the N–N separation R (in bohr). (b) The difference between the CCSD and ECCSD cluster operators T and the difference between the ECCSD cluster operators T and Σ , as defined by the quantity $d(Y, Z)$, equation (63), for the STO-3G N₂ molecule, as functions of the N–N separation R (in bohr).

length in N₂ ($R \approx 2.0$ bohr). This is why the CCSD and BECCSD/QECCSD/ECCSD wave functions and the corresponding energies (particularly, the expectation values of the Hamiltonian calculated with the CCSD and BECCSD/QECCSD/ECCSD wave functions) are virtually identical for the equilibrium and smaller values of R . The situation drastically changes when the triple bond in N₂ is stretched or broken. For $R > 3.0$ bohr, the differences between the CCSD and BECCSD/QECCSD/ECCSD operators T increase so much (*cf.* Fig. 3(b)) that the behavior of the CCSD method and the behavior of the BECCSD/QECCSD/ECCSD approaches at stretched nuclear geometries are totally different. As we have already discussed, the standard CCSD method completely fails at larger R values, whereas the BECCSD/QECCSD/ECCSD approaches provide relatively good results. Figure 3(b) illustrates another important feature of the ECCSD theory, namely, the similarity of the T and Σ operators in the equilibrium region and the significant difference between the T and Σ operators obtained in the ECCSD calculations in the region of larger N–N distances. As mentioned earlier, the lowest-order MBPT estimates of the operators Σ and T are identical (*cf.* Refs. [60–62,83,84]). In consequence, in the equilibrium region, where the MBPT series rapidly converges, we have $\Sigma \approx T$ (see Fig. 3(b)). The situation changes, when the convergence of the MBPT series is slow or when the MBPT series diverges, as is the case when the N–N bond is stretched or broken. For larger N–N separations, the operators Σ and T become completely different. Figure 3(b) provides us with a direct evidence that this is indeed what happens at larger R values.

2.3.2. The Arponen–Bishop ECCSD approach

So far, we have tested the ECCSD methods based on the ECC formalism of Piecuch and Bartlett. We have demonstrated considerable improvements offered by the ECCSD approximations when multiple bonds are broken and severe configurational quasi-degeneracies set in. The question is if similar improvements can be obtained when the original, bi-variational formulation of the ECC theory, proposed by Arponen and Bishop, is exploited. This question is addressed in this subsection.

The usefulness of the bi-variational ECCSD theory of Arponen and Bishop based on equations (39) and (43)–(46) in improving the results for multiple bond breaking becomes apparent when we examine the results for the STO-3G model of N_2 shown in Table 4 and Fig. 4. As one can see, the ECCSD method of Arponen and Bishop employing the ground-state RHF determinant as a reference provides remarkable improvements in the very poor description of the potential energy curve of N_2 by the standard CCSD method. The results are as good as those obtained with the ECCSD approach of Piecuch and Bartlett. Indeed, the huge negative errors in the CCSD results at larger N–N separations, which exceed -200 millihartree in the $R > 4.5$ bohr region, reduce to much smaller positive errors (on the order of 31–38 millihartree when $R > 4.5$ bohr) in the ECCSD/Arponen–Bishop case. As shown in Fig. 4, the ECCSD approach of Arponen and Bishop completely eliminates the pathological behavior of the standard CCSD method at larger N–N distances, restoring the variational description of the potential energy curve of N_2 at all internuclear separations. As in the case of the Piecuch–Bartlett theory, the ECCSD approach of Arponen and Bishop is capable of capturing the most essential non-dynamic correlation effects (which the small STO-3G basis set used in these calculations already describes) in spite of the use of the

Table 4. The ground-state energies of the N_2 molecule obtained for several internuclear separations R with the STO-3G basis set^a

R^b	Full CI	CCSD	QECCSD ^c	ECCSD ^c
1.5	−106.720117	1.102	0.886	0.885
2.0	−107.623240	3.295	1.898	1.897
2.5	−107.651880	9.220	3.443	3.427
3.0	−107.546614	13.176	3.909	3.757
3.5	−107.473442	−38.645	5.294	4.746
4.0	−107.447822	−140.376	15.815	14.148
4.5	−107.441504	−184.984	27.792	24.198
5.0	−107.439549	−200.857	35.335	30.590
5.5	−107.438665	−206.974	39.983	34.158
6.0	−107.438265	−209.538	42.609	36.082
7.0	−107.438054	−211.915	44.839	37.671
8.0	−107.438029	−213.431	45.508	38.161

^a The full CI energies are in hartree. The CCSD, QECCSD, and ECCSD energies are in millihartree relative to the corresponding full CI energy values. The lowest two occupied orbitals were kept frozen.

^b The N–N separation in bohr. The equilibrium value of R is 2.068 bohr.

^c The QECCSD and full ECCSD methods based on the Arponen–Bishop ECC theory.

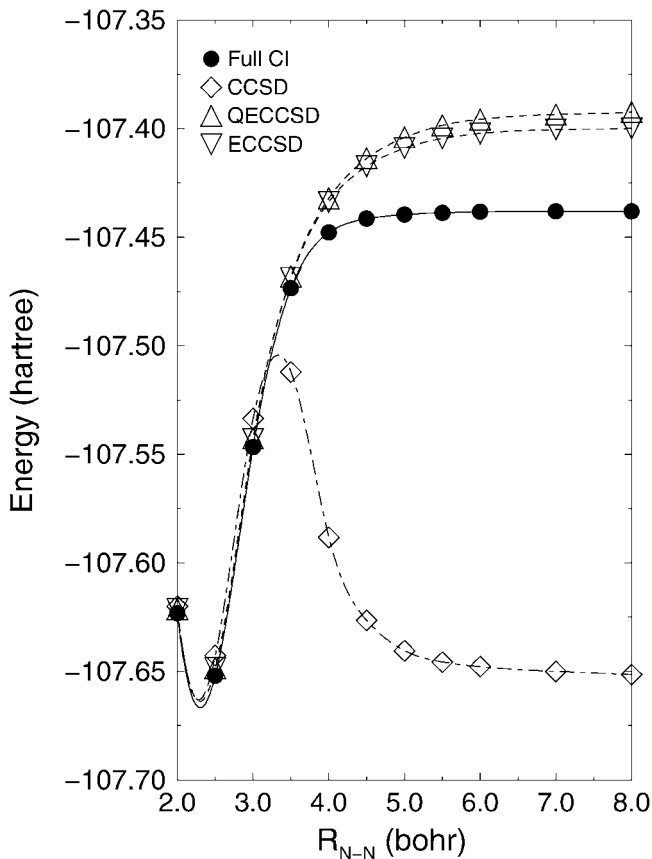


Fig. 4. Ground-state potential energy curves of the N_2 molecule, as described by the STO-3G basis set. The QECCSD and ECCSD methods are based on the Arponen–Bishop ECC theory.

single, spin- and symmetry-adapted, RHF determinant as a reference. The comparison of the CCSD and ECCSD potential energy curves for N_2 shown in Table 4 and Fig. 4 confirms once again that the T_1 and T_2 cluster components obtained in the ECCSD calculations are of much higher quality in the bond breaking region than the T_1 and T_2 clusters resulting from the standard CCSD calculations.

As shown in Table 4 and Fig. 4, the QECCSD/Arponen–Bishop results for the STO-3G model of the N_2 molecule, obtained by truncating the ECCSD energy functional at terms quadratic in $(\Sigma_1^\dagger + \Sigma_2^\dagger)$ (see equations (52)–(57)), are much better than the corresponding CCSD results and almost as good as the results of the full ECCSD calculations. The huge negative errors in the CCSD results in the $R > 4.5$ bohr region, which exceed -200 millihartree, reduce to much smaller positive errors on the order of 35–46 millihartree, when the QECCSD method is employed. As in the case of the full ECCSD approach, the QECCSD approximation employing the Arponen–Bishop ECC formalism eliminates the pathological behavior of the CCSD method at larger N–N distances, restoring the variational description of the potential energy curve of N_2 at all internuclear separations. The variational

Table 5. The ground-state energies of the N_2 molecule obtained for several internuclear separations R with the DZ basis set^a

Method	$0.75R_e$	R_e^b	$1.25R_e$	$1.5R_e$	$1.75R_e$	$2R_e$	$2.25R_e$
CCSD	3.132	8.289	19.061	33.545	17.714	-69.917	-120.836
CCSDT ^c	0.580	2.107	6.064	10.158	-22.468	-109.767	-155.656
CCSD(T) ^c	0.742	2.156	4.971	4.880	-51.869	-246.405	-387.448
CCSD(TQ _f) ^c	0.226	0.323	0.221	-2.279	-14.243	92.981	334.985
CCSDT(Q _f) ^d	0.047	-0.010	-0.715	-4.584	3.612	177.641	426.175
QECCSD ^e	2.506	6.236	13.609	23.485	31.060	40.085	49.741

^a All energies are in millihartree relative to the corresponding full CI energy values, which are -108.549027, -109.105115, -109.054626, -108.950728, -108.889906, -108.868239, and -108.862125 hartree at $R = 0.75R_e$, R_e , $1.25R_e$, $1.5R_e$, $1.75R_e$, $2R_e$, and $2.25R_e$, respectively. The lowest two occupied and the highest two unoccupied orbitals were frozen in correlated calculations.

^b The equilibrium value of R , $R_e = 2.068$ bohr.

^c From Ref. [31].

^d From Ref. [34].

^e The quadratic approximation to the full QECCSD theory of Arponen and Bishop.

and qualitatively correct behavior of the QECCSD method based on the Arponen–Bishop ECC theory is independent of the basis set. Indeed, as shown in Table 5 and Fig. 5, the QECCSD potential energy curve for the double zeta (DZ) [85] model of N_2 is much better than the corresponding CCSD curve. The QECCSD potential energy curve for the N_2 molecule obtained with the DZ basis set, shown in Fig. 5, is located above the full CI curve. The large negative errors in the CCSD results in the $R \geq 2R_e$ region of -70 to -121 millihartree ($R_e = 2.068$ bohr is the equilibrium value of R) are replaced by the considerably smaller positive errors of 40–50 millihartree when the QECCSD method is employed. As in the case of the STO-3G basis set, the QECCSD approach based on the Arponen–Bishop ECC theory eliminates the well pronounced hump on the CCSD potential energy curve, when the DZ basis set is employed.

Thus, the QECCSD approach exploiting the Arponen–Bishop ECC theory provides a practical method of capturing the large non-dynamic correlation effects in N_2 , in spite of the single-reference nature of the ECC formalism, in spite of the use of the RHF determinant in the QECCSD calculations, and, what is probably most remarkable, in spite of the two-body character of the QECCSD (or ECCSD) theory, which uses only one- and two-body cluster operators T_1 , T_2 , Σ_1 , and Σ_2 . As a matter of fact, the QECCSD results at larger internuclear separations of N_2 are much better than those obtained with the standard CC methods with singly, doubly, triply, and even quadruply excited clusters (*cf.* the QECCSD results in Table 5 and Fig. 5 with the corresponding CCSD(T), CCSDT, CCSD(TQ_f), and CCSDT(Q_f) results).

2.4. Conclusion

We can summarize this section by stating that the ECCSD approach of Piecuch and Bartlett, and its approximate BECCSD and QECCSD variants [74–76], and the ECCSD method of

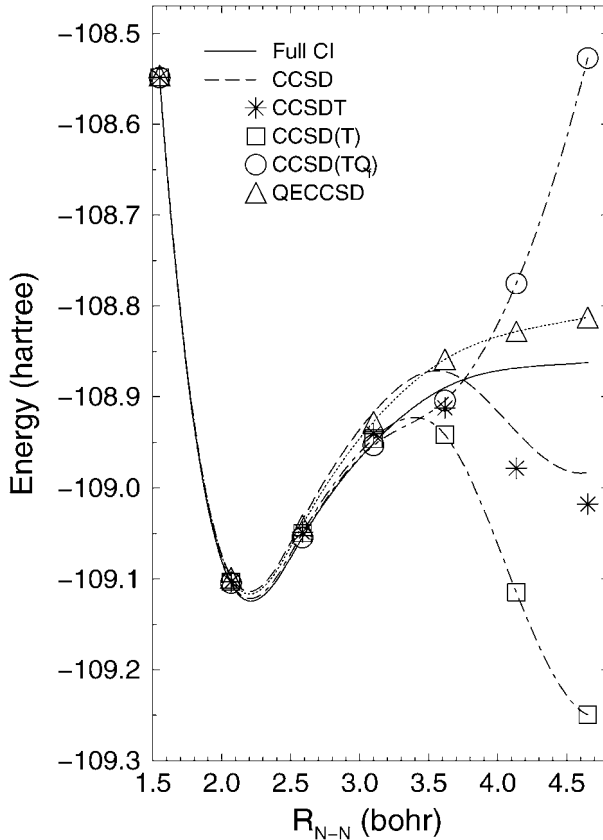


Fig. 5. Ground-state potential energy curves of the N_2 molecule, as described by the DZ basis set. QECCSD represents the quadratic version of the ECCSD theory of Arponen and Bishop.

Arponen and Bishop and its QECCSD variant [77] represent interesting new alternatives for improving the results of CC calculations for quasi-degenerate electronic states and bond breaking. The BECCSD, QECCSD, and full ECCSD methods remove the pervasive failing of the standard CCSD approach at larger internuclear separations and provide very good values of the T_1 and T_2 cluster amplitudes in the bond breaking region, in spite of using the RHF configuration as a reference and in spite of the two-body character of all ECCSD approximations. The BECCSD, QECCSD, and full ECCSD approaches improve the quality of the T_1 and T_2 cluster components so much that we can start thinking about using the BECCSD, QECCSD, or full ECCSD theories to design new single-reference *ab initio* methods for quantitative, high accuracy calculations for bond breaking and other cases of severe configurational quasi-degeneracy. For example, by having an access to relatively good T_1 and T_2 cluster amplitudes, resulting from the BECCSD, QECCSD, or ECCSD calculations, which are much better than the T_1 and T_2 clusters resulting from the standard CCSD calculations, we should be able to propose simple non-iterative corrections

to the BECCSD, QECCSD, or ECCSD energies, which may provide further improvements in the ECC results in the bond breaking region (see Section 3).

Based on a comparison of the ECCSD and QECCSD results for N_2 obtained with the Piecuch–Bartlett and Arponen–Bishop theories, we do not expect the differences between the ECC methods of Arponen and Bishop [50–59] and Piecuch and Bartlett [60] to be large in the context of bond breaking. It seems to us that the rigorously bi-variational character of the ECC formalism of Arponen and Bishop is of the secondary importance in the calculations of PESs involving bond breaking (*cf.* Section 2.3). Our experiences to date indicate that the most important factor that contributes to significant improvements in the quality of the T_1 and T_2 cluster components in the bond breaking region is the flexibility of the ECC theories, which rely on two independent sets of cluster amplitudes that are optimized by solving coupled systems of equations. The standard CC theory uses only one set of cluster amplitudes and this is not sufficient to obtain a correct description of multiple bond breaking by the standard CCSD method.

On the other hand, costs of the ECCSD calculations employing the ECC theory of Arponen and Bishop are somewhat smaller than those characterizing the ECCSD approach of Piecuch and Bartlett. This, in particular, applies to the QECCSD approximation, which is simpler when the Arponen–Bishop ECC theory is employed. The QECCSD method based on Arponen’s and Bishop’s formulation of the ECC theory is an \mathcal{N}^6 procedure. The relatively low cost of the QECCSD approximation, the single reference (“black-box”) character of the QECCSD calculations, and the qualitatively correct description of multiple bond breaking by the QECCSD approach make the QECCSD method an attractive theory for the design of non-iterative corrections to CC energies. These corrections are discussed next.

3. NON-ITERATIVE CORRECTIONS TO EXTENDED COUPLED-CLUSTER ENERGIES: GENERALIZED METHOD OF MOMENTS OF COUPLED-CLUSTER EQUATIONS

In Section 2, we showed that we can provide substantial improvements in the quality of the calculated potential energy curves and electronic quasi-degeneracies if we switch from the standard CCSD theory to its extended ECCSD counterpart. The question arises if we can improve the ECCSD (or QECCSD) results even further and obtain a more quantitative description of bond breaking by adding the *a posteriori* corrections to ECCSD energies that would be reminiscent of the popular triples and quadruples corrections of the CCSD(T) and CCSD(TQ_f) methods and that would eliminate failures of these methods at larger internuclear separations. In this section, we show that such corrections to ECCSD energies can be developed if we use the generalized version of the method of moments of CC equations (the MMCC theory) of Piecuch and Kowalski [11–13,30–32,74,75]. Before describing the generalized MMCC (GMMCC) approach, we discuss the original MMCC formalism.

3.1. The method of moments of coupled-cluster equations

The main idea of the original MMCC theory [11–13,30–32,74,75] and its most recent bi-orthogonal formulation [86,87] is that of the non-iterative energy correction

$$\delta_0^{(A)} \equiv E_0 - E_0^{(A)}, \quad (64)$$

which, when added to the energy $E_0^{(A)}$ obtained in some standard approximate CC calculation A , such as CCSD, recovers the exact, full CI, energy E_0 . The objective of the approximate MMCC methods is to approximate corrections $\delta_0^{(A)}$, such that the resulting MMCC energies, defined as

$$E_0^{(\text{MMCC})} = E_0^{(A)} + \delta_0^{(A)}, \quad (65)$$

are close to the corresponding full CI energies E_0 . The ground-state MMCC formalism can be extended to excited states [12,13,88–90] (*cf.* also Ref. [86]) and genuine multi-reference CC theories [32,91,92]. In this paper, we focus on the ground-state problem and merging the original single-reference MMCC formalism of Refs. [11–13,30–32,74,75] with the non-standard CC theories, such as the ECC method of Arponen and Bishop [50–59] (see Refs. [75,77]).

In the normal formulation of the ground-state MMCC theory, we use the non-iterative corrections $\delta_0^{(A)}$ to improve the results of the standard CC calculations. By the standard CC calculation, we mean any single-reference CC calculation in which the many-body expansion for the cluster operator T , defining the CC ground state $|\Psi_0\rangle$, equation (4), is truncated at some excitation level $m_A < N$ (recall that N is the number of electrons in a system) and in which we obtain the corresponding cluster amplitude equations by projecting the connected cluster form of the electronic Schrödinger equation, equation (15), on the n -tuply excited determinants $|\Phi_{i_1 \dots i_n}^{a_1 \dots a_n}\rangle = E_{i_1 \dots i_n}^{a_1 \dots a_n} |\Phi\rangle$ with $n = 1, \dots, m_A$, corresponding to the many-body components T_n included in the truncated form of T . The general form of the truncated cluster operator T , designated by $T^{(A)}$, defining the standard CC approximation A characterized by the excitation level m_A , is given by equation (21). An example of the standard CC approximation is the CCSD method. In this case, $m_A = 2$ and the cluster operator T is approximated by

$$T \approx T^{(\text{CCSD})} = T_1 + T_2, \quad (66)$$

where T_1 and T_2 are defined by equations (26) and (27), respectively. Other examples of the standard CC approximations are the full CCSDT, CCSDTQ, and CCSDTQP approaches mentioned in the [Introduction](#), in which $m_A = 3, 4$, and 5 , respectively.

The standard CC system of equations for the cluster amplitudes $t_{a_1 \dots a_n}^{i_1 \dots i_n}$ defining the T_n components of $T^{(A)}$ has the following general form:

$$\langle \Phi_{i_1 \dots i_n}^{a_1 \dots a_n} | \bar{H}^{(A)} | \Phi \rangle = 0, \quad i_1 < \dots < i_n, a_1 < \dots < a_n, \quad (67)$$

where $n = 1, \dots, m_A$ and

$$\bar{H}^{(A)} = e^{-T^{(A)}} H e^{T^{(A)}} = (H e^{T^{(A)}})_C \quad (68)$$

is the similarity-transformed Hamiltonian of the CC theory. In particular, the standard CCSD equations for the singly and doubly excited cluster amplitudes t_a^i and t_{ab}^{ij} defining operators T_1 and T_2 , respectively, are

$$\langle \Phi_i^a | \bar{H}^{(\text{CCSD})} | \Phi \rangle = 0, \quad (69)$$

$$\langle \Phi_{ij}^{ab} | \bar{H}^{(\text{CCSD})} | \Phi \rangle = 0, \quad i < j, a < b, \quad (70)$$

where $\bar{H}^{(\text{CCSD})}$ is the similarity-transformed Hamiltonian of the CCSD approach defined by equation (38). Once the system of equations, equation (67), is solved for $T^{(A)}$ (or equations (69) and (70) are solved for T_1 and T_2), the CC energy corresponding to the standard

approximation A is calculated as

$$E_0^{(A)} = \langle \Phi | \bar{H}^{(A)} | \Phi \rangle. \quad (71)$$

The fundamental formula of the ground-state MMCC formalism introduced in Refs. [11] and [30] (*cf.* also Refs. [12,30–32,74,75]), which expresses the energy difference $\delta_0^{(A)}$, equation (64), in terms of the generalized moments of the single-reference CC equations of method A , has the following form:

$$\delta_0^{(A)} \equiv E_0 - E_0^{(A)} = \sum_{n=m_A+1}^N \sum_{k=m_A+1}^n \frac{\langle \Psi_0 | C_{n-k}(m_A) M_k(m_A) | \Phi \rangle}{\langle \Psi_0 | e^{T^{(A)}} | \Phi \rangle}. \quad (72)$$

Here,

$$C_{n-k}(m_A) = (e^{T^{(A)}})_{n-k} \quad (73)$$

is the $(n-k)$ -body component of the wave operator $e^{T^{(A)}}$ defining the CC method A , $|\Psi_0\rangle$ is the full CI ground state, and

$$M_k(m_A) | \Phi \rangle = \sum_{i_1 < \dots < i_k, a_1 < \dots < a_k} \mathfrak{M}_{a_1 \dots a_k}^{i_1 \dots i_k}(m_A) | \Phi_{i_1 \dots i_k}^{a_1 \dots a_k} \rangle. \quad (74)$$

The coefficients $\mathfrak{M}_{a_1 \dots a_k}^{i_1 \dots i_k}(m_A)$ entering equation (74) represent the general moments of the CC equations of method A ,

$$\mathfrak{M}_{a_1 \dots a_k}^{i_1 \dots i_k}(m_A) = \langle \Phi_{i_1 \dots i_k}^{a_1 \dots a_k} | \bar{H}^{(A)} | \Phi \rangle. \quad (75)$$

By comparing equations (75) and (67), we can state that moments $\mathfrak{M}_{a_1 \dots a_k}^{i_1 \dots i_k}(m_A)$ entering $\delta_0^{(A)}$ represent the projections of the CC equations of method A on excited determinants $|\Phi_{i_1 \dots i_k}^{a_1 \dots a_k}\rangle$ with $k > m_A$ that are disregarded in the standard CC calculations.

Equation (72) states that by calculating quantities $C_{n-k}(m_A)$, equation (73), and moments $\mathfrak{M}_{a_1 \dots a_k}^{i_1 \dots i_k}(m_A)$, equation (75), with $k > m_A$, we can determine the non-iterative energy correction $\delta_0^{(A)}$ to the CC energy $E_0^{(A)}$ that recovers the full CI energy E_0 . The determination of moments $\mathfrak{M}_{a_1 \dots a_k}^{i_1 \dots i_k}(m_A)$ for the low-order CC methods, such as CCSD, is relatively straightforward (*cf.* equations (78)–(81)). The $C_{n-k}(m_A)$ terms entering equation (72) are easy to calculate too. The zero-body term, $C_0(m_A)$, equals 1; the one-body term, $C_1(m_A)$, equals T_1 ; the two-body term, $C_2(m_A)$, equals $T_2 + \frac{1}{2}T_1^2$ if $m_A \geq 2$; the three-body term, $C_3(m_A)$, equals $T_1T_2 + \frac{1}{6}T_1^3$ if $m_A = 2$ and $T_3 + T_1T_2 + \frac{1}{6}T_1^3$ if $m_A \geq 3$, *etc.* Thus, the above formula for $\delta_0^{(A)}$, equation (72), is an excellent starting point for developing non-iterative CC approaches, in which the ground-state energies are calculated by adding corrections $\delta_0^{(A)}$ to the standard CC energy $E_0^{(A)}$. For example, we can develop a hierarchy of approximations, in which the energy corrections based on equation (72) are added to the CCSD energies. In this case, the formula for the correction $\delta_0^{(\text{CCSD})}$, which must be added to the CCSD energy $E_0^{(\text{CCSD})}$ to recover the full CI energy E_0 , is

$$\delta_0^{(\text{CCSD})} \equiv E_0 - E_0^{(\text{CCSD})} = \sum_{n=3}^N \sum_{k=3}^{\min(n,6)} \frac{\langle \Psi_0 | C_{n-k}(2) M_k(2) | \Phi \rangle}{\langle \Psi_0 | e^{T_1+T_2} | \Phi \rangle}, \quad (76)$$

where

$$M_k(2)|\Phi\rangle = \sum_{i_1 < \dots < i_k, a_1 < \dots < a_k} \mathfrak{M}_{a_1 \dots a_k}^{i_1 \dots i_k}(2) |\Phi_{i_1 \dots i_k}^{a_1 \dots a_k}\rangle, \quad (77)$$

with moments $\mathfrak{M}_{a_1 \dots a_k}^{i_1 \dots i_k}(2)$, $k = 3-6$, defined as projections of the CCSD equations on triply, quadruply, pentuply, and hexuply excited determinants,

$$\begin{aligned} \mathfrak{M}_{abc}^{ijk}(2) &= \langle \Phi_{ijk}^{abc} | \bar{H}^{(\text{CCSD})} | \Phi \rangle \\ &= \langle \Phi_{ijk}^{abc} | \left[H_N \left(T_2 + T_1 T_2 + \frac{1}{2} T_2^2 + \frac{1}{2} T_1^2 T_2 + \frac{1}{2} T_1 T_2^2 + \frac{1}{6} T_1^3 T_2 \right) \right]_C | \Phi \rangle, \end{aligned} \quad (78)$$

$$\begin{aligned} \mathfrak{M}_{abcd}^{ijkl}(2) &= \langle \Phi_{ijkl}^{abcd} | \bar{H}^{(\text{CCSD})} | \Phi \rangle \\ &= \langle \Phi_{ijkl}^{abcd} | \left[H_N \left(\frac{1}{2} T_2^2 + \frac{1}{2} T_1 T_2^2 + \frac{1}{6} T_2^3 + \frac{1}{4} T_1^2 T_2^2 \right) \right]_C | \Phi \rangle, \end{aligned} \quad (79)$$

$$\mathfrak{M}_{abcde}^{ijklm}(2) = \langle \Phi_{ijklm}^{abcde} | \bar{H}^{(\text{CCSD})} | \Phi \rangle = \frac{1}{6} \langle \Phi_{ijklm}^{abcde} | [H_N(T_2^3 + T_1 T_2^3)]_C | \Phi \rangle, \quad (80)$$

$$\mathfrak{M}_{abcdef}^{ijklmn}(2) = \langle \Phi_{ijklmn}^{abcdef} | \bar{H}^{(\text{CCSD})} | \Phi \rangle = \frac{1}{24} \langle \Phi_{ijklmn}^{abcdef} | (H_N T_2^4)_C | \Phi \rangle. \quad (81)$$

The fact that we do not have to consider moments $\mathfrak{M}_{a_1 \dots a_k}^{i_1 \dots i_k}(2)$ with $k > 6$ is a consequence of the pairwise nature of the electron–electron interactions in the Hamiltonian, which cause moments $\mathfrak{M}_{a_1 \dots a_k}^{i_1 \dots i_k}(2)$ with $k > 6$ vanish.

The exact MMCC corrections $\delta_0^{(A)}$, equation (72), or $\delta_0^{(\text{CCSD})}$, equation (76), have the form of the complete many-body expansions involving all n -tuply excited configurations with $n = m_A + 1, \dots, N$, where N is the number of electrons in a system (*cf.* the summations over n in equations (72) and (76)). Thus, in order to develop practical methods based on the MMCC theory defined by equation (72), we must first truncate the many-body expansions for corrections $\delta_0^{(A)}$ or $\delta_0^{(\text{CCSD})}$ at some, preferably low, excitation level m_B satisfying $m_A < m_B < N$. This leads to the MMCC(m_A, m_B) schemes, in which we calculate the energy as follows [11–13,30–32,74,75]:

$$E_0^{(\text{MMCC})}(m_A, m_B) = E_0^{(A)} + \delta_0(m_A, m_B), \quad (82)$$

where $E_0^{(A)}$ is the energy obtained with the standard CC method A and

$$\delta_0(m_A, m_B) = \sum_{n=m_A+1}^{m_B} \sum_{k=m_A+1}^n \frac{\langle \Psi_0 | C_{n-k}(m_A) M_k(m_A) | \Phi \rangle}{\langle \Psi_0 | e^{T^{(A)}} | \Phi \rangle} \quad (83)$$

is the relevant MMCC correction. Examples of the MMCC(m_A, m_B) schemes are the basic MMCC(2, 3) and MMCC(2, 4) approximations, in which energies are calculated as follows [11–13,30–32,74,75]:

$$E_0^{(\text{MMCC})}(2, 3) = E_0^{(\text{CCSD})} + \frac{\langle \Psi_0 | M_3(2) | \Phi \rangle}{\langle \Psi_0 | e^{T_1+T_2} | \Phi \rangle}, \quad (84)$$

$$E_0^{(\text{MMCC})}(2, 4) = E_0^{(\text{CCSD})} + \frac{\langle \Psi_0 | \{M_3(2) + [M_4(2) + T_1 M_3(2)]\} | \Phi \rangle}{\langle \Psi_0 | e^{T_1+T_2} | \Phi \rangle}, \quad (85)$$

where $E_0^{(\text{CCSD})}$ is the CCSD ground-state energy. The MMCC(2, 3) approach requires that we only determine the triply excited moments $\mathfrak{M}_{abc}^{ijk}(2)$, equation (78). The MMCC(2, 4) method requires that we determine the triply excited moments $\mathfrak{M}_{abc}^{ijk}(2)$, equation (78), and the quadruply excited moments $\mathfrak{M}_{abcd}^{ijkl}(2)$, equation (79).

The second issue that has to be addressed before the MMCC(m_A, m_B) methods can be used in practice is the fact that in the exact MMCC theory the wave function $|\Psi_0\rangle$ that enters equations (72) and (76) is the exact, full CI, ground state. Thus, in order to propose the computationally tractable approaches based on the MMCC theory, we must approximate $|\Psi_0\rangle$ in some, preferably inexpensive, manner. Various ways of approximating $|\Psi_0\rangle$ in equations (83)–(85), leading to the completely renormalized (CR) CC methods [11–13,30–35,37,74,75], the quasi-variational and quadratic MMCC methods [74–76,93], the CI-corrected MMCC approaches [11–13,75,88,89,94], and the multireference MBPT-corrected MMCC approach [95,96]—all employing the CCSD values of T_1 and T_2 to construct the relevant corrections $\delta_0^{(\text{CCSD})}$ —have been suggested. For example, the CR-CCSD(T) method [11–13,30,31,33,35,37,74,75,97–99] is obtained by replacing the wave function $|\Psi_0\rangle$ in the MMCC(2, 3) formula, equation (84), by the MBPT(2)[SDT]-like expression

$$|\Psi_0^{\text{CCSD(T)}}\rangle = (1 + T_1 + T_2 + T_3^{[2]} + Z_3)|\Phi\rangle, \quad (86)$$

where T_1 and T_2 are the singly and doubly excited clusters obtained in the CCSD calculations, $T_3^{[2]}$ is an approximation of the connected triply excited clusters T_3 , defined by equation (61), and

$$Z_3|\Phi\rangle = R_0^{(3)}V_N T_1|\Phi\rangle \quad (87)$$

is the disconnected triples correction, which is responsible for the difference between the [T] and (T) triples corrections of the standard CCSD[T] and CCSD(T) approaches. The higher-order CR-CCSD(TQ) methods [11–13,30,31,33–35,74,75] are obtained in a similar manner, by inserting the MBPT(2)[SDTQ]-like expressions for $|\Psi_0\rangle$ into the MMCC(2, 4) formula, equation (85). For example, the wave function $|\Psi_0\rangle$ defining variant “b” of the CR-CCSD(TQ) approach (the CR-CCSD(TQ),b method) is defined as follows:

$$|\Psi_0^{\text{CCSD(TQ),b}}\rangle = |\Psi_0^{\text{CCSD(T)}}\rangle + \frac{1}{2}T_2^2|\Phi\rangle, \quad (88)$$

where $|\Psi_0^{\text{CCSD(T)}}\rangle$ is given by equation (86).

As shown in Refs. [11–13,30–35,37,74,75] and [96–100], the CR-CCSD(T) and CR-CCSD(TQ) approaches eliminate or considerably reduce the failures of the standard CCSD(T) and CCSD(TQ_f) methods at larger internuclear separations and for bi-radicals without making the calculations substantially more difficult or expensive. In particular, the CR-CCSD(T) and CR-CCSD(TQ) methods provide a very good description of single bond breaking. Similar remarks apply to the more recent locally renormalized extensions of the CR-CCSD(T) and CR-CCSD(TQ) approaches based on the numerator–denominator-connected variant of the MMCC formalism [101] (not discussed here). The recently formulated rigorously size extensive CR-CC methods, such as CR-CCSD(T)_ℓ or CR-CC(2, 3) (the original CR-CC methods slightly violate the strict size extensivity of the CC theory, at the level of ~0.5–1% of the correlation energy in the CR-CCSD(T) case [13]), based on the bi-orthogonal formulation of the MMCC theory (also not discussed here), pro-

vide even better, sometimes spectacular, results [86,87], even in the most difficult cases of balancing bi-radical and closed-shell regions of PESs encountered in studies of some metallo-enzymes, where multi-reference methods face considerable challenges [102]. Unfortunately, performance of all of these MMCC-based methods for multiply bonded systems can be much less impressive, partly due to the very poor quality of the singly and doubly excited cluster amplitudes resulting from the CCSD calculations, on which the CR-CCSD(T), CR-CCSD(TQ), and similar methods are based, in calculations involving multiple bond breaking. In this work, we examine an alternative approach, in which the MMCC corrections $\delta_0^{(A)}$ or $\delta_0^{(\text{CCSD})}$ are constructed using the cluster components obtained in the ECC or ECCSD calculations. As shown in Section 2, the ECCSD method provides much better values of T_1 and T_2 clusters than the CCSD approach when multiple bonds are stretched or broken, so that we may be able to improve the CR-CCSD(T) and CR-CCSD(TQ) results in cases where the standard CCSD values of T_1 and T_2 are of very poor quality. The use of the ECC or ECCSD values of cluster amplitudes in MMCC calculations requires the suitable generalization of the MMCC theory to non-standard CC methods, such as ECC, which is described in the next subsection.

3.2. The generalized MMCC formalism

Interestingly, equations (72) and (76) can be generalized to a situation where the truncated cluster operator $T^{(A)}$ is not determined by solving the standard CC equations, equation (67). Here is how this works: When the cluster operator $T^{(A)}$ is obtained in a non-standard way, we can no longer assume that the generalized moments $\mathfrak{M}_{a_1 \dots a_k}^{i_1 \dots i_k}(m_A)$ with $k = 1, \dots, m_A$ vanish; they only vanish in the standard CC case (*cf.* equations (67) and (75)). It has been shown in Refs. [13] and [30] that when moments $\mathfrak{M}_{a_1 \dots a_k}^{i_1 \dots i_k}(m_A)$ with $k = 1, \dots, m_A$ do not vanish, we have to use the following expression for the exact, full CI, energy E_0 instead of equation (72):

$$\begin{aligned} E_0 &= \sum_{n=0}^N \sum_{k=0}^n \frac{\langle \Psi_0 | C_{n-k}(m_A) M_k(m_A) | \Phi \rangle}{\langle \Psi_0 | e^{T^{(A)}} | \Phi \rangle} \\ &= M_0(m_A) + \sum_{n=1}^N \sum_{k=1}^n \frac{\langle \Psi_0 | C_{n-k}(m_A) M_k(m_A) | \Phi \rangle}{\langle \Psi_0 | e^{T^{(A)}} | \Phi \rangle}. \end{aligned} \quad (89)$$

Here, $M_0(m_A)$ designates the zero-body moment, which is calculated in exactly the same way as the CC energy $E_0^{(A)}$, *i.e.* (*cf.* equation (71)),

$$M_0(m_A) = \langle \Phi | \tilde{H}^{(A)} | \Phi \rangle. \quad (90)$$

Although the formulas for $M_0(m_A)$ and $E_0^{(A)}$ are identical, there is a fundamental difference between $M_0(m_A)$ and $E_0^{(A)}$. The energy $E_0^{(A)}$ is determined using the cluster amplitudes originating from the standard CC equations, equation (67), and $E_0^{(A)}$ is the energy expression used in the CC theory. The zero-body moment $M_0(m_A)$ can be computed with any cluster operator $T^{(A)}$, obtained, for example, by performing some non-standard calculations, such as the ECC calculations, and $M_0(m_A)$ does not have to represent the energy expression of the non-standard CC theory used to generate $T^{(A)}$ (*e.g.*, $M_0(m_A)$

does not represent the energy expression of the ECC formalism, which is given by equation (23)).

As in the case of the standard MMCC formalism defined by equation (72), the $C_{n-k}(m_A)$ and $M_k(m_A)|\Phi\rangle$ quantities entering equation (89) are defined by equations (73) and (74), respectively, although we must consider now all quantities $M_k(m_A)|\Phi\rangle$ with $k \geq 1$, not just those with $k > m_A$. In other words, since we no longer assume that the generalized moments $\mathfrak{M}_{a_1 \dots a_k}^{i_1 \dots i_k}(m_A)$ with $k = 1, \dots, m_A$ vanish, since equation (67) is no longer satisfied, we must consider all generalized moments $\mathfrak{M}_{a_1 \dots a_k}^{i_1 \dots i_k}(m_A)$, which a given cluster operator $T^{(A)}$ produces. In particular, if we want to use the T_1 and T_2 clusters to construct the full CI energy E_0 , which are no longer determined by solving the standard CCSD equations, we must use the following formula for the exact energy E_0 :

$$E_0 = M_0(2) + \sum_{n=1}^N \sum_{k=1}^{\min(n,6)} \frac{\langle \Psi_0 | C_{n-k}(2) M_k(2) | \Phi \rangle}{\langle \Psi_0 | e^{T_1+T_2} | \Phi \rangle}, \quad (91)$$

where $M_k(2)|\Phi\rangle$ is defined by equation (77). As one can see, equation (91) is very similar to equation (76). In particular, we do not have to consider moments $\mathfrak{M}_{a_1 \dots a_k}^{i_1 \dots i_k}(2)$ with $k > 6$, since for Hamiltonians containing up to two-body interactions the generalized moments $\mathfrak{M}_{a_1 \dots a_k}^{i_1 \dots i_k}(2)$ with $k > 6$ vanish, independent of the source of T_1 and T_2 clusters. There is, however, a difference between equations (76) and (91): in equation (91) we consider the singly and doubly excited moments, $\mathfrak{M}_a^i(2) = \langle \Phi_i^a | \bar{H}^{(\text{CCSD})} | \Phi \rangle$ and $\mathfrak{M}_{ab}^{ij}(2) = \langle \Phi_{ij}^{ab} | \bar{H}^{(\text{CCSD})} | \Phi \rangle$, respectively, which are no longer zeroed, along with moments $\mathfrak{M}_{a_1 \dots a_k}^{i_1 \dots i_k}(2)$ with $k = 3-6$ considered in the standard CCSD case; for comparison, equation (76) uses moments $\mathfrak{M}_{a_1 \dots a_k}^{i_1 \dots i_k}(2)$ with $k = 3-6$ only, since $\mathfrak{M}_a^i(2) = \mathfrak{M}_{ab}^{ij}(2) = 0$ in the standard CCSD case. The formulas for the $\mathfrak{M}_a^i(2)$ and $\mathfrak{M}_{ab}^{ij}(2)$ moments, entering equation (91), in terms of the T_1 and T_2 clusters, are identical to the left-hand sides of the standard CCSD equations. Thus, we obtain (cf. equations (69) and (70))

$$\mathfrak{M}_a^i(2) = \langle \Phi_i^a | \left[H_N \left(1 + T_1 + T_2 + \frac{1}{2} T_1^2 + T_1 T_2 + \frac{1}{6} T_1^3 \right) \right]_C | \Phi \rangle, \quad (92)$$

$$\mathfrak{M}_{ab}^{ij}(2) = \langle \Phi_{ij}^{ab} | \left[H_N \left(1 + T_1 + T_2 + \frac{1}{2} T_1^2 + T_1 T_2 + \frac{1}{6} T_1^3 + \frac{1}{2} T_2^2 + \frac{1}{2} T_1^2 T_2 + \frac{1}{24} T_1^4 \right) \right]_C | \Phi \rangle. \quad (93)$$

Equations (89) and (91) define the generalized version of the ground-state MMCC theory, designated as GMMCC. Clearly, the GMMCC theory reduces to the standard MMCC formalism if cluster components T_n defining operator $T^{(A)}$ are determined by solving the standard CC equations, equation (67). In this case, the $\mathfrak{M}_{a_1 \dots a_k}^{i_1 \dots i_k}(m_A)$ moments with $k = 1, \dots, m_A$ vanish and the summations $\sum_{n=1}^N \sum_{k=1}^n$ entering equation (89) reduce to $\sum_{n=m_A+1}^N \sum_{k=m_A+1}^n$, giving equation (72). The obvious advantage of equations (89) and (91) is that they are much more general than equations (72) and (76), enabling us to use the non-standard values of $T^{(A)}$ clusters. Otherwise, we use equations (89) and (91) in exactly the same way as equations (72) and (76). Thus, once the cluster components defining the truncated cluster operator $T^{(A)}$ are determined, we calculate the relevant moments $M_0(m_A)$ and $\mathfrak{M}_{a_1 \dots a_k}^{i_1 \dots i_k}(m_A)$ and use these moments to determine the ground-state energy E_0 .

In analogy to the normal MMCC theory discussed in Section 3.1, a few issues have to be addressed before using the GMMCC formalism in practical calculations. First of all, the exact GMMCC expressions, equations (89) or (91), represent the complete many-body expansions involving all n -tuply excited configurations with $n = 1, \dots, N$, where N is the number of electrons in a system (see the summations over n in equations (89) and (91)). Thus, in order to develop the computationally tractable GMMCC methods, we must first truncate the many-body energy expansions, equations (89) or (91), at some, preferably low, excitation level m_B , where $m_A < m_B < N$. This leads to the GMMCC(m_A, m_B) schemes, which are the non-standard analogs of the MMCC(m_A, m_B) approximations discussed in Section 3.1. By limiting ourselves to the wave functions $|\Psi_0\rangle$ that do not contain higher-than- m_B -tuply excited components relative to reference $|\Phi\rangle$ and by restricting the summation over n in equation (89) accordingly, we obtain the following energy expression for the GMMCC(m_A, m_B) methods:

$$E_0^{(\text{GMMCC})}(m_A, m_B) = M_0(m_A) + \sum_{n=1}^{m_B} \sum_{k=1}^n \frac{\langle \Psi_0 | C_{n-k}(m_A) M_k(m_A) | \Phi \rangle}{\langle \Psi_0 | e^{T^{(A)}} | \Phi \rangle}, \quad (94)$$

where $M_0(m_A)$ is defined by equation (90). The exact GMMCC formalism, equivalent to calculating the full CI energies, is obtained when $|\Psi_0\rangle$ in equation (94) is the full CI ground-state wave function and $m_B = N$. In this case, it is irrelevant what is the value of m_A and where is the cluster operator $T^{(A)}$ taken from. When $|\Psi_0\rangle$ is exact and $m_B = N$, equation (94) produces the exact energy, independent of the excitation level m_A and the source of cluster amplitudes defining $T^{(A)}$.

In this paper, we focus on the GMMCC(m_A, m_B) schemes with $m_A = 2$, which can be used to correct the results of the non-standard CCSD-like (*e.g.*, ECCSD or QECCSD) calculations. In analogy to the normal MMCC theory discussed in Section 3.1, two GMMCC(m_A, m_B) approximations are expected to be particularly useful: the GMMCC(2, 3) method and the GMMCC(2, 4) approach. According to equation (94), the GMMCC(2, 3) and GMMCC(2, 4) energies are calculated as follows:

$$\begin{aligned} E_0^{(\text{GMMCC})}(2, 3) &= M_0(2) + \langle \Psi_0 | \left\{ M_1(2) + [M_2(2) + T_1 M_1(2)] \right. \\ &\quad \left. + \left[M_3(2) + T_1 M_2(2) + \left(T_2 + \frac{1}{2} T_1^2 \right) M_1(2) \right] \right\} | \Phi \rangle \\ &\quad / \langle \Psi_0 | e^{T_1 + T_2} | \Phi \rangle, \end{aligned} \quad (95)$$

$$\begin{aligned} E_0^{(\text{GMMCC})}(2, 4) &= M_0(2) + \langle \Psi_0 | \left\{ M_1(2) + [M_2(2) + T_1 M_1(2)] \right. \\ &\quad \left. + \left[M_3(2) + T_1 M_2(2) + \left(T_2 + \frac{1}{2} T_1^2 \right) M_1(2) \right] \right. \\ &\quad \left. + \left[M_4(2) + T_1 M_3(2) + \left(T_2 + \frac{1}{2} T_1^2 \right) M_2(2) \right. \right. \\ &\quad \left. \left. + \left(T_1 T_2 + \frac{1}{6} T_1^3 \right) M_1(2) \right] \right\} | \Phi \rangle / \langle \Psi_0 | e^{T_1 + T_2} | \Phi \rangle. \end{aligned} \quad (96)$$

As one can see, in the case of the GMMCC(2, 3) approximation, we must calculate moments $\mathfrak{M}_a^i(2)$, $\mathfrak{M}_{ab}^{ij}(2)$, and $\mathfrak{M}_{abc}^{ijk}(2)$, using equations (92), (93), and (78), respectively, in addition to moment $M_0(2)$, equation (90). In the case of the GMMCC(2, 4) approach, we must determine moments $\mathfrak{M}_{abc}^{ijk}(2)$ and $\mathfrak{M}_{abcd}^{ijkl}(2)$, equations (78) and (79), respectively, along with moments $M_0(2)$, $\mathfrak{M}_a^i(2)$, and $\mathfrak{M}_{ab}^{ij}(2)$, equations (90), (92), and (93), respectively. Clearly, when the singly and doubly excited moments $\mathfrak{M}_a^i(2)$ and $\mathfrak{M}_{ab}^{ij}(2)$ vanish, the GMMCC(2, 3) and GMMCC(2, 4) energy expressions, equations (95) and (96), respectively, reduce to the MMCC(2, 3) and MMCC(2, 4) formulas given by equations (84) and (85). This can only happen when the T_1 and T_2 clusters are obtained by solving the standard CCSD equations, equations (69) and (70).

The second issue that needs to be addressed before the GMMCC(2, 3) and GMMCC(2, 4) methods and other GMMCC(m_A, m_B) approximations are used in practice is the issue of the wave function $|\Psi_0\rangle$ that enters equations (94)–(96), which in the exact theory is a full CI ground state. Clearly, in order to make the GMMCC(2, 3), GMMCC(2, 4), and other GMMCC(m_A, m_B) schemes usable in practical applications, we must suggest some approximate forms of $|\Psi_0\rangle$ that can be easily generated with one of the inexpensive *ab initio* approaches. Finally, the third issue is the source of the T_1 and T_2 cluster amplitudes which are needed to construct the GMMCC(2, 3) and GMMCC(2, 4) energy expressions, equations (95) and (96), respectively. As mentioned earlier, in calculating the GMMCC(2, 3) and GMMCC(2, 4) energies we would like to use the T_1 and T_2 cluster components which are more accurate in cases involving multiple bond breaking than those obtained in the standard CCSD calculations. As shown in Section 2, the T_1 and T_2 cluster components resulting from various types of ECCSD calculations are much better than their standard CCSD counterparts, when multiply bonded systems are examined. Thus, it is worth examining the possibility of combining the GMMCC(2, 3) and GMMCC(2, 4) schemes with the ECCSD methods. The resulting ECCSD(T), ECCSD(TQ), QECCSD(T), and QECCSD(TQ) approaches are discussed next.

3.3. The ECCSD(T), ECCSD(TQ), QECCSD(T), and QECCSD(TQ) methods and their performance in calculations for triple bond breaking in N_2

The ECCSD results for triple bond breaking in N_2 are so much better than their standard CCSD analogs that it is very important to analyze the effect of replacing the CCSD values of the T_1 and T_2 cluster components in the MMCC (*e.g.*, CR-CCSD(T) and CR-CCSD(TQ)) calculations by the ECCSD values of these clusters. Since the ECCSD and QECCSD methods are no longer the standard CC theories, so that we can no longer assume that the singly and doubly excited moments, $\mathfrak{M}_a^i(2)$ and $\mathfrak{M}_{ab}^{ij}(2)$, equations (92) and (93), respectively, vanish, we must use the GMMCC formalism discussed in Section 3.2 rather than the normal MMCC formalism discussed in Section 3.1 in such considerations. In the following, we test an idea of using the QECCSD and ECCSD values of T_1 and T_2 , resulting from the application of the Arponen–Bishop variant of the ECC theory, in the GMMCC calculations.

As explained in Section 3.2, in practice we are interested in a truncated form of the GMMCC theory that leads to relatively low costs of calculating the final energy. All of our tests to date, including the calculations for N_2 discussed below, indicate that the

lowest-order GMMCC scheme, employing the ECCSD or QECCSD values of T_1 and T_2 , which provides substantial improvements in the results for multiple bond breaking, is the GMMCC(2, 4) approach defined by equation (96). In this approach, we only consider the generalized moments $\mathfrak{M}_{a_1 \dots a_k}^{i_1 \dots i_k}(2)$ with $k = 1-4$, *i.e.*, moments corresponding to the projections of $\hat{H}^{(\text{CCSD})}|\Phi\rangle$ on singly, doubly, triply, and quadruply excited determinants. The lower-order GMMCC(2, 3) approach, defined by equation (95), employing the ECCSD or QECCSD values of T_1 and T_2 and ignoring the quadruply excited moments $\mathfrak{M}_{abcd}^{ijkl}(2)$, provides improvements too, but the neglect of the quadruply excited moments $\mathfrak{M}_{abcd}^{ijkl}(2)$ in the GMMCC calculations has a negative impact on the results for multiply bonded systems, such as N_2 .

As in all approximate MMCC calculations, we must decide what to do with the wave function $|\Psi_0\rangle$ that enters the GMMCC(2, 3) and GMMCC(2, 4) energy formulas, equations (95) and (96). Since we are mainly interested in the “black-box” GMMCC approaches of the CCSD(T) or CCSD(TQ) type and the effect of replacing the CCSD values of T_1 and T_2 clusters in the CR-CCSD(T) and CR-CCSD(TQ) calculations by the ECCSD values of these clusters, in this study of the performance of the GMMCC theory employing the ECCSD and QECCSD values of T_1 and T_2 , we use the same types of the wave functions $|\Psi_0\rangle$ in equations (95) and (96) as the wave functions $|\Psi_0^{\text{CCSD(T)}}\rangle$ and $|\Psi_0^{\text{CCSD(TQ),b}}\rangle$ used in the CR-CCSD(T) and CR-CCSD(TQ),b calculations (*cf.* equations (86) and (88)). Depending on the choice of $|\Psi_0\rangle$ and the precise source of T_1 and T_2 clusters for the GMMCC(2, 3) and GMMCC(2, 4) calculations, we introduce the following four approximations:

- ECCSD(T): The ECCSD(T) approach is defined as the GMMCC(2, 3) method, in which $|\Psi_0\rangle$ is defined by equation (86) and in which T_1 and T_2 clusters originate from the full ECCSD calculations of the Arponen–Bishop type.
- QECCSD(T): The QECCSD(T) approach is defined as the GMMCC(2, 3) method, in which $|\Psi_0\rangle$ is defined by equation (86) and in which T_1 and T_2 clusters originate from the QECCSD calculations of the Arponen–Bishop type.
- ECCSD(TQ): The ECCSD(TQ) approach is defined as the GMMCC(2, 4) method, in which $|\Psi_0\rangle$ is defined by equation (88) and in which T_1 and T_2 clusters originate from the full ECCSD calculations of the Arponen–Bishop type.
- QECCSD(TQ): The QECCSD(TQ) approach is defined as the GMMCC(2, 4) method, in which $|\Psi_0\rangle$ is defined by equation (88) and in which T_1 and T_2 clusters originate from the QECCSD calculations of the Arponen–Bishop type.

Based on the above definitions, it is easy to verify that the ECCSD(T)/QECCSD(T) energies can be calculated as follows:

$$E_0^{((\text{Q})\text{ECCSD(T)})} = M_0(2) + \frac{N^{(\text{T})}}{D^{(\text{T})}}, \quad (97)$$

where

$$\begin{aligned} N^{(\text{T})} = & \langle \Phi | T_1^\dagger M_1(2) | \Phi \rangle + \langle \Phi | T_2^\dagger [M_2(2) + T_1 M_1(2)] | \Phi \rangle \\ & + \langle \Phi | (T_3^{[2]} + Z_3)^\dagger \left[M_3(2) + T_1 M_2(2) + \left(T_2 + \frac{1}{2} T_1^2 \right) M_1(2) \right] | \Phi \rangle \end{aligned} \quad (98)$$

and

$$D^{(T)} = 1 + \langle \Phi | T_1^\dagger T_1 | \Phi \rangle + \langle \Phi | T_2^\dagger \left(T_2 + \frac{1}{2} T_1^2 \right) | \Phi \rangle \\ + \langle \Phi | (T_3^{[2]} + Z_3)^\dagger \left(T_1 T_2 + \frac{1}{6} T_1^3 \right) | \Phi \rangle, \quad (99)$$

with $T_3^{[2]}$ and Z_3 defined by equations (61) and (87), respectively, and T_1 and T_2 obtained in the ECCSD/QECCSD calculations. The ECCSD(TQ)/QECCSD(TQ) energies are calculated as

$$E_0^{((Q)\text{ECCSD(TQ)})} = M_0(2) + \frac{N^{(TQ)}}{D^{(TQ)}}, \quad (100)$$

where

$$N^{(TQ)} = N^{(T)} + \frac{1}{2} \langle \Phi | (T_2^\dagger)^2 \left[M_4(2) + T_1 M_3(2) + \left(T_2 + \frac{1}{2} T_1^2 \right) M_2(2) \right. \right. \\ \left. \left. + \left(T_1 T_2 + \frac{1}{6} T_1^3 \right) M_1(2) \right] | \Phi \rangle \right. \quad (101)$$

and

$$D^{(TQ)} = D^{(T)} + \frac{1}{2} \langle \Phi | (T_2^\dagger)^2 \left(\frac{1}{2} T_2^2 + \frac{1}{2} T_1^2 T_2 + \frac{1}{24} T_1^4 \right) | \Phi \rangle, \quad (102)$$

with $N^{(T)}$ and $D^{(T)}$ defined by equations (98) and (99), respectively, and T_1 and T_2 obtained in the ECCSD/QECCSD calculations.

The ECCSD(T)/QECCSD(T) methods reduce to the CR-CCSD(T) approach of Refs. [11] and [30] (*cf.* Section 3.1) if the T_1 and T_2 clusters originating from the ECCSD/QECCSD calculations are replaced in equations (97)–(99) by their standard CCSD values. Similarly, the ECCSD(TQ)/QECCSD(TQ) methods reduce to the CR-CCSD(T),b approach of Ref. [31] (*cf.* also Section 3.1) if the T_1 and T_2 clusters originating from the ECCSD/QECCSD calculations are replaced in equations (100)–(102) by their CCSD analogs. These straightforward relationships between the ECCSD(T)/QECCSD(T) and ECCSD(TQ)/QECCSD(TQ) methods, on the one hand, and the CR-CCSD(T) and CR-CCSD(T),b approaches, on the other hand, immediately imply that once the T_1 and T_2 clusters are determined by solving the ECCSD/QECCSD equations, the costs of calculating the ECCSD(T)/QECCSD(T) and ECCSD(TQ)/QECCSD(TQ) energies are essentially the same as the costs of the corresponding CR-CCSD(T) and CR-CCSD(T),b calculations or their standard CCSD(T) and CCSD(TQ_f) counterparts. In particular, the most expensive steps of the ECCSD/QECCSD-based ECCSD(T)/QECCSD(T) calculations (if we ignore the costs of the ECCSD/QECCSD calculations) scale as $n_o^3 n_u^4$. The most expensive steps of the ECCSD(TQ)/QECCSD(TQ) calculations (again, ignoring the costs of the ECCSD/QECCSD calculations) scale, depending on the implementation, as either $n_o^2 n_u^5$ or n_u^6 . The ECCSD(T) and ECCSD(TQ) methods are much less practical, since the underlying ECCSD calculations that provide T_1 and T_2 clusters have steps that scale as \mathcal{N}^{10} with the system size. However, the QECCSD(T) and QECCSD(TQ) methods are quite promising in this regard, since both the underlying QECCSD calculations that provide T_1 and T_2 clusters and the calculations of the final QECCSD(T) and QECCSD(TQ) energies, equations (97) and (100), respectively, have steps that scale, at worst, as $n_o^2 n_u^5$ or n_u^6 .

(\mathcal{N}^7 or \mathcal{N}^6 with the system size). We must keep in mind, however, that the QECCSD(T) and QECCSD(TQ) methods are approximations to the more complete ECCSD(T) and ECCSD(TQ) approaches. The questions, therefore, are:

- (i) Do the QECCSD(T) and QECCSD(TQ) methods provide the results of the full ECCSD(T) and ECCSD(TQ) quality?
- (ii) Are the QECCSD(T) and QECCSD(TQ) methods sufficiently accurate to eliminate the problems observed in the standard and completely renormalized CCSD(T) and CCSD(TQ) calculations for triple bond breaking in N_2 ?

The answers to both questions can be provided if we examine the results of the benchmark ECCSD(T), ECCSD(TQ), QECCSD(T), and QECCSD(TQ) calculations for N_2 shown in [Tables 6 and 7](#) and [Figs. 6 and 7](#), which we performed with the computer codes developed in Ref. [77].

As shown in [Table 6](#) and [Fig. 6](#), the ECCSD(TQ) approach employing the T_1 and T_2 clusters obtained in the full ECCSD (Arponen–Bishop) calculations is capable of providing spectacular improvements in the description of triple bond breaking in the N_2 molecule, as described by the STO-3G basis set, reducing the large unsigned errors in the CCSD and CR-CCSD(TQ),b results in the $R \geq 5.0$ bohr region, on the order of 201–213 and 39–54 millihartree, respectively, and the 31–38 millihartree errors in the ECCSD results to less than 4 millihartree. Remarkably enough, the ECCSD(TQ) results for the N_2 molecule, as described by the STO-3G basis set, in the entire $R \leq 8.0$ bohr ($\approx 4R_e$) region do not exceed ~ 4 millihartree, being much smaller in the $R \approx R_e$ region. As shown in [Table 6](#) and [Fig. 6](#), the ECCSD(TQ) potential energy curve is located only slightly above the full CI curve and there is no unphysical hump on it. Interestingly enough, the zero-body moment $M_0(2)$, equation (90), alone, calculated with the ECCSD values of T_1 and T_2 , which is corrected in the ECCSD(TQ) energy formula, equation (100), by adding terms expressed via moments $\mathfrak{M}_{a_1 \dots a_k}^{i_1 \dots i_k}(2)$ with $k = 1-4$, is a poor approximation to the exact, full CI, energy in the region of large N–N separations (see [Table 6](#)). This demonstrates the remarkable ability of the MMCC (or GMMCC) formalism to restore high accuracies in the bond breaking region, even when the CC or CC-like energy we are trying to correct (in this case, the $M_0(2)$ /ECCSD energy) is itself very poor.

The ECCSD(TQ) results for the STO-3G model of N_2 shown in [Table 6](#) and [Fig. 6](#) are very encouraging, but, as mentioned earlier, the ECCSD(TQ) approach is not too practical due to the expensive \mathcal{N}^{10} steps of the underlying ECCSD calculations. It is, therefore, important to examine if the more manageable QECCSD(TQ) approximation, which relies on the T_1 and T_2 clusters obtained in the QECCSD calculations and which is the \mathcal{N}^6 – \mathcal{N}^7 procedure, provides the results of the ECCSD(TQ) quality. The results in [Table 6](#) indicate that the QECCSD(TQ) and ECCSD(TQ) energies are virtually indistinguishable when the internuclear separation R does not exceed 3.5 bohr ($\approx 1.75R_e$). Only when the N–N separations exceed 3.5 bohr, the differences between the QECCSD(TQ) and ECCSD(TQ) results become larger. Although the errors in the QECCSD(TQ) results in the $R > 3.5$ bohr region are greater than the corresponding errors obtained with the ECCSD(TQ) method, the QECCSD(TQ) approach provides an excellent description of the potential energy curve of the STO-3G N_2 molecule, reducing the 35–46 millihartree errors in the QECCSD results and much larger errors in the CCSD and CR-CCSD(TQ),b results in the $R > 4.5$ bohr region to 5–6 millihartree (see [Table 6](#)). As in the ECCSD(TQ) case, the QECCSD(TQ) potential energy curve of the STO-3G N_2 molecule is located very

Table 6. The ground-state energies of the N_2 molecule obtained for several internuclear separations R with the STO-3G basis set.^a All ECC-related calculations were performed with the Arponen–Bishop ECC theory

Method	R^b											
	1.5	2.0	2.5	3.0	3.5	4.0	4.5	5.0	5.5	6.0	7.0	8.0
CCSD	1.102	3.295	9.220	13.176	−38.645	−140.376	−184.984	−200.857	−206.974	−209.538	−211.915	−213.431
CR-CCSD(TQ),b	0.202	0.687	2.497	4.483	6.168	−5.820	−26.557	−39.221	−46.162	−49.962	−53.158	−54.336
QECCSD	0.886	1.898	3.443	3.909	5.294	15.815	27.792	35.335	39.983	42.609	44.839	45.508
ECCSD	0.885	1.897	3.427	3.757	4.746	14.148	24.198	30.590	34.158	36.082	37.671	38.161
$M_0(2)/QECCSD^c$	0.704	0.503	−2.752	−6.337	16.028	65.713	111.844	143.639	163.434	175.122	185.091	187.896
$M_0(2)/ECCSD^d$	0.666	0.442	−2.878	−6.850	14.867	62.848	106.097	134.790	152.116	161.804	169.847	171.935
QECCSD(T) ^e	0.404	1.866	6.419	8.001	−0.985	2.822	12.915	22.336	28.225	31.847	35.046	35.988
ECCSD(T) ^f	0.404	1.865	6.405	7.836	−1.661	1.148	10.336	17.811	22.704	25.497	27.951	28.618
QECCSD(TQ) ^g	0.195	0.612	1.966	3.485	3.252	3.597	4.653	5.212	5.574	5.806	6.031	6.119
ECCSD(TQ) ^h	0.195	0.613	1.970	3.492	3.119	2.950	3.397	3.589	3.654	3.624	3.648	3.672

^a All energies are in millihartree relative to the corresponding full CI energy values, which are −106.720117, −107.623240, −107.651880, −107.546614, −107.473442, −107.447822, −107.441504, −107.439549, −107.438665, −107.438265, −107.438054, and −107.438029 hartree at $R = 1.5, 2.0, 2.5, 3.0, 3.5, 4.0, 4.5, 5.0, 5.5, 6.0, 7.0$, and 8.0 bohr, respectively. The lowest two occupied orbitals were frozen in correlated calculations.

^b The N–N separation in bohr. The equilibrium value of R is 2.068 bohr.

^c The zero-body moment or the CCSD-like energy expression, equation (90), calculated using the QECCSD values of T_1 and T_2 .

^d The zero-body moment or the CCSD-like energy expression, equation (90), calculated using the ECCSD values of T_1 and T_2 .

^e The GMMCC(2, 3) result obtained using the QECCSD values of T_1 and T_2 and $|\Psi_0\rangle$ defined by equation (86).

^f The GMMCC(2, 3) result obtained using the ECCSD values of T_1 and T_2 and $|\Psi_0\rangle$ defined by equation (86).

^g The GMMCC(2, 4) result obtained using the QECCSD values of T_1 and T_2 and $|\Psi_0\rangle$ defined by equation (88).

^h The GMMCC(2, 4) result obtained using the ECCSD values of T_1 and T_2 and $|\Psi_0\rangle$ defined by equation (88).

Table 7. The ground-state energies of the N₂ molecule obtained for several internuclear separations R with the DZ basis set^a

Method	0.75 R_e	R_e ^b	1.25 R_e	1.5 R_e	1.75 R_e	2 R_e	2.25 R_e
CCSD	3.132	8.289	19.061	33.545	17.714	−69.917	−120.836
CCSDT ^c	0.580	2.107	6.064	10.158	−22.468	−109.767	−155.656
CCSD(T) ^c	0.742	2.156	4.971	4.880	−51.869	−246.405	−387.448
CCSD(TQ) _f ^c	0.226	0.323	0.221	−2.279	−14.243	92.981	334.985
CCSDT(Q) _f ^d	0.047	−0.010	−0.715	−4.584	3.612	177.641	426.175
CR-CCSD(T) ^c	1.078	3.452	9.230	17.509	−2.347	−86.184	−133.313
CR-CCSD(TQ) _a ^c	0.448	1.106	2.474	5.341	1.498	−40.784	−69.259
CR-CCSD(TQ) _b ^c	0.451	1.302	3.617	8.011	13.517	25.069	14.796
QECCSD	2.506	6.236	13.609	23.485	31.060	40.085	49.741
$M_0(2)$ /QECCSD ^e	1.908	4.164	7.935	13.623	33.109	70.120	106.399
QECCSD(T) ^f	1.000	2.941	7.121	11.661	8.454	10.330	17.977
QECCSD(TQ) ^g	0.412	1.002	2.443	6.011	11.393	16.103	19.958

^a All energies are in millihartree relative to the corresponding full CI energy values, which are −108.549027, −109.105115, −109.054626, −108.950728, −108.889906, −108.868239, and −108.862125 hartree at $R = 0.75R_e$, R_e , $1.25R_e$, $1.5R_e$, $1.75R_e$, $2R_e$, and $2.25R_e$, respectively. The lowest two occupied and the highest two unoccupied orbitals were frozen in correlated calculations.

^b The equilibrium value of R , $R_e = 2.068$ bohr.

^c From Ref. [31].

^d From Ref. [34].

^e The zero-body moment or the CCSD-like energy expression, equation (90), calculated using the QECCSD values of T_1 and T_2 (obtained with the Arponen–Bishop ECC theory).

^f The GMMCC(2, 3) result obtained using the QECCSD values of T_1 and T_2 and $|\psi_0\rangle$ defined by equation (86) (obtained with the Arponen–Bishop ECC theory).

^g The GMMCC(2, 4) result obtained using the QECCSD values of T_1 and T_2 and $|\psi_0\rangle$ defined by equation (88) (obtained with the Arponen–Bishop ECC theory).

close to and above the exact, full CI curve (see Fig. 6). Thus, the QECCSD(TQ) approach provides a highly accurate description of the large non-dynamic correlation effects characterizing the N₂ molecule at larger N–N separations.

The question remains if the above observations obtained for the very small STO-3G basis apply to larger basis sets. In order to answer this question, we performed the QECCSD(TQ) calculations for the DZ model of N₂ (see Table 7 and Fig. 7). As shown in Table 7, the errors in the QECCSD(TQ) results are somewhat greater than in the case of the STO-3G basis set, but the overall patterns are the same. Thus, the QECCSD(TQ) method provides considerable improvements in the CCSD and QECCSD results, reducing the large negative, −70 to −121 millihartree, errors in the CCSD results in the $R = 2R_e$ – $2.25R_e$ region and the relatively large positive, 40–50 millihartree, errors in the QECCSD results in the same region to 16–20 millihartree. For smaller values of R , the improvements offered by the QECCSD(TQ) approach are even greater. For example, the QECCSD(TQ) method reduces the 6.236 and 8.289 millihartree errors in the QECCSD and CCSD energies at $R = R_e$ and the 23.485 and 33.545 millihartree errors in the QECCSD and CCSD energies at $R = 1.5R_e$ to 1.002 and 6.011 millihartree, respectively. As shown in Table 7 and Fig. 7,

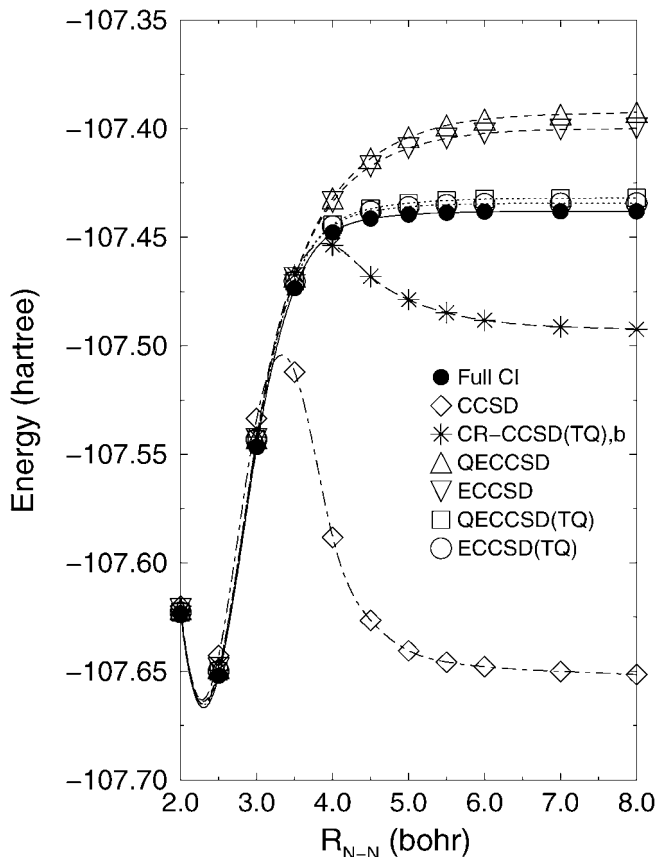


Fig. 6. Ground-state potential energy curves of the N_2 molecule as described by the STO-3G basis set. The QECCSD, ECCSD, QECCSD(TQ), and ECCSD(TQ) calculations were performed using the ECC theory of Arponen and Bishop.

the QECCSD(TQ) potential energy curve for the DZ N_2 molecule is located above the full CI curve and the QECCSD(TQ) approach completely eliminates the unphysical humps on the CR-CCSD(T) and CR-CCSD(TQ) curves, obtained with the CCSD values of T_1 and T_2 . This shows that the use of the QECCSD rather than CCSD values of the T_1 and T_2 clusters improves the quality of the results of the MMCC (*i.e.*, CR-CC) calculations. All of this is very encouraging, since the QECCSD(TQ) method is a relatively inexpensive single-reference approach employing the spin-adapted RHF reference. As shown in Table 7 and Fig. 7, all standard CC methods using the RHF determinant as a reference, including the very expensive CCSDT and CCSDT(Q_f) approaches, which require iterative steps that scale as \mathcal{N}^8 with the system size, completely break down at larger N–N separations. The QECCSD(TQ) method provides a smoother and more accurate description of triple bond breaking in N_2 , with the relatively small errors which monotonically increase with R , while eliminating the most essential pathologies observed in the standard CC calculations.

Interestingly enough, even the simplest QECCSD(T) method works reasonably well, when the DZ model of N_2 is examined (see Table 7), although one has to keep in mind

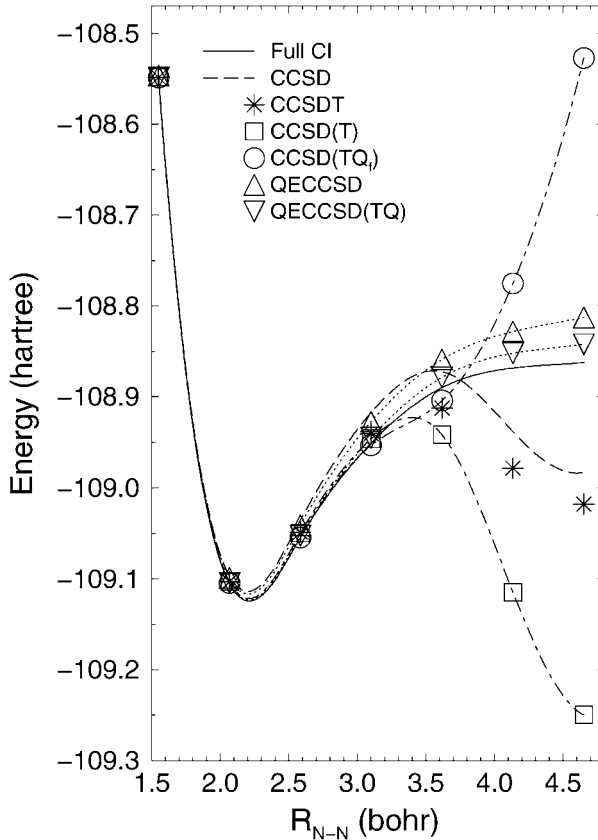


Fig. 7. Ground-state potential energy curves of the N_2 molecule as described by the DZ basis set. The QECCSD and QECCSD(TQ) calculations were performed using the ECC theory of Arponen and Bishop.

that the errors in the QECCSD(T) energies in the $R \leq 1.5R_e$ region are 2–3 times larger than in the QECCSD(TQ) case (see Table 7). Moreover, the QECCSD(T) energies do not vary with R as smoothly as the QECCSD(TQ) energies (*cf.* the nonmonotonic changes in errors in the QECCSD(T) results shown in Table 7). The same behavior is observed when the STO-3G basis set is employed. The calculations for the STO-3G basis set show that the QECCSD(T) and ECCSD(T) methods are incapable of providing significant improvements in the corresponding QECCSD and ECCSD results when the internuclear separation R becomes large (see Table 6). This is related to the absence of the quadruply excited moments $\mathcal{M}_{abcd}^{ijkl}(2)$ in the QECCSD(T) and ECCSD(T) energy expressions. It is interesting to observe, though, that the QECCSD(T) results for the DZ model of N_2 are much better than the results of the CR-CCSD(T) calculations (not to mention the CCSD(T) results), in which the quadruply excited moments $\mathcal{M}_{abcd}^{ijkl}(2)$ are neglected too. This shows once again that the T_1 and T_2 clusters resulting from QECCSD (and ECCSD) calculations are of much higher quality than the T_1 and T_2 clusters obtained with the standard CCSD approach, improving the results of the MMCC calculations.

3.4. Summary

We have demonstrated that the non-iterative ECCSD(TQ) and QECCSD(TQ) methods, obtained by merging the ECC formalism of Arponen and Bishop with the generalized version of the MMCC theory that enables one to use the non-standard cluster components to design the non-iterative corrections to CC energies, provide an accurate and variational description of potential energy surfaces involving multiple bond breaking with the ease of a single-reference “black-box” calculation. In particular, the GMMCC-based ECCSD(TQ) and QECCSD(TQ) approximations employing T_1 and T_2 clusters obtained in ECCSD and QECCSD calculations do not suffer from the non-variational collapse or unphysical behavior observed in the standard CCSD, CCSD(T), CCSD(TQ_f), CCSDT, and CCSDT(Q_f) calculations. The use of the ECCSD and QECCSD values of the singly and doubly excited clusters has a positive impact on improving the results of the MMCC calculations in the bond breaking region. In particular, the ECCSD(TQ) and QECCSD(TQ) methods employing the ECCSD and QECCSD values of T_1 and T_2 clusters improve the results of the CR-CCSD(T) and CR-CCSD(TQ) calculations for triple bond breaking in N₂, which also use the MMCC theory but rely on the T_1 and T_2 clusters obtained with the standard CCSD approach.

The test calculations discussed in this section show that the new GMMCC theory is a flexible formalism, which enables one to design the relatively inexpensive non-iterative CC methods employing the non-standard values of cluster components. The generalized version of the MMCC theory provides us with precise information about the many-body structure of the exact energy and the corrections that must be added to standard or non-standard CC energies to recover full CI results. This can be particularly valuable in situations involving multiple bond stretching or breaking, where the standard arguments based on MBPT fail due to the divergence of the MBPT series at larger internuclear separations. The fact that one can use the standard as well as non-standard cluster amplitudes in the GMMCC calculations is a very useful feature, which gives us an opportunity to improve the results by using non-traditional sources of cluster amplitudes that are more suitable for the applications of interest if the standard sources of these amplitudes are not sufficiently accurate. The results discussed in this section, in which we used the ECCSD and QECCSD methods to generate the T_1 and T_2 clusters for the GMMCC calculations, are a clear demonstration of how useful the idea of using the non-standard values of cluster amplitudes might be in the most challenging cases involving multiple bond breaking where all standard single-reference CC methods (including high level methods such as CCSDT or CCSDT(Q_f)) fail.

We tested a few ECCSD- and QECCSD-based GMMCC approximations, including ECCSD(T), QECCSD(T), ECCSD(TQ), and QECCSD(TQ). Although the best results are obtained with the ECCSD(TQ) method, we cannot recommend this method at this time for practical calculations due to the large costs of the underlying ECCSD calculations. The QECCSD(TQ) approach employing the QECCSD values of T_1 and T_2 clusters is more promising in this regard, offering a reasonably accurate description of large non-dynamic and substantial dynamic correlation effects with the computational steps that scale as \mathcal{N}^6 – \mathcal{N}^7 with the system size.

4. VIRTUAL EXACTNESS OF EXPONENTIAL WAVE FUNCTION EXPANSIONS EMPLOYING GENERALIZED ONE- AND TWO-BODY CLUSTER OPERATORS IN ELECTRONIC STRUCTURE THEORY

As demonstrated in Sections 2 and 3, we can considerably improve the description of chemical bond breaking and quasi-degenerate electronic states by performing the ECCSD calculations and by adding the suitably designed non-iterative corrections, based on the GMMCC formalism, to the ECCSD energies. The ECCSD approaches and the ECCSD-based GMMCC approaches are capable of eliminating the failures of the standard CCSD, CCSD(T), and CCSD(TQ_f) methods, in spite of the fact that we only use one- and two-body cluster operators in the ECCSD and ECCSD-based GMMCC calculations. Our positive experiences with the ECCSD-based methods imply that there is a lot of unexplored flexibility in the CC theories using only one- and two-body clusters. The natural question arises if one can improve the quality of many-electron wave functions based on the cluster expansions involving one- and two-body (or only two-body) cluster or correlation operators to a degree where the results become exact or, at least, virtually exact. After all, the many-electron Hamiltonians used in quantum chemistry and atomic and molecular physics do not contain higher-than-two-body terms. Thus, one may wonder if there is a way to obtain the exact or virtually exact description of many-electron systems with the CC-like theories that does not use higher-than-two-body operators to construct the corresponding many-particle wave functions. An issue of the exactness of the exponential cluster expansions employing two-body or one- and two-body correlation operators, as perceived by the authors of this work, is discussed in this section.

4.1. Theory

It is well known that one can always obtain the exact solution of the electronic Schrödinger equation within a given basis set by performing the full CI calculations. Unfortunately, the dimension of the full CI eigenvalue problem can easily run into astronomical figures, even for small many-electron systems. This can be easily verified by applying the well-known Weyl's formula [103] for the number $f(n, N, S)$ of spin-adapted electron configurations that enter the full CI expansion of an eigenstate of the electronic Hamiltonian H , *i.e.*,

$$f(n, N, S) = \frac{2S+1}{n+1} \binom{n+1}{N/2-S} \binom{n+1}{N/2+S+1}, \quad (103)$$

where n represents the number of correlated orbitals, N is the number of correlated electrons, S is the total spin of an eigenstate under consideration, and $\binom{m}{k} = m!/[k!(m-k)!]$ is the binomial coefficient. For example, a full CI calculation of a singlet electronic state for a system consisting of 10 electrons (*e.g.*, the HF molecule or the Ne atom) and described by only 20 orbitals requires using $f(20, 10, 0) = 52,581,816$ configurations. A modest increase of the number of orbitals from 20 to 30 results in a steep increase in the number of configurations defining the full CI problem to 4.04×10^9 . Those numbers should be compared with the much smaller numbers of 22,155 and 108,345 two-electron integrals defining the electronic Hamiltonians for the $n = 20$ and 30 cases, respectively. The point-group symmetry and other symmetries of the Hamiltonian can, on occasion, reduce the

dimension of the full CI problem, but savings resulting from the use of symmetry are minimal compared to the rapidly increasing numbers of configurations defining the full CI wave functions with n and N . Indeed, the realistic calculation for a 10 electron system would require using ~ 100 orbitals. According to equation (103), the $n = 100$, $N = 10$, and $S = 0$ case leads to an astronomical number of 9.94×10^{14} configurations in the corresponding full CI expansion. This should be compared to a much smaller number of 12,753,775 two-electron integrals defining the electronic Hamiltonian for the $n = 100$ case. Clearly, the numbers of full CI configurations would be significantly larger for $N > 10$ and for larger n values due to the factorial scaling of the dimension of the full CI problem with the system size. This should be contrasted with the relatively slow, n^4 -like, increase of the number of two-electron integrals defining the Hamiltonian H with n . Thus, there seems to be a conflict between the huge dimensionality of the full CI problem, which prevents us from performing exact *ab initio* calculations for larger systems, and the fact that the Hamiltonians for many-electron systems involve only one- and two-body integrals, whose numbers are much smaller than the numbers of full CI coefficients defining the exact wave functions. In spite of the tremendous progress in the area of full CI calculations and computer technology (*cf.*, *e.g.*, Ref. [104] and references therein), the exact *ab initio* calculations employing the full CI method remain limited to a few electron systems described by small (usually, $n \sim 20$ –30) basis sets.

4.1.1. The $\exp(X)$ conjecture

It has recently been suggested that it may be possible to represent the exact or virtually exact ground-state wave function of an arbitrary many-fermion pairwise interacting system by an exponential cluster expansion involving a general two-body or one- plus two-body correlation operator [105–111]. If these statements were true, completely new ways of performing *ab initio* quantum calculations for many-fermion (*e.g.*, many-electron) systems might be suggested, which could provide enormous reductions in computational requirements for accurate quantum calculations for pairwise-interacting many-fermion systems, eliminating the astronomical costs of generating the exact many-particle wave functions by solving the full CI eigenvalue problem. Specifically, it has been proposed that the exact ground-state wave function $|\Psi_0\rangle$ of a given many-fermion system described by the Hamiltonian

$$H = z_p^q c_p^\dagger c_q + \frac{1}{2} v_{pq}^{rs} c_p^\dagger c_q^\dagger c_s c_r, \quad (104)$$

containing up to two-body terms, obtained in a finite spin-orbital basis set, has the following simple form [105]:

$$|\Psi_0\rangle \equiv |\Psi_0(X)\rangle = e^X |\Phi_0\rangle, \quad (105)$$

where X is a general two-body operator and $|\Phi_0\rangle$ is a normalized reference state, which in principle is an arbitrary wave function that has a non-zero overlap with $|\Psi_0\rangle$, but in practice should provide us with a reasonable approximation of $|\Psi_0\rangle$. In equation (104) and equations presented below, we use, whenever possible, the Einstein summation convention over repeated upper and lower indices. As in the earlier sections, the c^p and c_p operators represent the usual creation and annihilation operators, respectively, associated with the one particle basis $\{p\}$. The $z_p^q = \langle p|z|q\rangle$ and $v_{pq}^{rs} = \langle pq|v|rs\rangle$ represent the usual one- and

two-particle integrals defining the Hamiltonian. In the language of second quantization,

$$X = X_2 = \frac{1}{2} x_{pq}^{rs} c^p c^q c_s c_r, \quad (106)$$

where x_{pq}^{rs} are some coefficients. According to Nooijen [105] (*cf.* also Refs. [110,111]), the number of independent coefficients x_{pq}^{rs} should be identical to the number of two-particle integrals v_{pq}^{rs} entering the Hamiltonian H , equation (104). One could redefine the operator X by considering the one- and two-body components in equation (106) [105,107,108] and write

$$X = X_1 + X_2 = x_p^q c^p c_q + \frac{1}{2} x_{pq}^{rs} c^p c^q c_s c_r, \quad (107)$$

but this is not absolutely necessary, since for a fixed number of particles (N), one can always rewrite the Hamiltonian H , equation (104), in terms of two-body terms only. A straightforward manipulation shows that

$$H = \frac{1}{2} h_{pq}^{rs} c^p c^q c_s c_r, \quad (108)$$

where

$$h_{pq}^{rs} = v_{pq}^{rs} + \frac{z_p^r \delta_q^s + \delta_p^r z_q^s}{N-1}, \quad (109)$$

with δ_p^q representing the usual Kronecker delta. On the other hand, it may be beneficial to use equation (107) rather than equation (106) in actual calculations, since the presence of one-body term $X_1 = x_p^q c^p c_q$ in the operator X may accelerate the convergence of the resulting wave functions and energies.

The above representation of the ground-state wave function, equation (105), is reminiscent of the exponential ansatz of the single-reference CC theory, equation (4). There is, however, a fundamental difference between equations (105) and (4). The cluster operator T entering equation (4) is defined in terms of the particle-hole excitation operators $E_{i_1 \dots i_n}^{a_1 \dots a_n}$, equation (7), where i_1, \dots, i_n (a_1, \dots, a_n) are the spin-orbitals that are occupied (unoccupied) in the reference configuration $|\Phi_0\rangle$ (which is then a single Slater determinant), and it contains all many-body terms T_n with $n = 1, \dots, N$ in the exact case. The operator X , equation (106), or its analog defined by equation (107), entering equation (105), has at most two-body terms, but of the general type (excitations, deexcitations, and all other combinations of indices p, q, r, s). Moreover, the reference configuration $|\Phi_0\rangle$ can be a multi-determinantal state. One could, of course, truncate the many-body expansion for the cluster operator T in equation (4) at a two-body component T_2 , equation (27), but then the resulting wave functions $e^{T_2}|\Phi_0\rangle$ and $e^{T_1+T_2}|\Phi_0\rangle$, which are used in the CCD and CCSD methods, respectively, are only approximate (and often not very accurate) wave functions. Thus, as we can see, there are significant differences between equations (105) and (4). However, because of the formal similarity of the CCD wave function, $e^{T_2}|\Phi_0\rangle$, and equation (105), Nooijen and Lotrich [112] and Van Voorhis and Head-Gordon [110] call the wave function ansatz defined by equations (105) and (106) generalized CCD (GCCD) (the wave function ansatz using equations (105) and (107) is then called generalized CCSD or GCCSD). A similar terminology has been used in Refs. [106–109].

4.1.2. Formal arguments in favor of the $\exp(X)$ conjecture (ground states)

There are several facts that speak in favor of the correctness of equation (105). Nooijen based his reasoning [105] on the fact that the number of two-body coefficients x_{pq}^{rs} is identical to the number of components of the Nakatsuji two-particle density equation [113], which is, in turn, equivalent to the time-independent Schrödinger equation for Hamiltonians containing up to two-body terms. The problem that was left unsolved by Nooijen is the solubility of a rather complicated exponential variant of the Nakatsuji density equation, which forms an essential part of Nooijen's analysis (*cf.* equation (11) in Ref. [105]). Van Voorhis and Head-Gordon based their reasoning [110] on the fact (exploited in Quantum Monte Carlo techniques) that one can always obtain the exact wave function by considering the expression

$$|\Psi_0\rangle = \lim_{t \rightarrow \infty} e^{Z_t} |\Phi_0\rangle, \quad (110)$$

where the two-body operator Z_t is defined as follows:

$$Z_t = -(H - E_0)t, \quad (111)$$

with E_0 representing the exact energy. They used equation (110) to write the two-body operator X defining the exact wave function $|\Psi_0\rangle$ via equation (105) as

$$X = -\lim_{t \rightarrow \infty} Z_t. \quad (112)$$

Similar arguments and equations have been presented by Nakatsuji [108,109], who also considered the conditions for the wave functions parameterized by two-body operators to be exact [106]. The problem with using equation (110) in this fashion is that the operator Z_t , equation (111), provides the exact wave function only in the $t \rightarrow \infty$ limit, whereas the operator X , equation (106) or (107), entering equation (105), is assumed to be a finite operator. This immediately implies that the operator X defining the exact wave function $|\Psi_0\rangle$ through equation (105) cannot be constrained to be of the Hamiltonian form, equation (111) (*cf.* below for additional remarks). Equation (110) does not open up the possibility of the existence of a finite two-body operator X , which is not necessarily defined through infinite coefficients x_{pq}^{rs} (which equation (112) produces). There also seem to exist some contradictions between statements made in Ref. [106] and Refs. [108,109]. The exactness of the GCCD or GCCSD wave functions was questioned in Ref. [106] and supported, to some extent, in Refs. [108,109] (see Refs. [114–118] for further debate; see the discussion below for additional comments). We will not go into the details of every paper that has been written until now on the subject. Clearly, the issue of the exactness of equation (105) is quite controversial and intriguing at the same time. Thus, from now on we focus on our own analyses, experiences, and observations, hoping that they will help the ongoing discussion of the issue of exactness of two-body cluster expansions defined by equation (105).

We recently provided a mathematical analysis, supported by numerical results [111], showing that the exact or, at least, the virtually exact ground state of a many-fermion system, described by the Hamiltonian containing one- and two-body terms, may indeed be represented by the exponential cluster expansion employing a general two-body operator, equation (105). In our analysis, we connected the problem with the Horn–Weinstein for-

mula for the exact energy [119],

$$\begin{aligned} E_0 &= \lim_{t \rightarrow \infty} \frac{\langle \Phi_0 | e^{-tH} H | \Phi_0 \rangle}{\langle \Phi_0 | e^{-tH} | \Phi_0 \rangle} \\ &= \lim_{t \rightarrow \infty} E_{0,t} = \lim_{t \rightarrow \infty} E(X_t), \end{aligned} \quad (113)$$

where

$$E_{0,t} \equiv E(X_t) = \frac{\langle \Phi_0 | e^{X_t^\dagger} H e^{X_t} | \Phi_0 \rangle}{\langle \Phi_0 | e^{X_t^\dagger} e^{X_t} | \Phi_0 \rangle} \quad (114)$$

and

$$X_t = -\frac{1}{2}tH, \quad (115)$$

and determined the operator X entering equation (105) through a direct minimization of the expectation value expression

$$E_0(\tilde{X}) = \frac{\langle \Phi_0 | e^{\tilde{X}^\dagger} H e^{\tilde{X}} | \Phi_0 \rangle}{\langle \Phi_0 | e^{\tilde{X}^\dagger} e^{\tilde{X}} | \Phi_0 \rangle} \quad (116)$$

over general two-body operators

$$\tilde{X} = \frac{1}{2} \tilde{x}_{pq}^{rs} c^p c^q c_s c_r. \quad (117)$$

This analysis (taken from Ref. [111]) is summarized below.

Let us consider the family \mathcal{M} of all two-body operators \tilde{X} , equation (117), that are defined by finite coefficients \tilde{x}_{pq}^{rs} and that have a general structure of the Hamiltonian H , equation (108). This means that \mathcal{M} consists of all two-body operators that are, for example, Hermitian, since H is Hermitian; that satisfy relations, such as $\tilde{x}_{pq}^{rs} = \tilde{x}_{qp}^{sr}$, since $h_{pq}^{rs} = h_{qp}^{sr}$, etc. Obviously, the number of independent parameters \tilde{x}_{pq}^{rs} is identical to the number of coefficients h_{pq}^{rs} or v_{pq}^{rs} defining the Hamiltonian. It should be noticed that all operators X_t , equation (115), and Z_t , equation (111), belong to \mathcal{M} , although \mathcal{M} is a much larger operator family, which contains infinitely many operators that are not multiples of H . This remark is important for the considerations discussed in this section, since one can always obtain the exact wave function and energy by applying equations (110) and (113), with Z_t and X_t defined by equations (111) and (115), respectively. As pointed out above, neither the operator Z_t nor its X_t analog can provide the exact description of a many-fermion system for a finite value of t . It is, therefore, essential to realize that we should search for the operator X defining $|\Psi_0\rangle$ via equation (105) by minimizing the expectation value expression, $E_0(\tilde{X})$, equation (116), over all operators in \mathcal{M} , without constraining these operators to be the multiples of the Hamiltonian, as implied by equations (111) and (115).

Let us, therefore, examine what the direct minimization of $E_0(\tilde{X})$ in \mathcal{M} can lead to. According to the Ritz variational principle, $E_0(\tilde{X})$ is bounded from below by the exact, full CI, energy, so that

$$E_0 \leq E_0(\tilde{X}) \quad (118)$$

for all operators $\tilde{X} \in \mathcal{M}$. This implies that there should exist a two-body operator $X \in \mathcal{M}$ that minimizes $E_0(\tilde{X})$. We can write

$$E_0(X) = \min_{\tilde{X} \in \mathcal{M}} E_0(\tilde{X}). \quad (119)$$

Obviously,

$$E_0 \leq E_0(X). \quad (120)$$

Let us now consider the energy expression $E_{0,t}$, equation (114), for an arbitrary (fixed) value of t . We can immediately write

$$E_0(X) < E_{0,t}, \quad (121)$$

since $E_0(X)$ is a minimum value of $E_0(\tilde{X})$, equation (116), in a space of all two-body operators \tilde{X} , whereas $E_{0,t} = E_0(X_t)$ is the value of $E_0(\tilde{X})$ at $\tilde{X} = X_t$ (cf. equations (116) and (114)). As a matter of fact, for a given value of t , one can always find a two-body operator Y from \mathcal{M} such that $E_0(Y) < E_{0,t}$. A trivial example of such operator might be provided by $X_{t'}$ with $t' > t$, since, as shown in Ref. [119], $E_{0,t}$, equation (114), is a monotonically decreasing function of t . However, since the operator family \mathcal{M} is much larger than the “one-dimensional” manifold of operators X_t , which are multiples of H , there is a chance that there exist two-body operators $Y \in \mathcal{M}$ which satisfy $E_0(Y) < E_{0,t}$ and which are not given by equation (115). This indicates that the operator X minimizing $E_0(\tilde{X})$ may very well be a finite operator (*i.e.*, defined by finite coefficients x_{pq}^{rs} and not obtained by considering the limiting case of the $t \rightarrow \infty$ operators X_t), although we cannot provide a rigorous mathematical proof that this is indeed the case and the existence of finite operator X may depend on the actual form of the reference state $|\Phi_0\rangle$, which does not have to be a single Slater determinant (see, *e.g.*, Refs. [114–116]). The existence of a finite operator $X \in \mathcal{M}$ that minimizes $E_0(\tilde{X})$ according to equation (119) and that is not of the Hamiltonian form is supported by the numerical calculations for a few many-electron systems [111] (see the discussion below).

Inequalities (120) and (121) can be combined into the following result:

$$E_0 \leq E_0(X) < E_{0,t}, \quad (122)$$

true for any value of t . In view of the Horn–Weinstein energy expression, equation (113), by considering the $t \rightarrow \infty$ limit in equation (122), we obtain the identity

$$E_0 = E_0(X). \quad (123)$$

Equation (123) implies that the two-body operator X , obtained by minimizing the expectation value expression $E_0(\tilde{X})$, equation (116), gives the exact energy E_0 and, by the virtue of the variational principle, the exact ground state $|\Psi_0\rangle$, as stated in equation (105).

The above analysis makes the exactness of equation (105) a possibility, but one should not treat it as a complete mathematical proof, since we cannot rigorously prove the existence of the finite coefficients x_{pq}^{rs} that would define the optimum operator X corresponding to the global minimum of $E_0(\tilde{X})$ for an arbitrary reference $|\Phi_0\rangle$. This would require proving that the manifold \mathcal{M} or the set of two-body correlation operators \tilde{X} is complete, which is a highly non-trivial statement which does not have to be true in general. Moreover, the existence of the finite coefficients x_{pq}^{rs} that would define the optimum operator X corresponding to the global minimum of $E_0(\tilde{X})$ is complicated by the highly non-linear nature of

the wave function ansatz defined by equation (105) which, unlike the standard CC ansatz, equation (4), employing the particle–hole excitation operator T , is a non-terminating series in the generalized cluster operator X . We can make, however, several useful observations. First, the reasoning presented above, which is based on combining the Horn–Weinstein energy formula, equation (113), with the minimization of $E_0(\tilde{X})$, has an advantage over the arguments given in Refs. [108–110] in that it frees us from necessarily assuming that the operator X can only be obtained by studying the $t \rightarrow \infty$ operators X_t , equation (115), or Z_t , equation (111). By minimizing $E_0(\tilde{X})$, equation (116), in a space of all two-body operators (or, equivalently, by minimizing $E_0(\tilde{X})$ in a finite-dimensional space of variables \tilde{x}_{pq}^{rs}), which is exactly how we obtained operator X in Ref. [111] (cf. the examples below), we may be able to find finite parameters x_{pq}^{rs} , defining the exact wave function $|\Psi_0\rangle$, precisely because the operator X is not constrained to be a multiple of the Hamiltonian. If the finite operator X , determined by some numerical procedure for minimizing $E_0(\tilde{X})$ in \mathcal{M} , is a local rather than a global minimum on the $E_0(\tilde{X})$ multi-parameter surface, then the resulting energy $E_0(X)$, calculated by substituting $\tilde{X} = X$ into equation (116), and the resulting wave function $|\Psi_0(X)\rangle$, equation (105), do not have to be mathematically exact. However, even in this case, the operator X may provide excellent results, opening up a possibility of using the exponential wave functions (105), with X defined by equation (106) (or (107)), in high accuracy *ab initio* calculations. Second, the mathematical analysis described above does not tell us anything about the specific form of the reference state $|\Phi_0\rangle$ that should be used in the calculations exploiting the $\exp(X)$ ansatz. It is possible, for example, that the finite parameters x_{pq}^{rs} that give the exact state $|\Psi_0(X)\rangle$ via equation (105) exist only for certain types of references $|\Phi_0\rangle$ that do not have to be represented by a single Slater determinant (based on the analyses presented in Refs. [114–116], it is rather unlikely that $|\Phi_0\rangle$ is a single determinant although there is no rigorous proof of this statement). It may happen, however, that highly accurate results are already obtained with the ordinary Hartree–Fock reference $|\Phi_0\rangle$ and the additional improvements are obtained by using a multi-determinantal reference state $|\tilde{\Phi}_0\rangle$ instead of $|\Phi_0\rangle$ in the definition of $|\Psi_0(X)\rangle$, equation (105). All of these issues are explored here by performing numerical calculations for a few small many-electron systems. Before, however, discussing a few numerical examples, we address the possibility of using the $\exp(X)$ ansatz in the excited-state calculations.

4.1.3. Extension of the $\exp(X)$ conjecture to excited states

The $\exp(X)$ conjecture was originally proposed for the ground states, but we can try to extend it to the excited states using the standard variational approach. For example, we can construct the trial wave function for the first excited state $|\Psi_1\rangle$ as

$$|\tilde{\Psi}_1(\tilde{X}^{(1)})\rangle = |\Psi_1(\tilde{X}^{(1)})\rangle - \langle\Psi_0|\Psi_1(\tilde{X}^{(1)})\rangle|\Psi_0\rangle. \quad (124)$$

Here,

$$|\Psi_0\rangle = \mathcal{N}_0 e^{X^{(0)}} |\tilde{\Phi}_0\rangle \quad (125)$$

is the previously obtained normalized ground state (\mathcal{N}_0 is the normalization factor, $X^{(0)}$ is the optimum two-body operator representing $|\Psi_0\rangle$, and $|\tilde{\Phi}_0\rangle$ is the single- or multi-determinantal reference state used in the calculation of $|\Psi_0\rangle$) and

$$|\Psi_1(\tilde{X}^{(1)})\rangle = \mathcal{N}_1 e^{\tilde{X}^{(1)}} |\tilde{\Phi}_1\rangle \quad (126)$$

is the normalized $\exp(X)$ -like form of the first excited state, where $|\tilde{\Phi}_1\rangle$ represents the reference state for $|\Psi_1\rangle$. By minimizing the energy functional

$$E_1(\tilde{X}^{(1)}) = \frac{\langle \tilde{\Psi}_1(\tilde{X}^{(1)}) | H | \tilde{\Psi}_1(\tilde{X}^{(1)}) \rangle}{\langle \tilde{\Psi}_1(\tilde{X}^{(1)}) | \tilde{\Psi}_1(\tilde{X}^{(1)}) \rangle} \quad (127)$$

over all two-body operators $\tilde{X}^{(1)} \in \mathcal{M}$, we obtain the energy of the first excited state and the corresponding wave function $|\Psi_1\rangle \equiv |\Psi_1(X^{(1)})\rangle$, where $X^{(1)}$ is the optimum value of $\tilde{X}^{(1)}$ obtained by minimizing $E_1(\tilde{X}^{(1)})$, equation (127).

For the k th excited state, we can define the trial wave function for variational calculations as

$$|\tilde{\Psi}_k(\tilde{X}^{(k)})\rangle = |\Psi_k(\tilde{X}^{(k)})\rangle - \sum_{m=0}^{k-1} \langle \Psi_m | \Psi_k(\tilde{X}^{(k)}) \rangle |\Psi_m\rangle, \quad (128)$$

where $|\Psi_m\rangle$, $m = 1, \dots, k-1$, are the previously computed lower-energy states and

$$|\Psi_k(\tilde{X}^{(k)})\rangle = \mathcal{N}_k e^{\tilde{X}^{(k)}} |\tilde{\Phi}_k\rangle \quad (129)$$

is the normalized $\exp(X)$ -like form of the k th excited state $|\Psi_k\rangle$, with $|\tilde{\Phi}_k\rangle$ representing the reference state for the k th excited state. By minimizing the energy functional

$$E_k(\tilde{X}^{(k)}) = \frac{\langle \tilde{\Psi}_k(\tilde{X}^{(k)}) | H | \tilde{\Psi}_k(\tilde{X}^{(k)}) \rangle}{\langle \tilde{\Psi}_k(\tilde{X}^{(k)}) | \tilde{\Psi}_k(\tilde{X}^{(k)}) \rangle} \quad (130)$$

over all two-body operators $\tilde{X}^{(k)} \in \mathcal{M}$, we obtain the energy of the k th excited state and the corresponding wave function $|\Psi_k\rangle \equiv |\Psi_k(X^{(k)})\rangle$, where $X^{(k)}$ is the optimum value of $\tilde{X}^{(k)}$.

Since excited states of many-electron systems are almost always very multi-determinantal and since they often have significant singly excited components, we may improve accuracies and accelerate the convergence of the numerical calculations for excited states based on equations (124)–(130) by using equation (107) (rather than equation (106)) to represent operator $\tilde{X}^{(k)}$, while obtaining the reference states $|\tilde{\Phi}_k\rangle$ by diagonalizing the Hamiltonian H in a small space spanned by a few Slater determinants that we believe are important to describe the ground and excited states of interest. This is what we did in our test excited-state calculations described below.

4.2. Numerical results

In our test calculations for a few many-electron systems, we first concentrated on the following two aspects of the $\exp(X)$ theory: (i) the existence of finite coefficients x_{pq}^{rs} defining the two-body operator X , equation (106), and (ii) the non-Hamiltonian nature of the operator X . Initially, we focused on the ground-state theory. We tested the exact ground-state theory, in which we used the unexpanded form of the exponential operator $e^{\tilde{X}}$ to define the $E_0(\tilde{X})$ energy rather than the truncated power series expansion in \tilde{X} . This was made possible by representing the operators H and \tilde{X} as matrices in the finite-dimensional N -electron Hilbert spaces relevant to a many-electron system under consideration (using all symmetry-adapted Slater determinants $|\Phi_0\rangle$ and $|\Phi_{i_1 \dots i_n}^{a_1 \dots a_n}\rangle$, $n = 1, \dots, N$, defining the

full CI problem, as basis states). In order to calculate the exact value of $E_0(\tilde{X})$, equation (116), in a given iteration of the numerical procedure used to minimize $E_0(\tilde{X})$, we first diagonalized the matrix representing \tilde{X} with some unitary matrix \tilde{U} to obtain the diagonal matrix $\tilde{D} = \tilde{U}\tilde{X}\tilde{U}^{-1}$. Next, we constructed $e^{\tilde{D}}$ by taking the exponentials of the diagonal elements of \tilde{D} . Finally, after constructing $e^{\tilde{D}}$, we calculated the matrix representing $e^{\tilde{X}}$ as $\tilde{U}^{-1}e^{\tilde{D}}\tilde{U}$ and applied it to a column vector representing $|\Phi_0\rangle$ to obtain $|\Psi_0(\tilde{X})\rangle$ according to equation (105). The value of $E_0(\tilde{X})$ was obtained by calculating $\langle\Psi_0(\tilde{X})|H|\Psi_0(\tilde{X})\rangle/\langle\Psi_0(\tilde{X})|\Psi_0(\tilde{X})\rangle$, using the matrices representing H and $|\Psi_0(\tilde{X})\rangle$, as described above. In order to determine the optimum operator X and the corresponding energy $E_0(X)$, we used the downhill simplex method [82] to minimize the energy $E_0(\tilde{X})$ in \mathcal{M} (recall that \mathcal{M} is a family of all two-body operators). Typically, our calculations required ~ 100 iterations to obtain a reasonably converged result, although in some cases we had to iterate much longer, particularly if we wanted to determine high decimal places. We realize that the numerical procedures used to obtain the optimum operator X are not suitable for routine calculations or for larger many-electron systems. The main point of this study is addressing the more fundamental question if the exact or virtually exact many-fermion wave functions can be represented by equation (105). In this context, the efficiency of the numerical procedures used to determine X is of no major importance.

Our test calculations were performed for a few many-electron systems, including, among others, the 8-electron/16-spin-orbital H8 model [120], which consists of eight hydrogen atoms arranged in a distorted octagonal configuration and described by the minimum basis set (MBS) obtained by placing one s function on each hydrogen atom. An example of the H8 model is very important for the discussion of the exactness of equation (105). This model provides us with a highly non-trivial situation, where the number of independent two-body parameters x_{pq}^{rs} , defining operator X , or the number of independent two-body integrals h_{pq}^{rs} , defining the Hamiltonian, is considerably smaller than the dimension of the corresponding N -electron Hilbert space. Indeed, the number of two-body parameters x_{pq}^{rs} defining operator X is in this case 186, whereas the number of all spin- and symmetry-adapted configurations defining the corresponding full CI problem is 468. The one-body parameters x_p^q that enter equation (107) do not change this situation. The total number of one- and two-body parameters defining X , equation (107), is 198, which is still a lot less than the number of full CI configurations describing the exact wave function. The H8 model is described by a single parameter α (in bohr), which describes the deviation of the geometry of the D_{2h} -symmetric H8 system from the regular octagon [120]. The following values of α were particularly important for testing: $\alpha = 1.0$ and $\alpha = 0.0001$. The $\alpha = 1.0$ H8 system is somewhat less demanding, since in this case the exact ground-state wave function is dominated by the RHF configuration $|\Phi_0\rangle$. The more demanding $\alpha = 0.0001$ H8 model is characterized by a strong configurational quasi-degeneracy of the ground electronic state involving the RHF reference $|\Phi_0\rangle$ and the doubly excited configuration $|\Phi_1\rangle$ of the HOMO–LUMO type [120].

The results of our calculations for the ground-state of the MBS H8 system are shown in Table 8. As we can see, the $\exp(X)$ ansatz gives remarkably accurate results for the ground-state of H8, even when the overlap of the reference state is as small as 0.668268, as is the case when $\alpha = 0.0001$ and we use the RHF determinant as a reference. Independent of the value of α , we obtain microhartree accuracies, which are a lot better than the accuracies resulting from various traditional CI and CC calculations. Our $\exp(X)$ calculations for the ground state employing two-body or one- plus two-body operators X are order of

Table 8. A comparison of the ground-state energies of the MBS H8 system obtained with the $\exp(X)$ -like wave functions, where $X = X_2$ (a purely two-body operator) or $X_1 + X_2$ (a sum of one- and two-body operators), with the exact, full CI, energies and energies obtained in various CI and CC calculations. Full CI energies are total energies in hartree and all other energies are errors relative to full CI (also in hartree). We also give the overlaps of the normalized ground-state wave functions obtained with the $\exp(X)$ ansatz and the full CI approach. The overlaps of the reference states $|\Phi_0\rangle$ and $|\tilde{\Phi}_0\rangle$ with the full CI ground-state wave function $|\Psi_0\rangle$ are given for comparison

Method (wave function)	Number of parameters in the wave function	$\alpha = 1.0$	$\alpha = 0.0001$
<i>Energies</i>			
Full CI	467	-4.352990	-4.204803
$\mathcal{N}_0 \exp(X_2) \Phi_0\rangle^a$	186	0.000008	0.000052
$\mathcal{N}_0 \exp(X_1 + X_2) \Phi_0\rangle^a$	198	0.000002	0.000020
$\tilde{\mathcal{N}}_0 \exp(X_1 + X_2) \tilde{\Phi}_0\rangle^b$	198	0.000005	0.000007
CISD	46	0.008396	0.022779
CISDT	146	0.007984	0.016064
CISDTQ	320	0.000254	0.000449
CCSD	46	0.000546	0.005034
CCSDT	146	0.000026	-0.008362
CCSDTQ	320	-0.000001	-0.000035
<i>Overlaps with a full CI wave function</i>			
$\mathcal{N}_0 \exp(X_2) \Phi_0\rangle^a$		0.999998	0.999987
$\mathcal{N}_0 \exp(X_1 + X_2) \Phi_0\rangle^a$		0.999999	0.999995
$\tilde{\mathcal{N}}_0 \exp(X_1 + X_2) \tilde{\Phi}_0\rangle^b$		0.999998	0.999998
$ \Phi_0\rangle^a$		0.939657	0.668268
$ \tilde{\Phi}_0\rangle^b$		0.942804	0.909461

^a $|\Phi_0\rangle$ is the ground-state RHF determinant.

^b $|\tilde{\Phi}_0\rangle = c_{00}|\Phi_0\rangle + c_{10}|\Phi_1\rangle$, where $|\Phi_0\rangle$ is the RHF determinant and $|\Phi_1\rangle$ is the doubly excited determinant of the (HOMO)² \rightarrow (LUMO)² type. The coefficients c_{00} and c_{10} defining the reference $|\tilde{\Phi}_0\rangle$ were obtained by diagonalizing the Hamiltonian in a space spanned by $|\Phi_0\rangle$ and $|\Phi_1\rangle$ and by selecting the lower energy eigenstate of H in this two-dimensional subspace as $|\tilde{\Phi}_0\rangle$.

magnitude more accurate than the CISD and CCSD calculations, which also use one- and two-body operators only. In fact, the $\exp(X)$ calculations provide a significantly better description of the ground state than the CISDTQ calculations employing one-, two-, three-, and four-body excitations. The number of parameters used to describe the CISDTQ wave function is much bigger than the number of parameters used to define our $\exp(X)$ wave functions. The results of our $\exp(X)$ calculations employing at most two-body operators are as good as or even better than the CCSDTQ results. In fact, by using one- and two-body parameters in X and the two-determinantal reference $|\tilde{\Phi}_0\rangle$ (see footnote “b” in Table 8), we obtain the results which are considerably better than those obtained with CCSDTQ, when the challenging case of the quasi-degenerate $\alpha = 0.0001$ H8 model is examined.

Table 9. Same as Table 8 for the first excited state of the 1A_g symmetry

Method (wave function)	Number of parameters in the wave function	$\alpha = 1.0$	$\alpha = 0.0001$
<i>Energies</i>			
Full CI	467	−3.998978	−4.144027
$\tilde{\mathcal{N}}_1 \exp(X_1 + X_2) \tilde{\Phi}_1\rangle^a$	198	0.000396	0.000020
CISD	46	0.059314	0.042374
CISDT	146	0.031697	0.009726
CISDTQ	320	0.001608	0.000435
EOMCCSD	46	0.019605	0.015011
EOMCCSDT	146	−0.003174	−0.010505
EOMCCSDTQ	320	−0.000140	−0.000384
<i>Overlaps with a full CI wave function</i>			
$\tilde{\mathcal{N}}_1 \exp(X_1 + X_2) \tilde{\Phi}_1\rangle^a$		0.999998	0.999992
$ \tilde{\Phi}_1\rangle^a$		0.791762	0.902255

^a $|\tilde{\Phi}_1\rangle = c_{01}|\Phi_0\rangle + c_{11}|\Phi_1\rangle$, where $|\Phi_0\rangle$ is the RHF determinant and $|\Phi_1\rangle$ is the doubly excited determinant of the $(\text{HOMO})^2 \rightarrow (\text{LUMO})^2$ type. The coefficients c_{01} and c_{11} defining the reference $|\tilde{\Phi}_1\rangle$ were obtained by diagonalizing the Hamiltonian in a space spanned by $|\Phi_0\rangle$ and $|\Phi_1\rangle$ and by selecting the higher energy eigenstate of H in this two-dimensional subspace as $|\tilde{\Phi}_1\rangle$.

As we can see, the presence of one-body operator $X_1 = x_p^q c^p c_q$ in X improves the convergence toward the full CI results. The use of a two-determinantal reference state $|\tilde{\Phi}_0\rangle$, which reflects the predominantly two-determinantal character of the ground-state wave function at $\alpha = 0.0001$, has a positive impact on the accuracy of $\exp(X)$ calculations. Even if our numerical procedures do not produce the exact (in a mathematical sense) energies, the microhartree accuracies, obtained with the exponential cluster expansions involving up to two-body operators only, are truly intriguing. The parameters x_{pq}^{rs} or x_p^q and x_{pq}^{rs} defining the optimum operators X are finite. For example, if we optimize X assuming that $X = X_2 = \frac{1}{2} x_{pq}^{rs} c^p c^q c_s c_r$, the largest values of x_{pq}^{rs} obtained in our ground-state calculations are 0.316845 at $\alpha = 1.0$ and 0.596623 at $\alpha = 0.0001$. The corresponding operators X do not commute with the Hamiltonian, so that the optimum X operators producing the highly accurate results in Table 8 are not of the Hamiltonian form.

In Table 9 we show the results of the $\exp(X)$ calculations for the first excited state of the 1A_g symmetry. This state is dominated by the RHF configuration $|\Phi_0\rangle$ and the doubly excited determinant of the HOMO–LUMO type $|\Phi_1\rangle$ in the quasi-degenerate, $\alpha = 0.0001$, region, so that it is natural to choose a two-determinantal state $|\tilde{\Phi}_1\rangle = c_{01}|\Phi_0\rangle + c_{11}|\Phi_1\rangle$ as a reference in our $\exp(X)$ calculations (see footnote “a” in Table 9). The $\exp(X)$ calculations for the first excited 1A_g state were performed using the numerical procedure described in Section 4.1.3. To facilitate our numerical effort, we considered the truncated form of the $\exp(X)$ expansion, where the $\exp(X)$ series is truncated at the X^{50} term. Since the optimum coefficients x_p^q and x_{pq}^{rs} are rather small (<1) and X^n enters the $\exp(X)$ expansion as $\frac{1}{n!} X^n$, the truncation of the $\exp(X)$ expansion at the $\frac{1}{50!} X^{50}$ term produces essentially no errors (errors that cannot be detected in numerical calculations with the dou-

ble precision Fortran). As shown in Table 9, the $\exp(X)$ calculations for the first excited 1A_g state of H8 at $\alpha = 0.0001$ produce microhartree accuracies. For $\alpha = 1.0$ we obtained a somewhat larger error on the order of 0.4 millihartree, but this can be understood if we realize that the reference state $|\tilde{\Phi}_1\rangle$ is not a good representation of the exact first excited-state wave function in this region of α , slowing down the convergence. We must realize, however, that this error is on the same order as the error resulting from the equation-of-motion (EOM) CCSDTQ calculations (for basic information about EOMCC methods, see, *e.g.*, Refs. [9,60,63]), which use a much larger number of parameters to define the corresponding wave function than the $\exp(X)$ expansion employing one- and two-body parameters only. For $\alpha = 0.0001$, the $\exp(X)$ calculations give a microhartree-level accuracy for the first excited 1A_g state of H8. None of the conventional CI or CC methods, including CISDTQ or even EOMCCSDTQ can produce the results of this quality.

4.3. Summary

Let us summarize the results discussed in this final section. By combining the theoretical arguments based on the Horn–Weinstein energy expression with variational principle and numerical calculations, we demonstrated that one can obtain the virtually exact description of pairwise interacting many-fermion systems, including molecular systems, by representing their ground- and excited-state wave functions by exponential cluster expansions employing general two-body or one- and two-body operators. Based on the evidence reported in this section, we can conclude that the optimum two-body or one- and two-body operators defining these cluster expansions are finite and not of the Hamiltonian form. Our results show that one can tremendously improve the description of many-electron wave functions without using higher-than-two-body cluster operators. All of this implies that there remains a lot of flexibility in the exponential cluster expansions, which was not utilized in the past. Based on the formal arguments and the extraordinarily high accuracies obtained in the calculations based on the $\exp(X)$ expansions, where X is a sum of one- and two-body components or a purely two-body operator, we can conclude that it is possible to formulate the virtually exact many-electron theories based on these kinds of expansions.

ACKNOWLEDGEMENTS

This work has been supported by the Chemical Sciences, Geosciences and Biosciences Division, Office of Basic Energy Sciences, Office of Science, U.S. Department of Energy (grant DE-FG02-01ER15228).

REFERENCES

- [1] F. Coester, *Nucl. Phys.* **7** (1958) 421.
- [2] F. Coester, H. Kümmel, *Nucl. Phys.* **17** (1960) 477.
- [3] J. Čížek, *J. Chem. Phys.* **45** (1966) 4256.
- [4] J. Čížek, *Adv. Chem. Phys.* **14** (1969) 35.
- [5] J. Čížek, J. Paldus, *Int. J. Quantum Chem.* **5** (1971) 359.

- [6] J. Paldus, in: S. Wilson, G. Diercksen (Eds.), *Methods in Computational Molecular Physics*, NATO Advanced Study Institute Series B: Physics, vol. 293, Plenum, New York, 1992, pp. 99–194.
- [7] R.J. Bartlett, in: D.R. Yarkony (Ed.), *Modern Electronic Structure Theory, Part I*, World Scientific, Singapore, 1995, pp. 1047–1131.
- [8] J. Gauss, in: P. von Raqué Schleyer, N.L. Allinger, T. Clark, J. Gasteiger, P.A. Kollman, H.F. Schaefer III (Eds.), *The Encyclopedia of Computational Chemistry*, vol. 1, Wiley, Chichester, 1998, pp. 615–636.
- [9] J. Paldus, X. Li, *Adv. Chem. Phys.* **110** (1999) 1.
- [10] T.D. Crawford, H.F. Schaefer III, *Rev. Comp. Chem.* **14** (2000) 33.
- [11] P. Piecuch, K. Kowalski, in: J. Leszczyński (Ed.), *Computational Chemistry: Reviews of Current Trends*, vol. 5, World Scientific, Singapore, 2000, pp. 1–104.
- [12] P. Piecuch, K. Kowalski, I.S.O. Pimienta, S.A. Kucharski, in: M.R. Hoffmann, K.G. Dyall (Eds.), *Low-Lying Potential Energy Surfaces*, vol. 828, Am. Chem. Soc., Washington, DC, 2002, pp. 31–64.
- [13] P. Piecuch, K. Kowalski, I.S.O. Pimienta, M.J. McGuire, *Int. Rev. Phys. Chem.* **21** (2002) 527.
- [14] G.D. Purvis III, R.J. Bartlett, *J. Chem. Phys.* **76** (1982) 1910.
- [15] M. Urban, J. Noga, S.J. Cole, R.J. Bartlett, *J. Chem. Phys.* **83** (1985) 4041.
- [16] K. Raghavachari, G.W. Trucks, J.A. Pople, M. Head-Gordon, *Chem. Phys. Lett.* **157** (1989) 479.
- [17] G.E. Scuseria, A.E. Scheiner, T.J. Lee, J.E. Rice, H.F. Schaefer III, *J. Chem. Phys.* **86** (1987) 2881.
- [18] G.E. Scuseria, C.L. Janssen, H.F. Schaefer III, *J. Chem. Phys.* **89** (1988) 7382.
- [19] T.J. Lee, J.E. Rice, *Chem. Phys. Lett.* **150** (1988) 406.
- [20] P. Piecuch, J. Paldus, *Int. J. Quantum Chem.* **36** (1989) 429.
- [21] P. Piecuch, J. Paldus, *Theor. Chim. Acta* **78** (1990) 65.
- [22] P. Piecuch, R. Toboła, J. Paldus, *Int. J. Quantum Chem.* **55** (1995) 133.
- [23] S.A. Kucharski, R.J. Bartlett, *J. Chem. Phys.* **108** (1998) 9221.
- [24] W.D. Laidig, P. Saxe, R.J. Bartlett, *J. Chem. Phys.* **86** (1987) 887.
- [25] K.B. Ghose, P. Piecuch, L. Adamowicz, *J. Chem. Phys.* **103** (1995) 9331.
- [26] P. Piecuch, V. Špirko, A.E. Kondo, J. Paldus, *J. Chem. Phys.* **104** (1996) 4699.
- [27] L. Adamowicz, P. Piecuch, K.B. Ghose, *Mol. Phys.* **94** (1998) 225.
- [28] P. Piecuch, S.A. Kucharski, R.J. Bartlett, *J. Chem. Phys.* **110** (1999) 6103.
- [29] P. Piecuch, S.A. Kucharski, V. Špirko, *J. Chem. Phys.* **111** (1999) 6679.
- [30] K. Kowalski, P. Piecuch, *J. Chem. Phys.* **113** (2000) 18.
- [31] K. Kowalski, P. Piecuch, *J. Chem. Phys.* **113** (2000) 5644.
- [32] K. Kowalski, P. Piecuch, *J. Mol. Struct. (Theochem)* **547** (2001) 191.
- [33] K. Kowalski, P. Piecuch, *Chem. Phys. Lett.* **344** (2001) 165.
- [34] P. Piecuch, S.A. Kucharski, K. Kowalski, *Chem. Phys. Lett.* **344** (2001) 176.
- [35] P. Piecuch, S.A. Kucharski, V. Špirko, K. Kowalski, *J. Chem. Phys.* **115** (2001) 5796.
- [36] P. Piecuch, K. Kowalski, I.S.O. Pimienta, *Int. J. Mol. Sci.* **3** (2002) 475.
- [37] M.J. McGuire, K. Kowalski, P. Piecuch, *J. Chem. Phys.* **117** (2002) 3617.
- [38] Y.S. Lee, R.J. Bartlett, *J. Chem. Phys.* **80** (1984) 4371.
- [39] Y.S. Lee, S.A. Kucharski, R.J. Bartlett, *J. Chem. Phys.* **81** (1984) 5906; *J. Chem. Phys.* **82** (1985) 5761 (Erratum).
- [40] J. Noga, R.J. Bartlett, M. Urban, *Chem. Phys. Lett.* **134** (1987) 126.
- [41] G.W. Trucks, J. Noga, R.J. Bartlett, *Chem. Phys. Lett.* **145** (1988) 548.
- [42] S.A. Kucharski, R.J. Bartlett, *Chem. Phys. Lett.* **158** (1989) 550.
- [43] J. Noga, R.J. Bartlett, *J. Chem. Phys.* **86** (1987) 7041; *J. Chem. Phys.* **89** (1988) 3401 (Erratum).
- [44] G.E. Scuseria, H.F. Schaefer III, *Chem. Phys. Lett.* **152** (1988) 382.
- [45] S.A. Kucharski, R.J. Bartlett, *Theor. Chim. Acta* **80** (1991) 387.
- [46] S.A. Kucharski, R.J. Bartlett, *J. Chem. Phys.* **97** (1992) 4282.
- [47] N. Oliphant, L. Adamowicz, *J. Chem. Phys.* **95** (1991) 6645.
- [48] P. Piecuch, L. Adamowicz, *J. Chem. Phys.* **100** (1994) 5792.
- [49] M. Musiał, S.A. Kucharski, R.J. Bartlett, *J. Chem. Phys.* **116** (2002) 4382.
- [50] J.S. Arponen, *Ann. Phys.* **151** (1983) 311.
- [51] J.S. Arponen, R.F. Bishop, E. Pajanne, *Phys. Rev. A* **36** (1987) 2519.
- [52] J.S. Arponen, R.F. Bishop, E. Pajanne, *Condensed Matter Theor.* **2** (1987) 357.
- [53] R.F. Bishop, J.S. Arponen, E. Pajanne, in: D. Mukherjee (Ed.), *Aspects of Many-Body Effects in Molecules and Extended Systems, Lecture Notes in Chemistry*, vol. 50, Springer-Verlag, Berlin, 1989, pp. 79–100.
- [54] R.F. Bishop, J.S. Arponen, *Int. J. Quantum Chem. Symp.* **24** (1990) 197.

- [55] J.S. Arponen, R.F. Bishop, *Ann. Phys.* **207** (1991) 171.
- [56] R.F. Bishop, N.I. Robinson, J.S. Arponen, *Condensed Matter Theor.* **5** (1990) 37.
- [57] R.F. Bishop, *Theor. Chim. Acta* **80** (1991) 95.
- [58] J.S. Arponen, *Phys. Rev. A* **55** (1997) 2686.
- [59] J.S. Arponen, R.F. Bishop, E. Pajanne, *Phys. Rev. A* **36** (1987) 2539.
- [60] P. Piecuch, R.J. Bartlett, *Adv. Quantum Chem.* **34** (1999) 295.
- [61] E.A. Salter, G.W. Trucks, R.J. Bartlett, *J. Chem. Phys.* **90** (1989) 1752.
- [62] E.A. Salter, R.J. Bartlett, *J. Chem. Phys.* **90** (1989) 1767.
- [63] J.F. Stanton, R.J. Bartlett, *J. Chem. Phys.* **98** (1993) 7029.
- [64] J.F. Stanton, R.J. Bartlett, *J. Chem. Phys.* **99** (1993) 5178.
- [65] S. Pal, *Theor. Chim. Acta* **66** (1984) 151.
- [66] S. Pal, *Phys. Rev. A* **33** (1986) 2240.
- [67] S. Pal, *Phys. Rev. A* **34** (1986) 2682.
- [68] K.B. Ghose, S. Pal, *Phys. Rev. A* **36** (1987) 1539.
- [69] N. Vaval, K.B. Ghose, S. Pal, *J. Chem. Phys.* **101** (1994) 4914.
- [70] N. Vaval, S. Pal, *Phys. Rev. A* **54** (1996) 250.
- [71] A.B. Kumar, N. Vaval, S. Pal, *Chem. Phys. Lett.* **295** (1998) 189.
- [72] N. Vaval, A.B. Kumar, S. Pal, *Int. J. Mol. Sci.* **2** (2001) 89.
- [73] N. Vaval, *Chem. Phys. Lett.* **318** (2000) 168.
- [74] P. Piecuch, K. Kowalski, P.-D. Fan, I.S.O. Pimienta, in: J. Maruani, R. Lefebvre, E. Brändas (Eds.), *Advanced Topics in Theoretical Chemical Physics, Progress in Theoretical Chemistry and Physics*, vol. 12, Kluwer Academic, Dordrecht, 2003, pp. 119–206.
- [75] P. Piecuch, K. Kowalski, I.S.O. Pimienta, P.-D. Fan, M. Lodriguito, M.J. McGuire, S.A. Kucharski, T. Kuś, M. Musiał, *Theor. Chem. Acc.* **112** (2004) 349.
- [76] P. Piecuch, I.S.O. Pimienta, P.-D. Fan, K. Kowalski, in: A. Wilson, K. Peterson (Eds.), *Recent Progress in Electron Correlation Methodology, ACS Symposium Series*, Am. Chem. Soc., Washington, DC, 2006, in press.
- [77] P.-D. Fan, K. Kowalski, P. Piecuch, *Mol. Phys.* **103** (2005) 2191.
- [78] J. Paldus, P. Piecuch, L. Pylypow, B. Jeziorski, *Phys. Rev. A* **47** (1993) 2738.
- [79] P. Piecuch, J. Paldus, *Phys. Rev. A* **49** (1994) 3479.
- [80] P. Piecuch, R. Toboła, J. Paldus, *Chem. Phys. Lett.* **210** (1993) 243.
- [81] W.J. Hehre, R.F. Stewart, J.A. Pople, *J. Chem. Phys.* **51** (1969) 2657.
- [82] *Numerical Recipes in Fortran: The Art of Scientific Computing*, Cambridge Univ. Press, Cambridge, UK, 1992.
- [83] S.A. Kucharski, R.J. Bartlett, *J. Chem. Phys.* **108** (1998) 5243.
- [84] S.A. Kucharski, R.J. Bartlett, *J. Chem. Phys.* **108** (1998) 5255.
- [85] T.H. Dunning, *J. Chem. Phys.* **53** (1970) 2823.
- [86] P. Piecuch, M. Włoch, J.R. Gour, A. Kinal, *Chem. Phys. Lett.* **418** (2005) 463.
- [87] P. Piecuch, M. Włoch, *J. Chem. Phys.* **123** (2005) 224105.
- [88] K. Kowalski, P. Piecuch, *J. Chem. Phys.* **115** (2001) 2966.
- [89] K. Kowalski, P. Piecuch, *J. Chem. Phys.* **116** (2002) 7411.
- [90] K. Kowalski, P. Piecuch, *J. Chem. Phys.* **120** (2004) 1715.
- [91] P. Piecuch, K. Kowalski, *Int. J. Mol. Sci.* **3** (2002) 676.
- [92] K. Kowalski, P. Piecuch, *Mol. Phys.* **102** (2004) 2425.
- [93] I.S.O. Pimienta, K. Kowalski, P. Piecuch, *J. Chem. Phys.* **119** (2003) 2951.
- [94] P. Piecuch, K. Kowalski, I.S.O. Pimienta, *Int. J. Mol. Sci.* **3** (2002) 475.
- [95] P. Piecuch, M. Włoch, M. Lodriguito, J.R. Gour, in: J.-P. Julien, J. Maruani, D. Mayou, S. Wilson, G. Delgado-Barrio (Eds.), *Recent Advances in the Theory of Chemical and Physical Systems, Progress in Theoretical Chemistry and Physics*, vol. 15, Springer-Verlag, Berlin, 2006, pp. 45–106.
- [96] M.D. Lodriguito, K. Kowalski, M. Włoch, P. Piecuch, *J. Mol. Struct. (Theochem)* **771** (2006) 89.
- [97] P. Piecuch, S.A. Kucharski, K. Kowalski, M. Musiał, *Comput. Phys. Commun.* **149** (2002) 71.
- [98] M.J. McGuire, P. Piecuch, K. Kowalski, S.A. Kucharski, M. Musiał, *J. Phys. Chem. A* **108** (2004) 8878.
- [99] M.J. McGuire, P. Piecuch, *J. Am. Chem. Soc.* **127** (2005) 2608.
- [100] A. Kinal, P. Piecuch, *J. Phys. Chem. A* **110** (2006) 367.
- [101] K. Kowalski, P. Piecuch, *J. Chem. Phys.* **122** (2005) 074107.
- [102] C.J. Cramer, M. Włoch, P. Piecuch, C. Puzzarini, L. Gagliardi, *J. Phys. Chem. A* **110** (2006) 1991.

- [103] H. Weyl, *The Classical Groups, Their Invariants and Representations*, Princeton Univ. Press, Princeton, NJ, 1946.
- [104] C.D. Sherrill, H.F. Schaefer III, *Adv. Quantum Chem.* **34** (1999) 143.
- [105] M. Nooijen, *Phys. Rev. Lett.* **84** (2000) 2108.
- [106] H. Nakatsuji, *J. Chem. Phys.* **113** (2000) 2949.
- [107] H. Nakatsuji, E.R. Davidson, *J. Chem. Phys.* **115** (2001) 2000.
- [108] H. Nakatsuji, *J. Chem. Phys.* **115** (2001) 2465.
- [109] H. Nakatsuji, *J. Chem. Phys.* **116** (2002) 1811.
- [110] T. Van Voorhis, M. Head-Gordon, *J. Chem. Phys.* **115** (2001) 5033.
- [111] P. Piecuch, K. Kowalski, P.-D. Fan, K. Jedziniak, *Phys. Rev. Lett.* **90** (2003) 113001.
- [112] M. Nooijen, V. Lotrich, *J. Chem. Phys.* **113** (2000) 4549.
- [113] H. Nakatsuji, *Phys. Rev. A* **14** (1976) 41.
- [114] S. Ronen, *Phys. Rev. Lett.* **91** (2003) 123002.
- [115] E.R. Davidson, *Phys. Rev. Lett.* **91** (2003) 123001.
- [116] D.A. Mazziotti, *Phys. Rev. A* **69** (2004) 012507.
- [117] D. Mukherjee, W. Kutzelnigg, *Chem. Phys. Lett.* **397** (2004) 174.
- [118] W. Kutzelnigg, D. Mukherjee, *Phys. Rev. A* **71** (2005) 022502.
- [119] D. Horn, M. Weinstein, *Phys. Rev. D* **30** (1984) 1256.
- [120] K. Jankowski, L. Meissner, J. Wasilewski, *Int. J. Quantum Chem.* **28** (1985) 931.

This page intentionally left blank

Angular Momentum Diagrams

Paul E.S. Wormer¹ and Josef Paldus²

¹*Theoretical Chemistry, Institute for Molecules and Materials, Radboud University Nijmegen,
Toernooiveld, 6525 ED Nijmegen, The Netherlands
E-mail: pwormer@teochem.ru.nl*

²*Department of Applied Mathematics, Department of Chemistry, and Guelph-Waterloo Center for Graduate
Work in Chemistry—Waterloo Campus, University of Waterloo, Waterloo, Ontario, Canada, N2L 3G1
E-mail: paldus@scienide.uwaterloo.ca*

Abstract

Starting from the simplest possible building blocks—a ket, a bra, a time-reversed ket, and a time-reversed bra—a diagrammatic formalism is developed for angular momentum coupling problems. The formalism comprises Clebsch–Gordan coefficients as well as $3jm$ -symbols. The idea of constructing invariants (internal lines) by contracting contragredient pairs of quantities is emphasized throughout. The Clebsch–Gordan series, and its extension to the coupling of more than two angular momenta, is introduced algebraically and diagrammatically. Recoupling between bases obtained in different coupling schemes is introduced and the connection between recoupling coefficients and irreducible $3nj$ -symbols is derived diagrammatically. The well-known diagrammatic rules due to Jucys and co-workers are derived by group theoretical means and simple rules for their practical exploitation are presented.

Contents

1. Introduction	60
2. The essentials of SU(2)	62
2.1. Exponential form of SU(2) elements	62
2.2. Second-quantized representation	63
2.3. Contragredient representations	67
2.4. Time reversal	69
2.5. Clebsch–Gordan series	71
3. Diagrams	74
3.1. Basic diagrammatic building blocks	74
3.2. Clebsch–Gordan diagrams	77
3.3. $1jm$ -symbol	80
3.4. Generalized Clebsch–Gordan coefficients	81
3.5. $3jm$ -symbols	83
3.6. Transition from CG coefficients to $3jm$ -symbols	87
4. Basic rules for angular momentum diagrams	89
4.1. Removal of a zero line	90
4.2. Factorization rules	92
4.3. Separation rules	97
5. Irreducible closed diagrams	101
5.1. $1j$ - and $3j$ -symbols	102
5.2. Recoupling and the $6j$ - and $9j$ -symbols	102
5.3. Properties of the $6j$ -symbol	106
The $6j$ -symbol is invariant under any permutation of its vertices	106
The $6j$ -symbol is invariant with respect to the interchange of the rows in any two of its columns	107

5.4. Properties of the $9j$ -symbol	110
5.5. Higher $3nj$ -symbols	113
6. Concluding remarks	113
Acknowledgement	115
Appendix: Summary of the graphical rules	115
Basic units	115
Basic rules	116
$1jm$ -symbol	116
Clebsch–Gordan coefficients and diagrams	116
$3jm$ -symbols and diagrams	117
Transition from CG to $3jm$ -diagrams	118
Diagram manipulation	118
Basic irreducible diagrams; $3nj$ -symbols	120
References	121

1. INTRODUCTION

The origins of the coupling problem for angular momenta can be traced back to the early—purely mathematical—work on invariant theory (Refs. [1,2]) by (Rudolf Friedrich) Alfred Clebsch (1833–1872) and Paul (Albert) Gordan (1837–1912), see Section 2.5. Even before the birth of quantum mechanics the formal analogy between chemical valence theory and binary invariant theory was recognized by eminent mathematicians as Sylvester [3], Clifford [4], and Gordan and Alexejeff [5]. The analogy, lacking a physical basis at the time, was criticized heavily by the mathematician E. Study and ignored completely by the chemistry community of the 1890s. After the advent of quantum mechanics it became clear, however, that chemical valences arise from electron-spin couplings, see, *e.g.*, Rumer, Teller, and Weyl [6] and that electron-spin functions are, in fact, binary forms of the type studied by Gordan and Clebsch.

Angular momentum is of great physical importance because it represents a constant of the motion for rotationally invariant systems. Although this observation is as true in classical mechanics as it is in quantum mechanics, it is not of great help in solving the problems of classical mechanics. However, quantum mechanics and the aid of symmetry in solving the Schrödinger equation, brought angular momentum theory to its prominence. From a mathematical viewpoint, this theory is equivalent to the study of the representation theory of the unitary unimodular group $SU(2)$. There is hardly a textbook on quantum theory that would not include a chapter or a section dealing with the orbital and spin angular momenta, not to mention a number of specialized publications on the subject, see, *e.g.*, Refs. [7–17]. (For a more exhaustive reference list Ref. [13] may be consulted.)

The present review introduces the diagrammatic representation of angular momentum theory. This representation is mainly due to Jucys¹ and his co-workers. In their 1962 book [18] Jucys, Levinson, and Vanagas (JLV) based their diagrams completely on $3j$ -symbols (which for reasons that will become clear later, will be referred to as $3jm$ -symbols from here on). In a later book Jucys and Bandzaitis [19] worked solely with Clebsch–Gordan (CG) coefficients. These coefficients have the advantage that they allow the formulation of an angular momentum problem in the most natural way, namely in terms of eigenkets and eigenbras of angular momentum operators. However, CG coefficients have

¹ Due to transcriptions from Lithuanian (which uses the Latin alphabet) into the Cyrillic alphabet and back, one often finds different spellings, *e.g.*, Yutsis, Yuzis, Ioucis, *etc.* The correct Lithuanian spelling is Jucys.

the disadvantage that their symmetry relations are awkward and that the reduction of an angular momentum problem to irreducible quantities (*i.e.*, $6j$ -, $9j$ -, \dots , $3nj$ -symbols) is difficult. El Baz and Castel [20] introduced a graphical formalism that incorporates both types of coefficients: $3jm$ -symbols and CG coefficients. The formalism introduced below is inspired by their work, but avoids two problems present in their formalism. In the first place El Baz and Castel identify a bra with a time-reversed ket and although both quantities transform identically under $SU(2)$, they are not the same. Second, they do not distinguish diagrammatically the unique pair of quantum numbers in a CG coefficient, which is an important characteristic of a CG coefficient.

In their 1993 book [21] Brink and Satchler (BS) present a diagrammatic formalism that has a large overlap with the JLV $3jm$ -formalism. The two differ mainly in that BS suppress line orientations when these may be freely flipped (*i.e.*, without introduction of phase). Furthermore, BS claim that their approach has the advantage over the JLV approach that CG coefficients can be handled, which allegedly cannot be done in the JLV formalism. Since BS simply use the fact that a CG coefficient is proportional to a $3jm$ -symbol and since they do not attempt to represent the proportionality factor diagrammatically, it is hard to endorse this advantage.

The diagrammatic technique of angular momentum theory can be, in principle, generalized to handle Racah–Wigner algebras of arbitrary compact groups. In this regard, we refer an interested reader to the monograph by Stedman [22] and to an extensive paper by Kibler and El Baz [23] and references therein. However, in this work we restrict our attention to the group $SU(2)$ and focus on the exploitation of graphical techniques of spin algebras for the angular momentum problems arising in atomic and molecular physics.

Before introducing diagrams, we shall briefly review the necessary parts of angular momentum theory in the first few sections. The components of the angular momentum operator span the Lie algebra of $SO(3)$ (the group of unimodular (unit determinant) orthogonal (rotation) operators on real three-dimensional vector space), as well as of $SU(2)$ (which consists of unimodular, unitary operators on complex two-dimensional vector space), and so the quantum theory of angular momentum is closely intertwined with the representation theory of these two groups.

The group $SU(2)$ has two simplifying properties that related groups, such as $SU(3)$, do not possess. In the first place, the conjugacy classes of $SU(2)$ are ambivalent, *i.e.*, contain with an element $U \in SU(2)$ also its inverse U^{-1} . This implies that the characters of U and U^{-1} are equal in any representation (rep). Since in a unitary rep the character of an element and of its inverse are each others complex conjugate, it follows from the ambivalent nature of its classes that all characters of any unitary rep of $SU(2)$ are real. As a result, every rep is equivalent to its complex conjugate rep. The second simplifying property of $SU(2)$ is that its irreducible representations (irreps) are multiplicity free. This means that the reduction of a direct product of two irreps will yield any irrep at most once. Wigner [24] calls groups that possess these two properties *simply reducible*. If $SU(2)$ and $SO(3)$ had not been simply reducible, a diagrammatic description of their representation theory would have been much more cumbersome.

The following notes also introduce the concept of mixed $3jm$ -symbols, recoupling, and the $6j$ -, $9j$ -, \dots , $3nj$ -symbols. It is the belief of the authors that $3nj$ -coefficients are easier to grasp diagrammatically than algebraically.

2. THE ESSENTIALS OF SU(2)

We review the necessary theory of the group SU(2). First, we show that a general element can be written in exponential form and then we introduce a second-quantized basis carrying irreps of SU(2). The concept of standard and contrastandard representations is introduced and the connection with time reversal is pointed out. Finally, the Clebsch–Gordan series is discussed. The summation convention over repeated indices is used throughout. Also, the Cartesian coordinates are labeled by (x, y, z) or $(1, 2, 3)$.

2.1. Exponential form of SU(2) elements

The *Pauli spin matrices* [25]

$$\sigma_x = \begin{pmatrix} 0 & 1 \\ 1 & 0 \end{pmatrix}, \quad \sigma_y = \begin{pmatrix} 0 & -i \\ i & 0 \end{pmatrix}, \quad \sigma_z = \begin{pmatrix} 1 & 0 \\ 0 & -1 \end{pmatrix} \quad (1)$$

satisfy the relations

$$\sigma_j \sigma_k = \delta_{jk} \mathbf{1} + i \varepsilon_{jkl} \sigma_l, \quad (2)$$

where ε_{jkl} (the Levi–Civita tensor) is the totally antisymmetric tensor of rank 3 defined by

$$\varepsilon_{ijk} = \det(\hat{e}_i, \hat{e}_j, \hat{e}_k) \quad \text{for } i, j, k = 1, 2, 3,$$

and $\hat{e}_1, \hat{e}_2, \hat{e}_3$ form a right-handed orthonormal set of vectors. From equation (2) follows immediately that

$$\sigma_j \sigma_k - \sigma_k \sigma_j \equiv [\sigma_j, \sigma_k] = 2i \varepsilon_{jkl} \sigma_l.$$

Thus, defining operators \hat{s}_j by the action on the usual spin- $\frac{1}{2}$ functions

$$\hat{s}_j(|\alpha\rangle, |\beta\rangle) = (|\alpha\rangle, |\beta\rangle) \frac{1}{2} \sigma_j, \quad j = 1, 2, 3, \quad (3)$$

we obtain the usual angular momentum commutation relations

$$[\hat{s}_j, \hat{s}_k] = i \varepsilon_{jkl} \hat{s}_l.$$

It is easily seen that a 2×2 unimodular ($\det = 1$), unitary matrix is parametrized by two complex numbers, because

$$\mathbf{U}^{-1} \equiv \begin{pmatrix} u_{11} & u_{12} \\ u_{21} & u_{22} \end{pmatrix}^{-1} = \det(\mathbf{U})^{-1} \begin{pmatrix} u_{22} & -u_{12} \\ -u_{21} & u_{11} \end{pmatrix} = \mathbf{U}^\dagger = \begin{pmatrix} u_{11}^* & u_{21}^* \\ u_{12}^* & u_{22}^* \end{pmatrix}.$$

Since $\det(\mathbf{U}) = 1$, it follows, if we set $u_{11} \equiv u$ and $u_{12} \equiv v$, that

$$\mathbf{U} = \begin{pmatrix} u & v \\ -v^* & u^* \end{pmatrix}, \quad u, v \in \mathbb{C}. \quad (4)$$

We can introduce real parameters a_i ,

$$\begin{pmatrix} u & v \\ -v^* & u^* \end{pmatrix} = \begin{pmatrix} a_0 - ia_3 & -ia_1 - a_2 \\ -ia_1 + a_2 & a_0 + ia_3 \end{pmatrix} = a_0 \mathbf{1} - i \vec{\sigma} \cdot \vec{a}$$

with $\vec{a} \equiv (a_1, a_2, a_3)$ and where

$$\det(\mathbf{U}) = |u|^2 + |v|^2 = a_0^2 + a_1^2 + a_2^2 + a_3^2 = 1.$$

This parametrization is often referred to as the Euler–Rodrigues parametrization. It indicates that as an analytic manifold the Lie group $\text{SU}(2)$ is the three-dimensional surface of the unit sphere S^3 in \mathbb{R}^4 . The sphere S^3 is covered exactly once (except for the poles $\varphi = 0$ and $\varphi = 2\pi$) by $(a_0, \vec{a}) = (\cos \frac{\varphi}{2}, \vec{n} \sin \frac{\varphi}{2})$, where \vec{n} is a vector that ranges over the whole unit sphere S^2 in \mathbb{R}^3 and $0 \leq \varphi \leq 2\pi$. Hence,

$$\mathbf{U}(\vec{n}, \varphi) = \mathbf{1} \cos \frac{\varphi}{2} - i(\vec{\sigma} \cdot \vec{n}) \sin \frac{\varphi}{2}. \quad (5)$$

Since \vec{n} is a unit vector and $\vec{n} \times \vec{n} = \vec{0}$, we have, using summation convention, from equation (2):

$$(\vec{\sigma} \cdot \vec{n})^2 \equiv n_j n_k \sigma_j \sigma_k = n_j n_k \delta_{jk} \mathbf{1} + i(\vec{n} \times \vec{n})_l \sigma_l = \mathbf{1}.$$

This implies for positive integer p

$$(\vec{\sigma} \cdot \vec{n})^{2p} = \mathbf{1} \quad \text{and} \quad (\vec{\sigma} \cdot \vec{n})^{2p+1} = \vec{\sigma} \cdot \vec{n}, \quad (6)$$

so that the general element of $\text{SU}(2)$ can be written as

$$\mathbf{U}(\vec{n}, \varphi) = e^{-i(\vec{\sigma} \cdot \vec{n})\varphi/2}. \quad (7)$$

We note, finally, that a rotation by 2π over a fixed axis \vec{n} does not correspond to the identity operator, but

$$\mathbf{U}(\vec{n}, 2\pi) = \mathbf{1} \cos \pi - i(\vec{\sigma} \cdot \vec{n}) \sin \pi = -\mathbf{1} \quad (\neq \mathbf{U}(\vec{n}, 0) = \mathbf{1}).$$

We thus have to consider $0 \leq \varphi \leq 4\pi$ to cover the whole of $\text{SU}(2)$ (and must restrict the range of \vec{n} to a unit hemisphere if the group is to be covered once).

2.2. Second-quantized representation

Schwinger [26] introduced a second-quantized representation of angular momentum operators $\mathcal{J}_x, \mathcal{J}_y, \mathcal{J}_z$, that satisfy the usual commutation relations

$$[\mathcal{J}_j, \mathcal{J}_k] = i\varepsilon_{jkl} \mathcal{J}_l, \quad j, k, l = x, y, z. \quad (8)$$

He represented also their eigenstates, which span carrier spaces of the $\text{SU}(2)$ irreps, in second-quantized form. These eigenstates of the total angular momentum operators \mathcal{J}^2 and \mathcal{J}_z , designated by $|j, m\rangle$, are labeled by the quantum numbers j and m , with j labeling a given irrep and m the basis states of this irrep, $m = -j, -j+1, \dots, j-1, j$, and transform in the usual manner under the action of the step up and step down operators $\mathcal{J}_+ \equiv \mathcal{J}_x + i\mathcal{J}_y$ and $\mathcal{J}_- \equiv \mathcal{J}_x - i\mathcal{J}_y$, respectively, namely

$$\mathcal{J}^2 |j, m\rangle = |j, m\rangle j(j+1), \quad (9a)$$

$$\mathcal{J}_z |j, m\rangle = |j, m\rangle m, \quad (9b)$$

$$\mathcal{J}_\pm |j, m\rangle = |j, m \pm 1\rangle \sqrt{(j \mp m)(j \pm m + 1)}. \quad (9c)$$

Since Schwinger's second-quantization representation is very compact and facilitates the transition to the corresponding contragredient form, it is essential for the diagrammatic representation considered here.

In order to introduce Schwinger's formalism it is useful to recall the well-known second-quantized representation of a one-dimensional harmonic oscillator with the Hamiltonian

$$H = \hbar\omega \left(b^\dagger b + \frac{1}{2} \right), \quad (10)$$

where the creation and annihilation operators b^\dagger and b satisfy the boson commutation relations

$$[b, b^\dagger] = 1, \quad [b^\dagger, b^\dagger] = [b, b] = 0, \quad (11)$$

and the energies E_n and eigenstates $|n\rangle$ are given by

$$E_n = \hbar\omega \left(n + \frac{1}{2} \right) \quad \text{and} \quad |n\rangle = \frac{(b^\dagger)^n}{\sqrt{n!}} |0\rangle, \quad (12)$$

with the action

$$b|0\rangle = 0, \quad (13a)$$

$$b|n\rangle = |n-1\rangle \sqrt{n}, \quad (13b)$$

$$b^\dagger|n\rangle = |n+1\rangle \sqrt{n+1}. \quad (13c)$$

The normalization of $|n\rangle$ is easily checked by application of the following "differentiation" rule

$$[b, (b^\dagger)^k] = k(b^\dagger)^{k-1}. \quad (14)$$

This result can easily be proved by mathematical induction. Considering the matrix element ($k \geq n$)

$$\langle k|n\rangle = \frac{1}{\sqrt{k!n!}} \langle 0|b^k (b^\dagger)^n |0\rangle = \frac{1}{\sqrt{k!n!}} n! \langle 0|b^{k-n} |0\rangle = \delta_{k,n},$$

we find that the kets $|n\rangle$ ($n = 0, 1, \dots$) are orthonormal.

Returning to SU(2), we recall that this is the dynamic symmetry group of the isotropic two-dimensional harmonic oscillator. The time-independent Schrödinger equation of such an oscillator separates into two uncoupled one-dimensional equations. The Hamiltonian is the sum of two single-mode Hamiltonians given in equation (10),

$$H = \hbar\omega \left(\sum_{i=1}^2 b_i^\dagger b_i + 1 \right). \quad (15)$$

Its eigenstates are simply tensorial products,

$$|n_1, n_2\rangle := |n_1\rangle \otimes |n_2\rangle.$$

Since b_1 and b_2 are related to independent (uncoupled) vibrational modes, the following commutation relations hold,

$$[b_i, b_j^\dagger] = \delta_{ij}, \quad [b_i, b_j] = [b_i^\dagger, b_j^\dagger] = 0, \quad i, j = 1, 2, \quad (16)$$

and their action on kets is the same as before, *cf.* equations (13a)–(13c). We can relate the eigenstates $|j, m\rangle$ to $|n_1, n_2\rangle$ by

$$n_1 = j + m \quad \text{and} \quad n_2 = j - m. \quad (17)$$

Thus,

$$|j, m\rangle \equiv |n_1, n_2\rangle = \frac{(b_1^\dagger)^{n_1} (b_2^\dagger)^{n_2}}{\sqrt{n_1! n_2!}} |0\rangle = \frac{(b_1^\dagger)^{j+m} (b_2^\dagger)^{j-m}}{\sqrt{(j+m)!(j-m)!}} |0\rangle, \quad (18)$$

where $|0\rangle \equiv |j = 0, m = 0\rangle = |n_1 = 0, n_2 = 0\rangle$ and $\mathcal{J}_i |0\rangle = 0$ ($i = x, y, z$). Equations (9c) can be rewritten as

$$\begin{aligned} \mathcal{J}_+ |n_1, n_2\rangle &= |n_1 + 1, n_2 - 1\rangle \sqrt{(n_1 + 1)n_2}, \\ \mathcal{J}_- |n_1, n_2\rangle &= |n_1 - 1, n_2 + 1\rangle \sqrt{n_1(n_2 + 1)}, \end{aligned} \quad (19)$$

so that

$$\mathcal{J}_+ = b_1^\dagger b_2 \equiv \mathcal{E}_{12}, \quad (20)$$

$$\mathcal{J}_- = b_2^\dagger b_1 \equiv \mathcal{E}_{21}. \quad (21)$$

The $j = 0$ “vacuum” state $|0\rangle$ is rotationally invariant, so that

$$\hat{U} |0\rangle = |0\rangle, \quad \hat{U} \in \text{SU}(2). \quad (22)$$

Writing for the general action of \hat{U} on basis vectors $|\sigma\rangle \equiv b_\sigma^\dagger |0\rangle$, which span a given SU(2) irrep,

$$\hat{U} |\sigma\rangle \equiv |\tilde{\sigma}\rangle = \sum_{\mu} |\mu\rangle U_{\mu\sigma}, \quad (23)$$

or, equivalently,

$$\tilde{b}_\sigma^\dagger = \sum_{\mu} b_\mu^\dagger U_{\mu\sigma}, \quad \tilde{b}_\sigma^\dagger |0\rangle = |\tilde{\sigma}\rangle, \quad (24)$$

we see that the rotational invariance of $|0\rangle$ and the unitarity of \hat{U} imply

$$\hat{U} b_\sigma^\dagger |0\rangle = \hat{U} b_\sigma^\dagger \hat{U}^\dagger \hat{U} |0\rangle = \hat{U} b_\sigma^\dagger \hat{U}^\dagger |0\rangle = \tilde{b}_\sigma^\dagger |0\rangle = \sum_{\mu} b_\mu^\dagger U_{\mu\sigma} |0\rangle,$$

or, succinctly,

$$\hat{U} b_\sigma^\dagger \hat{U}^\dagger = \sum_{\mu} b_\mu^\dagger U_{\mu\sigma}, \quad \hat{U} \in \text{SU}(2). \quad (25)$$

We see that the total Hamiltonian in equation (15), which contains implicitly a sum of kinetic and potential energy terms, is invariant under SU(2), while the separate kinetic and potential energy terms are invariant under $\text{SO}(2) \subset \text{SU}(2)$.

Generally we can write

$$\mathcal{J}_k = \frac{1}{2} \begin{pmatrix} b_1^\dagger & b_2^\dagger \end{pmatrix} \sigma_k \begin{pmatrix} b_1 \\ b_2 \end{pmatrix}, \quad \text{with } k = x, y, z. \quad (26)$$

Equivalently, using the operators \mathcal{E}_{ij} introduced above, $i, j = 1, 2$,

$$\mathcal{E}_{ij} = b_i^\dagger b_j, \quad (27)$$

we find that

$$\mathcal{J}_x = \frac{1}{2}(\mathcal{E}_{12} + \mathcal{E}_{21}), \quad (28a)$$

$$\mathcal{J}_y = -\frac{i}{2}(\mathcal{E}_{12} - \mathcal{E}_{21}), \quad (28b)$$

$$\mathcal{J}_z = \frac{1}{2}(\mathcal{E}_{11} - \mathcal{E}_{22}), \quad (28c)$$

and

$$\begin{aligned} \hat{\mathcal{J}}^2 &:= \hat{\mathcal{J}}_x^2 + \hat{\mathcal{J}}_y^2 + \hat{\mathcal{J}}_z^2 \\ &= \frac{1}{2}(\hat{\mathcal{J}}_+ \hat{\mathcal{J}}_- + \hat{\mathcal{J}}_- \hat{\mathcal{J}}_+) + \hat{\mathcal{J}}_z^2 \\ &= \frac{1}{2}(\mathcal{E}_{12}\mathcal{E}_{21} + \mathcal{E}_{21}\mathcal{E}_{12}) + \frac{1}{4}(\mathcal{E}_{11} - \mathcal{E}_{22})^2. \end{aligned} \quad (29)$$

It is important to note that the operators \mathcal{E}_{ij} possess the commutation relations

$$[\mathcal{E}_{ij}, \mathcal{E}_{mn}] = \delta_{jm}\mathcal{E}_{in} - \delta_{in}\mathcal{E}_{mj}, \quad i, j, m, n = 1, 2, \quad (30)$$

characterizing the generators of the general linear group GL(2) and thus of its subgroup SU(2).

The action of these operators on an arbitrary state $|j, m\rangle$ is now easily checked to be

$$\begin{aligned} \mathcal{E}_{11}|jm\rangle &= b_1^\dagger b_1|jm\rangle \\ &= [(j+m)!(j-m)!]^{-1/2} (j+m)b_1^\dagger (b_1^\dagger)^{j+m-1} (b_2^\dagger)^{j-m} |0\rangle \\ &= (j+m)|jm\rangle, \end{aligned} \quad (31)$$

where we used the differentiation rule:

$$b_1 (b_1^\dagger)^{j+m} (b_2^\dagger)^{j-m} |0\rangle = (j+m) (b_1^\dagger)^{j+m-1} (b_2^\dagger)^{j-m} |0\rangle.$$

In the same way,

$$\begin{aligned} \mathcal{E}_{22}|jm\rangle &= (j-m)|jm\rangle, \\ \mathcal{E}_{12}|jm\rangle &= [(j-m)(j+m+1)]^{1/2} |j, m+1\rangle, \\ \mathcal{E}_{21}|jm\rangle &= [(j+m)(j-m+1)]^{1/2} |j, m-1\rangle. \end{aligned} \quad (32)$$

Using these relationships, we easily recover equations (9a)–(9c), verifying that the Schwinger states (18) possess the usual properties of angular momentum states and span a single $(2j+1)$ -dimensional irrep of SU(2) labeled by j .

Note that for $j = \frac{1}{2}$, $m = \pm\frac{1}{2}$, we recover the standard spin up and spin down functions,

$$|\frac{1}{2}, \frac{1}{2}\rangle = b_1^\dagger |0\rangle \equiv \alpha(1), \quad |\frac{1}{2}, -\frac{1}{2}\rangle = b_2^\dagger |0\rangle \equiv \beta(1), \quad (33)$$

spanning the defining representation of SU(2). Due to the bosonic character of the b_i^\dagger , the states (18) are symmetric under permutation of the creation operators. This implies that

the kets (18) are the second-quantized representation of a system consisting of $2j$ spin- $\frac{1}{2}$ particles in a state of highest total spin j . Thus, for example,

$$\begin{aligned}\frac{1}{\sqrt{2}}b_1^\dagger b_1^\dagger|0\rangle &\leftrightarrow \alpha(1)\alpha(2), \\ b_1^\dagger b_2^\dagger|0\rangle &\leftrightarrow \frac{\alpha(1)\beta(2) + \beta(1)\alpha(2)}{\sqrt{2}}, \\ \frac{1}{\sqrt{2}}b_2^\dagger b_2^\dagger|0\rangle &\leftrightarrow \beta(1)\beta(2).\end{aligned}$$

To express the antisymmetric two-particle singlet state

$$\frac{\alpha(1)\beta(2) - \beta(1)\alpha(2)}{\sqrt{2}}$$

in second-quantized form, the boson operators must be equipped with a second subscript [27].

At this point it would be easy to construct the actual matrix irrep $\mathbf{D}^{(j)}$ as a polynomial in the matrix elements $U_{\mu\sigma}$ (cf. equation (25)) by using

$$\hat{U}b_1^\dagger b_1^\dagger b_1^\dagger \cdots |0\rangle = (\hat{U}b_1^\dagger \hat{U}^\dagger)(\hat{U}b_1^\dagger \hat{U}^\dagger)(\hat{U}b_1^\dagger \hat{U}^\dagger) \cdots \hat{U}|0\rangle \quad (34)$$

and $\hat{U}|0\rangle = |0\rangle$. Since we do not need the explicit form of $\mathbf{D}^{(j)}$ we skip this construction.

2.3. Contragredient representations

Recall that a non-singular matrix \mathbf{A} is in one-to-one correspondence with the contragredient matrix $\bar{\mathbf{A}} := (\mathbf{A}^{-1})^T$. For unitary matrices we have $\bar{\mathbf{U}} = (\mathbf{U}^\dagger)^T = \mathbf{U}^*$, i.e., a unitary matrix and its contragredient counterpart are connected by complex conjugation. In the terminology of Fano and Racah [9] the unitary *contrastandard* matrix rep $\bar{\mathbf{D}}(g)$ of a group G is the complex conjugate $\mathbf{D}(g)^*$ of the unitary *standard* matrix rep $\mathbf{D}(g)$. The concept of contragredience is important because it leads by contraction to group invariants. Indeed, suppose χ_i and $\bar{\chi}_i$ are bases of n -dimensional vector spaces V and \bar{V} that carry $\mathbf{D}(g)$ and $\bar{\mathbf{D}}(g)$, respectively, of the same group G . That is, for all $g \in G$,

$$g(\chi_i) = \sum_{j=1}^n \chi_j D(g)_{ji} \quad \text{and} \quad g(\bar{\chi}_i) = \sum_{j=1}^n \bar{\chi}_j \bar{D}(g)_{ji}.$$

The contraction of χ_i and $\bar{\chi}_i$ satisfies

$$\sum_{i=1}^n g(\chi_i)g(\bar{\chi}_i) = \sum_{i,j,k} \chi_j \bar{\chi}_k D(g)_{ji} \bar{D}(g)_{ki} = \sum_{j,k} \chi_j \bar{\chi}_k \delta_{jk} = \sum_{i=1}^n \chi_i \bar{\chi}_i, \quad (35)$$

and is therefore a group invariant.

For general groups the standard rep $\mathbf{D}(g)$ and the contrastandard rep $\bar{\mathbf{D}}(g)$ are not necessarily equivalent. It was pointed out in the Introduction that for groups with only ambivalent conjugacy classes the standard and contrastandard matrix reps are equivalent, because their characters are real, and so, since the classes of $\text{SU}(2)$ are ambivalent, its standard and contrastandard reps are equivalent.

Consider an orthonormal basis (for instance a Schwinger basis) of the $(2j+1)$ -dimensional space V which carries the irrep $\mathbf{D}^{(j)}$ of $SU(2)$. We refer to this basis as a *standard basis*. An orthonormal basis carrying $\mathbf{D}^{(j)*}$ is a *contrastandard basis*. The matrix \mathbf{Y} which transforms a contrastandard basis of the defining irrep into a standard one, is

$$\mathbf{Y} = \begin{pmatrix} 0 & -1 \\ 1 & 0 \end{pmatrix}. \quad (36)$$

This matrix has the desired property for the defining irrep of $SU(2)$, since it can be verified by matrix multiplication and the form (4) of \mathbf{U} that

$$\mathbf{Y}\mathbf{U}^*\mathbf{Y}^{-1} = \mathbf{U}. \quad (37)$$

The matrix \mathbf{Y} represents an active rotation around the y -axis \hat{e}_y over π . Indeed, from equation (5) we find

$$\begin{aligned} \hat{U}(\hat{e}_y, \pi)(|\alpha\rangle, |\beta\rangle) &= (|\alpha\rangle, |\beta\rangle)\mathbf{U}(\hat{e}_y, \pi) \\ &= (|\alpha\rangle, |\beta\rangle) \left[\mathbf{1} \cos \frac{\pi}{2} - i\sigma_y \sin \frac{\pi}{2} \right] \\ &= (|\alpha\rangle, |\beta\rangle) \begin{pmatrix} 0 & -1 \\ 1 & 0 \end{pmatrix} \equiv (|\alpha\rangle, |\beta\rangle)\mathbf{Y}. \end{aligned} \quad (38)$$

Since by equation (37) \mathbf{Y} maps a standard basis onto a contrastandard basis, it is often referred to as the $SU(2)$ *metric tensor*. In order to find the $SU(2)$ metric tensor for general j , we define a contrastandard set of boson operators. We recall the transformation rule equation (25) and define $\hat{Y} := U(\hat{e}_y, \pi) \in SU(2)$. Following common usage in tensor analysis, we distinguish upper and lower indices and define $(b^1)^\dagger$ and $(b^2)^\dagger$ by

$$((b^1)^\dagger, (b^2)^\dagger) := \hat{Y}(b_1^\dagger, b_2^\dagger)\hat{Y}^\dagger = (b_1^\dagger, b_2^\dagger)\mathbf{Y} = (b_2^\dagger, -b_1^\dagger). \quad (39)$$

Then the basis

$$|\overline{j}m\rangle := \frac{(b_1^\dagger)^{j+m}(b_2^\dagger)^{j-m}}{\sqrt{(j+m)!(j-m)!}}|0\rangle, \quad (40)$$

is contrastandard, because

- (i) $(b^1)^\dagger$ and $(b^2)^\dagger$ carry \mathbf{U}^* ,
- (ii) $|\overline{j}m\rangle$ is the same polynomial in $(b^1)^\dagger$ and $(b^2)^\dagger$ as $|jm\rangle$ is in b_1^\dagger and b_2^\dagger (cf. (18)),
- (iii) the vectors $|jm\rangle$ carry $\mathbf{D}^{(j)}$ (cf. (34)) and hence the $|\overline{j}m\rangle$ carry $\overline{\mathbf{D}}^{(j)}$.

Using $\hat{Y}^\dagger|0\rangle = |0\rangle$ (cf. (22)), we find from equations (39) and (40) that

$$|\overline{j}m\rangle = \hat{Y} \frac{(b_1^\dagger)^{j+m}(b_2^\dagger)^{j-m}}{\sqrt{(j+m)!(j-m)!}}|0\rangle = \hat{Y}|jm\rangle,$$

as well as

$$|\overline{j}m\rangle = (-1)^{j-m} \frac{(b_1^\dagger)^{j-m}(b_2^\dagger)^{j+m}}{(j+m)!(j-m)!}|0\rangle = (-1)^{j-m}|j, -m\rangle, \quad (41)$$

which imply the following important relation

$$|\overline{j}m\rangle = \hat{Y}|jm\rangle = (-1)^{j-m}|j, -m\rangle. \quad (42)$$

Wigner [24] introduced the $SU(2)$ metric tensor as the tensor that transforms a standard to a contrastandard basis vector:

$$|\overline{j\bar{m}}\rangle = \sum_{m'} |jm'\rangle \begin{pmatrix} j \\ m'm \end{pmatrix}, \quad (43)$$

where the tensor elements, referred to as the *Wigner 1jm-symbols*, have the following explicit form

$$\begin{pmatrix} j \\ m'm \end{pmatrix} := D^{(j)}(\mathbf{Y})_{m'm} = (-1)^{j-m} \delta_{m', -m}, \quad (44)$$

as can be verified using equation (42) and upon noting that $\mathbf{D}^{(j)}(\mathbf{Y})$ is the matrix of \hat{Y} in the basis $|jm\rangle$. Since $SU(2)$ has “double group” character, *i.e.*,

$$\mathbf{D}^{(j)}(\mathbf{Y})\mathbf{D}^{(j)}(\mathbf{Y}) = (-1)^{2j} \mathbf{1}^{(j)},$$

or explicitly,

$$\sum_{m'} \begin{pmatrix} j \\ mm' \end{pmatrix} \begin{pmatrix} j \\ m'\tilde{m} \end{pmatrix} = (-1)^{2j} \delta_{m\tilde{m}}$$

(in the case of half-integer j a rotation by 2π is minus the identity), we find that

$$\begin{pmatrix} j \\ m'm \end{pmatrix} = (-1)^{2j} \begin{pmatrix} j \\ mm' \end{pmatrix}, \quad (45)$$

so that also

$$\begin{pmatrix} j \\ mm' \end{pmatrix} = (-1)^{j+m} \delta_{m, -m'}. \quad (46)$$

This antisymmetry of the $SU(2)$ metric tensor for half-integer j is the source of unpleasant phase factors, of which we shall keep track by orienting the lines in the diagrams introduced later.

2.4. Time reversal

It is of interest to relate the operator \hat{Y} to the operation of *time reversal*. We define the time-reversal operator ϑ by its action on the dynamical variables of position \vec{q} , linear momentum \vec{p} , and spin \vec{s} (the vector operator with components defined in equation (3)):

$$\vartheta \vec{q} \vartheta^\dagger = \vec{q}, \quad (47a)$$

$$\vartheta \vec{p} \vartheta^\dagger = -\vec{p}, \quad (47b)$$

$$\vartheta \vec{s} \vartheta^\dagger = -\vec{s}, \quad (47c)$$

$$\langle \vartheta \psi | \vartheta \phi \rangle \langle \vartheta \phi | \vartheta \psi \rangle = \langle \psi | \phi \rangle \langle \phi | \psi \rangle. \quad (47d)$$

Note that the requirements (47a) and (47b) imply that the orbital angular momentum $\vec{q} \times \vec{p}$ is antisymmetric under time reversal. Condition (47c) for the spin angular momentum is introduced by analogy. Finally, we require that Born’s transition probability is left invariant by ϑ , *i.e.*, condition (47d). Wigner [8] proved that this last requirement implies that ϑ is unitary and either linear or antilinear. (Note that the sufficiency of this requirement is immediately obvious.) Considering the angular momentum commutation relations we find

two possibilities

$$\vartheta[\hat{J}_j, \hat{J}_k]\vartheta^\dagger = \sum_l \vartheta(i\varepsilon_{jkl}\hat{J}_l)\vartheta^\dagger = \pm i \sum_l \varepsilon_{jkl}\vartheta\hat{J}_l\vartheta^\dagger = \mp i \sum_l \varepsilon_{jkl}\hat{J}_l,$$

where the upper sign holds if ϑ is linear and the lower if ϑ is antilinear. Since, on the other hand,

$$\vartheta[\hat{J}_j, \hat{J}_k]\vartheta^\dagger = [\vartheta\hat{J}_j\vartheta^\dagger, \vartheta\hat{J}_k\vartheta^\dagger] = [-\hat{J}_j, -\hat{J}_k] = i \sum_l \varepsilon_{jkl}\hat{J}_l,$$

it follows that ϑ is antilinear, and in view of equation (47d) ϑ is antiunitary. Recall that an antiunitary operator satisfies the following turnover rule

$$\langle \vartheta\psi | \vartheta\phi \rangle = \langle \phi | \psi \rangle = \langle \psi | \phi \rangle^*,$$

and from $\vartheta\vartheta^\dagger = 1$,

$$\langle \vartheta^\dagger\psi | \phi \rangle = \langle \psi | \vartheta\phi \rangle^*.$$

Time reversal is one of the fundamental symmetries observed in nature. To date there is no experimental evidence that casts doubt on the general validity of this symmetry for electromagnetic interactions. In a time-independent formalism, the name of this symmetry may be somewhat puzzling. We notice, however, that classically linear momentum changes sign under time reversal, while position does not. These basic symmetries are preserved in the quantum mechanical definition of ϑ . The reader will note that a simple sign change of the time variable, $t \rightarrow -t$, will not provide a satisfactory definition of time reversal in quantum mechanics, since this would also change the sign of the energy, as follows immediately from the time dependent Schrödinger equation. In fact, the requirement that the energy is conserved is consistent with the antilinearity of the time-reversal operator.

It is easily verified that the operators \mathcal{J}_k in equations (28a)–(28c) satisfy $\vartheta\mathcal{J}_k\vartheta^\dagger = -\mathcal{J}_k$ if we assume

$$\vartheta(b_1^\dagger, b_2^\dagger)\vartheta^\dagger = e^{i\phi}(b_1^\dagger, b_2^\dagger)\mathbf{Y}.$$

Here $e^{i\phi}$ is an overall phase factor; below we shall argue that we can make the choice $\phi = 0$. The matrix \mathbf{Y} is given in equation (36).

We next observe that the time-reversal operator commutes with the elements of SU(2). This can be readily seen by the use of the exponential representation (7) of a general element $\hat{U} \in \text{SU}(2)$. Using the antilinearity of ϑ we have for the p th term in the expansion of the exponential that

$$\vartheta[-i\varphi\boldsymbol{\sigma} \cdot \vec{n}]^p\vartheta^\dagger = [-i\varphi\boldsymbol{\sigma} \cdot \vec{n}]^p.$$

From this the commutation of \hat{U} and ϑ follows. From the antilinearity of ϑ and the commutation rule $[\hat{U}, \vartheta] = 0$ just found, we can immediately conclude that $\{\vartheta|jm\rangle\}$ forms a contrastandard basis. Indeed, applying ϑ to the defining relation

$$\hat{U}|jm\rangle = \sum_{m'} D^{(j)}(U)_{m'm}|jm'\rangle,$$

yields

$$\vartheta\hat{U}|jm\rangle = \hat{U}\vartheta|jm\rangle = \sum_{m'} D^{(j)}(U)_{m'm}^*\vartheta|jm'\rangle.$$

Hence, $\hat{Y}|jm\rangle$ and $\vartheta|jm\rangle$ span the very same irrep of $SU(2)$. From Schur's lemma and the orthonormality of the basis used follows that

$$\hat{Y}|jm\rangle = e^{i\phi_j} \vartheta|jm\rangle,$$

where the phase factor does not depend on m . Thus, a natural choice for the phase of $|jm\rangle$ is such that $\exp[i\phi_j]$ is unity,² so that we can write, using equation (42),

$$\vartheta|jm\rangle \equiv |\vartheta(jm)\rangle = (-1)^{j-m}|j, -m\rangle.$$

Although \hat{Y} and ϑ have now the same effect on $|jm\rangle$, they are not identical operators, since the one is linear and the other antilinear. By introducing the *complex conjugation operator* K_0 we can find an operator relationship between Y and ϑ . We define K_0 by

$$K_0(c|\psi\rangle + c'|\psi'\rangle) := c^*|\psi\rangle + c'^*|\psi'\rangle,$$

so that it is antilinear. We can then write that

$$\vartheta = \hat{Y} K_0,$$

where \hat{Y} represents a rotation by π around the y -axis, see equation (38). Since $K_0^2 = 1$, so that

$$\vartheta^2|jm\rangle = Y^2|jm\rangle = (-1)^{2j}|jm\rangle, \quad (48)$$

we find that for half-integer j neither \hat{Y} nor ϑ are involutory.³

We wish to end this section by pointing out that the bras $\{\langle jm|\}$ also form a contrastandard basis of $SU(2)$, *i.e.*,

$$\langle jm|\hat{U}^\dagger = \langle \hat{U}(jm)| = \sum_{m'} D^{(j)}(U)_{m'm}^* \langle jm'|.$$

We must emphasize, however, that the bra vectors span a different space (the dual space) than the ket vectors, so that there can be no linear relationship relating bras with kets. Furthermore, the process of Hermitian conjugation is involutory,

$$|jm\rangle^{\dagger\dagger} = |jm\rangle.$$

This already implies that we cannot represent $\vartheta|jm\rangle$ and $\langle jm|$ by the same diagram (see below), although both carry the very same irrep of $SU(2)$.

2.5. Clebsch–Gordan series

To define the CG series we consider spaces V_{j_1} and V_{j_2} carrying standard irreps $D^{(j_1)}$ and $D^{(j_2)}$ of $SU(2)$. The basis $|j_1, m_1\rangle$, $m_1 = -j_1, \dots, j_1$, consist of eigenfunctions of J^2 and J_z . The same holds for $|j_2, m_2\rangle$. The tensor product space $V_{j_1} \otimes V_{j_2}$ carries the reducible Kronecker product representation $D^{(j_1)} \otimes D^{(j_2)}$. Reduction of the tensor space

² Note, however, that spherical harmonics with the widely used Condon and Shortley phase convention do not satisfy this choice, and differ by the phase factor $(-i)^j$ from the $|jm\rangle$ introduced here.

³ An operator A is involutory if $A^2 = 1$.

under $SU(2)$ yields

$$V_{j_1} \otimes V_{j_2} = \sum_{j=|j_1-j_2|}^{j_1+j_2} \oplus V_j, \quad (49)$$

where V_j carries the irrep $D^{(j)}$ of $SU(2)$. It is proved in textbooks by Lie-algebraic techniques that this reduction is multiplicity free, *i.e.*, the irrep $D^{(j)}$ occurs once in this reduction. Also the range of j , indicated in equation (49) is proved in textbooks. Equation (49) constitutes the Clebsch–Gordan theorem, proved in 1869 by the German mathematician Paul Gordan [28], who used techniques from invariant theory developed by his colleague Alfred Clebsch.

Designating the orthonormal basis for V_j by $\{|j, m\rangle\}$, we can insert the resolution of the identity in the tensor product space and write

$$|j_1 m_1\rangle \otimes |j_2 m_2\rangle = \sum_{j=|j_1-j_2|}^{j_1+j_2} \sum_{m=-j}^j |jm\rangle \langle jm|j_1 m_1; j_2 m_2\rangle, \quad (50)$$

where we introduced the notation $|j_1 m_1\rangle \otimes |j_2 m_2\rangle \equiv |j_1 m_1; j_2 m_2\rangle$. As it is common to refer to equation (50) as the $SU(2)$ *Clebsch–Gordan (CG) series*, we will follow this practice. The inner product $\langle jm|j_1 m_1; j_2 m_2\rangle$ is a *Clebsch–Gordan (CG) coefficient*. These coefficients transform an orthonormal basis of $V_{j_1} \otimes V_{j_2}$ into another one and form a unitary matrix \mathbf{C} , which decomposes the Kronecker product representation into irreducible blocks,

$$\mathbf{C}[\mathbf{D}^{(j_1)}(\hat{U}) \otimes \mathbf{D}^{(j_2)}(\hat{U})] \mathbf{C}^\dagger = \sum_j \oplus \mathbf{D}^{(j)}(\hat{U}), \quad \hat{U} \in SU(2).$$

This relationship exhibits the fact that the CG coefficients depend only on the irreps of $SU(2)$ and not on a particular realization of V_{j_1} and V_{j_2} , so that we can choose $|j_1 m_1\rangle$ and $|j_2 m_2\rangle$ arbitrarily in the derivation of CG coefficients. The first derivation of an algebraic formula for CG coefficients was given by Wigner in his famous 1931 book [8]. The following expression for the CG coefficients is due to Van der Waerden [29] and is the most symmetric one of the various existing forms, see, *e.g.*, Ref. [13] for a derivation,

$$\begin{aligned} \langle jm|j_1 m_1; j_2 m_2\rangle &= \delta_{m, m_1+m_2} \Delta(j_1, j_2, j) \\ &\times \sum_t (-1)^t [(2j+1)(j_1+m_1)(j_1-m_1)! \\ &\times (j_2+m_2)(j_2-m_2)(j+m)(j-m)!]^{1/2} \\ &\times [t!(j_1+j_2-j-t)!(j_1-m_1-t)! \\ &\times (j_2+m_2-t)(j-j_2+m_1+t)(j-j_1-m_2+t)!]^{-1}, \end{aligned} \quad (51)$$

where

$$\Delta(j_1, j_2, j) \equiv \left[\frac{(j_1+j_2-j)!(j_1-j_2+j)!(-j_1+j_2+j)!}{(j_1+j_2+j+1)!} \right]^{1/2},$$

and the sum runs over all values of t which do not lead to negative factorials.

The symmetry properties of the CG coefficients are

$$(i) \quad \langle jm|j_1 m_1; j_2 m_2\rangle = \langle j_1 m_1; j_2 m_2|jm\rangle,$$

- (ii) $\langle jm|j_1m_1; j_2m_2\rangle = (-1)^{j_1+j_2-j}\langle j, -m|j_1, -m_1; j_2, -m_2\rangle,$
- (iii) $\langle jm|j_1m_1; j_2m_2\rangle = (-1)^{j_1+j_2-j}\langle jm|j_2m_2; j_1m_1\rangle,$
- (iv) $\langle jm|j_1m_1; j_2m_2\rangle = \left[\frac{2j+1}{2j_2+1}\right]^{1/2} \langle j_2m_2|jm; \vartheta(j_1m_1)\rangle.$

For $j = m = 0$, CG coefficients are equal to

$$(v) \quad \langle 00|j_1m_1; j_2m_2\rangle = \delta_{j_1j_2}\delta_{m_1,-m_2}(-1)^{j_1-m_1}(2j_1+1)^{-1/2}.$$

We will prove these properties:

- (i) The CG coefficients are defined as an inner product in equation (50); their explicit form shows that they are real. Hence,

$$\langle jm|j_1m_1; j_2m_2\rangle = \langle j_1m_1; j_2m_2|jm\rangle^* = \langle j_1m_1; j_2m_2|jm\rangle.$$

- (ii) From the unitarity of the time reversal operator ϑ and the realness of CG coefficients follows that

$$\begin{aligned} \langle jm|j_1m_1; j_2m_2\rangle &= \langle jm|\vartheta^\dagger\vartheta|j_1m_1; j_2m_2\rangle = \langle \vartheta(jm)|\vartheta(j_1m_1); \vartheta(j_2m_2)\rangle \\ &= (-1)^{j+j_1+j_2}(-1)^{-(m+m_1+m_2)}\langle j, -m|j_1, -m_1; j_2, -m_2\rangle. \end{aligned}$$

Since $m = m_1 + m_2$ and m is a half-integer if and only if j is a half-integer, we find that

$$(-1)^{-(m+m_1+m_2)} = (-1)^{-2m} = (-1)^{-2j}.$$

- (iii) The explicit form for CG coefficients, equation (51), is invariant with respect to a simultaneous interchange $j_1 \leftrightarrow j_2$ and $m_1 \leftrightarrow -m_2$, which implies that $m \rightarrow -m$ and thus

$$\begin{aligned} \langle jm|j_1m_1; j_2m_2\rangle &= \langle j, -m|j_2, -m_2; j_1, -m_1\rangle = (-1)^{j_1+j_2-j}\langle jm|j_2m_2; j_1m_1\rangle. \end{aligned}$$

- (iv) Make simultaneous replacements $j \leftrightarrow j_2$ and $m \leftrightarrow -m_2$ in the explicit expression for CG coefficients, equation (51), and change the summation variable t to $j_1 - m_1 - t$. Observe that except for the first factor $(2j+1)^{1/2}$ and the phase $(-1)^t$ they leave the expression (51) invariant. Thus

$$\begin{aligned} \langle jm|j_1m_1; j_2m_2\rangle &= \left[\frac{2j+1}{2j_2+1}\right]^{1/2} (-1)^{j_1-m_1}\langle j_2, -m_2|j_1m_1; j, -m\rangle \\ &= \left[\frac{2j+1}{2j_2+1}\right]^{1/2} (-1)^{j_1-m_1}\langle j_2m_2|jm; j_1, -m_1\rangle \\ &= \left[\frac{2j+1}{2j_2+1}\right]^{1/2} \langle j_2m_2|jm; \vartheta(j_1m_1)\rangle. \end{aligned}$$

- (v) Follows by applying rule (iv) to the identity

$$\langle j_1m_1|j_2m_2; 00\rangle = \delta_{j_1j_2}\delta_{m_1m_2}.$$

3. DIAGRAMS

We shall now introduce the basic concepts of a graphical technique, sometimes referred to as the graphical method of spin algebras, which is designed to facilitate the manipulation of complicated expressions involving CG coefficients, their simplification and evaluation.

Our presentation will be based on the well-defined transformation properties of CG coefficients, which follow immediately from their definition as a vector space inner product, given in the preceding section. The four group-theoretical characteristics of special importance in this respect are:

- (1) the SU(2) irrep to which the state belongs (*i.e.*, its j -quantum number),
- (2) the row of the irrep according to which the state transforms (its m -quantum number),
- (3) the variance of the state (does the state transform according to a standard or a contrastandard irrep?),
- (4) and finally, is the state a bra or a ket?

3.1. Basic diagrammatic building blocks

We first introduce a diagrammatic representation for various states which enter the inner products (*i.e.*, Clebsch–Gordan coefficients) considered. We must emphasize that our graphical technique is intended to manipulate these inner products and not the states themselves. Moreover, the inner products are always real, so that the diagrams are invariant under a simultaneous Hermitian conjugation of all states.

We draw the vertices arising in the CG diagrams as half circles, and adhere to the following rules.

CONVENTION C1. A state transforming according to a *standard* rep is designated by an oriented line *leaving* a vertex, while a state transforming according to a *contrastandard* rep is represented by a line *entering* a vertex.

CONVENTION C2. A *ket* is represented by a *single arrow* and a *bra* by a *double arrow*.

CONVENTION C3. An n -fold tensor product is represented by n lines attached to a single vertex. The vertex sign defines the order in the tensor product: a *minus sign* indicates a *clockwise* and a *plus sign* a *counter clockwise* reading. Note that this corresponds to the sense of rotation around an axis pointing towards the reader. Evidently, when only one line is attached to a vertex, a node sign is superfluous.

We thus have the following states:

$$|jm\rangle \rightarrow \text{D} \rightarrow \overset{j \ m}{\longrightarrow} \equiv \overset{j \ m}{\longleftarrow} \text{D}, \quad (52a)$$

$$\langle jm| \rightarrow \text{D} \xleftarrow{j \ m} \equiv \xrightarrow{j \ m} \text{D}, \quad (52b)$$

$$|\vartheta(jm)\rangle \equiv \vartheta|jm\rangle \rightarrow \text{D} \xleftarrow{j \ m} \equiv \xrightarrow{j \ m} \text{D}, \quad (52c)$$

$$\langle \vartheta(jm) | \equiv \langle jm | \vartheta^\dagger \rightarrow \text{D} \xrightarrow{j \ m} \equiv \xleftarrow{j \ m} \text{D}. \quad (52d)$$

For a tensor product we have

$$|j_1 m_1; \dots; j_n m_n\rangle := |j_1 m_1\rangle \otimes \dots \otimes |j_n m_n\rangle$$

As an example of a mixed standard-contrastandard tensor we give

$$|\vartheta(j_1 m_1); j_2 m_2\rangle := (\vartheta | j_1 m_1) \rangle \otimes |j_2 m_2\rangle \rightarrow \text{D} \begin{matrix} \nearrow j_1 m_1 \\ \searrow j_2 m_2 \end{matrix}.$$

An inner product of two states is then represented as

$$\langle j_1 m_1 | j_2 m_2 \rangle = \delta_{j_1 j_2} \delta_{m_1 m_2}$$

$$\rightarrow \xrightarrow{j_1 \ m_1} | \xrightarrow{j_2 \ m_2} := \xrightarrow{j_1 \ m_1} \text{D} \xrightarrow{j_2 \ m_2} \quad (53)$$

and, for tensor product states, as

$$\langle j_1 m_1; \dots; j_n m_n | j'_1 m'_1; \dots; j'_n m'_n \rangle$$

The central concept of graphical techniques is that of *contraction*, representing the formation of an SU(2) invariant by summing over the m -quantum number of a product of a standard and a contrastandard state. We introduce the following four possible prototypes for a contraction.

CONVENTION C4.

(i) *Ket-bra contraction* (projector):

$$\sum_m |jm\rangle \langle jm| = \sum_m \text{D} \xrightarrow{j \ m} \xleftarrow{j \ m} \text{D} = \text{D} \xrightarrow{j} \text{D}.$$

$$\sum_m \langle \vartheta(jm) | \langle jm | \longrightarrow \text{D} \text{---} \overset{j}{\longleftarrow} \text{D},$$
$$\sum_m \text{---} \rangle^j m \text{---} = \text{---} \rangle^j m \text{---} \langle^j = \text{---} \rangle^j \text{---} \langle^j.$$

- Only lines which preserve the orientation can be contracted.
- Contraction of a single-arrowed line with a double-arrowed line produces an unoriented line.
- Contraction of two single-arrowed lines yields a single-arrowed line with preserved orientation.
- Contraction of two double-arrowed lines again produces a single-arrowed line, but with reversed orientation.

$$\begin{array}{c} j_1 m_1 \\ \nearrow \\ j_3 m_3 \longrightarrow \text{---} | \text{---} \\ \searrow \\ j_2 m_2 \end{array} := \begin{array}{c} j_1 m_1 \\ \nearrow \\ j_3 m_3 \longrightarrow \text{---} \circ \text{---} \\ \searrow \\ j_2 m_2 \end{array} = \langle j_3 m_3 | j_1 m_1; j_2 m_2 \rangle.$$

The symmetry properties of the CG coefficient (Section 2.5) are diagrammatically represented as follows (for conciseness we replace the label $j_k m_k$ by k , $k = 1, 2, 3$):

(i) $\langle j_3 m_3 | j_1 m_1; j_2 m_2 \rangle = \langle j_1 m_1; j_2 m_2 | j_3 m_3 \rangle$

(58)

(ii) $\langle j_3 m_3 | j_1 m_1; j_2 m_2 \rangle = \langle \vartheta(j_3 m_3) | \vartheta(j_1 m_1); \vartheta(j_2 m_2) \rangle$

(59)

(iii) $\langle j_3 m_3 | j_1 m_1; j_2 m_2 \rangle = (-1)^{j_1+j_2-j_3} \langle j_3 m_3 | j_2 m_2; j_1 m_1 \rangle$

(60)

(iv) $\langle j_3 m_3 | j_1 m_1; j_2 m_2 \rangle = \sqrt{\frac{[j_3]}{[j_2]}} \langle j_2 m_2 | j_3 m_3; \vartheta(j_1 m_1) \rangle$

(61)

with $[j_k] := 2j_k + 1, k = 1, 2, 3$.

(v) $\langle j_3 m_3 | j_1 m_1; j_2 m_2 \rangle = (-1)^{2j_2} \sqrt{\frac{[j_3]}{[j_1]}} \langle j_1 m_1 | \vartheta(j_2 m_2); j_3 m_3 \rangle$

(62)

Rule (62) results from successive application of rules (60), (61) and again (60).

Since the states $|jm\rangle$ form also an orthonormal basis for the tensorial product space spanned by $|j_1 m_1; j_2 m_2\rangle$, for certain fixed j_1 and j_2 and with $m_1 = -j_1, \dots, j_1$ and

$m_2 = -j_2, \dots, j_2$, we find the first orthogonality relation

$$\sum_{j=|j_1-j_2|}^{j_1+j_2} \sum_{m=-j}^j \langle j_1 m_1; j_2 m_2 | j m \rangle \langle j m | j_1 m'_1; j_2 m'_2 \rangle \\ = \langle j_1 m_1; j_2 m_2 | j_1 m'_1; j_2 m'_2 \rangle = \delta_{m_1 m'_1} \delta_{m_2 m'_2},$$

which can be represented graphically as follows:

$$\sum_j \left(\begin{array}{c} j_1, m_1 \\ \nearrow \\ j_2, m_2 \end{array} \right) + \left(\begin{array}{c} j_1, m'_1 \\ \nearrow \\ j_2, m'_2 \end{array} \right) = \begin{array}{c} j_1, m_1 \\ \nearrow \\ j_2, m_2 \end{array} + \begin{array}{c} j_1, m'_1 \\ \nearrow \\ j_2, m'_2 \end{array} = \begin{array}{c} j_1, m_1 \\ \nearrow \\ j_2, m_2 \end{array} + \begin{array}{c} j_1, m'_1 \\ \nearrow \\ j_2, m'_2 \end{array}. \quad (63)$$

In order to obtain the second orthogonality relation, we first define a $3j$ -symbol⁴ or *triangular delta* by

$$\{j, j_1, j_2\} = \begin{cases} 1 & \text{if } |j_1 - j_2| \leq j \leq j_1 + j_2, \\ 0 & \text{otherwise.} \end{cases}$$

We can write

$$\sum_{m_1 m_2} \langle j m | j_1 m_1; j_2 m_2 \rangle \langle j_1 m_1; j_2 m_2 | j' m' \rangle \\ = \{j, j_1, j_2\} \{j_1, j_2, j'\} \langle j m | j' m' \rangle = \delta_{jj'} \delta_{mm'} \{j, j_1, j_2\},$$

or graphically,

$$\begin{array}{c} j_1 \\ \nearrow \\ j, m \end{array} + \begin{array}{c} j_1 \\ \nearrow \\ j', m' \end{array} = \{j, j_1, j_2\} \begin{array}{c} j, m \\ \nearrow \\ j_2, m' \end{array}.$$

Taking $j = j'$, $m = m'$ and summing over m , we obtain

$$\{j, j_1, j_2\} = [j]^{-1} \sum_{m, m_1, m_2} \langle j m | j_1 m_1; j_2 m_2 \rangle \langle j_1 m_1; j_2 m_2 | j m \rangle,$$

so that diagrammatically $\{j, j_1, j_2\}$ can be represented by an “oyster” diagram

$$\{j, j_1, j_2\} = [j]^{-1} \begin{array}{c} j_1 \\ \nearrow \\ j \\ \searrow \\ j_2 \end{array}. \quad (64)$$

⁴ We wish to stress that the $3j$ -symbol must not be confused with the $3jm$ -symbol introduced below. Confusion is possible since the latter is often referred to by other authors as a $3j$ -symbol.

3.3. $1jm$ -symbol

We have seen in Section 2.4 that the time-reversal operator transforms a standard state into a contrastandard one and vice versa. Thus, the matrix representation of ϑ plays the role of a metric tensor and we now write

$$\begin{pmatrix} j \\ mm' \end{pmatrix} = \langle jm | \vartheta(jm') \rangle. \quad (65)$$

The facts $\vartheta^\dagger \vartheta = 1$ and $\vartheta^2 = (-1)^{2j}$ imply that

$$\begin{aligned} \langle jm | \vartheta(jm') \rangle &= \langle jm | \vartheta^\dagger \vartheta(jm') \rangle = \langle \vartheta(jm) | \vartheta^2(jm') \rangle^* \\ &= (-1)^{2j} \langle jm' | \vartheta(jm) \rangle. \end{aligned} \quad (66)$$

The $1jm$ -symbols are real, since

$$\begin{pmatrix} j \\ mm' \end{pmatrix} = (-1)^{j-m'} \langle jm | j, -m' \rangle = (-1)^{j-m'} \delta_{m, -m'} = (-1)^{j+m} \delta_{m, -m'},$$

in agreement with equations (44) and (46). Clearly the identity (66) is equivalent to the antisymmetry (equation (45)) of the metric tensor (equation (65)).

Diagrammatically we can represent the $1jm$ -symbol in one of the following ways as equation (66) implies:

$$\begin{aligned} \begin{array}{c} j \quad m \\ \longrightarrow \end{array} \mid \begin{array}{c} j \quad m' \\ \longleftarrow \end{array} &= (-1)^{2j} \begin{array}{c} j \quad m \\ \longleftarrow \end{array} \mid \begin{array}{c} j \quad m' \\ \longrightarrow \end{array} \\ &= \begin{array}{c} j \quad m \\ \longleftarrow \end{array} \mid \begin{array}{c} j \quad m' \\ \longrightarrow \end{array} = (-1)^{2j} \begin{array}{c} j \quad m \\ \longrightarrow \end{array} \mid \begin{array}{c} j \quad m' \\ \longleftarrow \end{array}. \end{aligned} \quad (67)$$

Algebraic equivalents of these diagrams are, respectively,

$$\begin{aligned} \langle jm | \vartheta(jm') \rangle &= (-1)^{2j} \langle \vartheta(jm) | jm' \rangle \\ &= \langle \vartheta(jm') | jm \rangle = (-1)^{2j} \langle jm' | \vartheta(jm) \rangle, \end{aligned}$$

and, as we just saw,

$$\langle jm | \vartheta(jm') \rangle = (-1)^{j-m'} \delta_{m, -m'} = (-1)^{j+m} \delta_{m, -m'}. \quad (68)$$

The transformation of a ket to a contrastandard one, cf. equation (43),

$$\vartheta |jm\rangle = \sum_{m'} |jm'\rangle \begin{pmatrix} j \\ m'm \end{pmatrix} = (-1)^{j-m} |j, -m\rangle, \quad (69)$$

reads graphically

$$\begin{array}{c} \mid \end{array} \begin{array}{c} j \quad m \\ \longleftarrow \end{array} = \sum_{m'} \begin{array}{c} \mid \end{array} \begin{array}{c} j \quad m' \\ \longrightarrow \end{array} \begin{array}{c} j \quad m' \\ \longrightarrow \end{array} \mid \begin{array}{c} j \quad m \\ \longleftarrow \end{array} = \begin{array}{c} \mid \end{array} \begin{array}{c} j \\ \longrightarrow \end{array} \begin{array}{c} j \quad m \\ \longrightarrow \end{array} \mid \begin{array}{c} j \quad m \\ \longleftarrow \end{array} \quad (70)$$

which confirms that contraction yields a projection operator on the space V_j with its restriction $\hat{1}_j$ being the unit operator in V_j ,

$$\begin{array}{c} \mid \end{array} \begin{array}{c} j \\ \longrightarrow \end{array} \begin{array}{c} \mid \end{array} = \sum_{m'} |jm'\rangle \langle jm'| = \hat{1}_j. \quad (71)$$

The $1jm$ -symbol is also closely related to the coupling of two angular momenta to a zero momentum. The latter will be represented by a dashed line. Clearly, if one of the coupled momenta vanishes, we have that

$$\langle jm|j'm'; 00\rangle = \langle jm|00; j'm'\rangle = \langle jm|j'm'\rangle = \delta_{jj'}\delta_{mm'}$$

or

$$(72)$$

Recalling the symmetry relations given in Section 2.5, we can write

$$\begin{aligned} \langle 00|jm; j'm'\rangle &= \langle jm; j'm'|00\rangle = [j']^{-1/2}\langle j'm'|00; \vartheta(jm)\rangle \\ &= [j']^{-1/2}\langle j'm'|\vartheta(jm)\rangle = \delta_{jj'}[j]^{-1/2} \begin{pmatrix} j \\ m'm \end{pmatrix} \\ &= \delta_{jj'}\delta_{m,-m'}(-1)^{j-m}[j]^{-1/2}, \end{aligned} \quad (73)$$

which can be represented graphically as

$$(74)$$

or any one of the other equivalent forms of the $1jm$ -symbol shown in equation (67). This implies that the zero angular momentum line can always be eliminated from our diagrams by the use of rule (72) or (74). We do not present other possibilities, since we shall give the general rule below, when we introduce a more symmetric representation of the coupling coefficients.

3.4. Generalized Clebsch–Gordan coefficients

When coupling more than two angular momenta to resulting j and m we are faced with a multiplicity problem, since we get generally more than one linearly independent state for a given j and m . To achieve a unique labeling of states we thus need additional labels; these can be supplied through quantum numbers characterizing intermediate couplings. We employ the *genealogy* (i.e., the set of intermediate coupling j -quantum numbers) with respect to a certain *coupling scheme* (the sequence of pairwise couplings) to resolve the multiplicity problem. Designating the genealogy by (α) we thus define the *generalized CG series* as

$$|(\alpha)jm\rangle = \sum_{m_1, \dots, m_n} |j_1 m_1; \dots; j_n m_n\rangle \langle j_1 m_1; \dots; j_n m_n | (\alpha)jm\rangle,$$

where $\langle j_1 m_1; \dots; j_n m_n | (\alpha)jm\rangle$ is a *generalized CG coefficient*.

To be more specific we consider the case of three angular momenta and the coupling scheme $((j_1 j_2) j_3)$. A state with an intermediate quantum number j_{12} is given by the generalized CG series

$$\begin{aligned} & |((j_1 j_2) j_{12} j_3) jm\rangle \\ &= \sum_{m_1, m_2, m_3} |j_1 m_1; j_2 m_2; j_3 m_3\rangle \langle j_1 m_1; j_2 m_2; j_3 m_3 | ((j_1 j_2) j_{12} j_3) jm \rangle. \end{aligned} \quad (75)$$

By definition

$$\begin{aligned} & \langle j_1 m_1; j_2 m_2; j_3 m_3 | ((j_1 j_2) j_{12} j_3) jm \rangle \\ &= \sum_{m_{12}} \langle j_1 m_1; j_2 m_2 | j_{12} m_{12} \rangle \langle j_{12} m_{12}; j_3 m_3 | jm \rangle, \end{aligned} \quad (76)$$

i.e., we first couple j_1 and j_2 to the angular momentum j_{12} , and then the ket $|j_{12} m_{12}\rangle$ is coupled with $|j_3 m_3\rangle$ to the final j and m . When we replace for simplicity the labels j_k, m_k by k , we have diagrammatically

$$\begin{aligned} & \langle j_1 m_1; j_2 m_2; j_3 m_3 | ((j_1 j_2) j_{12} j_3) jm \rangle \\ &= \sum_{m_{12}} \begin{array}{c} \text{Diagram 1: } \text{Three incoming lines labeled 1, 2, 3. Lines 1 and 2 are coupled at a vertex to form an intermediate line labeled } j_{12}. \text{ This line } j_{12} \text{ is then coupled with line 3 at a second vertex to form the final line labeled } j \text{ with quantum number } m. \end{array} \\ &= \begin{array}{c} \text{Diagram 2: } \text{A tree diagram where lines 1 and 2 are coupled at a vertex to form } j_{12}, \text{ which is then coupled with line 3 at another vertex to form } j \text{ with quantum number } m. \end{array} \end{aligned} \quad (77)$$

Another possible coupling scheme is, for example, $(j_1 (j_2 j_3))$, which yields the following CG coefficient

$$\begin{aligned} & \langle j_1 m_1; j_2 m_2; j_3 m_3 | (j_1 (j_2 j_3) j_{23}) jm \rangle = \\ & \begin{array}{c} \text{Diagram 3: } \text{A tree diagram where lines 2 and 3 are coupled at a vertex to form an intermediate line labeled } j_{23}. \text{ This line } j_{23} \text{ is then coupled with line 1 at a second vertex to form the final line labeled } j \text{ with quantum number } m. \end{array} \end{aligned} \quad (78)$$

In the general case, when coupling N angular momenta, the generalized CG coefficient will be diagrammatically represented by a tree with $N + 1$ external lines and $N - 1$ CG type vertices, whose internal structure reflects the chosen coupling scheme. Since the internal (contracted) lines are invariant, it is not difficult to see that the $SU(2)$ transformation properties of these quantities are fully determined by the external lines. We will elaborate on this point in Section 4, where we shall exploit this fact by deriving various rules for manipulation of diagrams. First, however, we shall consider another diagrammatic representation of CG-like quantities, which better reflects their inherent symmetry properties.

The symmetry properties of CG coefficients (see Section 2.5) reflect the asymmetry of the basic coupling problem and, consequently, have quite an awkward diagrammatic representation (*cf.* Section 3.2). We shall thus introduce quantities which are proportional to CG coefficients but have much nicer symmetry properties, namely the so-called $3j$ -symbols [24]. To avoid confusion with the triangular deltas $\{j_1, j_2, j_3\}$ we refer to them as $3jm$ -symbols.

and

[illegible]

$$\langle \vartheta(j_2 m_2); \vartheta(j_3 m_3) | j_1 m_1 \rangle = (-1)^{2j_2+2j_3} \langle j_2 m_2; j_3 m_3 | \vartheta(j_1 m_1) \rangle,$$
$$\begin{aligned}
& \text{Diagram 1: A vertex with three external lines. Line 3 enters from the left, line 1 exits to the top-right, and line 2 exits to the bottom-right.} \\
& = (-1)^{2j_2} \left(\frac{[j_3]}{[j_1]} \right)^{1/2} \text{Diagram 2: A vertex with three external lines. Line 1 enters from the left, line 2 exits to the top-right, and line 3 exits to the bottom-right.} \\
& = (-1)^{2j_3} \left(\frac{[j_3]}{[j_1]} \right)^{1/2} \text{Diagram 3: A vertex with three external lines. Line 1 enters from the left, line 2 exits to the top-right, and line 3 exits to the bottom-right.} , \quad (81)
\end{aligned}$$

we see that both resulting generalized CG coefficients, equations (79) and (80), are identical. We obtain a unique state

$$|(j_1 j_2 j_3) 00\rangle := |((j_1 j_2) j_{12} j_3) 00\rangle \equiv |(j_1 (j_2 j_3) j_{23}) 00\rangle,$$

and can define the $3jm$ -symbol by the relation

$$\langle (j_1 j_2 j_3) 00 | =: (-1)^{j_1 - j_2 + j_3} \sum_{m_1 m_2 m_3} \langle j_1 m_1; j_2 m_2; j_3 m_3 | \begin{pmatrix} j_1 & j_2 & j_3 \\ m_1 & m_2 & m_3 \end{pmatrix}. \quad (82)$$

Since the left-hand side of this equation is $SU(2)$ invariant ($j = 0$) and the tensor product $\langle j_1 m_1; j_2 m_2; j_3 m_3 |$ transforms as a triple Kronecker product of contrastandard irreps, the $3jm$ -symbol transforms as a triple product of standard irreps. Indeed, the defining equation (82) gives for $U \in SU(2)$

$$\begin{aligned} & (-1)^{j_1 - j_2 + j_3} \begin{pmatrix} j_1 & j_2 & j_3 \\ m_1 & m_2 & m_3 \end{pmatrix} \\ &= \langle (j_1 j_2 j_3) 00 | j_1 m_1; j_2 m_2; j_3 m_3 \rangle \\ &= \langle (j_1 j_2 j_3) 00 | U^\dagger U | j_1 m_1; j_2 m_2; j_3 m_3 \rangle \\ &= (-1)^{j_1 - j_2 + j_3} \\ &\quad \times \sum_{\mu_1 \mu_2 \mu_3} \begin{pmatrix} j_1 & j_2 & j_3 \\ \mu_1 & \mu_2 & \mu_3 \end{pmatrix} D^{(j_1)}(U)_{\mu_1 m_1} D^{(j_2)}(U)_{\mu_2 m_2} D^{(j_3)}(U)_{\mu_3 m_3}. \end{aligned} \quad (83)$$

For the graphical representation of the $3jm$ -symbol we realize that the three angular momenta appear in the ket and are standard, so that they must be represented by single-arrowed outgoing lines. Accordingly we set⁵

$$\begin{pmatrix} j_1 & j_2 & j_3 \\ m_1 & m_2 & m_3 \end{pmatrix} =: \begin{array}{c} \begin{array}{c} \uparrow j_2 m_2 \\ \bullet \\ \swarrow j_1 m_1 \quad \searrow j_3 m_3 \end{array} \end{array},$$

the minus sign at the vertex indicating a clockwise reading in accordance with our conventions.

The $3jm$ -symbol times $(-1)^{j_1 - j_2 + j_3}$, as defined by equation (82), is equal to the generalized CG coefficient on the left-hand side of equations (79) and (80). The second of these equations states that

$$(-1)^{j_1 - j_2 + j_3} \begin{pmatrix} j_1 & j_2 & j_3 \\ m_1 & m_2 & m_3 \end{pmatrix} = [j_1]^{-1/2} \langle j_2 m_2; j_3 m_3 | \vartheta(j_1 m_1) \rangle, \quad (84)$$

which implies the following relationship between the $3jm$ - and CG coefficients

$$\begin{pmatrix} j_1 & j_2 & j_3 \\ m_1 & m_2 & m_3 \end{pmatrix} = [j_1]^{-1/2} (-1)^{j_2 - j_3 - m_1} \langle j_1, -m_1 | j_2 m_2; j_3 m_3 \rangle. \quad (85)$$

This relation is often used as the definition of a $3jm$ -symbol.

⁵ When no confusion can arise, we shall again replace the label $j_k m_k$ simply by k and for the contracted lines j_k by k .

Let us now investigate some basic properties of the $3jm$ -symbol. We see immediately from equation (85) that the $3jm$ -symbol vanishes unless

$$m_1 + m_2 + m_3 = 0. \quad (86)$$

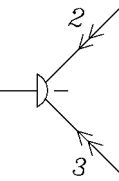
It is also easy to see that it is symmetric or antisymmetric under the permutation of its columns. Indeed, using the symmetry property (iii) of CG coefficients (equation (60)) together with equation (84) we find that

$$\begin{pmatrix} j_1 & j_2 & j_3 \\ m_1 & m_2 & m_3 \end{pmatrix} = (-1)^{j_1+j_2+j_3} \begin{pmatrix} j_1 & j_3 & j_2 \\ m_1 & m_3 & m_2 \end{pmatrix}. \quad (87)$$

Further, a $3jm$ -symbol is invariant under a cyclic permutation of all three columns,

$$\begin{pmatrix} j_2 & j_3 & j_1 \\ m_2 & m_3 & m_1 \end{pmatrix} = \begin{pmatrix} j_1 & j_2 & j_3 \\ m_1 & m_2 & m_3 \end{pmatrix},$$

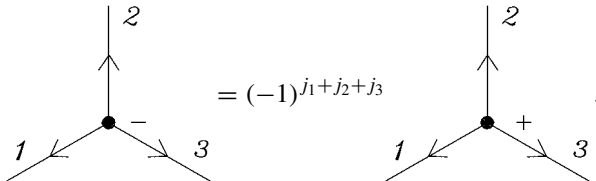
as can be seen easily by applying the cyclic permutation (1 2 3) to equation (79),

$$(-1)^{j_2-j_3+j_1} \begin{pmatrix} j_2 & j_3 & j_1 \\ m_2 & m_3 & m_1 \end{pmatrix} = (-1)^{2j_1} [j_1]^{-1/2} \rightarrow \text{diagram}$$


applying equation (84) to the right-hand side and observing that $j_1 - j_2 + j_3$ is integer, so that $(-1)^{2j_1-2j_2+2j_3} = 1$. Since the permutations (1 2 3) and (2 3) generate all $3!$ permutations of the three columns, we have found the general rule:

A $3jm$ -symbol is invariant under an even permutation of its columns and obtains the phase factor $(-1)^{j_1+j_2+j_3}$ upon an odd permutation of its columns.

The invariance of a $3jm$ -symbol with respect to cyclic permutations is reflected in the three-fold symmetry of the $3jm$ -diagram, while the relationship (87) leads to the rule for the reversal of vertex sign:



$$= (-1)^{j_1+j_2+j_3}.$$

It is also useful to define mixed standard-contrastandard $3jm$ -symbols, such as, for example,

$$\begin{pmatrix} \mu_1 & j_2 & j_3 \\ j_1 & m_2 & m_3 \end{pmatrix} := (-1)^{j_1-j_2+j_3} \langle (j_1 j_2 j_3) 00 | \vartheta(j_1 \mu_1); j_2 m_2; j_3 m_3 \rangle. \quad (88)$$

This symbol obviously transforms as $D^{(j_1)*} \otimes D^{(j_2)} \otimes D^{(j_3)}$, which we indicate by placing the magnetic quantum number μ_1 in the upper row of the $3jm$ -symbol. It is easy to see that we can lower and raise the magnetic quantum number using the $1jm$ -symbol. Indeed,

applying equation (69) we obtain

$$\begin{aligned}
 \begin{pmatrix} \mu_1 & j_2 & j_3 \\ j_1 & m_2 & m_3 \end{pmatrix} &= (-1)^{j_1-j_2+j_3} \sum_{m_1} \langle (j_1 j_2 j_3) 00 | j_1 m_1; j_2 m_2; j_3 m_3 \rangle \begin{pmatrix} j_1 \\ m_1 \mu_1 \end{pmatrix} \\
 &= \sum_{m_1} \begin{pmatrix} j_1 & j_2 & j_3 \\ m_1 & m_2 & m_3 \end{pmatrix} \begin{pmatrix} j_1 \\ m_1 \mu_1 \end{pmatrix} \\
 &= (-1)^{j_1-\mu_1} \begin{pmatrix} j_1 & j_2 & j_3 \\ -\mu_1 & m_2 & m_3 \end{pmatrix}. \tag{89}
 \end{aligned}$$

Thus, to *raise* a quantum number we put the $1jm$ -symbol on the *right* (and sum over the common index). Graphically, this raising is represented by an arrow reversal, since

$$\begin{pmatrix} \mu_1 & j_2 & j_3 \\ j_1 & m_2 & m_3 \end{pmatrix} = \sum_{m_1} \begin{pmatrix} \mu_1 & j_2 & j_3 \\ j_1 & m_2 & m_3 \end{pmatrix} + \begin{pmatrix} \mu_1 & j_2 & j_3 \\ j_1 & m_2 & m_3 \end{pmatrix} = \sum_{m_1} \begin{pmatrix} \mu_1 & j_2 & j_3 \\ j_1 & m_2 & m_3 \end{pmatrix} + \begin{pmatrix} \mu_1 & j_2 & j_3 \\ j_1 & m_2 & m_3 \end{pmatrix}$$

as implied by equations (70) and (71).

To lower a magnetic quantum number, we write (cf. equation (65))

$$|jm\rangle = \sum_{\mu} |\vartheta(j\mu)\rangle \langle \vartheta(j\mu) | jm \rangle = \sum_{\mu} \begin{pmatrix} j \\ m \mu \end{pmatrix} |\vartheta(j\mu)\rangle,$$

which reads graphically

$$\begin{pmatrix} j & m \\ m & \mu \end{pmatrix} = \sum_{\mu} \begin{pmatrix} j & m \\ m & \mu \end{pmatrix} = \sum_{\mu} \begin{pmatrix} j & m \\ m & \mu \end{pmatrix}$$

If we use this relationship in the first equation (83) and recall the definition of the mixed $3jm$ -symbol, given in equation (88), we get

$$\begin{aligned}
 \begin{pmatrix} j_1 & j_2 & j_3 \\ m_1 & m_2 & m_3 \end{pmatrix} &= \sum_{\mu_1} \begin{pmatrix} j_1 \\ m_1 \mu_1 \end{pmatrix} \begin{pmatrix} \mu_1 & j_2 & j_3 \\ j_1 & m_2 & m_3 \end{pmatrix} \\
 &= (-1)^{j_1+m_1} \begin{pmatrix} -m_1 & j_2 & j_3 \\ j_1 & m_2 & m_3 \end{pmatrix}. \tag{90}
 \end{aligned}$$

Thus, to *lower* a magnetic quantum number we put the $1jm$ -symbol on the *left*. Of course, raised and lowered $3jm$ -symbols are closely related. When we substitute $-m_1 = \mu_1$ in the last equation and use that $j_1 + m_1$ is an integer number, we immediately recover equation (89).

Clearly we can raise or lower the magnetic quantum numbers *independently in each column*. Correspondingly, this implies an independent arrow reversal for each of the corresponding lines of the $3jm$ -diagram. This operation implies certain symmetry properties which follow from the (anti)unitarity of ϑ and the invariance of $\langle (j_1 j_2 j_3) 00 |$ under ϑ , which yield

$$\langle (j_1 j_2 j_3) 00 | j_1 m_1; j_2 m_2; j_3 m_3 \rangle = \langle (j_1 j_2 j_3) 00 | \vartheta(j_1 m_1); \vartheta(j_2 m_2); \vartheta(j_3 m_3) \rangle$$

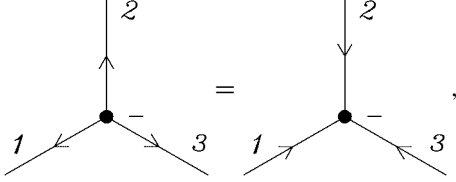
or

$$\begin{pmatrix} j_1 & j_2 & j_3 \\ m_1 & m_2 & m_3 \end{pmatrix} = \begin{pmatrix} m_1 & m_2 & m_3 \\ j_1 & j_2 & j_3 \end{pmatrix}. \quad (91)$$

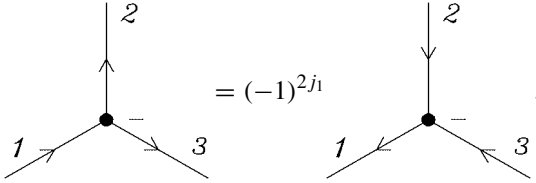
In a very similar manner we obtain from equations (48) and (88)

$$\begin{pmatrix} m_1 & j_2 & j_3 \\ j_1 & m_2 & m_3 \end{pmatrix} = (-1)^{2j_1} \begin{pmatrix} j_1 & m_2 & m_3 \\ m_1 & j_2 & j_3 \end{pmatrix}. \quad (92)$$

Graphically equation (91) gives the rule



and equation (92):



Note that in the latter rule the line with the unique variance determines the phase.

Finally, it is important to remark that also a mixed $3jm$ -symbol is invariant under an even permutation of its columns and obtains the phase factor $(-1)^{j_1+j_2+j_3}$ upon an odd permutation of its columns, which is due to the fact that the raising and lowering operations can be applied to any column independently.

3.6. Transition from CG coefficients to $3jm$ -symbols

Almost all physical problems involving coupling of angular momenta find their most natural formulation in terms of CG coefficients. On the other hand, the $3jm$ -symbols are easier to manipulate and lead to simpler graphical rules in view of their symmetry. We thus find it best to formulate the initial problem in terms of CG diagrams and transform them subsequently to $3jm$ -diagrams, using the rules which will be given shortly. We then construct the final resulting diagrams, simplify and evaluate them using the rules which will be expounded in the remainder of this work.

It is, of course, possible to formulate all the rules in terms of CG diagrams (see, *e.g.*, Ref. [19]) or to employ a unified CG– $3jm$ representation [30]. In any case, however, either more complicated rules result or the generality must be sacrificed.

The transition rules that we now introduce are found by inspection. We will demonstrate their application on several examples in order to convince ourselves that they are correct.

RULES (Transformation from CG to $3jm$ -coefficients).

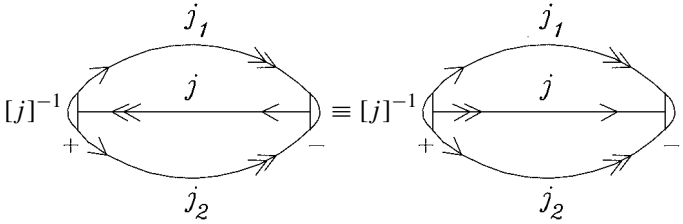
1. Conserve the variance and labeling of all lines and replace double arrows by single arrows.

2. Change the vertex sign.
3. Multiply by $[j]^{1/2} \equiv (2j+1)^{1/2}$, where j labels the unique line of the CG coefficient.
4. Multiply by $(-1)^{2j}$ for each line j marked by an outgoing double arrow (a time-inverted bra).
5. Multiply by $(-1)^{2j}$, where j is the first non-unique line in the CG diagram. The first non-unique line is defined as the first line which is met when going in the direction indicated by the node sign starting from a single arrow unique line and in the opposite direction for a double arrow unique line.

To remember more easily rule 5, we recall that, loosely speaking, the bra is the complex conjugate of the ket, so that the association of *complex* with *contra* may provide a useful mnemonics.

In Table 1 we give a number of illustrations of the transformation rules with both the graphical and the algebraic form in each case. We illustrate rule 5 by a curved arrow ending at the first non-unique line. The transition rules for individual CG coefficients can be also applied to resulting CG diagrams containing contracted lines. In such a case we first assign arrows to the lines, which often gives us certain freedom.

Consider, for example, the diagram of the triangular delta, equation (64). Two of the possible arrow assignments are



Application of the transition rules leads to, respectively,

$$\begin{aligned}
 & (-1)^{2j_1+2j_2} \begin{array}{c} \xrightarrow{j_1} \\ \text{---} j \text{---} \\ \xleftarrow{j_2} \end{array} \begin{array}{c} \bullet \\ + \end{array} \equiv (-1)^{2j+2j_1+2j_2} \begin{array}{c} \xrightarrow{j_1} \\ \text{---} j \text{---} \\ \xrightarrow{j_2} \end{array} \begin{array}{c} \bullet \\ - \end{array} \\
 & \hspace{15em} = \{j_1, j_2, j_3\}. \tag{93}
 \end{aligned}$$

Note that $(-1)^{2j+2j_1+2j_2} = 1$ and $(-1)^{2j_1+2j_2} = (-1)^{2j}$, so that we have here an illustration of the rule of arrow reversal (cf. (57)), which also holds for $3jm$ -diagrams.

Although it is irrelevant which arrow assignment we choose, as the above example illustrates, it must, of course, be done in a consistent way. The two non-unique lines that are attached to a given CG vertex must be both of the same type (*i.e.*, either both bra or both ket lines). Further, a non-oriented contracted line must be composed of a bra and a ket, and an oriented line must consist either of two ket lines in the same direction or of two bra lines in opposite direction, as implied by the contraction Convention C4. In practical applications it is of course best to make the $\text{CG} \rightarrow 3jm$ conversion first, before drawing the resulting diagrams, as already indicated above.

Table 1. Examples of transformation from CG to $3jm$ -diagrams

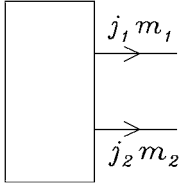
1.		$= [j_3]^{1/2}(-1)^{2j_2}$	
	$\langle j_3 m_3 j_1 m_1; j_2 m_2 \rangle$	$= [j_3]^{1/2}(-1)^{2j_2}$	$\begin{pmatrix} j_1 & m_3 & j_2 \\ m_1 & j_3 & m_2 \end{pmatrix}$
2.		$= [j_3]^{1/2}(-1)^{2j_2+2j_3}$	
	$\langle \vartheta(j_3 m_3) j_1 m_1; j_2 m_2 \rangle$	$= [j_3]^{1/2}(-1)^{2j_1}$	$\begin{pmatrix} j_1 & j_3 & j_2 \\ m_1 & m_3 & m_2 \end{pmatrix}$
3.		$= [j_3]^{1/2}(-1)^{2j_1}$	
	$\langle j_1 m_1; j_2 m_2 \vartheta(j_3 m_3) \rangle$	$= [j_3]^{1/2}(-1)^{2j_1}$	$\begin{pmatrix} m_1 & m_3 & m_2 \\ j_1 & j_3 & j_2 \end{pmatrix}$
4.		$= [j_3]^{1/2}(-1)^{2j_1+2j_2+2j_3}$	
	$\langle \vartheta(j_2 m_2); \vartheta(j_1 m_1) j_3 m_3 \rangle$	$= [j_3]^{1/2}(-1)^{2j_1}$	$\begin{pmatrix} j_1 & j_2 & j_3 \\ m_1 & m_2 & m_3 \end{pmatrix}$
5.		$= [j_3]^{1/2}(-1)^{4j_2}$	
	$\langle \vartheta(j_2 m_2); j_1 m_1 j_3 m_3 \rangle$	$= [j_3]^{1/2}$	$\begin{pmatrix} m_1 & j_2 & j_3 \\ j_1 & m_2 & m_3 \end{pmatrix}$

4. BASIC RULES FOR ANGULAR MOMENTUM DIAGRAMS

In the preceding section we have introduced the basic concepts of graphical techniques of spin algebras and formulated the rules for the conversion of CG diagrams into

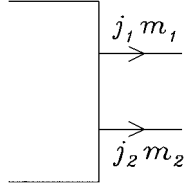
$3jm$ -diagrams. From now on we shall restrict our attention to the latter and will derive the rules which will enable us to reduce any angular momentum problem to the computation of canonical $3nj$ -symbols, $n = 1, 2, \dots$, by expressing the kinematic part of a given angular momentum problem in terms of these symbols. The dynamic part, however, which is contained in the so-called reduced matrix elements, must be treated separately for each case.

In deriving the graphical rules we shall distinguish closed and open diagrams and will represent them as closed and open boxes,



(a)

and



(b)

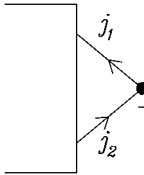
(94)

respectively. Thus, the diagram (94a) represents a graph with an arbitrary number of $3jm$ -vertices and with all lines contracted except those which are shown explicitly, namely the lines labeled $j_1 m_1$ and $j_2 m_2$. Referring to the contracted lines which connect two $3jm$ -vertices as the *internal lines* and to the uncontracted ones as the *free* or *external lines*, we can also say that a closed diagram represented by a full box, as in (94a), contains only internal lines, and all the free lines must be shown explicitly. With an open box, diagram (94b), we then represent a graph which may possess additional free lines to those indicated explicitly. Since some of the rules hold only for closed diagrams, this distinction is important.

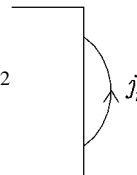
4.1. Removal of a zero line

We prove the following rules for the removal of a zero line, which hold provided that j_1 and j_2 are distinct lines.

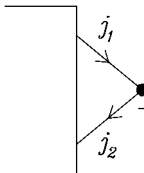
RULE 1.



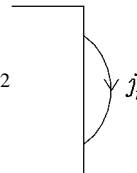
$\cdots = \delta_{j_1 j_2} [j_1]^{-1/2}$



(95)



$\cdots = \delta_{j_1 j_2} [j_1]^{-1/2}$



(96)

Thus, when the lines j_1 and j_2 run in the direction indicated by the vertex sign, the vertex with attached zero line can be replaced by the factor $\delta_{j_1 j_2} [j_1]^{-1/2}$.

PROOF. Assuming that j_1 and j_2 are distinct lines, we may reverse the direction of the j_2 line and write

$$\begin{aligned}
 & \left[\begin{array}{c} j_1 \\ \text{---} \\ j_2 \end{array} \right] \text{---} = (-1)^{2j_2} \left[\begin{array}{c} j_1 \\ \text{---} \\ j_2 \end{array} \right] \text{---} \\
 & = (-1)^{2j_2} \sum_{m_1 m_2} \left[\begin{array}{c} j_1 m_1 \\ \text{---} \\ j_2 m_2 \end{array} \right] \text{---} .
 \end{aligned}$$

Converting to a CG vertex and using equation (74) we find

$$\begin{aligned}
 & \left[\begin{array}{c} j_1 m_1 \\ \text{---} \\ j_2 m_2 \end{array} \right] \text{---} = (-1)^{2j_1} \left[\begin{array}{c} j_1 m_1 \\ \text{---} \\ j_2 m_2 \end{array} \right] \text{---} = \delta_{j_1 j_2} (-1)^{2j_1} [j_1]^{-1/2} \left[\begin{array}{c} j_1 m_1 \\ \text{---} \\ j_2 m_2 \end{array} \right] \text{---} .
 \end{aligned}$$

Using, further, the completeness relation, equation (71), we get the first rule, (95),

$$\begin{aligned}
 & \left[\begin{array}{c} j_1 \\ \text{---} \\ j_2 \end{array} \right] \text{---} = \delta_{j_1 j_2} [j_1]^{-1/2} \left[\begin{array}{c} j_1 \\ \text{---} \\ j_2 \end{array} \right] \text{---} = \delta_{j_1 j_2} [j_1]^{-1/2} \left[\begin{array}{c} j_1 \\ \text{---} \\ j_1 \end{array} \right] \text{---} .
 \end{aligned}$$

The second rule, (96), follows directly from the first when we note that

$$\begin{aligned}
 & \left[\begin{array}{c} j_1 \\ \text{---} \\ j_2 \end{array} \right] \text{---} = (-1)^{3j_1+3j_2} \left[\begin{array}{c} j_1 \\ \text{---} \\ j_2 \end{array} \right] \text{---} = \delta_{j_1 j_2} (-1)^{2j_1} [j_1]^{-1/2} \left[\begin{array}{c} j_1 \\ \text{---} \\ j_1 \end{array} \right] \text{---} .
 \end{aligned}$$

The use of the rule for arrow reversal then gives the desired result. \square

REMARK. It is of interest to consider the case—which we explicitly excluded—that j_1 and j_2 label the same line and for which the proof above does not apply. Since by equation (72)

$$\begin{aligned}
 & \left[\begin{array}{c} j m \\ \text{---} \\ j m \end{array} \right] \text{---} = [j]^{-1/2} \left[\begin{array}{c} j m \\ \text{---} \\ j m \end{array} \right] \text{---} = [j]^{-1/2} \langle j m | j m; 00 \rangle = [j]^{-1/2} ,
 \end{aligned}$$

we find that

$$\begin{aligned}
 \text{Loop } j \text{ with } + \text{ sign} &= \sum_m \text{Diagram with two lines } j, m \text{ and } + \text{ sign} \\
 &= \sum_m \text{Diagram with two lines } j, m \text{ and } - \text{ sign} = \text{Loop } j \text{ with } - \text{ sign} = [j]^{1/2}.
 \end{aligned}$$

Recalling that the non-oriented loop represents $[j] \equiv 2j + 1$, equation (55), we get the rule

$$\text{Loop } j \text{ with } + \text{ sign} = \text{Loop } j \text{ with } - \text{ sign} = [j]^{-1/2} \text{Loop } j \equiv [j]^{1/2}, \quad (97)$$

which differs from the general rules (95) and (96) in that the resulting line is non-oriented. It is essential that the loop is non-oriented, because otherwise the rule of arrow reversal would predict that the two oriented loops differ by a factor $(-1)^{2j}$.

4.2. Factorization rules

A $3jm$ -symbol, being an inner product by equation (83), is an $SU(2)$ invariant. On the other hand, it transforms as a triple Kronecker product of irreps, equation (83). A similar observation leads to the well-known Wigner–Eckart theorem, which states that the matrix element of an irreducible tensor operator between eigenstates of J^2 can be factored into an invariant quantity (the so-called reduced matrix element) and a quantity that reflects the transformation properties of the matrix element. The latter quantity is a mixed $3jm$ -symbol (or a CG coefficient).

We shall first show that the transformation properties of a diagram are solely determined by its free lines. Following the proof of the Wigner–Eckart theorem we then obtain a factorization of the diagram into an invariant quantity and a quantity that carries the transformation properties of the diagram.

Consider a diagram with n $3jm$ -vertices (the proof works equally well for CG graphs). Transforming all the states with $U \in SU(2)$, the diagram, on the one hand, remains invariant and, on the other hand, transforms as a $3n$ -fold Kronecker product of D matrices. However, the D matrices that correspond to internal lines cancel one another in view of their unitarity. Indeed, by definition, a contracted line consists of a standard and a contra-standard quantity, say a ket and a time-reversed ket, so that

$$\begin{aligned}
 U \sum_m |jm; \vartheta(jm)\rangle &= \sum_{m, \mu, \mu'} D^{(j)}(U)_{\mu m} D^{(j)}(U)_{\mu' m}^* |j\mu; \vartheta(j\mu')\rangle \\
 &= \sum_{\mu, \mu'} \delta_{\mu \mu'} |j\mu; \vartheta(j\mu')\rangle = \sum_{\mu} |j\mu; \vartheta(j\mu)\rangle.
 \end{aligned}$$

(The invariance of contractions of other types is proved in a similar manner, *cf.* also equation (35).) Thus, the transformation properties of a diagram are defined solely and uniquely

by its free lines. We next state and prove the following very useful rule for the closing of a diagram with two external lines.

RULE 2.

$$= \delta_{j_1 j_2} \delta_{m_1 m_2} [j_1]^{-1} \quad (98)$$

PROOF. We denote the diagram on the left-hand side by $G \begin{pmatrix} j_1 & m_2 \\ m_1 & j_2 \end{pmatrix}$ and apply $U \in \text{SU}(2)$ obtaining

$$\begin{aligned} U G \begin{pmatrix} j_1 & m_2 \\ m_1 & j_2 \end{pmatrix} &= G \begin{pmatrix} j_1 & m_2 \\ m_1 & j_2 \end{pmatrix} \\ &= \sum_{\mu_1, \mu_2} D^{(j_1)}(U)_{\mu_1 m_1} D^{(j_2)}(U)_{\mu_2 m_2}^* G \begin{pmatrix} j_1 & \mu_2 \\ \mu_1 & j_2 \end{pmatrix}. \end{aligned}$$

Since all unitary groups are compact, their “volume” is well defined, and designating the volume of $\text{SU}(2)$ by V , we find using the great orthonormality relations and integrating over the whole group, that

$$\begin{aligned} V G \begin{pmatrix} j_1 & m_2 \\ m_1 & j_2 \end{pmatrix} &= \sum_{\mu_1, \mu_2} G \begin{pmatrix} j_1 & \mu_2 \\ \mu_1 & j_2 \end{pmatrix} \int D^{(j_1)}(U)_{\mu_1 m_1} D^{(j_2)}(U^{-1})_{m_2 \mu_2} dV \\ &= \sum_{\mu_1, \mu_2} G \begin{pmatrix} j_1 & \mu_2 \\ \mu_1 & j_2 \end{pmatrix} \delta_{j_1 j_2} \delta_{\mu_1 \mu_2} \delta_{m_1 m_2} V [j_1]^{-1} \\ &= \delta_{j_1 j_2} \delta_{m_1 m_2} V [j_1]^{-1} \sum_{\mu_1} G \begin{pmatrix} j_1 & \mu_1 \\ \mu_1 & j_1 \end{pmatrix}, \end{aligned}$$

so that

$$\begin{aligned} G \begin{pmatrix} j_1 & m_2 \\ m_1 & j_2 \end{pmatrix} &= \delta_{j_1 j_2} \delta_{m_1 m_2} [j_1]^{-1} \sum_{\mu_1} G \begin{pmatrix} j_1 & \mu_1 \\ \mu_1 & j_1 \end{pmatrix} \\ &= \delta_{j_1 j_2} \delta_{m_1 m_2} [j_1]^{-1} \quad \text{[Diagram: vertical rectangle with a curved line on the right labeled } j_1 \text{ with a checkmark]} \end{aligned}$$

In a similar way we can prove the following rule:

$$= \delta_{j 0} \delta_{m 0} \quad (99)$$

which states that the only $\text{SU}(2)$ invariant quantity transforming according to the irrep (j) of $\text{SU}(2)$ is one transforming according to the identity irrep $j = 0$. We must emphasize

that the above two rules hold irrespective of whether the diagram consists of CG vertices, $3jm$ -vertices or a mixture of both. In the case of two free lines, the proof simply rests on the fact that one line is standard and the other one contrastandard.

To derive similar rules for diagrams with more than two free lines we simply precouple the lines, thus reducing their number. This is most easily done by exploiting the identity

$$\sum_j [j] \begin{array}{c} j_1 m_1 \nearrow \\ \bullet + \\ j_2 m_2 \nearrow \end{array} \begin{array}{c} \leftarrow j \\ \bullet - \\ \leftarrow j \end{array} \begin{array}{c} j_1 m'_1 \nearrow \\ \bullet - \\ j_2 m'_2 \searrow \end{array} = \delta_{m_1 m'_1} \delta_{m_2 m'_2}, \quad (100)$$

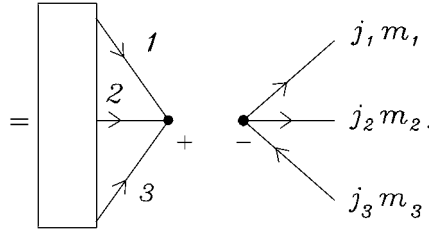
which follows immediately from the corresponding orthogonality relation for CG coefficients, equation (63). \square

RULE 3. A diagram can be factorized over three lines by the use of

$$\begin{array}{|l} \\ \\ \end{array} \begin{array}{c} \xrightarrow{j_1 m_1} \\ \xrightarrow{j_2 m_2} \\ \xleftarrow{j_3 m_3} \end{array} = \begin{array}{|l} \\ \\ \end{array} \begin{array}{c} 1 \\ 2 \\ 3 \end{array} \begin{array}{c} \nearrow \\ \bullet + \\ \nearrow \end{array} + \begin{array}{|l} \\ \\ \end{array} \begin{array}{c} \nearrow \\ \bullet - \\ \searrow \end{array} \begin{array}{c} j_1 m_1 \\ j_2 m_2 \\ j_3 m_3 \end{array}. \quad (101)$$

PROOF. Applying the identity (100) and the separation rule (98), we obtain

$$\begin{aligned} \begin{array}{|l} \\ \\ \end{array} \begin{array}{c} \xrightarrow{j_1 m_1} \\ \xrightarrow{j_2 m_2} \\ \xleftarrow{j_3 m_3} \end{array} &= \sum_j (-1)^{2j} [j] \sum_{m'_1 m'_2} \begin{array}{|l} \\ \\ \end{array} \begin{array}{c} \xrightarrow{j_1 m'_1} \\ \xrightarrow{j_2 m'_2} \\ \xleftarrow{j_3 m_3} \end{array} \begin{array}{c} \nearrow \\ \bullet + \\ \nearrow \end{array} \begin{array}{c} \leftarrow j \\ \bullet - \\ \leftarrow j \end{array} \begin{array}{c} \nearrow \\ \bullet - \\ \searrow \end{array} \begin{array}{c} 1 \\ 2 \end{array} \\ &= \sum_{jm} (-1)^{2j} [j] \begin{array}{|l} \\ \\ \end{array} \begin{array}{c} 1 \\ 2 \\ 3 \end{array} \begin{array}{c} \nearrow \\ \bullet + \\ \nearrow \end{array} \begin{array}{c} j m \\ j m \\ j m \end{array} \begin{array}{c} \nearrow \\ \bullet - \\ \searrow \end{array} \begin{array}{c} 1 \\ 2 \end{array} \\ &= (-1)^{2j_3} \begin{array}{|l} \\ \\ \end{array} \begin{array}{c} 1 \\ 2 \\ 3 \end{array} \begin{array}{c} \nearrow \\ \bullet + \\ \nearrow \end{array} \begin{array}{c} 1 \\ 2 \\ 3 \end{array} \begin{array}{c} \nearrow \\ \bullet - \\ \searrow \end{array} \begin{array}{c} 1 \\ 2 \\ 3 \end{array} \end{aligned}$$



Similar rules hold for other possible orientations of external lines (see the example below). \square

Note that we have achieved the same factorization as in the Wigner–Eckart theorem. The closed diagram is invariant under $SU(2)$, and the mixed $3jm$ -symbol has the transformation properties of the original diagram, characterized by two standard (outgoing) lines and one contrastandard (ingoing) line. The positions of the plus and minus vertex signs in the final result may be interchanged, since $(-1)^{2(j_1+j_2+j_3)} = 1$.

In the case of more than three external lines we can simply factor out the corresponding generalized CG coefficient or its $3jm$ -equivalent. Thus, in the case of four external lines, we find the following rule.

RULE 4. A diagram can be separated over four lines by the use of the following rule,

$$\begin{aligned}
 & \text{Diagram with box and 4 lines} = \sum_{jm} \sum_{j'm'} [j][j'] (-1)^{2j} \text{Diagram with box and 4 lines} \\
 & = \sum_j [j] \text{Diagram with box and 4 lines} \times \sum_m (-1)^{2j} jm \text{Diagram with 4 lines} \\
 & = \sum_j [j] \text{Diagram with box and 4 lines} \text{Diagram with 4 lines}
 \end{aligned} \tag{102}$$

Note that both j lines could also be oriented downward and that the vertex signs are arbitrary as long as they are opposite for vertices associated with identically labeled lines.

It should now be clear how to handle the cases with more than four free lines. However, since n free lines, $n > 3$, give rise to $n - 3$ summations over the intermediate quantum numbers, the factorization rule is seldom used for more than four free lines.

When we meet open diagrams whose free lines have variances different from those used in the above given factorization rules, we proceed in the same way as we did in the raising and lowering of the magnetic quantum numbers in $3jm$ -symbols, Section 3.5. Namely, we use either one of the following rules:

$$\begin{aligned} \text{Diagram with } j, m \text{ and } \mu \text{ lines} &= \sum_{\mu} \text{Diagram with } j, \mu \text{ and } \mu \text{ lines} \rightarrow \text{Diagram with } j, m \text{ and } \mu \text{ lines}, \\ \text{Diagram with } j, m \text{ and } \mu \text{ lines} &= \sum_{\mu} \text{Diagram with } j, \mu \text{ and } \mu \text{ lines} \rightarrow \text{Diagram with } j, m \text{ and } \mu \text{ lines}, \end{aligned}$$

which converts the free line to the required variance, and then apply the factorization rule to the line labeled by the summation index μ . For example,

$$\begin{aligned} &\text{Diagram with } 1 \text{ and } 2 \text{ lines} = \sum_{\mu_2} \text{Diagram with } 1 \text{ and } j_2, \mu_2 \text{ lines} \rightarrow \text{Diagram with } 2 \text{ lines} \\ &= \sum_{\mu_2} \delta_{j_1 j_2} \delta_{m_1 \mu_2} [j_1]^{-1} \text{Diagram with } 1 \text{ and } j_2, \mu_2 \text{ lines} \rightarrow \text{Diagram with } 2 \text{ lines} \\ &= \delta_{j_1 j_2} \delta_{m_1, -m_2} [j_1]^{-1} (-1)^{j_1 - m_1} \text{Diagram with } 1 \text{ and } j_2, \mu_2 \text{ lines}, \end{aligned} \quad (103)$$

where we used $\langle \vartheta(j_2 \mu_2) | j_2 m_2 \rangle = (-1)^{j_2 + m_2} \delta_{-\mu_2, m_2}$ (equation (67)) for the $1jm$ -symbol. Similarly,

$$\begin{aligned} &\text{Diagram with } 1, 2 \text{ and } 3 \text{ lines} = \sum_{\mu_3} \text{Diagram with } 1, 2 \text{ and } j_3, \mu_3 \text{ lines} \rightarrow \text{Diagram with } 3 \text{ lines} \\ &= \sum_{\mu_3} \text{Diagram with } 1, 2 \text{ and } j_3, \mu_3 \text{ lines} \rightarrow \text{Diagram with } 3 \text{ lines} \end{aligned}$$

$$= \text{[Diagram]} \quad (104)$$

4.3. Separation rules

The factorization rules imply immediately the following separation rules.

1. *Separation over one line:*

$$= \delta_{j,0} \text{[Diagram]} \quad (105)$$

The zero angular momentum lines can then be eliminated by the use of rule (95), (96), or (97).

2. *Separation over two lines:*

$$= \sum_{m_1 m_2} (-1)^{2j_2} \text{[Diagram]} \quad (106)$$

Clearly, both resulting j_1 lines can also be oriented in the upward direction. Similarly, if the j_1 and j_2 lines run in opposite directions in the connected diagram at the left-hand side, then so do the resulting lines in the separated diagram.

3. *Separation over three lines:* Using the factorization rule equation (104), we can prove that

$$= \text{[Diagram]} \quad (107)$$

We could also formulate the rules for separation over more than three lines. However, such rules may be difficult to apply, particularly within complicated diagrams, and it is generally advisable to proceed by substituting one or more intermediate summation lines. We have already applied this technique of pairwise precoupling in the factorization of

diagrams with three and four external lines. After a sufficient number of summation lines have been introduced, the diagram may be factored using one of the separation rules given above.

The substitution of a summation line is accomplished by the following rule, which is a direct consequence of equation (100),

$$\begin{array}{|c|} \hline \\ \hline \end{array} \begin{array}{c} \xrightarrow{1} \\ \xrightarrow{2} \end{array} \begin{array}{|c|} \hline \\ \hline \end{array} = \sum_x [x] \begin{array}{|c|} \hline \\ \hline \end{array} \begin{array}{c} \xrightarrow{1} \\ \xrightarrow{2} \end{array} \begin{array}{c} \bullet \\ + \end{array} \begin{array}{c} \xleftarrow{x} \\ \xleftarrow{-} \end{array} \begin{array}{c} \bullet \\ - \end{array} \begin{array}{c} \xrightarrow{1} \\ \xrightarrow{2} \end{array} \begin{array}{|c|} \hline \\ \hline \end{array} . \quad (108)$$

This rule is easy to remember: we first orient the lines to be coupled so that they run in the same direction. We insert a summation line that runs in the opposite direction. The vertex signs are chosen in such a way that the order of the three angular momenta j_1 , j_2 , and x is the same for both vertices. (Note that the diagram is invariant with respect to the interchange of vertex signs.) An analogous rule holds also for the case of crossing lines.

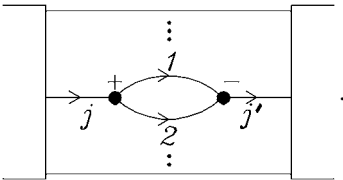
4. *Separation over four lines:* We separate over four lines, as an example, precoupling j_2 and j_3 ,

$$\begin{array}{|c|} \hline \\ \hline \end{array} \begin{array}{c} \xrightarrow{1} \\ \xrightarrow{2} \\ \xrightarrow{3} \\ \xrightarrow{4} \end{array} \begin{array}{|c|} \hline \\ \hline \end{array} = \sum_x [x] \begin{array}{|c|} \hline \\ \hline \end{array} \begin{array}{c} \xrightarrow{1} \\ \xrightarrow{2} \\ \xrightarrow{3} \\ \xrightarrow{4} \end{array} \begin{array}{c} \bullet \\ + \end{array} \begin{array}{c} \xleftarrow{x} \\ \xleftarrow{-} \end{array} \begin{array}{c} \bullet \\ - \end{array} \begin{array}{c} \xrightarrow{1} \\ \xrightarrow{2} \\ \xrightarrow{3} \\ \xrightarrow{4} \end{array} \begin{array}{|c|} \hline \\ \hline \end{array} \\ = \sum_x [x] \begin{array}{|c|} \hline \\ \hline \end{array} \begin{array}{c} \xrightarrow{1} \\ \xrightarrow{2} \\ \xrightarrow{3} \\ \xrightarrow{4} \end{array} \begin{array}{c} \bullet \\ + \end{array} \begin{array}{c} \xrightarrow{x} \\ \xrightarrow{+} \end{array} \begin{array}{c} \bullet \\ + \end{array} \begin{array}{c} \xrightarrow{1} \\ \xrightarrow{2} \\ \xrightarrow{3} \\ \xrightarrow{4} \end{array} \begin{array}{|c|} \hline \\ \hline \end{array} . \quad (109)$$

To end the discussion of the separation rules we point out that the factorization rules represent a special case of the separation rules when one of the diagrams is an empty diagram. It thus suffices to remember the separation rules only.

We will end this section by giving four examples in which the separation rules are illustrated.

EXAMPLE 1. As an illustration of the two-line separation rule (106), we consider the removal of a loop, *i.e.*, a diagram of the type



Pulling down the loop sufficiently far and observing that the loop is a closed diagram, we can apply (106) for the lines j and j' , obtaining

$$\begin{array}{c} \text{Diagram 1: A rectangular box with four vertical lines. The left and right lines are connected at the bottom by a loop. The loop has two vertices, each with a dot. The left vertex is labeled '+' and the right vertex is labeled '-'. The loop is labeled with '1' and '2'. The top and bottom lines are labeled 'j' and 'j' respectively. } \end{array} = (-1)^{2j} \delta_{jj'} [j]^{-1} \begin{array}{c} \text{Diagram 2: A rectangular box with four vertical lines. The left and right lines are connected at the bottom by a loop. The loop has two vertices, each with a dot. The left vertex is labeled '+' and the right vertex is labeled '-'. The loop is labeled with '1' and '2'. The top and bottom lines are labeled 'j' and 'j' respectively. } \end{array}$$

We have already met both the CG and the $3jm$ -forms of the “oyster” (the $3j$ -symbol) diagram (equations (64) and (93), respectively). The $3jm$ -form is equal to the triangular delta $\{j, j_1, j_2\}$ (which is unity when the triangular conditions hold).

EXAMPLE 2. To illustrate a separation over three and four lines, we consider the example given in Fig. 1 where we precoupled j_5 and j_6 . Clearly, we could also first apply the precoupling rule (108) to the lines j_1 and j_2 in Fig. 1 and then factor over the three lines.

EXAMPLE 3. As another example we consider the diagram G in Fig. 2. There are two obvious ways of separation over the four lines, vertically: j'_1, j'_2, j'_3, j'_4 (represented by $1', 2', 3', 4'$), and horizontally: j_1, j_2, j_5, j_6 . In the first case we get the diagram in Fig. 3. The second possibility leads clearly to the same final result. The resulting four diagrams are irreducible and cannot be factored into smaller closed diagrams. In Section 5 we shall return to these closed diagrams.

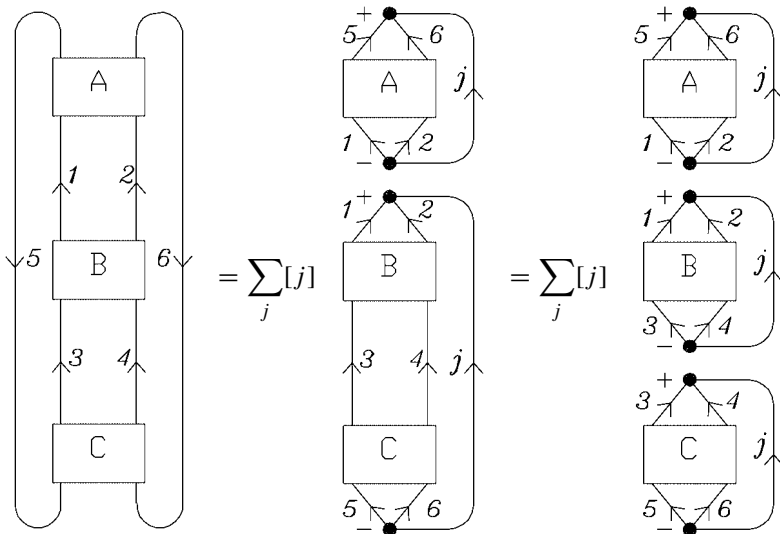


Fig. 1. An illustration of a separation over four lines (Example 2).

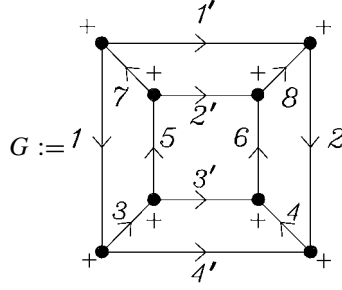


Fig. 2. The initial diagram of [Example 3](#).

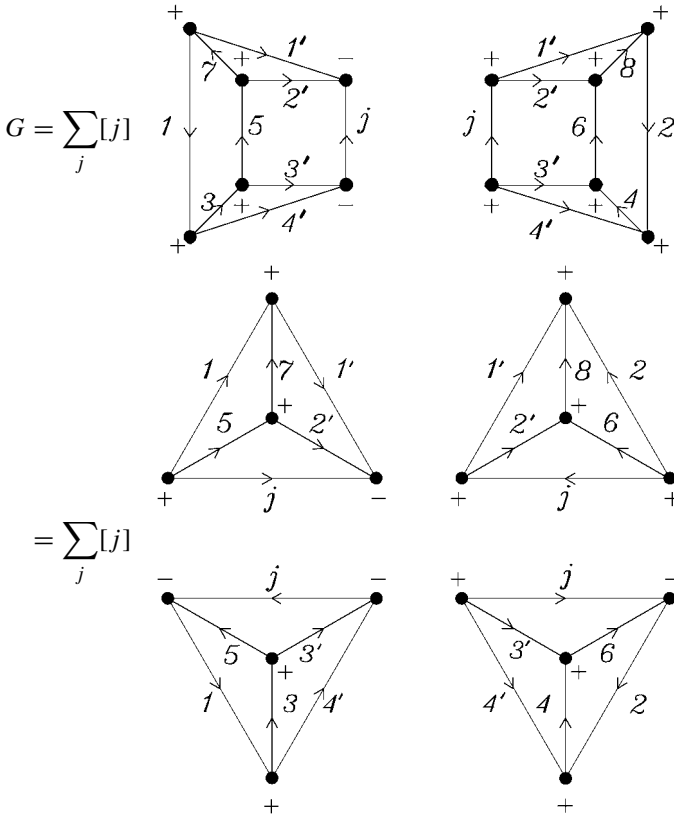


Fig. 3. The diagram of [Fig. 2](#) ([Example 3](#)) after separation over four lines.

EXAMPLE 4. There is also a less obvious way to factor G of [Fig. 2](#). To clarify this possibility, we first convert G into a form ([Fig. 4](#)) that is topologically the same as the diagram in [Fig. 2](#). By using equation (100) we now precouple j_1 and j_2 and draw the summation line j vertically in the center of the diagram. Then we separate three times over three lines. The diagrams on the right-hand side of [Fig. 4](#) are also irreducible. In fact, they can be easily redrawn into the “tetrahedral” shape used in the first factorization of G , see [Fig. 3](#).

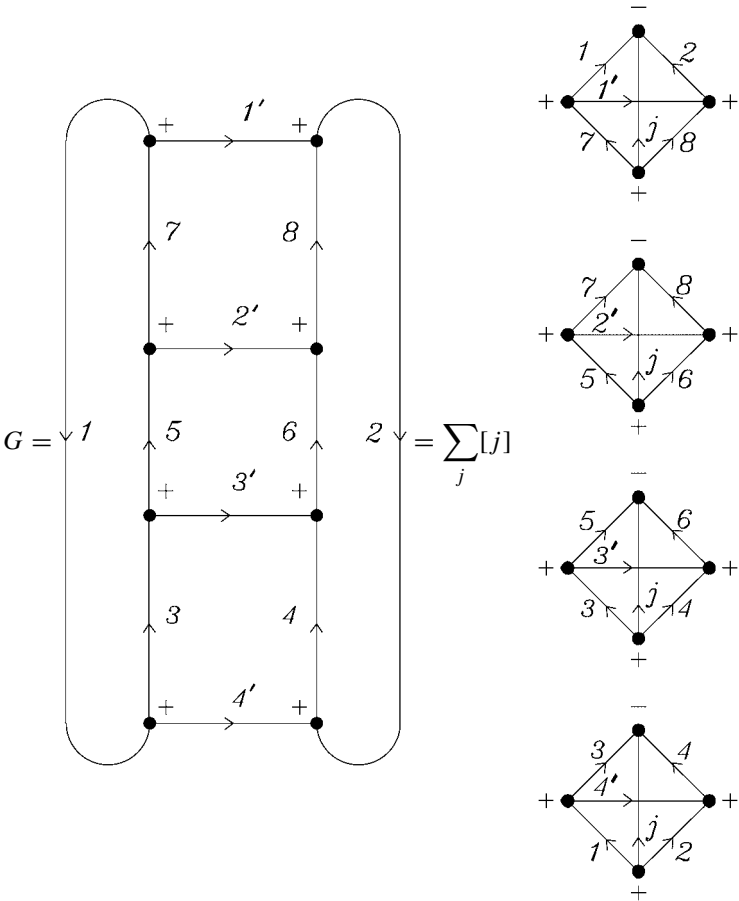


Fig. 4. Separation of the diagram of Example 4. Note that G is the same diagram as in Fig. 2.

Note that the different diagrams in the previous two examples contain different angular momenta and, consequently, are related in a non-trivial way (through a so-called sum rule).

5. IRREDUCIBLE CLOSED DIAGRAMS

The main objective of graphical methods for the study of an angular momentum problem is to reduce it to the form of a product of standard quantities that are easy to handle and to evaluate. We have seen how to factor a general open diagram into a product of a closed diagram and a diagram representing a generalized CG coefficient. The latter diagram is clearly the simplest possible diagram containing a given number of external lines. We thus turn our attention to the closed diagrams.

A closed diagram is *reducible* if it can be separated into a product of closed diagrams, otherwise it is *irreducible*. The factorization of a closed diagram into irreducible components provides clearly the utmost simplification of the angular momentum problem.

Suppose we have an irreducible diagram consisting of $k > 0$ vertices. Since three lines are attached to every vertex and every line connects two vertices, the total number of lines equals $3k/2$. Hence, the number of vertices in an irreducible diagram must be even, say $k = 2n$, $n = 1, 2, \dots$. We thus find the general result that an irreducible diagram consists of $3n$ lines and $2n$ vertices. Since each line is labeled by a quantum number j , we speak of $3nj$ -symbols.

5.1. $1j$ - and $3j$ -symbols

We have already encountered a closed (and irreducible) diagram containing one line and no vertices ($k = 0$), namely

$$\sum_m \langle jm | jm \rangle = [j] \equiv 2j + 1 = \text{---} \bigcirc \text{---}^j.$$

It is appropriate to refer to this non-oriented loop as a $1j$ -symbol.

The $3j$ -symbol (or triangular delta) was already introduced in Section 2.5 in CG form (see Section 3.5 for the $3jm$ -form),

$$\{j_1, j_2, j_3\} = [j_2]^{-1} \begin{array}{c} \text{---} \overset{1}{\curvearrowright} \text{---} \\ \text{---} \overset{2}{\text{---}} \text{---} \\ \text{---} \underset{3}{\curvearrowleft} \text{---} \end{array} \begin{array}{c} + \quad \quad - \end{array} = \begin{array}{c} \text{---} \overset{1}{\curvearrowright} \text{---} \\ \text{---} \overset{2}{\text{---}} \text{---} \\ \text{---} \underset{3}{\curvearrowleft} \text{---} \end{array} \begin{array}{c} - \quad \quad + \end{array}.$$

Its value is zero or unity depending on whether the three angular momenta satisfy the triangular condition. The $3jm$ -representation of $\{j_1, j_2, j_3\}$ shows clearly its symmetry: A transposition of two of the three angular momenta gives the phase $(-1)^{2J}$, where $J := j_1 + j_2 + j_3$. Since J is an integer, it follows that the $3j$ -symbol is invariant under permutations.

5.2. Recoupling and the $6j$ - and $9j$ -symbols

Because the $6j$ -, $9j$ -, and higher symbols appear naturally in the problem of recoupling of three, four (and more) angular momenta, we first discuss this problem before turning to the study of their properties.

We have seen in Section 3.4 that we can couple three or more angular momenta by different coupling schemes. This does not imply that eigenstates of J^2 , obtained by different coupling schemes, are linearly independent. Indeed, states obtained in one coupling scheme can be expressed as linear combinations of states obtained by another coupling scheme. This is called *recoupling*. Recoupling is a basis transformation in tensor product space $V_{j_1} \otimes V_{j_2} \otimes \dots \otimes V_{j_n}$, where V_{j_k} is a $(2j_k + 1)$ -dimensional carrier space of an irrep of $SU(2)$. Specification of a coupling scheme (genealogy) leads to a basis for this space and another coupling scheme gives another basis; recoupling transforms the one basis into the other.

To be more specific we first consider the case of three angular momenta. In Section 3.4 we have considered two coupling schemes, namely $((j_1 j_2) j_{12} j_3)$ and $(j_1 (j_2 j_3) j_{23})$. We

relate the states obtained by these different couplings by

$$\begin{aligned} & |((j_1 j_2) j_{12} j_3) j m\rangle \\ &= \sum_{j_{23}, j', m'} |(j_1 (j_2 j_3) j_{23}) j' m'\rangle \langle (j_1 (j_2 j_3) j_{23}) j' m' | ((j_1 j_2) j_{12} j_3) j m \rangle. \end{aligned}$$

The expansion coefficients arising in this basis transformation are *recoupling coefficients*. The recoupling coefficient obviously vanishes unless $j = j'$ and $m = m'$, and we shall see shortly that it is independent of m . Both facts follow immediately from the diagrammatic rules.

In order to obtain a graphical representation of the recoupling coefficients, we substitute the resolution of the identity, expressed in terms of the uncoupled basis, obtaining the generalized CG coefficients of Section 3.4 (see (77) and (78)). Thus,

$$\begin{aligned} R &:= \langle (j_1 (j_2 j_3) j_{23}) j' m' | ((j_1 j_2) j_{12} j_3) j m \rangle \\ &= \sum_{m_1 m_2 m_3} \langle (j_1 (j_2 j_3) j_{23}) j' m' | j_1 m_1; j_2 m_2; j_3 m_3 \rangle \\ &\quad \times \langle j_1 m_1; j_2 m_2; j_3 m_3 | ((j_1 j_2) j_{12} j_3) j m \rangle \\ &= \sum_{m_1 m_2 m_3} \end{aligned}$$

Transition to $3jm$ -diagrams and introduction of the notation

$$[j_1, j_2, \dots, j_k] := \prod_{i=1}^k [j_i] \equiv \prod_{i=1}^k (2j_i + 1), \quad k > 0,$$

gives

$$\begin{aligned} R &= [j, j', j_{12}, j_{23}]^{1/2} \end{aligned}$$

$$= \delta_{jj'} \delta_{mm'} [j_{12}, j_{23}]^{1/2} \end{aligned} \quad (110)$$

where in the last step we have applied the rule (98). The closed diagram that we have obtained cannot be further factored into closed diagrams in a non-trivial way: it is *irreducible*. (Note that by the rule (101) an oyster type diagram can be separated off from each corner; this, however, is a trivial factorization.)

The diagram of the recoupling coefficient is proportional to Wigner's $6j$ -symbol, which is defined graphically as

$$\left\{ \begin{matrix} j_1 & j_2 & j_3 \\ j'_1 & j'_2 & j'_3 \end{matrix} \right\} := \text{Diagram} \quad (111)$$

This definition may be remembered by noting that j_1 , j_2 , and j_3 appear on the central vertex in the order indicated by the vertex sign. The angular momentum j'_k appears on the edge opposite j_k , $k = 1, 2, 3$. Hence, the direction of j'_1 , j'_2 , j'_3 is also dictated by the central vertex sign. All vertices have the same sign. Obviously, the graph can be drawn in several different forms, which imply its symmetry properties. We shall address this problem in the next section.

Bringing the diagram in equation (110) to this standard form, we finally get

$$\begin{aligned} R &\equiv \langle (j_1(j_2 j_3) j_{23}) j' m' | ((j_1 j_2) j_{12} j_3) j m \rangle \\ &= \delta_{jj'} \delta_{mm'} (-1)^{j_1+j_2+j_3+j} [j_{12}, j_{23}]^{1/2} \\ &= \delta_{jj'} \delta_{mm'} (-1)^{j_1+j_2+j_3+j} [j_{12}, j_{23}]^{1/2} \left\{ \begin{matrix} j_1 & j_2 & j_{12} \\ j_3 & j & j_{23} \end{matrix} \right\}. \end{aligned} \quad (112)$$

We next consider the recoupling of four angular momenta, where several coupling schemes are again possible. We can couple sequentially, one angular momentum after another, or we can also couple pairwise, in which case we have the possible coupling schemes $((j_1 j_2)(j_3 j_4))$, $((j_1 j_3)(j_2 j_4))$, and $((j_1 j_4)(j_2 j_3))$. All recoupling problems can be easily treated by the graphical techniques. As an example we consider the recoupling

$$\begin{aligned} &|((j_1 j_2) j_{12} (j_3 j_4) j_{34}) j m \rangle \\ &= \sum_{j_{13}, j_{24}} |((j_1 j_3) j_{13} (j_2 j_4) j_{24}) j m \rangle \\ &\quad \times \left[\sum_{m_1 m_2 m_3 m_4} \langle ((j_1 j_3) j_{13} (j_2 j_4) j_{24}) j m | j_1 m_1; j_2 m_2; j_3 m_3; j_4 m_4 \rangle \right. \\ &\quad \left. \times \langle j_1 m_1; j_2 m_2; j_3 m_3; j_4 m_4 | ((j_1 j_2) j_{12} (j_3 j_4) j_{34}) j m \rangle \right]. \end{aligned} \quad (113)$$

The expression in square brackets is the recoupling coefficient expressed in terms of generalized CG coefficients and has the following graphical representation

$$\sum_{\substack{m_1 m_2 \\ m_3 m_4}} - \begin{array}{c} \text{Diagram 1: A diamond shape with four vertices. Top vertex: } 24 \text{ (in), } 2 \text{ (out), } 4 \text{ (out). Bottom vertex: } 13 \text{ (in), } 3 \text{ (out), } 1 \text{ (out). Left vertex: } 24 \text{ (in), } 2 \text{ (out), } 13 \text{ (in). Right vertex: } 2 \text{ (in), } 3 \text{ (out), } 12 \text{ (out). Internal lines: } jm \text{ (horizontal), } jm \text{ (vertical). Signs: } + \text{ at top and bottom, } - \text{ at left and right.} \end{array} + \gamma + \begin{array}{c} \text{Diagram 2: A hexagon with six vertices. Top-left: } 24 \text{ (in), } 2 \text{ (out), } 13 \text{ (in). Top-right: } 2 \text{ (in), } 3 \text{ (out), } 12 \text{ (out). Bottom-left: } 13 \text{ (in), } 3 \text{ (out), } 1 \text{ (out). Bottom-right: } 3 \text{ (in), } 4 \text{ (out), } 34 \text{ (out). Internal lines: } j \text{ (horizontal), } j \text{ (vertical), } j \text{ (diagonal). Signs: } - \text{ at top-left and bottom-right, } + \text{ at top-right and bottom-left.} \end{array}. \quad (114)$$

The factor γ which arises from the transition to the $3jm$ -representation and from application of equation (98) to the free lines with jm labels is easily found to be

$$\begin{aligned} \gamma &= [j_{13}, j, j_{24}, j_{34}, j, j_{12}]^{1/2} [j]^{-1} (-1)^{2j_3+2j_{24}+2j_4+2j_3+2j_{12}+2j_1} \\ &= [j_{13}, j_{24}, j_{34}, j_{12}]^{1/2}. \end{aligned} \quad (115)$$

The hexagonal diagram in equation (114) is proportional to Wigner's $9j$ -symbol, which we define as

$$\left\{ \begin{array}{ccc} j_1 & j_2 & j_3 \\ j_4 & j_5 & j_6 \\ j_7 & j_8 & j_9 \end{array} \right\} := + \begin{array}{c} \text{Diagram 3: A hexagon with six vertices. Top-left: } 1 \text{ (in), } 3 \text{ (out), } 4 \text{ (in). Top-right: } 3 \text{ (in), } 5 \text{ (out), } 8 \text{ (in). Bottom-left: } 4 \text{ (in), } 7 \text{ (out), } 6 \text{ (in). Bottom-right: } 5 \text{ (in), } 6 \text{ (out), } 9 \text{ (in). Internal lines: } 2 \text{ (horizontal), } 7 \text{ (vertical), } 8 \text{ (diagonal). Signs: } - \text{ at top-left and bottom-right, } + \text{ at top-right and bottom-left.} \end{array}. \quad (116)$$

To remember this definition we note that:

- The vertex signs on the perimeter of the hexagon alternate.
- The nodes with minus signs define the rows of the $9j$ -symbol and those with plus signs define its columns.
- The order within the rows and columns is also defined by the node signs.
- The arrows always point from the positive to negative vertices.

In the next section we shall show that there are different, though equivalent, ways of representing the $9j$ -symbol, which reflect its various symmetries.

In order to bring the $9j$ -symbol of equation (114), defining the recoupling coefficient, to the standard form, equation (116), we first flip all the vertex signs. This does not change the phase since

$$(-1)^{2(j_1+j_3+j_{13})+2(j_2+j_4+j_{24})+2(j_{12}+j_{34}+j)} = 1.$$

Reversing, further, the orientation on intermediately coupled lines again keeps the phase unchanged, since

$$(-1)^{2(j_{13}+j_{24}+j_{34}+j_{12})} = (-1)^{4j} = 1,$$

so that we finally get

$$\begin{aligned} & \langle (j_1 j_3) j_{13} (j_2 j_4) j_{24} j m | (j_1 j_2) j_{12} (j_3 j_4) j_{34} j m \rangle \\ &= [j_{13}, j_{24}, j_{12}, j_{34}]^{1/2} \left\{ \begin{matrix} j_1 & j_2 & j_{12} \\ j_3 & j_4 & j_{34} \\ j_{13} & j_{24} & j \end{matrix} \right\}. \end{aligned} \quad (117)$$

5.3. Properties of the $6j$ -symbol

We see from the defining equation (111) that the $6j$ -symbol can be written as the following complete contraction of four $3jm$ -symbols

$$\begin{aligned} \left\{ \begin{matrix} j_1 & j_2 & j_3 \\ j'_1 & j'_2 & j'_3 \end{matrix} \right\} &= \sum_{\substack{m_1, m_2, m_3 \\ m'_1, m'_2, m'_3}} \begin{pmatrix} m_1 & m_2 & m_3 \\ j_1 & j_2 & j_3 \end{pmatrix} \begin{pmatrix} j_1 & m'_2 & j'_3 \\ m_1 & j'_2 & m'_3 \end{pmatrix} \\ &\quad \times \begin{pmatrix} j'_1 & j_2 & m'_3 \\ m'_1 & m_2 & j'_3 \end{pmatrix} \begin{pmatrix} m'_1 & j'_2 & j_3 \\ j'_1 & m'_2 & m_3 \end{pmatrix}. \end{aligned} \quad (118)$$

Since the following four relations must hold,

$$0 = m_1 + m_2 + m_3 = m_1 - m'_2 + m'_3 = m'_1 + m_2 - m'_3 = -m'_1 + m'_2 + m_3,$$

the sum is, in fact, only a double sum. Each $3jm$ -symbol, being proportional to a CG coefficient, is given by a single sum (cf. (51)), so that a $6j$ -symbol represents a six-fold summation. However, through a series of ingenious substitutions, Racah [31] was able to reduce the 6-fold summation to the following formula (for details, see [13], Chapter 3, Appendix A)

$$\begin{aligned} & \left\{ \begin{matrix} j_1 & j_2 & j_3 \\ j'_1 & j'_2 & j'_3 \end{matrix} \right\} \\ &= \Delta(j_1 j_2 j_3) \Delta(j_1 j'_2 j'_3) \Delta(j'_1 j_2 j'_3) \Delta(j'_1 j'_2 j_3) \\ &\quad \times \sum_t (-1)^t (t+1)! \\ &\quad \times [(t - j_1 - j_2 - j_3)! (t - j_1 - j'_2 - j'_3)! (t - j'_1 - j_2 - j'_3)! \\ &\quad \times (t - j'_1 - j'_2 - j_3)! (j_1 + j_2 + j'_1 + j'_2 - t)! \\ &\quad \times (j_1 + j_3 + j'_1 + j'_3 - t)! (j_2 + j_3 + j'_2 + j'_3 - t)!]^{-1}, \end{aligned} \quad (119)$$

where

$$\Delta(abc) := \left[\frac{(a+b-c)!(a-b+c)!(-a+b+c)!}{(a+b+c+1)!} \right]^{1/2}.$$

The sum over t is restricted by the requirement that the factorials occurring in (119) are non-negative.

The $6j$ -symbol is invariant under any permutation of its vertices

Hence, its symmetry group is the permutation group S_4 , which is of order $4!$ (all permutations of 4 distinct objects). By considering the diagram of the $6j$ -symbol one easily proves

this symmetry. Indeed,

$$\begin{aligned} \left\{ \begin{matrix} j_1 & j_2 & j_3 \\ j'_1 & j'_2 & j'_3 \end{matrix} \right\} &= \left\{ \begin{matrix} j_a & j_b & j_c \\ j'_a & j'_b & j'_c \end{matrix} \right\} = \left\{ \begin{matrix} j_a & j'_b & j'_c \\ j'_a & j_b & j_c \end{matrix} \right\} \\ &= \left\{ \begin{matrix} j'_a & j_b & j'_c \\ j_a & j'_b & j_c \end{matrix} \right\} = \left\{ \begin{matrix} j'_a & j'_b & j_c \\ j_a & j_b & j'_c \end{matrix} \right\}, \end{aligned} \quad (120)$$

where $(a \ b \ c)$ is any permutation of $(1 \ 2 \ 3)$. For instance, the invariance with respect to the transposition of the first and last column follows by interchanging the vertices C and D in the following diagram:

$$\begin{aligned} \left\{ \begin{matrix} j_1 & j_2 & j_3 \\ j'_1 & j'_2 & j'_3 \end{matrix} \right\} &= \begin{array}{c} \text{Diagram 1: Triangle ABC with central vertex A. Signs: A(-), B(-), C(-), D(-). Lines: 1 (A-B), 2 (A-C), 3 (A-D), 1' (B-C), 2' (C-D), 3' (D-B).} \end{array} \\ &= \begin{array}{c} \text{Diagram 2: Triangle ABC with central vertex A. Signs: A(+), B(+), C(+), D(+). Lines: 1 (A-B), 2 (A-C), 3 (A-D), 1' (B-C), 2' (C-D), 3' (D-B).} \end{array} \\ &= \begin{array}{c} \text{Diagram 3: Triangle ABC with central vertex A. Signs: A(-), B(-), C(-), D(-). Lines: 1 (A-B), 2 (A-C), 3 (A-D), 1' (B-C), 2' (C-D), 3' (D-B).} \end{array} = \left\{ \begin{matrix} j_3 & j_2 & j_1 \\ j'_3 & j'_2 & j'_1 \end{matrix} \right\}. \end{aligned} \quad (121)$$

It is easily checked that the phase arising from the conversion of the second diagram into the third one equals unity. The second diagram represents, in fact, another canonical form which is easy to remember: all vertices carry the same sign, the lines on the perimeter are oriented in the direction indicated by the signs, and all lines attached to the central vertex are ingoing (or outgoing).

The $6j$ -symbol is invariant with respect to the interchange of the rows in any two of its columns

Consider for instance the cyclic permutation $(A \ B \ C)$ applied to the first diagram of equa-

tion (121), which gives

$$\begin{aligned}
 \left\{ \begin{matrix} j_1 & j_2 & j_3 \\ j'_1 & j'_2 & j'_3 \end{matrix} \right\} &= \text{Diagram 1} \\
 &= (-1)^{2j_2+2j_3+2j'_2+2j'_3} \text{Diagram 2} = \left\{ \begin{matrix} j'_1 & j'_2 & j_3 \\ j_1 & j_2 & j'_3 \end{matrix} \right\},
 \end{aligned}$$

where we used $(-1)^{2j_2+2j_3} = (-1)^{2j'_2+2j'_3} = (-1)^{2j_1}$.

Besides the 24 symmetry operations, equation (120), there exists an additional symmetry, first found by Regge [32] by inspection of the Racah formula for the $6j$ -symbol. We forego a discussion of the Regge symmetry and only mention it here for completeness.

The graphical method is very powerful for deriving sum rules. For example,

$$\sum_{j_1} [j_1] (-1)^{2j_1} \left\{ \begin{matrix} j_1 & j_2 & j_3 \\ j'_1 & j_2 & j_3 \end{matrix} \right\} = \{j'_1, j_2, j_3\}.$$

To prove this we use the completeness relation, equation (100), and obtain

$$\begin{aligned}
 \sum_{j_1} [j_1] &= \text{Diagram 3} \\
 &= \sum_{j_1} [j_1] + \text{Diagram 4} \\
 &= (-1)^{2j_2} + \text{Diagram 5} \\
 &= \{j'_1, j_2, j_3\}.
 \end{aligned}$$

Similarly, setting $j'_2 = j_3$ and $j'_3 = j_2$, we get

$$\sum_{j_1} [j_1] (-1)^{j_1+j_2+j_3} \left\{ \begin{matrix} j_1 & j_2 & j_3 \\ j'_1 & j_3 & j_2 \end{matrix} \right\}$$

$$\begin{aligned}
&= (-1)^{2j_3} \sum_{j_1} [j_1] \\
&\quad \begin{array}{c} \text{Diagram: A triangle with vertices. Top vertex is labeled '+'. Bottom-left and bottom-right vertices are labeled '-'. Edges are labeled: top-left to top-right is '3' (downward), top-right to top-left is '2' (upward), top-left to bottom-left is '3' (downward), top-right to bottom-right is '2' (downward), and bottom-left to bottom-right is 'j_1' (downward).} \end{array} \\
&= (-1)^{2j_3} \begin{array}{c} \text{Diagram: Two circles. Left circle has a clockwise arrow labeled '3'. Right circle has a clockwise arrow labeled '2'. They are connected by a horizontal line with a leftward arrow labeled 'j_1' and a '-' sign below it.} \end{array} \\
&= \delta_{j_1', 0} \begin{array}{c} \text{Diagram: Two circles. Left circle has a clockwise arrow labeled '3' and a '+' sign below it. Right circle has a clockwise arrow labeled '2' and a '-' sign below it. They are connected by a dashed horizontal line.} \end{array} = \delta_{j_1', 0} [j_2, j_3]^{1/2},
\end{aligned}$$

where we have used the separation rule (105) and the zero line removal rule (97).

The well-known orthogonality relation for $6j$ -symbols, which states that, apart from the factor $[j_1, j_1']^{1/2}$, the $6j$ -symbols form an orthogonal matrix for fixed j_2, j_3, j_2' , and j_3' ,

$$\sum_{j_1} [j_1] \begin{Bmatrix} j_1 & j_2 & j_3 \\ j_1' & j_2' & j_3' \end{Bmatrix} \begin{Bmatrix} j_1 & j_2 & j_3 \\ j_1'' & j_2' & j_3' \end{Bmatrix} = \delta_{j_1', j_1''} [j_1']^{-1} \{j_1', j_2', j_3\} \{j_1', j_2, j_3'\},$$

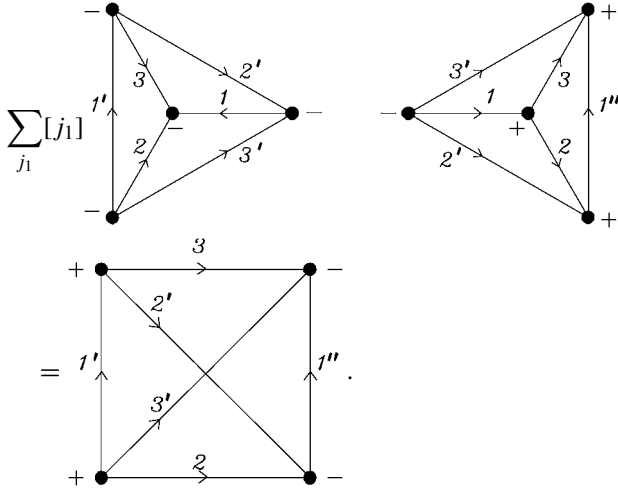
can also be easily proved. We simply use the rule (109) for a separation over the four lines in reverse direction (note that the required phase change equals unity) obtaining

$$\begin{aligned}
&\sum_{j_1} [j_1] \begin{array}{c} \text{Diagram: A complex network of lines and vertices. Top-left vertex is '+', top-right is '-'. Bottom-left and bottom-right are '+'. Edges are labeled: top-left to top-right is '3', top-right to top-left is '2'', top-left to bottom-left is '2', top-right to bottom-right is '3'', and bottom-left to bottom-right is 'j_1' (labeled '1' in the middle).} \end{array} \\
&= \begin{array}{c} \text{Diagram: Two large loops. Left loop has a clockwise arrow labeled '2'' and a '+' sign below it. Right loop has a clockwise arrow labeled '3' and a '-' sign below it. They are connected by a horizontal line with a leftward arrow labeled 'j_1' (labeled '1' in the middle).} \end{array} \\
&= \delta_{j_1', j_1''} [j_1']^{-1} \begin{array}{c} \text{Diagram: Two smaller loops. Top loop has a clockwise arrow labeled '3' and a '+' sign below it. Bottom loop has a clockwise arrow labeled '2' and a '+' sign below it. They are connected by a horizontal line with a leftward arrow labeled 'j_1' (labeled '1' in the middle).} \end{array}
\end{aligned}$$

Similarly, the well-known sum rule

$$\sum_{j_1} [j_1] (-1)^{j_1 + j_1' + j_1''} \begin{Bmatrix} j_1 & j_2 & j_3 \\ j_1' & j_2' & j_3' \end{Bmatrix} \begin{Bmatrix} j_1 & j_2 & j_3 \\ j_1'' & j_2' & j_2' \end{Bmatrix} = \begin{Bmatrix} j_1'' & j_2 & j_2' \\ j_1' & j_3 & j_3' \end{Bmatrix} \quad (122)$$

can also be derived by the use of the following version of the separation rule (109), where now, in view of equation (108), the vertices involving crossing lines have the same signs, so that



By bringing these $6j$ -diagrams to their canonical form and dividing out the phases thus arising, equation (122) easily follows.

We also see that the $6j$ -diagram reduces to the $3j$ -type *oyster* diagram when one of the angular momenta vanishes. Thus, applying the rule (96) for the zero line removal, we find that

$$\left\{ \begin{matrix} j_1 & j_2 & j_3 \\ j'_1 & j'_2 & 0 \end{matrix} \right\} = \delta_{j_1 j'_1} \delta_{j_2 j'_2} (-1)^{j_1 + j_2 + j_3} [j_1, j_2]^{-1/2} \{j_1, j_2, j_3\}.$$

5.4. Properties of the $9j$ -symbol

The $9j$ -symbol is defined as a contraction of six $3jm$ -symbols, equation (116), and can be computed as a triple sum over the magnetic quantum numbers of the product of these $3jm$ -symbols. An alternative route is to express it as a single sum over a product of three $6j$ -symbols,

$$\left\{ \begin{matrix} j_1 & j_2 & j_3 \\ j'_1 & j'_2 & j'_3 \\ j''_1 & j''_2 & j''_3 \end{matrix} \right\} = \sum_x [x] (-1)^{R+2x} \left\{ \begin{matrix} j_1 & j_2 & j_3 \\ x & j''_1 & j'_1 \end{matrix} \right\} \left\{ \begin{matrix} j'_1 & j'_2 & j'_3 \\ j''_2 & x & j_2 \end{matrix} \right\} \left\{ \begin{matrix} j''_1 & j''_2 & j''_3 \\ j'_3 & j_3 & x \end{matrix} \right\}, \quad (123)$$

where

$$R = \sum_{i=1}^3 (j_i + j'_i + j''_i). \quad (124)$$

This expression can be proved graphically as shown in Fig. 5.

The $9j$ -symbol has a symmetry group of order 72, *i.e.*, there are 72 operations permuting its quantum numbers that conserve its absolute value. In the first place, it is invariant under

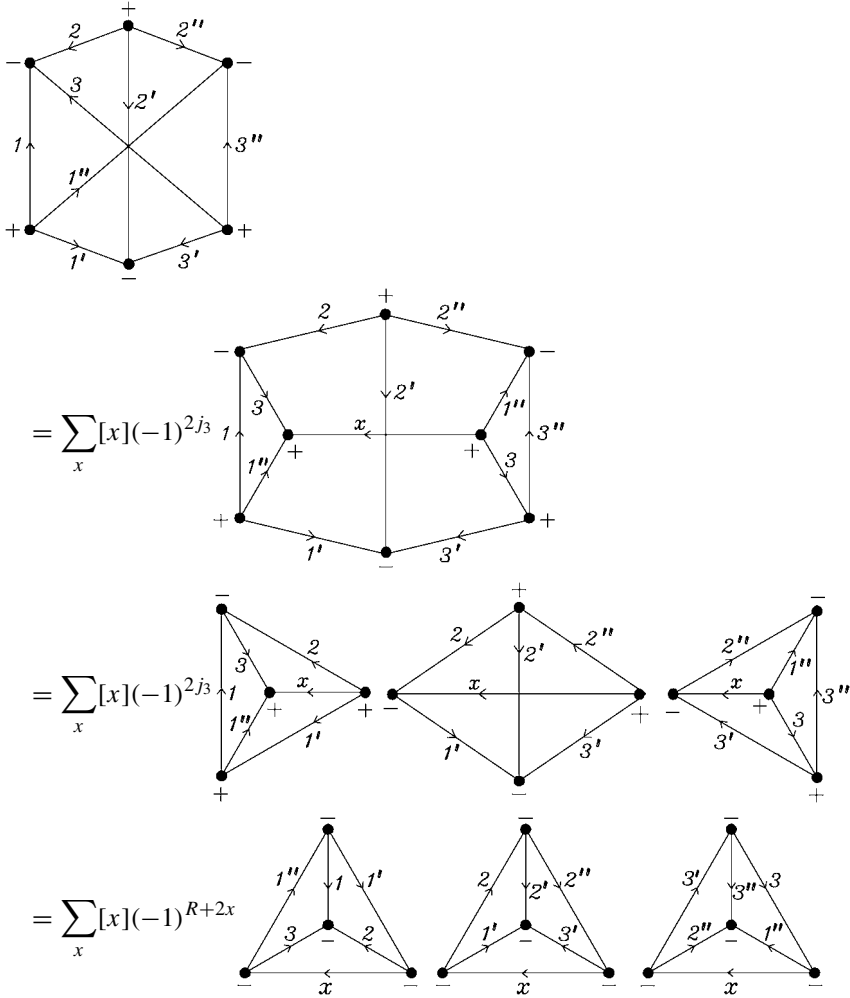


Fig. 5. Graphical derivation of equation (123), which gives a $9j$ -symbol as a sum of a product of three $6j$ -symbols.

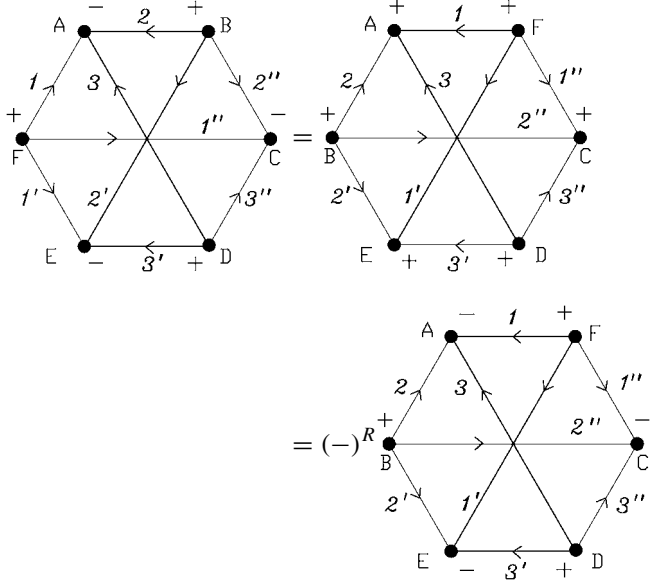
cyclic permutations of its rows and columns. This follows immediately from the definition, equation (116), which does not specify the j -value that should appear in the upper left-hand corner of the $9j$ -symbol, and from the three-fold symmetry of the corresponding unlabeled $9j$ -diagram. Thus

$$\left\{ \begin{matrix} j_1 & j_2 & j_3 \\ j'_1 & j'_2 & j'_3 \\ j''_1 & j''_2 & j''_3 \end{matrix} \right\} = \left\{ \begin{matrix} j'_1 & j'_2 & j'_3 \\ j''_1 & j''_2 & j''_3 \\ j_1 & j_2 & j_3 \end{matrix} \right\} = \left\{ \begin{matrix} j_2 & j_3 & j_1 \\ j'_2 & j'_3 & j'_1 \\ j''_2 & j''_3 & j''_1 \end{matrix} \right\} = \dots$$

A transposition of the first two columns, however, changes the phase since

$$\left\{ \begin{matrix} j_1 & j_2 & j_3 \\ j'_1 & j'_2 & j'_3 \\ j''_1 & j''_2 & j''_3 \end{matrix} \right\} = (-1)^R \left\{ \begin{matrix} j_2 & j_1 & j_3 \\ j'_2 & j'_1 & j'_3 \\ j''_2 & j''_1 & j''_3 \end{matrix} \right\}.$$

This is proved graphically as follows:



where $R \equiv j_1 + j_2 + j_3 + j'_1 + j'_2 + j'_3 + j''_1 + j''_2 + j''_3$, equation (124), is due to the sign reversal at nodes A, E, and C. Since a transposition and a cyclic permutation generate the whole permutation group S_3 , this rule holds for all transpositions of the columns.

Any closed diagram is invariant under a simultaneous reversal of all arrows and all node signs. If we perform this operation on the 9j-diagram, we interchange the rows and columns of the 9j-symbol (i.e., we transpose the corresponding 3×3 matrix). Hence, the 9j-symbol is invariant with respect to a simultaneous interchange of its rows and columns, which implies that it obtains the phase $(-1)^R$ under an odd permutation of its rows. Thus, to summarize:

The 9j-symbol is invariant under any even permutation of its rows or columns and obtains the phase $(-1)^R$ in case of an odd permutation of its rows or columns.

The graphical technique can be again very useful in deriving various sum rules for the 9j-symbols. We leave this to the reader as an exercise.

Finally, if one of the angular momenta vanishes, a 9j-symbol reduces to a 6j-symbol. For example, when $j''_3 = 0$, we get

$$\begin{Bmatrix} j_1 & j_2 & j_3 \\ j'_1 & j'_2 & j'_3 \\ j''_1 & j''_2 & 0 \end{Bmatrix} = \delta_{j_3 j'_3} \delta_{j''_1 j'_1} (-1)^{j_2 + j_3 + j'_1 + j''_1} [j_3, j'_1]^{-1/2} \begin{Bmatrix} j_1 & j_2 & j_3 \\ j'_2 & j'_1 & j'_1 \\ j''_1 & j''_2 & 0 \end{Bmatrix}.$$

We again easily verify this rule graphically, since

$$= \delta_{j_3 j'_3} \delta_{j_1'' j_2''} [j_3, j_1'']^{-1/2} (-1)^{2j_3+2j_1''} j_1$$

$$= \delta_{j_3 j'_3} \delta_{j_1'' j_2''} [j_3, j_1'']^{-1/2} (-1)^{j_2+j_3+j_1'+j_1''}$$

5.5. Higher $3nj$ -symbols

The number of closed irreducible diagrams rapidly increases with increasing n . For $n \geq 4$ there exist two $3nj$ -symbols, whose symmetries can be displayed by writing their arguments on a cylindrical band. In the case of a $3nj$ -symbol of the first kind the band is twisted (a Möbius strip) and in the case of a $3nj$ -symbol of the second kind, it is not. For $n = 4$ these are the only irreducible diagrams, but when $n > 4$ there exist additional, less symmetric, irreducible $3nj$ -symbols. It can be shown that there are five $15j$ -symbols, 18 $18j$ -symbols, 84 $21j$ -symbols, and 576 $24j$ -symbols, indicating the rapid increase in their number. Many of these symbols, their symmetries, reductions and sum rules have been examined in detail by Jucys and co-workers [18,19]. Should we encounter any one of such diagrams, we shall express them as *sums* over the products of lower-order $3nj$ -symbols as we did above for the $6j$ - and $9j$ -symbols.

6. CONCLUDING REMARKS

In closing this exposition of the graphical methods of angular momentum theory we wish to briefly point out some of the applications of this technique, particularly as it pertains to the

field of the molecular electronic structure investigations. Clearly, the angular momentum theory is relevant in any study of rotationally invariant systems and motion in isotropic space, ranging from elementary particle and both classical and quantum field theories to atomic and molecular structure investigations.

Of particular interest and utility are those applications in which this approach is closely linked with other graphical or diagrammatic techniques. Typical representatives of such approaches are those based on Feynman-like or many-body perturbation theory (MBPT) diagrams, which enable an efficient and “graphic” pictorial implementation of the time-independent Wick theorem in the framework of the second-quantization formalism. In the case of atomic systems, both the orbital and spin angular momentum can be handled in this way [33–35], while in molecular studies one is most often concerned with spin couplings, leading to the so-called spin-adapted version of various approaches to the molecular electronic structure.

Perhaps the simplest exploitation of the latter kind deals with the direct evaluation of the spin-adapted configuration interaction (CI) or shell model matrix elements when considering only low-excitation orders (see, *e.g.*, Refs. [33–37]). A more general exploitation of this type is then based on the permutation or symmetric group representation theory [38] or on the unitary group approach (UGA) (see, *e.g.*, Refs. [27,39–41]). The graphical methods also proved to be very useful in elucidating the relationship between the permutation group S_N and unitary group $U(n)$ approaches [42–44]. In fact, the diagrammatic method is very convenient to compute spin eigenstates adapted to canonical subgroup chains embedded within S_N or $U(n)$ and Hamiltonian matrix elements between such states [45].

Although in UGA one can completely rely on the algebraic approach [27,39–41], the realization that the Gel’fand–Tsetlin states are equivalent (up to a phase factor) to those arising from the Yamanouchi–Kotani coupling scheme enabled an efficient handling of the two-electron contributions in UGA or graphical UGA (GUGA) [46] via the introduction of suitable “segment values” [47–50]. (Note, however, that GUGA is based on a very different type of diagrams, which not only enable a global representation of the two-column Gel’fand–Tsetlin basis but afford much insight as well.)

Similarly as in variational CI approaches, the diagrammatic technique described in this work has also been successfully exploited when designing the spin-adapted versions of the coupled cluster (CC) formalism, both at the single-reference [51–54] and multireference [55,56] levels, as well as in related approaches [57,58].

In the theory of long-range intermolecular forces angular momentum recoupling plays an important role due to the fact that the multipole expansion of the intermolecular part of the electronic Hamiltonian appears naturally in terms of coupled spherical tensor operators (the multipoles). In second- and higher-order perturbation theory it is convenient to pre-couple the multipoles on each monomer to irreducible monomer tensors. This requires a recoupling of the multipoles arising in the multipole expansion [59]. This recoupling was applied by Piecuch [60–64] to systems consisting of N closed-shell monomers through third-order of intermolecular perturbation. The graphical technique proved indispensable to handle the very complicated angular momentum algebra arising in this work. Also the theory of long-range interaction-induced properties of collisional complexes [65] benefited greatly from the aid of the diagrammatic technique. Recently the long-range interaction energy between atoms in arbitrary angular momentum states was worked out [66]. Here it was recognized diagrammatically that an $18j$ -symbol appeared, which was a

useful insight because it showed that the complicated expression was simplified to the utmost.

Finally, the graphical methods of angular momentum coupling proved to be useful even in the analysis of experimental data, as exemplified by the studies of angular distribution in photoionization experiments. For example, they facilitate the derivation of the phenomenological equations for the analysis of angular distribution of photoelectrons from resonant two-photon ionization of alkali atoms with hyperfine interactions by relying on the graphical method and the so-called Liouville representation [67]. As stated in the just quoted paper [67], “graphical representation helps one to visualize the physics and simplifies and organizes the computations”.

ACKNOWLEDGEMENT

One of the authors (J. Paldus) wishes to acknowledge the continued support by the National Science and Engineering Research Council of Canada. He also appreciates the hospitality of the Wissenschaftskolleg in Berlin, where the work on the preliminary version of this chapter was carried out.

APPENDIX: SUMMARY OF THE GRAPHICAL RULES

In this section the most important diagrammatic rules are reviewed.

Basic units

Vectors and arrow directions:

$$\begin{aligned} |jm\rangle &= \text{---}\leftarrow\!\!\!\lrcorner, & |\vartheta(jm)\rangle &= (-1)^{j-m}|j,-m\rangle = \text{---}\rightarrow\!\!\!\lrcorner, \\ \langle jm| &= \text{---}\!\!\!\searrow, & \langle\vartheta(jm)| &= (-1)^{j-m}\langle j,-m| = \text{---}\!\!\!\swarrow. \end{aligned}$$

Tensor products:

$$|j_1 m_1; j_2 m_2; \dots; j_N m_N\rangle =$$

Orthonormality:

$$\langle jm|j'm'\rangle = \delta_{jj'}\delta_{mm'} = \begin{array}{c} jm \qquad \qquad j'm' \\ \longrightarrow \longrightarrow | \longrightarrow \end{array}.$$

Basic rules

Contractions:

$$\begin{aligned}
 \sum_m \text{D} \xrightarrow{j m} & \quad \xrightarrow{j m} \text{D} = \text{D} \xrightarrow{j} \text{D}, \\
 \sum_m \text{D} \xleftarrow{j m} & \quad \xleftarrow{j m} \text{D} = \text{D} \xleftarrow{j} \text{D}, \\
 \sum_m \text{D} \xrightarrow{j m} & \quad \xrightarrow{j m} \text{D} = \text{D} \xrightarrow{j} \text{D}, \\
 \sum_m \text{D} \xleftarrow{j m} & \quad \xleftarrow{j m} \text{D} = \text{D} \xleftarrow{j} \text{D}.
 \end{aligned}$$

Arrow reversals:

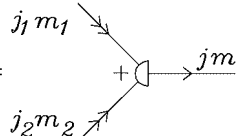
$$\begin{aligned}
 \left[\right] \xrightarrow{j} \left[\right] &= (-1)^{2j} \left[\right] \xleftarrow{j} \left[\right], \\
 \sum_{\mu} \left[\right] \xrightarrow{j \mu} & \quad \xrightarrow{j \mu} \left[\right] \xleftarrow{j m} \left[\right] = \left[\right] \xleftarrow{j m}, \\
 \sum_{\mu} \left[\right] \xleftarrow{j \mu} & \quad \xleftarrow{j \mu} \left[\right] \xrightarrow{j m} \left[\right] = \left[\right] \xrightarrow{j m}.
 \end{aligned}$$

1jm-symbol

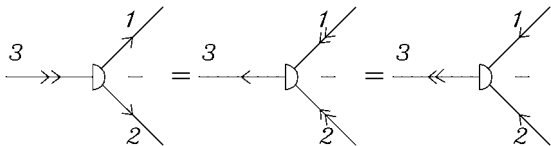
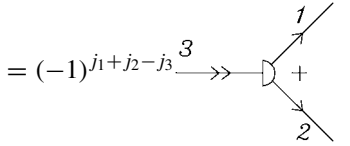
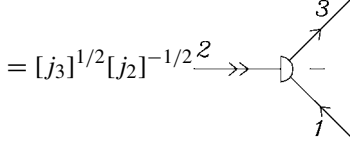
$$\begin{aligned}
 \left(\begin{matrix} j \\ m' m \end{matrix} \right) &\equiv \langle j m' | \vartheta(j m) \rangle, \\
 \left(\begin{matrix} j \\ m m' \end{matrix} \right) &\equiv \langle \vartheta(j m') | j m \rangle = (-1)^{2j} \langle j m' | \vartheta(j m) \rangle = (-1)^{2j} \left(\begin{matrix} j \\ m' m \end{matrix} \right), \\
 \xrightarrow{j m'} \xleftarrow{j m} &= (-1)^{2j} \xrightarrow{j m'} \xleftarrow{j m}, \\
 \langle j m' | \vartheta(j m) \rangle &= \xrightarrow{j m'} \xleftarrow{j m} = (-1)^{j+m'} \delta_{m', -m} = (-1)^{j-m} \delta_{m', -m}, \\
 \langle \vartheta(j m') | j m \rangle &= \xleftarrow{j m'} \xrightarrow{j m} = (-1)^{j-m'} \delta_{m', -m} = (-1)^{j+m} \delta_{m', -m}.
 \end{aligned}$$

Clebsch–Gordan coefficients and diagrams

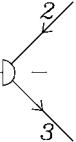
$$\langle j m | j_1 m_1; j_2 m_2 \rangle = \xrightarrow{j m} \text{D} \begin{matrix} \nearrow j_1 m_1 \\ \searrow j_2 m_2 \end{matrix}$$

$$= \langle j_1 m_1; j_2 m_2 | j m \rangle =$$


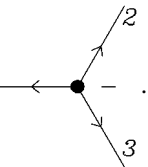
Symmetries:


$$= (-1)^{j_1 + j_2 - j_3}$$

$$= [j_3]^{1/2} [j_2]^{-1/2}$$


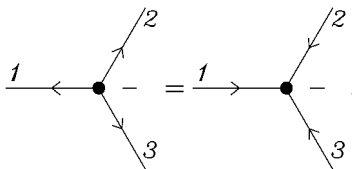
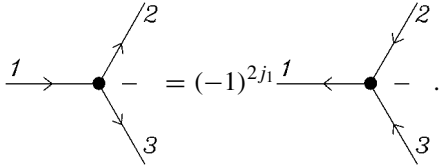
$[j_k] \equiv 2j_k + 1$

$$= (-1)^{2j_2} [j_3]^{1/2} [j_1]^{-1/2}$$


3 *j m*-symbols and diagrams

$$\begin{pmatrix} j_1 & j_2 & j_3 \\ m_1 & m_2 & m_3 \end{pmatrix} =$$


Symmetries:


$$= (-1)^{2j_1}$$


(The line with unique variance determines the phase obtained by reversal of all arrows.)

To *raise* a magnetic quantum number contract the $3jm$ -symbol with the $1jm$ -symbol on the *right*; to *lower* a magnetic quantum number contract the $3jm$ -symbol with the $1jm$ -symbol on the *left*.

EXAMPLE.

$$\sum_m \begin{pmatrix} j_1 & j_2 & j_3 \\ m & m_2 & m_3 \end{pmatrix} \begin{pmatrix} j_1 \\ mm_1 \end{pmatrix} = \begin{pmatrix} m_1 & j_2 & j_3 \\ j_1 & m_2 & m_3 \end{pmatrix}$$

Raising and lowering can be performed on any column independently.

Vertex sign reversal:

Transition from CG to $3jm$ -diagrams

Apply the following operations in order to convert a CG into a $3jm$ -vertex:

1. Conserve variances (arrow directions).
2. Invert vertex sign.
3. Multiply by $\sqrt{[j]}$, where j labels the unique line of the CG diagram.
4. Multiply for every outgoing double arrow by $(-1)^{2j}$, where j is the label of the double-arrowed line.
5. Multiply also by $(-1)^{2j}$, where j is the *first* non-unique line met when going around the vertex starting at the unique line. If the unique line is a *ket* we go in the direction of the node sign. If the unique line is a *bra* ('complex') we go contra the direction of the node sign.

See Table 1 in Section 3.6 for illustrations of CG to $3jm$ -transitions.

Diagram manipulation

Closed boxes do not have free lines other than the ones shown explicitly, open boxes can have any number of free lines.

Removal of a zero line:

Let lines go in the direction indicated by the vertex sign, then take the vertex out:

$$\begin{array}{c}
 \left[\begin{array}{c} \xrightarrow{j_1} \\ \xrightarrow{j_2} \end{array} \right] \bullet_+ \text{---} = \delta_{j_1 j_2} [j_1]^{-1/2} \left[\begin{array}{c} \xrightarrow{j_1} \end{array} \right] \\
 \left[\begin{array}{c} \xrightarrow{j_1} \\ \xrightarrow{j_2} \end{array} \right] \bullet_- \text{---} = \delta_{j_1 j_2} [j_1]^{-1/2} \left[\begin{array}{c} \xrightarrow{j_1} \end{array} \right]
 \end{array}$$

Exception to this rule:

$$\left[\begin{array}{c} \xrightarrow{j} \end{array} \right] \bullet_+ \text{---} = \left[\begin{array}{c} \xrightarrow{j} \end{array} \right] \bullet_- \text{---} = \left[\begin{array}{c} \xrightarrow{j} \end{array} \right] = [j]^{-1/2} \equiv [j]^{1/2}.$$

Insertion of a summation line:

Let j_1 and j_2 run in the same direction; x then runs in the opposite direction. Choose vertex signs such that the three lines have the same order on both new vertices. This rule holds for crossing lines as well.

$$\left[\begin{array}{c} \xrightarrow{j_1} \\ \xrightarrow{j_2} \end{array} \right] = \sum_x [x] \left[\begin{array}{c} \xrightarrow{j_1} \\ \xrightarrow{j_2} \end{array} \right] \bullet_+ \xleftarrow{x} \bullet_- \left[\begin{array}{c} \xrightarrow{j_1} \\ \xrightarrow{j_2} \end{array} \right].$$

Separation over one line:

$$\left[\begin{array}{c} \xrightarrow{j} \end{array} \right] = \delta_{j,0} \text{---} \left[\begin{array}{c} \end{array} \right]. \quad (125)$$

Separation over two lines:

$$\left[\begin{array}{c} \xrightarrow{j_1} \\ \xrightarrow{j_2} \end{array} \right] = \delta_{j_1 j_2} [j_1]^{-1} \left[\begin{array}{c} \xrightarrow{j_1} \end{array} \right] \left[\begin{array}{c} \xrightarrow{j_1} \end{array} \right]. \quad (126)$$

Separation over three lines:

$$\left[\begin{array}{c} \xrightarrow{j_1} \\ \xrightarrow{j_2} \\ \xrightarrow{j_3} \end{array} \right] = \left[\begin{array}{c} \xrightarrow{j_1} \\ \xrightarrow{j_2} \\ \xrightarrow{j_3} \end{array} \right] \bullet_+ \left[\begin{array}{c} \xrightarrow{j_1} \\ \xrightarrow{j_2} \\ \xrightarrow{j_3} \end{array} \right] \bullet_- \left[\begin{array}{c} \xrightarrow{j_1} \\ \xrightarrow{j_2} \\ \xrightarrow{j_3} \end{array} \right]. \quad (127)$$

In rules (125)–(127) the diagrams on the right-hand side may be open, and in particular they may be empty. In that case we recover the factorization rules (99), (95), and (101), respectively.

Basic irreducible diagrams; $3nj$ -symbols

$n = 1$; $3j$ -symbol:

$$\{j_1, j_2, j_3\} = [j_2]^{-1} \begin{array}{c} \xrightarrow{j_1} \\ \text{---} \xrightarrow{j_2} \text{---} \\ \xrightarrow{j_3} \end{array} \begin{array}{c} \text{+} \end{array} = \begin{array}{c} \xrightarrow{j_1} \\ \text{---} \xrightarrow{j_2} \text{---} \\ \xrightarrow{j_3} \end{array} \begin{array}{c} \text{+} \end{array}.$$

The diagram is totally symmetric under permutations.

$n = 2$; $6j$ -symbol:

$$\left\{ \begin{array}{ccc} j_1 & j_2 & j_3 \\ k_1 & k_2 & k_3 \end{array} \right\} = \begin{array}{c} \text{---} \\ \nearrow k_2 \quad \nwarrow k_3 \\ \text{---} \xrightarrow{j_1} \text{---} \\ \nwarrow j_3 \quad \nearrow j_2 \\ \text{---} \end{array} \begin{array}{c} \text{---} \\ \text{---} \end{array}$$

$$= \begin{array}{c} \text{---} \\ \nearrow k_3 \quad \nwarrow k_2 \\ \text{---} \xrightarrow{j_1} \text{---} \\ \nwarrow j_2 \quad \nearrow j_3 \\ \text{---} \end{array} \begin{array}{c} \text{---} \\ \text{---} \end{array} = - \begin{array}{c} \text{---} \\ \nearrow j_1 \quad \nwarrow j_3 \\ \text{---} \xrightarrow{j_2} \text{---} \\ \nwarrow k_3 \quad \nearrow k_1 \\ \text{---} \end{array} \begin{array}{c} \text{---} \\ \text{---} \end{array}.$$

In the “tetrahedral” form of the $6j$ -symbol all node signs are the same, and arrows on the perimeter are directed as indicated by the node signs. Arrows on the central node are either all outgoing or all ingoing. The “diamond” form is obtained from the “tetrahedral” form by pulling the interior vertex outside.

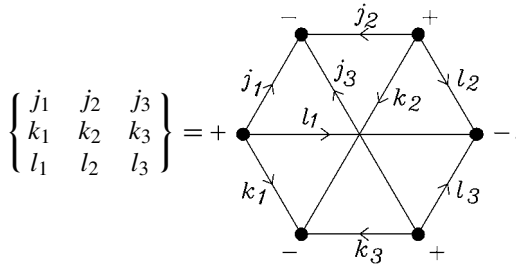
Symmetries:

$$\left\{ \begin{array}{ccc} j_1 & j_2 & j_3 \\ k_1 & k_2 & k_3 \end{array} \right\} = \left\{ \begin{array}{ccc} j_a & j_b & j_c \\ k_a & k_b & k_c \end{array} \right\} = \left\{ \begin{array}{ccc} j_a & k_b & k_c \\ k_a & j_b & j_c \end{array} \right\}$$

$$= \left\{ \begin{array}{ccc} k_a & j_b & k_c \\ j_a & k_b & j_c \end{array} \right\} = \left\{ \begin{array}{ccc} k_a & k_b & j_c \\ j_a & j_b & k_c \end{array} \right\},$$

where $(a \ b \ c)$ is any permutation of $(1 \ 2 \ 3)$.

$n = 3$; 9j-symbol:



The node signs on the perimeter alternate. The negative nodes give the rows and the positive nodes the columns of the 9j-symbol.

Symmetries:

$$\left\{ \begin{matrix} j_1 & j_2 & j_3 \\ k_1 & k_2 & k_3 \\ l_1 & l_2 & l_3 \end{matrix} \right\} = \left\{ \begin{matrix} j_1 & k_1 & l_1 \\ j_2 & k_2 & l_2 \\ j_3 & k_3 & l_3 \end{matrix} \right\} \\ = (-1)^R \left\{ \begin{matrix} j_a & j_b & j_c \\ k_a & k_b & k_c \\ l_a & l_b & l_c \end{matrix} \right\} = (-1)^R \left\{ \begin{matrix} j_a & k_a & l_a \\ j_b & k_b & l_b \\ j_c & k_c & l_c \end{matrix} \right\},$$

where

$$R = \begin{cases} j_1 + j_2 + j_3 + k_1 + k_2 + k_3 + l_1 + l_2 + l_3 & \text{if } (a \ b \ c) \text{ is odd,} \\ 0 & \text{if } (a \ b \ c) \text{ is even.} \end{cases}$$

REFERENCES

- [1] R.F.A. Clebsch, *Theorie der binären algebraischen Formen*, Teubner, Leipzig, 1872.
- [2] P. Gordan, *Über das Formensystem binären Formen*, Teubner, Leipzig, 1875.
- [3] J.J. Sylvester, *Am. J. Math.* **1** (1878) 64.
- [4] W.K. Clifford, *Am. J. Math.* **1** (1878) 126.
- [5] P. Gordan, W.G. Alexejeff, *Z. Phys. Chem.* **35** (1900) 610.
- [6] G. Rumer, E. Teller, H. Weyl, *Gött. Nachr. Math.-Phys. Klasse* **499** (1932).
- [7] M.E. Rose, *Theory of Angular Momentum*, Wiley, New York, 1957.
- [8] E.P. Wigner, *Group Theory and Its Applications to the Quantum Mechanics of Atomic Spectra*, Academic Press, New York, 1959, originally published as *Gruppentheorie und ihre Anwendung auf die Quantenmechanik der Atomspektren*, Vieweg, Braunschweig, 1931, translated to English by J.J. Griffin.
- [9] U. Fano, G. Racah, *Irreducible Tensorial Sets*, Academic Press, New York, 1959.
- [10] A.R. Edmonds, *Angular Momentum in Quantum Mechanics*, second ed., Princeton Univ. Press, Princeton, 1960.
- [11] B.R. Judd, *Operator Techniques in Atomic Spectroscopy*, McGraw-Hill, New York, 1963.
- [12] L.C. Biedenharn, H. van Dam, *Quantum Theory of Angular Momentum*, Academic Press, New York, 1965.
- [13] L.C. Biedenharn, J.D. Louck, *Angular Momentum in Quantum Physics, Encyclopedia of Mathematics*, vol. 8, Addison-Wesley, Reading, 1981.
- [14] D.A. Varshalovich, A.N. Moskalev, V.K. Khersonskii, *Quantum Theory of Angular Momentum*, World Scientific, Singapore, 1988, originally published in Russian by Nauka, Leningrad, 1975.
- [15] R.N. Zare, *Angular Momentum: Understanding Spatial Aspects in Chemistry and Physics*, Wiley, New York, 1988.
- [16] M. Danos, V. Gillet, *Angular Momentum Calculus in Quantum Physics*, World Scientific, Singapore, 1990.

- [17] J.D. Louck, in: G.W.F. Drake (Ed.), *Atomic, Molecular, & Optical Physics Handbook*, Am. Inst. of Phys, Woodbury, NY, 1996, pp. 6–55; second ed., Springer-Verlag, New York, 2006, pp. 9–74.
- [18] A. Jucys, I.B. Levinson, V.V. Vanagas, *The Theory of Angular Momentum*, Israel Program for Scientific Translation, Jerusalem, 1962, translated from the 1960 Russian edition by A. Sen and A.R. Sen.
- [19] A. Jucys, A.A. Bandzaitis, *Theory of Angular Momentum in Quantum Mechanics*, Lithuanian Academy of Sciences, Vilnius, 1965 [in Russian].
- [20] A. El Baz, B. Castel, *Graphical Methods of Spin Algebras*, Dekker, New York, 1972.
- [21] D.M. Brink, G.R. Satchler, *Angular Momentum*, third ed., Clarendon, Oxford, 1993.
- [22] G.E. Stedman, *Diagram Techniques in Group Theory*, Cambridge Univ. Press, Cambridge, 1990.
- [23] M. Kibler, E. El Baz, *Int. J. Quantum Chem.* **16** (1979) 1161.
- [24] E.P. Wigner, reprinted in: Biedenharn and van Dam [12].
- [25] W. Pauli, *Z. Phys.* **43** (1927) 601.
- [26] J.S. Schwinger, reprinted in: Biedenharn and van Dam [12].
- [27] J. Paldus, in: H. Eyring, D. Henderson (Eds.), *Theoretical Chemistry: Advances and Perspectives*, vol. 2, Academic Press, New York, 1976, pp. 131–290.
- [28] P. Gordan, *J. Reine Angew. Math.* **69** (1869) 1.
- [29] B.L. van der Waerden, *Die gruppentheoretische Methode in der Quantenmechanik*, Springer-Verlag, Berlin, 1932.
- [30] I. Lindgren, J. Morrison, *Atomic Many-Body Theory*, second ed., Springer-Verlag, New York, 1986.
- [31] G. Racah, *Phys. Rev.* **62** (1942) 438.
- [32] T. Regge, *Nuovo Cimento* **11** (1959) 116.
- [33] V.V. Tolmachev, *Adv. Chem. Phys.* **14** (1969) 471.
- [34] J.S. Briggs, *Rev. Mod. Phys.* **43** (1971) 189.
- [35] B.G. Adams, J. Paldus, *Phys. Rev. A* **24** (1981) 2302.
- [36] J. Paldus, B.G. Adams, J. Čížek, *Int. J. Quantum Chem.* **11** (1977) 813.
- [37] B.G. Adams, J. Paldus, J. Čížek, *Int. J. Quantum Chem.* **11** (1977) 849.
- [38] J. Paldus, P.E.S. Wormer, *Phys. Rev. A* **18** (1978) 827.
- [39] J. Paldus, *J. Chem. Phys.* **61** (1974) 5321.
- [40] J. Paldus, in: D.G. Truhlar (Ed.), *Mathematical Frontiers in Computational Chemical Physics*, IMA Series, vol. 15, Springer-Verlag, Berlin, 1988, pp. 262–299.
- [41] J. Paldus, *Contemp. Math.* **160** (1994) 209.
- [42] P.E.S. Wormer, J. Paldus, *Int. J. Quantum Chem.* **16** (1979) 1307.
- [43] J. Paldus, P.E.S. Wormer, *Int. J. Quantum Chem.* **16** (1979) 1321.
- [44] P.E.S. Wormer, J. Paldus, *Int. J. Quantum Chem.* **18** (1980) 841.
- [45] P.E.S. Wormer, in: M.F. Guest, S. Wilson (Eds.), *Proceedings of the Daresbury Study Weekend*, Science Research Council, Daresbury, Warrington, 1979, pp. 49–59.
- [46] I. Shavitt, in: D.G. Truhlar (Ed.), *Mathematical Frontiers in Computational Chemical Physics*, IMA Series, vol. 15, Springer-Verlag, Berlin, 1988, pp. 300–349.
- [47] J. Paldus, M.J. Boyle, *Physica Scripta* **21** (1980) 295.
- [48] J. Paldus, in: M.F. Guest, S. Wilson (Eds.), *Proceedings of the Daresbury Study Weekend*, Science Research Council, Daresbury, Warrington, 1980, pp. 40–48.
- [49] J. Paldus, M.J. Boyle, *Phys. Rev. A* **22** (1980) 2299.
- [50] M.J. Boyle, J. Paldus, *Phys. Rev. A* **22** (1980) 2316.
- [51] J. Paldus, *J. Chem. Phys.* **67** (1977) 303.
- [52] B.G. Adams, J. Paldus, *Phys. Rev. A* **20** (1979) 1.
- [53] M. Takahashi, J. Paldus, *J. Chem. Phys.* **85** (1986) 1486.
- [54] P. Piecuch, J. Paldus, *Int. J. Quantum Chem.* **36** (1989) 429.
- [55] P. Piecuch, J. Paldus, *Theor. Chim. Acta* **83** (1992) 69.
- [56] P. Piecuch, J. Paldus, *J. Chem. Phys.* **101** (1994) 5875.
- [57] P. Piecuch, J. Paldus, *Theor. Chim. Acta* **78** (1990) 65.
- [58] A.E. Kondo, P. Piecuch, J. Paldus, *J. Chem. Phys.* **102** (1995) 6511.
- [59] P.E.S. Wormer, Ph.D. thesis, University of Nijmegen, 1975.
- [60] P. Piecuch, *Int. J. Quantum Chem.* **25** (1984) 449.
- [61] P. Piecuch, *J. Math. Phys.* **27** (1986) 2165.
- [62] P. Piecuch, in: J. Maruani (Ed.), *Molecules in Physics, Chemistry and Biology, Topics in Molecular Organization and Engineering*, vol. 2, Kluwer Academic, Dordrecht, 1988, pp. 417–505.

- [63] P. Piecuch, *Mol. Phys.* **66** (1989) 805.
- [64] P. Piecuch, *Acta Phys. Pol. A* **77** (1990) 453.
- [65] T.G.A. Heijmen, R. Moszynski, P.E.S. Wormer, A. van der Avoird, *Mol. Phys.* **89** (1996) 81.
- [66] R.V. Krems, G.C. Groenenboom, A. Dalgarno, *J. Phys. Chem. A* **108** (2004) 8941.
- [67] R.-L. Chien, *J. Chem. Phys.* **81** (1984) 4023.

This page intentionally left blank

Chemical Graph Theory—The Mathematical Connection

Ivan Gutman

Faculty of Science, University of Kragujevac, 34000 Kragujevac, Serbia
E-mail: gutman@kg.ac.yu

Abstract

The impact that research done in chemical graph theory (CGT) had and has on “serious” or “pure” mathematics is examined. Although this impact is minor, it is not fully negligible. By means of two case studies we intend to demonstrate the following general features of the *CGT* \rightarrow *Mathematics* connection: (a) Scholars familiar with chemistry design a mathematical model of the examined chemical phenomena; (b) such a model may require the usage of non-trivial mathematical objects and methods, and may lead to difficult and interesting mathematical problems; (c) in order to grasp the significance of a particular mathematical object/method/problem of CGT, mathematicians need a very long time, sometimes as much as 20–30 years; (d) once this significance is recognized, a vigorous mathematical research begins; (e) mathematicians usually generalize and extend the original object/method/problem of CGT, and the results they obtain may be lacking value for CGT. The two case studies pertain to the *graph energy* and the *connectivity* (or *Randić*) *index*.

Contents

1. Prologue	125
2. Introduction	126
3. The first case study: Graph energy	127
4. The second case study: Connectivity (Randić) index	130
5. More examples	132
5.1. Hückel molecular orbitals and graph spectral theory	132
5.2. Wiener index and graph distance	133
5.3. Kekulé structures and perfect matchings	133
6. Concluding remarks	133
Acknowledgement	134
References	134

1. PROLOGUE

The field of research that we nowadays call *chemical graph theory* (CGT) originated in the 1870s, when the great British mathematician Arthur Cayley published the paper “*On the mathematical theory of isomers*” [1], followed by some half a dozen of other chemico-mathematical treatises. About the same time the British–American mathematician James Joseph Sylvester wrote the following pompous sentence [2]:

It may not be wholly without interest to some of the readers of “Nature” to be made acquainted with an analogy that has recently forcibly impressed me between branches

of human knowledge apparently so dissimilar as modern chemistry and modern algebra.

A somewhat less enthusiastic opinion on the same matter is found in an article [3] produced a century later:

Sylvester unveiled his “algebro-chemical theory” whose aim was to apply the methods of classical invariant theory to the then rapidly developing science of molecular chemistry. As far as we can tell, his theory was never taken very seriously by chemists, and not developed any further by mathematicians, and so died a perhaps well-deserved death.

Already as a student, in the 1960s, the present author became fascinated by the fact that both chemistry and algebra may be viewed as sciences that investigate the results of various operations on certain objects—on algebraic structures in algebra, and on molecular structures in chemistry. The main difference would be that in algebra the rules by which the operations act are chosen and precisely defined by mathematicians, whereas in chemistry these rules are laws of Nature and need to be discovered by chemists. Pursuing these ideas, the author encountered graph theory as early as in 1971 [4,5], and has remained active in CGT ever since. Thirty years later, in his inaugural lecture at the Serbian Academy of Sciences and Arts he summarized his efforts as follows [6]:

Some of my scientific activities may be viewed as an attempt to investigate and understand chemical notions from an algebraic point of view, and to apply various algebraic concepts, objects, methods and techniques to chemistry. This turned out to be successful only to a limited degree, but to arrive at such a conclusion I spent most of my life.

Anyway, as someone who interacted and cooperated with both chemists (*e.g.*, [4]) and mathematicians (*e.g.*, [5]), and whose scientific interests and results oscillated between chemistry (*e.g.*, [4]) and mathematics (*e.g.*, [5]), the author of this text believes himself to be qualified and competent to witness about the *mathematical connection* of CGT, and to try to establish some of its general features.

2. INTRODUCTION

A perennial problem of both mathematics and natural sciences is why the phenomena occurring in Nature are so successfully described by mathematical formalism. Some scholars are of the opinion that this is so because our Universe and the objects in it are constructed (by a Creator) so as to obey the laws of mathematics (or, to go to the extreme, that the Universe consists of mathematical objects). Another possibility would be that mathematics and its laws are constructed (by men) so as to agree with the phenomena occurring in Nature. The true answer (if such exists at all) may be somewhere in between.

There are numerous compelling examples of how examination of Nature stimulated progress in certain areas of mathematics and, probably, served as a road sign for choosing one among several possible directions in which one could go. In what follows we outline in due detail a few such examples, related to CGT. Before doing this we wish to remind the reader that graph theory (or, more generally, discrete mathematics) belongs to the less important and less valued parts of “pure” mathematics. As a consequence, whichever impact CGT would have on the researches done in graph theory, this would have little or

no influence on the direction and speed of development of the mainstream of mathematical sciences. Thus, the reader—especially if he is a mathematician—should not expect to much.

Yet, the mere fact that some concepts conceived and developed in CGT penetrated into “pure” graph theory (and therefore into “pure” mathematics) is something the members of the chemical–graph-theoretical community should be proud of. This gives us hope that not everything done in CGT will be viewed by those who come after us as an “*an exercise in chemical futility*” [7].

3. THE FIRST CASE STUDY: GRAPH ENERGY

Within the framework of the Hückel molecular orbital (HMO) approximation [8,9], the total energy of the π -electrons of a conjugated molecule is expressed as

$$E_{\pi} = \sum_j g_j E_j, \quad (1)$$

where E_j is the energy of the j th molecular orbital, g_j is the respective occupation number, and the summation embraces all molecular orbitals. Without being aware of this, Hückel in 1930s employed graph spectral theory.¹ When this fact was recognized [10], equation (1) could be rewritten as

$$E_{\pi} = \sum_{j=1}^n g_j (\alpha + \beta \lambda_j) = n_{\pi} \alpha + \beta \sum_{j=1}^n g_j \lambda_j. \quad (2)$$

In equation (2) α and β are the standard parameters of the HMO theory [9], n_{π} is the number of π -electrons, whereas n and $\lambda_1, \lambda_2, \dots, \lambda_n$ are, respectively, the number of vertices and the eigenvalues of the underlying molecular graph [11]. The non-trivial term on the right-hand side of (2) is

$$E = \sum_{j=1}^n g_j \lambda_j$$

which in the case of molecules in their ground electronic state, and assuming that the graph eigenvalues are labeled in a non-increasing order:

$$\lambda_1 \geq \lambda_2 \geq \dots \geq \lambda_n$$

reads

$$E = \begin{cases} 2 \sum_{j=1}^{n/2} \lambda_j & \text{if } n \text{ is even,} \\ 2 \sum_{j=1}^{(n-1)/2} \lambda_j + \lambda_{(n+1)/2} & \text{if } n \text{ is odd.} \end{cases} \quad (3)$$

In HMO theory E is usually referred to as the total π -electron energy (expressed in the units of the carbon–carbon resonance integral β , the so-called β units) [9,11–13].

The form of equation (3) is so awkward that it hardly would capture the attention of a single mathematician. Fortunately, the right-hand side of (3) can often be simplified. Namely,

¹ More data on this matter are found in Section 5.1.

for the majority of molecular graphs of conjugated systems of interest in chemistry,

$$\begin{cases} \lambda_{n/2} \leq 0 \leq \lambda_{n/2+1} & \text{if } n \text{ is even,} \\ \lambda_{(n+1)/2} = 0 & \text{if } n \text{ is odd.} \end{cases} \quad (4)$$

In particular, as a consequence of the pairing theorem [9,14], (4) holds for the molecular graphs of all alternant hydrocarbons. However, (4) is obeyed also by numerous non-alternant hydrocarbons. If (4) is satisfied, then the right-hand side of (3) becomes equal to twice the sum of the positive-valued eigenvalues of the molecular graph. Because the sum of all graph eigenvalues is equal to zero, we arrive at

$$E = \sum_{j=1}^n |\lambda_j|. \quad (5)$$

Expression (5) was known to George Hall in 1955 [15], and was explicitly stated by Klaus Ruedenberg in 1961 [16]. It could well be that Charles Coulson knew it already in 1940 [17].

Until the end of the 1970s, numerous mathematical results were obtained in the theory of HMO total π -electron energy. Of these we mention the following:

- The Coulson integral formula [17]:

$$E = \frac{1}{\pi} \int_{-\infty}^{+\infty} \left[n - \frac{ix\phi'(G, ix)}{\phi(G, ix)} \right] dx, \quad (6)$$

where G denotes the molecular graph, $\phi(G, x)$ is its characteristic polynomial, $\phi'(G, x) = (d/dx)\phi(G, x)$, and $i = \sqrt{-1}$.

- The McClelland inequalities [18]:

$$\sqrt{2m + n(n-1)|\det \mathbf{A}|^{2/n}} \leq E \leq \sqrt{2mn}, \quad (7)$$

where m is the number of edges of the molecular graph, and \mathbf{A} is its adjacency matrix.

- The improved McClelland estimates [19]:

$$U \leq 2mn - E^2 \leq (n-1)U \quad \text{for all conjugated systems,} \quad (8)$$

$$2U \leq 2mn - E^2 \leq (n-2)U \quad \text{for alternant systems,} \quad (9)$$

where $U = 2m - n|\det \mathbf{A}|^{2/n}$.

- The acyclic species with extremal E [20]:

$$E(S_n) < E(T_n) < E(P_n), \quad (10)$$

where S_n and P_n stand for the n -vertex star and n -vertex path, respectively, and T_n is any n -vertex tree different from S_n and P_n .

Without a single exception, all the results obtained for E , in particular (6)–(10), assumed (either explicitly or tacitly) that the condition (4) is satisfied and, thus, that equation (5) is applicable; for a recent discussion on this matter see [21]. Bearing this in mind, and realizing that (5) would be much more attractive to mathematically thinking people than (3), this author launched the concept of *graph energy* [22].

DEFINITION 1. Let G be a graph on n vertices, and let $\lambda_1, \lambda_2, \dots, \lambda_n$ be its eigenvalues. The *energy* of the graph G , denoted by $E(G)$, is the sum of the absolute values of the eigenvalues of G , i.e.,

$$E(G) = \sum_{j=1}^n |\lambda_j|. \quad (11)$$

At the first glance there is no difference between (5) and (11). However, whereas the right-hand side of (5) was viewed as chemically meaningful only if the underlying graph belongs to the restricted class of “Hückel molecular graphs” [11,12], the right-hand side of (11) is (by definition) applicable to all graphs. Whereas (3) calls for a certain physico-chemical interpretation, the quantity in (11) is just an abstract mathematical notion that needs not be interpreted at all.²

Paper [22], in which Definition 1 was proposed for the first time, is hard to find in science libraries. However, the concept of graph energy was elaborated in due detail also in the book [12], and elsewhere [23,24].

It was expected that mathematicians will become interested in graph energy, because (by Definition 1) this quantity is a symmetric function of the graph eigenvalues.³ This indeed happened, but with an enormous delay.

In the twenty-years period 1978–1997 there was practically no mathematical research on graph energy. In 1983 the Chinese mathematician Fuji Zhang published two papers concerned with $E(G)$ [25,26]. In the 1980s Siemion Fajtlowicz, by means of his computer-aided conjecture-generator *Graffiti* arrived at a few conjectures involving the sum of the positive eigenvalues of graphs [27,28], of which some were eventually verified by a group of French mathematicians [29].

Near the end of the 20th century a dramatic change occurred. In addition to mathematical works coauthored by the present author [21,30–38], a large number of mathematicians entered the field, producing by the end of 2005 over 30 papers [39–75]. In Summer 2003 the first mathematical conference was organized (in Belgaun, India), devoted solely to graph energy. This happened exactly 25 years after the concept of graph energy was put forward [22], but almost half a century after equation (5) appeared in the chemical literature.

It is not our aim to review the current mathematical research on graph energy. In brief: lower and upper bounds for $E(G)$ are established; for a variety of classes of graphs, the species having extremal (minimum and maximum) energy are characterized; the existence, structure and construction of n -vertex graphs for which $E(G) > 2n - 2$ (referred to as “hyperenergetic”) are examined; pairs and families of graphs having equal energies (referred to as “equienergetic”) are discovered. Some exquisite results obtained along these lines are:

- Among connected n -vertex graphs the n -vertex star has minimum energy [30].

² Some colleagues criticized the name “energy” proposed for $E(G)$. In order to vindicate this choice recall that in the same way as we distinguish between “curl” (in vector calculus) and “curl” (of hair), “filter” (in topology) and “filter” (in laboratory), an algebraic and a poetic “ideal”, a group-theoretic and a florist’s “wreath”, “matrix” (in algebra) and “matrix” (mold for casting metal), etc., we should distinguish between “energy” (as defined by (11)) and “energy” in molecular science and thermodynamics.

³ Recall that symmetric functions are a classical topic in algebra.

- If G is an n -vertex graph, then $E(G) \leq \frac{n}{2}(1 + \sqrt{n})$, with equality if and only if G is strongly regular [76] with parameters

$$\left(n, \frac{n + \sqrt{n}}{2}, \frac{n + 2\sqrt{n}}{4}, \frac{n + 2\sqrt{n}}{4}\right)$$

in which case G has maximum energy among n -vertex graphs [46]. Maximum-energy graphs of this kind are shown to exist [46] for $n = 4^{k+2}$, $k = 1, 2, \dots$, that is for $n = 64, 256, 1024, 4096, \dots$. For other values of n the structure of the maximum-energy graphs is not known.

- The line graph of the complete graph is hyperenergetic [41].
- Let G_1 and G_2 be two n -vertex regular graphs, both of degree r , $r \geq 3$. Then the second iterated line graphs of G_1 and G_2 are equienergetic [37].
- The energy of the Cartesian product [77] of two graphs is equal to the product of the energies of these graphs [62].

The above listed results possess an evident mathematical beauty. Their chemical relevance is hard to envisage.

4. THE SECOND CASE STUDY: CONNECTIVITY (RANDIĆ) INDEX

It was observed long ago that many properties of organic molecules depend on the extent of branching of the carbon-atom skeleton. When graph-based approaches started to be used in the study of structure–property relations, it immediately became clear that some quantitative measure of molecular branching is needed. Such measures are often referred to as “branching indices”. One of the first branching indices was proposed by Milan Randić in 1975 [78].⁴ This quantity is nowadays called the “connectivity index” or “Randić index” and is usually denoted by $\chi = \chi(G)$; in the mathematical literature it sometimes appears under the name “Randić weight”, and is sometimes denoted by $R = R(G)$. In one paper (written in Chinese) the name “randic” was used for χ .

In CGT the connectivity index achieved a rapid and enormous success. It soon became the most popular and most frequently employed structure descriptor, used in innumerable QSPR and QSAR studies. It soon was generalized (to “higher-order connectivity indices”) and parametrized (so as to be applicable to heteroatom-containing species). It is the only structure descriptor on which books are written [80–82]. For details on chemical applications of the connectivity index see the books [80,81], the reviews [83–85], and elsewhere [86–90], as well as the references cited therein.

DEFINITION 2. Let G be a graph on n vertices, possessing at least one edge. Let v_1, v_2, \dots, v_n be the vertices of G , and let the edge connecting the vertices v_i and v_j be denoted by (ij) . The degree (number of first neighbors) of the vertex v_i is denoted by δ_i . Then the *connectivity index* or *Randić index* of G is

$$\chi(G) = \sum_{(ij)} \frac{1}{\sqrt{\delta_i \delta_j}} \quad (12)$$

⁴ The structure descriptor introduced by Harold Wiener in 1947 [79], nowadays known as Wiener index, could be viewed as the first branching index of CGT.

with the summation going over all pairs of adjacent vertices, *i.e.*, over all edges of G . If the graph G has no edges, then $\chi(G) = 0$.

The situation with the mathematical investigations of the connectivity index is similar, yet more drastic as in the case of energy. In the period 1975–1987 *not a single* result on χ was reported that could be characterized as mathematical. Even worse, in 1988 a group of Swedish mathematicians published a lampoon [91] entitled “*Use of molecular connectivity indices in socio-historical and business management studies*”, in which (among other things) they “used” the Randić index to approximately calculate the phone numbers of the employees of a fish cannery in Storuman, Sweden.

The turn happened slightly before 1998. Namely, in 1998 a paper appeared, entitled “*Graphs of extremal weights*”, authored by two distinguished mathematicians (both of Hungarian origin), Béla Bollobás and Paul Erdős [92]. In this paper the “Randić weight” was examined and a difficult theorem for it proven (see below). The preprint of the paper [92] circulated among mathematicians several years before 1998, and thus many of them were familiar with it long before its actual publication. Somewhat later another paper by Erdős was published [93]. Both [92,93] appeared years after Erdős’s death.

Now, whereas Bollobás belongs among the top graph theoreticians of our time, Paul Erdős (1913–1996) is considered to be one of the greatest mathematicians of the 20th century. He had great authority and influence. Because Erdős spent some of his precious time on the study of the connectivity index, in the eyes of mathematicians there could be no doubt: the connectivity index is worth their attention, and it is an interesting mathematical object, offering numerous difficult problems.

Anyway, the rush started in 1998 and, so far, shows no sign of attenuation. We compiled over 50 references, published in 1998 and later, in which mathematical results on the connectivity index and its generalizations are reported [92–146], and this list is certainly not complete.

In mathematical investigations of the connectivity index the focus was on two main, mutually related, problems [82]: to find lower and upper bounds for χ (preferably the best possible), and to determine the graphs (within a class considered) having minimum and maximum values for χ . The main results along these lines are the following:

- Among connected n -vertex graphs the n -vertex star has minimum Randić index, equal to $\sqrt{n-1}$ [92].
- Among n -vertex graphs the maximum value of the Randić index is $n/2$, attained by all graphs in which every component is a regular graph. (This relatively straightforward result has been independently proven by several authors. It, for instance, is a direct consequence of the identity (13).)
- Among n -vertex trees the path P_n has maximum Randić index [96,98,118]. (The tree with minimum χ is, of course, the star S_n .)
- If G is an n -vertex graph without isolated vertices, then [100]

$$\chi(G) = \frac{n}{2} - \sum_{(ij)} \left(\frac{1}{\sqrt{\delta_i}} - \frac{1}{\sqrt{\delta_j}} \right)^2 \quad (13)$$

where the notation is same as in Definition 2.

- If G is a connected n -vertex graph and $\mu_1 \geq \mu_2 \geq \dots \geq \mu_{n-1} > \mu_n = 0$ are its Laplacian eigenvalues, then [121]

$$\frac{n}{2}(1 - k\mu_1) \leq \chi(G) \leq \frac{n}{2}(1 - k\mu_{n-1}),$$

where

$$k = \left(\frac{1}{n} \sum_{i=1}^n \frac{1}{\delta_i} \right) - \left(\frac{1}{n} \sum_{i=1}^n \frac{1}{\sqrt{\delta_i}} \right)^2.$$

When conceiving his branching index [78], Randić hesitated whether to define it via equation (12) or as

$$\chi_{-1}(G) = \sum_{(ij)} \frac{1}{\delta_i \delta_j}.$$

This motivated the mathematicians to think of the generalized version of the connectivity index, viz.,

$$\chi_\lambda(G) = \sum_{(ij)} (\delta_i \delta_j)^\lambda, \quad (14)$$

where λ is some real number.

Already Bollobás and Erdős [92] considered the case $\lambda = +1$. In the meantime, numerous results on such generalized Randić indices have accumulated, valid either for some particular value of λ or for λ belonging to a certain interval. For details on this matter see the book [82]. As an interesting result we mention here the finding [97,109] that among n -vertex trees the star has minimum χ_{-1} , but if $n \geq 10$, then the tree with maximum χ_{-1} is not the path P_n . The maximum- χ_{-1} trees have not yet been fully characterized.

Much as in the case of graph energy, the mathematical results obtained for the connectivity index $\chi(G)$ and its generalizations $\chi_\lambda(G)$, $\lambda \neq -1/2$, are not lacking depth and elegance. The assessment of their usefulness for CGT and chemistry in general is left to the reader.

5. MORE EXAMPLES

In order to provide additional support for the conclusions stated in the subsequent section, we give—without going into details—a few more examples of how ideas from chemistry (and CGT in particular) influenced mathematical developments.

5.1. Hückel molecular orbitals and graph spectral theory

Intending to explain by means of quantum theory the extraordinary stability of benzene, Erich Hückel formulated an approach [8] that nowadays is known under the name *Hückel molecular orbital theory* (HMO theory). This occurred in the 1930s when Hückel published a series of papers, all in German language, in German journals. In that time graph spectral theory did not exist, and Hückel was fully unaware that the mathematics he was using would one day become part of algebraic graph theory.

In 1940 Charles Coulson obtained results [14,17] that in essence are theorems of graph spectral theory. Many more results of the same kind followed in the 1940s and early 1950s [147–157].

The first mathematical paper on graph spectral theory was published by the German mathematicians Lothar Collatz and Ulrich Sinogowitz [158]. It is known that the work published in 1957 was done much earlier, in part, during World War II. There seems to be no evidence that Collatz and Sinogowitz knew about HMO theory, but this not so unlikely possibility should not be automatically disregarded.

Anyway, graph spectral theory was used in chemistry some 10–20 years before any research in this area was done by mathematicians. Whether or not these chemical applications influenced and stimulated the formation of the respective mathematical discipline cannot be decided from the available data.

5.2. Wiener index and graph distance

In a paper [79], probably published too early, Harold Wiener defined a structure descriptor that (in modern words) is equal to the sum of distances between all pairs of vertices of the molecular graph (of an alkane). Twenty years later mathematicians started to examine the very same quantity [159], being, of course, fully unaware of Wiener's work. It took additional ten years until (partially thanks to the efforts of the present author) the name “Wiener index” entered into the vocabulary of (mathematical) graph theory, and until colleagues active in CGT started to appreciate what was obtained by mathematicians. In the meantime numerous results were discovered two or more times. For details see the review [160].

5.3. Kekulé structures and perfect matchings

Determining the number K of Kekulé structures in benzenoid hydrocarbons is a classical problem of theoretical chemistry. Major progress along these lines was achieved already in the 1950s. In that time the first combinatorial expressions for K were reported [161]. In addition, an intriguing algebraic relation: $K = \sqrt{|\det \mathbf{A}|}$ was obtained [156], in which \mathbf{A} denotes the adjacency matrix of the respective molecular graph. In spite of much work in this area, and numerous papers that were continuously published in the chemical literature, mathematicians needed more than 30 years to recognize the significance and value of the problem. The first mathematical paper concerned with “perfect matchings in hexagonal systems” (equivalent to “Kekulé structures in benzenoid molecules”) was published by Horst Sachs [162]. He attempted to find necessary and sufficient conditions for the existence of Kekulé structures, a problem that in CGT was open for a long time. The solution of the problem was obtained within just one year, but by other mathematicians [163,164]; for details see the reviews [165,166].

6. CONCLUDING REMARKS

The examples outlined in the previous sections show that research done in CGT had some impact on “pure” mathematics. Although this impact is minor, it is not negligible. Our

examples suggest that there may be a general (or, at least, a frequently occurring) pattern characteristic for the *CGT* \rightarrow *Mathematics* connection:

- Scholars familiar with chemistry design a mathematical model of the examined chemical phenomena.⁵
- Such a model may require the usage of non-trivial mathematical objects and methods, and may lead to difficult and interesting mathematical problems.
- In order to grasp the significance of a particular mathematical object/method/problem of CGT, mathematicians need a very long time, sometimes as much as 20–30 years.
- Once this significance is recognized, many mathematicians begin (almost simultaneously) to do research in this area. This results in a great number of papers, published within a short period of time.
- Mathematicians have a great tendency to generalize and extend the original object/method/problem of CGT, and the results they obtain may be lacking value for CGT.

All over the world mathematicians are under pressure to do applied research. For them, whatever they do in CGT or in connection with CGT is “applied in chemistry”. Knowing this, one would expect a reasonably large interest towards CGT. This, however, is not the case. There may be two main reasons for this.

First, there are numerous other fields of science where a skilled mathematician can find topics for applied or “applied” research. In the eyes of many mathematicians, chemistry is not worth much attention. Physics and biology, operations research, and computer science, not to mention sciences related to business and banking, attract the mathematicians far more than chemistry, and CGT in particular.

Second, directions of research and preferences in mathematics have their own intrinsic logic. What a mathematician will choose to examine depends to a great extent on tradition and his feeling what is “interesting”, “beautiful” and “non-trivial”, and much less on what is “useful” (for someone else). Here again CGT does not perform well.

In spite of all this, the fact is that in the past chemical graph theory inspired some genuine mathematical studies, and contributed a bit to the progress of mathematical sciences. We are confident that this will continue also in the future.

ACKNOWLEDGEMENT

The author tanks Professor Douglas J. Klein (Galveson) for useful comments and suggestions.

REFERENCES

- [1] A. Cayley, *Philos. Mag.* **67** (1874) 444.
- [2] J.J. Sylvester, *Nature* **17** (1877/1878) 284.
- [3] P.J. Oliver, C. Shakiban, *Adv. Math.* **75** (1989) 212.
- [4] A. Graovac, I. Gutman, N. Trinajstić, T. Živković, *Theor. Chim. Acta* **26** (1972) 67.
- [5] D.M. Cvetković, I. Gutman, *Mat. Vesnik (Belgrade)* **9** (1972) 141.

⁵ For this mathematical skills are necessary. Yet, so far not a single successful mathematical model of chemical phenomena was invented by professional mathematicians.

- [6] I. Gutman, *Bull. Acad. Serbe Sci. Arts Cl. Math. Natur.* **124** (2003) 11.
- [7] G. Binsch, *Naturwiss.* **60** (1973) 369.
- [8] E. Hückel, *Z. Phys.* **70** (1931) 204.
- [9] C.A. Coulson, B. O'Leary, R.B. Mallion, *Hückel Theory for Organic Chemists*, Academic Press, London, 1978.
- [10] H.H. Günthard, H. Primas, *Helv. Chim. Acta* **39** (1956) 1645.
- [11] A. Graovac, I. Gutman, N. Trinajstić, *Topological Approach to the Chemistry of Conjugated Molecules*, Springer-Verlag, Berlin, 1977.
- [12] I. Gutman, O.E. Polansky, *Mathematical Concepts in Organic Chemistry*, Springer-Verlag, Berlin, 1986.
- [13] I. Gutman, *J. Serb. Chem. Soc.* **70** (2005) 441.
- [14] C.A. Coulson, G.S. Rushbrooke, *Proc. Cambridge Philos. Soc.* **36** (1940) 193.
- [15] G.G. Hall, *Proc. Roy. Soc. London Ser. A* **229** (1955) 251.
- [16] K. Ruedenberg, *J. Chem. Phys.* **34** (1961) 1884.
- [17] C.A. Coulson, *Proc. Cambridge Philos. Soc.* **36** (1940) 201.
- [18] B.J. McClelland, *J. Chem. Phys.* **54** (1971) 640.
- [19] I. Gutman, *Chem. Phys. Lett.* **24** (1974) 283.
- [20] I. Gutman, *Theor. Chim. Acta* **45** (1977) 79.
- [21] I. Gutman, M. Mateljević, *J. Math. Chem.* **39** (2006) 259.
- [22] I. Gutman, *Ber. Math. Statist. Sect. Forschungszentrum Graz* **103** (1978) 1.
- [23] I. Gutman, *J. Math. Chem.* **1** (1987) 123.
- [24] I. Gutman, in: A. Betten, A. Kohert, R. Laue, A. Wassermann (Eds.), *Algebraic Combinatorics and Applications*, Springer-Verlag, Berlin, 2001, pp. 196–211.
- [25] F. Zhang, *Kexue Tongbao* **28** (1983) 726.
- [26] F. Zhang, Z. Lai, *Sci. Exploration* **3** (1983) 12.
- [27] S. Fajtlowicz, *Congr. Numer.* **60** (1987) 187.
- [28] S. Fajtlowicz, *Discrete Math.* **72** (1988) 113.
- [29] O. Favaron, M. Mahéo, J.F. Saclé, *Discrete Math.* **111** (1993) 197.
- [30] G. Caporossi, D. Cvetković, I. Gutman, P. Hansen, *J. Chem. Inf. Comput. Sci.* **39** (1999) 984.
- [31] I. Gutman, L. Pavlović, *Bull. Acad. Serbe Sci. Arts Cl. Math. Natur.* **118** (1999) 35.
- [32] J.H. Koolen, V. Moulton, I. Gutman, *Chem. Phys. Lett.* **320** (2000) 213.
- [33] H.B. Walikar, I. Gutman, P.R. Hampiholi, H.S. Ramane, *Graph Theory Notes N.Y.* **51** (2001) 14.
- [34] I. Gutman, Y. Hou, *MATCH Commun. Math. Comput. Chem.* **43** (2001) 17.
- [35] Y. Hou, I. Gutman, *MATCH Commun. Math. Comput. Chem.* **43** (2001) 29.
- [36] Y. Hou, I. Gutman, C.W. Woo, *Linear Algebra Appl.* **356** (2002) 27.
- [37] H.S. Ramane, H.B. Walikar, S.B. Rao, B.D. Acharya, P.R. Hampiholi, S.R. Jog, I. Gutman, *Kragujevac J. Math.* **26** (2004) 5.
- [38] H.S. Ramane, H.B. Walikar, S.B. Rao, B.D. Acharya, P.R. Hampiholi, S.R. Jog, I. Gutman, *Appl. Math. Lett.* **18** (2005) 679.
- [39] J. Li, X. Wang, *Acta Appl. Math.* **14** (1998) 443.
- [40] F. Zhang, H. Li, *Discrete Appl. Math.* **92** (1999) 71.
- [41] H.B. Walikar, H.S. Ramane, P.R. Hampiholi, in: R. Balakrishnan, H.M. Mulder, A. Vijayakumar (Eds.), *Graph Connections*, Allied Publishers, New Delhi, 1999, pp. 120–123.
- [42] H. Li, *J. Math. Chem.* **25** (1999) 145.
- [43] F. Zhang, H. Li, in: P. Hansen, P. Fowler, M. Zheng (Eds.), *Discrete Mathematical Chemistry*, Amer. Math. Soc., Providence, 2000, pp. 385–392.
- [44] F. Zhang, Z. Li, L. Wang, *Chem. Phys. Lett.* **337** (2001) 125.
- [45] F. Zhang, Z. Li, L. Wang, *Chem. Phys. Lett.* **337** (2001) 131.
- [46] J. Koolen, V. Moulton, *Adv. Appl. Math.* **26** (2001) 47.
- [47] H.B. Walikar, H.S. Ramane, *Kragujevac J. Sci.* **23** (2001) 51.
- [48] H.B. Walikar, H.S. Ramane, *Kragujevac J. Sci.* **23** (2001) 63.
- [49] H.B. Walikar, H.S. Ramane, P.R. Hampiholi, in: R. Nadarajan, P.R. Kandasamy (Eds.), *Mathematical and Computational Models*, Allied Publishers, New Delhi, 2001, pp. 306–312.
- [50] Y. Hou, *J. Math. Chem.* **29** (2001) 163.
- [51] Y. Hou, *Linear Multilinear Algebra* **49** (2002) 347.
- [52] Y. Hou, *J. Syst. Sci. Math. Sci.* **23** (2003) 491.
- [53] D.A. Morales, *Int. J. Quantum Chem.* **88** (2002) 317.

- [54] D.A. Morales, *Int. J. Quantum Chem.* **93** (2003) 20.
- [55] J. Koolen, V. Moulton, *Graphs Combin.* **19** (2003) 131.
- [56] J. Rada, A. Tineo, *Linear Algebra Appl.* **372** (2003) 333.
- [57] J. Rada, A. Tineo, *J. Math. Anal. Appl.* **289** (2004) 446.
- [58] B. Zhou, *MATCH Commun. Math. Comput. Chem.* **51** (2004) 111.
- [59] B. Zhou, *Kragujevac J. Sci.* **26** (2004) 5.
- [60] L. Ye, R.S. Chen, *MATCH Commun. Math. Comput. Chem.* **52** (2004) 193.
- [61] R. Balakrishnan, *Linear Algebra Appl.* **387** (2004) 287.
- [62] D. Stevanović, *Linear Multilinear Algebra* **53** (2005) 67.
- [63] W. Yan, L. Ye, *Appl. Math. Lett.* **18** (2005) 1046.
- [64] J.A. Peña, L. Mendoza, J. Rada, *Discrete Math.* **302** (2005) 77.
- [65] J. Zhang, B. Zhao, *J. Math. Chem.* **37** (2005) 423.
- [66] D.A. Morales, *J. Math. Chem.* **38** (2005) 389.
- [67] A. Yu, M. Lu, F. Tian, *MATCH Commun. Math. Comput. Chem.* **53** (2005) 441.
- [68] W. Yan, L. Ye, *MATCH Commun. Math. Comput. Chem.* **53** (2005) 449.
- [69] W. Lin, X. Guo, H. Li, *MATCH Commun. Math. Comput. Chem.* **54** (2005) 363.
- [70] F. Li, B. Zhou, *MATCH Commun. Math. Comput. Chem.* **54** (2005) 379.
- [71] G. Indulal, A. Vijayakumar, *MATCH Commun. Math. Comput. Chem.* **55** (2006) 83.
- [72] B. Zhou, *MATCH Commun. Math. Comput. Chem.* **55** (2006) 91.
- [73] A. Chen, A. Chang, W.C. Shiu, *MATCH Commun. Math. Comput. Chem.* **55** (2006) 95.
- [74] I. Šparlinski, *Linear Algebra Appl.* **414** (2006) 378.
- [75] W.H. Wang, A. Chang, L.Z. Zhang, D.Q. Lu, *J. Math. Chem.* **39** (2006) 231.
- [76] A. Brouwer, A. Cohen, A. Neumaier, *Distance Regular Graphs*, Springer-Verlag, Berlin, 1989.
- [77] W. Imrich, S. Klavžar, *Product of Graphs—Structure and Recognition*, Wiley, New York, 2000.
- [78] M. Randić, *J. Am. Chem. Soc.* **97** (1975) 6609.
- [79] H. Wiener, *J. Am. Chem. Soc.* **69** (1947) 17.
- [80] L.B. Kier, L.H. Hall, *Molecular Connectivity in Chemistry and Drug Research*, Academic Press, New York, 1976.
- [81] L.B. Kier, L.H. Hall, *Molecular Connectivity in Structure-Activity Analysis*, Wiley, New York, 1986.
- [82] X. Li, I. Gutman, *Mathematical Aspects of Randić-Type Molecular Structure Descriptors*, Univ. Kragujevac, Kragujevac, 2006.
- [83] L.H. Hall, in: D.H. Rouvray (Ed.), *Computational Chemical Graph Theory*, Nova Press, New York, 1990, pp. 202–233.
- [84] S.P. Gupta, *Chem. Rev.* **91** (1991) 1109.
- [85] L. Pogliani, *Chem. Rev.* **100** (2000) 3827.
- [86] L. Pogliani, *J. Phys. Chem.* **99** (1995) 925.
- [87] L. Pogliani, *J. Phys. Chem.* **103** (1999) 1598.
- [88] L. Pogliani, *J. Mol. Struct. (Theochem)* **466** (1999) 1.
- [89] E. Estrada, *J. Phys. Chem. A* **106** (2002) 9085.
- [90] E. Estrada, *Internet Electron. J. Mol. Design* **1** (2002) 360.
- [91] J.T. Edward, E. Johanson, S. Wold, *Graph Theory Notes N.Y.* **15** (1988) 26.
- [92] B. Bollobás, P. Erdős, *Ars Combin.* **50** (1998) 225.
- [93] B. Bollobás, P. Erdős, A. Sarkar, *Discrete Math.* **200** (1999) 5.
- [94] O. Araujo, J.A. de la Peña, *Linear Algebra Appl.* **283** (1998) 171.
- [95] O. Araujo, J.A. de la Peña, *J. Chem. Inf. Comput. Sci.* **38** (1998) 827.
- [96] P. Yu, *J. Math. Study* **31** (1998) 225.
- [97] L.H. Clark, J.W. Moon, *Ars Combin.* **54** (1999) 223.
- [98] G. Caporossi, I. Gutman, P. Hansen, *Comput. Chem.* **23** (1999) 469.
- [99] I. Gutman, O. Miljković, G. Caporossi, P. Hansen, *Chem. Phys. Lett.* **306** (1999) 366.
- [100] I. Gutman, O. Araujo, J. Rada, *ACH Models Chem.* **137** (2000) 653.
- [101] O. Araujo, J. Rada, *J. Math. Chem.* **27** (2000) 201.
- [102] I. Gutman, O. Araujo, D.A. Morales, *Indian J. Chem.* **39A** (2000) 381.
- [103] I. Gutman, L. Pavlović, O. Miljković, *Bull. Acad. Serbe Sci. Arts Cl. Math. Natur.* **121** (2000) 1.
- [104] I. Gutman, O. Araujo, D.A. Morales, *J. Chem. Inf. Comput. Sci.* **40** (2000) 572.
- [105] I. Gutman, O. Miljković, *MATCH Commun. Math. Comput. Chem.* **41** (2000) 75.
- [106] L. Pavlović, I. Gutman, *Novi Sad J. Math.* **31** (2001) 53.

- [107] I. Gutman, *Croat. Chem. Acta* **75** (2002) 357.
- [108] I. Gutman, *J. Serb. Chem. Soc.* **67** (2002) 99.
- [109] I. Gutman, M. Lepović, D. Vidović, L.H. Clark, *Indian J. Chem. A* **41** (2002) 457.
- [110] O. Araujo, J. Rada, *Ars Combin.* **62** (2002) 65.
- [111] C. Delorme, O. Favaron, D. Rautenbach, *Discrete Math.* **257** (2002) 29.
- [112] D. Rautenbach, *Discrete Math.* **271** (2003) 335.
- [113] L. Pavlović, *Discrete Appl. Math.* **127** (2003) 615.
- [114] L. Pavlović, *Kragujevac J. Math.* **25** (2003) 55.
- [115] M. Fischermann, A. Hoffmann, D. Rautenbach, L. Volkmann, *Discrete Appl. Math.* **128** (2003) 375.
- [116] J. Rada, C. Uzcátegui, *Discrete Appl. Math.* **128** (2003) 447.
- [117] P. Hansen, H. Mélot, *J. Chem. Inf. Comput. Sci.* **43** (2003) 1.
- [118] G. Caporossi, I. Gutman, P. Hansen, L. Pavlović, *Comput. Biol. Chem.* **27** (2003) 85.
- [119] J. Rada, O. Araujo, *MATCH Commun. Math. Comput. Chem.* **49** (2003) 15.
- [120] X. Li, H. Zhao, *MATCH Commun. Math. Comput. Chem.* **50** (2004) 57.
- [121] M. Lu, H. Liu, F. Tian, *MATCH Commun. Math. Comput. Chem.* **51** (2004) 149.
- [122] X. Li, Y. Yang, *MATCH Commun. Math. Comput. Chem.* **51** (2004) 155.
- [123] H. Zhao, X. Li, *MATCH Commun. Math. Comput. Chem.* **51** (2004) 167.
- [124] Y. Hu, X. Li, Y. Yuan, *MATCH Commun. Math. Comput. Chem.* **52** (2004) 119.
- [125] Y. Hu, X. Li, Y. Yuan, *MATCH Commun. Math. Comput. Chem.* **52** (2004) 129.
- [126] X. Li, Y. Yang, *MATCH Commun. Math. Comput. Chem.* **52** (2004) 147.
- [127] X. Li, X. Wang, B. Wei, *MATCH Commun. Math. Comput. Chem.* **52** (2004) 157.
- [128] J. Rada, *MATCH Commun. Math. Comput. Chem.* **52** (2004) 167.
- [129] J. Gao, M. Lu, *MATCH Commun. Math. Comput. Chem.* **53** (2005) 377.
- [130] L. Zhang, B. Wu, *MATCH Commun. Math. Comput. Chem.* **54** (2005) 189.
- [131] X. Li, J. Zheng, *MATCH Commun. Math. Comput. Chem.* **54** (2005) 195.
- [132] J.A. Rodriguez, J.M. Sigarreta, *MATCH Commun. Math. Comput. Chem.* **54** (2005) 403.
- [133] H. Li, M. Lu, *MATCH Commun. Math. Comput. Chem.* **54** (2005) 417.
- [134] Y. Hu, X. Li, Y. Shi, T. Xu, I. Gutman, *MATCH Commun. Math. Comput. Chem.* **54** (2005) 425.
- [135] H. Lu, B. Zhou, *MATCH Commun. Math. Comput. Chem.* **54** (2005) 435.
- [136] Y. Hu, X. Li, Y. Yuan, *MATCH Commun. Math. Comput. Chem.* **54** (2005) 441.
- [137] B. Wu, L. Zhang, *MATCH Commun. Math. Comput. Chem.* **54** (2005) 455.
- [138] X. Pan, H. Liu, J. Xu, *MATCH Commun. Math. Comput. Chem.* **54** (2005) 465.
- [139] X. Lu, L. Zhang, F. Tian, *J. Math. Chem.* **38** (2005) 677.
- [140] J. Rada, C. Uzcátegui, *Discrete Appl. Math.* **150** (2005) 232.
- [141] H. Liu, M. Lu, F. Tian, *Discrete Appl. Math.* **154** (2005) 106.
- [142] Y. Hu, Y. Jin, X. Li, L. Wang, *MATCH Commun. Math. Comput. Chem.* **55** (2006) 119.
- [143] X. Li, J. Zheng, *MATCH Commun. Math. Comput. Chem.* **55** (2006) 381.
- [144] X. Li, L. Wang, Y. Zhang, *MATCH Commun. Math. Comput. Chem.* **55** (2006) 391.
- [145] X. Pan, J. Xu, C. Yang, *MATCH Commun. Math. Comput. Chem.* **55** (2006) 409.
- [146] H. Liu, M. Lu, F. Tian, *MATCH Commun. Math. Comput. Chem.* **55** (2006) 419.
- [147] C.A. Coulson, H.C. Longuet-Higgins, *Proc. Roy. Soc. London Ser. A* **191** (1947) 39.
- [148] C.A. Coulson, H.C. Longuet-Higgins, *Proc. Roy. Soc. London Ser. A* **192** (1947) 16.
- [149] C.A. Coulson, H.C. Longuet-Higgins, *Proc. Roy. Soc. London Ser. A* **193** (1948) 447.
- [150] C.A. Coulson, H.C. Longuet-Higgins, *Proc. Roy. Soc. London Ser. A* **193** (1948) 456.
- [151] C.A. Coulson, H.C. Longuet-Higgins, *Proc. Roy. Soc. London Ser. A* **195** (1948) 188.
- [152] C.A. Coulson, J. Jacobs, *J. Chem. Soc.* (1949) 2805.
- [153] I. Samuel, *C. R. Acad. Sci. Paris* **229** (1949) 1236.
- [154] C.A. Coulson, *Proc. Cambridge Philos. Soc.* **46** (1950) 202.
- [155] H.C. Longuet-Higgins, *J. Chem. Phys.* **18** (1950) 265.
- [156] M.J.S. Dewar, H.C. Longuet-Higgins, *Proc. Roy. Soc. London Ser. A* **214** (1952) 482.
- [157] E. Heilbronner, *Helv. Chim. Acta* **36** (1953) 170.
- [158] L. Collatz, U. Sinogowitz, *Abh. Math. Sem. Univ. Hamburg* **21** (1957) 63.
- [159] R.C. Entringer, D.E. Jackson, D.A. Snyder, *Czechoslovak Math. J.* **26** (1976) 283.
- [160] A.A. Dobrynin, R. Entringer, I. Gutman, *Acta Appl. Math.* **66** (2001) 211.
- [161] M. Gordon, W.H.T. Davison, *J. Chem. Phys.* **20** (1952) 428.
- [162] H. Sachs, *Combinatorica* **4** (1984) 89.

- [163] A.V. Kostochka, in: *Proc. 30th Int. Sci. Colloquium TH Ilmenau, Graphen und Netzwerke—Theorie und Anwendungen, Ilmenau*, 1985, pp. 49–52.
- [164] F. Zhang, R. Chen, X. Guo, *Graphs Combin.* **1** (1985) 383.
- [165] I. Gutman, S.J. Cyvin, *J. Serb. Chem. Soc.* **53** (1988) 391.
- [166] F. Zhang, X. Guo, R. Chen, *Top. Curr. Chem.* **153** (1990) 181.

Atomic Charges *via* Electronegativity Equalization: Generalizations and Perspectives

Alexander A. Oliferenko^{1,2}, Sergei A. Pisarev², Vladimir A. Palyulin²,
and Nikolai S. Zefirov²

¹*Pacific Northwest National Laboratory, Richland, WA 99352, USA*

E-mail: aleksandr.oliferenko@pnl.gov

²*Department of Chemistry, Moscow State University, Moscow 119992, Russia*

Abstract

Since the atomic point charges came into wide use as the electrostatic part of modern molecular force fields, dozens of empirical and semiempirical charge calculation methods were developed over the last few decades. Many of them employ electronegativity equalization, one of the DFT cornerstone principles. We show that algebraically all known electronegativity equalization schemes can be divided into two different groups with respect to the underlying mathematical formalism and the degree to which electronegativity is equalized. Methods of the first group are based on the generalized hardness matrix formalism and provide complete electronegativity equalization, whereas another group of methods invokes the Laplacian matrix formalism and results in a redistribution of electronegativity rather than complete equalization. A new principle of electronegativity relaxation is introduced. Electronegativity identified with electrical potential is viewed as a harmonic function satisfying a discrete Laplace equation with Dirichlet boundary conditions. A Markov chain formalism for solving such equations is developed. Some numerical results of chemical interest are discussed. Application of atomic charges in different areas of molecular modeling is overviewed.

Contents

1. Introduction	140
2. Two approaches to electronegativity redistribution	141
2.1. Complete electronegativity equalization through the generalized hardness matrix	142
Method of Mullay (1984–1986) [34–36]	144
EEM of Mortier and co-workers (1985–1986) [11,33]	144
QEq method of Rappe and Goddard (1991) [44]	145
2.2. Electronegativity relaxation through the Laplacian matrix	146
Common algebraic formalism	147
Method of Del Re	148
Method of Gasteiger and Marsili	148
Kirchhoff Charge Model	149
3. Principle of electronegativity relaxation	149
3.1. Electronegativity relaxation as a discrete Dirichlet problem	149
3.2. Markov chain formalism	150
4. Numerical examples	152
5. Chemical applications of atomic charges	153
6. Conclusions	153
References	154

1. INTRODUCTION

It is generally recognized now that knowledge of charge distribution is fundamental for chemical theory and vital for modeling of biomolecular and material-science systems. The usual way of representing the electronic charge distribution is as partial atomic charges, which are assigned to each atom in a molecule and measured in fractions of the elementary charge. Such a view of fixed atomic charges is no better than a useful idealization, because one hardly can imagine a totally relaxed real molecule free of any sort of excitation due to interaction with other particles, emissions or physical fields. Although atomic charges are not a physical observable, nor does there exist a quantum-mechanical operator whose expectation values are the atomic charges, this concept is extremely useful in the description of electrostatic properties of molecules and molecular complexes.

Quantum chemistry provides a way of estimating molecular charge distributions through different population analysis techniques; those by Mulliken [1], Löwdin [2], and Weinhold *et al.* [3] are well known and described elsewhere. To derive reasonable atomic charges using these techniques one has to obtain a full molecular wavefunction from a high level of non-empirical theory. The Bader “atoms in molecules” theory, AIM [4], derives the zeroth-order atomic moments (atomic charges) by integrating the electron density over atomic basins. Possible sources of the density are either *ab initio* wavefunctions or X-ray diffraction experiments. Another important molecular feature that can be extracted from MO-LCAO calculations is the molecular electrostatic potential (MEP). Several methods have been proposed to reproduce the non-empirical MEP with point charges (the so-called ESP-charges) obtained by a statistical fit [5–8]. Hard computational demands are the reason why the population analysis techniques and AIM integration are limited to small molecules only and hardly applicable to macromolecular objects of biological and nanotechnological interest. Much less time-consuming semiempirical SCF theory can provide highly reasonable atomic charges through an appropriate parameterization, as has been demonstrated by Cramer and Truhlar [9].

There is a rapidly growing need of the computer-aided molecular and material design field in computationally inexpensive charge calculation schemes. Many of the schemes discussed below may be referred to as “quasi-quantum” since they use quantum chemical ideas such as the electronic chemical potential and its equalization but rarely or never resort to real quantum mechanical computational machinery. Instead of nuclei and electrons these quasi-quantum schemes deal with classical chemical concepts such as atoms and bonds comprising a molecular backbone.

The paper is organized as follows: electronegativity equalization methods divided into two categories with respect to the underlying matrix formalism are discussed in Section 2. In Section 3 we present a new view of electronegativity redistribution and show that changes in electronegativity of the constituent atoms upon formation of a molecule can be viewed to result from the action of the electronegativity relaxation principle, which is identified as a boundary value problem. According to the relaxation principle, electronegativity redistributes itself to meet first the local arithmetic mean principle, in distinction to Sanderson’s theory and DFT where electronegativity obeys the global geometric mean principle, much as occurs with the minimization of the Gibbs free energy of a phase. Section 4 provides some numerical results of atomic charge calculation according to the method outlined in Section 2. Section 5 covers some important applications of “quasi-quantum” atomic charges in drug design, biomolecular simulations, and materials science.

2. TWO APPROACHES TO ELECTRONEGATIVITY REDISTRIBUTION

The electronegativity concept is a very important atomistic idea, which is widely used in modern chemistry. Analyses of molecular structure, reactivity patterns, and intermolecular interactions [10], as well as derivations of atomic charges [11] are the chemical areas of using this concept. Originally put forward by Pauling [10], the electronegativity concept evolved in the work of Mulliken [12], of Allred and Rochow [12], of Sanderson [13], and lastly with very many density-functional theorists [14]. DFT relates electronegativity to the negative of the molecular chemical potential [15], which appears in the DFT equations as the first derivative of energy with respect to the electron occupation number. By definition, any potential tends to be redistributed or ultimately equalized, as does the chemical potential on the formation of a molecule. This property of the chemical potential gives rise to two different views of the electronegativity redistribution.

As assumed by Sanderson's geometric mean postulate [13] and as is considered within the DFT-based electronegativity equalization method (EEM) [11], atomic *in situ* electronegativities are all equal over the whole system, and the common value is the geometric mean of the original atomic quantities. DFT treats electronegativity by analogy with chemical thermodynamics: the electron gas is brought to equilibrium (a molecule is in its ground state) when its chemical potential becomes equal over the whole system, and the equalized chemical potential minimizes the energy of the system.

However, apart from the complete electronegativity-equalization approach within DFT, there are approaches exploiting the idea of partial or incomplete electronegativity equalization [16–18]. Such incomplete electronegativity equalization implies that atoms in a molecule retain certain amounts of their own electronegativities, which are not equal to a mean value. Whereas the derivation of electronegativity within DFT borrows ideas from classical thermodynamics, the other electronegativity redistribution concepts rely upon different classical theories. For example, the approach being developed by the present authors [19–22] and implicitly the Del Re [16] method are based on the theory of electrical circuits. Here, the molecule is represented by an electrical network composed of nodes (junction points), corresponding to atoms and conducting branches, which are identified with chemical bonds. Similar structural models appear in mathematical chemical works of Golender *et al.* [23] and of Klein and co-workers [24,25]. In our model electronegativities of the constituent atoms are associated with electric potentials in the nodes of a closed electrical network, hence they may be redistributed, rather than being obligatorily equalized. The net amounts of the electronic charge transferred upon formation of the molecule are associated with currents flowing through the resistive network. This is because the model is discrete and the currents are defined as amounts of the charge stuck in each of the discrete time states. Further we shall refer to our approach as to the Kirchhoff Charge Model (KCM), emphasizing that our method of atomic charge calculation is based on Kirchhoff's electricity laws. In turn, Kirchhoff's electricity laws are the manifestation of a very general principle of evolution of dynamic systems. Thus the classical theory of electrical circuits has recently been reformulated in the framework of quantum chaotic dynamics and solid state physics. Quantum network theory [26] attempts to quantize electrical circuits and considers quantum electric networks as the low-frequency limit of quantum optics. Signal transmission lines play the role of resistors of a usual electrical network, and the Kirchhoff electricity laws turned out to be the correct Heisenberg equations of motion.

Table 1. Correspondence between DFT and electrical networks

Property	DFT	Electrical circuits theory
Potential	χ , electronegativity	V , voltage
Resistance	η , hardness	R , resistance
Conductance	$s = 1/\eta$, softness	C , conductance
Current (charge transfer)	$\Delta N_{ij} = (\chi_i - \chi_j)/\eta_{ij}$	$i_{ij} = (v_i - v_j)/R_{ij}$
Energy	$E = E_0 + \chi \Delta N + \eta(\Delta N)^2$	$E = E_0 + v_i + R i^2$
Reciprocity	$\Delta N_{ij} = -\Delta N_{ji}$	$i_{ij} = -i_{ji}$
Charge conservation	$\sum_i \sum_j \Delta N_{ij} = 0, \pm 1, \dots$	$\sum_j i_{ij} = 0$

Non-dissipative quantum conductances in networks are studied in [27], where the authors relate the discrete Laplacian of a graph to a Hamiltonian in the tight-binding approximation with the potential due to the nuclei being constant or simply zero. Classical and quantum dynamics of multi-channel scattering of particles gives rise to a new, rapidly growing area of mathematical physics, the quantum graph theory [28–30]. The term graph is reserved here and throughout the paper for a combinatorial or topological entity, a subject of graph theory [31]. In the chemical language a quantum graph is a weighted graph equipped with self-loops and multiple edges along with a second-order difference or differential operator defined on the graph edges as well as boundary conditions defined on the graph vertices. The Kirchhoff charge model is thus a quantum graph with the difference Laplacian operator (represented by the Laplacian matrix) and Dirichlet boundary conditions. In the light of the above considerations the principle of electronegativity relaxation seems to be substantiated to an extent not less than for the complete electronegativity equalization of DFT. At the same time we note a significant similarity between DFT and theory of electrical networks as seen from Table 1.

The main difference between the DFT electronegativity equalization and the Kirchhoff electronegativity relaxation is how they meet the charge conservation law: KCM complies with charge conservation both locally through Kirchhoff's current rule (the algebraic sum of all charge transfers at any atom is zero), and globally (the algebraic sum of all atomic charges is equal to the system's formal charge), whereas DFT demands only the global charge conservation.

2.1. Complete electronegativity equalization through the generalized hardness matrix

Usually the reasoning starts with a hypothetic atomic energy E as a continuous and differentiable function of N , where N is the electron occupation number. As it follows from DFT, the ground state energy E of an atom in a molecule can be expanded as a power series in N in the vicinity of $\Delta N = 0$ at a constant external potential:

$$E(N) = E^0 + \frac{\partial E}{\partial N} \Delta N + \frac{1}{2} \frac{\partial^2 E}{\partial N^2} (\Delta N)^2 + \dots + . \quad (1)$$

It is generally believed that the expansion up to the second term is sufficient. As DFT identifies electronegativity χ as the first derivative of energy E with respect to the number

of electrons and hardness η as the second derivative, differentiation of (1) immediately gives a basis for electronegativity equalization and calculation of atomic charges:

$$\chi = \chi^0 + \eta^0 q, \quad (2)$$

where the zero superscript refers to the characteristics of non-interacting atoms, and the amount of the electronic charge transferred (ΔN) is now denoted as q . For a diatomic molecule AB one composes a set of equations

$$\begin{aligned} \chi_A &= \chi_A^0 + \eta_A^0 q_A, \\ \chi_B &= \chi_B^0 + \eta_B^0 q_B \end{aligned} \quad (3)$$

and imposes two subsidiary constraints to make the equations solvable:

$$q_A = -q_B \quad \text{and} \quad \chi_A = \chi_B = \chi_M \quad (4)$$

with the second constraint being the essence of the complete electronegativity equalization principle. Resolving these equations of (3) for q under the given constraints, we obtain the charge transferred from atom A to atom B upon formation of molecule AB:

$$q = \frac{\chi_B^0 - \chi_A^0}{\eta_A^0 + \eta_B^0}. \quad (5)$$

This formalism works well in case of a diatomic molecule, but in multi-atomic molecules it generally fails because the charges generated are not connectivity-dependent, and if too casually implemented, may not obey the charge conservation condition. To force the charge conservation some new physically relevant terms are added to equations (3) as electronegativity corrections for the molecular environment. Without loss of generality we can conclude that the various methods, exploiting the complete electronegativity equalization principle, differ only in the nature of the additional terms added to equations (3), whereas the underlying algebraic formalism is the same. Then a set of simultaneous equations (3) is solved for unknown atomic charges q_i . In matrix form it can be written as follows:

$$\begin{pmatrix} \mathbf{H} & \mathbf{1} \\ \mathbf{1}^T & 0 \end{pmatrix} \begin{pmatrix} \mathbf{q} \\ -\chi \end{pmatrix} = \begin{pmatrix} -\chi^0 \\ Q \end{pmatrix}. \quad (6)$$

A similar matrix notation was used in [32] for writing the EEM (Electronegativity Equalization Method) equations [11] in the brief and convenient form. Equation (6) is more general: the main block of the block matrix in the left-hand side of equation (6) is a generalized hardness matrix \mathbf{H} . The particular form of this matrix varies in different complete electronegativity equalization methods, which generally do not respect molecular connectivity, but instead take into account all pair-wise interatomic interactions. In terms of graph theory such a complete relation can be expressed through the sum of the adjacency matrix \mathbf{A} of a complete graph weighted by a matrix \mathbf{H}_{ij} , containing all pair-wise interatomic contributions, and a diagonal matrix $\text{diag}(h_{ii})$ whose diagonal elements are atomic (or intraatomic, following the terminology of [33]) hardnesses. In symbolic notation it is written as follows: $\mathbf{H} = \mathbf{A} * \mathbf{H}_{ij} + \text{diag}(h_{ii})$, where “*” stands for the matrix component-wise (Hadamard) multiplication.

The generalized hardness matrix formed in such a way needs to be augmented by column vector $\mathbf{1}$, containing all 1, its transpose $\mathbf{1}^T$, and zero in the lower right corner to explicitly include constraints (4) into equation (6). Other components of equation (6) are the column

vector of unknown atomic charges, \mathbf{q} , the vector of initial free-atom electronegativities, χ^0 , the equalized electronegativity χ (still unknown but common for all the atoms), and the total charge of the system under study, Q . Once the hardness matrix, initial electronegativities, and the total charge of the system of interest have been determined, the matrix equation (6) can easily be solved for the unknown charges by inversion of the augmented hardness matrix:

$$\begin{pmatrix} \mathbf{q} \\ -\chi \end{pmatrix} = \begin{pmatrix} \mathbf{H} & \mathbf{1} \\ \mathbf{1}^T & 0 \end{pmatrix}^{-1} \begin{pmatrix} -\chi^0 \\ Q \end{pmatrix}. \quad (7)$$

Therefore, the only distinguishing feature of the various methods are the elements of matrix \mathbf{H} . Below we list all complete EEM methods in a chronological order and discuss briefly their features.

Method of Mullay (1984–1986) [34–36]

In the Mullay method equations (3) take the following form:

$$\chi_i = \chi_i^0 + \frac{3}{2}\chi_i^0 q_i + \sum_{i \neq j} \frac{1}{2}\chi_i^0 q_j. \quad (8)$$

Here we can see that both atomic and interatomic hardness values are expressed through the free-atom electronegativity χ_i^0 , and the hardness matrix is defined as

$$\mathbf{H}^M = \{h_{ij}\} = \begin{cases} \frac{3}{2}\chi_i^0, & \text{if } i = j, \\ \frac{1}{2}\chi_i^0, & \text{if } i. \end{cases} \quad (9)$$

The atomic electronegativity parameters χ_i^0 were approximated by Mullay with the following formula: $\chi_i^0 = 1.67G_i(Z^2/n_e^2) + 0.41$, where G_i is a linear function of the p -character of the i th orbital, and Z and n_e are the effective screened nuclear charge and the effective principal quantum number, respectively, both calculated according to Slater's rules. Multiple group electronegativities were calculated by Mullay and it was shown that on the average it satisfactorily reproduced ESCA chemical shifts and *ab initio* charge calculations. The method is not aimed to produce atomic charges reliable enough to approximate dipole or higher electrostatic moments.

EEM of Mortier and co-workers (1985–1986) [11,33]

This is the most well-developed approach to complete electronegativity equalization developed in the framework of DFT with the use of previous results of Sanderson [13], Huheey [17], and Nalewajski [37]. The respective electronegativity equalization formula is given by

$$\chi_i = \chi_i^* + 2\eta_i^* q_i + \sum_{i \neq j}^N \frac{q_j}{R_{ij}}. \quad (10)$$

As a physically relevant additional term, accounting for interatomic hardness, the EEM authors take the Madelung-type potential q_j/R_{ij} , with atomic hardnesses being diagonal

elements of the hardness matrix \mathbf{H} . In this setting matrix \mathbf{H} takes the following values:

$$\mathbf{H}^{\text{EEM}} = \{h_{ij}\} = \begin{cases} 2\eta_i^*, & \text{if } i = j, \\ \frac{1}{R_{ij}}, & \text{if } i \neq j. \end{cases} \quad (11)$$

It should be emphasized that the electronegativity and hardness parameters within EEM are not straightforwardly selected from experimental data or calculated but searched out through an optimization protocol to reproduce *ab initio* Mulliken atomic charges calculated in the STO-3G basis. Therefore, the “atom in a molecule” electronegativity (and hardness) values $\chi_i^* = \chi_i^0 + \Delta\chi_i$ are made up of two terms: the free-atom experimental electronegativities χ_i^0 , and corrections $\Delta\chi_i$ for the molecular surrounding, subjected to optimization. No special provisions are applied to the molecular electron density, it is implicit that spherical atomic densities are condensed to the corresponding nuclei.

The method of Mortier has given an impetus to further explosive progress in the EEM development. Dozens of publications have suggested new parameterizations and new applications of the complete EEM principle in many fields of chemistry, molecular modeling, and materials science, see Ref. [38] and references therein. These new parameterizations amount to more thorough fitting of the $\Delta\chi_i$ corrections [39,40], or to developing new off-diagonal elements of the hardness matrix [41–43].

QEq method of Rappe and Goddard (1991) [44]

The QEq method originates from the same DFT premises much as for EEM, however, the way of selecting the hardness matrix elements within QEq is different. Electronegativity equalization is given by

$$\chi_i = \chi_i^0 + J_{ii}^0 q_i + \sum_{i \neq j}^N q_j J_{ij}. \quad (12)$$

Here, the one-center two-electron integral, J_{ii}^0 , is employed for filling the principal diagonal of matrix \mathbf{H}^{QEq} . It is quite justified since J_{ii}^0 is commonly considered as a measure of atomic hardness, in many cases the semiempirically estimated repulsion integral J_{ii}^0 and η are identically equal to each other because they are calculated from the same spectroscopic data. For a geometry-dependent term in equation (12) Rappe and Goddard used an approximate two-center integral linearly related to the interatomic distance between centers i and j :

$$\mathbf{H}^{\text{QEq}} = \{h_{ij}\} = \begin{cases} J_{ii}^0, & \text{if } i = j, \\ J_{ij}, & \text{if } i \neq j. \end{cases} \quad (13)$$

To provide a more accurate mutual screening of closely located atoms the authors allowed the electron density to extend by using of Slater-type spherically symmetric basis functions. Thus, J_{ij} of all atoms besides hydrogen depend solely on the inter-atomic separations. Hydrogen, because of its unique coreless nature, was treated in a more complex way. It was adopted that the two-center repulsion between the hydrogen and another atom depends not only on the inter-nuclear separation, but also on the atomic charge on the hydrogen. This charge dependence of hardness is implied upon taking the next higher term in the expansion presented by equation (1). Such a setting necessarily requires additional

steps of self-consistent calculations, so QEq is an iteration method and thus is more time-consuming than EEM. The method has been further improved by the Goddard group as the Dynamic Charge Equilibration (DQEq) method [45] for use with a force field designed for modeling of crystal structures and amorphous materials.

Finally, mention may be made of other charge calculation schemes, exploiting the same Sanderson–DFT principle of electronegativity equalization. Since the mathematical formalism used is identical to that above described we do not give many details here. What is really worth noting is the chemical-potential-equalization (CPE) method of York and Yang [46], which was also considered by its authors and later reflected in the literature [38] as a generalization for the EEM and QEq. The electron density is represented within the CPE as a set of Gaussian basis functions (*cf.* Slater-type functions in the QEq) and the hardness matrix elements are optimized to fit DFT local density calculations (*cf.* experimental parameters of the EEM). The fluctuating-charge (FC) model of Berne *et al.* [47] utilizes the general electronegativity equalization formalism and the same basis function representation of the electron density as in the QEq method, however, to force the charge conservation over a multi-molecular system, the atomic charges are treated as dynamical variables with fictitious masses. Equations of “motion” for the charges are written according to Newton’s second law, and the method of undetermined Lagrange multipliers is used to provide necessary constraints.

2.2. Electronegativity relaxation through the Laplacian matrix

As was noted above DFT invokes a thermodynamic analogy for treating the electron density as an electron gas in the field of nuclei. By contrast, the model we develop consists of atoms and interaction channels among them and uses the computational formalism of theory of electrical circuits. Generally, this formalism is a special case of the general probabilistic approach to solving physical problems where differential equations arise, which is based on random walks [48,49] or Markov chains [50]. Both representations are operationally equivalent and provide a common mathematical ground for many distant at first glance areas such as theory of electrical networks, classical potential theory, and Brownian motion. Of our interest is the well-known electrical problem: given a network architecture and external potentials generating a stationary electric field, to find potentials inside the network. This problem is reduced to solving the Laplace equation with Dirichlet boundary conditions and has a unique solution. As for practical purposes only potentials at the nodes of the network matter, the potential function becomes discrete, and the problem is readily formalized in terms of matrices associated with graphs representing electrical networks [49]. The external potentials form a discrete boundary and the discrete Laplace equation is solved for unknown interior potentials. In the discrete setting the differential Laplacian operator is substituted by its discrete analog, the Laplacian matrix of a graph [51]. Since molecular structure is also often represented by discrete, graph-theoretical models with no real geometry assigned, it comes at no surprise that the Laplacian matrix is intensively studied by chemists [52–54]. Moreover, some atomic charge calculation schemes implicitly or explicitly make use of this formalism. Historically, one of the earliest charge calculation methods and the first one utilizing the Laplacian matrix formalism is that proposed by Del Re in 1958 [16]. This approach has been further developed in the works of Allinger *et al.* [55] and Fliszar and Chretien [56]. A different

but related approach was set out by Gasteiger and Marsili in 1978 [57] and, finally, a new method, explicitly relying upon the Laplacian formalism, has been elaborated in the works of the present authors [19–22,58].

Common algebraic formalism

The connectivity of a molecular graph is often expressed in the form of an adjacency matrix or a Laplacian matrix. The element a_{ij} of the adjacency matrix is equal either to zero if there is no edge connecting vertices i and j or is equal to the multiplicity of the respective edge. The Laplacian matrix, \mathbf{L} , of graph G on n vertices and m edges is defined in the following way:

$$\mathbf{L} = (l_{ij}) = \begin{cases} -c, & i \sim j, i \neq j, \\ d_i, & i = j, \\ 0, & \text{otherwise,} \end{cases} \quad (14)$$

where c is the multiplicity of the edge connecting vertices i and j , d_i is the degree of i th vertex (being the count of all edges attached to the i th vertex). The sign \sim means atoms i and j are connected by a common edge. Matrix \mathbf{L} can be constructed in two possible ways:

$$\mathbf{L} = \mathbf{D} - \mathbf{A}, \quad (15a)$$

$$\mathbf{L} = \mathbf{B}^T \mathbf{B}, \quad (15b)$$

where $\mathbf{D} = (d_{ij})$ is the $n \times n$ diagonal degree matrix of graph G , \mathbf{A} is the respective adjacency matrix, \mathbf{B} is the $n \times m$ incidence matrix [31] of the graph G with selected edge directions, and \mathbf{B}^T is its transpose. The multiplicative notation (15b) is more convenient because it readily enables the construction of a Laplacian matrix of a weighted graph:

$$\mathbf{L} = \mathbf{B}^T \mathbf{W} \mathbf{B}, \quad (16)$$

where \mathbf{W} is the diagonal $m \times m$ weight matrix whose element w_{ii} is a weight assigned to a specific edge. In the weighted case multiplicity c stands for the edge weight and the vertex degree d_i is equal to the algebraic sum of weights of all the edges incident to vertex i .

Let us assume that the discrete potential function is electronegativity, with boundary being some known standard χ_i^0 values. Equations (17) relate standard, unperturbed electronegativity values to equilibrated ones, χ_i , through the weighted Laplacian matrix:

$$\mathbf{L}\chi = \chi^0 \quad \text{or} \quad \mathbf{B}^T \mathbf{W} \mathbf{B} \chi = \chi^0. \quad (17)$$

Unknown effective values of χ_i are found by solving equation (17):

$$\chi = \mathbf{L}^{-1} \chi^0, \quad (18)$$

where \mathbf{L}^{-1} is the inverse (generally speaking, generalized inverse) of \mathbf{L} . As χ^0 stands for orbital electronegativities in volts (V), and matrix \mathbf{W} is a diagonal bond softness matrix (whose elements may be taken $1/(\eta_i + \eta_j)$ as a crude approximation) with softness units e/V [62], then atomic charges q_i are obtained in the electronic charge units (e):

$$\mathbf{q} = \chi - \chi^0 = \mathbf{L}^{-1} \chi^0 - \chi^0 = (\mathbf{L}^{-1} - \mathbf{I}) \chi^0. \quad (19)$$

Equation (19) transforms point potentials (electronegativities) into discrete currents (charges).

Method of Del Re

The Del Re semiempirical design is to calculate charge transfers over the bonded framework on the formation of a molecule. It uses a Hückel-type Hamiltonian with some additional parameters to be optimized against experimental dipole moments. These parameters are vertex weights δ_i^0 (reduced electronegativities), edge weights γ_{ij} (analog of chemical hardness), and bond characteristics ε_{ij} (derived from bond dissociation energies). The set of simultaneous equations is written according to

$$\delta_i = \delta_i^0 + \sum_{i \sim j} \delta_j \gamma_{ij} \quad (20)$$

and the resulting charge-transfer components are calculated from effective electronegativities δ_i of neighboring atoms: $Q_{ij} = (\delta_i - \delta_j)/2\varepsilon_{ij}$. Obviously, equation (20) can be readily written in the form of matrix equation (17) and the elements of matrix **L** are as follows:

$$\mathbf{L} = (l_{ij}) = \begin{cases} -\gamma_{i(j)}, & i \sim j, i \neq j, \\ 1, & i = j, \\ 0, & \text{otherwise.} \end{cases} \quad (21)$$

It should be mentioned that, because of the parameterization, matrix **L** in the Del Re method is not generally symmetrical, *i.e.*, in some cases (bonds C–H, C–Cl, N–H, O–H) $\gamma_{ij} \neq \gamma_{ji}$. Unknown δ_i are obtained through solving equation (18), *i.e.*, by the inversion of matrix **L**, then charge transfer components Q_{ij} are calculated, and lastly, atomic charges are derived by common algebra.

Method of Gasteiger and Marsili

In an effort to remedy the well-known shortcoming of the original Sanderson electronegativity equalization scheme [13], when atoms of the same sort in isomeric groups attain the same charge, Gasteiger and Marsili [18,57] proposed a new approach to charge calculation based on an iterative difference scheme, where reduced electronegativity differences converge to a limit in six to eight iterations. This scheme provides a good illustration to the above-described algebraic formalism. As the Laplacian matrix given by equation (15b) is a discrete analog of a second-order differential operator, matrix **B** acts as the first differentiation (more precisely the first difference), and matrix **B**^T acts as the second difference. Thus matrix **B** is a discrete analog of the gradient of a function, and its action on the electronegativity vector results in electronegativity differences across bonded atoms. Hence, it follows that the Gasteiger–Marsili formalism can be expressed by the matrix equation

$$\mathbf{q} = \mathbf{WB}\chi, \quad (22)$$

where χ is the orbital electronegativity vector and **W** is the diagonal weight matrix with element w_{ii} being the product of a normalizing factor and a damping factor. Normalization is achieved by dividing the electronegativity differences by the orbital electronegativity of *i*th atom (or *j*th atom if its orbital electronegativity is smaller) in the +1 state, χ_i^+ . However, in this setting the molecule under study turns out to be a set of disjoint bonds. To make the bond interaction possible, a computational loop is introduced by the multiple application of equation (22) with variable electronegativity (to be recalculated according to the Iczkowski and Margrave equation [59] at each step of the algorithm) and variable

damping factor $(1/2)^\alpha$ (α is the number of the current cycle of the loop). The damping factor is meant for simulating a returning potential which prevents complete electronegativity equalization. All the charge transfers are collected over all iterations and summed up to give final atomic charges.

Kirchhoff Charge Model

The first contribution to KCM was done by Zefirov and Kirpichenok in 1987 [58]. The basic finding of this earlier method is to use logarithms of Sanderson's electronegativity values in order to go from exponential equations to linear ones. Likewise a set of simultaneous equations is written but not in an explicit matrix form as equation (17), and there is no direct reference to the electrical network analogy. Further progress has been achieved in the works of Oliferenko *et al.* [19–22] where the explicit Laplacian matrix formalism is first presented. The current version of our model outlined by equations (16)–(19) is based on the matrix \mathbf{L} factorization (16) with bond hardness explicitly included, so atomic charges produced by equation (19) are in correct units and, as will be demonstrated below, their numerical values are quite reasonable.

3. PRINCIPLE OF ELECTRONEGATIVITY RELAXATION

3.1. Electronegativity relaxation as a discrete Dirichlet problem

As electronegativity χ is identified with the electrostatic [60] or chemical potential [15], it is thought of here as a harmonic function, satisfying the molecular Laplace equation

$$\nabla^2 \chi(\mathbf{r}) = 0. \quad (23)$$

Since electronegativity is defined here as a discrete function, the position function $\chi(\mathbf{r})$ is replaced by an electronegativity vector χ , whose components are assigned to each atomic site of a molecule. Such a transition from the geometric to the discrete level and back is a correctly defined operation [61]. It is performed by restricting $\chi(\mathbf{r})$ to the vertex set of graph G or, if back, by embedding the graph into the 3D space. The structure of the molecule is known and the Dirichlet boundary conditions are formed by standard electronegativities χ^0 :

$$\chi|_S = f(\chi^0). \quad (24)$$

Discrete boundary S is represented by self loops attached to each of the graph vertices. In different representations the self loops symbolize either current sources in the electrical model, or infinite leads of quantum graphs, or absorbing states in the Markov chain formalism.

This Dirichlet problem is formulated as follows: equilibrium electronegativity values (molecular interior) are uniquely determined by the original, unperturbed electronegativity values (boundary) and the molecular structure (topology or geometry depending on the model used). One can anticipate that original electronegativity values smooth out on the relaxation, because the property of being a harmonic function makes electronegativity satisfying the averaging property: the value of a function at any interior point is equal to the average of the neighboring values.

The electronegativity relaxation principle goal to uncover equilibrium or *in situ* electronegativity is readily achieved by solving the molecular Laplace equation with the help of Markov chains.

3.2. Markov chain formalism

There is a close relation between the discrete potential theory outlined above and Markov chains with a discrete state space. A Markov chain is well represented by a graph, with the graph vertices corresponding to Markov-chain discrete states, and the graph edges corresponding to transitions between the states. This means that weights assigned to graph edges may be identically equal to transition probabilities in the Markov chain sense. All transition probabilities are normally written in the form of a probability matrix. Electron motion in the field of fixed nuclei can be considered as transitions among different states with varying probability, or, equivalently, as a simple random walk on a network formed by the nuclei. Thus it is possible to represent charge transfers caused by electronegativity differences at neighboring atoms by means of a molecular Markov chain. Such Markov chain for a water molecule is depicted in Fig. 1. The transition probabilities if not specified are fully determined by the atomic valence numbers (vertex degrees), *i.e.*, by molecular connectivity. In this general case the edge weights in Fig. 1 are equal to the inverse vertex degrees. If they are specified, for example, by bond hardness values, the latter serve as a weight function controlling transition probabilities.

The states of this Markov chain fall into two categories: absorbing states are those which can never be left by a randomly walking particle, and non-absorbing states which are all transient states.

Absorbing and non-absorbing states correspond to the boundary and interior, respectively. In Fig. 1 absorbing states are numbered first, then interior atoms O and H are numbered 4, 5, and 6. This is done to enable the so called canonical form of the probability matrix \mathbf{P} ,

$$\mathbf{P} = \begin{array}{c|cccccc} \mathbf{1} & 1 & 0 & 0 & 0 & 0 & 0 \\ \mathbf{2} & 0 & 1 & 0 & 0 & 0 & 0 \\ \mathbf{3} & 0 & 0 & 1 & 0 & 0 & 0 \\ \mathbf{4} & 1/3 & 0 & 0 & 0 & 1/3 & 1/3 \\ \mathbf{5} & 0 & 1/2 & 0 & 1/2 & 0 & 0 \\ \mathbf{6} & 0 & 0 & 1/2 & 1/2 & 0 & 0 \end{array}, \quad \mathbf{P} = \begin{pmatrix} \mathbf{I} & \mathbf{0} \\ \mathbf{R} & \mathbf{Q} \end{pmatrix}.$$

Matrix \mathbf{P} is a block matrix with \mathbf{I} being the $n \times n$ identity matrix and $\mathbf{0}$ being zero matrix of appropriate dimensions. \mathbf{R} and \mathbf{Q} are special matrices, which contain all information about the transitions. The transition matrix \mathbf{P} has the following useful property:

$$\mathbf{P}f = f \quad \text{if and only if } f \text{ is a regular (harmonic) function.} \quad (25)$$

Equation (25) rearranged as $\mathbf{P}f - f = 0$ and then $(\mathbf{P} - \mathbf{I})f = 0$ leads to a Markov chain formulation of the Laplace equation, in which $(\mathbf{P} - \mathbf{I})$ is an analog of ∇^2 . Higher powers n of matrix \mathbf{P} are relevant for practical tasks. When $n \rightarrow \infty$ (our numerical experiments showed that for practical purposes $n = 8 \div 20$ is sufficient) matrix \mathbf{P} takes the form shown below, with the block matrix \mathbf{C} being the inverse Laplacian matrix \mathbf{L}^{-1} given by

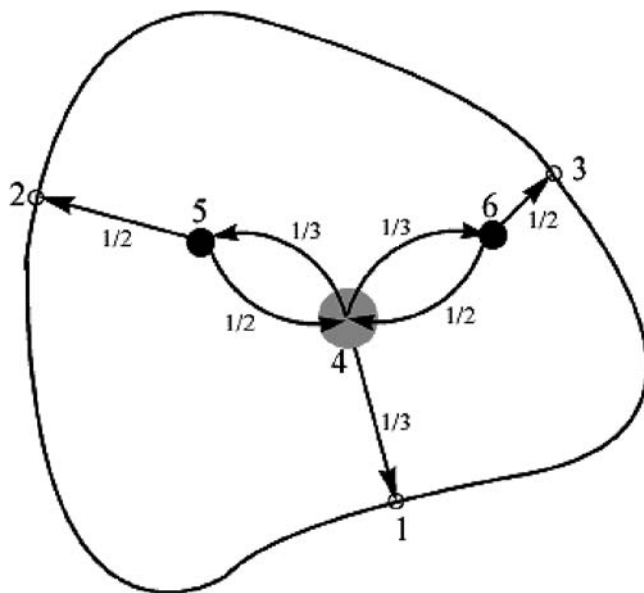


Fig. 1. Representation of a water molecule by a Markov chain.

equation (18):

$$\mathbf{P} = \begin{pmatrix} \mathbf{I} & \mathbf{0} \\ \mathbf{R} & \mathbf{Q} \end{pmatrix} \xrightarrow{n \rightarrow \infty} \begin{pmatrix} \mathbf{I} & \mathbf{0} \\ \mathbf{C} & \mathbf{0} \end{pmatrix} = \mathbf{P}^\infty.$$

Hence the Laplacian matrix notation (18) and the probabilistic notation (26) are equivalent because in both cases we obtain the same result, *i.e.*, equilibrium electronegativity values: either $\chi = \mathbf{L}^{-1} \chi^0$ or

$$\mathbf{P}^\infty \begin{pmatrix} \chi^0 \\ 0 \end{pmatrix} = \begin{pmatrix} \chi^0 \\ \chi \end{pmatrix}. \quad (26)$$

The Markov chain form of equation (23) is given by equation (27), which look like a true Laplace equation with Dirichlet boundary conditions:

$$(\mathbf{P}^\infty - \mathbf{I}) \begin{pmatrix} \chi^0 \\ \chi \end{pmatrix} = \begin{pmatrix} 0 \\ 0 \end{pmatrix}. \quad (27)$$

In equation (27) \mathbf{I} stands for an identity matrix which dimension is the same as the dimension of \mathbf{P} . The dimension of \mathbf{P} is $2n \times 2n$ because the number of boundary vertices is exactly the same as the number of atoms in a molecule.

The conclusion is that the discrete Laplacian and Markov chain formulations of the electronegativity relaxation principle are equivalent in the operational sense and both provide solutions of the molecular Laplace equation (equilibrium electronegativities) at approximately the same computational cost.

4. NUMERICAL EXAMPLES

To provide some numerical examples of the Kirchhoff atomic charges we calculated them for a set of simple molecules. Such a small set of representative molecules was selected just to get an idea as to how the scheme described by equations (16)–(19) works and what are the trends in the atomic charge variation. As parameters of the method we use orbital electronegativities and hardnesses calculated by Bergman and Hinze [62]. Second row hydrides CH_4 , NH_3 , H_2O , and HF , successively substituted fluoromethanes, formaldehyde, ethylene, acetylene, and benzene are given in Fig. 2 with point charges assigned to appropriate atomic sites. It is clearly seen that the charge variation in the series of the second row hydrides corresponds to their expected polarity, and the numerical values resemble

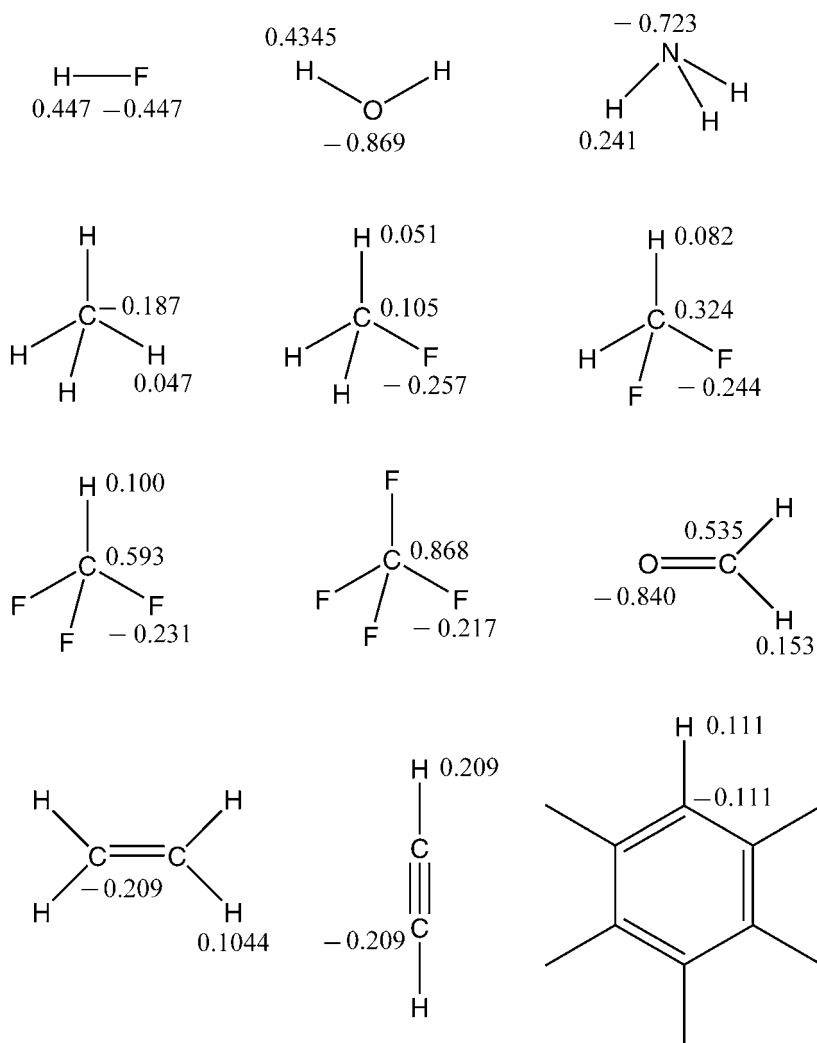


Fig. 2. Examples of atomic charge calculations.

those that could be obtained through an *ab initio* calculation or an MEP-fitting procedure. A similar trend is observed in the series methane, ethylene, benzene, acetylene, with the most acidic acetylenic hydrogen—in agreement with experiment. Successive fluorine substitution of methane results in a marked accumulation of positive charge on the carbon atom rather than the negative charge depletion on the fluorine atoms, which is in line with the previous theoretical study of Wiberg and Rablen [63]. Technically, the incidence matrix **B** is formed by writing all possible edges of a molecular graph under study, with separate lines for each self loops and each multiple edge. Such an explicit account of multiple bonds is critical for unsaturated species, and one sees in Fig. 2 that the charge distributions of formaldehyde, ethylene, acetylene, and benzene are quite reasonable.

5. CHEMICAL APPLICATIONS OF ATOMIC CHARGES

The above considered charge calculation schemes are widely used in modern molecular modeling and simulation for the fast assessment of electrostatic interaction energy. Atomic charges feature very largely in virtually all available commercial software packages for biomolecular and materials science modeling. Del Re and Gasteiger–Marsili charges have been implemented into the SYBYL software package [64] and are actively used for rapid estimation of electrostatic potential around molecules. The charge equilibration method of Rappe and Goddard [44] was designed to meet the needs of molecular dynamics in a polarizable electrostatic model, and it has found its use in force fields such as Universal Force Field [65], as it implemented in ArgusLab [66], and the QEq–Morse stretch force field [45]. The Electronegativity Equalization Method has been extensively used in the Charge Sensitivity Analysis of catalysis and molecular and atomic clusters [38]. Another important application of atomic charges is that in QSAR studies where they are used as global molecular descriptors [22,67] or local atomic characteristics like in the CoMFA [68] or MFTA method [69].

6. CONCLUSIONS

The intent of this work is to analyze various electronegativity equalization schemes from a rather general, algebraic point of view, to perceive common features and, hopefully, to elucidate common algebraic structures underlying at first glance so different techniques. It is shown that many methods formulated in different physical terms appear to be equivalent in their mathematical sense. A deep understanding of algebraic relationships among different methods of molecular modeling and simulation should be useful in the selection of adequate models and in further development of the field.

Another aim of this work is to generalize and refine our previously developed approach to atomic charge calculation. We show that an alternative electronegativity redistribution principle—the electronegativity relaxation principle—is possible and is consistent with physical considerations as well as with chemical intuition and experience. This principle and calculation schemes derived thereof can find their use in studies of molecular structure and reactivity as well as in the derivation of inexpensive atomic charges for drug design and nanotechnology simulations, areas of human activity where computational expenses are otherwise extremely huge.

REFERENCES

- [1] R.S. Mulliken, Electronic population analysis on LCAO–MO molecular wave functions, I, *J. Chem. Phys.* **23** (1955) 1833–1840.
- [2] P.O. Löwdin, On the non-orthogonality problem, *Adv. Quantum Chem.* **5** (1970) 185–199.
- [3] A. Reed, R. Weinstock, F. Weinhold, Natural population analysis, *J. Chem. Phys.* **83** (1985) 735–746.
- [4] R.F.W. Bader, *Atoms in Molecules: A Quantum Theory*, Clarendon, Oxford, 1990.
- [5] F.A. Momany, Determination of partial atomic charges from *ab initio* molecular electrostatic potentials. Application to formamide, methanol, and formic acid, *J. Phys. Chem.* **82** (1978) 592–601.
- [6] U.C. Singh, P.A. Kollman, An approach to computing electrostatic charges for molecules, *J. Comp. Chem.* **5** (1984) 129–145.
- [7] L.E. Chirlian, M.M. Francl, Atomic charges derived from electrostatic potentials—a detailed study, *J. Comp. Chem.* **8** (1987) 894–905.
- [8] C.M. Breneman, K.B. Wiberg, Determining atom-centered monopoles from molecular electrostatic potentials—the need for high sampling density in formamide conformational-analysis, *J. Comp. Chem.* **11** (1990) 361–373.
- [9] J.W. Storer, D.J. Giesen, C.J. Cramer, D.G. Truhlar, Class IV charge models—a new semiempirical approach in quantum chemistry, *J. Comp. Aided Mol. Des.* **9** (1995) 87–110.
- [10] L. Pauling, *The Nature of the Chemical Bond*, Cornell Univ. Press, Ithaca, 1960.
- [11] W.J. Mortier, K. Van Genechten, J. Gasteiger, Electronegativity equalization: Application and parametrization, *J. Am. Chem. Soc.* **107** (1985) 829–835.
- [12] J.E. Huheey, *Inorganic Chemistry*, Harper & Row, New York, 1983.
- [13] R.T. Sanderson, *Chemical Bonds and Bond Energy*, Academic Press, New York, 1976.
- [14] R.G. Parr, W. Yang, *Density Functional Theory of Atoms and Molecules*, Oxford Univ. Press, New York, 1976, Clarendon, Oxford, 1976.
- [15] R.G. Parr, R.A. Donnelly, M. Levy, W.E. Palke, Electronegativity: The density functional viewpoint, *J. Chem. Phys.* **68** (1978) 3801–3807.
- [16] G. Del Re, A simple MO–LCAO method for the calculation of charge distribution in saturated organic molecules, *J. Chem. Soc.* (1958) 4031–4040.
- [17] J.E. Huheey, The electronegativity of groups, *J. Phys. Chem.* **69** (1965) 3284–3291.
- [18] J. Gasteiger, M. Marsili, Iterative partial equalization of orbital electronegativity—a rapid access to atomic charges, *Tetrahedron* **36** (1980) 3219–3228.
- [19] A.A. Oliferenko, V.A. Palyulin, S.A. Pisarev, A.V. Neiman, N.S. Zefirov, Novel point charge models: Reliable instrument for molecular electrostatics, *J. Phys. Org. Chem.* **14** (2001) 355–369.
- [20] A.A. Oliferenko, V.A. Palyulin, N.S. Zefirov, A method for calculating partial charges of atoms in a molecule, based on a new principle of electronegativity equalization, *Doklady Chemistry* **368** (1999) 209–212.
- [21] A.A. Oliferenko, V.A. Palyulin, A.V. Neiman, N.S. Zefirov, A new topological model for the calculation of partial atomic charges, *Doklady Chemistry* **375** (2000) 281–284.
- [22] A.A. Oliferenko, P.V. Krylenko, V.A. Palyulin, N.S. Zefirov, A new scheme for electronegativity equalization as a source of electronic descriptors: Application to chemical reactivity, *SAR & QSAR Environ. Res.* **13** (2002) 297–305.
- [23] V.E. Golender, V.V. Drboglav, A.B. Rosenblit, Graph-potential method and its application for chemical information processing, *J. Chem. Inf. Comput. Sci.* **21** (1981) 196–204.
- [24] D.J. Klein, M. Randic, Resistance distance, *J. Math. Chem.* **12** (1993) 81–95.
- [25] D.J. Klein, N.H. March, Electron density in chemically bonded materials and the chemical network model, *Theochem* **337** (1995) 257–264.
- [26] B. Yurke, J.S. Denker, Quantum network theory, *Phys. Rev. A* **29** (1984) 1419–1437.
- [27] J.E. Avron, A. Raveh, B. Zur, Adiabatic quantum transport in multiply connected systems, *Rev. Mod. Phys.* **60** (1988) 873–915.
- [28] T. Kottos, U. Smilansky, Periodic orbit theory and spectral statistics for quantum graphs, *Ann. Phys.* **274** (1999) 76–124.
- [29] F. Barra, P. Gaspard, Transport and dynamics on open quantum graphs, *Phys. Rev. E* **65** (2001) 016205.
- [30] P. Kuchment, Quantum graphs: I. Some basic structures, *Waves Random Media* **14** (2004) S107–S128.
- [31] F. Harary, *Graph Theory*, Addison-Wesley, Reading, MA, 1969.
- [32] P. Bultinck, R. Carbo-Dorca, Algebraic relationships between conceptual DFT quantities and the electronegativity equalization hardness matrix, *Chem. Phys. Lett.* **364** (2002) 357–362.

- [33] W.J. Mortier, S.K. Ghosh, S. Shankar, Electronegativity equalization method for the calculation of atomic charges in molecules, *J. Am. Chem. Soc.* **108** (1986) 1770–1775.
- [34] J. Mullay, Atomic and group electronegativities, *J. Am. Chem. Soc.* **106** (1984) 5842–5847.
- [35] J. Mullay, Calculation of group electronegativities, *J. Am. Chem. Soc.* **107** (1985) 7271–7275.
- [36] J. Mullay, A simple method for calculating atomic charges in molecules, *J. Am. Chem. Soc.* **108** (1986) 1770–1775.
- [37] R. Nalewajski, Electrostatic effects in interactions between hard (soft) acids and bases, *J. Am. Chem. Soc.* **106** (1984) 944–945.
- [38] P. Geerlings, F. De Proft, W. Langenaeker, Conceptual density functional theory, *Chem. Rev.* **103** (2003) 1793–1873.
- [39] P. Bultinck, W. Langenaeker, P. Lahorte, F. De Proft, P. Geerlings, M. Waroquier, J.P. Tollenaere, The electronegativity equalization method I: Parametrization and validation for atomic charge calculation, *J. Phys. Chem. A* **106** (2002) 7887–7894.
- [40] G. Menegon, K. Shimizu, J.P.S. Farah, L.G. Dias, H. Shaimovich, Parametrization of the electronegativity equalization method based on the charge model 1, *Phys. Chem. Chem. Phys.* **4** (2002) 5933–5936.
- [41] F. De Proft, W. Langenaeker, P. Geerlings, A nonempirical electronegativity equalization scheme. Theory and applications using isolated atom properties, *Theochem* **339** (1995) 45–55.
- [42] Z.Z. Yang, C.S. Wang, Atom-bond electronegativity equalization method. 1. Calculation of the charge distribution in large molecules, *J. Phys. Chem. A* **101** (1997) 6315–6321.
- [43] S.L. Njo, J. Fan, B. van de Graaf, Extending and simplifying the electronegativity equalization method, *J. Mol. Catalysis A: Chem.* **134** (1998) 79–88.
- [44] A.K. Rappe, W.A. Goddard, Charge equilibration for molecular dynamics simulations, *J. Phys. Chem.* **95** (1991) 3358–3363.
- [45] J. Sefcik, E. Demiralp, T. Gagin, W.A. Goddard III, Dynamic charge equilibration–morse stretch force field: Application to energetics of pure silica zeolites, *J. Comp. Chem.* **23** (2002) 1507–1514.
- [46] D.M. York, W. Yang, A chemical potential equalization method for molecular simulations, *J. Chem. Phys.* **104** (1996) 159–172.
- [47] S.W. Rick, S.J. Stuart, B.J. Berne, Dynamical fluctuating charge force fields: Application to liquid water, *J. Chem. Phys.* **101** (1994) 6141–6156.
- [48] F. Spitzer, *Principles of Random Walks*, Springer-Verlag, New York, 1976.
- [49] P.G. Doyle, J.L. Snell, *Random Walks and Electric Networks*, Math. Assoc. of America, 1984.
- [50] J.G. Kemeny, J.L. Snell, A.W. Knapp, *Denumerable Markov Chains*, Springer-Verlag, New York, 1976.
- [51] S. Guattery, G.L. Miller, Graph embeddings and Laplacian eigenvalues, *SIAM J. Matrix Anal. Appl.* **21** (2000) 703–723.
- [52] N. Trinajstić, D. Babić, S. Nikolić, D. Plavšić, D. Amić, Z. Mihalić, The Laplacian matrix in chemistry, *J. Chem. Inf. Comput. Sci.* **34** (1994) 368–376.
- [53] D.J. Klein, Geometry, graph metrics, and Wiener, *Comm. Math. Chem. (MATCH)* **35** (1997) 7–27.
- [54] D.J. Klein, J.L. Palacios, M. Randić, N. Trinajstić, Random walks and chemical graph theory, *J. Chem. Inf. Comput. Sci.* **44** (2004) 1521–1525.
- [55] L. Dozen-Micović, D. Jeremić, N.L. Allinger, Treatment of electrostatic effects within the molecular mechanics method, *J. Am. Chem. Soc.* **105** (1983) 1716–1722.
- [56] S. Fliszar, S. Chretien, On simple, accurate calculations of atomic charges, bond properties and molecular energies, *Theochem* **618** (2002) 133–146.
- [57] J. Gasteiger, M. Marsili, A new model for calculating atomic charges in molecules, *Tetrahedron Lett.* **34** (1978) 3181–3184.
- [58] N.S. Zefirov, M.A. Kirpichenok, F.F. Izmailov, M.I. Trofimov, A new calculational scheme for electronegativity equalization according to Sanderson’s principle, *Dokl. Akad. Nauk* **304** (1989) 887–891.
- [59] R.P. Iczkowski, J.L. Margrave, Electronegativity, *J. Am. Chem. Soc.* **83** (1961) 3547–3551.
- [60] W. Gordy, A new method of determining electronegativity from other atomic properties, *Phys. Rev.* **69** (1946) 604–607.
- [61] B. Mohar, Some applications of Laplace eigenvalues on graphs, in: G. Hahn, G. Sabidussi (Eds.), *Graph Symmetry: Algebraic Methods and Applications*, NATO ASI Ser. C497, Kluwer, 1997, pp. 225–275.
- [62] D. Bergman, J. Hinze, Electronegativity and charge distribution, *Structure and Bonding* **66** (1987) 145–190.
- [63] K.B. Wiberg, P.R. Rablen, Origin of the stability of carbon tetrafluoride: Negative hyperconjugation reexamined, *J. Am. Chem. Soc.* **115** (1993) 614–625.
- [64] SYBYL, Completely Integrated Environment for Computational Chemistry and Molecular Modeling, <http://www.tripos.com>.

- [65] A.K. Rappe, C.J. Casewit, K.S. Colwell, W.A. Goddard III, W.M. Skiff, UFF, a full periodic table force field for molecular mechanics and molecular dynamics simulations, *J. Am. Chem. Soc.* **114** (25) (1992) 10024–10035.
- [66] ArgusLab 4.0 by Mark Thompson, <http://www.arguslab.com>.
- [67] A.R. Katritzky, S. Sild, M. Karelson, QSAR treatment of solvent scales, *J. Chem. Inf. Comput. Sci.* **39** (1999) 684–691.
- [68] R.D. Cramer III, D.E. Patterson, J.D. Bunce, Comparative molecular field analysis (CoMFA). 1. Effect of shape on binding of steroids to carrier proteins, *J. Am. Chem. Soc.* **110** (1988) 5959–5967.
- [69] V.A. Palyulin, E.V. Radchenko, N.S. Zefirov, Molecular field topology analysis method in QSAR studies of organic compounds, *J. Chem. Inf. Comput. Sci.* **40** (2000) 659–667.

Fast Padé Transform for Exact Quantification of Time Signals in Magnetic Resonance Spectroscopy

Dževad Belkić

Karolinska Institute, P.O. Box 260, S-171 76 Stockholm, Sweden

E-mail: dzevad.belkic@ki.se

Abstract

This work employs the fast Padé transform (FPT) for spectral analysis of theoretically generated time signals. The spectral characteristics of these synthesised signals are reminiscent of the corresponding data that are measured experimentally via encoding digitised free induction decay curves from a healthy human brain using Magnetic Resonance Spectroscopy (MRS). In medicine, *in vivo* MRS is one of the most promising non-invasive diagnostic tools, especially in oncology, due to the provided biochemical information about functionality of metabolites of the scanned tissue. For success of such diagnostics, it is crucial to carry out the most reliable quantifications of the studied time signals. This quantification problem is the harmonic inversion via the spectral decomposition of the given time signal into its damped harmonic constituents. Such a reconstruction finds the unknown total number of resonances, their complex frequencies and the corresponding complex amplitudes. These spectral parameters of the fundamental harmonics give the peak positions, widths, heights, and phases of all the physical resonances. As per the unified theory of quantum-mechanical spectral analysis and signal processing, the FPT represents the exact solver of the quantification problem, which is mathematically ill-conditioned. The exact and unique solution via the FPT is valid for any noiseless synthesised time signal built from an arbitrary number of damped complex exponentials. These attenuated harmonics can appear as a linear combination with both stationary and non-stationary amplitudes. Such sums produce time signals that yield Lorentzian (non-degenerate) and non-Lorentzian (degenerate) spectra for isolated and overlapped resonances from MRS. We give a convergent validation for these virtues of the FPT. This is achieved through the proof-of-principle investigation by developing an algorithmic feasibility for robust and efficient computations of the exact numerical solution of a typical quantification problem from MRS. The systematics in the methodology designed in the present study represent a veritable paradigm shift for solving the quantification problem in MRS with special ramifications in clinical oncology. This is implied by the explicit demonstration of the remarkable ability of the fast Padé transform to unambiguously quantify all the customary spectral structures, ranging from isolated resonances to those that are tightly overlapped and nearly confluent.

Contents

1. Introduction	158
2. Challenges with quantification of time signals from MRS	161
3. The quantum-mechanical concept of resonances in scattering and spectroscopy	168
4. Resonance profiles	171
5. The role of quantum mechanics in signal processing	172
6. Suitability of the fast Padé transform for signal processing	174
7. Fast Padé transforms inside and outside the unit circle	175
7.1. Description of the background contribution by the off-diagonal FPT	176
7.2. Diagonal and para-diagonal FPT	178
7.3. Determination of the exact number of resonances by the concept of the Froissart doublets (pole-zero cancellations)	183

8. Results	184
8.1. Tabular data	187
8.1.1. Exact input data for the spectral parameters of 25 resonances	187
8.1.2. Convergence of numerical values of the reconstructed spectral parameters for varying signal length N/M ($M = 1-32$)	189
8.1.3. Numerical values of the reconstructed spectral parameters near full convergence for 3 partial signal lengths $N_p = 180, 220, 260$	193
8.1.4. Extended accuracy of numerical values of the reconstructed spectral parameters near full convergence for partial signal lengths $N_p = 180, 220$	194
8.1.5. Extended accuracy of numerical values of the reconstructed spectral parameters at a quarter $N/4$ and the full signal length N	195
8.2. Absorption total shape spectra	197
8.2.1. Absorption total shape spectra or absorption envelope spectra	197
8.2.2. Padé and Fourier convergence rates of absorption total shape spectra	201
8.3. Residual spectra and consecutive difference spectra	203
8.3.1. Residual or error absorption total shape spectra	203
8.3.2. Residual or error absorption total shape spectra near full convergence	206
8.3.3. Consecutive difference spectra for absorption envelope spectra	206
8.3.4. Consecutive differences for absorption envelope spectra near full convergence	209
8.4. Absorption component shape spectra of individual resonances	209
8.4.1. Absorption component spectra and metabolite maps	209
8.4.2. Absorption component spectra and envelope spectra near full convergence	212
8.5. Distributions of poles and spectral parameters in their complex planes	212
8.5.1. Distributions of poles and spectral parameters in the $FPT^{(+)}$	212
8.5.2. Distributions of poles and spectral parameters in the $FPT^{(-)}$	216
8.5.3. Convergence of complex frequencies in the $FPT^{(-)}$	216
8.5.4. Convergence of absolute values of amplitudes in the $FPT^{(-)}$	219
8.5.5. Distributions of complex frequencies in the $FPT^{(\pm)}$ near full convergence	219
8.5.6. Distributions of absolute values of amplitudes in the $FPT^{(\pm)}$ near full convergence	223
9. Discussion	223
10. Conclusion	228
Acknowledgements	232
References	232

1. INTRODUCTION

Among the leading and fastest developing non-invasive diagnostic methods in medicine are Magnetic Resonance Spectroscopy (MRS) and Magnetic Resonance Spectroscopic Imaging (MRSI), which is alternatively called Chemical Shift Imaging (CSI) [1–6]. In particular, MRSI is a hybrid of MRS and Magnetic Resonance Imaging (MRI). While MRS deals with a single voxel, MRSI provides information from multiple voxels. The hybrid nature of MRSI is in sharing spectroscopic and anatomical information with MRS and MRI, respectively. In both MRS and MRSI, *in vivo* time signals, or equivalently, free induction decay (FID) curves, are encoded and spectrally analysed by solving an inverse problem called quantification. This problem consists of reconstructing biochemical information about diagnostically important metabolites of the examined tissue. The retrieved information gives the sought quantitative data such as abundance, *i.e.*, concentrations of metabolites, their relaxation times, *etc.* The obtained results are compared with the corresponding normal findings or standards from control groups of healthy volunteers in order to assign the identified spectral patterns from patients with a particular disease. Thus through an adequate theoretical interpretation of measurements on patients, both MRS and MRSI

can help diagnosticians in drawing inferences from spectral information which is usually very different for healthy and diseased tissues.

Mathematically, the quantification problem consists of using the encoded FIDs to reconstruct the true number of harmonic transients together with the pairs of spectral parameters that are complex-valued physical quantities—the frequencies and the corresponding amplitudes. These frequencies and amplitudes are the sole elements of the fundamental harmonics that build the studied FID. Each harmonic transient has its resonant frequency, relaxation time, intensity, and phase that completely characterise the underlying normal-mode damped oscillations in the given FID. Such four real-valued parameters can be identified directly from the reconstructed complex frequencies and amplitudes that, moreover, give the peak areas of the associated resonance profiles in the corresponding spectrum. Finally, relative concentrations of metabolites can also be obtained, since these quantities are proportional to the computed peak areas. Here, constants of proportionality are the fixed concentrations of certain chosen reference metabolites, *e.g.*, water in normal, healthy tissue. The total number of harmonic transients, as a quantifiable entity, can also be reconstructed during the spectral analysis of the given FID.

By definition, quantification is recognised as one of the main problems from quantum theory of resonances and spectroscopy [5]. Thus, the general quantum-mechanical relaxation formalism can be exploited for solving the quantification problem from *in vivo* MRS and MRSI. With this goal, we use the quantum-mechanical signal processing and spectral analysis through the Green function implemented algorithmically via the fast Padé transform (FPT) to obtain the frequency spectrum as the unique quotient of two polynomials. This form of a rational quantum response function to the external perturbation (static and gradient magnetic fields, radio-frequency pulses) is dictated both by the quantum origin of MRS or MRSI and the resolvent form (operator Padé approximant) of the Green operator of the examined system. The FPT encompasses two different versions of the Green function, with the incoming and outgoing boundary conditions, inside and outside the unit circle of the complex harmonic variable z . The former and the latter variants of the FPT coincide, respectively, with the causal and anti-causal Padé- z transform from mathematical statistics and the engineering literature on signal processing. In the present work, we illustrate how the FPT solves the quantification problem exactly by extracting the sought spectral parameters, using a synthesised FID generated theoretically, but nevertheless intrinsically based upon realistic and typical data as customarily encoded via MRS and MRSI from the brain of a healthy volunteer.

In both MRS and MRSI, it is of great importance to avoid encoding long FIDs. This is because the exponentially damped envelopes of these FIDs become completely embedded in noise at long total acquisition times T . It is the fast Fourier transform (FFT) which requires long T to increase its frequency resolution which is equal to $2\pi/T$. Thus relying upon the FFT, one is caught here in a vicious circle facing two diametrically opposing tendencies—resolution enhancement necessitates a long T but this, in turn, brings more noise which is an impediment to the very sought improvement in the spectral quality. The usual practice with the FFT is to patch these drawbacks by using shorter bandwidths or window sizes that, however, are unsatisfactory due to the resulting spectral deformations via Gibbs ringing and reduced resolution.

A deeper reason for which these attempts in the FFT have not met with success is in the fact that the Fourier analysis ignores the structure of the investigated FID. Namely, in the FFT all FIDs encoded with the same T have the same universal resolution $2\pi/T$

irrespective of their internal structure. This limits the FFT to shape estimations alone [5]. However, every FID has a structure which is quantifiable by certain parameters. In practice, neither this structure nor the related parameters of the studied FID are known prior to signal processing. The task of spectral analysis is to reveal or reconstruct these unknowns from the given FID, and this is achieved by performing spectral decomposition which, in turn, obviates the need for long T . Moreover, in the ensuing parametric estimation, as opposed to the Fourier non-parametric processing, resolution is not determined exclusively T . As mentioned, the structural parameters are the fundamental frequencies and the associated amplitudes as the building elements of damped harmonics from the investigated FID.

Particularly noticeable algorithms for spectral decomposition can be found among the class of methods known as convergence accelerators and analytical continuators of Fourier series and sequences. For a given bandwidth, the FFT converges linearly at a slow rate $1/N$ with increasing signal length N . This convergence can be accelerated significantly. One of the convergence accelerators which is studied in this work is the FPT which exhibits at least a quadratic convergence $1/N^2$ with a systematically augmented N . Moreover, near full convergence as a function of the varying signal length, the FPT has the so-called spectral convergence, which is the term used to denote a spectacular exponential convergence rates to the exact values of the sought parameters. This translates directly into two simultaneous achievements, resolution enhancement and shortening the FID. With this, the Fourier dichotomy that “a resolution enhancement cannot be obtained without prolonging T ”, becomes obsolete. Operationally, this accomplishment of the FPT is traced back to modelling the spectrum by a quotient of two unique polynomials, instead of just one polynomial encountered in the FFT. Additionally, we show in this work that the same achievement can alternatively be obtained by analytical continuation in lieu of convergence acceleration. Analytical continuation is a powerful concept of Cauchy by which a divergent sequence is induced or forced to converge. For example, if a given series in powers of the harmonic variable z (as the Green function representing the exact spectrum in the present analysis) is convergent outside the unit circle ($|z| > 1$), it will be automatically divergent inside the unit circle ($|z| < 1$). An analytical continuator in the role of a signal processor comes here to rescue the situation by analytically continuing the Green function to become well defined also inside the unit circle and, thus, throughout the complex frequency plane excepting the singular points (poles). On top of being a convergence accelerator, the FPT is also an analytical continuator. A number of illustrations with an FID from MRS will be presented in this work with the proof of cross validation demonstrating that both convergence acceleration and analytical continuation by the FPT yield exactly the same true spectral parameters.

Clearly, the total number of the reconstructed metabolites is unknown prior to quantification of FIDs from MRS and MRSI. Therefore, this information, or more precisely the full number of resonances must be added to the existing list of the other two unknown quantities, the complex frequencies and amplitudes, in the quantification problem from MRS and MRSI [5]. In other words, similarly to the sought fundamental frequencies and amplitudes, the total number of resonances ought to be reliably reconstructed from the given spectrally analysed FID encoded via MRS or MRSI. This is clinically important in the overall effort to establish MRS and MRSI as routine diagnostic tools in hospitals with physician confidence raised to the level at least comparable to the firm status of MRI. Moreover, clinicians have higher expectations from applications of MRS and MRSI because these non-invasive methods can provide invaluable metabolic information about functionality of the examined

tissue. This new biochemical information from MRS and MRSI about the tissue content complements the usual anatomical information provided by MRI.

Thus far, in signal processing within *in vivo* MRS and MRSI, the common practice has been to use *ad hoc* guesses for the number of resonances, as done in all fittings of Fourier-reconstructed spectral line-shapes by some pre-assigned expansion functions or model *in vitro* spectra. These fittings are non-unique and subjective, such that the guessed number leads to either under- or over-fitting by under- or over-estimating the true number of physical, *i.e.*, genuine resonances. This is hardly acceptable to diagnostics, since the former and the latter surmising are associated, respectively, with missing some genuine and finding some non-physical, *i.e.*, spurious resonances. By contrast, the FPT considers the total number of resonances on the same footing as the fundamental complex frequencies and amplitudes, meaning that all these three latter quantities are viewed as the unknowns of the quantification problem. Thus, the full number of resonances need not be guessed any longer nor should it be known or given in advance. The Padé-based quantification in MRS and MRSI can yield the total number of resonances with the highest reliability, as in the case of the reconstructed frequencies and amplitudes.

The unique capability of the FPT to reconstruct the true total number of physical resonances is due to the fact that this estimator is the only exact filter for FIDs built from harmonics in the form of damped complex exponentials with stationary and/or non-stationary polynomial-type amplitudes. Precisely these FIDs are predicted by the quantum-mechanical description of magnetic resonance phenomena and, moreover, such data are encoded clinically via MRS/MRSI when strict experimental conditions are met (adequate shimming of static magnetic field to reduce inhomogeneities, proper suppression of the giant water resonance in, *e.g.*, neuro-diagnostics, *etc.*).

To provide the unequivocal proof for these statements, it is mandatory to consider an exactly solvable model problem with all the controllable, *i.e.*, precisely known input data. In this work, we illustrate on a synthesised FID how the FPT determines unequivocally the exact total number of resonances as well as all the fundamental frequencies and amplitudes. The exact number of resonances is reconstructed using the powerful concept of pole–zero cancellations, *i.e.*, the Froissart doublets—a phenomenon unique to the Padé polynomial quotient, which is the form of the spectrum in the FPT.

Specifically, the present study will focus on MRS, but the developed methodology will remain valid also for MRSI. This is due to the fact that FIDs from MRS and MRSI are of the same type.

2. CHALLENGES WITH QUANTIFICATION OF TIME SIGNALS FROM MRS

At present, versatile Magnetic Resonance (MR) modalities in medical diagnostics are widely considered as one of the fastest expanding fields of the cross-disciplinary research in medical physics. Nevertheless, the most recent vivid progress particularly in MRS and MRSI, also uncovered the fact that the indispensable signal processing meets with huge challenges in reliably extracting information about biochemical and physical functionality of the most clinically relevant metabolites of the investigated tissue. This type of information could be obtained by MRS and MRSI under the assumption of achieving high quality, both in encoding and signal processing. Specifically, in encoding due care ought to be taken

of the magnetic field shimming and water and/or fat suppression. As to signal processing, it is mandatory to be able to carry out unequivocal, accurate and robust quantifications of the concentrations of metabolites of the examined tissue. As mentioned, quantification consists of spectral decomposition of the encoded FID into its harmonic constituents. Such a synthesis is achieved mathematically once the encoding has been performed, because quantitative information cannot be extracted directly from the encoded raw FID without resorting to signal processing.

In the framework of MRS, the signal processor which has been most frequently used is the FFT. The FFT is employed to efficiently convert the encoded FID to the frequency domain with a spectrum of resonances. However, such a transformation is merely a qualitative description of metabolites of the studied tissue. Each metabolite has a molecular structure which might contain more than one resonance. This leads to a number of congested peaks in a typical spectrum of metabolites. Among such spectral structures, unambiguous quantification of overlapping resonances presents a considerable challenge for adequate theoretical interpretation of encoded data. Attractiveness for processing FIDs by the FFT within MRS is largely due the stability and efficiency of automatic computations via the fast $N \ln_2 N$ algorithm for any fixed signal length N whenever $N = 2^s$ ($s = 0, 1, 2, \dots$). For a given FID, the FFT spectrum has a simple stick structure and, as such, it exists only at the Fourier grid frequencies $2\pi k/T$ ($0 \leq k \leq N - 1$). Here, T is the total acquisition time $T = N\tau$, whereas $\tau > 0$ is the sampling rate, or equivalently, the dwell time, which is equal to the inverse of the selected bandwidth. Clearly, for a theoretically synthesised FID, T has the same significance as the total acquisition time in measurement, but actually it is called the total duration of the FID. Naturally, no encoded FID is zero for any realistically selected T . Nevertheless, the common practice with the FFT is to artificially double the original FID length by adding zeros, and this is called zero filling or zero padding. As a result, the length of the resulting FFT spectrum is also doubled. The supplementary N frequencies in the FFT spectrum give a simple sinc-interpolation characterised by wiggling side lobes around each genuine resonance. A drawback of such an outcome, especially for any two closely spaced resonances, is that the sinc side lobes coupled with truncation artefacts might interfere constructively or destructively to yield extraneous peaks or dips. Any extraneous or spurious spectral peak is a false and unphysical structure which is not a part of the true information contained in the investigated FID. This sinc-interpolation cannot be systematically improved, as empirical practice shows that no enhanced spectral quality is achieved by introducing additional zeros into the FID beyond the first doubling of N .

The mentioned truncation artefacts in the FFT are spectral deformations known as Gibbs oscillations that stem from the experimental impossibility to encode infinitely long FIDs. On the other hand, only FIDs of infinite length can give the exact Fourier coefficients. Therefore, the FFT itself can give merely some approximate Fourier coefficients for any encoded FIDs. In encoding of an FID, the first selected quantity is the bandwidth. The second selected quantity is the signal length N , so that T is automatically fixed. However, the unavoidable truncation in the time domain is critically determined by τ itself. This occurs because τ is the only quantity determining the Nyquist frequency $1/(2\tau)$ as the largest frequency which can be sampled for a fixed bandwidth. The Nyquist frequency sets the upper limit to the frequency content of the FID prior to encoding. Hence, it is such a limit which leads to unavoidable truncation errors in the time domain, since no FID can be limited simultaneously in the two conjugate domains—time and frequency. The role of a concrete value of N appears on the level of indicating the actual extent of the

truncation error. A large enough N means that the total truncation error will be dominated by noise. Gibbs oscillations are reduced for a long FID, but the resulting signal-to-noise ratio (SNR) is diminished. A better SNR is obtained for a shorter FID, but this enhances Gibbs oscillations. Thus in the FFT, a longer FID reduces spectral deformations, but also worsens SNR. This trouble is unsolvable using only the FFT because of its fundamental drawback—the lack of extrapolation features.

The resolution in the FFT is defined by $\omega_{\min} = 2\pi/T$. Thus, all the FIDs with the same T , irrespective of their internal structure, will have the same resolution which is fixed prior to processing by the FFT. In other words, the resolving power in the FFT is pre-determined by the separation between any two adjacent Fourier grid points $2\pi k/N$ ($0 \leq k \leq N-1$). The minimal frequency separation ω_{\min} is also called the Rayleigh bound or the Fourier uncertainty principle. In signal processing, two kinds of spectral shapes are encountered. These are the component shape spectra and the total shape spectrum. The component shape spectra are the spectra for every separate resonance, and they can be generated only via parametric estimators. The total shape spectrum represents the sum of all the separate component shape spectra. The total shape spectrum is also the envelope spectrum. This stems from the fact that a constructive and destructive interference of all the individual resonances yields the total spectral shape. The FFT as a non-parametric processor can give only envelope spectra. For this reason, the FFT and other non-parametric processors are called envelope estimators. By contrast, parametric estimators are able to yield both component and total shape spectra, since they can obtain the peak positions, widths, heights, and phases of individual physical resonances. The main difference between these two categories of processors is in the kind of the information extracted from the input FID. Non-parametric processors can give merely qualitative information, which is an apparent information seen on graphs of spectral shapes. However, more important quantitative information can be obtained by parametric estimators through unfolding the hidden spectral structure of the apparent envelope. Crucially, parametric methods can reconstruct the quantitative features of resonances (peak position, width, height, phase) as the essential ingredient for estimates of concentrations and relaxation times of the most clinically relevant metabolites of the examined tissue.

The spectral parameters of resonances that determine concentrations and relaxation times of metabolites are the complex frequencies and the corresponding complex residues (amplitudes) as the main constituents of the damped harmonics from the associated FID. Surprisingly, with all its drawbacks, fitting is still most frequently employed in MRS for estimation of these critically important spectral parameters. Here, envelope spectra from the FFT are fitted by least square (LS) adjustments of some assumed resonance line-shapes such as Lorentzians, Gaussians, or their sum. Similar LS techniques are also employed in the time domain by fitting a sum of damped complex exponentials or Gaussians or their product to a given FID. Examples of such fitting recipes are VAPRO (variable projection) [7], AMARES (advanced method for accurate, robust and efficient spectral fitting) [8], etc. As another option to these fittings of every individual peak, similar LS adjustments of the given *in vivo* FFT spectrum as a whole are also frequently practised with MRS data. This can be done via, e.g., the ‘linear combination of model’ (LCModel) *in vitro* spectra [9]. The LCModel uses a separately encoded FID on a phantom to set up a basis of model *in vitro* spectra that are subsequently fitted to the studied *in vivo* spectrum which is subjected to quantification. Such model metabolites from *in vitro* spectra can alternatively be pre-selected from the corresponding data banks if available for the concrete case.

These fittings can use some prior information to constrain the variations of the adjusted parameters during nonlinear minimisations of the LS residuals. Such residuals are defined as the difference between the observed envelopes of spectra or FIDs and the corresponding modelled data. In practice, such fittings are set up by means of iterations. In particular, the LCModel uses the Levenberg–Marquardt nonlinear fitting algorithm [10] and gives some error assessments of the Kramer–Rao type or the like. The most serious drawback of all the existing fitting recipes is non-uniqueness, as the same envelope spectrum can be freely adjusted to have any subjectively chosen number of resonances. Moreover, the prior information customarily used in LS fittings in MRS can easily lead to biased estimates in quantification even when the assessed Kramer–Rao bounds decrease [11,12]. This is partially due to the usage of non-orthogonal expansion sets. With such sets, any change of the weighted sum of the squares of the LS residuals, caused by alterations of one or more adjustable parameters, could largely be compensated by independent variations of all the remaining free parameters [13].

Conceptually different from fitting, there exists another strategy for signal processing in MRS. This is quantum-mechanical spectral analysis which converts the quantification problem from MRS into the Schrödinger eigenvalue problem of the evolution matrix or the Hankel (data) matrix. Here, diagonalisation of such matrices yields the spectral parameters. Rigorously the same results can alternatively be obtained without diagonalisation by solving the corresponding secular equation through rooting the characteristic polynomial. Being parametric and non-iterative, this kind of estimator can unequivocally reconstruct the unknown complex frequencies and amplitudes of each physical resonance. With such processors, these main resonance parameters are retrieved first, and it is only afterwards that the corresponding component and total shape spectra can be constructed, if desired. In other words, this represents a completely different methodology from fitting estimators that need the pre-computed envelope spectrum prior to their attempts to quantify the encoded data. These two distinctly different approaches—ambiguous fittings and unambiguous quantum estimation—are anticipated to give appreciably different results, particularly regarding closely overlapping resonances. Experience shows that spectra in MRS are abundant with tightly overlapped resonances. These latter spectral structures are often of primary clinical importance.

An example of quantum-mechanical parametric estimators is the Hankel–Lanczos Singular Value Decomposition (HLSVD) which is in frequent use within MRS [14]. The HLSVD arranges the encoded raw FID points $\{c_n\}$ as a data matrix of the Hankel form $\{c_{i+j+1}\}$, which is subsequently diagonalised to yield the fundamental complex frequencies for the reconstructed harmonics from the time signal. The associated complex amplitudes are extracted in the HLSVD subsequently through a description of the studied FID by a linear combination of complex damped exponentials with time-independent amplitudes. Such a description yields a system of linear equations for the sought amplitudes. This latter system uses all the found frequencies, including both the genuine and the spurious ones. Such a mix of frequencies is disadvantageous, since the admixture of even a slight amount of extraneous frequencies could severely undermine the reliability of the estimates for the amplitudes in the HLVSVD. Another drawback of the HLSVD is the fact that from the onset it is designed to work only with Lorentzian line-shapes, despite the abundant appearance of non-Lorentzians in all spectra encountered in MRS with encoded FIDs. In practice, the HLSVD is implemented for an over-determined system of linear equations. In such a system, the number of equations is larger than the number of

the unknowns. Consequently, the redundant input information from the data matrix leads to the so-called singular eigenvalues. These are the nearly zero eigenvalues that cause the inverse of the diagonalised Hankel matrix to become almost singular. Removing such singular values reduces the rank of the investigated matrix, and this occurrence is an integral part of the procedure called the singular value decomposition (SVD).

A powerful and versatile quantum-mechanical processor for parametric estimations which simultaneously lifts both of the mentioned restrictions of the HLSVD is the FPT which has been intensively used in MRS [5]. The FPT can be set up in both the time and the frequency domain of estimations. This is achievable through a number of numerical and algebraic algorithms that invariably give the spectrum in the form of the quotient of two uniquely determined frequency-dependent polynomials. Such rational polynomials can be in several different forms, *e.g.*, the most general non-diagonal P_L/Q_K ($K \geq L$), diagonal P_K/Q_K , para-diagonal P_{K-1}/Q_K , *etc.* For example, in the case of the diagonal quotient where both polynomials have the same degree K , the algebraic condition for a strictly determined system is given by $2K = N$. In other words, here at least $2K$ FID points are needed to obtain K frequencies and K amplitudes, since in a determined system, the number of equations is equal to the number of the unknown quantities. While remaining in the same computational framework, the FPT comprises both the usual Padé approximant (PA) and the causal Padé z -transform (PzT). The PA is a well-known method from numerical analysis and the theory of approximations whose most important branch is the class of rational functions. Similarly, the PzT is also a well-known method from signal processing and statistical mathematics [15]. The PA and the PzT variants of the FPT are defined with their initial convergence ranges lying outside and inside the unit circle in the complex harmonic variable plane, or the z -plane. The acronyms for these two versions of the FPT are $\text{FPT}^{(-)}$ and $\text{FPT}^{(+)}$, respectively. It is important to emphasise that the $\text{FPT}^{(+)}$ does not diverge outside the unit circle and neither does the $\text{FPT}^{(-)}$ inside the unit circle. This crucial feature is secured by the universal Cauchy principle of analytical continuation. Such a principle applied to the $\text{FPT}^{(+)}$ prolongs its initial convergence region, which is inside the unit circle, to the complementary domain outside the unit circle. Likewise, the same Cauchy principle when used in connection with the $\text{FPT}^{(-)}$, extends its initial convergence region, which is outside the unit circle, to the complementary domain inside the unit circle. Thus, in the case of both the $\text{FPT}^{(+)}$ and the $\text{FPT}^{(-)}$, their respective initial and extended convergence regions cover the entire complex frequency plane, with the exception of poles as points of singularity. Unification of these two computationally different algorithms into a single concept and methodology yields the clause ‘Padé transform’ in the acronym FPT. Further, the adjective ‘fast’ in the FPT stands to indicate that the envelope spectra from the FPT can optionally be computed by the fast $N \ln_2 N$ algorithm as always done in the FFT. Such an option is implemented through acceleration of Fourier sequences by the well-known Wynn ε -non-linear recursion. The Wynn algorithm has been invented to alleviate a cumbersome direct evaluation of quotients of Hankel determinants that enter the definition of the Shanks transform [5]. The Shanks transform is an extension of the Aitken extrapolation (Δ^2 -extrapolation) from one to an arbitrary number of harmonics. When a sequence or a series to be non-linearly transformed is comprised of partial sums, as is the case in the acceleration of Fourier sequences by the Wynn algorithm in the frequency domain, the Shanks transform is identical to the Padé approximant. In such a case, the Wynn ε -algorithm is simply a recursive generation of the Padé approximants in a frequency-by-frequency sweeping throughout a chosen window in the spectrum or in

the whole Nyquist range. In the present context of MRS, the Wynn recursion is extremely efficient if applied to many frequencies because the Fourier sequences to be accelerated are very short, containing barely a dozen pre-computed FFT spectra of increasing length, $N = 2^s$ ($s = 0, 1, \dots$) [16]. These sequences are short since the full length of a typical FID encoded at clinical scanners by means of MRS for a chosen bandwidth does not ordinarily go beyond $N = 2048$, and this corresponds to 2^s for $s = 11$. By construction, the FPT is set up to work for both Lorentzian (non-degenerate) and non-Lorentzian (degenerate) spectra. The latter degenerate spectra include peaks due to multiple roots of the denominator polynomial Q_K in the defining quotient from the FPT. Crucially, being a rational response function, the FPT is simultaneously an interpolator and extrapolator. A particularly important feature of the FPT is extrapolation, since it leads directly to resolution enhancement. Unlike the FFT, resolution ω_{ave} in the FPT is not restricted critically by T . Instead ω_{ave} depends upon the average density of resonances in the given frequency window. Such a circumstance permits resolution enhancement below the Rayleigh limit, $\omega_{\text{ave}} < \omega_{\text{min}}$ [17–19].

Among users of fitting prescriptions for *in vivo* MRS, there is a perception that, in general, successful quantification should include some kind of prior information. This is certainly untrue for non-fitting algorithms such as the FPT or HLSVD. The real reason for which some prior information is used at all in fitting recipes should be clarified. Ample evidence proves that fittings in MRS customarily employ certain chosen prior information (*e.g.*, a fixed ratios among the heights or widths of some resonant peaks or the like), exclusively to constrain the possibly wide variations of the otherwise free adjustable parameters. Without such constraints, fittings usually yield inadequate reconstructions since, as mentioned, changing some free parameters could easily lead to large and unphysical variations in the other adjustable parameters. Such a basic defect of fitting is then generalised by the users of fittings to state that all the adequate algorithms for quantification should introduce prior information. This generalisation is misleading. In principle, certain physically motivated prior information could be readily imposed to the Padé estimation, but this is not indispensable. The adequate prior information to the Schrödinger eigenproblem is already inherently introduced by the proper initial or boundary condition. Moreover, according to the main working postulate of quantum mechanics, the reconstructed total Schrödinger eigenstate contains the whole information about the studied system. Hence, there is no need to impose any other prior information, since the correct solution of the Schrödinger eigenproblem leads to the true eigenspectrum with the sought complex-valued fundamental frequencies and amplitudes. Should some among these spectral parameters obey certain relationships that are known to exist prior to quantification, such relationships would be also inherently ingrained in the investigated FID and, hence, extractable from the retrieved Schrödinger eigenspectrum with no imposed constraints. As mentioned, the FPT is a quantum-mechanical eigenproblem solver [5]. This method employs directly or indirectly the Schrödinger equation, which can be solved exactly in a finite-dimensional space through the Krylov or the Lanczos basis set functions [5]. Within the FPT, computation is done by systematically enlarging the dimension of the Schrödinger or, equivalently, the Krylov state space with the purpose of monitoring and detecting constancy of the retrieved spectral parameters. This represents a procedure of proven validity for demonstrating that the information uncovered from the given FID is complete, without the need to introduce any constraint by some prior information. Therefore, prior information used in fitting techniques becomes superfluous and unsubstantiated by quantum-mechanical spectral analysis,

which quantifies MRS data without any fitting, as has previously been demonstrated within the FPT [17–19] and this will also be illustrated in the present work. Even describing FIDs from MRS by linear combinations of complex damped exponentials with both stationary and non-stationary amplitudes, as done in the FPT, cannot be considered as an imposed, constrained relationship. This comes from the fact that precisely such a relationship follows directly from the two main entities of quantum physics—the exact evolution operator and the related auto-correlation functions.

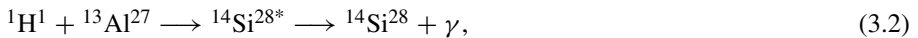
Recent vigorous advances of Padé methodology in MRS and MRI have made it evident that the FPT is a very reliable and robust signal processor, which gives the full and intrinsically cross-validated spectral information of great significance for medical diagnostics [20–27]. Such a finding from the MR literature is reminiscent of the well-established status of the general Padé theory over the years across inter-disciplinary scientific and engineering research, including physics, chemistry, biology, signal processing, system theory, circuit theory, speech pattern recognition, *etc.* The most recent review of the versatile use of the PA in such vastly different research branches has been reported in [5]. Further, relevance of the FPT for medical diagnostics, particularly in clinical oncology has also been thoroughly analysed [6]. We re-emphasise that the PA and the FPT belong to the same general Padé methodology. The acronym FPT in the Padé method emphasises a particular, transform-type property for obtaining envelope spectra without reconstructing the spectral parameters at all [5,16]. More importantly, it has been shown in quantum chemistry that the FPT can carry out parametric analysis of theoretically generated and experimentally measured FIDs through extremely accurate computation of complex frequencies and amplitudes of the reconstructed physical resonances [17–19]. Such a conclusion is also relevant to medicine, especially when quantifying FIDs that are encoded from patients via MRS or MRSI. In these reconstructions, the quantification problem is recognised as the harmonic inversion problem and/or the complex-valued power moment problem [5]. The task of this inverse problem is to reconstruct the proper number K of physical resonances, as well as their true fundamental complex frequencies and amplitudes $\{\omega_k, d_k\}$ ($1 \leq k \leq K$) that build the given FID, which is the only input data available.

The present work applies the FPT to the quantification problem in MRS using a synthesised FID from MRS. The input complex frequencies and amplitudes in the FID are selected according to other similar data in the MRS literature. Such an FID yields the absorption total shape spectrum with the main physical characteristics reminiscent of a high-resolution spectrum from an associated FID encoded clinically from a healthy human brain by means of MRS at an external static field $B_0 = 1.5$ T and a short echo time of 20 ms [28]. The remaining characteristics of such a synthesised FID are also of the same customary type as in encoding on a clinical scanner via MRS, *e.g.*, the signal length is $N = 1024$ and the bandwidth is 1000 Hz such that $\tau = 1$ ms. In order to secure a robust error analysis and cross-validation of the obtained results, both versions of the FPT via the $\text{FPT}^{(+)}$ and the $\text{FPT}^{(-)}$ are employed throughout. One of the main objectives of the exemplified quantification in MRS is to assess the overall performance of the FPT for parametric estimation of a fully controlled theoretical FID without noise. Some 25 input resonances with their 100 spectral parameters are chosen to generate the FID. The FPT is scrutinised rigorously against these entry data by testing for the possibility of reconstructing all the spectral parameters exactly. These testings also aim at verifying whether the FPT is stable and reliable while retrieving the total number of resonances as well as their

complex frequencies and amplitudes by exhausting, *e.g.*, at most one half of the full signal length N [12]. A successful outcome of such a testing would have far reaching ramifications beyond one-dimensional (1D) MRS and become also important for two-dimensional (2D) MRS, 2D MRSI as well as three-dimensional (3D) MRSI and MRI. In particular, for 2D MRS, one of the total acquisition times is a fraction of the corresponding value from 1D MRS. Therefore, whenever the 2D FFT is employed to compute cross-correlation plots using *in vivo* 2D FIDs encoded via 2D MRS, low-resolution results are obtained along the frequency axis associated with the short total acquisition time [29]. In such cases, no appreciable improvement in the results of the FFT is achieved by zero filling of the FID on the short time axis. Hence, the need for signal processors that possess extrapolation features. Such features are automatically built into the FPT via modelling the response function by polynomial quotients. These latter rational functions describe adequately and realistically the manner in which the examined physical system responds to external perturbations. As opposed to the FFT, the FPT predicts that the system's answer to these excitations is non-linear. Here, non-linearity of the FPT can turn into an advantage through the possibility of diminishing the influence of noise on the reconstructed data.

3. THE QUANTUM-MECHANICAL CONCEPT OF RESONANCES IN SCATTERING AND SPECTROSCOPY

In collisions between two nuclei, certain transformations called nuclear transmutations are possible. For example, if the projectile is proton (${}^1\text{H}^1$) and the target is carbon (${}^6\text{C}^{12}$) or aluminium (${}^{13}\text{Al}^{27}$), the following nuclear reactions called radiative capture could take place:



with emission of the photon γ . In the part ${}^1\text{H}^1 + {}^6\text{C}^{12} \rightarrow {}^7\text{N}^{13*}$ from (3.1), or in the like part ${}^1\text{H}^1 + {}^{13}\text{Al}^{27} \rightarrow {}^{14}\text{Si}^{28*}$ from (3.2), the so-called compound nucleus of nitrogen (${}^7\text{N}^{13*}$) or silicium (${}^{14}\text{Si}^{28*}$) is formed in an excited state as indicated by the star superscript. These excited states are unstable and they decay via radiative de-excitations of the type ${}^7\text{N}^{13*} \rightarrow {}^7\text{N}^{13} + \gamma$ or ${}^{14}\text{Si}^{28*} \rightarrow {}^{14}\text{Si}^{28} + \gamma$.

It is well known that cross-sections $\sigma(E)$, as a function of the incident energy E , for resonant nuclear scattering of particles is excellently described by the single- or multi-level Breit–Wigner (BW) formula [30]. This latter formula is either a single Lorentzian of the type:

$$\sigma(E) \approx \sigma_1 \propto \frac{\Gamma_1^2/4}{(E - E_1)^2 + \Gamma_1^2/4}, \quad (3.3)$$

or a linear combination of a number of such Lorentzians,

$$\sigma(E) \approx \sigma_K \propto \sum_{k=1}^K \frac{\Gamma_k^2/4}{(E - E_k)^2 + \Gamma_k^2/4}, \quad (3.4)$$

where E_k is a resonance energy and Γ_k is the resonance width.¹ In the original derivation, Breit and Wigner [30] obtained their dispersion formula or resonance formula by using a perturbation method similar to the Weisskopf–Wigner theory of dispersion of light by atomic systems. The first adequate derivation of the BW formula from a quantum-mechanical scattering wave function for particle scatterings is due to Siegert [31]. Siegert used the perturbation formalism of quantum scattering theory. Importantly, his introduction of decaying states of a compound system comprised of a projectile and a target is very plausible. This stems from the nature of the initial problem in which one wants to describe an experimental finding that at certain energies of the compound system, the cross-sections for a collision between a projectile and a target become unusually large. Such an occurrence falls precisely into the category of the universal phenomenon of the resonance effect, irrespective of its origin (mechanical, quantum-mechanical, acoustic, wave-like, *etc.*) and, therefore, it would be natural to inquire whether the observed enhancement could be inferred directly from the very definition of the cross-section $\sigma(E)$. The cross-section $\sigma(E)$, in the units of area for a collisional event is a ratio between the outgoing and incoming particle flux $F^{(-)}$ and $F^{(+)}$:

$$\sigma(E) \propto \frac{F^{(-)}}{F^{(+)}}. \quad (3.5)$$

Therefore, it follows that $\sigma(E) \rightarrow \infty$ whenever $F^{(+)} \rightarrow 0$. In other words the cross-section will become singular if the incoming wave $F^{(+)}$ is absent. This leads to a natural perception of a compound state of the projectile-target system as a state describing the annihilation of the incoming wave. In other words a compound state is a state with an energy which makes the cross-section singular, in the sense of being enormously large. Hence the resonance effect. In this picture, the target captures (absorbs) the projectile and they both proceed to coexist temporarily as a compound system. However, such a compound is unstable or metastable and, hence, prone to decay once the decay time $1/\Gamma_k$ has elapsed. The inverse resonance width $1/\Gamma_k$ is the lifetime of the k th metastable state. Alternatively, we could say that the compound system relaxes with the relaxation time $1/\Gamma_k$. This critical identification in the definition of $\sigma(E)$ gives the signature of the resonance effect as the singularities of the cross-sections at certain values of complex energy E'_k of the compound system. Siegert's hypothesis of a complex-valued energy $E'_k = E_k - i\Gamma_k/2$ of the compound system at the resonance is rooted in the fact these states have a definite width $\Gamma_k \neq 0$, since they will eventually decay. As opposed to true discrete states, that have zero widths and are located at the negative energy axis, the resonance states have positive energies. Thus, a resonance state is described by a wave packet localised on the positive part of the real energy axis. The real and the imaginary part of the complex resonance energy are the position and the width of the corresponding peak in the variation of the cross-section $\sigma(E)$ with energy E . This resonant maximum in $\sigma(E)$ at $E \approx E_k$ appears as being superimposed on top of a smoothly varying background described by a certain regular function $f(E)$. Being located in the complex energy plane, the resonance energies could be generally classified as sharp and broad. The singularities in $\sigma(E)$ associated with E_k near the real energy axis (small Γ_k) lead to well-delineated resonances. They appear as sharp peaks or resonant cross-sections:

$$\sigma_k(E) \equiv \sigma(E_k). \quad (3.6)$$

¹ Throughout, we shall use the units in which the reduced Planck constant is equal to unity ($\hbar = 1$), so that the energy and frequency can be interchangeably employed as synonyms, $E = \hbar\omega = \omega$.

In such a case, the total cross-section $\sigma(E)$ near the resonant energy in the single- and multi-level BW formulae can be approximated by:

$$\sigma(E) \approx f(E) + \sigma_1(E), \quad \sigma(E) \approx f(E) + \sum_{k=1}^K \sigma_k(E). \quad (3.7)$$

The non-singular function $f(E)$ describes a background which might contain contributions from broad resonances with large widths Γ_k . Physically, as mentioned, the BW formula describes an absorption of an incident particle or a wave by a target. Therefore, $\sigma_k(E)$ is proportional to an absorption spectrum $A(E)$, which is the real part of the complex-valued spectrum $F(E)$:

$$F(E) = i \frac{C_1}{(E - E_1) + i\Gamma_1/2} \equiv A_1(E) + iD_1(E), \quad (3.8)$$

where C_1 is a constant and $D_1(E)$ is a dispersion spectrum,

$$A_1(E) = C_1 \frac{\Gamma_1/2}{(E - E_1)^2 + \Gamma_1^2/4}, \quad D_1(E) = C_1 \frac{E - E_1}{(E - E_1)^2 + \Gamma_1^2/4}. \quad (3.9)$$

As it stands, in the case of a single-level BW formula, the function $F(E)$ is recognised as the simplest PA to $F_{\text{ex}}(E)$ with a numerator and denominator polynomial of the degree 0 and 1, as customarily symbolised by $[0/1]$:

$$F(E) = [0/1]_{F_{\text{ex}}}(E), \quad (3.10)$$

where $F_{\text{ex}}(E)$ is the sought exact complex-valued spectrum. Likewise the multi-level BW formula for $F(E)$ is seen to be the PA of the order $[(K - 1)/K]$ to $F_{\text{ex}}(E)$:

$$F(E) = i \sum_{k=1}^K \frac{C_k}{(E - E_k) + i\Gamma_k/2} \equiv \frac{P_{K-1}(E)}{Q_K(E)} = [(K - 1)/K]_{F_{\text{ex}}}(E), \quad (3.11)$$

where $P_{K-1}(E)$ and $Q_K(E)$ are the numerator and denominator polynomial of degree $K - 1$ and K . This complex spectrum can also be written as a sum of its absorption and dispersion spectrum $A(E)$ and $D(E)$:

$$F(E) = i \sum_{k=1}^K \frac{C_k}{(E - E_k) + i\Gamma_k/2} \equiv A(E) + iD(E), \quad (3.12)$$

$$A(E) = \sum_{k=1}^K A_k(E) \equiv \sum_{k=1}^K C_k \frac{\Gamma_k/2}{(E - E_k)^2 + \Gamma_k^2/4}, \quad (3.13)$$

$$D(E) = \sum_{k=1}^K D_k(E) \equiv C_k \frac{E - E_k}{(E - E_k)^2 + \Gamma_k^2/4}. \quad (3.14)$$

Of course, the same BW formulae for one or many levels also apply directly to spectroscopy. This brief and elementary reminder indicates that the Padé approximant is naturally ingrained into the adequate physical description of a resonance phenomenon. Therefore, from the onset, this method has every chance of yielding the proper theoretical predictions and explanation of resonance data that are measured experimentally, as is indeed the case not only in physics, but also throughout interdisciplinary research

[5]. The outlined quantum-mechanical concept of resonances is deeply rooted in one of the most fundamental quantities in physics, called the scattering matrix or S -matrix. The S -matrix is used to transform the incoming to the outgoing total scattering wave function $\Psi^{(+)}$ and $\Psi^{(-)}$ for the initial and final state of the considered system [32]:

$$\Psi^{(-)}(E) = S(E)\Psi^{(+)}(E). \quad (3.15)$$

The incoming and outgoing particle fluxes $F^{(+)}$ and $F^{(-)}$ can be computed from $\Psi^{(+)}$ and $\Psi^{(-)}$. Therefore, the cross-section $\sigma(E)$ from (3.5) can be obtained from $S(E)$. As such, the elements of the S -matrix can account for all the feature of cross-sections, including resonances. In particular, $S(E)$ is an analytic function in the complex energy plane with singularities given by poles and branch cuts. The poles of $S(E)$ give the Lorentzian resonances in $\sigma(E)$. A function which has poles must be a rational function and so is $S(E)$. Therefore, it comes as no surprise that the matrix elements of the S -matrix are the Padé approximants, that are the simplest rational function given by the quotient of two polynomials, as in (3.11). The purpose of this discussion is to highlight the critical feature of the Padé approximant, namely the fact that this method is inseparable from quantum-mechanics and its leading mathematical formulations as well as implementations.

4. RESONANCE PROFILES

As discussed, scattering theory predicts on physical grounds that the most natural spectral line-shape is the Lorentzian profile. The name Lorentzian for a bell-shaped profile of a spectral line originates from optics where Lorentz [33] used a dispersion-type function as in (3.3). In mathematics, a Lorentzian is known under the name of the Cauchy distribution. There are other line-shapes, such as the Gauss and the Voigt profiles. The Voigt [34] profile is a convolution integral of a Lorentzian by a Gaussian. Therefore, the Voigt function appears as a broadened Lorentzian or, equivalently, a narrowed Gaussian depending which of the two constituents (Lorentzian or Gaussian) is viewed as the primary profile. The Voigt profile has originally been introduced in optics to accounts for the Doppler broadening (via Gaussians) of the primary line-shapes given by dispersion functions (Lorentzians) which describe absorption spectra [34]. Since then many applications of the Voigt profile arose in diverse fields, including MRS. The Voigt frequency profile, as a symmetric function, is intermediate to a Gaussian and a Lorentzian, thus reducing to the former or to the latter function in the pertinent limiting cases of the two widths. Not too far from the centre $\omega \approx \omega_1$, the Lorentz and the Gauss distributions look alike. However, the difference between these two functions becomes appreciable away from the centre where a Lorentzian decreases more slowly than a Gaussian with the augmented value of the frequency variable ω . Mathematically, a Lorentz function is the one-sided Fourier integral of an exponentially damped oscillatory wave function. Physically, an oscillator (a pendulum, an atom, a molecule, *etc.*) exposed to a certain external influence will start its damped harmonic oscillations of a type of forced excitations as a response to a perturbation. Such a response function associated with exponentially attenuated harmonic oscillations is a pure Lorentzian in the absence of any other external disturbances. A convolution (folding) of two or more Voigtians gives a single Voigt frequency profile. This is reminiscent of the well-known fact that a convolution of two or more Gaussians (Lorentzians) yields a single Gaussian (Lorentzian). In plasma physics, the Doppler broadening of spectral lines stems from statistical velocity distributions of emitting atoms. According to Boltzmann's ther-

modynamical theory of gases, the average velocity and plasma temperature are directly proportional to each other. At temperatures far from Bose–Einstein condensation, the velocity distribution of atoms appears to be Maxwellian and for this reason the mentioned Doppler broadening has a Gaussian profile. In some other applications, the Voigt function can alternatively be conceived of as a primary Gaussian profile, which is subsequently narrowed by a convolution with a Lorentzian due collisions of atoms.

In MRS, inhomogeneity of static magnetic fields is often modelled by Gaussian broadenings of the basic Lorentzian profiles that originate from absorption of radio-frequency photons. In practice, the Voigt convolution used in MRS has often been considerably simplified by a linear combination of Lorentzians and Gaussians with some constant fitting coefficients [35]. However, the Voigt convolution integral can be calculated analytically.² In particular, it can be shown that the Voigt convolution integral is the real part of the exponentially modulated error-function of a complex independent variable (also called the probability function or the w -function). The error-function of a complex variable can be generated quickly to within machine accuracy by the Gautschi [36] continued fraction algorithm. With this latter algorithm, the Voigt frequency profile could be used extensively without previous simplifications as a sum of a Gaussian and a Lorentzian. Of course, there is also the Voigt time profile. It is given by the inverse Fourier integral of the Voigt frequency profile. The explicit result of such an inversion is given by $\exp(-\alpha t - \beta t^2)$, where t is time ($t \geq 0$). This follows from the convolution theorem according to which the Fourier integrals of two functions convolved in the frequency domain are reduced in the time domain to the ordinary product of the two inverse Fourier transforms. Specifically, the one-sided inverse Fourier integral (from zero to infinity) of a Lorentzian $\propto 1/(\alpha^2 + \omega^2)$ is $\propto \exp(-\alpha t)$, whereas that of a Gaussian $\propto \exp(-\omega^2/\beta^2)$ is $\propto \exp(-\beta t^2)$. Hence, the Voigt time profile is given by $\exp(-\alpha t - \beta t^2)$.

5. THE ROLE OF QUANTUM MECHANICS IN SIGNAL PROCESSING

The dynamics of time-evolving physical systems in quantum mechanics are described by the Schrödinger equation $\hat{U}(\tau)|\gamma_k\rangle = u_k|\gamma_k\rangle$. This is the eigenvalue problem of the evolution operator $\hat{U} = \exp(-i\hat{\Omega}\tau)$, where $\hat{\Omega}$ is the system operator which is the kernel of the dynamics and $u_k = \exp(-i\omega_k\tau)$. Decay to zero of u_k at the infinite time requires that $\text{Im}(\omega_k) < 0$. Physically, $\hat{\Omega}$ represents the energy operator derived from the Hamiltonian which is the total energy (kinetic + potential) of the system. To encompass resonances with complex energies, the operator $\hat{\Omega}$ needs to be non-Hermitian, *i.e.*, $\hat{\Omega}^\dagger \neq \hat{\Omega}$. For a given ‘Hamiltonian’ $\hat{\Omega}$ of the investigated system, the direct spectral analysis consists of extracting the spectral set comprised of all the eigenfrequencies and eigenfunctions $\{\omega_k, \gamma_k\}$. This is customarily done by solving the Schrödinger eigenvalue problem through, *e.g.*, diagonalisation of the operator $\hat{\Omega}$ using certain conveniently chosen basis functions from a set which is complete, or locally complete. In practice, what is actually needed are the complex frequencies $\{\omega_k\}$ and the corresponding complex amplitudes $\{d_k\}$. The amplitudes are obtained by squaring the projection of the full state vector γ_k onto the initial state Φ_0 of the system, $d_k = (\Phi_0|\gamma_k)^2$. The absolute values $\{|d_k|\}$ relate to the intensity of the spectral line-shapes, whereas $\{\text{Re}(\omega_k)\}$ and $\{\text{Im}(\omega_k)\}$ are the positions and the widths of the

² This is especially needed when this convolution is repeatedly used many times in the course of an iterative analysis, *e.g.*, in various LS estimations of spectra.

resonances in the spectrum of the considered system. In this way, by obtaining the spectral parameters $\{\omega_k, d_k\}$ for the known system operator $\hat{\Omega}$, quantum mechanics examines the structure of matter on any specified level (nuclear, atomic, molecular, *etc.*). This is the direct quantification problem.

The reason for which the quantity \hat{U} is called the evolution operator becomes immediately apparent by considering the time-dependent Schrödinger equation $(i\partial/\partial t)\Phi(t) = \hat{\Omega}\Phi(t)$. For conservative systems, the ‘Hamiltonian’ operator $\hat{\Omega}$ is stationary so that the solution $\Phi(t)$ of this latter equation can be obtained in the simple form $\Phi(t) = \hat{U}(t)\Phi(0)$. This expression tells us that the state of the system $\Phi(t)$ at any instant t will be known as soon as the initial state $\Phi(0) = \Phi(t=0) \equiv \Phi_0$ is given at $t=0$ along with the operator $\hat{\Omega}$. Hence determinism of quantum mechanics. The generation of $\Phi(t)$ at any time $t > 0$ is accomplished by application of the operator $\hat{U}(t)$ onto $\Phi(0)$. It is this mapping which justifies the name of the time evolution operator for \hat{U} . Spectral problems can equivalently be solved within another powerful quantum-mechanical formalism called the Green operator that are generated by means of the resolvent operator, *i.e.*, $\hat{G}(u) = (u\hat{1} - \hat{U})^{-1}$.

Physical systems develop in time through correlated dynamics. Correlations between any two states of the same system are ingrained in the definition of the evolution operator $\hat{U}(t)$ which relates $\Phi(0)$ with $\Phi(t)$. However, operators are not experimentally measurable quantities (*i.e.*, they are not observables) and, therefore, a passage to scalar quantities is needed. This is achieved by the projection technique through projection of one state onto the other using the scalar or inner product. For example, to correlate $\Phi(t)$ and $\Phi(0)$ with the result in the field of scalars, we form the inner product $C(t) \equiv (\Phi(0)|\Phi(t))$. The ensuing quantity $C(t)$ is called the auto-correlation function, since it correlates the same system to itself in two different states $\Phi(t)$ and $\Phi(0)$. Moreover, since $\Phi(t) = \hat{U}\Phi(0)$, we see that $C(t)$, in fact, correlates the state $\Phi(0)$ to the same vector $\Phi(0)$ weighted with the evolution operator, so that $C(t) = (\Phi_0|\hat{U}(t)|\Phi_0)$.

The main working postulate of quantum mechanics is that the whole information about a general studied system is contained in the wave function of the system. Such stationary and non-stationary wave functions are the mentioned state vectors Υ and $\Phi(t)$, respectively. The mathematical expression which transcends this statement is the assurance of the existence of the global (or at least the local) completeness relation $\sum_{k=1}^K \hat{\pi}_k = \hat{1}$, where $\hat{\pi}_k$ is the projection operator $\hat{\pi}_k = |\Upsilon_k\rangle\langle\Upsilon_k|$. Here, completeness refers to the complete information. The interpretation of the completeness relation rests upon the probabilistic meaning of quantum mechanics and all its entities. For example, the state vector $|\Upsilon_k\rangle$ and its dual counterpart $\langle\Upsilon_k|$ represent the probability densities of finding the system in the state described by these wave functions. Knowing everything about the studied system amounts to achieving the maximum probability which is equal to 1, and this is what is stated by the mentioned completeness relation in the operator form. The same statement can also be written in the scalar form by placing the completeness relation in a matrix element between the initial state and this gives $\sum_{k=1}^K d_k = 1$, where d_k is the scalar amplitude d_k defined by $d_k = (\Phi_0|\hat{\pi}_k|\Phi_0) = (\Phi_0|\Upsilon_k)^2$, in agreement with the already quoted expression for d_k . Thus, one of the ways of verifying the completeness relation is to check whether the sum of all the amplitudes $\{d_k\}$ ($1 \leq k \leq K$) is equal to unity. Note that every form (operational or scalar) of the completeness relation implicitly contains the information about the frequencies $\{\omega_k\}$ since Υ_k and d_k correspond to ω_k .

The holders of the complete information, the states vectors Υ and $\Phi(t)$, are derived from the system operator $\hat{\Omega}$. This implies that the whole sought information is also con-

tained in $\hat{\Omega}$, or equivalently, in $\hat{U}(t)$. On the other hand, the total evolution operator $\hat{U}(t)$ is the main ingredient of $C(t)$. Therefore, the previously stated quantum-mechanical postulate also means that everything one could possibly learn about any studied system is ingrained in the auto-correlation function $C(t)$. Although the same full information is available from γ , $\Phi(t)$, $\hat{\Omega}$, $\hat{U}(t)$ on the one hand, and from $C(t)$ on the other, the auto-correlation functions are more manageable, as they are observables. Being a scalar, the quantity $C(t)$ possesses a functional form which is given by its dependence upon the independent variable t . Therefore, since $C(t)$ inherits the entire information about the investigated generic system, it is very important to know the quantum-mechanical prediction for the shape of the auto-correlation function. To see how the auto-correlation function $C(t)$ looks when plotted against the variation of time t , it is sufficient to invoke the spectral representation of $\hat{U}(t)$. The latter representation is readily obtained through multiplication of the defining exponential $\exp(-i\hat{\Omega}t)$ for $\hat{U}(t)$ by the unity operator $\hat{1}$, which is taken from the completeness relation to yield $\hat{U}(t) = \sum_{k=1}^K \exp(-i\omega_k t) \hat{\pi}_k$. Thus, the preservation of the full information from the system, used in this derivation, *imposes* the spectral representation of the evolution operator as the sum of K complex damped exponentials with the operator amplitudes $\hat{\pi}_k$. Inserting this representation for $\hat{U}(t)$ into $C(t)$ gives $C(t) = \sum_{k=1}^K d_k \exp(-i\omega_k t)$. Hence, the shape of the quantum-mechanical auto-correlation functions is given by a linear combination of K complex damped exponentials with the scalar amplitudes d_k . This is not a fitting model for $C(t)$ introduced by hand. Rather, it is the shape of the auto-correlation function *dictated* by the form $\exp(-i\hat{\Omega}t)$ of the quantum-mechanical evolution operator $\hat{U}(t)$. Such a form of $C(t)$ corresponds precisely to time signals $c(t)$ in many fields. This establishes the equivalence between quantum-mechanical auto-correlation functions and time signals. Hence, a direct connection between quantum mechanics and signal processing as two otherwise totally separated branches. Such a link is of a fundamental nature, because a proper mathematical modelling in signal processing can only be done with an adequate physical description of the studied phenomenon, and quantum mechanics amply fulfils this request [5].

6. SUITABILITY OF THE FAST PADÉ TRANSFORM FOR SIGNAL PROCESSING

Independent of whether a mathematical model is assumed for the description of a given signal or not, the FPT appears as an optimal estimator especially in MRS. This can be understood from a twofold argument which runs as follows. Given any time signal c_n , described by a sum of attenuated complex exponentials $c_n = \sum_{k=1}^K d_k u_k^n$ with, e.g., stationary amplitudes $\{d_k\}$, the exact spectrum is given by $\sum_{k=1}^K d_k / (u - u_k)$ at any $u = \exp(-i\omega\tau)$. The indicated sum can explicitly be performed to give the polynomial quotient $P_{K-1}(u)/Q_K(u)$, which is the para-diagonal FPT. A similar reasoning can be extended to a more general time signal given as a linear combination of damped complex exponentials with non-stationary polynomial-type amplitudes. Therefore, the FPT is optimal for processing signals modelled as indicated. This is anticipated, since the FPT is the exact theory if a function to be modelled is itself a rational polynomial. Algorithmically, the FPT yields the unique quantification in MRS by rooting the characteristic equation $Q_K(u) = 0$. The results are the reconstructed K values for the complex harmonics $\{u_k\}$ from the input time signal. Moreover, the associated amplitudes $\{d_k\}$ are retrieved with no additional effort in computations

by employing the Cauchy residue formula $d_k \propto P_{K-1}(u_k)[(d/du)Q_K(u)]_{u=u_k}$ for all the distinct roots ($u_p \neq u_q$, $p \neq q$). After extracting the spectral parameters $\{u_k, d_k\}$, the corresponding non-degenerate Lorentzian spectrum in the complex mode is generated using the Heaviside partial fractions $\sum_{k=1}^K d_k/(u - u_k)$. This analysis extends readily to encompass the multiple roots of $Q_K(u)$ to treat strictly overlapping (degenerate) resonances.

When no model is assumed for c_n , the ensuing exact spectrum is the Green function given as the Maclaurin expansion $G(u) = \sum_{n=0}^{\infty} c_n u^{-n-1}$. Also in this case the FPT is optimal, since its non-diagonal polynomial quotient $P_L(u)/Q_K(u)$ has the best description of $G(u)$ through the first $L + K$ expansion terms. This is achieved via the exact agreement between the partial sum $\sum_{n=0}^{L+K} c_n u^{-n-1}$ from $G(u) = \sum_{n=0}^{\infty} c_n u^{-n-1}$ which is truncated at $n = L + K$ and the Maclaurin series of $P_L(u)/Q_K(u)$ through the first $L + K$ terms, as follows from the definition of the FPT, i.e., $P_L(u)/Q_K(u) - G(u) = \mathcal{O}(u^{-L-K-1})$. Here, symbol $\mathcal{O}(u^{-L-K-1})$ is the remainder which represents a series in terms of $u^{-L-K-1-n}$ ($n \geq 0$) with certain expansion coefficients. In order to reach consistency, the discussed two results (with and without modelling of the examined FID) need to be connected. To this end, we insert the modelled time signal $c_n = \sum_{k=1}^K d_k u_k^n$ into the exact model-free spectrum $G(u) = \sum_{n=0}^{\infty} c_n u^{-n-1}$. This infinite Maclaurin sum from the Green function can be carried out exactly by means of the geometric series, so that $G(u) = \sum_{k=1}^K d_k/(u - u_k)$, which is recognised as the para-diagonal FPT, $P_{K-1}(u)/Q_K(u)$. Therefore, the generic spectrum $G(u)$ with no modelling of the time signal is reduced, when the signal is subsequently supposed to be model-dependent, to the identical result as the one from a different and independent analysis. This establishes the consistency of the two representations. Furthermore, when spectral analysis is carried out directly in the time domain via the Shanks algorithm [5], the FPT is seen to be the *exact* filter for a general signal given in the most customary form of a sum of complex damped exponentials with stationary and/or time-dependent amplitudes. Overall, the two presented arguments for a modelled and non-modelled time signals illustrate the optimal suitability of the FPT for MRS.

7. FAST PADÉ TRANSFORMS INSIDE AND OUTSIDE THE UNIT CIRCLE

Among all the existing signal processors, the FPT is a particularly important method due to its self-contained cross-validation. This is because the FPT, as a system function which is formulated to model an optimal response to generic external perturbations, possesses two complementary versions. These equivalent variants, $\text{FPT}^{(+)}$ and $\text{FPT}^{(-)}$, are initially defined in two entirely different convergence regions located inside ($|z| < 1$) and outside ($|z| > 1$) the unit circle, respectively [21,22]. This method works equally well in both the time and the frequency domain. For example, in the frequency domain, both the $\text{FPT}^{(+)}$ and the $\text{FPT}^{(-)}$ have a common starting point, which is the same input spectrum given by the truncated power series representation of the finite-rank Green function:

$$G_N(z^{-1}) = \frac{1}{N} \sum_{n=0}^{N-1} c_n z^{-n}, \quad (7.1)$$

$$z = e^{i\omega\tau}. \quad (7.2)$$

The expansion coefficients in (7.1) are the signal points $\{c_n\}$ ($0 \leq n \leq N - 1$), where N is

the total length. The time signal from the Green function is equivalent to the quantum-mechanical auto-correlation function. By the adopted convention from the theory of the z -transform, the Green function (7.1) is defined as an expansion in powers of the inverse z^{-1} of the harmonic variable. This means that in the limit $N \rightarrow \infty$, the series (7.1) is convergent outside and divergent inside the unit circle, $|z| > 1$ and $|z| < 1$, respectively. The initial convergence regions of the $\text{FPT}^{(+)}$ and the $\text{FPT}^{(-)}$ are within $|z| < 1$ and $|z| > 1$, where the superscripts \pm stand to indicate the power ± 1 of the expansion harmonic variable, $z^{\pm 1}$. In accord with the general Padé methodology for the input power expansions such as in (7.1), both response functions or spectra in the $\text{FPT}^{(\pm)}$ are the unique rational polynomials $P_L^{\pm}(z^{\pm 1})/Q_K^{\pm}(z^{\pm 1})$ in $z^{\pm 1}$ such that the sum of their degrees L and K is less than or equal to N :

$$G_N(z^{-1}) - G_{L,K}^{\pm}(z^{\pm 1}) = \mathcal{O}(z^{\pm L+K\pm 1}), \quad (7.3)$$

$$G_{L,K}^{\pm}(z^{\pm 1}) = \frac{P_L^{\pm}(z^{\pm 1})}{Q_K^{\pm}(z^{\pm 1})}, \quad (7.4)$$

$$L + K \leq N, \quad (7.5)$$

where $z^{+1} \equiv z^+ = z$ and $z^{-1} \equiv z^- = 1/z$. Here, symbols $\mathcal{O}(z^{\pm L+K\pm 1})$ are remainders that represent the Maclaurin series beginning with the powers $\pm L + K \pm 1$ of the expansion variables $z^{\pm 1}$. The direct meaning of the $\mathcal{O}(z^{\pm L+K\pm 1})$ symbols from (7.3) is seen if the Green–Padé functions $G_{L,K}^{\pm}(z^{\pm 1})$ are developed in their own Maclaurin series. The resulting series agree exactly with the partial sum G_{L+K} containing the first $L + K \leq N$ terms of the original Green function G_N . In such a case, the remaining $N - L - K$ terms from G_N and $G_{L,K}^{\pm}$ are different, and they are all collected in the corresponding $\mathcal{O}(z^{\pm L+K\pm 1})$ symbols in (7.3). In other words, $\mathcal{O}(z^{\pm L+K\pm 1})$ represent the series that start from $z^{\pm L+K\pm 1}$. For brevity, given these remarks, (7.3) can be rewritten as:

$$G_N(z^{-1}) = G_{L,K}^{\pm}(z^{\pm 1}), \quad (7.6)$$

under the convention that the left- and the right-hand sides are equal only up to the neglected terms of the orders $\mathcal{O}(z^{\pm L+K\pm 1})$. By definition, the rational polynomial $G_{L,K}^+(z)$ and $G_{L,K}^-(z^{-1})$ are the Padé approximations to the finite-rank Green function G_N and, therefore, they are also called the Green–Padé functions. In these functions, $P_L^{\pm}(z^{\pm 1})$ and $Q_K^{\pm}(z^{\pm 1})$ are the numerator and denominator polynomial of the degrees L and K :

$$P_L^{\pm}(z^{\pm 1}) = \sum_{r=r^{\pm}}^L p_r^{\pm} z^{\pm r}, \quad Q_K^{\pm}(z^{\pm 1}) = \sum_{s=0}^K q_s^{\pm} z^{\pm s}, \quad (7.7)$$

where $r^+ = 1$ and $r^- = 0$. Since both Green functions, $G_N(z^{-1})$ and $G_{L,K}^-(z^{-1})$, have the same independent variables z^{-1} , it is clear that the $\text{FPT}^{(-)}$ is the usual PA which is denoted in the standard way by $[L/K]_{G_N}(z^{-1})$. However, as opposed to the input z -transform $G_N(z^{-1})$, the alternative Green–Padé function $G_{L,K}^+(z)$ is defined in terms of the variable z and, as such, the $\text{FPT}^{(+)}$ is recognised as the causal PzT.

7.1. Description of the background contribution by the off-diagonal FPT

From a mathematical viewpoint, the concrete values of the degrees L and K of the polynomials $P_L^{\pm}(z^{\pm 1})$ and $Q_K^{\pm}(z^{\pm 1})$ in the general Green–Padé functions $G_{L,K}(z^{\pm 1})$ from (7.4)

can be any positive integers, provided that their sum does not exceed the total number of the available signal points as stated in (7.5). However, from a physical point of view, the situation is quite different. The input FID contains a very definite number of harmonics, and this number is equal to K . Although K is not known prior to spectral analysis, this does not mean that K can be varied arbitrarily as regularly done in all fittings in MRS as well as in the HLSVD. Quite the contrary, the unknown true value K must be unequivocally reconstructed from the input FID, just like its unknown fundamental frequencies and amplitudes, as is the case in the FPT.

Two cases are especially important in applications of the FPT. These are the diagonal ($L = K$) and para-diagonal ($L = K - 1$) variants of the fast Padé transforms that will be denoted in a simplified way as:

$$G_K^\pm(z^{\pm 1}) \equiv G_{K,K}^\pm(z^{\pm 1}), \quad \bar{G}_K^\pm(z^{\pm 1}) \equiv G_{K-1,K}^\pm(z^{\pm 1}), \quad (7.8)$$

$$G_K^\pm(z^{\pm 1}) = \frac{P_K^\pm(z^{\pm 1})}{Q_K^\pm(z^{\pm 1})}, \quad (7.9)$$

$$\bar{G}_K^\pm(z^{\pm 1}) = \frac{\bar{P}_{K-1}^\pm(z^{\pm 1})}{Q_K^\pm(z^{\pm 1})}. \quad (7.10)$$

The diagonal Green–Padé functions $G_K^\pm(z^{\pm 1})$ can always be expressed as a sum of a constant term and the corresponding para-diagonal form, say $\bar{G}_K^\pm(z^{\pm 1})$:

$$G_K^\pm(z^{\pm 1}) = b_K^\pm + \bar{G}_K^\pm(z^{\pm 1}), \quad (7.11)$$

$$\bar{G}_K^\pm(z^{\pm 1}) = \frac{\bar{P}_{K-1}^\pm(z^{\pm 1})}{Q_K^\pm(z^{\pm 1})}, \quad (7.12)$$

$$\bar{P}_{K-1}^\pm(z^{\pm 1}) = \sum_{r=r^\pm}^{K-1} \bar{p}_r^\pm z^{\pm r}, \quad (7.13)$$

$$\bar{p}_r^\pm = p_r^\pm - b_K^\pm q_r^\pm, \quad b_K^\pm = \frac{p_K^\pm}{q_K^\pm}. \quad (7.14)$$

In MRS, all absorption spectra computed from encoded FIDs are always seen to have rather elevated backgrounds located below the main physical resonances. Such backgrounds are thought to be due to large macromolecules that all the fitting techniques from MRS treat vaguely by adjusting some 3 or 4 expansion coefficients of an *ad hoc* third or fourth degree least-square polynomial. This background polynomial is afterwards superficially patched with whichever basis set is used for the remaining resonances in the fitted spectrum. In contradistinction with this, the FPT can describe the background accurately and quite naturally by the off-diagonal Green–Padé functions $G_{L,K}^\pm(z^{\pm 1})$ for $L > K$ due to the following simple relationship:

$$\frac{P_L^\pm(z^{\pm 1})}{Q_K^\pm(z^{\pm 1})} = B_{L-K}^\pm(z^{\pm 1}) + \frac{A_K^\pm(z^{\pm 1})}{Q_K^\pm(z^{\pm 1})}. \quad (7.15)$$

Here $B_{L-K}^\pm(z^{\pm 1})$ are the polynomials of degree $L - K > 0$ for the description of the background contribution to a spectrum in MRS. The remaining resonances are described by the diagonal Green–Padé functions $A_K^\pm(z^{\pm 1})/Q_K^\pm(z^{\pm 1})$, where $A_K^\pm(z^{\pm 1})$ are the numerator

polynomials of the same degree K as the denominators $Q_K^\pm(z^{\pm 1})$. This latter quotient could also be replaced by the para-diagonal Green–Padé functions $\tilde{A}_{K-1}^\pm(z^{\pm 1})/Q_K^\pm(z^{\pm 1})$ in which case the degree of the new polynomial for the background would be increased accordingly by 1:

$$\frac{P_L^\pm(z^{\pm 1})}{Q_K^\pm(z^{\pm 1})} = \tilde{B}_{L-K+1}^\pm(z^{\pm 1}) + \frac{\tilde{A}_{K-1}^\pm(z^{\pm 1})}{Q_K^\pm(z^{\pm 1})}. \quad (7.16)$$

Of course, the expressions (7.15) and (7.16) are written merely to indicate that a modelling of the background of macromolecules is accomplished naturally by a simple division in the Padé quotients. Such a division can factor out a background polynomial, so that the remaining quotient describes the main resonances. In practice, whenever a given spectrum to be modelled contains a rolling and smoothly varying background as in MRS, we would not first extract $P_L^\pm(z^{\pm 1})/Q_K^\pm(z^{\pm 1})$ for $L > K$ and then perform divisions as, *e.g.*, in (7.15) to single out macromolecules from other resonances. Rather, we would set up the Padé models with these two contributions that are manifested distinctly from the onset *via*:

$$G_N(z^{-1}) \approx B_{L-K}^\pm(z^{\pm 1}) + \frac{A_K^\pm(z^{\pm 1})}{Q_K^\pm(z^{\pm 1})}, \quad (7.17)$$

with the diagonal polynomial quotient, or with the corresponding para-diagonal ratio,

$$G_N(z^{-1}) \approx \tilde{B}_{L-K+1}^\pm(z^{\pm 1}) + \frac{\tilde{A}_{K-1}^\pm(z^{\pm 1})}{Q_K^\pm(z^{\pm 1})}. \quad (7.18)$$

The expansion coefficients of the background polynomials $B_{L-K}^\pm(z^{\pm 1})$ as well as those of the remaining two main polynomials in the quotients $A_K^\pm(z^{\pm 1})/Q_K^\pm(z^{\pm 1})$ would be extracted simultaneously from the system of linear equations that is inherent, *e.g.*, in (7.17). In such a way, the background and the main physical resonances would be treated in concert without any artificial patching of one contribution to the other.

7.2. Diagonal and para-diagonal FPT

In the remaining part of this study, we shall deal only with the diagonal and para-diagonal forms of the FPT^(±). The initial step in the algorithms of the FPT^(±) consists of extracting the Padé polynomials $P_K^\pm(z^{\pm 1})$ and $Q_K^\pm(z^{\pm 1})$ from the given set of the input time signal points $\{c_n\}$. The road towards this end has already been paved by the very definition the FPT^(±) from (7.6) which itself permits extraction of the expansion coefficients $\{p_r^\pm\}$ and $\{q_s^\pm\}$ of $P_K^\pm(z^{\pm 1})$ and $Q_K^\pm(z^{\pm 1})$. To proceed this way in the FPT⁽⁺⁾ or the FPT⁽⁻⁾, it is necessary to multiply (7.6) for $L = K$ by $Q_K^+(z)$ or $Q_K^-(z^{-1})$, and then equalise the coefficients of the same powers of the expansion variables. In the case of the FPT⁽⁺⁾, the results are the following two systems of linear equations for $\{q_s^+\}$ and $\{p_r^+\}$:

$$\sum_{s=1}^K q_s^+ c_{m+s} = -c_m, \quad 0 \leq m \leq I, \quad (7.19)$$

$$p_k^+ = \sum_{r=0}^{K-k} c_r q_{k+r}^+, \quad 1 \leq k \leq K, \quad (7.20)$$

where $I = N - K - 1$. Likewise, for the $\text{FPT}^{(-)}$, the associated systems of two linear equations for the expansion coefficients $\{q_s^-\}$ and $\{p_r^-\}$ are:

$$\sum_{s=1}^K q_s^- c_{K+m-s} = -c_{K+m}, \quad 1 \leq m \leq I, \quad (7.21)$$

$$p_k^- = \sum_{r=0}^k c_r q_{k-r}^-, \quad 0 \leq k \leq K. \quad (7.22)$$

The coefficients q_0^\pm can be freely set to unity in (7.19) and (7.21). The equivalent matrix forms of the systems of equations (7.19)–(7.22) can also be written as in [5]. It should be noted that the expansion coefficients $\{q_s^-\}$ and $\{q_s^+\}$ of the polynomial $Q_K^-(z^{-1})$ and $Q_K^+(z)$ have the meaning of the forward and backward prediction coefficients in the $\text{FPT}^{(-)}$ and the $\text{FPT}^{(+)}$, respectively. In other words, once all the K coefficients $\{q_s^-\}$ are determined, (7.21) can be used to predict the new, unavailable time signal points from a linear combination of the known data. Hence, extrapolation of the $\text{FPT}^{(-)}$ directly in the time domain. Similarly, when all the K coefficients $\{q_s^+\}$ are obtained, (7.19) can be used to recur backwards and retrieve the old time signals points. The fidelity of such a retrieval is a check for the accuracy of the computed coefficients $\{q_s^+\}$. Computations of the polynomial expansion coefficients $\{p_r^+\}$ and $\{q_s^+\}$ are greatly simplified by the fact that the two systems of equations (7.19) and (7.20) are actually decoupled. The same is true for $\{p_r^-\}$ and $\{q_s^-\}$ from the two systems of equations (7.21) and (7.22). Therefore, in the $\text{FPT}^{(+)}$ or the $\text{FPT}^{(-)}$, only the system (7.19) or (7.21) for the coefficients $\{q_s^+\}$ or $\{q_s^-\}$ must be solved, respectively. Namely, when the sets $\{q_s^\pm\}$ are found, it is not necessary to solve the linear equations from (7.20) and (7.22) for the remaining coefficients $\{p_r^+\}$ or $\{p_r^-\}$. This is because for the known sets $\{q_s^\pm\}$, the equations (7.20) and (7.22) themselves are the analytical results for $\{p_k^+\}$ and $\{p_k^-\}$, respectively. As to the systems of linear equations (7.19) and (7.21), for the coefficients $\{q_s^+\}$ and $\{q_s^-\}$, we use exclusively the standard Matlab algorithms, including the usual SVD for a refinement of the found solutions.

The Green–Padé spectra $G_K^\pm(z^{\pm 1})$ are meromorphic functions, meaning that the only singularities they have are their poles. Therefore, their poles are the same as the corresponding zeros of the denominator polynomials $Q_K^\pm(z^{\pm 1})$. This implies that the $\text{FPT}^{(\pm)}$ are capable of determining all the fundamental complex frequencies $\{\omega_k^\pm\}$ ($1 \leq k \leq K$), counted with their multiplicities, if they exist, by solving the characteristic equations:

$$Q_K^\pm(z^{\pm 1}) = 0. \quad (7.23)$$

These are also the secular equations that give the roots in terms of the harmonic variables z_k^\pm via:

$$z_k^\pm \equiv e^{\pm i\omega_k^\pm \tau}, \quad \text{Im}(\omega_k^\pm) > 0. \quad (7.24)$$

Physical, *i.e.*, genuine roots are associated with the property $\text{Im}(\omega_k^\pm) > 0$ which signifies that all the K poles $\{z_k^+\}$ and $\{z_k^-\}$ are located inside and outside the unit circle, respectively. The fundamental frequencies ω_k^\pm are obtained from z_k^\pm as:

$$\omega_k^\pm = \mp \frac{i}{\tau} \ln(z_k^\pm), \quad \ln(z_k^\pm) = \ln(|z_k^\pm|) + \text{Arg}(z_k^\pm). \quad (7.25)$$

For non-degenerate resonances, a fixed fundamental frequency corresponds to one amplitude alone. Such resonances produce purely Lorentzian line-shapes in the associated spectrum. In the Padé spectral analysis, these amplitudes are the Cauchy residue of the corresponding Green–Padé functions. For example,

$$d_k^\pm = \lim_{z^{\pm 1} \rightarrow z_k^{\pm 1}} \{(z^{\pm 1} - z_k^{\pm 1}) \tilde{G}_K^\pm(z^{\pm 1})\} = \frac{\tilde{P}_{K-1}^\pm(z_k^\pm)}{[(d/dz^{\pm 1}) Q_K^\pm(z^{\pm 1})]_{z^{\pm 1}=z_k^\pm}}. \quad (7.26)$$

Here, only the k th frequency determines the k th amplitude. Hence non-degeneracy. The Padé reconstructions for the true phases ϕ_k of the k th resonance are given by $\phi_k^\pm \equiv \text{Arg}(d_k^\pm)$. The absolute values of the amplitudes, $|d_k^\pm|$, are not the only spectral parameters that determine the height of the corresponding resonance peak. This becomes clear from the following ersatz spectrum:

$$E_K(\omega) = -i \sum_{k=1}^K \frac{|d_k|}{\omega - \omega_k}. \quad (7.27)$$

This Heaviside partial fraction representation can be summed up to give a ratio of a numerator and denominator polynomial of degree $K - 1$ and K , respectively. Therefore, $E_K(\omega)$ is a para-diagonal FPT in variable ω [17]. For brevity, the superscripts \pm in (7.27) are omitted. The absorption ersatz spectrum associated with (7.27) is a sum of K pure Lorentzians:

$$\text{Re} \left(-i \sum_{k=1}^K \frac{|d_k|}{\omega - \omega_k} \right) = \sum_{k=1}^K \frac{|d_k| \text{Im}(\omega_k)}{[(\omega - \text{Re}(\omega_k))^2 + [\text{Im}(\omega_k)]^2]}. \quad (7.28)$$

Here, the height h_k of the k th Lorentzian, $|d_k| \text{Im}(\omega_k) / [(\omega - \text{Re}(\omega_k))^2 + [\text{Im}(\omega_k)]^2]$, is obtained at the resonance position $\omega = \text{Re}(\omega_k)$ as:

$$h_k \equiv \lim_{\omega \rightarrow \text{Re}(\omega_k)} \frac{|d_k| \text{Im}(\omega_k)}{[(\omega - \text{Re}(\omega_k))^2 + [\text{Im}(\omega_k)]^2]} = \frac{|d_k|}{\text{Im}(\omega_k)}. \quad (7.29)$$

Hence, the height h_k of the k th Lorentzian peak is determined by the two spectral parameters, $|d_k|$ and $\text{Im}(\omega_k)$, rather than by $|d_k|$ alone. This is illustrated in Section 8. The outlined procedure completes the determination of all the fundamental complex frequencies and the corresponding complex amplitudes. These spectral parameters give the sought four peak parameters (position, width, height, phase) for each of the K Lorentzian resonances in the spectra computed by both variants of the FPT.

For the same input Maclaurin sum (7.1), the uniqueness of the FPT implies that the $\text{FPT}^{(+)}$ and the $\text{FPT}^{(-)}$ must yield the identical frequencies and amplitudes $\{\omega_k^+, d_k^+\}$ and $\{\omega_k^-, d_k^-\}$. Moreover, these reconstructed spectral parameters ought to be equal to the true complex frequencies and amplitudes $\{\omega_k, d_k\}$ from the given FID:

$$\omega_k^+ = \omega_k^- = \omega_k, \quad d_k^+ = d_k^- = d_k. \quad (7.30)$$

These equalities are satisfied when the values for all the retrieved spectral parameters $\{\omega_k^\pm, d_k^\pm\}$ have converged as a function of the increased number of the signal points, as demonstrated in Section 8. Furthermore, in this self-contained cross-checking, the FPT can also discriminate with certainty between the genuine and spurious resonances.

The overall significance of this kind of an intrinsic cross-validation within the $\text{FPT}^{(\pm)}$ is in avoiding altogether the conventional need to compare different processors that could mutually agree, but this would not necessarily mean that they reconstructed the true spectral parameters. The $\text{FPT}^{(+)}$ and the $\text{FPT}^{(-)}$ have a joint conceptual design for a system response function through the Green–Padé functions $G_K^+(z)$ and $G_K^-(z^{-1})$ within the same general Padé mathematical methodology. Nevertheless, these versions of the FPT are computationally so complementary that they should rightly be conceived as the two distinct strategies for the same problem. Their essential difference is in that the $\text{FPT}^{(-)}$ accelerates slowly convergent series [21], whereas the $\text{FPT}^{(+)}$ transforms divergent series into convergent ones by the Cauchy analytical continuation principle [22]. As mentioned, for the diagonal cases $[K/K]_{G_N}(z^{-1})$, the optimal performances of the $\text{FPT}^{(-)}$ and the $\text{FPT}^{(+)}$ are anticipated for $N = 2K$ and $N > 2K$, respectively. The two conditions $N = 2K$ and $N > 2K$ give, respectively, the algebraically determined and over-determined system of linear equations for the expansion coefficients p_r^\pm and q_s^\pm of the polynomials $P_K^\pm(z^{\pm 1})$ and $Q_K^\pm(z^{\pm 1})$ that are the most critical part of the computation. These expansion coefficients must be determined very accurately to provide the highest precision for the reconstructed fundamental frequencies and amplitudes. Such accuracy is achieved in the present computations and the results are illustrated in Section 8.

Having carried out an accurate extraction of all the fundamental frequencies and amplitudes $\{\omega_k^\pm, d_k^\pm\}$ from the input FID, the Green–Padé spectra can immediately be constructed in their complex modes given by the Heaviside partial fractions:

$$\tilde{G}_K^\pm(z^{\pm 1}) = \frac{\tilde{P}_{K-1}^\pm(z^{\pm 1})}{Q_K^\pm(z^{\pm 1})} = \sum_{k=1}^K \frac{d_k^\pm}{z^{\pm 1} - z_k^\pm}. \quad (7.31)$$

An alternative representation can also be set up by using exclusively the roots of the numerator and denominator polynomials. Thus, solving the equation:

$$\tilde{P}_{K-1}^\pm(z^{\pm 1}) = 0, \quad (7.32)$$

will give the roots that we denote by $\{\tilde{z}_k^\pm\}$ ($1 \leq k \leq K-1$),

$$\tilde{z}_k^\pm \equiv e^{\pm i\omega_k^\pm \tau}. \quad (7.33)$$

Therefore, using the two sets of roots $\{z_k^\pm\}$ and $\{\tilde{z}_k^\pm\}$ we can express $\tilde{G}_K^\pm(z^{\pm 1})$ in the canonical forms that are equivalent to (7.31):

$$\frac{\tilde{P}_{K-1}^\pm(z^{\pm 1})}{Q_K^\pm(z^{\pm 1})} = \frac{\tilde{p}_{K-1}^\pm}{q_K^\pm} \frac{\prod_{k=1}^{K-1} (z^{\pm 1} - \tilde{z}_k^\pm)}{\prod_{k=1}^K (z^{\pm 1} - z_k^\pm)}. \quad (7.34)$$

Taking the Cauchy residues of (7.34) leads to the corresponding expressions for the Padé amplitudes:

$$d_k^\pm = \frac{\tilde{p}_{K-1}^\pm}{q_K^\pm} \frac{\prod_{k'=1}^{K-1} (z_k^\pm - \tilde{z}_{k'}^\pm)}{\prod_{k'=1, k' \neq k}^K (z_k^\pm - z_{k'}^\pm)}. \quad (7.35)$$

This is equivalent to (7.26). Such a procedure applies only to those line-shapes that are of the purely Lorentzian forms for a non-degenerate spectrum where all the fundamental frequencies are different from each other. This permits the reconstruction of the corresponding FID as a sum of K attenuated complex harmonics whose amplitudes d_k^\pm are independent

of time, *i.e.*, stationary:

$$c_n = \sum_{k=1}^K d_k^{\pm} e^{in\omega_k^{\pm}\tau}, \quad \text{Im}(\omega_k^{\pm}) > 0. \quad (7.36)$$

The outlined concept needs to be modified if some coincident (confluent) fundamental frequencies are present in the input FID. Here, more than one amplitude is associated with the same given frequency. This is described by the multiple roots of the characteristic polynomials $Q_K^{\pm}(z^{\pm 1})$. The associated line-shapes are non-Lorentzians and they correspond to the degenerate part of the whole spectrum. Let $J \leq K$ be the number of the degenerate fundamental frequencies in the input FID, and let the k th degenerate frequency has the multiplicity m_k whose maximal value is denoted by M_k :

$$M_k = \max\{m_k\}, \quad M_1 + M_2 + \cdots + M_J = K. \quad (7.37)$$

Here, $1 \leq m_k \leq M_k$, where $m_k > 1$ means that the k th root of Q_K^{\pm} is repeated m_k times. The case $m_k = 1$ corresponds to non-degeneracy. If all the multiplicities m_k of the k th root of $Q_K^{\pm}(z^{\pm 1})$ are taken into account, the Cauchy residues of the polynomial quotients $\tilde{P}_K^{\pm}(z^{\pm 1})/Q_K^{\pm}(z^{\pm 1})$ are obtained as:

$$D_{k,m_k}^{\pm} = \frac{\tilde{P}_{K-1}^{\pm}(z_k^{\pm})}{[(d/dz^{\pm 1})^{m_k} Q_K^{\pm}(z^{\pm 1})]_{z^{\pm 1}=z_k^{\pm}}}. \quad (7.38)$$

This generalises (7.26) to the case of the coinciding fundamental frequencies. The corresponding expressions that extend (7.31) to the case of the simultaneous presence of both simple and multiple roots of $Q_K^{\pm}(z^{\pm 1})$ in the $\text{FPT}^{(\pm)}$ are given by the mixed complex spectra:

$$\tilde{G}_K^{\pm}(z^{\pm 1}) = \frac{\tilde{P}_{K-1}^{\pm}(z^{\pm 1})}{Q_K^{\pm}(z^{\pm 1})} = \sum_{k=1}^J \sum_{m_k=1}^{M_k} \frac{D_{k,m_k}^{\pm}}{(z^{\pm 1} - z_k^{\pm})^{m_k}}. \quad (7.39)$$

From here, a general form of the FID can be reconstructed with the appearance of both degenerate and non-degenerate fundamental frequencies. In particular, the degenerate part of such an FID contains the confluent harmonics given by a linear combination of damped complex exponentials with the coefficients that are time-dependent (non-stationary) amplitudes $d_{k,n}^{\pm}$. This latter time dependence has the form of a polynomial of degree M_k , so that the corresponding FID becomes:

$$c_n = \sum_{k=1}^J d_{k,n}^{\pm} e^{in\omega_k^{\pm}\tau}, \quad \text{Im}(\omega_k^{\pm}) > 0, \quad (7.40)$$

$$d_{n,k}^{\pm} = \sum_{m_k=1}^{M_k} D_{k,m_k}^{\pm} (n\tau)^{m_k-1}. \quad (7.41)$$

It is seen that very simple analytical formulae also exist in the $\text{FPT}^{(\pm)}$ for degenerate amplitudes of non-Lorentzian spectral line-shapes with confluent resonances that have exactly the same real parts of their complex fundamental frequencies. This analysis proves that the two Green–Padé variants, the $\text{FPT}^{(+)}$ and the $\text{FPT}^{(-)}$, can treat both Lorentzian and non-Lorentzian spectra on the same footing. These non-degenerate and degenerate spectra are associated with FIDs described by the linear combinations of K attenuated complex exponentials with stationary and non-stationary amplitudes, respectively.

7.3. Determination of the exact number of resonances by the concept of the Froissart doublets (pole–zero cancellations)

The accurate reconstruction of the unknown true number K of the genuine resonances in the given FID is essential. This number is determined exactly in the FPT. In the FPT, K can be retrieved in both the time and the frequency domain analysis, using the Shanks transform [5] and the Froissart doublets [37], respectively. For either (7.36) or (7.40), the Shanks transform, $e_K(c_0)$, is proportional to a quotient of two Hankel determinants:

$$e_K(c_0) \propto \frac{H_K(c_0)}{H_{K+1}(c_0)}. \quad (7.42)$$

The analysis shows that whenever the given FID is comprised of exactly K non-degenerate or degenerate damped complex harmonics, (7.42) is reduced to:

$$e_K(c_0) = 0. \quad (7.43)$$

This result represents the signature for the detection of the exact K in the time domain. Numerically, the Hankel determinants are not computed directly, since this is not practical for high dimensions. Instead, the required ratio of such determinants is computed recursively using the Wynn ε -algorithm. The Wynn recursion is derived from a recursion which connects four neighbouring elements in a table of the Padé approximants of the varying order. In other words, the recursive algorithm for the Shanks transform is one of the algorithms of the general Padé methodology.

In the frequency domain, the exact Padé-reconstruction of the true number K can be accomplished by using the powerful concept of the Froissart doublets, *i.e.*, the pole–zero cancellations:

$$z_k^\pm = \tilde{z}_k^\pm. \quad (7.44)$$

Since K is not known prior to the analysis, the computation via the FPT would proceed by increasing gradually and systematically the order S in the Green–Padé functions $G_S^\pm(z^{\pm 1})$. These changes in S would cause the fluctuations in the reconstructed functions. Eventually, S would reach a value after which such fluctuations would cease to exist within a demanded level of accuracy. Such a value of the order S represents the sought K . This constancy of the reconstructed values is attained, *e.g.*, via (7.34) which leads to cancellation of all the terms in the Padé numerator and denominator polynomials, when the computation is continued beyond the stabilised value of the order in the Green–Padé functions:

$$\frac{P_{K+m}^\pm(z^{\pm 1})}{Q_{K+m}^\pm(z^{\pm 1})} = \frac{P_K^\pm(z^{\pm 1})}{Q_K^\pm(z^{\pm 1})}, \quad m = 1, 2, 3, \dots \quad (7.45)$$

Moreover, it follows from (7.35) that whenever $z_k^\pm = \tilde{z}_k^\pm$, the amplitudes of the poles from the Froissart doublets are zero:

$$d_k^\pm = 0 \quad \text{for } z_k^\pm = \tilde{z}_k^\pm. \quad (7.46)$$

Further, pole–zero cancellations also take place if the computations find multiplicities in $\{z_k^\pm\}$ even for an FID whose spectrum is known to be non-degenerate. In such a case, the same degeneracies also appear in $\{\tilde{z}_k^\pm\}$, and this gives the degenerate Froissart doublets whose subsequent elimination via the pole–zero cancellations yields the non-degenerate

spectrum. Moreover, the pole–zero cancellation also occurs prior to detection of the true K for all the spurious poles that are cancelled by the corresponding spurious zeros. In other words, the Froissart doublets represent a powerful way of deciding whether a reconstructed resonance is genuine or spurious. Spurious resonances can appear in spectral analysis based upon both noise-free and noise-corrupted (synthesised or encoded) FIDs. Therefore, the concept of the Froissart doublets could advantageously be used as a robust and reliable procedure for separating the physical from non-physical (noise) information. In the end, all the Froissart doublets are discarded, so that the list of the reconstructed spectral parameters $\{\omega_k^\pm, d_k^\pm\}$ contains only the physical information. The outlined main properties of mathematical modelling via the Green–Padé functions illustrate the optimal suitability of the FPT for solving reconstruction problems from MRS.

8. RESULTS

Guided by the type of time signals customarily encountered in MRS, we shall study a synthesised noise-free FID, which is a linear combination of K damped complex exponentials with stationary amplitudes as in (7.36):

$$c_n = \sum_{k=1}^K d_k e^{in\omega_k\tau}, \quad \text{Im}(\omega_k) > 0, 0 \leq n \leq N-1, \quad (8.1)$$

where $K = 25$ and $N = 1024$. The corresponding exact complex-valued spectrum is given by the finite-rank Green function (7.1). Reconstruction of the spectral parameters from such noiseless FIDs is essential for formulating the unambiguous theoretical standards for the validity assessments of an adequately designed estimator, such as the FPT. In fact, the quantification problem in MRS can be kept under full control throughout the analysis only with synthesised noise-free FIDs. In such a case, one knows exactly all the expectation from the theory, so that the remaining part of the investigation can be focused on testing the appropriateness of the employed algorithms. Subsequently, corrupting such idealised FIDs with random Gaussian noise, and solving the quantification problem, will enable one to get a handle on more realistic data that are reminiscent of *in vivo* FIDs encoded via MRS. In both noise-free and noise-corrupted synthesised FIDs, the true spectral parameters are recognised through detection of their stability or constancy for gradually varying the partial signal length N/M ($M > 1$). This anticipated constancy of reconstructed parameters is predicted by the well-known Hazi–Taylor stabilisation method from resonant scattering theory [38]. According to the stabilisation method, the computed eigenenergies will attain their constant values if the dimension of the used finite-rank Hamiltonian matrix is augmented by systematically enlarging the size of the box in which the examined physical system is enclosed. Such a procedure can readily be implemented in the FPT with the purpose of disentangling the physical part of the FID from its noise. This is accomplished by differentiating the stable from unstable transients. The former and the latter transients are identified as genuine (physical) and non-physical (spurious, noisy), respectively. This procedure has been tested and shown to be reliable within the FPT applied to ion cyclotron resonance mass spectroscopy (ICRMS) [17,18] and to nuclear magnetic resonance (NMR) [19]. Similarly, the FPT has also been tested using encoded FIDs from MRS as reported in [11] and [20–25]). In these studies, the convergence rate and resolving power of the FPT for envelope spectra have been established in relation to the FFT. Com-

parative analyses within the FPT and the FFT are important whenever the FFT spectra with the full FID are of such a high quality that they could be used as the gold standard in their own category of envelope spectra. This was indeed the case in the investigations from [11] and [20–25] focused on FIDs of high SNR as encoded via MRS [39] at the magnetic field strengths of 4 T and 7 T from a healthy human brain. One of the main conclusions that emerged from these investigations was that the FPT achieves at least twice better resolution than the FFT for the same fraction N/M of the full signal length N . Remarkably, this was the case even for $M = 2$ when $N/2$ signal points are used in both the FPT and FFT. These findings are equivalent to saying that the FPT can reach the same resolution as the FFT by exhausting only the first half $N/2$ of the full signal length N . Such a distinct out-performance of the FFT by the FPT for envelope spectra stemming from FIDs encoded with high SNR is expected to be even sharper for synthesised time signals [12].

Including the envelope spectra in the present work is instructive for the reason of facilitating a direct link between the results reported here and those from earlier investigations within MRS using the FPT. This, in turn, would permit another consistency check of our previous conclusions. Nevertheless, it is essential to go beyond comparisons between the Padé and Fourier envelope spectra, by reporting explicitly the results of quantifications. Of course, such results of the FPT for the numerical values of the spectral parameters reconstructed from *in vivo* MRS FIDs have also been implicitly present in our studies on envelope spectra. This was the case because such reported envelope spectra have systematically been constructed via the Heaviside partial fraction expansions that can be computed only after reconstruction of the complex frequencies and the corresponding amplitudes of all the physical resonances. The explicit reporting on these numerical values of the spectral parameters has not been made in the mentioned studies on MRS, since our initial interest was mainly in comparing the convergence rates of the FPT and the FFT. Such comparisons are possible only within envelope spectra, since these are the only spectra obtainable by the FFT. In an envelope spectrum of the FPT via the Heaviside representation, the sum is carried out over all the spectral parameters, so that the information on the inherently performed quantification is not transparent. For checking purposes, an envelope spectrum in the FPT could also be computed directly through a frequency-by-frequency evaluation of the defining polynomial quotient without prior reconstruction of the spectral parameters.

The current study goes beyond reporting on the envelope spectra by giving the explicit numerical values of the reconstructed spectral parameters. In this regard, the most stringent test is the exact retrieval of the known complex frequencies and amplitudes, and this becomes possible for a synthesised FID. Such a typical FID is considered in this section by choosing their spectral parameters reminiscent of the corresponding time signals encoded via MRS. The quantification problem for this synthesised FID will be solved using both variants of the FPT, inside and outside the unit circle, the $\text{FPT}^{(+)}$ and the $\text{FPT}^{(-)}$, respectively. Strictly, the theory of synthesised noise-free input FIDs predicts that these two versions of the FPT ought to yield the same results once convergence has been achieved in all the spectral parameters, and this is set up to be tested here. Such a testing is important, since with noisy FIDs encoded via MRS, as those studied in [11,24,25], the usage of both the $\text{FPT}^{(+)}$ and the $\text{FPT}^{(-)}$ is necessary for an intrinsic cross-validation of estimations. According to this cross-validation, the only acceptable reconstructions will be the ones found jointly by both the $\text{FPT}^{(+)}$ and the $\text{FPT}^{(-)}$. The algebraic structure of these two versions of the FPT are different, and designed to work in the two complementary regions of the complex plane for the harmonic variable z . The $\text{FPT}^{(+)}$ and the $\text{FPT}^{(-)}$ operate in

the first and the fourth quadrant of the complex z -plane, respectively. Critically, these two opposite regions are sharply different relative to the expected locations of spurious poles, stemming from the computations and the encoded FID. Thus, in the case of the $\text{FPT}^{(+)}$, it is anticipated that there will be a distinct separation of the physical poles (inside the unit circle, $|z| < 1$) from the non-physical ones (outside the unit circle, $|z| > 1$). This separation should advantageously facilitate robust and stable estimations by the $\text{FPT}^{(+)}$ whenever noise is present in the studied FIDs. Such an expectation needs to be checked, especially because the $\text{FPT}^{(+)}$ has to carry out the numerically difficult and ill-conditioned task of analytical continuation by inducing convergence into the input Maclaurin sum (7.1) which diverges inside the unit circle when N is increased. By contrast, the $\text{FPT}^{(-)}$ accelerates the already convergent input sum (7.1), and this is computationally easier than analytical continuation. However, the $\text{FPT}^{(-)}$ has its own challenge to separate the genuine from the spurious poles that are mixed together within the same region outside the unit circle. As such, the major properties of the $\text{FPT}^{(+)}$ and the $\text{FPT}^{(-)}$ are complementary to each other in more than one way. Therefore, each of these two versions of the FPT must strike a trade-off independently in order to achieve optimal performance. The outlined important differences between the $\text{FPT}^{(+)}$ and the $\text{FPT}^{(-)}$ lend support to the usage of both versions of the FPT even for noiseless FIDs for which the genuine resonances are known exactly, so that spurious poles can be identifiable with fidelity. The positive outcomes from the presently designed testing on a synthesised time signal should encourage similar scrutiny of the FPT while attempting to differentiate between the genuine and spurious resonances in FIDs encoded by means of MRS.

The present work has the focus on quantification of FIDs from MRS. For this reason, the synthesised FID is selected to have the main physical features of importance to clinical diagnostics that rely upon similar FIDs encoded via MRS. Such a similarity is accomplished by taking the concrete numerical values of the complex fundamental frequencies and the amplitudes in the synthesised FID to be reminiscent of the corresponding tabulated data from the MRS literature. Moreover, the FID generated theoretically with such spectral parameters gives the absorption total shape spectrum of the type of a similar highly resolved spectrum due to an FID encoded via MRS from a healthy human brain at short echo time (20 ms) at the magnetic field strength $B_0 = 1.5 \text{ T}$ [28].

The overall findings and the detailed interpretation from this section are expounded in Sections 8.1–8.5. These results are obtained employing a sequence of partial signal lengths N/M ($M = 8\text{--}32$) as well as the full length N of the FID.

- Section 8.1 reports the tabular data for all the numerical values of the spectral parameters (both the input and the reconstructed). This includes Section 8.1.1 via the exact input data (Table 1) and Sections 8.1.2–8.1.5 for convergence of numerical values of the Padé-reconstructed spectral parameters (Tables 2–5).
- Section 8.2 has Section 8.2.1 with the absorption total shape spectra (Fig. 1) and Section 8.2.2 for the comparative convergence rates of envelope spectra obtained using the FFT and the FPT for varying N/M (Figs. 2 and 3).
- Section 8.3 proceeds with Sections 8.3.1–8.3.4 for the residual or error spectra and the consecutive difference spectra (Figs. 4–7). Sections 8.3.1–8.3.4 constitute a part of the intrinsic error analysis in the FPT with no recourse to the FFT or to any other estimator.
- Section 8.4 contains the absorption component shape spectra and the envelope spectra (Sections 8.4.1 and 8.4.2 with Figs. 8 and 9). The absorption component shape spectra

refer to every individual resonance. The sum of all these elementary constituent spectra represents the corresponding absorption total shape spectra or the envelope spectra. On Fig. 8 also indicated are the acronyms via the map of the human brain MR-detectable metabolites corresponding to a part of the examined resonances.

- Section 8.5 is presented through six Sections. These are: Section 8.5.1 for the distributions of complex frequencies and amplitudes, as well as poles, depicted via the harmonic variables for the constituent resonances in the associated complex planes as reconstructed by the $\text{FPT}^{(+)}$ after full convergence (Fig. 10), Section 8.5.2 which is the same as Section 8.5.1, except for the usage of the $\text{FPT}^{(-)}$ (Fig. 11), Sections 8.5.3–8.5.6 with the convergence rates of the complex frequencies and the amplitudes of the reconstructed resonances for increasing partial signal length (Figs. 12–15).

8.1. Tabular data

8.1.1. Exact input data for the spectral parameters of 25 resonances

Table 1 shows the exact input data of all the spectral parameters for 25 complex attenuated exponentials that constitute the presently synthesised time signal (8.1). These parameters are the fundamental frequencies and the amplitudes. Hereafter, $\text{Re}(f_k)$ and $\text{Im}(f_k)$ are the real and imaginary parts of the complex frequencies, respectively. The real-valued frequencies $\text{Re}(f_k)$ are equivalently called the chemical shifts. The quantities $|d_k|$ represent the absolute values of the corresponding amplitudes. All the individual phases ϕ_k of the amplitudes d_k are chosen with the zero values, so that $d_k = |d_k| \exp(i\phi_k) = |d_k|$. Such a selection for phases is customary for spectral analysis of synthesised FIDs in MRS [40]. Of course, this is not a restriction at all to the FPT which can process FIDs with any phases ϕ_k . The decay time constants $\{\lambda_k\}$ are also given in Table 1. They are proportional to the transverse relaxation times T_{2k} that are connected with the inverses of the imaginary frequency by:

$$\text{Im}(f_k)[\text{ppm}] = \frac{1}{\lambda_k[\text{s}]f_L[\text{Hz}]}, \quad (8.2)$$

where f_L is the Larmor precession frequency, which is equal to 63.864 MHz at $B_0 = 1.5$ T. As usual in MRS, the frequencies $\text{Re}(f_k)$ and $\text{Im}(f_k)$ are given in the dimensionless units of parts per million (ppm), λ_k is expressed in seconds (s), and $|d_k|$ in arbitrary units (au). Furthermore, chemical shifts $\text{Re}(f_k)$ given in ppm and hertz (Hz) are related by:

$$\text{Re}(f_k)[\text{ppm}] = 4.68 - \frac{1}{f_L} \text{Re}(f_k)[\text{Hz}], \quad (8.3)$$

where 4.68 ppm is the resonance frequency of water. In the case of imaginary frequencies $\text{Im}(f_k)$ expressed in ppm and Hz the following relationship exists:

$$\text{Im}(f_k)[\text{ppm}] = \frac{1}{f_L} \text{Im}(f_k)[\text{Hz}]. \quad (8.4)$$

The fundamental spectral parameters yield directly the peak areas for the resonances. Moreover, each peak area is proportional to the dimensionless concentration of the given metabolite, C_{met} , associated with the considered resonance. In this relationship, the proper

Table 1. Twelve digit accurate numerical values for all the input spectral parameters: the real $\text{Re}(f_k)$ and the imaginary $\text{Im}(f_k)$ part of the complex frequencies f_k , and the absolute values $|d_k|$ of the complex amplitudes d_k of 25 damped complex exponentials from the synthesised time signal (8.1) similar to a short echo time (~ 20 ms) encoded FID via MRS at the magnetic field strength $B_0 = 1.5$ T from a healthy human brain [28]. Every phase $\{\phi_k\}$ of the amplitudes is equal to zero, *i.e.*, each d_k is purely real, $d_k = |d_k| \exp(i\phi_k) = |d_k|$. Damping constants λ_k in seconds are the inverses of $\text{Im}(f_k)$ in hertz. For further details, see Section 8.1.1

Input data for spectral parameters of a synthesised time signal or FID				
k	$\text{Re}(f_k)$ [ppm]	$\text{Im}(f_k)$ [ppm]	λ_k [s]	$ d_k $ [au]
1	0.98502473596	0.17990454132	0.08703656793	0.12201438595
2	1.11200735795	0.25658576222	0.06102549766	0.16102435946
3	1.54801569651	0.17204176445	0.09101437597	0.13503495848
4	1.68903251243	0.11770094141	0.13303439755	0.03401357349
5	1.95901267177	0.06238000851	0.25101429458	0.05600564965
6	2.06502549764	0.03125251772	0.50102439657	0.17102439945
7	2.14500325695	0.05002523921	0.31300747541	0.11603475947
8	2.26101647683	0.06237900579	0.25101832954	0.09202435471
9	2.41102372957	0.06237378866	0.25103932547	0.08501859743
10	2.51903189374	0.03599397181	0.43502489568	0.03700394835
11	2.67601743561	0.03282529729	0.47701849258	0.00803647948
12	2.67601743562	0.06237738980	0.25102483259	0.06301432946
13	2.85502875659	0.01612534721	0.97103483280	0.00502795766
14	3.00901597366	0.06391028570	0.24500397175	0.06503678451
15	3.06703789325	0.03599475800	0.43501539396	0.10101385935
16	3.23902967517	0.05002180933	0.31302893761	0.09600832983
17	3.30101465479	0.06390252530	0.24503372532	0.06502839735
18	3.48103472769	0.03106586849	0.50403463972	0.01101473944
19	3.58401439546	0.02821222528	0.55501732587	0.03603369658
20	3.69403619626	0.03632796252	0.43102537951	0.04101734593
21	3.80302562621	0.02390555006	0.65500579542	0.03102743954
22	3.94401583739	0.04153212404	0.37701596520	0.06800491864
23	3.96503824982	0.06237466622	0.25103579355	0.01303736963
24	4.27101643509	0.05493564932	0.28502937575	0.01601435735
25	4.68000000000	0.13614144169	0.11501474964	0.11302794375

dimension of the concentration is introduced through the constant of proportionality as an overall multiplying factor. Such a proportionality constant represents the concentration of a reference metabolite, C_{ref} , which is expressed in units of mMol/gr per wet weight (ww). Different numerical values for C_{ref} are chosen for different tissues. For example, for FIDs encoded via MRS in, *e.g.*, grey matter of the healthy human brain, the reference metabolite is frequently taken to be NAA (nitrogen acetyl aspartate) or H_2O (water), in which case the usual concentrations are $C_{\text{ref}}(\text{NAA}) = 6$ mMol/(gr ww) [28] or $C_{\text{ref}}(\text{H}_2\text{O}) = 85$ mMol/(gr ww) [41].

The presentation of the results and their analysis is facilitated by referring to resonances by their numbers k where $1 \leq k \leq K$ ($K = 25$). These numbers are ordered in such a way that the first resonance is a lipid (Lip) and the 25th is water (H_2O). In, *e.g.*, proton MRS, the following abbreviations are used for some of the major MR-detectable metabolites: H_2O , Cho (choline), Cr (creatine), Glu (glutamine), Gln (glutamate), Ins (inositol), NAA, Ala (alanine), Lip, *etc.* High-quality *in vivo* FIDs encoded via proton MRS are obtained with excellent shimming and water suppression. In such FIDs, the residual water content does not seriously disturb determination of concentration of the neighbouring metabolites. To mimic this situation closely, the presently synthesised FID is set up to contain the residual water metabolite. This resonance will have a small and broad shape determined by the chosen values of the parameters $|d_{25}|$ and $\text{Im}(f_{25})$ seen at the chemical shift 4.68 ppm on the 25th line in Table 1. Inspection of the values of all the other fundamental parameters for the synthesised FID from Table 1 indicates that the corresponding exact absorption spectrum, defined as the real part of the associated complex-valued spectrum, will possess a variety of structures, including isolated, overlapped, tightly overlapped, and nearly degenerate resonances. In particular, the exact absorption component shape spectra for the clinically most informative chemical shifts (0–5 ppm), will have isolated, but still closely packed resonances, that are associated with the following 10 peaks: $k = 8, 9, 10, 13, 18, 19, 20, 21, 24, 25$ located at chemical shifts 2.261 ppm, 2.411 ppm, 2.519 ppm, 2.855 ppm, 3.481 ppm, 3.584 ppm, 3.694 ppm, 3.803 ppm, 4.271 ppm, 4.680 ppm, respectively. Additionally, the overlapped resonances will appear corresponding to these 11 peaks: $k = 1, 2$ (0.985 ppm, 1.112 ppm), $k = 3, 4$ (1.548 ppm, 1.689 ppm), $k = 5, 6, 7$ (1.959 ppm, 2.065 ppm, 2.145 ppm), $k = 14, 15$ (3.009 ppm, 3.067 ppm), and $k = 16, 17$ (3.239 ppm, 3.301 ppm). Also, the tightly overlapped resonances will show up as the following 2 peaks: $k = 22, 23$ (3.944 ppm, 3.965 ppm). These latter resonances are apart from each other by 0.021 ppm. Further, there will be almost degenerate resonances emerging at these 2 peaks separated by 10^{-11} ppm: $k = 11, 12$ (2.67601742561 ppm, 2.67601742562 ppm). Such two nearly coincident peaks, in the absorption total shape spectrum, will be unresolved in their appearance as a single resonance. Conceivably, in this doublet of near degeneracy, all the conventional fitting techniques would fail to detect the small peak which is $k = 11$. Indeed there is no justifiable reason to initialise fitting using two peaks for a resonance which manifestly appears as a single structure. Even if here a fitting begins with the two pre-assigned modelling resonances, disregarding the appearance of a bell-shaped single peak, then no rationale could be given for avoiding to select, *e.g.*, 3 or 4 or a higher number of small peaks below the dominant peak $k = 12$ in the $k = 11$ and 12 doublet. This points to one of the basic ambiguities with fittings from MRS such as VAPRO, AMARES, LCModel, *etc.* Specifically, the drawback of these fittings is in their non-uniqueness in dealing with the inverse quantification problem in MRS. This near-degeneracy $k = 11$ and 12 in the presently synthesised FID raises substantially the overall challenge for spectral analysis by any estimator, including the FPT.

8.1.2. Convergence of numerical values of the reconstructed spectral parameters for varying signal length N/M ($M = 1\text{--}32$)

Table 2 displays the detailed convergence rates of the numerical values of the complex frequencies and amplitudes for the reconstructed resonances by the $\text{FPT}^{(-)}$ using 6 partial signal lengths ($N/32 = 32$, $N/16 = 64$, $N/8 = 128$, $N/4 = 256$, $N/2 = 512$) as well as the full FID ($N = 1024$). In particular, panels (i)–(iii) of Table 2 display the spectral

Table 2. Convergence rates within 4 digit accuracy for the numerical values of the complex frequencies and amplitudes reconstructed by solving the quantification problem in the $\text{FPT}^{(-)}$ at systematically increased signal length. For further details, see Section 8.1.2

Convergence of spectral parameters in fast Padé transform, $\text{FPT}^{(-)}$: signal length N/M , $N = 1024$

k	$\text{Re}(f_k^-)$ [ppm]	$\text{Im}(f_k^-)$ [ppm]	$ d_k^- $ [au]	k	$\text{Re}(f_k^-)$ [ppm]	$\text{Im}(f_k^-)$ [ppm]	$ d_k^- $ [au]
(i) $M = 32, N/32 = 32$				(ii) $M = 16, N/16 = 64$			
1	1.010	0.205	0.223	1	0.989	0.180	0.130
3	1.514	0.421	0.251	2	1.121	0.241	0.148
4	1.642	0.097	0.039	3	1.562	0.207	0.195
6	2.065	0.069	0.340	5	2.029	0.012	0.026
12	2.638	0.276	0.423	6	2.055	0.071	0.376
15	3.054	0.138	0.414	9	2.475	0.194	0.315
17	3.377	0.037	0.017	10	2.589	0.054	0.060
23	3.972	0.113	0.230	15	3.058	0.051	0.161
24	4.092	0.086	0.088	16	3.237	0.071	0.178
25	4.681	0.135	0.111	19	3.564	0.045	0.035
				21	3.778	0.068	0.075
				22	3.941	0.048	0.087
				24	4.269	0.055	0.016
				25	4.680	0.136	0.113

parameters of the detected 10, 14, and 20 resonances at $N/32 = 32$, $N/16 = 64$, and $N/8 = 128$, respectively. Of course, these latter findings represent only the approximate values for the corresponding exact input data for the parameters. This occurs because here the numbers of the used signal points ($N/M \leq 128$) are insufficient. Panels (iv)–(vi) of Table 2 show the spectral parameters found at $N/4 = 256$, $N/2 = 512$, and $N = 1024$, respectively. These latter results should be compared with the corresponding input data from Table 1. It then follows from, *e.g.*, panel (iv) of Table 2 for a quarter ($N/4 = 256$) of the full signal length N that the $\text{FPT}^{(-)}$ has retrieved the entire set of 25 resonances with all their exact values for every single spectral parameters. Moreover, it is stunning that these reconstructed spectral parameters remain totally unaltered, even after attaining full convergence, when further signal points are included beyond $N/4$. This is documented on panels (v) and (vi) for $N/2 = 512$ and $N = 1024$, respectively. Such a remarkable occurrence, as a unique feature of the Padé polynomial quotient, *e.g.*, P_K^-/Q_K^- , is credited to the pole–zero cancellation, or equivalently, the Froissart doublets, as analysed in Section 7.3. A sure signature of reconstruction of the true number K of resonances is provided by the attained convergence of the spectral parameters. If one keeps increasing K in the

Table 2. (Continued)

Convergence of spectral parameters in fast Padé transform, $\text{FPT}^{(-)}$: signal length N/M , $N = 1024$

k	$\text{Re}(f_k^-)$ [ppm]	$\text{Im}(f_k^-)$ [ppm]	$ d_k^- $ [au]	k	$\text{Re}(f_k^-)$ [ppm]	$\text{Im}(f_k^-)$ [ppm]	$ d_k^- $ [au]
(iii) $M = 8, N/8 = 128$				(iv) $M = 4, N/4 = 256$			
1	0.985	0.180	0.122	1	0.985	0.180	0.122
2	1.112	0.256	0.160	2	1.112	0.257	0.161
3	1.546	0.169	0.123	3	1.548	0.172	0.135
4	1.704	0.133	0.051	4	1.689	0.118	0.034
5	2.014	0.073	0.347	5	1.959	0.062	0.056
6	2.044	0.043	0.329	6	2.065	0.031	0.171
7	2.157	0.036	0.039	7	2.145	0.050	0.116
				8	2.261	0.062	0.092
9	2.351	0.015	0.007	9	2.411	0.062	0.085
10	2.510	0.130	0.200	10	2.519	0.036	0.037
				11	2.676	0.033	0.008
12	2.654	0.049	0.061	12	2.676	0.062	0.063
13	2.809	0.018	0.001	13	2.855	0.016	0.005
				14	3.009	0.064	0.065
15	3.072	0.053	0.184	15	3.067	0.036	0.101
16	3.231	0.078	0.208	16	3.239	0.050	0.096
17	3.366	0.036	0.011	17	3.301	0.064	0.065
				18	3.481	0.031	0.011
19	3.588	0.021	0.024	19	3.584	0.028	0.036
20	3.700	0.041	0.047	20	3.694	0.036	0.041
21	3.803	0.027	0.037	21	3.803	0.024	0.031
22	3.944	0.045	0.084	22	3.944	0.042	0.068
				23	3.965	0.062	0.013
24	4.271	0.055	0.016	24	4.271	0.055	0.016
25	4.680	0.136	0.113	25	4.680	0.136	0.113

ratio P_K^-/Q_K^- even after convergence has been achieved, the converged results for the Padé quotient in the $\text{FPT}^{(-)}$ will not change. This happens because the new poles from Q_{K+m}^- will be precisely the same as the new zeros of P_{K+m}^- . In such a case, the pole–zero cancellation occurs in the Padé quotient, $P_{K+m}^-/Q_{K+m}^- = P_K^-/Q_K^-$, as per (7.45), where m is any positive integer. This is checked to hold true exactly in the present computation as seen on panels (iv)–(vi) of Table 2. Synergistically, the same computation proves that all the amplitudes $\{d_k^-\}$ associated with the poles from the Froissart doublets are identical to zero, as in (7.46). Theoretically, the strict algebraic condition $2K = N$ implies that only 50 time signal points should suffice for the $\text{FPT}^{(-)}$ to reconstruct exactly all the 25 unknown complex frequencies and 25 complex amplitudes. Instead, panel (iv) of Table 2 shows that full convergence is achieved with the first 256 time signal points. The reason for this is that the

Table 2. (*Continued*)

Convergence of spectral parameters in fast Padé transform, $\text{FPT}^{(-)}$: signal length N/M , $N = 1024$

k	$\text{Re}(f_k^-)$ [ppm]	$\text{Im}(f_k^-)$ [ppm]	$ d_k^- $ [au]	k	$\text{Re}(f_k^-)$ [ppm]	$\text{Im}(f_k^-)$ [ppm]	$ d_k^- $ [au]
(v) $M = 2, N/2 = 512$				(vi) $M = 1, N = 1024$			
1	0.985	0.180	0.122	1	0.985	0.180	0.122
2	1.112	0.257	0.161	2	1.112	0.257	0.161
3	1.548	0.172	0.135	3	1.548	0.172	0.135
4	1.689	0.118	0.034	4	1.689	0.118	0.034
5	1.959	0.062	0.056	5	1.959	0.062	0.056
6	2.065	0.031	0.171	6	2.065	0.031	0.171
7	2.145	0.050	0.116	7	2.145	0.050	0.116
8	2.261	0.062	0.092	8	2.261	0.062	0.092
9	2.411	0.062	0.085	9	2.411	0.062	0.085
10	2.519	0.036	0.037	10	2.519	0.036	0.037
11	2.676	0.033	0.008	11	2.676	0.033	0.008
12	2.676	0.062	0.063	12	2.676	0.062	0.063
13	2.855	0.016	0.005	13	2.855	0.016	0.005
14	3.009	0.064	0.065	14	3.009	0.064	0.065
15	3.067	0.036	0.101	15	3.067	0.036	0.101
16	3.239	0.050	0.096	16	3.239	0.050	0.096
17	3.301	0.064	0.065	17	3.301	0.064	0.065
18	3.481	0.031	0.011	18	3.481	0.031	0.011
19	3.584	0.028	0.036	19	3.584	0.028	0.036
20	3.694	0.036	0.041	20	3.694	0.036	0.041
21	3.803	0.024	0.031	21	3.803	0.024	0.031
22	3.944	0.042	0.068	22	3.944	0.042	0.068
23	3.965	0.062	0.013	23	3.965	0.062	0.013
24	4.271	0.055	0.016	24	4.271	0.055	0.016
25	4.680	0.136	0.113	25	4.680	0.136	0.113

$\text{FPT}^{(-)}$ produces both genuine and spurious resonances. Namely, in the polynomial quotient P_K^-/Q_K^- , spurious poles and spurious zeros from the denominator and the numerator, respectively, come in the pairs as the Froissart doublets and, therefore, cancel each other. In this way, every addition of more time signal points yields new Froissart doublets, but simultaneously another process takes place, and that is stabilisation of the values of the reconstructed physical spectral parameters. Ultimately, a saturation is attained when the total number of genuine resonances ceases to fluctuate as prescribed by (7.45). In this case, all the spectral parameters become constant for varying partial signal length. The described stabilisation is the pattern through which the $\text{FPT}^{(-)}$ determines, with certainty, the true total number K of genuine resonances. Here, for the studied FID, such a stabilisation occurs by actually using less than a quarter $N/4 = 256$ of the full FID by exhausting the

first 200 signal points (not shown in Table 2 where all the signal lengths are of the form 2^s with s being a positive integer). This would give $K = 100$, but the elimination of all the Froissart doublets finally gives the exact total number $K = 25$ of the genuine resonances in a Froissart-cleaned spectrum.

8.1.3. Numerical values of the reconstructed spectral parameters near full convergence for 3 partial signal lengths $N_P = 180, 220, 260$

Table 3 for the reconstructed spectral parameters from the $FPT^{(+)}$ (left column) and the $FPT^{(-)}$ (right column) zooms into a narrow convergence range with 3 partial signal lengths $N_P = 180, 220, 260$. This is suggested by Table 2 where all the parameters are seen to

Table 3. Convergence rates within 4 digit accuracy for the numerical values of the complex frequencies and amplitudes reconstructed by solving the quantification problem in the $FPT^{(+)}$ and $FPT^{(-)}$ at three partial signal lengths near convergence: $N_P = 180, 220, 260$. For further details, see Section 8.1.3

Spectral parameters near full convergence, $FPT^{(+)}$ (left) and $FPT^{(-)}$ (right)							
k	$\text{Re}(f_k^+)$ [ppm]	$\text{Im}(f_k^+)$ [ppm]	$ d_k^+ $ [au]	k	$\text{Re}(f_k^-)$ [ppm]	$\text{Im}(f_k^-)$ [ppm]	$ d_k^- $ [au]
(i) $N_P = 180$				(iv) $N_P = 180$			
1	0.985	0.180	0.122	1	0.985	0.180	0.122
2	1.112	0.257	0.161	2	1.112	0.257	0.161
3	1.548	0.172	0.135	3	1.548	0.172	0.135
4	1.689	0.118	0.034	4	1.689	0.118	0.034
5	1.959	0.062	0.056	5	1.959	0.062	0.056
6	2.065	0.031	0.171	6	2.065	0.031	0.171
7	2.145	0.050	0.115	7	2.145	0.050	0.115
8	2.261	0.063	0.094	8	2.261	0.063	0.094
9	2.411	0.064	0.089	9	2.411	0.064	0.089
10	2.518	0.036	0.036	10	2.518	0.036	0.037
12	2.676	0.054	0.066	12	2.676	0.054	0.066
13	2.855	0.014	0.004	13	2.856	0.015	0.004
14	3.014	0.054	0.058	14	3.011	0.059	0.059
15	3.065	0.037	0.113	15	3.066	0.037	0.108
16	3.242	0.054	0.121	16	3.240	0.051	0.104
17	3.302	0.052	0.044	17	3.299	0.060	0.061
18	3.482	0.027	0.009	18	3.480	0.030	0.011
19	3.585	0.028	0.036	19	3.584	0.028	0.035
20	3.694	0.037	0.042	20	3.694	0.036	0.041
21	3.803	0.024	0.031	21	3.803	0.024	0.031
22	3.945	0.042	0.072	22	3.944	0.041	0.067
23	3.970	0.057	0.010	23	3.964	0.061	0.014
24	4.271	0.055	0.016	24	4.271	0.055	0.016
25	4.680	0.136	0.113	25	4.680	0.136	0.113

Table 3. (*Continued*)

Spectral parameters near full convergence, FPT ⁽⁺⁾ (left) and FPT ⁽⁻⁾ (right)							
k	$\text{Re}(f_k^+)$ [ppm]	$\text{Im}(f_k^+)$ [ppm]	$ d_k^+ $ [au]	k	$\text{Re}(f_k^-)$ [ppm]	$\text{Im}(f_k^-)$ [ppm]	$ d_k^- $ [au]
(ii) $N_P = 220$				(v) $N_P = 220$			
1	0.985	0.180	0.122	1	0.985	0.180	0.122
2	1.112	0.257	0.161	2	1.112	0.257	0.161
3	1.548	0.172	0.135	3	1.548	0.172	0.135
4	1.689	0.118	0.034	4	1.689	0.118	0.034
5	1.959	0.062	0.056	5	1.959	0.062	0.056
6	2.065	0.031	0.171	6	2.065	0.031	0.171
7	2.145	0.050	0.116	7	2.145	0.050	0.116
8	2.261	0.062	0.092	8	2.261	0.062	0.092
9	2.411	0.062	0.085	9	2.411	0.062	0.085
10	2.519	0.036	0.037	10	2.519	0.036	0.037
11	2.676	0.031	0.007	11	2.676	0.033	0.008
12	2.676	0.062	0.064	12	2.676	0.062	0.063
13	2.855	0.016	0.005	13	2.855	0.016	0.005
14	3.009	0.064	0.065	14	3.009	0.064	0.065
15	3.067	0.036	0.101	15	3.067	0.036	0.101
16	3.239	0.050	0.096	16	3.239	0.050	0.096
17	3.301	0.064	0.065	17	3.301	0.064	0.065
18	3.481	0.031	0.011	18	3.481	0.031	0.011
19	3.584	0.028	0.036	19	3.584	0.028	0.036
20	3.694	0.036	0.041	20	3.694	0.036	0.041
21	3.803	0.024	0.031	21	3.803	0.024	0.031
22	3.944	0.042	0.068	22	3.944	0.042	0.068
23	3.965	0.062	0.013	23	3.965	0.062	0.013
24	4.271	0.055	0.016	24	4.271	0.055	0.016
25	4.680	0.136	0.113	25	4.680	0.136	0.113

have reached their convergence in the interval $[N/8, N/4] = [128, 256]$. Prior to full convergence, at the lowest partial signal length considered in Table 3 ($N_P = 180$) on panels (i) and (iv), the peak $k = 11$ is undetected in the FPT^(±). However, full convergence of the whole set of the unknowns in both versions of the FPT is reached at $N_P = 220$ on panels (ii) and (v). This convergence is maintained at $N_P = 260$ on panels (iii) and (vi).

8.1.4. Extended accuracy of numerical values of the reconstructed spectral parameters near full convergence for partial signal lengths $N_P = 180, 220$

Table 4 shows the extended number of digits to highlight the achieved accuracy of the reconstructed spectral parameters from the FPT⁽⁻⁾ near full convergence at the 2 partial signal lengths $N_P = 180, 220$. On panel (i) at $N_P = 180$, prior to full convergence, the

Table 3. (Continued)

Spectral parameters near full convergence, $\text{FPT}^{(+)}$ (left) and $\text{FPT}^{(-)}$ (right)							
k	$\text{Re}(f_k^+)$ [ppm]	$\text{Im}(f_k^+)$ [ppm]	$ d_k^+ $ [au]	k	$\text{Re}(f_k^-)$ [ppm]	$\text{Im}(f_k^-)$ [ppm]	$ d_k^- $ [au]
(iii) $N_P = 260$				(vi) $N_P = 260$			
1	0.985	0.180	0.122	1	0.985	0.180	0.122
2	1.112	0.257	0.161	2	1.112	0.257	0.161
3	1.548	0.172	0.135	3	1.548	0.172	0.135
4	1.689	0.118	0.034	4	1.689	0.118	0.034
5	1.959	0.062	0.056	5	1.959	0.062	0.056
6	2.065	0.031	0.171	6	2.065	0.031	0.171
7	2.145	0.050	0.116	7	2.145	0.050	0.116
8	2.261	0.062	0.092	8	2.261	0.062	0.092
9	2.411	0.062	0.085	9	2.411	0.062	0.085
10	2.519	0.036	0.037	10	2.519	0.036	0.037
11	2.676	0.033	0.008	11	2.676	0.033	0.008
12	2.676	0.062	0.063	12	2.676	0.062	0.063
13	2.855	0.016	0.005	13	2.855	0.016	0.005
14	3.009	0.064	0.065	14	3.009	0.064	0.065
15	3.067	0.036	0.101	15	3.067	0.036	0.101
16	3.239	0.050	0.096	16	3.239	0.050	0.096
17	3.301	0.064	0.065	17	3.301	0.064	0.065
18	3.481	0.031	0.011	18	3.481	0.031	0.011
19	3.584	0.028	0.036	19	3.584	0.028	0.036
20	3.694	0.036	0.041	20	3.694	0.036	0.041
21	3.803	0.024	0.031	21	3.803	0.024	0.031
22	3.944	0.042	0.068	22	3.944	0.042	0.068
23	3.965	0.062	0.013	23	3.965	0.062	0.013
24	4.271	0.055	0.016	24	4.271	0.055	0.016
25	4.680	0.136	0.113	25	4.680	0.136	0.113

number of the exact reconstructed digits varies from 2 to 7. However, on panel (ii) at $N_P = 220$, a spectacular increase in accuracy through all the 12 input digits is obtained for every single reconstructed spectral parameter. This demonstrates that the $\text{FPT}^{(-)}$ has the spectral convergence, *i.e.*, the exponential convergence rate to the exact numerical values of all the reconstructed fundamental frequencies and amplitudes.

8.1.5. *Extended accuracy of numerical values of the reconstructed spectral parameters at a quarter $N/4$ and the full signal length N*

Table 5 displays the extended number of digits for the obtained accuracy of the reconstructed spectral parameters from the $\text{FPT}^{(-)}$ at a quarter $N/4 = 256$ and the full signal length $N = 1024$ on panels (i) and (ii), respectively. These two panels give the identical

Table 4. Extended accuracy all the way up to 12 exact digits for the numerical values of the complex frequencies and amplitudes reconstructed by solving the quantification problem in the $\text{FPT}^{(-)}$ near full convergence at the partial signal lengths $N_P = 180, 220$. Notice, especially (Table 4 continued), that using only 220 signal points out of 1024 entries available from the full FID, the $\text{FPT}^{(-)}$ resolves unequivocally the two near degenerate frequencies separated from each other by 10^{-11} ppm. For further details, see Section 8.1.4

Frequency and amplitude quantification near full convergence, $\text{FPT}^{(-)}$						
k	$\text{Re}(f_k^-)$ [ppm]	Exact digits	$\text{Im}(f_k^-)$ [ppm]	Exact digits	$ d_k^- $ [au]	Exact digits
(i) Partial signal length $N_P = 180$						
Prior to full convergence: Accuracy with 2–7 exact digits						
1	0.9850348	5	0.1799096	6	0.1220452	5
2	1.1120277	5	0.2565547	5	0.1609685	4
3	1.5480023	5	0.1720240	5	0.1349621	4
4	1.6890921	4	0.1177028	6	0.0340169	5
5	1.9589387	4	0.0623701	5	0.0558901	4
6	2.0649992	4	0.0312327	4	0.1707180	4
7	2.1452561	4	0.0498941	3	0.1153226	3
8	2.2613813	4	0.0629439	3	0.0939629	3
9	2.4107480	4	0.0636112	3	0.0885553	3
10	2.5177852	3	0.0357790	4	0.0365775	4
12	2.6756790	4	0.0542728	2	0.0659905	2
13	2.8555634	3	0.0145633	3	0.0044935	3
14	3.0111192	3	0.0585441	3	0.0592624	2
15	3.0660875	3	0.0367422	3	0.1077829	2
16	3.2404581	3	0.0510575	3	0.1040292	2
17	3.2992316	3	0.0604341	3	0.0609218	2
18	3.4798617	3	0.0301797	3	0.0104799	3
19	3.5841194	4	0.0278830	4	0.0353843	3
20	3.6943017	4	0.0362691	5	0.0408387	4
21	3.8030785	4	0.0239524	4	0.0310989	4
22	3.9440716	4	0.0413624	3	0.0670324	3
23	3.9638513	2	0.0613914	3	0.0141695	3
24	4.2710159	6	0.0549367	6	0.0160150	5
25	4.6800001	7	0.1361411	7	0.1130274	6

12 digit accurate results, and the same is checked to be true also for one half of the full signal length, $N/2 = 512$. The joint findings from Tables 4 and 5 prove that the FPT remains stable beyond the stage at which full convergence is reached, so that adding further signal points does not change the stabilised results. Such a feature is very important for the overall robustness of the FPT in quantification within MRS.

Table 4. (Continued)

Frequency and amplitude quantification near full convergence, $FPT^{(-)}$						
k	$Re(f_k^-)$ [ppm]	Exact digits	$Im(f_k^-)$ [ppm]	Exact digits	$ d_k^- $ [au]	Exact digits
(ii) Partial signal length $N_p = 220$						
Full convergence: Machine accuracy with 12 exact digits						
1	0.98502473596	12	0.17990454132	12	0.12201438595	12
2	1.11200735795	12	0.25658576222	12	0.16102435946	12
3	1.54801569651	12	0.17204176445	12	0.13503495848	12
4	1.68903251243	12	0.11770094141	12	0.03401357349	12
5	1.95901267177	12	0.06238000851	12	0.05600564965	12
6	2.06502549764	12	0.03125251772	12	0.17102439945	12
7	2.14500325695	12	0.05002523921	12	0.11603475947	12
8	2.26101647683	12	0.06237900579	12	0.09202435471	12
9	2.41102372957	12	0.06237378866	12	0.08501859743	12
10	2.51903189374	12	0.03599397181	12	0.03700394835	12
11	2.67601743561	12	0.03282529729	12	0.00803647948	12
12	2.67601743562	12	0.06237738980	12	0.06301432946	12
13	2.85502875659	12	0.01612534721	12	0.00502795766	12
14	3.00901597366	12	0.06391028570	12	0.06503678451	12
15	3.06703789325	12	0.03599475800	12	0.10101385935	12
16	3.23902967517	12	0.05002180933	12	0.09600832983	12
17	3.30101465479	12	0.06390252530	12	0.06502839735	12
18	3.48103472769	12	0.03106586849	12	0.01101473944	12
19	3.58401439546	12	0.02821222528	12	0.03603369658	12
20	3.69403619626	12	0.03632796252	12	0.04101734593	12
21	3.80302562621	12	0.02390555006	12	0.03102743954	12
22	3.94401583739	12	0.04153212404	12	0.06800491864	12
23	3.96503824982	12	0.06237466622	12	0.01303736963	12
24	4.27101643509	12	0.05493564932	12	0.01601435735	12
25	4.68000000000	12	0.13614144169	12	0.11302794375	12

8.2. Absorption total shape spectra

8.2.1. Absorption total shape spectra or absorption envelope spectra

Figure 1 depicts, on panels (i) and (ii), the real $Re(c_n)$ and imaginary $Im(c_n)$ part, respectively, of the complex-valued synthesised FID $\{c_n\}$ ($0 \leq n \leq N - 1$) computed from (8.1) by employing the spectral parameters given in Table 1. The full signal length of the FID is $N = 1024$, the selected bandwidth is 1000 Hz, which sets the sampling rate to $\tau = 1$ ms, so that the total duration time is $T = N\tau = 1.024$ s. Panel (iii) of Fig. 1 shows the initial convergence regions of the $FPT^{(+)}$ and the $FPT^{(-)}$ situated inside and outside the unit circle $|z| < 1$ and $|z| > 1$ in the complex planes of the harmonic variables z^+ and z^- , respectively. However, since the Padé spectra are rational functions given by the quotients

Table 5. Persistent, twelve digit accuracy for the numerical values for all the 25 complex frequencies and amplitudes reconstructed by solving the quantification problem by the $\text{FPT}^{(-)}$ at $N/4 = 256$ and $N = 1024$. Constancy of all the spectral parameters is steadily maintained beyond the partial signal length $N_p = 220$ where the first machine accurate convergence occurs. For further details, see Section 8.1.5

Preserved machine accuracy for frequencies and amplitudes, $\text{FPT}^{(-)}$						
k	$\text{Re}(f_k^-)$ [ppm]	Exact digits	$\text{Im}(f_k^-)$ [ppm]	Exact digits	$ d_k^- $ [au]	Exact digits
(i) Signal length $N/4 = 256$						
Full convergence: Machine accuracy with 12 exact digits						
1	0.98502473596	12	0.17990454132	12	0.12201438595	12
2	1.11200735795	12	0.25658576222	12	0.16102435946	12
3	1.54801569651	12	0.17204176445	12	0.13503495848	12
4	1.68903251243	12	0.11770094141	12	0.03401357349	12
5	1.95901267177	12	0.06238000851	12	0.05600564965	12
6	2.06502549764	12	0.03125251772	12	0.17102439945	12
7	2.14500325695	12	0.05002523921	12	0.11603475947	12
8	2.26101647683	12	0.06237900579	12	0.09202435471	12
9	2.41102372957	12	0.06237378866	12	0.08501859743	12
10	2.51903189374	12	0.03599397181	12	0.03700394835	12
11	2.67601743561	12	0.03282529729	12	0.00803647948	12
12	2.67601743562	12	0.06237738980	12	0.06301432946	12
13	2.85502875659	12	0.01612534721	12	0.00502795766	12
14	3.00901597366	12	0.06391028570	12	0.06503678451	12
15	3.06703789325	12	0.03599475800	12	0.10101385935	12
16	3.23902967517	12	0.05002180933	12	0.09600832983	12
17	3.30101465479	12	0.06390252530	12	0.06502839735	12
18	3.48103472769	12	0.03106586849	12	0.01101473944	12
19	3.58401439546	12	0.02821222528	12	0.03603369658	12
20	3.69403619626	12	0.03632796252	12	0.04101734593	12
21	3.80302562621	12	0.02390555006	12	0.03102743954	12
22	3.94401583739	12	0.04153212404	12	0.06800491864	12
23	3.96503824982	12	0.06237466622	12	0.01303736963	12
24	4.27101643509	12	0.05493564932	12	0.01601435735	12
25	4.68000000000	12	0.13614144169	12	0.11302794375	12

of two polynomials, the Cauchy analytical continuation principle lifts the restrictions of the initial convergence regions. Specifically, the Cauchy principle extends the initial convergence region $|z| < 1$ to $|z| > 1$ for the $\text{FPT}^{(+)}$, and similarly $|z| > 1$ to $|z| < 1$ for the $\text{FPT}^{(-)}$. As such, both the $\text{FPT}^{(+)}$ and the $\text{FPT}^{(-)}$ remain computable throughout the complex frequency plane without encountering any divergent regions, with the exception of fundamental frequencies of the examined FID that are simultaneously the singular points (poles) of the system's response function. The small dots seen on panel (iii) rep-

Table 5. (Continued)

Preserved machine accuracy for frequencies and amplitudes, FPT ⁽⁻⁾						
k	$\text{Re}(f_k^-)$ [ppm]	Exact digits	$\text{Im}(f_k^-)$ [ppm]	Exact digits	$ d_k^- $ [au]	Exact digits
(ii) Signal length $N = 1024$						
Full convergence: Machine accuracy with 12 exact digits						
1	0.98502473596	12	0.17990454132	12	0.12201438595	12
2	1.11200735795	12	0.25658576222	12	0.16102435946	12
3	1.54801569651	12	0.17204176445	12	0.13503495848	12
4	1.68903251243	12	0.11770094141	12	0.03401357349	12
5	1.95901267177	12	0.06238000851	12	0.05600564965	12
6	2.06502549764	12	0.03125251772	12	0.17102439945	12
7	2.14500325695	12	0.05002523921	12	0.11603475947	12
8	2.26101647683	12	0.06237900579	12	0.09202435471	12
9	2.41102372957	12	0.06237378866	12	0.08501859743	12
10	2.51903189374	12	0.03599397181	12	0.03700394835	12
11	2.67601743561	12	0.03282529729	12	0.00803647948	12
12	2.67601743562	12	0.06237738980	12	0.06301432946	12
13	2.85502875659	12	0.01612534721	12	0.00502795766	12
14	3.00901597366	12	0.06391028570	12	0.06503678451	12
15	3.06703789325	12	0.03599475800	12	0.10101385935	12
16	3.23902967517	12	0.05002180933	12	0.09600832983	12
17	3.30101465479	12	0.06390252530	12	0.06502839735	12
18	3.48103472769	12	0.03106586849	12	0.01101473944	12
19	3.58401439546	12	0.02821222528	12	0.03603369658	12
20	3.69403619626	12	0.03632796252	12	0.04101734593	12
21	3.80302562621	12	0.02390555006	12	0.03102743954	12
22	3.94401583739	12	0.04153212404	12	0.06800491864	12
23	3.96503824982	12	0.06237466622	12	0.01303736963	12
24	4.27101643509	12	0.05493564932	12	0.01601435735	12
25	4.68000000000	12	0.13614144169	12	0.11302794375	12

resent both the exact input harmonic variables $z_k^{\pm 1} = \exp(\pm i\omega_k \tau)$ and the corresponding Padé counterparts $z_k^{\pm} = \exp(\pm i\omega_k^{\pm} \tau)$ reconstructed with $N/4 = 256$, where $\omega_k = 2\pi f_k$ and $\omega_k^{\pm} = 2\pi f_k^{\pm}$. Also drawn on panel (iii) are two small squares and circles inside and outside the unit circle locating the positions of the first and the 25th damped harmonics for lipid and water denoted by Lip and H₂O, respectively. These are the two end points of the complex harmonic variable interval within which all the 25 studied resonances are seen to reside. The similar small circles and squares for the remaining 23 resonances on both sides of the circumference $|z| = 1$ are not drawn on panel (iii) to avoid clutter. However, they will be shown at a later stage of the analysis on Figs. 10 and 11. Panels (iv) and (v) in Fig. 1 give the two Padé absorption envelope spectra from the Heaviside partial fractions of the FPT⁽⁺⁾ and the FPT⁽⁻⁾, respectively, computed using a quarter of the signal

TIME and FREQUENCY DOMAIN DATA in MAGNETIC RESONANCE SPECTROSCOPY

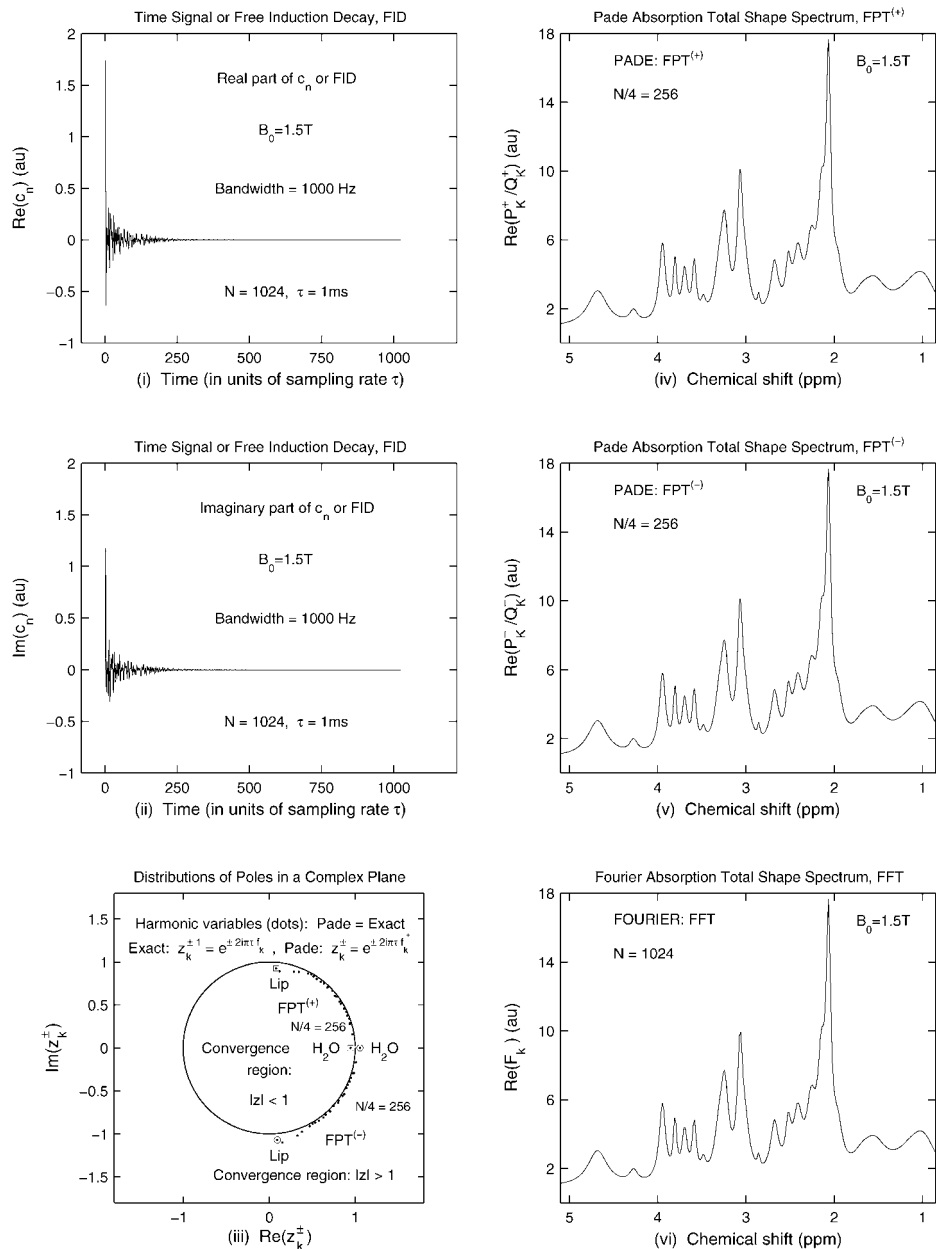


Fig. 1. The synthesised time signal and the associated absorption total shape spectra in the $FPT^{(\pm)}$ and the FFT. The convergence regions in the $FPT^{(+)}$ and the $FPT^{(-)}$, inside and outside the unit circle, respectively, are shown on panel (iii). For further details, see Section 8.2.1.

length ($N/4 = 256$). These results are identical to those obtained with $N/2 = 512$ and $N = 1024$ as dictated by the corresponding numerical values of the spectral parameters from panels (iv)–(vi) in Table 2. Panel (vi) in Fig. 1 shows the Fourier absorption envelope spectrum evaluated via the FFT employing the full FID with $N = 1024$. Comparing panels (iv)–(vi) in Fig. 1, exactly zero-valued spectra are obtained from the difference between any two selected pairs of these spectra. Such differences are called the residual or error spectra and they will be explicitly displayed on Fig. 4. Of course, when the FFT is used in these residuals, subtraction of the Fourier from the Padé spectra is possible only if the FPT is also computed at the Fourier grid points for chemical shifts. This present finding about the error spectra sharpens the corresponding conclusion from our previous studies [11,24,25] where one half of the whole FID was required for the FPT to obtain negligible residuals. In the current investigation, the FPT exhausts only the first quarter of the full FID to attain the resolution of the FFT (which employs the whole time signal) and thereby gives the zero-valued residual spectra. Nevertheless, we re-emphasise that the FIDs used in [11,24,25] were encoded FIDs with noise despite their excellent SNRs, whereas in the present work we use a theoretically constructed noiseless time signal. On all the panels from the right column in Fig. 1, the abscissae are the chemical shifts, *i.e.*, $\text{Re}(f_k)$ (in ppm), and the ordinates are the intensities (in au) of the structures in the envelope spectra. The Fourier and the Padé absorption envelope spectra are denoted by $\text{Re}(F_k)$ with $0 \leq k \leq N - 1$ and $\text{Re}(P_K^\pm/Q_K^\pm)$ as the real parts of the corresponding complex-valued spectra, $F \equiv F_k$ and $P_K^\pm/Q_K^\pm \equiv P_K^\pm(z^{\pm 1})/Q_K^\pm(z^{\pm 1})$, respectively. The Fourier spectrum F_k can be obtained from (7.1), provided that $G_N(z^{-1})$ is evaluated at the Fourier grid points, $F_k = G_N(\exp(-2i\pi k/N))$. It is customary in NMR and MRS that chemical shifts in ppm are shown graphically in descending order when passing from left to right on the abscissa. In the present case, this implies that the largest resonant frequency (water at 4.68 ppm) for resonance $k = 25$ is situated on the far-most left corner of the whole interval for chemical shifts on the abscissa. Such conventions, notations, nomenclature, and units will also apply to other figures, but will not be restated in the captions.

8.2.2. Padé and Fourier convergence rates of absorption total shape spectra

Figure 2 gives the convergence rates of the absorption envelope spectra from the FFT and the $\text{FPT}^{(-)}$ at 3 partial signal lengths ($N/32 = 32$, $N/16 = 64$, $N/8 = 128$). The left and the right columns of this figure are for the Fourier and the Padé spectra via panels (i)–(iii) and (iv)–(vi), respectively. In particular, inspecting the Fourier panels (i) and (ii) together with the Padé panels (iv) and (v) in Fig. 2, striking differences are seen between the FFT and the $\text{FPT}^{(-)}$ at the two shortest investigated signal lengths $N/32 = 32$ and $N/16 = 64$. It is clear that the FFT gives no spectroscopic information whatsoever on panels (i) and (ii). These latter Fourier spectra exhibit only very broad and uninterpretable bumps near 2 ppm and 3 ppm. On the other hand, the $\text{FPT}^{(-)}$ on panel (iv) with merely $N/32 = 32$ delineates several physical resonances, *e.g.*, the Lipid complex located between 1 ppm and 2 ppm, NAA near 2 ppm, Cr around 3 ppm as well as close to 4 ppm, Cho in the vicinity of 4.3 ppm and H_2O near 4.7 ppm, where only the clearly visible spectral structures are mentioned. Remarkably, despite using only 32 signal points out of 1024, these Padé-reconstructed resonance profiles on panel (iv) in Fig. 2 are quite reasonable. Here, some of these line-shapes in the FPT are rather broad, since 32 signal points yield an insufficient accuracy in the estimates for the exact values of the spectral parameters.

CONVERGENCE of ABSORPTION TOTAL SHAPE SPECTRA (FFT: LEFT, FPT: RIGHT);
SIGNAL LENGTH N/M , $N=1024$, $M=8-32$

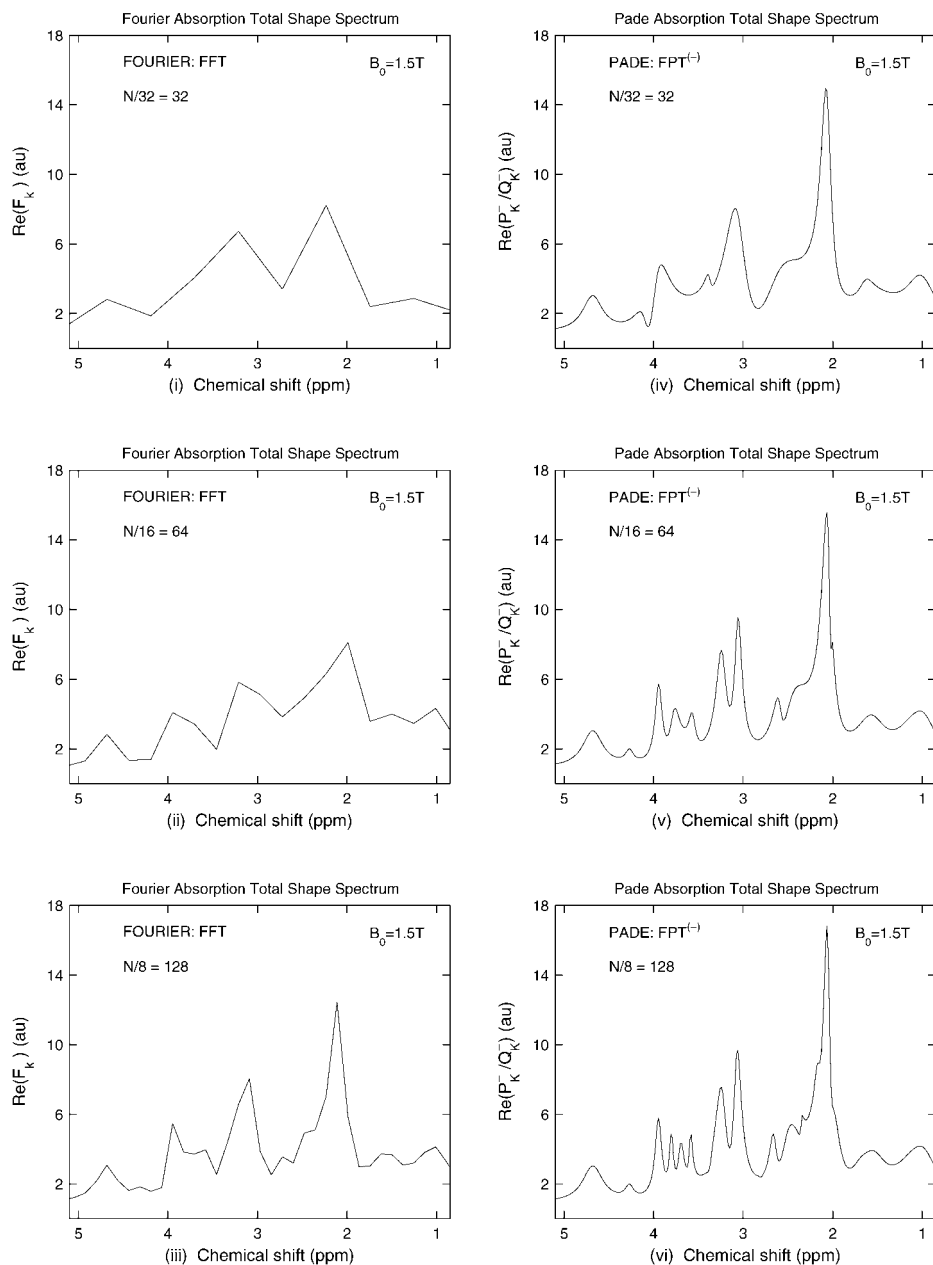


Fig. 2. Convergence rates of absorption total shape spectra from the FFT (left column) and the FPT⁽⁻⁾ (right column) at the varying signal length $N/32 = 32$, $N/16 = 64$, $N/8 = 128$. For further details, see Section 8.2.2.

However, increasing the input information by employing $N/16 = 64$ signal points, the performance of the $\text{FPT}^{(-)}$ is substantially enhanced, as documented on panel (v) in Fig. 2. We see that the initial estimates for the Padé envelope spectra from panel (iv) are now significantly improved. This indicates that a more accurate reconstruction of the exact spectral parameters is performed by the FPT at $N/16 = 64$ than at $N/32 = 32$, as is also evident from the associated numerical values listed on panel (ii) in Table 2. Moreover, the same panel (v) in Fig. 2 shows some 4 additional resonances that are excellently reconstructed by the $\text{FPT}^{(-)}$. These are the peaks corresponding to NAA near 2.7 ppm, Cho close to 3.2 ppm, Ins around 3.6 ppm, and Glu in the vicinity of 3.8 ppm. Especially referring to the corresponding spectra from the FFT on panels (i) and (ii) in Fig. 2, the results of the $\text{FPT}^{(-)}$ from panels (iv) and (v), although still incomplete, nevertheless clearly indicate a good trend towards a better convergence rate in the Padé analysis relative to the Fourier technique. This expectation is further consolidated on panels (iii) and (vi) at $N/8 = 128$ on Fig. 2 for the FFT and the $\text{FPT}^{(-)}$, respectively.

Figure 3 continues with comparisons of the total shape spectra from Fig. 2 by involving more signal points via $N/4 = 256$, $N/2 = 512$, $N = 1024$ to yield the results shown on panels (i)–(iii) for the FFT and (iv)–(vi) for the $\text{FPT}^{(-)}$. With a quarter ($N/4 = 256$) of the full FID, the FFT on panel (i) in Fig. 3 has not obtained the adequate estimates for NAA, Cr, and Cho that are the three diagnostically most informative metabolites. This continues to be the case even with one half ($N/2 = 512$) of the full FID as seen on panel (ii) in Fig. 3, where the FFT still underestimates the true height of NAA. Eventually, only when the whole signal length $N = 1024$ is exhausted, the correct estimates are obtained by the FFT for the exact absorption total shape spectrum, as shown on panel (iii) in Fig. 3. This compares unfavourably with the $\text{FPT}^{(-)}$ shown on panel (iv) in Fig. 3, where full convergence to the exact input result is reached by utilising only a quarter $N/4 = 256$ of the full signal length N . The same conclusion within the $\text{FPT}^{(-)}$ holds true also for one half $N/2$ and the full length N of the input FID as seen on panels (v) and (vi). Considered jointly, Figs. 2 and 3 give a powerful illustration of the out-performance of the FFT by the $\text{FPT}^{(-)}$ with respect to the convergence rate for the varying partial signal length N/M ($M = 2\text{--}32$). This is understood by reference to panels (i) and (ii) in Fig. 1. There it is seen that the studied FID becomes negligible after the first $N/4 = 256$ data points, *i.e.*, after $T/4 = 256$ ms. Thus, any estimator with a resolution which is not exclusively determined by $T = N\tau$ should be able to perform accurate reconstructions by employing only the first quarter of the full FID. Precisely such an expectation is realised by the $\text{FPT}^{(-)}$, as shown in Fig. 3. However, the resolving power $2\pi/T$ in the FFT is pre-fixed only by T , so that the full FID is needed to arrive at a converged envelope spectrum. The $\text{FPT}^{(+)}$ also gives the absorption total shape spectra (not shown) that are either very close or identical to the corresponding results of the $\text{FPT}^{(-)}$ from Figs. 2 and 3. This type of a cross-validation between the two variants of the Padé-based reconstructions increases the overall fidelity in the FPT.

8.3. Residual spectra and consecutive difference spectra

8.3.1. Residual or error absorption total shape spectra

Figure 4 shows the residual or error absorption total shape spectra in the $\text{FPT}^{(-)}$. These spectra are obtained via subtraction of the absorption total shape spectra for the full length

CONVERGENCE of ABSORPTION TOTAL SHAPE SPECTRA (FFT: LEFT, FPT: RIGHT);
SIGNAL LENGTH N/M , $N=1024$, $M=1-4$

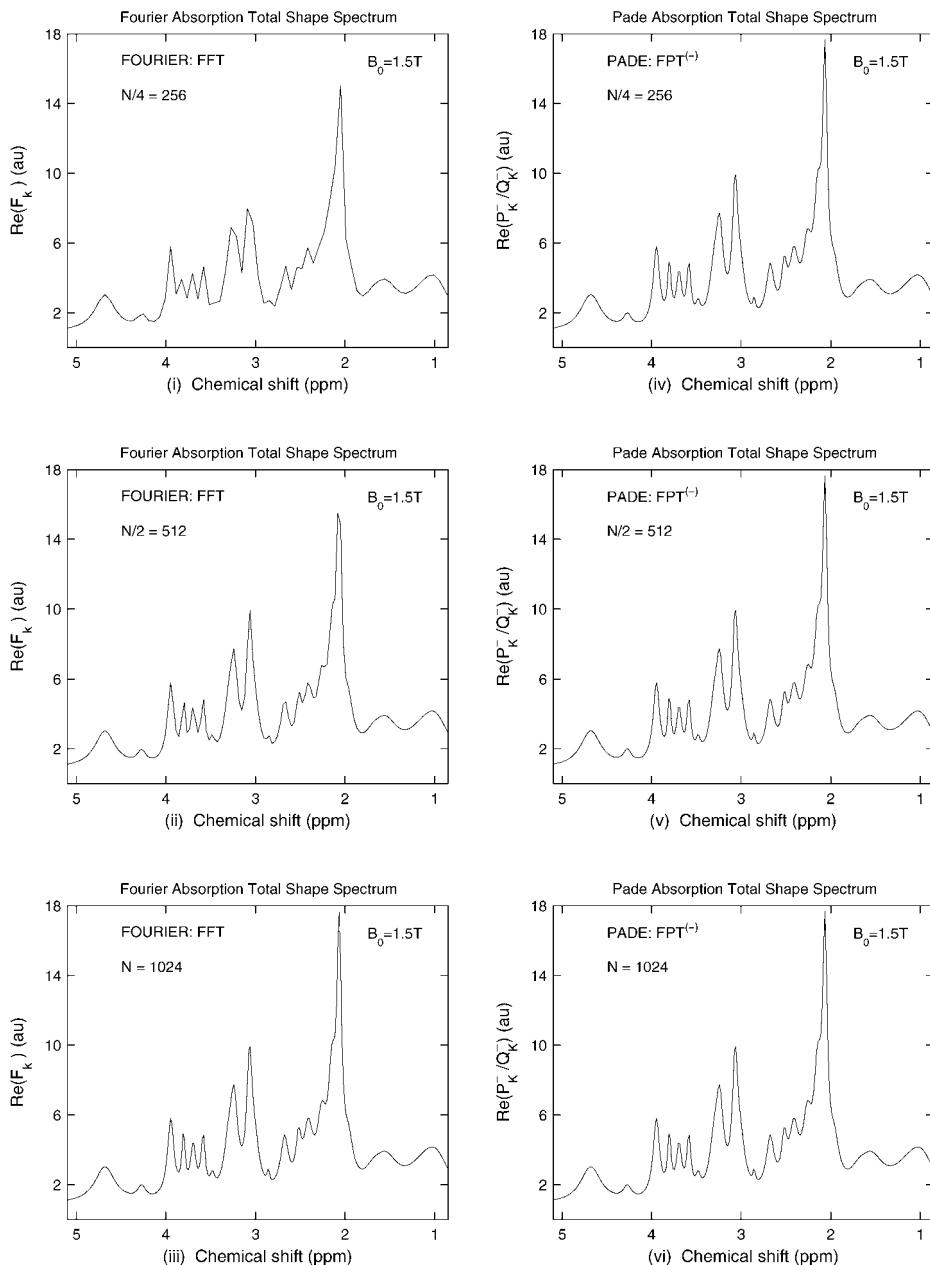


Fig. 3. Convergence rates of absorption total shape spectra from the FFT (left column) and the FPT⁽⁻⁾ (right column) at the varying signal length $N/4 = 256$, $N/2 = 512$, $N = 1024$. For further details, see Section 8.2.2.

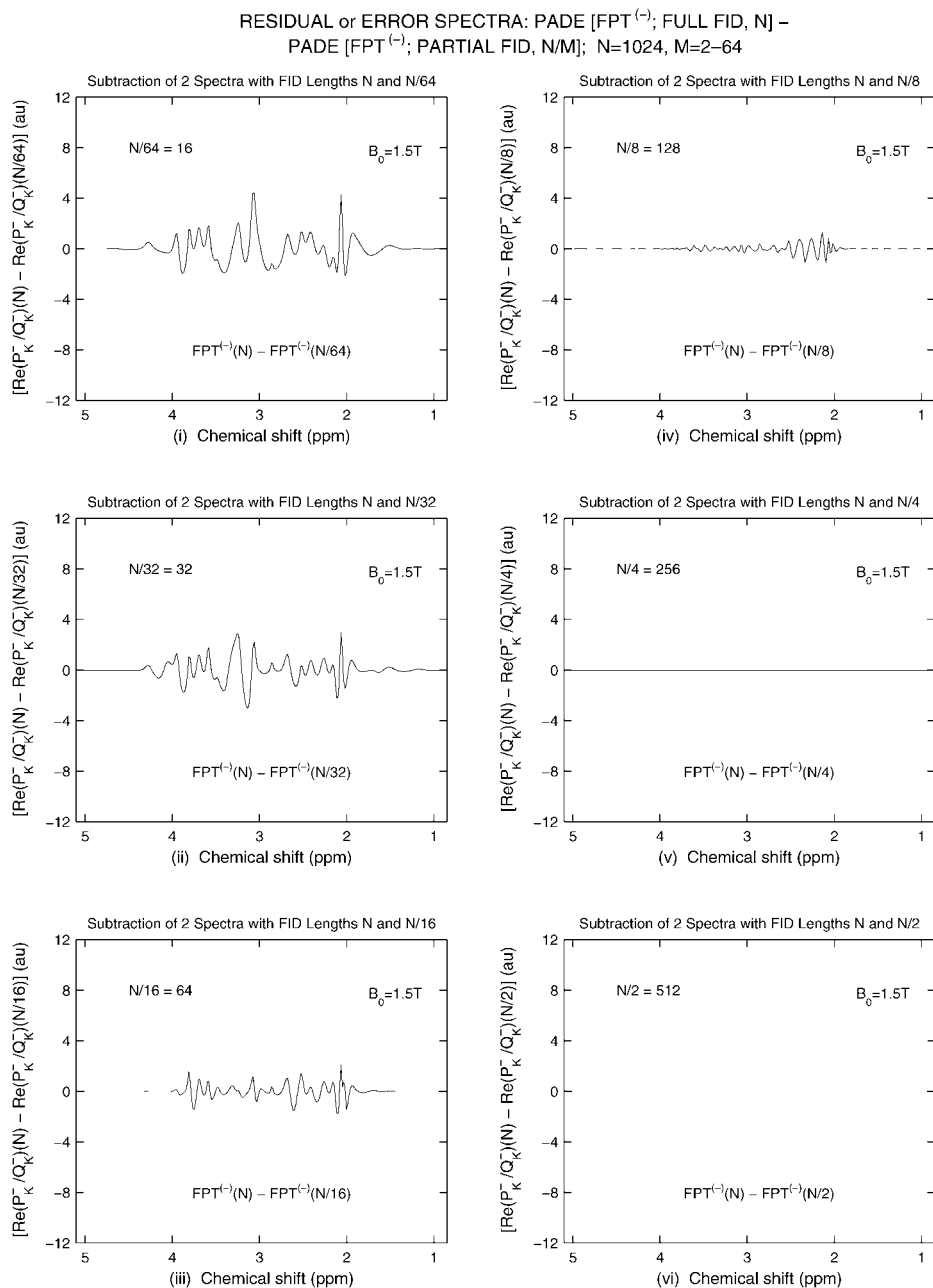


Fig. 4. Residual spectra or, equivalently, error spectra for absorption total shape spectra from the FPT⁽⁻⁾ at the varying signal length $N/64 = 8$, $N/32 = 32$, $N/16 = 64$, $N/8 = 128$, $N/4 = 256$, $N/2 = 512$, $N = 1024$. For further details, see Section 8.3.1.

from those for the partial lengths, $\text{Re}(P_K^-/Q_K^-)[N] - \text{Re}(P_K^-/Q_K^-)[N/M]$. Here, we use the label $[L]$ to indicate that, in total, L signal points are employed, where L is either N or N/M , and N is the full signal length ($N = 1024$), with M being the truncation number ($M = 2, 4, 8, 16, 32$). As such, the number $N/M < N$ represents the partial signal length. An overall extremely stable and fast convergence within the $\text{FPT}^{(-)}$ seen earlier on Figs. 2 and 3, is further impacted onto the residual spectra from Fig. 4 via a systematic decline in the global error. Thus, already with a quarter $N/4 = 256$ of the full FID, the error spectra become zero throughout the entire frequency range. This situation persists at $N/M > 256$. Hence, the partial length $N/4$ could rightly be utilised instead of N in the computation of these error spectra. In other words, the new differences $\text{Re}(P_K^-/Q_K^-)[N/4] - \text{Re}(P_K^-/Q_K^-)[N/M]$ for $M = 2, 8, 16, 32$ would look precisely the same as those on panels (i)–(iv) and (vi). Of course, in this latter context, panel (v) is not mentioned, since in this subplot the error spectrum would be zero by definition, $\text{Re}(P_K^-/Q_K^-)[N/4] - \text{Re}(P_K^-/Q_K^-)[N/M] \equiv 0$ for $M = 4$. In any event, the residual spectrum in the $\text{FPT}^{(-)}$ converges fully by using at most the first quarter of the whole FID, as anticipated from panel (iv) on Fig. 3. This finding is also true for the $\text{FPT}^{(+)}$ (not shown), as could similarly be expected from Fig. 1, where the identical absorption total shape spectra are obtained in both the $\text{FPT}^{(+)}$ and the $\text{FPT}^{(-)}$ at $N/4$.

8.3.2. Residual or error absorption total shape spectra near full convergence

Figure 5 displays the residual absorption total shape spectra in the $\text{FPT}^{(+)}$ (left column) and the $\text{FPT}^{(-)}$ (right column) computed via $\text{Re}(P_K^-/Q_K^-)[N] - \text{Re}(P_K^-/Q_K^-)[N_P]$, where $N_P = 180, 220, 260$. In other words, this figure has a focus on the range of the partial signal length near full convergence. It can be seen that all the shown residual or error spectra in both variants of the FPT are practically equal to zero throughout the considered frequency range. This proves full convergence of all the total shape spectra even at $N_P = 180$ where the peak $k = 11$ is absent as seen earlier on panels (iv) and (i) of Tables 3 and 4, respectively.

8.3.3. Consecutive difference spectra for absorption envelope spectra

Figure 6 depicts the consecutive difference absorption envelope spectra obtained in the $\text{FPT}^{(-)}$. Such spectra are constructed through subtraction of the absorption envelope spectra at the two consecutive signal lengths via $\text{Re}(P_K^-/Q_K^-)[N/M] - \text{Re}(P_K^-/Q_K^-)[N/(2M)]$. Here, following the notation from Fig. 4, the same symbol $[L]$ implies that L signal points are employed. However, in Fig. 6, the number L is either N/M or $N/(2M)$, where again N is the full signal length ($N = 1024$) and M is the truncation number ($M = 2, 4, 8, 16, 32, 64$). These consecutive difference spectra are seen in Fig. 6 to be zero at $M = 4$, and the same finding also extends to $M < 4$. Such a result, through an alternative error analysis, confirms again that the $\text{FPT}^{(-)}$ has reached full convergence with only a quarter of the whole FID. This is also true for the $\text{FPT}^{(+)}$ (not shown). The main rationale for displaying the consecutive difference spectra in Fig. 6, even though the error spectra have already been analysed on Fig. 4, is in illuminating the finer details of the convergence rate on the local level by using the adjacent values of the signal length. This is a valuable supplement to the estimates of the global error available from the associated error spectra $\text{Re}(P_K^-/Q_K^-)[N] - \text{Re}(P_K^-/Q_K^-)[N/M]$ from Fig. 4. Obviously, the latter formula is also a difference spectrum for a varying

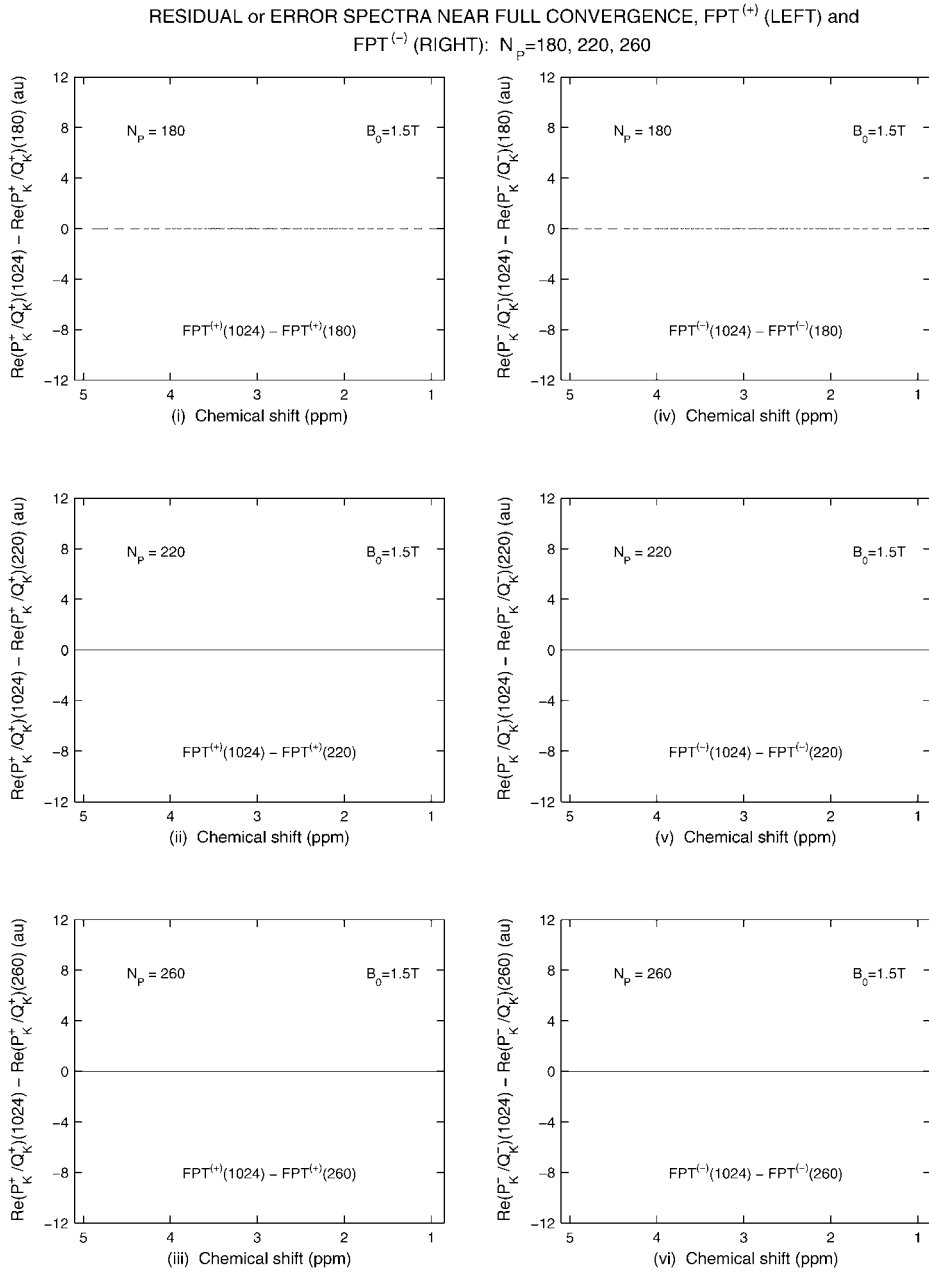


Fig. 5. Residual spectra or error spectra for absorption total shape spectra from the $\text{FPT}^{(-)}$ near full convergence at three partial signal lengths $N_p = 180, 220, 260$. For further details, see Section 8.3.2.

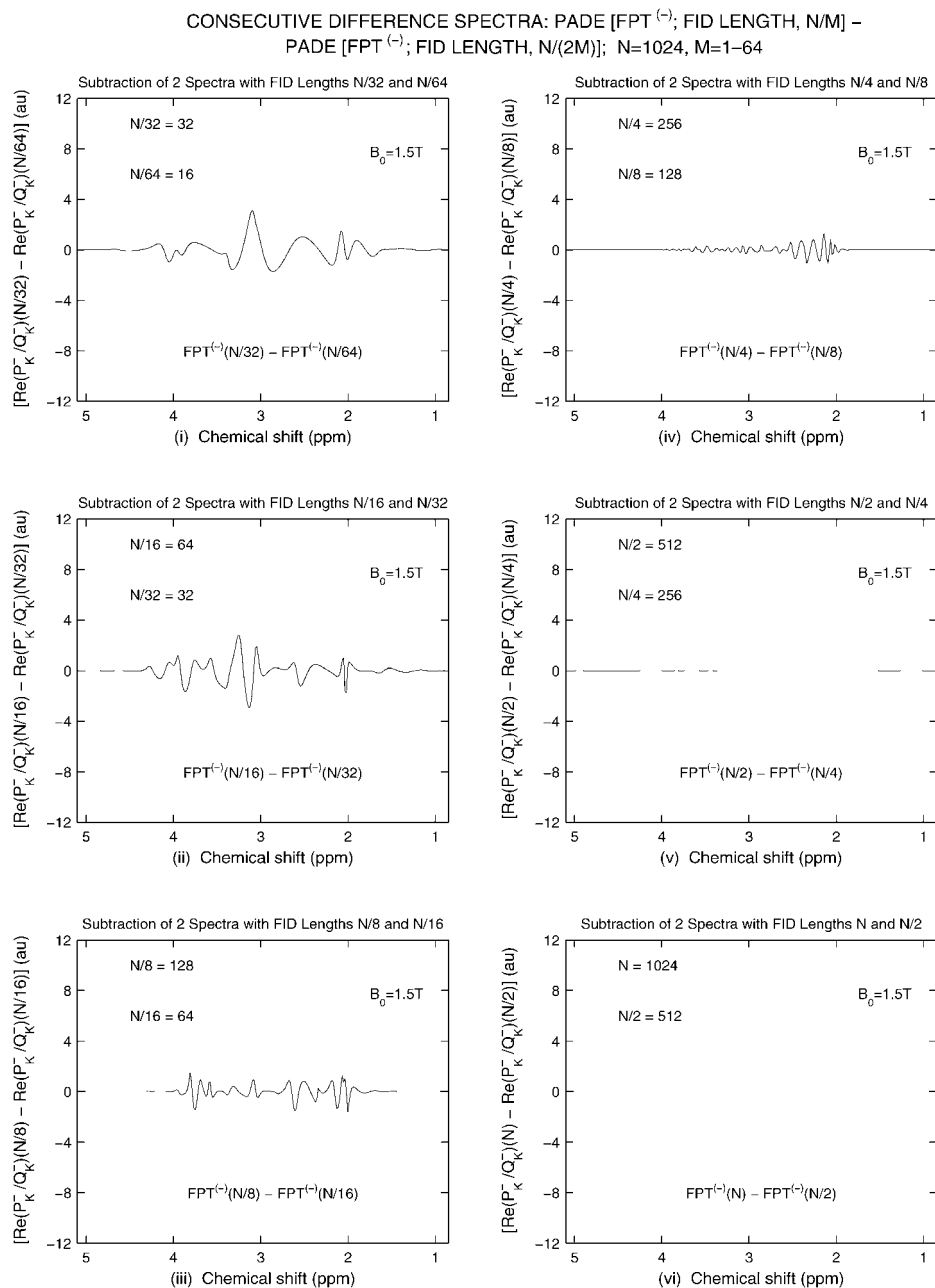


Fig. 6. Consecutive difference spectra for absorption total shape spectra from the FPT⁽⁻⁾ at the varying signal length $N/64 = 8$, $N/32 = 32$, $N/16 = 64$, $N/8 = 128$, $N/4 = 256$, $N/2 = 512$, $N = 1024$. For further details, see Section 8.3.3.

partial length N/M which, however, occurs only in the second term, while the full signal length N is always fixed in the first term $\text{Re}(P_K^-/Q_K^-)[N]$. Clearly, the details on panels (i)–(iii) on Figs. 4 and 6 are different, because of the lack of full convergence at $N/M < 256$. Nevertheless, even though convergence has not been reached yet at $N/8 = 128$ on panel (iv), the data for $\text{Re}(P_K^-/Q_K^-)[N] - \text{Re}(P_K^-/Q_K^-)[N/8]$ on Fig. 4 and $\text{Re}(P_K^-/Q_K^-)[N/4] - \text{Re}(P_K^-/Q_K^-)[N/8]$ on Fig. 6 are identical. As mentioned, this is due to the fact that the first terms in the differences $\text{Re}(P_K^-/Q_K^-)[N]$ and $\text{Re}(P_K^-/Q_K^-)[N/4]$ give the same results.

8.3.4. Consecutive differences for absorption envelope spectra near full convergence

Figure 7 depicts the consecutive difference spectra in the $\text{FPT}^{(+)}$ (left column) and the $\text{FPT}^{(-)}$ (right column) computed via $\text{Re}(P_K^-/Q_K^-)[N_P] - \text{Re}(P_K^-/Q_K^-)[N'_P]$, where $N_P = 180, 220, 260$ and $N'_P = 140, 180, 220$. This emphasises a narrow region around full convergence. Panels (i) and (iv), prior to full convergence of the absorption envelope spectra, show some residual structures located in the frequency interval 2–4 ppm. However, all such residuals are gone on the middle and lower panels yielding practically zero-valued difference spectra.

8.4. Absorption component shape spectra of individual resonances

8.4.1. Absorption component spectra and metabolite maps

Figure 8 compares the results of the $\text{FPT}^{(+)}$ and the $\text{FPT}^{(-)}$ as shown on the left and right column, respectively. The relevant details regarding panels (i) and (iv) as well as (ii) and (v) of Fig. 8 are already outlined in Section 8.2 on Fig. 1. However, important additional information on panels (ii) and (v) for the absorption envelope spectra is given via the display of the usual acronyms that locate the positions of the major MR-detectable metabolites associated with resonances stemming from FIDs encoded via MRS from a healthy human brain. Here, the same acronyms for several resonances (Cho, Glu, NAA) are seen at more than one chemical shift. This is a consequence of the so-called J-coupling [3]. On panels (iii) and (vi) in Fig. 8, the absorption component shape spectra are presented for each individual resonance. By definition, the sums of all of such component shape spectra yield the associated total shape spectra from panels (ii) and (iv) of Fig. 8. As is clear from panels (iii) and (vi) in Fig. 8, only a quarter $N/4 = 256$ of the full FID is necessary for both the $\text{FPT}^{(+)}$ and the $\text{FPT}^{(-)}$ to completely resolve all the individual resonances, including the peaks that are isolated ($k = 8, 9, 10, 13, 18, 19, 20, 21, 24, 25$), overlapped ($k = 1, 2, k = 3, 4, k = 5, 6, 7, k = 14, 15, k = 16, 17$), tightly overlapped ($k = 22, 23$) as well as nearly degenerate ($k = 11, 12$). Moreover, it is seen on panels (iii) and (vi) of this figure, that the component shape spectra coincide in the $\text{FPT}^{(+)}$ and the $\text{FPT}^{(-)}$. Such an observation is consistent with the conclusion from Fig. 1, where the corresponding total shape spectra on panels (iv) and (v) are found to be the same in the $\text{FPT}^{(+)}$ and the $\text{FPT}^{(-)}$. This is expected from the definition of the total shape spectrum in the FPT via the sum of the component shape spectra of all the constituent resonances. Clearly, this will be the case only for unique reconstructions like those in the FPT. This should be contrasted to the non-uniqueness of all fittings. In such reconstructions, a given absorption total shape spectrum is fitted by some pre-assigned component shape spectra that, however, might differ widely in nearly all the essential details from the corresponding exact counterparts.

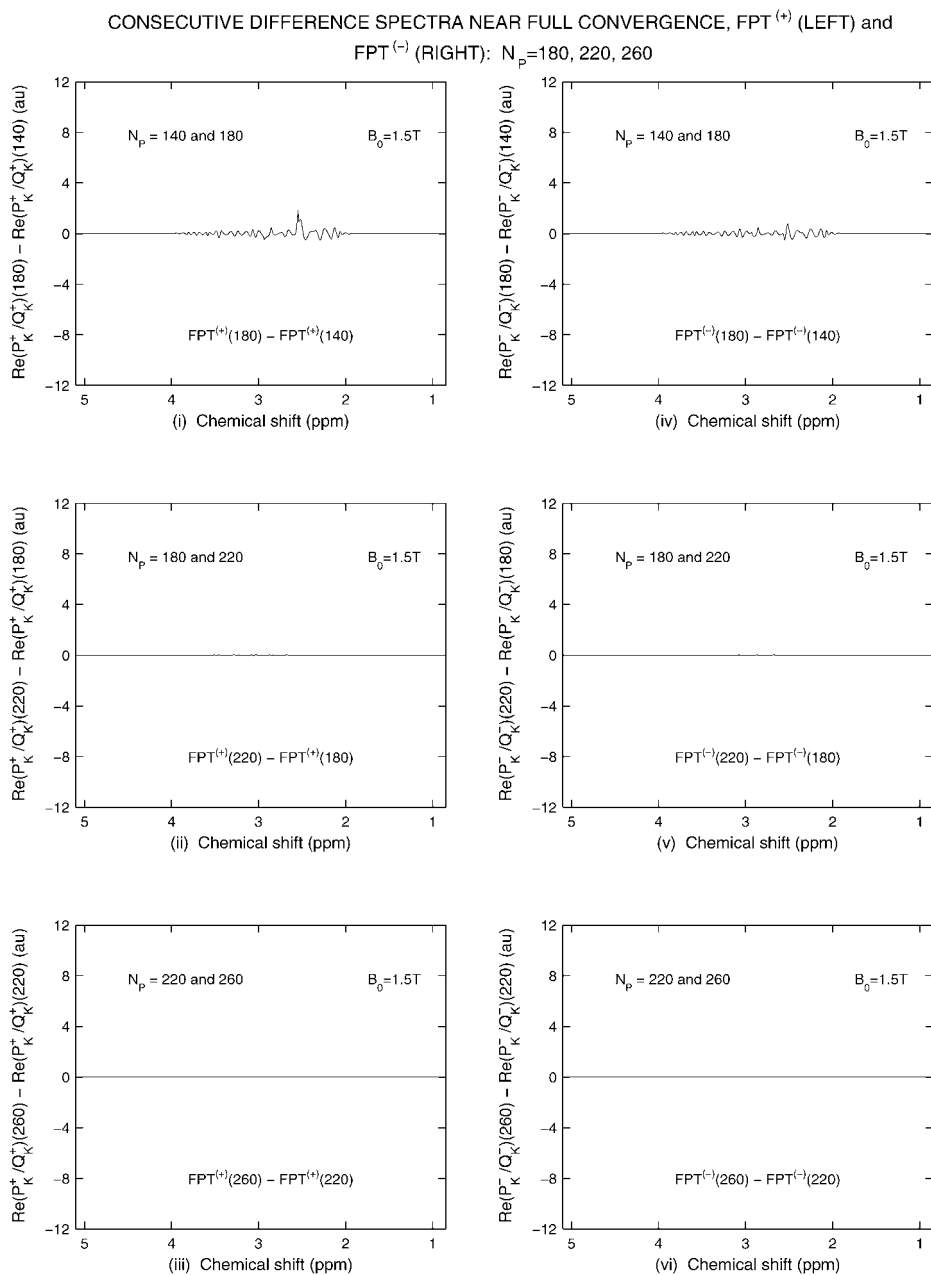


Fig. 7. Consecutive difference spectra for absorption total shape spectra from the FPT⁽⁻⁾ near full convergence at three partial signal lengths $N_p = 180, 220, 260$. For further details, see Section 8.3.4.

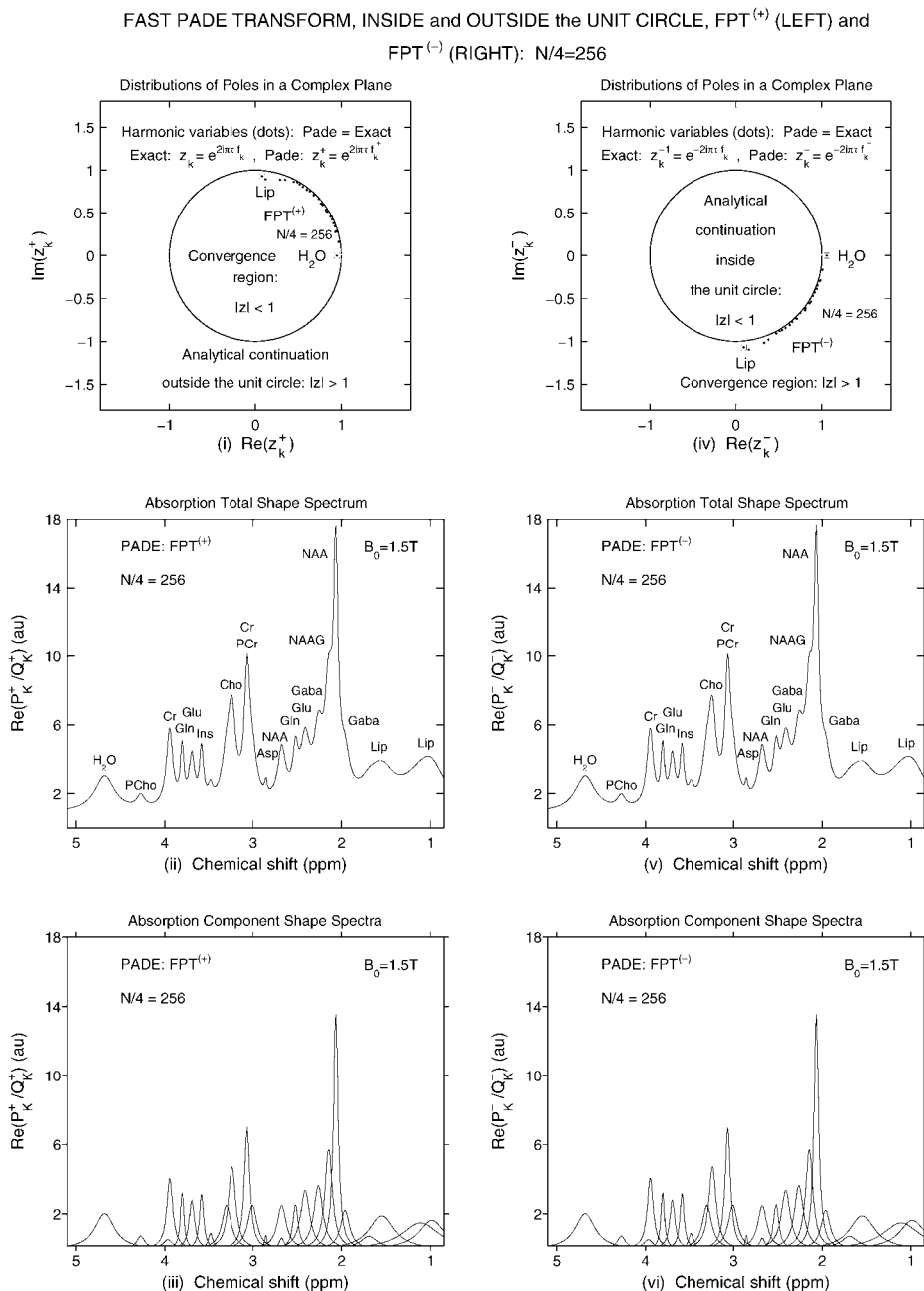


Fig. 8. The initial convergence regions (top panels), absorption total shape spectra (middle panels) and absorption component shape spectra (bottom panels) in the $FPT^{(+)}$ (left column) and the $FPT^{(-)}$ (right column). The middle panels display the usual acronyms for the main MR-detectable metabolites in the healthy human brain. For further details, see Section 8.4.1.

8.4.2. Absorption component spectra and envelope spectra near full convergence

Figure 9 shows absorption component shape spectra (left column) and total shape spectra (right column) from the $\text{FPT}^{(-)}$ computed near full convergence at 3 partial signal lengths $N_p = 180, 220, 260$. All the 3 panels on the right column for the total shape spectra reached full convergence. As to the left column for the component shape spectra, full convergence is achieved at $N_p = 220, 260$. On panel (i) for the component shape spectra at $N_p = 180$, the peak $k = 11$ is missing, and the peak $k = 12$ is over-estimated. Moreover, the area of the 12th peak is over-estimated precisely by the amount of the area of the absent 11th peak. As a result of this latter compensation, the total shape spectrum has not felt that either deficiency took place. In other words, the envelope spectrum on panel (iv) for $N_p = 180$ achieved full convergence despite the missing peak $k = 11$ and the associated over-estimation of peak $k = 12$. Such a full convergence is reflected in the corresponding zero-valued residual or error spectrum for $N_p = 180$ shown on panel (iv) in Fig. 5. This proves that residual or error spectra might be a necessary, but not a sufficient condition for reliability of estimation. Therefore, it is always prudent to pass beyond the point where full convergence has been reached for the first time (in this case above $N_p = 180$) in order to make sure that the anomalies of the type from panels (i) and (iv) from Fig. 9 do not occur in the final results. Such final results are obtained for $N_p = 220, 260$ and shown on panels (ii) and (iii) for the components as well as panels (v) and (vi) for the envelopes.

8.5. Distributions of poles and spectral parameters in their complex planes

8.5.1. Distributions of poles and spectral parameters in the $\text{FPT}^{(+)}$

Figure 10 provides further insights into the exact quantification within the $\text{FPT}^{(+)}$. Here, as earlier in Figs. 1 and 8, all the obtained results are for $N/4 = 256$. The absorption total shape spectrum is displayed on panel (iv) where the individual numbers of resonances are placed near the related peaks. Thus each well-resolved isolated resonance is marked by the corresponding separate number, e.g., $k = 8, 9$, etc., Likewise, the overlapped, tightly overlapped and nearly degenerate resonances are labelled as the sum of the pertinent peak numbers, e.g., $k = 1 + 2$ or $k = 5 + 6 + 7$, etc. Further, panel (v) in Fig. 10 shows the absorption component shape spectra of the constituent resonances $k = 1-25$, and all the individual numbers are indicated for an easier comparison with panel (iv) on the same figure. In this way, the hidden structures are clearly delineated in these component shape spectra. Such hidden peaks are the overlapped ($k = 1 + 2, 3 + 4, 5 + 6 + 7, 14 + 15, 16 + 17$), tightly overlapped ($k = 22 + 23$), and nearly degenerate ($k = 11 + 12$) resonances. As before, the resonance positions $\text{Re}(f_k^+)$ as chemical shifts are in descending order on the abscissa when going from left to right. As to the ordinate, if only panel (vi) for the distribution of resonance frequencies in the corresponding complex plane is analysed without relation to other panels in Fig. 10, there does not seem to be a need for inverting the imaginary frequency $\text{Im}(f_k^+)$. However, panel (vi) is most instructive if it is not viewed only independently of the other panels, but also in its relation to the rest of the panels in Fig. 10. Here, especially panels (v) and (vi) should be inspected together, since they are complementary. It is for this reason that we decided to use the descending order for the values of $\text{Im}(f_k^+)$ when going from bottom to top of the ordinate axis. In this way, the ordinate is also inverted similarly to the abscissa on Fig. 10. Such a convention on panel

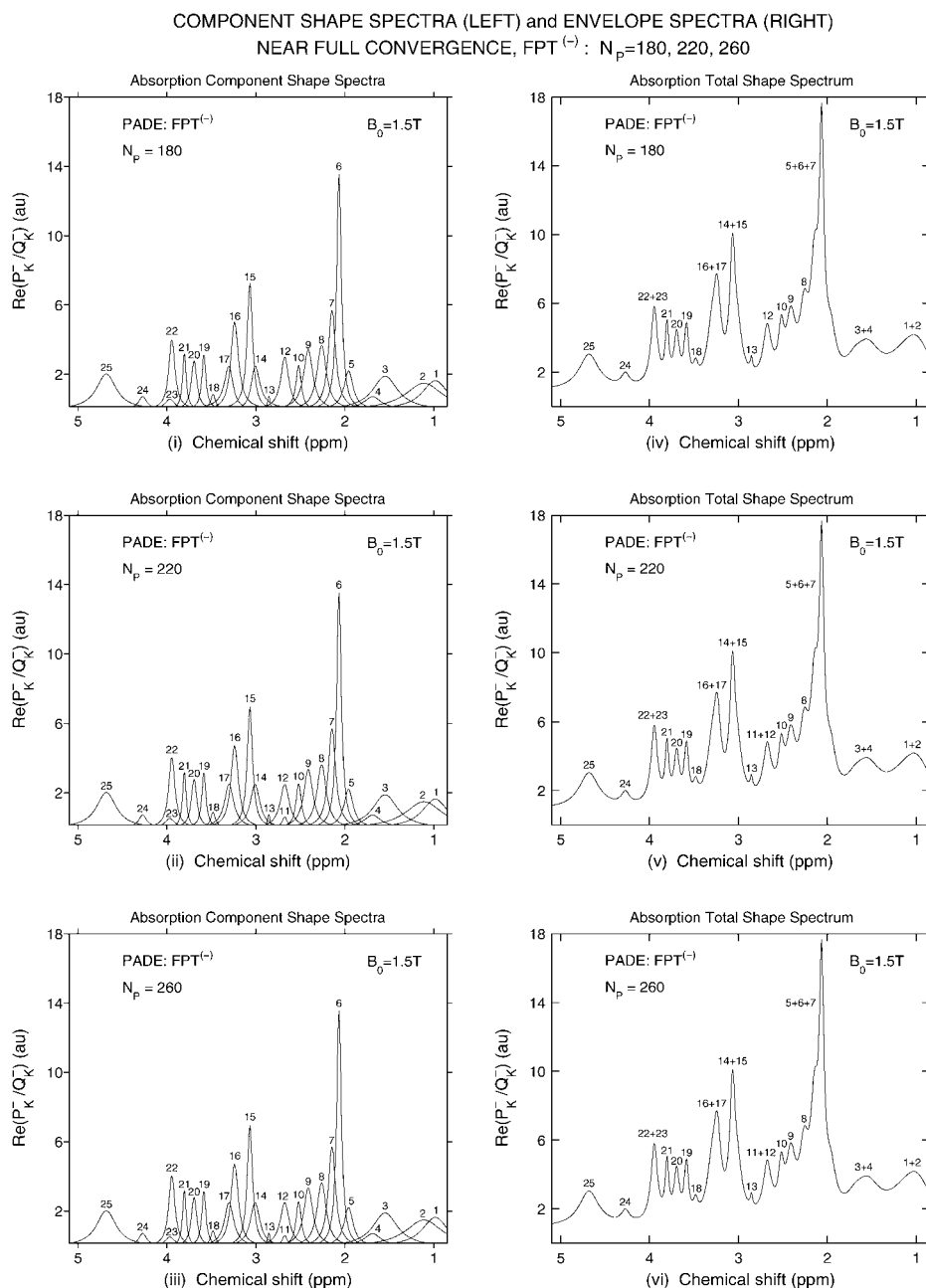


Fig. 9. Absorption component shape spectra (left column) and absorption total shape spectra (right column) from the $FPT^{(-)}$ near full convergence at three partial signal lengths $N_p = 180, 220, 260$. On panel (iv) for $N_p = 180$, the total shape spectrum reached full convergence, despite the fact that on panel (i) for the corresponding component shape spectra, the 11th peak is missing and the 12th peak is over-estimated. For further details, see Section 8.4.2.

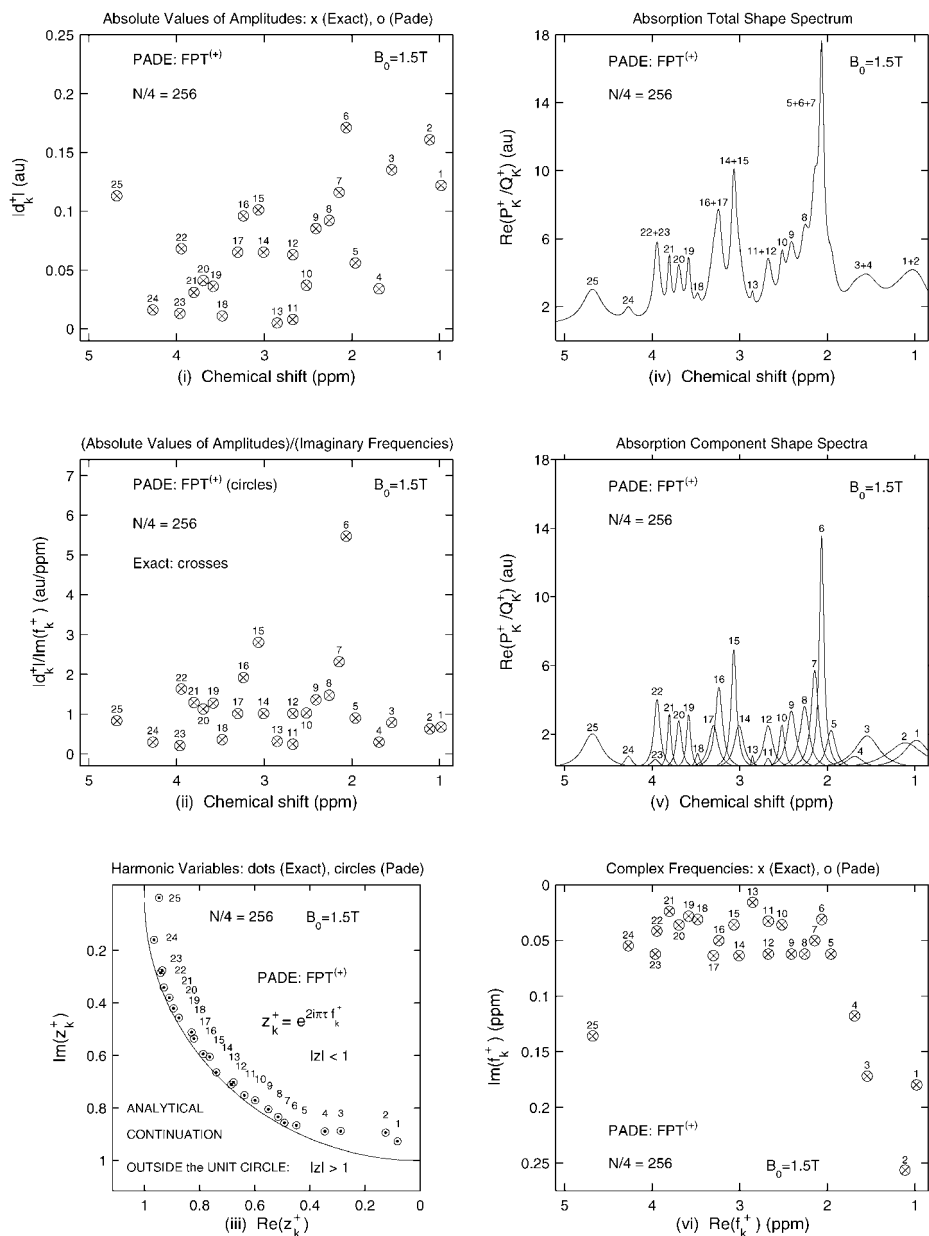
EXACT QUANTIFICATION by FAST PADE TRANSFORM, INSIDE the UNIT CIRCLE, FPT⁽⁺⁾: N/4=256

Fig. 10. Configurations of the reconstructed spectral parameters in the FPT⁽⁺⁾. Panel (i): the absolute values $|d_k^+|$ of the amplitudes d_k^+ for varying chemical shift. Panel (ii): the ratios $|d_k^+|/\text{Im}(f_k^+)$ that are proportional to the peak heights. Panel (iii): distributions of poles expressed through the harmonic variable z_k^+ in the complex z^+ -plane. Panel (vi): distributions of the fundamental complex frequencies f_k^+ in the complex f^+ -plane. For further details, see Section 8.5.1.

(vi) gives an appealing layout for the configuration of the poles of complex frequencies according to the kind of resonances displayed on panel (v). This is particularly informative given that panel (v) is placed right above panel (vi) on the same Fig. 10. Here, as seen on panel (v), most resonances, *e.g.*, $k = 5\text{--}24$ are quite narrow as implied by the rather small values of $\text{Im}(f_k^+)$, so that these imaginary frequencies are not far from the real axis. Consequently, these resonances appear on panel (vi) in a group in the middle part of this subplot. On the other hand, panel (v) in Fig. 10 also shows broader resonances, *e.g.*, $k = 1\text{--}4$ and $k = 25$ with larger values of $\text{Im}(f_k^+)$ and, therefore, such imaginary frequencies are deeper in the complex plane. Hence, these resonances are quite distant from the real axis, as seen on the far left and the far right parts of panel (vi). In addition to panel (vi) in Fig. 10, graphical presentations of the reconstructed and the input data for the spectral parameters are also shown on panels (i)–(iii). In particular, panel (i) in Fig. 10 displays the distribution of the absolute values of the amplitudes at different chemical shifts. It follows from panel (i) that the quantities $|d_k^+|$ do not represent the heights of the absorption peaks from panels (iv) and (v) as announced in Section 2. Rather, the absorption peak heights are directly proportional to the quotient $|d_k^+|/\text{Im}(f_k^+)$ as pointed out in Section 2. Thus in Fig. 10, panel (ii) shows the distribution of the quotients of the absolute values of the amplitudes and the imaginary frequencies. We see from panel (ii) that all the 25 ratios $|d_k^+|/\text{Im}(f_k^+)$ are indeed proportional to the heights of the corresponding peaks in the absorption component shape spectra from panel (v) in Fig. 10, as anticipated in Section 2. Panel (iii) from Fig. 10 depicts, in the complex z^+ -plane, the distribution of the Padé poles contained in the complex harmonic variable z_k^+ . This is recognised as the zoomed version of panels (iii) or (i) from Fig. 1 or Fig. 8, respectively. The difference is in showing only the first quadrant in Fig. 10, because the rest of the complex z^+ -plane does not contain any physical resonance. Further, panel (iii) from Figs. 1 and 10 differ in arrangements of the values of $\text{Re}(z_k^+)$ and $\text{Im}(z_k^+)$. Unlike chemical shifts, no particular reason exists in Fig. 1 or Fig. 10 to abandon the universal convention of the ascending order of the values for $\text{Re}(z_k^+)$ when passing from left to right on the abscissa, and similarly for the ascending order of the values of $\text{Im}(z_k^+)$ when going from bottom to top on the ordinate. As such, this usual practice is seen on panel (iii) in Fig. 1 as well as on panels (i) and (iv) of Fig. 8. However, as to panel (iii) in Fig. 10, both axes $\text{Re}(z_k^+)$ and $\text{Im}(z_k^+)$ are reversed. This implies that the values on the abscissa and ordinate on panel (iii) of Fig. 10 are arranged in descending order when passing from left to right on the abscissa and from bottom to top on the ordinate, respectively. Such a twofold inversion on panel (vi) in Fig. 10 is made to follow the arrangements of $\text{Re}(f_k^+)$ and $\text{Im}(f_k^+)$ that are both depicted in descending order when going from left to right on the abscissa or from bottom to top on the ordinate. This convenient layout shows that all the Padé poles $k = 1\text{--}25$ are aligned consecutively one after another from left to right regarding the abscissa. The same poles $k = 1\text{--}25$ are also packed together along the circumference ($|z| = 1$) of the unit circle in such a way that they follow each other according to their consecutive numbers from inside the unit circle by being aligned upward with respect to the ordinate. Panel (iii) in Fig. 10 shows that the poles contained in the harmonic variable z_k^+ are less scattered from each other relative to the associated distributions of the complex frequencies from panel (vi) in the same figure. The reason for this is in the exponential function of the complex frequency which is plotted on panel (iii), whereas the frequency itself is shown on panel (vi) in Fig. 10. It is seen on panel (iii) in Fig. 10 that all the retrieved poles extracted by the $\text{FPT}^{(+)}$ are located inside the unit circle ($|z| < 1$), as anticipated. In particular, narrow resonances $k = 5\text{--}24$ are seen

to be near the circumference ($|z| = 1$) of the unit circle. By contrast, the broad resonances shown on panel (iii) in Fig. 10, such as $k = 1-4$ and $k = 25$, are seen to lie farther from the border line $|z| = 1$.

8.5.2. Distributions of poles and spectral parameters in the $\text{FPT}^{(-)}$

Figure 11 is of the same kind as Fig. 10. The difference is that Fig. 11 shows the results of the $\text{FPT}^{(-)}$. The interpretation of the results from the $\text{FPT}^{(+)}$ as presented on panels (i), (ii), and (iv)–(vi) in Fig. 10 also applies to the corresponding findings from the $\text{FPT}^{(-)}$ shown on panels (i), (ii) and (iv)–(vi) in Fig. 11. Such an observation comes from the fact that the $\text{FPT}^{(+)}$ and the $\text{FPT}^{(-)}$ yield the indistinguishable spectral parameters for the same number $N/4 = 256$ of signal points as stated in Section 8.1.2. However, panel (iii) is different in Figs. 10 and 11, since the presented information here concerns the two complementary regions of the initial convergence, inside and outside the unit circle, for the $\text{FPT}^{(+)}$ and the $\text{FPT}^{(-)}$, respectively. To match the configuration from panel (iii) in Fig. 10, the Padé poles contained in the harmonic variable z_k^- , as shown in the complex z^- -plane on panel (iii) in Fig. 11, are plotted with the values of $\text{Im}(z_k^-)$ in ascending order when passing from bottom to top of the ordinate. This is opposite to the ordering of $\text{Im}(z_k^+)$ on panel (iii) in Fig. 10 as expected, since $\text{Im}(z_k^+) > 0$ and $\text{Im}(z_k^-) < 0$. Therefore, the Padé-reconstructed results by the $\text{FPT}^{(+)}$ and the $\text{FPT}^{(-)}$ for the harmonic variables z_k^+ and z_k^- are located in the first and the fourth quadrant of the complex z^+ - and z^- -planes, respectively. This is clear from panel (iii) of Fig. 1 or on panels (i) and (iv) of Fig. 8. Moreover, it can be seen on panel (iii) in Fig. 11 that all the resonances reconstructed by means of the $\text{FPT}^{(-)}$ lie outside the unit circle ($|z| > 1$), as expected.

8.5.3. Convergence of complex frequencies in the $\text{FPT}^{(-)}$

Figure 12 shows the way in which the complex fundamental frequencies retrieved by the $\text{FPT}^{(-)}$ are configured in the complex frequency plane when using 6 partial signal lengths ($N/32 = 32$, $N/16 = 64$, $N/8 = 128$, $N/4 = 256$, $N/2 = 512$) and the full FID ($N = 1024$). Thus, panels (i)–(iii) illustrate the frequency distribution of the 10, 14, and 20 resonances that are retrieved with $N/32 = 32$, $N/16 = 64$ and $N/8 = 128$, respectively. It should be pointed out that the ordinate axis on panel (i) is enlarged with respect to all other panels in Fig. 12. Such an adjustment is due to a larger scatter of the two retrieved imaginary frequencies from the corresponding exact values. This scatter is found to surpass the window 0–0.275 ppm which is common to the remaining 5 ordinate axes on panels (ii)–(vi) in Fig. 12. Further, on panels (iv)–(vi) in Fig. 12, we show the complex frequencies retrieved with $N/4 = 256$, $N/2 = 512$ and $N = 1024$, respectively. Notice that on panel (iv) for $N/4 = 256$, the exact frequencies and the associated Padé-reconstructed values are found to be in full agreement with each other. In addition, the plot on panel (iv) coincides with the plots on panels (v) and (vi) for $N/2 = 512$ and $N = 1024$, respectively. This graphical illustration of the complete agreement between the full set of the exact $\{f_k\}$ and the reconstructed $\{f_k^-\}$ frequencies, where the latter quantities are computed by the $\text{FPT}^{(-)}$ with the signal lengths $N/4 = 256$, $N/2 = 512$, and $N = 1024$, is expected from panels (iv)–(vi) in Table 2.

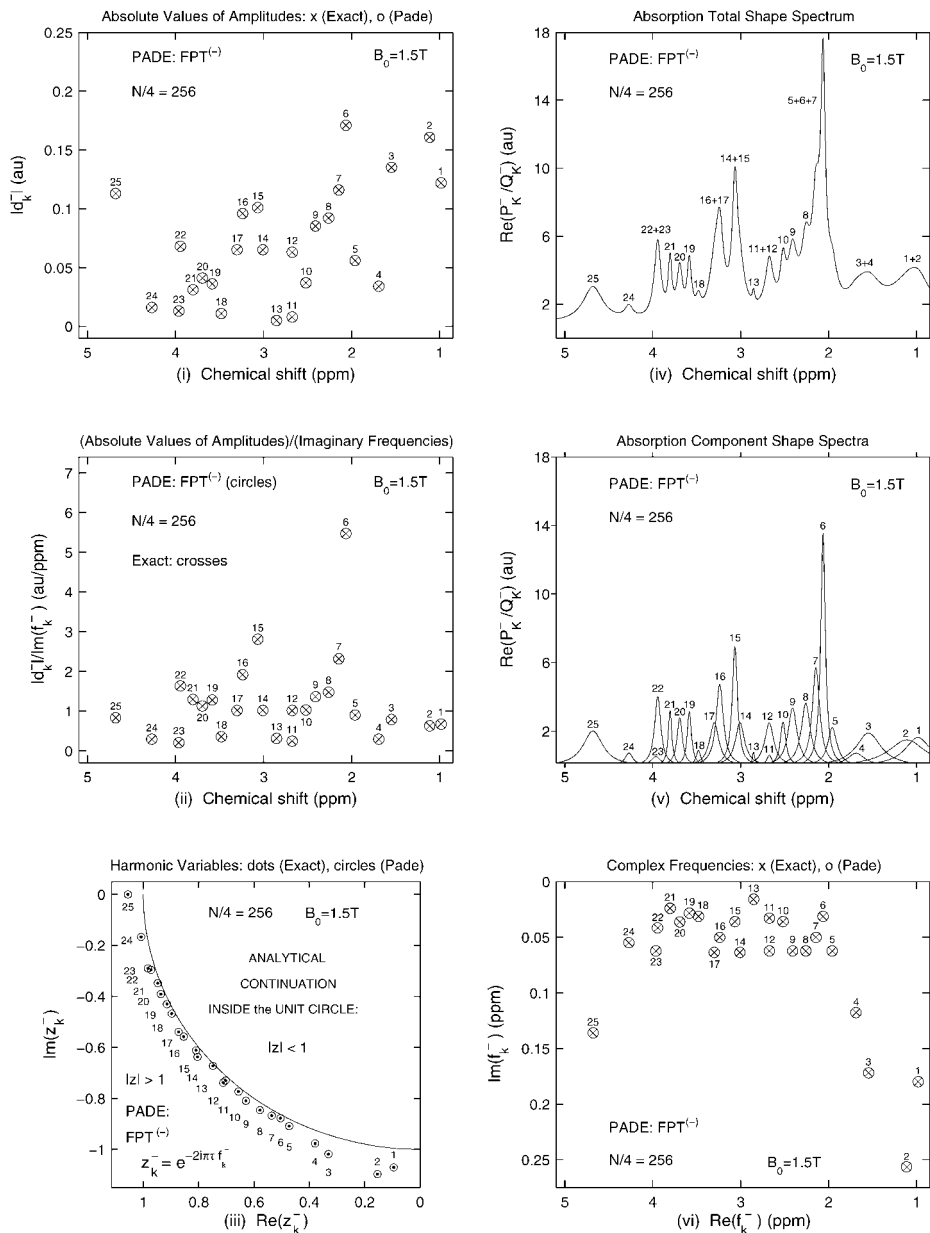
EXACT QUANTIFICATION by FAST PADE TRANSFORM, OUTSIDE the UNIT CIRCLE, FPT⁽⁻⁾ : N/4=256

Fig. 11. Configurations of the reconstructed spectral parameters in the FPT⁽⁻⁾. Panel (i): the absolute values $|d_k^-|$ of the amplitudes d_k^- for varying chemical shift. Panel (ii): the ratios $|d_k^-|/\text{Im}(f_k^-)$ that are proportional to the peak heights. Panel (iii): distributions of poles expressed through the harmonic variable z_k^- in the complex z^- -plane. Panel (vi): distributions of the fundamental complex frequencies f_k^- in the complex f^- -plane. For further details, see Section 8.5.2.

CONVERGENCE of COMPLEX FREQUENCIES in $FPT^{(-)}$: SIGNAL LENGTH N/M , $N=1024$, $M=1-32$

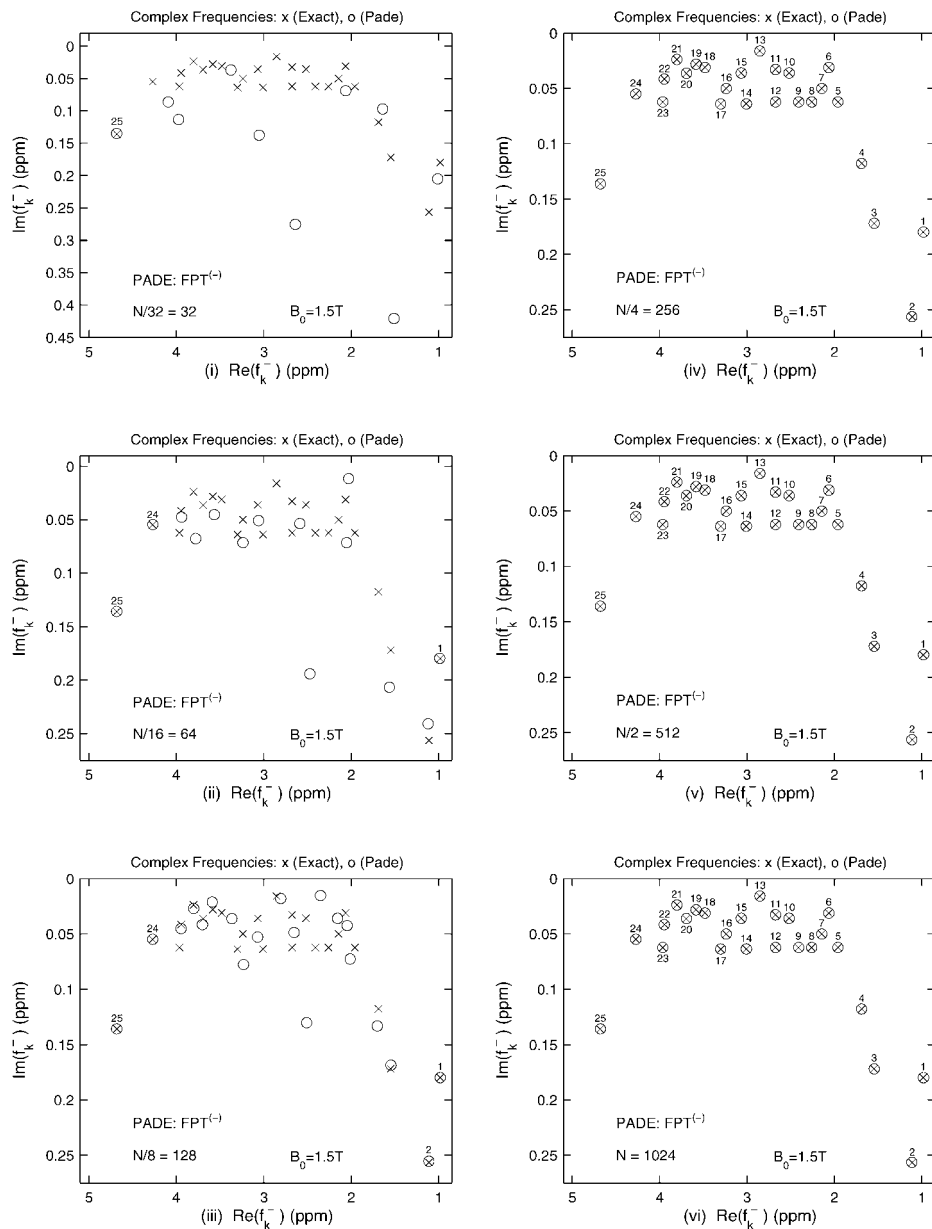


Fig. 12. Convergence of the fundamental complex frequencies reconstructed by the $FPT^{(-)}$ for varying signal lengths $N/32 = 32$, $N/16 = 64$, $N/8 = 128$, $N/4 = 256$, $N/2 = 512$, $N = 1024$. For further details, see Section 8.5.3.

8.5.4. Convergence of absolute values of amplitudes in the $\text{FPT}^{(-)}$

Figure 13 shows the distributions of the absolute values of amplitudes (related to the corresponding fundamental frequencies) as reconstructed using the $\text{FPT}^{(-)}$. These distributions are computed as a function of chemical shifts by employing the same sequence of the signal lengths as in Fig. 12, i.e., $N/32 = 32$, $N/16 = 64$, $N/8 = 128$, $N/4 = 256$, $N/2 = 512$ and $N = 1024$. On panels (i)–(iii) in Fig. 13 we display the amplitude distributions of the 10, 14, and 20 resonances reconstructed for $N/32 = 32$, $N/16 = 64$, and $N/8 = 128$, respectively. The ordinate axes on the whole left column via panels (i)–(iii) in Fig. 13 are seen as enlarged relative to panels (iv)–(vi) in the same figure. A like enlargement was also needed in Fig. 12 for the distribution of the retrieved complex frequencies, but merely on panel (i) for the shortest partial signal length $N/32 = 32$. Thus the reconstructed $|d_k^-|$'s are more scattered from the associated exact values than in the case of corresponding complex frequencies $\{f_k^-\}$ on the left column in Fig. 12. This implies that, prior to convergence, there is larger sensitivity of the reconstructed absolute values of the amplitudes on panels (i)–(iii) in Fig. 13, relative to the corresponding complex frequencies on panels (i)–(iii) on Fig. 12, when both sets of spectral parameters are computed with the same partial signal length in the interval $N/M < N/4 = 256$. This is expected, since the complex frequencies $\{f_k^-\}$ extracted by the $\text{FPT}^{(-)}$ are based only upon the roots of the denominator polynomial Q_K^- . However, the absolute values of the amplitudes $\{|d_k^-|\}$ rely upon both the numerator P_K^- and denominator Q_K^- polynomials, as per (7.26). Of course, any extra numerical inaccuracies that are due to the additional parameters to be obtained for the expansion coefficients $\{p_r^-\}$ in P_K^- yield more pronounced departures from the exact results for the amplitudes than for the frequencies, before full convergence has been achieved. Also, the reconstructed amplitudes converge more slowly than the corresponding frequencies for the investigated FID, because it is difficult to obtain the exact zero values for all the phases $\{\phi_k^-\}$ as in the associated exact set $\{\phi_k\}$. Such a circumstance is reflected on panels (i)–(iii) in Fig. 13, because here the non-converged $|d_k^-|$'s contain an admixture of $\text{Im}(d_k^-) \neq 0$, i.e., $\phi_k^- \neq 0$ and, hence, in these cases we have $|d_k^-| \neq d_k^-$. On the other hand, on panels (iv)–(vi) in Fig. 13, all the 25 absolute values of the amplitudes $\{|d_k^-|\}$ exhibit the feature $\text{Im}(d_k^-) = 0$ or, equivalently, $\phi_k^- = 0$. Therefore, in the cases of panels (iv)–(vi) in Fig. 13, it follows that $|d_k^-| = d_k^-$ as in the corresponding exact values for $|d_k|$ from Table 1, where $\phi_k = 0$, so that $|d_k| = d_k$ ($1 \leq k \leq K$). In the FPT , any inaccuracies in the intermediate stage of computations should disappear for all the 25 reconstructed amplitudes as soon as convergence takes place. This anticipation, which is based on theoretical grounds, is actually fulfilled already at $N/M \geq N/4 = 256$ as seen on panels (iv)–(vi) in Fig. 13 where a quarter, one half and full signal length are employed, respectively. Such a graphical visualisation stems from the exact agreement between all the absolute values of the amplitudes in the input data (Table 1) and the corresponding values obtained by the $\text{FPT}^{(-)}$ with $N/4 = 256$, $N/2 = 512$, and $N = 1024$ (Table 2).

8.5.5. Distributions of complex frequencies in the $\text{FPT}^{(\pm)}$ near full convergence

Figure 14 gives the distributions of the complex fundamental frequencies reconstructed by the $\text{FPT}^{(+)}$ (left column) and the $\text{FPT}^{(-)}$ (right column) near full convergence at 3 partial signal lengths $N_p = 180, 220, 260$. On panels (i) and (iv) at $N_p = 180$, the frequency for peak $k = 11$ is absent from the reconstructed parameters in the $\text{FPT}^{(+)}$ and the $\text{FPT}^{(-)}$.

CONVERGENCE of ABSOLUTE VALUES of AMPLITUDES in $\text{FPT}^{(-)}$:
SIGNAL LENGTH N/M , $N=1024$, $M=1-32$

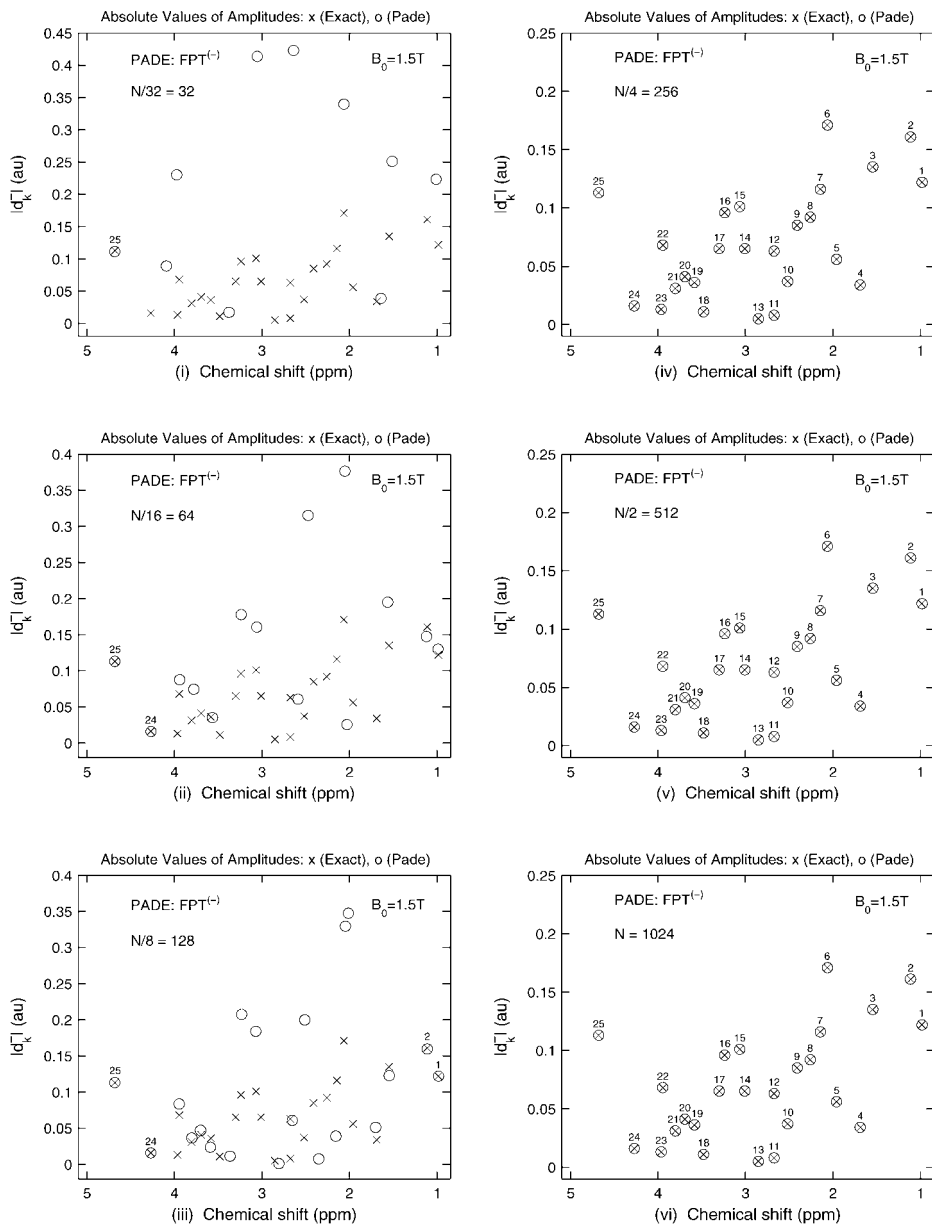


Fig. 13. Convergence of the absolute values of the amplitudes reconstructed by the $\text{FPT}^{(-)}$ at varying signal lengths $N/32 = 32$, $N/16 = 64$, $N/8 = 128$, $N/4 = 256$, $N/2 = 512$, $N = 1024$. For further details, see Section 8.5.4.

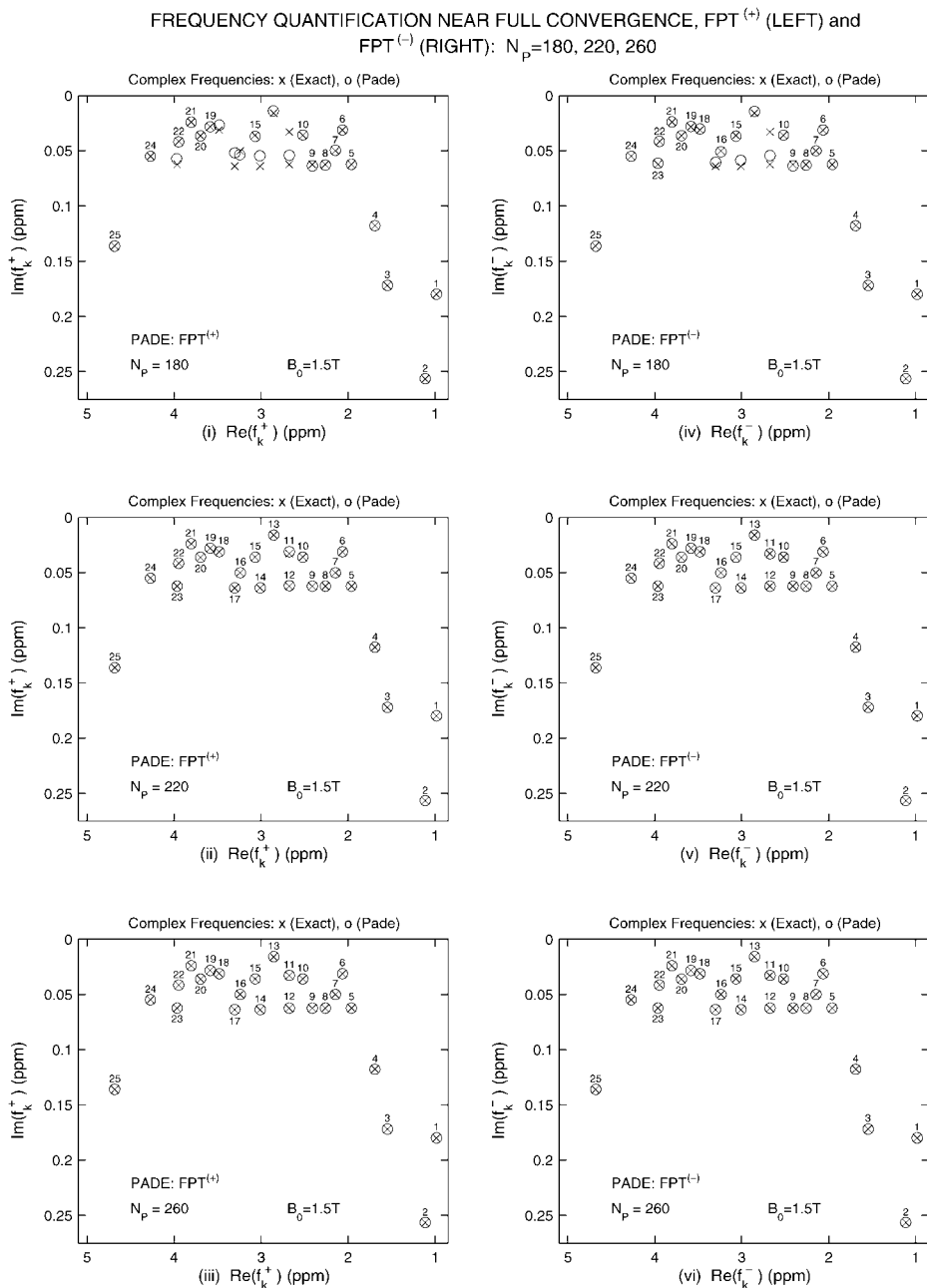


Fig. 14. Convergence of the fundamental complex frequencies reconstructed by the FPT⁽⁻⁾ near full convergence at the three signal lengths $N_p = 180, 220, 260$. For further details, see Section 8.5.5.

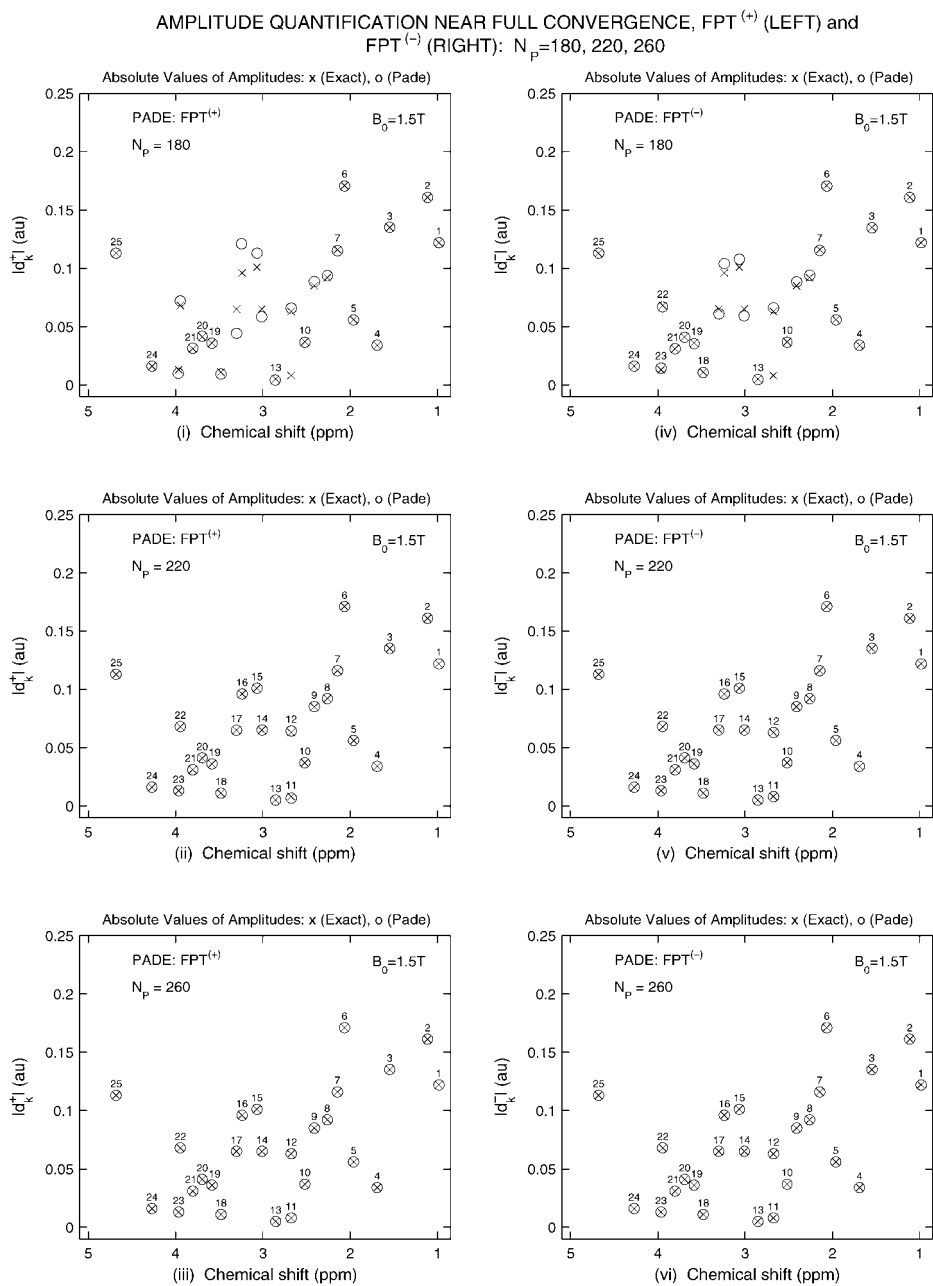


Fig. 15. Convergence of the absolute values of the amplitudes reconstructed by the FPT⁽⁻⁾ near full convergence at the three partial signal lengths $N_p = 180, 220, 260$. For further details, see Section 8.5.6.

However, at $N_P = 220$ the missing 11th peak is recovered by both variants of the FPT as seen on panels (ii) and (v). Such a stable estimation persists on panels (iii) and (vi) at $N_P = 260$.

8.5.6. Distributions of absolute values of amplitudes in the $FPT^{(\pm)}$ near full convergence

Figure 15 displays the absolute values of the amplitudes reconstructed by the $FPT^{(+)}$ (left column) and the $FPT^{(-)}$ (right column) near full convergence at 3 partial signal lengths $N_P = 180, 220, 260$. Full convergence is reached in the $FPT^{(\pm)}$ at $N_P = 220$ on panel (ii) as well as panel (v), and this is maintained on panels (iii) and (vi) at $N_P = 260$. However, the most interesting information is actually provided prior to full convergence in the $FPT^{(-)}$ by inspecting, *e.g.*, panel (iv) from Figs. 14 and 15, especially by making reference to panels (i) and (iv) of Fig. 9 for the component and total shape spectra. To recall, Fig. 9 shows that the converged total shape spectrum from panel (iv) is obtained without achieving convergence of the component spectra. This occurred due to a compensation effect—the 11th peak was missing, and the 12th peak was over-estimated. Panel (iv) in Figs. 14 and 15 gives the explanation for this compensation. Peak $k = 12$ on panel (iv) in Fig. 14 has a smaller imaginary frequency than the corresponding exact value, $\text{Im}(f_{12}^-) < \text{Im}(f_{12})$. By contrast, panel (iv) in Fig. 15 shows that $d_{12}^- > d_{12}$ and, therefore, $d_{12}^- / \text{Im}(f_{12}^-) > d_{12} / \text{Im}(f_{12})$. On the other hand, the ratio $d_k^- / \text{Im}(f_k^-)$ is proportional to the height h_k^- of the k th peak. The height h_k itself is proportional to the k th peak area which is, in turn, proportional to the concentration of the k th resonance. Therefore, the over-estimation of the peak $k = 12$ stems from the observed relation $h_{12}^- > h_{12}$. Furthermore, an inspection of the numerical values of these spectral parameters from Table 4 proves that the area of the 12th peak is over-estimated precisely by the corresponding amount of the missing 11th peak. Hence the compensation effect (which leads to the occurrence that the total shape spectrum on panel (iv) in Fig. 9 has reached convergence despite the absence of the peak $k = 11$ and the over-estimation of the peak $k = 12$). This also illustrates how risky it is to use an envelope spectrum to uncover the corresponding component spectra as is customarily attempted in most fitting routines used in MRS and beyond.

9. DISCUSSION

Single voxel *in vivo* MRS uses encoded FIDs to extract biochemical information about concentrations of clinically informative metabolites of the examined tissue. This is critically important for, *e.g.*, cancer diagnostics, because malignant tumours, benign processes, and healthy tissue usually differ significantly in their spectral information. These diagnostically crucial differences are detectable by MRS which can yield the initial information for the assignment of a particular disease to the identified spectral pattern of the scanned tissue. It is well known that *in vitro* MRS, which employs strong external magnetic fields, can resolve some 50 or so resonances [6]. This gives invaluable diagnostic information about tissue metabolites with high resolution and excellent SNR. However, such an excellent performance of *in vitro* MRS is absent from the corresponding *in vivo* MRS on clinical scanners that operate at considerably weaker fields and, therefore, yield information with poorer SNR. Moreover, the usual information from *in vivo* MRS is limited to a relatively small number of metabolites that can be resolved and eventually quantified for the purpose

of clinical diagnostics. A major reason for this problem is the fact that signal processing for *in vivo* MRS relies predominantly upon the FFT. Such a drawback of *in vivo* MRS could be considerably mitigated by employing high-resolution signal processors, *e.g.*, the FPT. Especially because of its capability to resolve closely overlapped resonances, the FPT can be advantageously applied to clinical FIDs encoded by *in vivo* MRS at short echo times. Most frequently, FIDs encoded via MRS use long echo times, because a larger number of short-lived tightly packed resonances create enormous problems to attempts at quantification by processing via fitting techniques that are non-unique. Furthermore, the powerful extrapolation characteristics of the FPT imply that long total acquisition times of encoded FIDs, as required by the FFT, are not indispensable. Such extrapolation advantages of the FPT also improve SNR relative to the FFT. Poor SNR has been cited in the literature as one of the major obstacles to the overall diagnostic performance of MRS [6,42].

Single voxel MRS complements MRI which provides only anatomical information about the spatial distribution of water and fat in the scanned tissue. Synergistically combining MRS and MRI gives multiple voxel MRSI, which provides both spatial distribution and biochemical information about many metabolites from the examined tissue. Originally, MRS was imported to medicine from basic laboratory research in physics and chemistry where it is known as NMR, which is one of the best spectroscopic methods available. However, accompanying well-developed theoretical methods in the corresponding signal processing from physics and chemistry [5] have not yet been widely imported to MRS. This situation ought to be improved on a more satisfying and deeper level in this extremely beneficial inter-disciplinary cross-fertilisation.

The information which is sought from the tissue via MRS is acquired in two separate stages. In the first instance, experimental measurement is employed for encoding a number of FIDs in a scanner.³ Subsequently, in the second step, theoretical methods are used through mathematical processing to quantify the averaged FID. The results of signal processing are the spectral parameters. These parameters are used to generate a frequency spectrum which has a number of peaks representing resonances at different chemical shifts. Such peaks can be isolated, overlapped, tightly overlapped, nearly degenerate, or degenerate (confluent). Every metabolite is linked to one or more resonances. The extracted spectral parameters determine the areas of these peaks in the frequency spectrum. The peak areas are proportional to the sought concentrations of metabolites. The retrieved spectral parameters for every individual resonance are the pairs of the fundamental complex frequencies and the associated complex amplitudes. The peak position or chemical shift is the real part of the complex frequency. The peak width is proportional to the imaginary part of the complex frequency. The relaxation times of metabolites are proportional to the inverse of the imaginary frequencies. The peak height is proportional to the quotient of the absolute value of the amplitude and the associated imaginary frequency. The phase of the individual harmonic component of the FID is the argument, *i.e.*, the phase of the complex amplitude. Thus, the reconstructed spectral parameters yield all the quantitative physical and biochemical information about metabolites of the scanned tissue, such as their concentrations, relaxation times, *etc.* The process of reconstruction of the pairs of complex-valued spectral parameters and the true number of resonances for the given FID represents an inverse nonlinear problem. In many research areas, this type of problem is encountered under a number of different names, *e.g.*, spectral analysis, harmonic analysis or complex-valued

³ Usually the number of encoded FIDs is of the order of 200. These measured FIDs are afterwards averaged to improve SNR. The averaged FID is subjected to signal processing.

moment problem (mathematics), harmonic inversion (physics, chemistry), quantification (medicine: MRS, MRSI), *etc.*

Importantly, signal processing plays a pivotal role in MRS. This is due to the fact that the most clinically relevant quantitative information about the examined tissue cannot be extracted from encoded FIDs without theoretical methods. These mathematical methods are necessary to properly interpret the measured time signals. Such theoretical interpretation of the encoded data, through solving the underlying inverse problem, yields the clinically sought information about metabolites' relaxation times, concentrations and the like. All of this is accomplished via an adequate reconstruction of the frequency-dependent parameters for the spectral profiles of the unknown fundamental components that are ingrained in the encoded FID. Generally, an inverse problem consists of finding the causes from the observation or measurement of the effects of the investigated phenomenon. Nearly all important measurements in science belong to the category of inverse problems. Inverse problems are extremely abundant in medicine. They are the essence of many powerful diagnostic tools without which modern hospitals would be basically non-functional. The most prominent examples of these versatile diagnostic modalities, that originate from basic research in physics and chemistry, are NMR, MRI, MRS, MRSI, CT (computerised tomography), PET (positron emission tomography), SPECT (single photon emission computerised tomography), US (ultrasound), *etc.* The common feature of these powerful diagnostic methods is the impossibility for direct interpretations of the measurements. Such a situation is rescued by the unavoidable recourse to theory whose mathematical methods are capable of solving reconstruction or inverse problems that are inherent in all the mentioned diagnostic modalities.

Surprisingly, for too long a time now, signal processing in MRS has been dominated by the FFT. Such an occurrence is at variance with the quantification problem, which is the very goal of MRS. The FFT is a non-quantifying estimator of envelope spectra. This qualitative information is usually complemented in MRS by fitting either encoded FIDs or Fourier spectra. These fittings employ some free, LS-adjusted parameters in attempts to quantify the MRS data. However, none of the fitting prescriptions from MRS can give the unequivocal solution for the mentioned inverse problem. In other words, fittings cannot yield the unique estimates for the sought spectral parameters that are the positions, widths and heights of the peak profiles, nor about the total number of resonances. This is the case because any given total shape spectrum (envelope) could always be fitted by many different sets of component shape spectra. Each set contains a number of metabolites. However, any fixed resonance can be of vastly different spectral characteristics when passing from one to another sets of component shape spectra. Hence, the non-uniqueness of fittings in MRS. This typically leads to two difficulties in practice, such as over-fitting and under-fitting. Over-fitting retrieves some non-existent, *i.e.*, spurious metabolites. Under-fitting fails to reconstruct some of the existing, *i.e.*, genuine metabolites. In both cases, a fitting bias is in guessing the number of the physical resonances. This could severely hamper diagnostics that are supposed to be aided by signal processing. For example, in brain tumour diagnostics via MRS, several inconclusive findings have been reported with contradictions depending on whether some typical metabolites were included or excluded from the basis set of *in vitro* spectra used in the LCModel for fitting the corresponding *in vivo* data [43,44].

All fitting algorithms available in MRS use the customary LS adjustments. This is accomplished in either the time or the frequency domain. In the frequency domain, fittings try to adjust the given total shape spectrum by a chosen model in order to reconstruct the most

important component shape spectra of individual resonances and their spectral parameters. As stated earlier, the LS technique is a minimisation of the LS residual, which represents the squared difference between the input and the modelled information. Any selected model in fittings is based upon variations of the free parameters until eventually a minimum of the LS residual is found. Almost invariably, the found extremum represents a local rather than the more correct global minimum. Often the varying parameters are constrained by some conditions to facilitate fittings. Likewise, in the time domain, the studied FID is fitted in MRS via adjustable parameters to match the damped oscillations in the encoded raw data. Irrespective of the studied domain (time or frequency), the fitting algorithms from MRS invariably use non-orthogonal expansion functions. Usually, such basis sets are damped complex exponentials, Gaussians and/or their combinations as implemented in VAPRO, AMARES, *etc.* Alternatively, rather than modelling individual resonances, fittings in MRS also use the whole model spectra with some pre-selected metabolites that play the role of a non-orthogonal basis set expansion as done in the LCModel. In all such fittings, non-orthogonality of expansion sets implies that any alteration in the weighted sum of the LS residuals caused by a change of one or more adjustable parameters in the selected mathematical model, could largely be compensated by totally independent variations of all the other free parameters [13]. This arbitrariness becomes especially severe when the number of adjustable parameters in fittings is not small. Such a mathematical ill-conditioning leads to non-uniqueness of all the LS fitting algorithms currently used in MRS. Contrary to this drawback of fittings, the FPT provides the unique reconstructions. In particular, in the FPT, the complex frequencies are unequivocally determined by solving the characteristic equation, which as the so-called secular equation is equivalent to the Schrödinger equation [17]. This leaves no room whatsoever for freedom in ‘varying’ the amplitudes, since they are unambiguously fixed by their definitions as the Cauchy residues (7.26) or (7.35) of the Green–Padé functions. There is also the uniqueness proof for these amplitudes. This proof demonstrates that, for the same set of retrieved complex frequencies, all different ways of computing the associated amplitudes must give the identical results [5]. Thus, the fundamental frequencies for the genuine resonances reconstructed via, *e.g.*, the HLSVD and the FPT under the same conditions ought to coincide with each other. Consequently, despite the fact that in the HLSVD the amplitudes are computed by solving a system of linear equations, rather than through the analytical expression of the FPT, the results from both methods must be the same. This should serve as a check to the numerical solutions for the amplitudes in the HLSVD. Obviously, the procedure in the FPT is optimal for the amplitudes of resonances encountered in MRS, since these Padé residues are available in the closed, analytical formula (7.26) or (7.35).

In MRS, it is often argued that the so-called biochemical prior information from fittings should be exported to other non-fitting algorithms. Such claims advocate that the overall quality of quantification is pre-determined by some prior information. However, the ‘biochemical’ prior information used in MRS is most often a pre-determined relationship, *e.g.*, fixed phases or amplitude ratios or quotients of peak areas of some resonances (or imposed connections among widths of several peaks in a selected part of the spectrum or throughout the Nyquist interval, *etc.*), as done in VAPRO, AMARES and LCModel. In other words, these claims imply that this type of prior information should be considered as a prerequisite for successful quantifications in MRS. This is incorrect, because the introduction of this type of prior information represents merely an attempt to mitigate the effect of subjectivity of fittings. Such attempts via some imposed constraints germane only to fitting try to

reduce the error from under- or over-estimation of subjectively pre-selected metabolites in an expansion set. In this way, *e.g.*, under-fitting would result in an overestimation of the true values of the spectral parameters because of the lack of a sufficient number of resonances in an expansion sets. Such an outcome is due to some attempts to minimise the said LS residuals. As especially unwelcome to medical diagnostics via MRS, this minimisation can overestimate the peak areas and this, in turn, would undermine the estimates for the related concentrations. The fitted peak areas are influenced by attempts to minimise the error from the missing genuine resonances in a chosen basis set by over-weighting the relative contribution from the included resonances.

These outlined basic drawbacks of fitting approaches to quantifications in MRS also point to the need for alternative estimations of spectral parameters. Such non-fitting strategies should not contain any free parameters and, moreover, they should yield the unique solution for restoration of the unknown harmonic components from FIDs in MRS. From the onset, the FPT is optimally suited to fulfil this goal of quantifications in MRS. This is understood by referring to the fact that the FPT is the exact filter for all the FIDs built from attenuated complex exponentials with stationary and non-stationary amplitudes that yield Lorentzian and non-Lorentzian spectra in MRS. Here, the word filter signifies an operation applied to the said FID with the result given by a baseline constant c_∞ . This constant is the limiting stationary value of the FID from which all the harmonics (transients) have been filtered out in a transformation whose outcome is equivalent to taking the limit of infinite times ($n\tau \rightarrow \infty$) in the considered set $\{c_n\}$. Such an exact filter is the Shanks transform which is, in fact, the FPT applied directly in the time domain [5]. The implicit time limiting process $t \rightarrow \infty$, which goes hand-in-hand with the Shanks transform, nicely illustrates the extrapolation features of the time-domain version of the FPT. Explicitly, the Shanks transform is defined as a quotient of two Hankel determinants. In the case of higher dimensions, these determinants are not practical for extensive numerical computations. Nevertheless, the Shanks transform is salvaged by the Wynn ε -algorithm which computes the ratios of the two Hankel determinant recursively. However, this latter recursion is nothing but yet another computational algorithm in the FPT. That these statements about filtering of harmonics from an FID are plausible, it suffices to recall a simpler and more familiar accelerator called the Aitken extrapolation, or equivalently, the Δ^2 -process [10]. If an FID has only one harmonic ($K = 1$), then the Aitken transformation is the exact filter in the above-defined sense. A direct generalisation of the Aitken transform to an FID with any higher number of harmonics ($K > 1$) represents the Shanks transform as the multi-exponential version of the single-exponential time signal.

Overall, the Padé methodology is not just another spectral analyser added to a sequence of the already existing ones. On top of its technical virtues of the uniqueness and exactness for solving the quantification problem in MRS, the most fundamental feature which singles out the Padé methodology from the conventional signal processors is that it is not only a powerful computational framework. More importantly, the Padé methodology is implicitly or explicitly a cornerstone of the very formulation of the Schwinger variational principles, the Heisenberg scattering matrix, the Green function, to name only a few of the leading strategies in the most successful physics theory—quantum mechanics [5].

10. CONCLUSION

The present investigation has the focus upon the exact solution of the quantification problem for noiseless synthesised time signals, or equivalently, free induction decays (FID) encountered in Magnetic Resonance Spectroscopy (MRS). For this purpose, we employ the fast Padé transform (FPT). The quantification problem in MRS is known to be the mathematically ill-conditioned harmonic inversion, which also goes under the equivalent names of spectral analysis, reconstruction or spectral decomposition. Here, an FID is given, whereas its building components as the damped fundamental harmonics are unknown. Specifically, the sought spectral parameters are the complex frequencies and the associated complex amplitudes. These extracted quantities can be interpreted to yield the physical and biochemical information about the metabolites in the tissue from which the FID has been encoded.

It is shown numerically that the quantification problem in MRS can be solved exactly by means of the FPT applied to a synthesised noiseless time signal. The particular values of the complex frequencies and amplitudes for the chosen 25 resonances in the synthesised FID are similar to those characterising short echo time FIDs encoded from a healthy human brain via proton MRS at $B_0 = 1.5$ T with a typical bandwidth 1000 Hz and the signal length 1024. Similarity between the presently synthesised time signal and FIDs encoded via *in vivo* MRS is further enhanced by assuring that the selected spectral parameters yield isolated, overlapped, tightly overlapped, and nearly degenerate Lorentzian resonances at different chemical shifts as abundantly present in the measured data. Chemical shifts are the resonant frequencies of the tissue protons. These shifts are much smaller than the Larmor precessing frequency of protons' magnetisation vectors around the axis of the external static magnetic field of the strength B_0 . Nevertheless, it is this small correction to the Larmor frequency that makes MRS happen. Without such corrections all the scanned protons would resonate at the same Larmor frequency and, therefore, the spectrum will exhibit a single peak. This would indeed be the case if all the protons under investigation were free. However, protons are bound in a variety of molecular compounds in the tissue. The electronic clouds of different molecules are able to produce different shieldings of protons' magnetic fields. Such shieldings cause protons to resonate with the external field at frequencies that are slightly shifted relative to the Larmor frequency as a function of the protons' chemical surrounding. Nevertheless, especially for the human brain metabolites investigated via proton MRS, the span of this shifting is relatively small. In particular, for the human brain investigated via proton MRS, most of the chemical shifts associated with the main part of a customary spectrum are situated between 0 ppm and 5 ppm. Of course, this latter range is only a fraction of the whole Nyquist interval. The chosen resonances of our synthesised FID correspond to a linear combination of damped complex exponentials with stationary amplitudes. This leads to a non-degenerate, Lorentzian spectrum. However, the FPT can also treat degenerate resonances that yield a non-Lorentzian spectrum. In this case, the FID is a sum of damped complex exponentials with non-stationary, *i.e.*, time-dependent amplitudes.

The FPT can perform both parametric and non-parametric estimations. The former is accomplished by solving the quantification problem, whereas the latter is done in a transform-type manner via a frequency-by-frequency computation of the response function without the need to reconstruct any spectral parameters. We presently elaborate the two different versions of the FPT denoted by $\text{FPT}^{(+)}$ and $\text{FPT}^{(-)}$. They unify the conven-

tional Padé approximant (PA) and the standard causal Padé z -transform (PzT), where z is the frequency-dependent complex harmonic variable. These two versions of the FPT are set up using the same truncated input Maclaurin series expansion for the exact spectrum given by the Green function of the studied system. The expansion coefficients in this Maclaurin development are the time signal points that are equivalent to the quantum-mechanical auto-correlation functions. Both the $\text{FPT}^{(+)}$ and the $\text{FPT}^{(-)}$ are the unique polynomial quotients in their respective independent variables z and $1/z$, respectively. Consequently, the initial convergence regions of the $\text{FPT}^{(+)}$ and the $\text{FPT}^{(-)}$ are inside ($|z| < 1$) and outside ($|z| > 1$) the unit circle. However, being rational analytical functions, both polynomial quotients automatically expand their initial validities to the whole complex plane of the harmonic variables as secured by the Cauchy principle of analytical continuation. As such, the $\text{FPT}^{(+)}$ and the $\text{FPT}^{(-)}$ are computable everywhere excepting the singular points given by the poles that represent the locations of fundamental frequencies from the examined FID. When the Maclaurin series is defined in the variable $1/z$, as in the present study, then this exact Green function expansion is convergent for $|z| > 1$ and divergent for $|z| < 1$, respectively. Therefore, the $\text{FPT}^{(+)}$ analytically continues a divergent series forcing it to converge for $|z| < 1$. On the other hand, the $\text{FPT}^{(-)}$ accelerates the convergence rate of an already convergent series for $|z| > 1$. However, there is more to the principle of analytical continuation than transforming an initial series in terms of $1/z$ into another series in powers of z . Analytical continuation also means that a function originally defined, *e.g.*, only for real frequencies, can be mapped into another more general function of complex frequencies. This is achieved by both the $\text{FPT}^{(+)}$ and the $\text{FPT}^{(-)}$ and, in this sense, they both perform analytical continuation. If the defining polynomial quotients from the $\text{FPT}^{(+)}$ and the $\text{FPT}^{(-)}$ are expanded in their own Maclaurin series, they must coincide with the original Maclaurin expansion at a fixed order depending on the degrees of the numerator and denominator polynomials. This means that all the converged results from the $\text{FPT}^{(+)}$ and the $\text{FPT}^{(-)}$ ought to be the same. Hence the uniqueness of the FPT. Such an internal cross-validation of the FPT is confirmed in the present numerical illustrations by carrying out the exact reconstructions of all the input spectral parameters. Moreover, the FPT succeeds to arrive at this accomplishment by employing only a quarter of the full FID.

For the given FID, the spectrum in the FPT can be set up, *e.g.*, in its diagonal form as the quotient of two unique polynomials P_K/Q_K . The sought exact number of resonances due to the fundamental harmonics from an FID is determined unequivocally in the FPT by the degree K of the denominator polynomial Q_K . By contrast, all other estimators used in MRS, and especially fitting algorithms, merely guess the true number K . The FPT takes an entirely different approach by conceiving the exact number K of resonances as yet another spectral parameter to be determined along with the frequencies and amplitudes by solving the quantification problem. In fact, the whole strategy of the FPT is so orthogonal to the common practice with attempted quantifications in MRS that the Padé methodology should rightly be considered as a paradigm shift. The FPT does not require any envelope spectrum such as the one from the FFT or any other processor to extract the spectral parameters. Quite the contrary, the FPT first extracts the complex frequencies and the corresponding amplitudes from the input raw data and the spectral analysis can end at this point. If desired, the shape spectra in any mode can be constructed afterwards, when all the spectral parameters become available. Moreover, the numerical work involved in solving the quantification problem by the FPT is straightforward. Thus, complex resonant frequencies are reconstructed exactly by obtaining the roots of the denominator polynomial Q_K , even

for large degree K , *via*, *e.g.*, the equivalent eigenvalues of the corresponding Hessenberg matrix. This latter polynomial is recognised as the characteristic or secular polynomial from quantum mechanics and linear algebra in numerical analysis. Upon finding these fundamental frequencies, the corresponding unique amplitudes are also readily extracted from the analytical expression for the Cauchy residue of the quotient P_K/Q_K in contrast to solving a system of linear equations as done in, *e.g.*, Hankel–Lanczos Singular Value decompositions, Linear Predictor, *etc.* These remarkable features illustrate the ease with which the FPT so naturally arrives at the most reliable quantifications in MRS. A robust algorithmic implementation of the FPT, as done in the present study using exclusively the standard Matlab routines, requires minimal computational effort. Moreover, the obtained results are shown to be numerically exact despite the usual finite precision arithmetic with the attendant round-off errors. It is explicitly demonstrated that by using only a quarter of the full time signal length, the FPT can reconstruct exactly all the spectral parameters of the investigated 25 resonances, including the isolated, overlapped, tightly overlapped, and nearly degenerate peaks.

Interestingly, the Fourier analysis itself lends support to the Padé analysis. Namely, it is well known from the Fourier analysis, that the exact one-sided Fourier integral from zero to infinity over a time signal from MRS, modelled by a linear combination of damped complex exponentials with constant amplitudes, is given precisely by the corresponding sum of Lorentzians that, in turn, represents the frequency spectrum. Further, still staying within the Fourier analysis, this latter sum is expressed explicitly in the representation of the Heaviside partial fractions. However, when the sum over these partial fractions is formally carried out, the result is invariably the ratio of two unique polynomials, which is then recognised as the standard Padé approximant. Nevertheless, the Fourier analysis stops short of making this latter statement explicitly. However, the underlying truth here is that the exact spectrum for these FIDs is a rational function given by a polynomial quotient. Hence, for such classes of functions that describe adequately the typical spectra encountered in MRS, the Padé approximant is, in fact, the exact theory. This should leave no doubt about which processor should be considered as optimal for MRS.

These remarks illustrate that already the Fourier analysis, in fact, paves the road for a natural introduction of the Padé-based MRS. Moreover, such observations also cohere fully with an independent formulation of the FPT. Namely, the Maclaurin series or, equivalently, the familiar z -transform, the Green function and its Heaviside partial fraction representation containing implicitly the Padé polynomial quotient, are all ingrained in the FPT from the onset with no reference to the Fourier integral or Fourier analysis. Furthermore, although the starting point of the FPT might provisionally be these expansions for the exact spectrum, the final result of the Padé spectral analysis is ultimately the set of the fundamental frequencies and amplitudes as the reconstructed attenuated harmonic components of the FID from the time domain. Precisely the same results are also obtained if the starting point of the analysis is taken to be the FID rather than its spectrum. In other words, the process of estimation in the FPT is done by treating the time and frequency domain on the same footing and simultaneously. Both ways (time and frequency domain analysis) invariably lead to precisely the same characteristic equation or the eigenproblem whose solutions are the spectral parameters. Thus for the full quantitative information about the system it suffices to give these parameters as the fundamental frequencies and the corresponding amplitudes without necessarily specifying the way in which they might subsequently be employed (*e.g.*, to construct spectra in various modes, to retrieve the given time signal

or to extrapolate it to unmeasured values, *etc.*). The robustness of any examined system with respect to the external excitations or perturbations is judged by its ability to maintain stability. Optimal stability, in many systems across interdisciplinary fields ranging from engineering to applied and basic science, is modelled by rational response functions via polynomial quotients as predicted by the Padé analysis. Hence, rather than defining such rational polynomials through their frequency representations of the Heaviside partial fractions, it is enough to provide simply the defining parameters of these functions as the fundamental frequencies and amplitudes. This is reminiscent of an alternative definition of an ordinary single polynomial, not necessarily through its development in powers of the independent variable, but rather via the set of all its parameters as the expansion coefficients. These general concepts of the Padé-based MRS make the border between the time and frequency domain analysis elusive, as they should be. This is opposed to fittings that are strictly limited, from the onset, to be either time or frequency domain techniques, depending on whether the FID or its spectrum is chosen to adjust the free parameters using some mathematical models.

From the beginning, the quantification analysis in MRS is a mathematically ill-conditioned problem as mentioned. This is caused by the lack of a continuous dependence of the sought solution upon the input data. Such an inherent difficulty of the problem itself, not of the employed methods, can possibly lead to large variations in the reconstructed spectral parameters even for relatively small uncertainties in the given encoded FID. The origin of these uncertainties or perturbations can be multifaceted, including various systematic experimental errors, statistical effects manifested as noise of varying levels, *etc.* On top of this, the methods of spectral analysis can add their own uncertainties through the computational round-off errors, algorithmic instabilities, *etc.* Therefore, attempts to handle simultaneously all these kinds of corruption of the analysed data are usually met with enormous difficulties especially for newly designed methods such as the FPT for the special purpose of MRS. Instead, a more prudent approach to this very challenging problem would be to assess the validity and the overall performance of a given processor in a systematic way by using first the realistically synthesised FIDs (noise-free and noise-corrupted) and then to extend the full spectral analysis to encoded time signals. In the case of a theoretically generated FID, the fundamental frequencies and amplitudes are known, so that the focus of the analysis should be placed upon the tests of the accuracy, robustness, and reliability of the estimator. Especially important are synthesised noiseless time signals that deserve a special investigation as done in the present work, because all the steps of the analysis from the input data to the finally reconstructed information can be fully controlled. In such a case, we prove in this study that the FPT is capable of achieving an unprecedented high performance in all the critical aspects of solving exactly the quantification problem in MRS.

From the high-resolution spectral analysis presented in this work for noiseless synthesised time signals, with the obtained results and their importance for furthering the field of MRS, encouraging especially the applications in clinical oncology, the following key question emerges. Is it feasible to exploit the reported stunning reliability of the fast Padé transform, as per all the vital predictions of the quantum-mechanical spectral analysis and signal processing, to carry out the most accurate and robust quantification in MRS also for noise-corrupted synthesised as well as encoded *in vivo* FIDs? The answer in the affirmative to this central question is already known from our recent studies on the level of estimation of envelope spectra computed by the FPT using FIDs encoded by *in vivo* MRS.

Although in these investigations, quantification problems have explicitly been solved by the FPT prior to construction of such spectra, the concrete detailed information especially about the sensitivity of all the reconstructed fundamental frequencies and amplitudes to the presence of noise in the encoded time signals have not yet been reported. This needs to be done systematically for both synthesised noise-corrupted and encoded FIDs. In a work to appear shortly, we have completed this essential and most demanding task by extending strictly the Padé methodology to noise-polluted time signals. As a preview, we emphasise that the role of the Froissart doublets or pole–zero cancellation for differentiation between genuine and spurious harmonics, as demonstrated presently for noiseless FIDs, becomes of critical importance also for distinguishing the physical from the non-physical, *i.e.*, noise-contaminated content in encoded time signals.

ACKNOWLEDGEMENTS

This work has been supported by the Swedish National Science Foundation (Vetenskapsrådet), Stockholm City Council for Research, Development and Education (FoUU), Swedish Cancer Society (Cancerföreningen), and the Karolinska Institute Research Fund.

REFERENCES

- [1] Z.-P. Liang, P.C. Lauturber, *Principles of Magnetic Resonance Imaging: A Signal Processing Prospective*, IEEE Press Series in Biomedical Engineering, IEEE, New York, 2000.
- [2] H. Günther, *NMR Spectroscopy: Basic Principles, Concepts and Applications in Chemistry*, second ed., Wiley, Chichester, 1992.
- [3] R. Freeman, *A Handbook of Nuclear Magnetic Resonance*, second ed., Addison-Wesley/Longman, Edinburgh, 1997.
- [4] D.W. McRobbie, E.A. Moore, M.J. Graves, M.R. Prince, *MRI from Picture to Proton*, Cambridge Univ. Press, Cambridge, 2003.
- [5] Dž. Belkić, *Quantum-Mechanical Signal Processing and Spectral Analysis*, Institute of Physics Publishing, Bristol, 2004 (and references therein).
- [6] K. Belkić, *Molecular Imaging through Magnetic Resonance for Clinical Oncology*, Cambridge International Science Publishing, Cambridge, 2004 (and references therein).
- [7] J.W.C. van der Veen, R. de Beer, P.R. Luyten, D. van Ormondt, *Magn. Reson. Med.* **6** (1988) 92.
- [8] L. Vanhamme, A. van den Boogaart, S. van Haffel, *J. Magn. Reson.* **129** (1997) 35.
- [9] S.W. Provencher, *Magn. Reson. Med.* **30** (1993) 672.
- [10] W.H. Press, S.A. Teukolsky, W.T. Vetterling, B.P. Flannery, *Numerical Recipes*, second ed., Cambridge Univ. Press, Cambridge, 1992.
- [11] Dž. Belkić, K. Belkić, *Phys. Med. Biol.* **51** (2006) 1049.
- [12] Dž. Belkić, *Phys. Med. Biol.* **51** (2006) 2633.
- [13] A.A. Istratov, *Rev. Sci. Instr.* **70** (1999) 1233.
- [14] W.W.F. Pijnappel, A. van den Boogaart, R. de Beer, D. van Ormondt, *J. Magn. Reson.* **7** (1992) 122.
- [15] A. Sidi, *Practical Extrapolation Methods: Theory and Applications*, Cambridge Univ. Press, Cambridge, 2003.
- [16] Dž. Belkić, *Nucl. Instr. Methods Phys. Res. A* **471** (2001) 165.
- [17] Dž. Belkić, P.A. Dando, J. Main, H.S. Taylor, *J. Chem. Phys.* **133** (2000) 6542.
- [18] Dž. Belkić, P.A. Dando, H.S. Taylor, J. Main, S.-K. Shin, *J. Phys. Chem. A* **104** (2000) 11677.
- [19] M. Dechamps, I. Burghardt, C. Derouet, G. Bodenhausen, Dž. Belkić, *J. Chem. Phys.* **113** (2000) 1630.
- [20] Dž. Belkić, *Magn. Reson. Mater. Phys. Biol. Med.* **15** (2002) 36.
- [21] Dž. Belkić, *Nucl. Instr. Methods Phys. Res. A* **525** (2004) 366.
- [22] Dž. Belkić, *Nucl. Instr. Methods Phys. Res. A* **525** (2004) 372.

- [23] D.Ž. Belkić, *Nucl. Instr. Methods Phys. Res. A* **525** (2004) 379.
- [24] D.Ž. Belkić, K. Belkić, *Int. J. Quantum Chem.* **105** (2005) 493.
- [25] D.Ž. Belkić, K. Belkić, *Phys. Med. Biol.* **50** (2005) 4385.
- [26] M.F. Callaghan, D.J. Larkman, J.V. Hajnal, *Magn. Reson. Med.* **54** (2005) 1490.
- [27] D.C. Williamson, H. Hawes, N.A. Thacker, S.R. Williams, *Magn. Reson. Med.* **55** (2006) 762.
- [28] J. Frahm, H. Bruhn, M.L. Gyngell, K.D. Merboldt, W. Hanicke, R. Sauter, *Magn. Reson. Med.* **1** (1989) 79.
- [29] M.A. Thomas, L.N. Ryner, M.P. Mehta, P.A. Turski, J.A. Sorenson, *J. Magn. Reson. Imag.* **6** (1996) 453.
- [30] G. Breit, E. Wigner, *Phys. Rev.* **49** (1936) 519.
- [31] A.J.F. Siegert, *Phys. Rev.* **56** (1939) 750.
- [32] D.Ž. Belkić, *Principles of Quantum Scattering Theory*, Institute of Physics Publishing, Bristol, 2003.
- [33] H.A. Lorentz, *Proc. Roy. Acad. Amsterdam* **13** (1914) 134.
- [34] W. Voigt, *Münch. Ber.* (1912) 603.
- [35] A. Freise, E. Spencer, I. Marshall, J. Higinbotham, *Bull. Magn. Reson.* **17** (1995) 302.
- [36] W. Gautschi, *SIAM J. Numer. Anal.* **7** (1970) 187.
- [37] M. Froissart, Approximation de Padé: application à la physique des particules élémentaires *CNRS, RCP, Programme n° 29, Strasbourg* **9** (1969) 1.
- [38] A.U. Hazi, H.S. Taylor, *Phys. Rev. A* **1** (1970) 1109.
- [39] I. Tkáč, P. Andersen, G. Adriany, H. Merkle, K. Uğurbil, A. Grueter, *Magn. Reson. Med.* **46** (2001) 451.
- [40] E. Cabanes, S. Confort-Gouny, Y. Le Fur, F. Simond, P.J. Cozzone, *J. Magn. Reson.* **150** (2001) 116.
- [41] D.J. Drost, W.R. Riddle, G.D. Clarge, *Med. Phys.* **29** (2002) 2177.
- [42] R. Katz-Brull, P.T. Lavin, R.E. Lekinski, *J. Natl. Cancer Inst.* **94** (2002) 1197.
- [43] Y.-D. Cho, G.-H. Choi, S.-P. Lee, J.-K. Kim, *Magn. Reson. Imag.* **21** (2003) 663.
- [44] K.S. Opstad, S.W. Provencher, B.A. Bell, J.R. Griffiths, F.A. Howe, *Magn. Reson. Med.* **49** (2003) 632.

This page intentionally left blank

Probing the Interplay between Electronic and Geometric Degrees-of-Freedom in Molecules and Reactive Systems

Roman F. Nalewajski

Department of Theoretical Chemistry, Jagiellonian University, R. Ingardena 3, 30-060 Cracow, Poland

Abstract

The Density-Functional Theory (DFT) description of molecular equilibria in both the externally *closed* (N -controlled) and *open* (μ -controlled) systems, where N denotes the system overall number of electrons and μ stands for its chemical potential, equal to that of the external reservoir of electrons, is explored within the Born–Oppenheimer approximation. The complementary *Electron-Following* (EF) and *Electron-Preceding* (EP) perspectives on molecular processes are examined, in which the external potential due to nuclei and the system electron density, respectively, provide the local state-variable of the molecular ground-state. In the chemical-softness representation of the EF perspective, which directly refers to the Born–Oppenheimer approximation of the wave-function theory, the external potential due to the system nuclei constitutes the independent state-parameter, with the electron distribution “following” the movements of the nuclei. In the chemical-hardness representation of the EP approach, in the spirit of DFT, the ground-state electron density determines the equilibrium state of the molecule. Its displacements create conditions for (“precede”) the movements of the nuclei in the spirit of the Hellmann–Feynman theorem. The equivalence of these two formulations is stressed and their complementarity in the complete theory of the electronic/geometrical structure and chemical reactivity is stressed. The associated quadratic Taylor expansions of the corresponding “thermodynamic” potentials for each representation are discussed. A distinction is made between the equilibrium (“horizontal”) and non-equilibrium (“variational”) expansions of the corresponding density functionals. In each Legendre-transformed representation the generalized “potentials” (first partials) and charge “sensitivities” (second partials) are summarized and interpreted as prospective descriptors of reactivity phenomena and external conditions of molecular processes. These basic concepts of the DFT reactivity theory include the global and local softness (hardness) quantities of the electron “gas”, the electronic and nuclear Fukui functions, and the theory basic kernels: the density linear-response function of the closed molecular systems, and the softness/hardness kernels of the externally open systems. The fundamental relations between these basic quantities are summarized and interpreted. In each representation the transformations between the system *perturbations*, *i.e.*, displacements of the system independent state-parameters, and the equilibrium linear *responses* of the conjugate (dependent, unconstrained) quantities are formulated in terms of the relevant charge sensitivities.

The equilibrium, ground-state coupling between the electronic and geometrical degrees-of-freedom of both closed and open molecular systems is then explored within the geometrical representations, which use the explicit dependence of the Legendre-transforms of the system Born–Oppenheimer potential-energy-surface on the nuclear coordinates or forces. Specific descriptors measuring this dependence are identified and discussed. The minimum-energy coordinates, formulated within the compliant approach to the combined electronic–nuclear structures of molecular systems, are introduced and discussed within both the global and atomic resolutions of the ground-state electron density. Of great importance in chemistry is the related condensed description of *Atoms-in-Molecules* (AIM). The relevant AIM-discretized Legendre-transformed descriptions of molecular states are established. They involve the atomic electron populations and chemical potentials, as well as the atomic external-potential quantities per electron. Such state-parameters of bonded atoms are defined using the “shape”-factors of atomic electron densities. The transformations between the AIM perturbations and responses are explored in alternative Legendre-transformed representations. The populational normal modes, which represent the independent (decoupled) coordinates for changing the system electronic structure, are introduced and the mapping

relations between the nuclear coordinates and electron populations of constituent atoms are summarized for the externally closed and open molecules, in both the EF and EP perspectives. These direct “translators” between the concomitant trajectories in the nuclear-position and the atomic electron-population spaces, respectively, embody the main trends of the intuitive *bond-length-variation* rules of Gutmann.

The equilibrium states and charge sensitivities of reactants in the Donor–Acceptor (DA) reactive systems are discussed. The *mutually* open and closed reactants are examined for both the *externally* open and closed arrangements of the basic and acidic subsystems. The *in situ* hardness and softness (or Fukui function) quantities defined by the derivatives of the system electronic energy with respect to the amount of the internal charge transfer are introduced and expressed through the corresponding condensed descriptors of both reactants. The implications of the equilibrium and stability criteria for the DA reactive systems are explored and regimes of the internal and external stability/instability are identified in terms of relations between the off-diagonal hardness in the reactant resolution, which reflect a charge coupling between the two subsystems, and the arithmetic and geometric averages of the diagonal hardnesses of both reactants in the DA complex. Within the information-theoretic approach to molecular subsystems, which justifies the so-called “stockholder” partition of the overall, molecular electron density, the *entropic* charge sensitivities of reactants are introduced. They represent the populational derivatives of the entropy deficiency in the subsystem resolution. The relevant chain-rule expressions demonstrate that these novel quantities, e.g., the *charge-transfer affinities* (entropic “forces”) unite the energy derivatives (Fukui functions) and the entropy-deficiency conjugates of the subsystem densities. The corresponding *in situ* information quantities for the internal charge transfer in the externally closed systems are also explored. The stockholder subsystems are shown to correspond to the equilibrium amount of CT, marking the vanishing affinities for the flow of electrons between the basic and acidic reactants. The reactant missing-information descriptors reflect the entropic variational principles, which define the electron densities of stockholder subsystems.

Contents

1. Introduction	236
2. Summary of basic relations	241
2.1. Chemical-softness representation	241
2.2. Chemical-hardness representation	248
2.3. Transformations between perturbations and responses	254
3. Electronic and nuclear sensitivities in geometric representations	256
3.1. Principal representation and its derivative quantities	256
3.2. Legendre-transformed representations	258
4. Minimum-energy coordinates in compliance formalism	263
5. Compliant indices of atoms-in-molecules	265
6. Atomic resolution—A reappraisal	271
7. Collective charge displacements and mapping relations	276
8. Concepts for reacting molecules	282
8.1. Equilibrium states and charge sensitivities of reactants	282
8.2. <i>In situ</i> quantities in donor–acceptor systems	290
8.3. Implications of equilibrium and stability criteria	292
8.4. Entropic charge sensitivities of reactants	294
9. Conclusion	299
References	301

1. INTRODUCTION

NOTE: Throughout paper, for example, \mathbf{P} is a square/rectangular matrix, \mathbf{P} denotes a row vector, and P stands for scalar quantity. The atomic units will be used throughout the paper. The broken (solid) vertical lines separating molecular subsystems denote their mutually open (closed) status, e.g., in reactive systems.

Although in the molecular world the distinction between the “intensive” and “extensive” state-parameters is blurred [1–3], we often refer to the molecular number of electrons N

as the *global* “extensive” parameter, since the overall number of electrons in the composite system is the sum of the corresponding average values for each component. Accordingly, the energy-conjugate of N , the chemical potential μ of electrons, is often referred to as the global “intensive” parameter of state. The N -controlled systems are externally-*closed* while the μ -controlled systems can be regarded as externally-open, being coupled to the hypothetical electron reservoir, which fixes the system chemical potential. The physical processes in both these types of molecular systems and their fragments have been systematically approached using the linear-response approximation of the Charge Sensitivity Analysis (CSA) [1–17].

The system internal degrees-of-freedom have either electronic or nuclear (geometric) origins. The global state-variables N and μ , of the system as a whole, or the local density of electrons $\rho(\mathbf{r})$ are electronic in character, while the positions of atomic nuclei $\mathbf{R} = \{\mathbf{R}_\alpha\}$ or their energy conjugates, the forces on nuclei $\mathbf{F} = \{\mathbf{F}_\alpha\}$, and the external potential $v(\mathbf{r})$ describe the complementary, geometric aspect of the molecular structure. In the molecular-fragment resolution, *e.g.*, in the atoms-in-molecules (AIM) description, a similar distinction applies to parameters describing the internal equilibria in molecular subsystems. For example, the electronic parameters of state of bonded atoms $\{N_\alpha, \mu_\alpha, \rho_\alpha(\mathbf{r})\}$ index the atomic average number of electrons $N_\alpha[\rho_\alpha] = \int \rho_\alpha(\mathbf{r}) d\mathbf{r}$, its chemical potential, and atomic electron density, respectively. The nuclear variables of AIM may involve either their condensed external potential variables $\mathbf{V} = \{V_\alpha\}$ or their local variants $\mathbf{v}(\mathbf{r}) = \{v_\alpha(\mathbf{r})\}$ [2–4,7–10]. The latter can be hypothetically manipulated separately or they can be set to the molecular (bare-nucleus) external potential, $\mathbf{v}(\mathbf{r}) = v(\mathbf{r})\mathbf{I} = \{v_\alpha(\mathbf{r}) = v(\mathbf{r})\}$ [3,4,6]. Alternatively, one uses the atomic effective (embedded) potentials $v_\alpha^{\text{eff}}(\mathbf{r}) = \{v_\alpha^{\text{eff}}(\mathbf{r})\}$, which take into account the presence of remaining atoms. The atomic densities $\rho_\alpha(\mathbf{r}) = \{\rho_\alpha(\mathbf{r})\}$ represent their ground-state distributions: $\rho_\alpha = \rho_\alpha[N_\alpha, v_\alpha^{\text{eff}}]$ or $\rho_\alpha = \rho_\alpha[\mu_\alpha, v_\alpha^{\text{eff}}]$ [3,4,6,17].

It should be also observed that some important parameters of state of both molecules and their parts exhibit a mixed electronic-and-nuclear origin. Consider, *e.g.*, the relative external potential of the Euler equation for the equilibrium electron density $\rho = \rho[N, v]$ in Density Functional Theory (DFT) [1,18],

$$u(\mathbf{r}) = v(\mathbf{r}) - \mu = -\frac{\delta F[\rho]}{\delta \rho(\mathbf{r})}, \quad (1)$$

which results from the variational principle for the minimum of the system electronic energy $E_v[\rho] = \int v(\mathbf{r})\rho(\mathbf{r}) d\mathbf{r} + F[\rho]$ subject to the constraint of the system prescribed number of electrons, $N[\rho] = \int \rho(\mathbf{r}) d\mathbf{r} = N$:

$$\delta\{E_v[\rho] - \mu N[\rho]\} = 0. \quad (2)$$

The universal functional $F[\rho]$ generates the sum of electronic kinetic and repulsion energies, and the system chemical potential plays the role of the Lagrange multiplier enforcing the constraint. Clearly, the relative external potential of equation (1) is of the mixed character, since it measures the local nuclear “variable” $v(\mathbf{r})$ against the global electronic variable μ .

One also encounters such parameters in the molecular fragment resolution [3,4,6,17]. The subsystem analog of equation (2),

$$\delta\left\{\mathcal{E}_v[\rho] - \sum_\alpha \mu_\alpha N_\alpha[\rho_\alpha]\right\} = 0, \quad (3)$$

where the electronic energy [3,17],

$$\mathcal{E}_v[\rho] = \int v(\mathbf{r}) \left[\sum_{\alpha} \rho_{\alpha}(\mathbf{r}) \right] d\mathbf{r} + \mathcal{F}[\rho] = \int v(\mathbf{r}) \rho(\mathbf{r}) d\mathbf{r} + \mathcal{F}[\rho] \equiv E_v[\rho], \quad (4)$$

contains the subsystem-resolved universal functional $\mathcal{F}[\rho]$. The latter can be split into the additive (a) and non-additive (na) contributions [3,4]:

$$\mathcal{F}[\rho] = \sum_{\alpha} F[\rho_{\alpha}] + \mathcal{F}^{\text{na}}[\rho] \equiv \mathcal{F}^{\text{a}}[\rho] + \mathcal{F}^{\text{na}}[\rho] \equiv F[\rho]. \quad (5)$$

The Euler equation resulting from equation (3), *i.e.*, the subsystem ground-state relation,

$$u_{\alpha}(\mathbf{r}) = \left\{ v(\mathbf{r}) + \frac{\delta \mathcal{F}^{\text{na}}[\rho]}{\delta \rho_{\alpha}(\mathbf{r})} \right\} - \mu_{\alpha} \equiv v_{\alpha}^{\text{eff}}(\mathbf{r}) - \mu_{\alpha} = -\frac{\delta F[\rho_{\alpha}]}{\delta \rho_{\alpha}(\mathbf{r})}, \quad (6)$$

is then isomorphic with equation (1), the Euler equation for the whole system, when one substitutes (μ, v) with $(\mu_{\alpha}, v_{\alpha}^{\text{eff}})$, respectively. Again, the external potential $v(\mathbf{r})$ introduces the nuclear component into the relative potential $u_{\alpha}(\mathbf{r})$ of subsystem α , while both the embedding potential of this fragment in the molecule,

$$v_{\alpha}^{\text{e}}(\mathbf{r}) = \frac{\delta \mathcal{F}^{\text{na}}[\rho]}{\delta \rho_{\alpha}(\mathbf{r})}, \quad (7)$$

and the subsystem chemical potential μ_{α} determine the electronic component of $u_{\alpha}(\mathbf{r})$.

In the “electron-following” (EF) perspective [3,6,19–21] of the standard Born–Oppenheimer (BO) approximation the external potential $v(\mathbf{r})$ due to the nuclei carries the information about the system geometry and constitutes the independent *local* parameter of state. The (N, v) variables of the ground-state in the closed molecular system constitute the natural set of independent state-variables in the Schrödinger wave-function theory of the molecular structure, since they uniquely define the electronic Hamiltonian $\hat{H}(N, v)$. The other set of the global state-variables, (μ, v) , uniquely identifies the ground-state of the open molecule in contact with an external reservoir of electrons.

The corresponding specifications of the constrained equilibria in molecular subsystems [2–10], admitting separate external potentials and electron reservoirs for each molecular fragment, may involve alternative subsystem discretizations of the external potential variables. In the closed subsystems their equilibrium electron densities $\rho(\mathbf{r})$ can be identified by one of the following state specifications: (N, V) , (N, v) (or (N, v^{eff})), and (N, v) . In open subsystems, in contact with the separate reservoirs of electrons, the alternative state-variables accordingly read: (μ, V) , (μ, v) (or (μ, v^{eff})), and (μ, v) .

The Hellmann–Feynman theorem identifies the ground-state electron density $\rho(\mathbf{r})$ or its subsystem contributions $\rho_{\alpha}(\mathbf{r})$ as the energy-conjugates of the external potential variables. In the closed molecular system the ground-state energy $E_v[\rho[N, v]] = E[N, v]$, while in the open molecule $E_v[\rho[\mu, v]] = E[\mu, v]$. In the subsystem resolution one finds $\mathcal{E}_v[\rho[N, v]] = \mathcal{E}_v[N, v] = \mathcal{E}_v[N, v]$, for the closed molecular fragments, and $\mathcal{E}_v[\rho[\mu, v]] = \mathcal{E}_v[\mu, v] = \mathcal{E}_v[\mu, v]$, for open subsystems. The energy-conjugates of the external potential variable(s) are identified as the corresponding electron densities:

$$\rho(\mathbf{r}) = \left(\frac{\partial E[N, v]}{\partial v(\mathbf{r})} \right)_N = \left(\frac{\partial \mathcal{E}[N, v]}{\partial v(\mathbf{r})} \right)_N, \quad \rho_{\alpha}(\mathbf{r}) = \left(\frac{\partial \mathcal{E}[N, v]}{\partial v_{\alpha}(\mathbf{r})} \right)_N \quad (8a)$$

or

$$\rho(\mathbf{r}) = \left(\frac{\partial E[\mu, v]}{\partial v(\mathbf{r})} \right)_{\mu} = \left(\frac{\partial \mathcal{E}[\mu, v]}{\partial v(\mathbf{r})} \right)_{\mu}, \quad \rho_{\alpha}(\mathbf{r}) = \left(\frac{\partial \mathcal{E}[\mu, v]}{\partial v_{\alpha}(\mathbf{r})} \right)_{\mu}. \quad (8b)$$

Therefore, in the EF formulation the electron distributions represent the unconstrained (dependent) local state-variables of molecular systems: $\rho = \rho[v]$. In other words, the electrons “follow” the displacements of the system nuclei. This selection of the dependent (ρ) and independent (v) local state-variables generates the chemical-softness kernel $\sigma(\mathbf{r}, \mathbf{r}')$ of the reactivity theory [1–17] and hence can be classified as the chemical-softness representation of molecular states.

These roles of the local state-parameters are reversed in the electron-preceding (EP) perspective [3,6,19–21] of DFT, which can be also referred to as the chemical-hardness representation, since it defines another key concept of the electronic-structure/reactivity theory—the chemical-hardness kernel $\eta(\mathbf{r}, \mathbf{r}')$, the inverse of $\sigma(\mathbf{r}, \mathbf{r}')$ [1–17]. In the EP approach the electron density is regarded as the controlling, independent parameter of state, while the external potential responds to the specified redistribution of electrons, thus representing a dependent (unconstrained) state-variable: $v = v[\rho]$. In other words, in this reverse perspective the shifts in the electron distribution create conditions for (precede) the movements of nuclei, in the spirit of the Hellmann–Feynman theorem. This way of approaching molecular changes is quite common in the chemical reactivity theory [2–10]. Indeed, chemists often envisage the key manipulation of the system electronic structure as the primary cause of the desired reconstruction of the geometrical structure determined by the nuclear positions, *e.g.*, breaking/forming the specified bonds in the molecule.

One requires both these representations to tackle general issues in the theory of electronic structure of molecules and their chemical reactivity. The wave-function and density-functional formulations of the quantum theory of the electronic structure of molecular systems thus emerge as the complementary descriptions, which together provide theoretical framework of the “complete” theory of chemical reactivity. The emergence of the modern DFT [1,18,22–24] has provided the hitherto missing theoretical framework of the EP perspective. It has also generated a new impetus for formulating new approaches to many classical problems in chemistry [1–11]. For example, the origin of chemical bonding, identity of AIM, factors determining the nature and relative importance of alternative reaction sites and pathways in large reactive and catalytic systems, stability of molecular charge distribution, similarity of molecules, electron localization in molecules, *etc.*, have been all approached afresh. This theory offers an alternative point of view, from which one can approach the diverse physical/chemical properties and processes involving atomic, molecular, and reactive systems. This novel perspective is much in the spirit of the old Electronegativity-Equalization (EE) approach of Sanderson [25] to the equilibrium (ground-state) distribution of electrons in molecular systems.

In DFT the Frontier-Electron theory of Fukui [26–28] has been given a more rigorous foundation in terms of the related density-response index called the electronic Fukui Function (FF) [1–5,29–34]:

$$f(\mathbf{r}) = \left(\frac{\partial \rho(\mathbf{r})}{\partial N} \right)_v = \frac{\partial^2 E[N, v]}{\partial N \partial v(\mathbf{r})} = \left(\frac{\partial \mu}{\partial v(\mathbf{r})} \right)_N, \quad \int f(\mathbf{r}) d\mathbf{r} = 1. \quad (9)$$

It follows from the preceding equation that the electronic FF has a double physical interpretation. On one hand, it reflects the normalized response in the system electron density, the

energy-conjugate of the external potential in the EF perspective, to a unit shift in the system global average number of electrons. This derivative is calculated for the fixed external potential, *i.e.*, the rigid molecular geometry. On the other hand, it measures the response in the system chemical potential of electrons, the energy-conjugate of the global number of electrons N , per unit shift in the local value of the external potential. The latter interpretation shows that electronic FF indeed reflects the closed-system coupling between the molecular electronic (μ) and nuclear (v , geometric) structures.

The corresponding nuclear FF (NFF) [1–5,35–41] row vector $\boldsymbol{\varphi}_\alpha = [\varphi_{\alpha,x}, \varphi_{\alpha,y}, \varphi_{\alpha,z}] = \{\varphi_{\alpha,s}\}$ has been introduced to “translate” a given ΔN displacement directly into the conjugate responses of the system ground-state forces acting on the nuclei, $\mathbf{F} = \{\mathbf{F}_\alpha = -\nabla_\alpha W[N, \mathbf{R}]\}$,

$$\boldsymbol{\varphi}_\alpha[N, \mathbf{R}] = \left(\frac{\partial \mathbf{F}_\alpha[N, \mathbf{R}]}{\partial N} \right)_v = -\frac{\partial^2 W[N, v(\mathbf{R})]}{\partial N \partial \mathbf{R}_\alpha} = \left(\frac{\partial \mu[N, \mathbf{R}]}{\partial \mathbf{R}_\alpha} \right)_N^T, \quad (10)$$

where the total BO-potential for nuclear motions

$$W[N, v(\mathbf{R})] = E[N, v(\mathbf{R})] + V_{\text{nn}}(\mathbf{R}) \equiv W(N, \mathbf{R}), \quad (11)$$

$$V_{\text{nn}}(\mathbf{R}) = \sum_\alpha \sum_{\beta > \alpha} \frac{Z_\alpha Z_\beta}{|\mathbf{R}_\alpha - \mathbf{R}_\beta|}, \quad (12)$$

denotes the nuclear-repulsion energy, $\mathbf{R} = \{\mathbf{R}_\alpha\}$ groups the nuclear positions, and $\partial/\partial \mathbf{R}_\alpha = \nabla_\alpha$ stands for the gradient with respect to the position \mathbf{R}_α of nucleus α . A reference to equation (10) shows that NFF measures the normalized response in the force acting on nucleus α per unit displacement in the global number of electrons. The cross-differentiation identity (Maxwell relation) also implies that this index can be alternatively interpreted as the response in the system electronic chemical potential per unit displacement in the nuclear position \mathbf{R}_α , thus coupling the electronic (dependent) global variable μ with the nuclear position-vector \mathbf{R}_α .

In defining the NFF we have, in fact, introduced yet another, *geometric* representation of the molecular ground-state in the externally-closed molecule, (N, \mathbf{R}) , for the fixed identity (charges) of the nuclei, in which the nuclear positions \mathbf{R} replace the external potential $v(\mathbf{R})$ in the list of independent state-parameters. The corresponding set for the molecule coupled to the electron reservoir then reads (μ, \mathbf{R}) . In the AIM (subsystem) resolution one accordingly defines the geometric representations in terms of (N, \mathbf{R}) or (μ, \mathbf{R}) .

Therefore, both the electronic and nuclear FF represent examples of the reactivity concepts, which probe the coupling between the geometric and electronic structures in molecules [1–5,38–42]. In fact, these two reactivity indices of the EF-perspective are mutually related through the chain-rule transformation:

$$\begin{aligned} \boldsymbol{\varphi}_\alpha(\mathbf{R}) &= -\frac{\partial^2 W[N, v(\mathbf{R})]}{\partial N \partial \mathbf{R}_\alpha} = -\frac{\partial^2 E[N, v(\mathbf{R})]}{\partial N \partial \mathbf{R}_\alpha} \\ &= -\frac{\partial}{\partial N} \int \left(\frac{\delta E[N, v]}{\delta v(\mathbf{r})} \right)_N \left(\frac{\partial v[\mathbf{r}; \mathbf{R}]}{\partial \mathbf{R}_\alpha} \right)^T d\mathbf{r} \\ &= -\int f(\mathbf{r}) \left(\frac{\partial v[\mathbf{r}; \mathbf{R}]}{\partial \mathbf{R}_\alpha} \right)^T d\mathbf{r} \equiv -\int f(\mathbf{r}) \mathbf{G}_\alpha(\mathbf{r}; \mathbf{R}) d\mathbf{r}. \end{aligned} \quad (13)$$

The transformation matrix $\mathbf{G}(\mathbf{r}; \mathbf{R}) = \{G_\alpha(\mathbf{r}; \mathbf{R})\} \equiv \partial v(\mathbf{r}; \mathbf{R})/\partial \mathbf{R} = \{G_k(\mathbf{r}; \mathbf{R})\}$, for translating the electronic FF into its nuclear analog, $\boldsymbol{\varphi} = \{\varphi_\alpha = -\int f(\mathbf{r})\mathbf{G}_\alpha(\mathbf{r}; \mathbf{R}) d\mathbf{r}\}$, is determined in the preceding equation as the geometric derivative, with respect to nuclear coordinates, of the external potential $v(\mathbf{r}; \mathbf{R})$.

It should be emphasized that both these reactivity indices belong to the same chemical softness representation of molecular states, reflecting the EF-perspective of the standard BO approximation. The electronic index depends on the electron-position argument and it discriminates the reactivities of alternative sites in the molecule with respect to the nucleophilic or electrophilic attack by an approaching agent. The nuclear index, a function of nuclear positions (molecular geometry), similarly establishes trends in the system geometry relaxation, which accompany a test displacement in the system global number of electrons. An alternative way of probing the coupling between the electronic and nuclear degrees-of-freedom in molecular systems is through their direct mapping relations [2,8,10,16,43] (see Section 7), which are implied by the ground-state Euler equation (1). They provide a theoretical basis for the intuitive bond-length variation rules of Gutmann [44].

2. SUMMARY OF BASIC RELATIONS

2.1. Chemical-softness representation

The partial energy-conjugates of the ground-state electronic energy $E[N, v]$, with respect to the state-parameters (N, v) of this principal representation of the closed (N -controlled) molecular system in the EF-description, include the ground-state chemical potential [1–5, 45–49] and electron density:

$$\left(\frac{\partial E[N, v]}{\partial N}\right)_v = \mu, \quad \left(\frac{\partial E[N, v]}{\partial v(\mathbf{r})}\right)_N = \rho(\mathbf{r}), \quad (14)$$

where in the second derivative we have used the Hellmann–Feynman theorem (8a). These derivatives determine the corresponding first differential of the electronic energy:

$$dE[N, v] = \mu dN + \int \rho(\mathbf{r}) dv(\mathbf{r}) d\mathbf{r}. \quad (15)$$

The second partial derivatives of $E[N, v]$ determine the system principal charge sensitivities. They include the global hardness [1–5,50], of the molecule as a whole, given by the diagonal derivative with respect to N :

$$\eta = \left(\frac{\partial^2 E[N, v]}{\partial N^2}\right)_v = \left(\frac{\partial \mu}{\partial N}\right)_v. \quad (16)$$

It represents the inverse of the associated global softness descriptor:

$$S = \left(\frac{\partial N}{\partial \mu}\right)_v = \frac{1}{\eta}. \quad (17)$$

It should be stressed that both the system chemical potential and global hardness/softness descriptors are defined for the fixed external potential due to nuclei, *i.e.*, for the rigid molecular geometry. Later in this work we shall examine the alternative *compliance* measures of

such purely-electronic response properties, for the relaxed (equilibrium) molecular geometry.

The mixed derivative defines the electronic FF of equation (9), while the diagonal derivative with respect to external potential gives rise to the density Linear Response (LR) function [12,51]:

$$\beta(\mathbf{r}, \mathbf{r}') = \left(\frac{\partial^2 E[N, v]}{\partial v(\mathbf{r}) \partial v(\mathbf{r}')} \right)_N = \left(\frac{\partial \rho(\mathbf{r}')}{\partial v(\mathbf{r})} \right)_N = \beta(\mathbf{r}', \mathbf{r}). \quad (18)$$

It represents the “softness”-kernel of the externally-closed molecular system, which also measures the coupling between the local electronic (ρ) and nuclear (v) state-parameters of the molecular ground-state.

These derivatives determine the quadratic Taylor expansion of the system electronic energy in terms of powers of displacements (ΔN , Δv) in its state-parameters:

$$\begin{aligned} \Delta^{(1+2)} E[N, v] \\ = \mu \Delta N + \int \rho(\mathbf{r}) \Delta v(\mathbf{r}) d\mathbf{r} \\ + \frac{1}{2} \left[\eta (\Delta N)^2 + 2 \Delta N \int f(\mathbf{r}) \Delta v(\mathbf{r}) d\mathbf{r} + \iint \Delta v(\mathbf{r}) \beta(\mathbf{r}, \mathbf{r}') \Delta v(\mathbf{r}') d\mathbf{r} d\mathbf{r}' \right]. \end{aligned} \quad (19)$$

This expansion is “horizontal” in character, since the energy difference $\Delta E[N, v] = E[N + \Delta N, v + \Delta v] - E[N, v]$, is determined as the difference of two ground-state energies, for the displaced and initial electronic Hamiltonians, $\hat{H}(N + \Delta N, v + \Delta v)$ and $\hat{H}(N, v)$, respectively:

$$E[N + \Delta N, v + \Delta v] = E_{v+\Delta v}[\rho[N + \Delta N, v + \Delta v]]. \quad (20)$$

It follows from equation (1) that there exist one-to-one matching between the relative external potential u and the ground-state density ρ , $\rho \leftrightarrow u$, so that these equilibrium-matched local state-variables are unique functionals of each other: $\rho = \rho[u]$ and $u = u[\rho]$.

The related perturbative approaches for molecular subsystems have also been proposed, *e.g.*, those describing reactants in the bimolecular reactive system $M_R = A-B$, where for definiteness A and B denote the acidic (electron-acceptor) and basic (electron-donor) subsystems, respectively. In such an approach each reactant $X = (A, B)$ is attributed an average number of electrons, N_X , and the effective external potential v_X^{eff} , which includes the relevant embedding contribution due to the presence of the other reactant. For the given (fixed) geometry of subsystems in M_R each reactant undergoes displacements (ΔN_X , Δv_X^{eff}) in its effective state-parameters (N_X , v_X^{eff}) in M_R , relative to the corresponding values (N_X^0 , v_X^0) in the separated-reactant limit. The corresponding second-order change in the system electronic energy can then be expressed using the appropriately generalized Taylor expansion (19). These Taylor series in the subsystem resolution provide a formal basis for most of the DFT treatments of molecular reactants perturbed by the presence of the reaction partner or a catalyst [1–11,33–43,52–61]. In the N -controlled (closed) reactive systems the shifts in the subsystem average number of electrons $dN = (dN_A, dN_B)$ are due to the internal CT between reactants, $N_{\text{CT}} = dN_A = -dN_B > 0$, while the shifts in reactant effective external potentials $\Delta \mathbf{v}^{\text{eff}}(\mathbf{r}) = \{\Delta v_A^{\text{eff}}(\mathbf{r}), \Delta v_B^{\text{eff}}(\mathbf{r})\}$ originate from the presence and subsequent changes in the geometry and the electronic structure of the complementary subsystem. These perturbations of the reactive system generate the reor-

ganization of electronic structure on both reactants, which in turn determines the forces acting on their nuclei towards the new (displaced) equilibrium configuration.

The alternative “vertical” form of a quadratic energy expansion corresponds to the fixed external potential v . It results from expanding the variational Hohenberg–Kohn energy functional in the spirit of the EP-perspective,

$$E_v[\rho'] = \int v(\mathbf{r})\rho'(\mathbf{r}) d\mathbf{r} + F[\rho'], \quad (21)$$

in powers of density displacements $\Delta\rho'(\mathbf{r}) = \rho'(\mathbf{r}) - \rho(\mathbf{r})$, of the trial density $\rho'(\mathbf{r})$ with respect to the initial ground-state density $\rho = \rho[N, v]$,

$$\Delta^{(1+2)} E_v[\rho'] = \mu\Delta N + \frac{1}{2} \iint \Delta\rho'(\mathbf{r})\eta(\mathbf{r}, \mathbf{r}')\Delta\rho'(\mathbf{r}') d\mathbf{r} d\mathbf{r}'. \quad (22)$$

Here the hardness kernel of the EP-perspective, for the rigid geometry of the molecule,

$$\begin{aligned} \eta(\mathbf{r}, \mathbf{r}') &= \left(\frac{\partial^2 E_v[\rho]}{\partial\rho(\mathbf{r})\partial\rho(\mathbf{r}')} \right)_v = \frac{\delta^2 F[\rho]}{\delta\rho(\mathbf{r})\delta\rho(\mathbf{r}')} = \left(\frac{\partial\mu(\mathbf{r}')}{\partial\rho(\mathbf{r})} \right)_v = \left(\frac{\partial\mu(\mathbf{r})}{\partial\rho(\mathbf{r}')} \right)_v \\ &= -\frac{\delta u(\mathbf{r}')}{\delta\rho(\mathbf{r})} = -\frac{\delta u(\mathbf{r})}{\delta\rho(\mathbf{r}')}. \end{aligned} \quad (23)$$

In this vertical Taylor expansion the displaced electron density $\rho' = \rho + \Delta\rho'$ is no longer equilibrium-matched with respect to the “frozen” external potential v .

Consider next the open (μ -controlled) molecular systems in equilibrium with the hypothetical external electron reservoir exhibiting the chemical potential $\mu = \mu_{\mathfrak{M}}$. It is characterized by the grand-potential $\Omega[\mu, v]$,

$$\begin{aligned} \Omega[\mu, v] &= E - \left(\frac{\partial E[N, v]}{\partial N} \right)_v N = E - N\mu = \Omega[u, \rho[u]] \equiv \Omega[u] \\ &= \int u(\mathbf{r})\rho(\mathbf{r}) d\mathbf{r} + F[\rho] \equiv \Omega_u[\rho], \end{aligned} \quad (24)$$

where the relative external potential is defined in equation (1). It corresponds to the Legendre-transformed representation of the system electronic energy $E[N, v]$, in which the chemical potential replaces the number of electrons in the list of state-parameters. The first differential of the grand-potential reads:

$$\begin{aligned} d\Omega[\mu, v] &= -N d\mu + \int \rho(\mathbf{r}) dv(\mathbf{r}) d\mathbf{r} = \int \rho(\mathbf{r}) du(\mathbf{r}) d\mathbf{r} \\ &= d\Omega_u[\rho[u]] = d\Omega[u]. \end{aligned} \quad (25)$$

It should be observed that this quantity constitutes the auxiliary functional of the Hohenberg–Kohn (HK) variational principle (2), in which the extra term supplementing the electronic energy, $-\mu N[\rho]$, enforces the correct normalization of the optimum density. This minimum principle allows one to express the grand-potential as the minimum of searches over the trial (ensemble average) numbers of electrons $\{N'\}$ or the ensemble-average (variational) densities $\{\rho'\}$:

$$\begin{aligned} \Omega[\mu, v] &= \min_{N'} \{ E[N', v] - \mu N' \} = \min_{\rho'} \{ E_v[\rho'] - \mu N[\rho'] \} \\ &= \min_{\rho'} \Omega_u[\rho'] = \Omega_u[\rho[u]] = \Omega[u]. \end{aligned} \quad (26)$$

These u -constrained searches deliver the optimum electronic parameters, the grand-ensemble average number of electrons $N = \int \rho(\mathbf{r}) d\mathbf{r}$ and the ensemble ground-state density ρ , which match the fixed (independent) state-parameter $u(\mathbf{r})$ of the open molecular system. The latter is now determined by quantities characterizing both the system nuclei (v) and the external reservoir of electrons (μ).

As also seen in the foregoing equation, the relative external potential $u(\mathbf{r})$ defines the equilibrium state in this EF-representation of open-systems. The grand-potential conjugate of the relative external potential is the grand-ensemble average density

$$\rho(\mathbf{r}) = \frac{\delta \Omega_u[\rho]}{\delta u(\mathbf{r})}. \quad (27)$$

The partial conjugates of $\Omega[u] = \Omega[\mu, v]$ define the grand-potential conjugates of the open system global and local state-variables, respectively,

$$\left(\frac{\partial \Omega[\mu, v]}{\partial \mu} \right)_v = -N, \quad \left(\frac{\partial \Omega[\mu, v]}{\partial v(\mathbf{r})} \right)_\mu = \rho(\mathbf{r}). \quad (28)$$

The second of these relations expresses the Hellmann–Feynman theorem for an open molecular system (8b).

The corresponding charge sensitivities are defined by the second partials of the grand-potential. They include the (rigid-geometry) global softness of equation (17),

$$S = \left(\frac{\partial N}{\partial \mu} \right)_v = - \left(\frac{\partial^2 \Omega[\mu, v]}{\partial \mu^2} \right)_v, \quad (29)$$

the mixed-derivative defining the local softness of the electron gas in a molecule,

$$s(\mathbf{r}) = \frac{\partial^2 \Omega[\mu, v]}{\partial \mu \partial v(\mathbf{r})} = \left(\frac{\partial \rho(\mathbf{r})}{\partial \mu} \right)_v = - \left(\frac{\partial N}{\partial v(\mathbf{r})} \right)_\mu = - \frac{\delta N}{\delta u(\mathbf{r})}, \quad (30)$$

and the softness kernel,

$$\begin{aligned} \sigma(\mathbf{r}, \mathbf{r}') &= - \left(\frac{\partial^2 \Omega[\mu, v]}{\partial v(\mathbf{r}) \partial v(\mathbf{r}')} \right)_\mu = - \left(\frac{\partial \rho(\mathbf{r}')}{\partial v(\mathbf{r})} \right)_\mu = - \left(\frac{\partial \rho(\mathbf{r})}{\partial v(\mathbf{r}')} \right)_\mu = \sigma(\mathbf{r}', \mathbf{r}) \\ &= - \frac{\delta^2 \Omega[u]}{\delta u(\mathbf{r}) \delta u(\mathbf{r}')} = - \frac{\delta \rho(\mathbf{r})}{\delta u(\mathbf{r}')} = - \frac{\delta \rho(\mathbf{r}')}{\delta u(\mathbf{r})}. \end{aligned} \quad (31)$$

The latter constitutes the inverse of the hardness kernel of equation (23):

$$\int \eta(\mathbf{r}, \mathbf{r}'') \sigma(\mathbf{r}'', \mathbf{r}') d\mathbf{r}'' = \delta(\mathbf{r} - \mathbf{r}'). \quad (32)$$

The grand-potential can be also regarded as the Legendre-transform of the density functional for the electronic energy $E_v[\rho] \equiv E[\rho; v]$, where the semicolon separates the system dependent (electronic) variable $\rho = \rho[N, v]$ from the independent nuclear parameter v :

$$\begin{aligned} \Omega_u[\rho] &= E_v[\rho] - \int \frac{\delta E_v[\rho]}{\delta \rho(\mathbf{r})} \rho(\mathbf{r}) d\mathbf{r} = E_v[\rho] - \int \mu(\mathbf{r}) \rho(\mathbf{r}) d\mathbf{r} \\ &= E_v[\rho] - \mu N[\rho]. \end{aligned} \quad (33)$$

Above, we have used the ground-state equalization of the local chemical potential $\mu(\mathbf{r})$ (see (1)) at the global level μ , which characterizes the molecule as a whole:

$$\mu(\mathbf{r}) \equiv \frac{\delta E_v[\rho]}{\delta \rho(\mathbf{r})} = v(\mathbf{r}) + \frac{\delta F[\rho]}{\delta \rho(\mathbf{r})} = \mu. \quad (34)$$

In the local Legendre-transformation (33) of the density functional for electronic energy the local value of the ground-state density $\rho(\mathbf{r})$ has thus been replaced by its energy conjugate, the local (equalized) chemical potential $\mu(\mathbf{r}) = \mu$ as the independent parameter of state.

The ground-state functional derivatives of $\Omega_u[\rho]$ then read:

$$\begin{aligned} \frac{\delta \Omega_u[\rho]}{\delta \rho(\mathbf{r})} &= u(\mathbf{r}) + \frac{\delta F[\rho]}{\delta \rho(\mathbf{r})} = 0 \quad \text{and} \\ \frac{\delta^2 \Omega_u[\rho]}{\delta \rho(\mathbf{r}) \delta \rho(\mathbf{r}')} &= \frac{\delta^2 F[\rho]}{\delta \rho(\mathbf{r}) \delta \rho(\mathbf{r}')} = \eta(\mathbf{r}, \mathbf{r}'). \end{aligned} \quad (35)$$

The first of these relations expresses the Euler equation for the ground-state density (see (1)). It implies that $\rho = \rho[u]$ and thus $\Omega_u[\rho[u]] = \Omega[u]$, as indeed confirmed by the differential of equation (25). The vanishing first-derivative in the preceding equation shows that the grand-potential is stationary with respect to displacements from the ground-state density, in accordance with the HK variational principle of equation (2).

The derivatives of equations (27)–(31) define the (“horizontal”) quadratic Taylor expansion of the grand-potential in terms of powers of displacements ($\Delta\mu$, Δv), or equivalently $\Delta u = \Delta v - \Delta\mu$, relative to the reference values (μ, v) , or $u = v - \mu$, determining the initial (equilibrium) grand-ensemble density $\rho = \rho[u]$:

$$\begin{aligned} \Delta^{(1+2)} \Omega[\mu, v] &= -N \Delta\mu + \int \rho(\mathbf{r}) \Delta v(\mathbf{r}) d\mathbf{r} \\ &\quad + \frac{1}{2} \left[-S(\Delta\mu)^2 + 2\Delta\mu \int s(\mathbf{r}) \Delta v(\mathbf{r}) d\mathbf{r} - \iint \Delta v(\mathbf{r}) \sigma(\mathbf{r}, \mathbf{r}') \Delta v(\mathbf{r}') d\mathbf{r} d\mathbf{r}' \right] \\ &= \int \Delta u(\mathbf{r}) \rho(\mathbf{r}) d\mathbf{r} - \frac{1}{2} \iint \Delta u(\mathbf{r}) \sigma(\mathbf{r}, \mathbf{r}') \Delta u(\mathbf{r}') d\mathbf{r} d\mathbf{r}'. \end{aligned} \quad (36)$$

This series approximates to the second-order the horizontal-displacements on the grand-potential surface $\Omega_u[\rho[u]] = \Omega[u]$, with the electron density satisfying the HK Euler equation (1) for the displaced relative external potential $u'(\mathbf{r}) = u(\mathbf{r}) + \Delta u(\mathbf{r})$: $\rho' = \rho[u']$.

Alternatively, using derivatives of the associated density functional $\Omega[\mu, v] = \Omega_u[\rho[u]]$ one arrives at the corresponding “vertical” (variational) expansion of the density functional $\Omega_u[\rho']$ for the fixed relative potential u and a trial density $\rho' = \rho + \Delta\rho'$, around the ground-state density ρ :

$$\Delta^{(1+2)} \Omega_u[\rho'] = \Delta^{(2)} \Omega_u[\rho'] = \frac{1}{2} \iint \Delta\rho'(\mathbf{r}) \eta(\mathbf{r}, \mathbf{r}') \Delta\rho'(\mathbf{r}') d\mathbf{r} d\mathbf{r}'. \quad (37)$$

There is a fundamental difference between these two expansions of the grand-potential. In equation (36) energy displacement is horizontal in character, approximating, to the second order, the shift along the *equilibrium* grand-potential surface, while equation (37) determines the quadratic change in the grand-potential due the *trial* density ρ' , which in general differs from the corresponding equilibrium-match of the fixed relative external potential u : $\rho' \neq \rho[u]$.

The subsystem-generalization of expansion (36) establishes a framework for the DFT treatment of reactants in an open reactive system, which is free to exchange electrons with external reservoirs [1–11,33–43,52–61]. In reactant resolution each subsystem $X = (A, B)$ exhibits displacements $(\Delta\mu_X, \Delta v_X)$ or $\Delta u_X = \Delta v_X - \Delta\mu_X$ in its independent state-parameters (μ_X, v_X) or $u_X = v_X - \mu_X$, relative to the separate-reactant values, due to a perturbing presence of the reaction partner. The reactant-resolved perturbational expansions of the coupled, interacting reactants in an open M_R define the chemical softness description of reacting species coupled to an external electron reservoir, *e.g.*, when they are chemisorbed on a surface of a catalyst [2,7,8].

These derivative properties of the closed and open molecular systems (or reactants) are mutually related. For example, in the closed molecular system, in which density displacements conserve the fixed (integer) number of electrons N , the internal hardness kernel of the closed molecular system

$$\eta^{\text{int}}(\mathbf{r}, \mathbf{r}') = -\left(\frac{\partial v(\mathbf{r}')}{\partial \rho(\mathbf{r})}\right)_N = -\beta^{-1}(\mathbf{r}, \mathbf{r}'), \quad (38)$$

reflects the equilibrium response in the system external potential to the polarizational (N -conserving) displacement of the system electron density. It differs from the hardness kernel $\eta(\mathbf{r}, \mathbf{r}')$ of equation (35), which additionally includes the external-CT contribution. These two normalized potential responses to local density displacements represent the basic kernels of the “inverse”, chemical-hardness representation, which will be the subject of the next section. Indeed, in both these charge sensitivities the primary perturbation $\delta\rho(\mathbf{r})$ is electronic in character while the monitored responses $\delta v(\mathbf{r}')$ or $\delta u(\mathbf{r}')$ are of nuclear (geometric) origin.

As we have already indicated in equation (32) the softness kernel of the EF-description is the inverse of the hardness kernel. This directly follows from the functional chain-rule

$$\int \sigma(\mathbf{r}, \mathbf{r}'') \eta(\mathbf{r}'', \mathbf{r}') d\mathbf{r}'' = \int \frac{\delta\rho(\mathbf{r}'')}{\delta u(\mathbf{r})} \frac{\delta u(\mathbf{r}')}{\delta\rho(\mathbf{r}'')} d\mathbf{r}'' = \frac{\delta u(\mathbf{r}')}{\delta u(\mathbf{r})} = \delta(\mathbf{r}' - \mathbf{r}). \quad (39)$$

This kernel can be expressed in terms of the LR function of equation (18), measuring the *closed*-system density response, and the extra term present only in *open* molecular systems, which involves the electronic FF (see (9)) and the system global softness of (see equations (17), (29)) [12]:

$$\begin{aligned} \sigma(\mathbf{r}, \mathbf{r}') &= \eta(\mathbf{r}', \mathbf{r})^{-1} = -\frac{\delta\rho(\mathbf{r}')}{\delta u(\mathbf{r})} = -\left(\frac{\partial\rho(\mathbf{r}')}{\partial v(\mathbf{r})}\right)_\mu \\ &= -\left(\frac{\partial\rho(\mathbf{r}')}{\partial v(\mathbf{r})}\right)_N - \left(\frac{\partial N}{\partial v(\mathbf{r})}\right)_\mu \left(\frac{\partial\rho(\mathbf{r}')}{\partial N}\right)_v \\ &= -\beta(\mathbf{r}, \mathbf{r}') + s(\mathbf{r})f(\mathbf{r}') = -\beta(\mathbf{r}, \mathbf{r}') + f(\mathbf{r})Sf(\mathbf{r}') \\ &\equiv \sigma^{\text{int}}(\mathbf{r}, \mathbf{r}') + \sigma^{\text{CT}}(\mathbf{r}, \mathbf{r}'). \end{aligned} \quad (40)$$

The first contribution in the above expression measures the density response due to the system internal polarizational, for the fixed N , while the second component reflects the effects due to the external CT.

In the preceding equation we have used the alternative expression for the local softness,

$$s(\mathbf{r}) = \left(\frac{\partial\rho(\mathbf{r})}{\partial\mu}\right)_v = \left(\frac{\partial\rho(\mathbf{r})}{\partial N}\right)_v \left(\frac{\partial N}{\partial\mu}\right)_v = f(\mathbf{r})S, \quad (41)$$

which also represents the rigid-geometry response property of electrons. The global and local softnesses combine the additive contributions from the softness-kernel:

$$\begin{aligned} S &= \left(\frac{\partial N}{\partial \mu} \right)_v = \iint \frac{\delta \rho(\mathbf{r}')}{\delta u(\mathbf{r})} \left(\frac{\delta u(\mathbf{r})}{\delta \mu} \right)_v d\mathbf{r} d\mathbf{r}' = \iint \sigma(\mathbf{r}, \mathbf{r}') d\mathbf{r} d\mathbf{r}' \\ &= \int \left(\frac{\partial \rho(\mathbf{r})}{\partial \mu} \right)_v d\mathbf{r} = \int s(\mathbf{r}) d\mathbf{r}, \end{aligned} \quad (42)$$

where

$$s(\mathbf{r}) = \int \sigma(\mathbf{r}, \mathbf{r}') d\mathbf{r}'. \quad (43)$$

Therefore, the electronic FF represents the normalized measure of the local softness:

$$f(\mathbf{r}) = \frac{s(\mathbf{r})}{S} = s(\mathbf{r})\eta, \quad \int f(\mathbf{r}) d\mathbf{r} = 1. \quad (44)$$

The global hardness of equation (16) can be similarly expressed as the FF-weighted average of the hardness kernel:

$$\begin{aligned} \eta &= \left(\frac{\partial \mu}{\partial N} \right)_v = \iint \left(\frac{\partial \rho(\mathbf{r})}{\partial N} \right)_v \left(\frac{\partial^2 E_v[\rho]}{\partial \rho(\mathbf{r}) \partial \rho(\mathbf{r}')} \right)_v \left(\frac{\partial \rho(\mathbf{r}')}{\partial N} \right)_v d\mathbf{r} d\mathbf{r}' \\ &= \iint f(\mathbf{r})\eta(\mathbf{r}, \mathbf{r}') f(\mathbf{r}') d\mathbf{r} d\mathbf{r}'. \end{aligned} \quad (45)$$

The same result is obtained for the local hardness of the ground-state distribution of electrons, defined by the derivative

$$\begin{aligned} \eta(\mathbf{r}) &= \left(\frac{\partial \mu(\mathbf{r})}{\partial N} \right)_v = \int \left(\frac{\partial^2 E_v[\rho]}{\partial \rho(\mathbf{r}) \partial \rho(\mathbf{r}')} \right)_v \left(\frac{\partial \rho(\mathbf{r}')}{\partial N} \right)_v d\mathbf{r}' \\ &= \int \eta(\mathbf{r}, \mathbf{r}') f(\mathbf{r}') d\mathbf{r}' = \left(\frac{\partial \mu}{\partial N} \right)_v = \eta. \end{aligned} \quad (46)$$

The last equation expresses the local-hardness equalization rule, which is a direct consequence of the chemical potential equalization principle of equation (34).

All relations between the ground-state charge sensitivities of open and closed molecular systems can be derived using the Euler equation (1) and the relevant functional chain-rule transformations or the equivalent Jacobian manipulations of the defining derivatives. The subsystem-resolved analogs of the global quadratic Taylor expansions of this section provide a flexible theoretical framework for the two-reactant treatment of diverse phenomena in chemical reactivity, covering both displacements in the global electronic (N or μ) and the local nuclear (v , \mathbf{F} , or \mathbf{R}) degrees-of-freedom of the molecular subsystems in bimolecular reactive systems $M_R = A-B$. This description can adequately treat both the “promoted” state of the closed reactants at the intermediate polarization, P-stage of a chemical reaction, when the overall number of electrons on each subsystem is fixed, and at the final equilibrium state of the mutually-open reactants, at the CT-stage of a chemical reaction, when electrons can freely flow between reactants. This perturbative DFT approach naturally connects to the conventional stages, in which the reaction mechanism is described in chemistry: the initial v -driven polarization of the mutually closed reactants being followed by the N -driven CT between the already polarized species.

This chemical-softness representation of either closed or open molecular systems, in which the external potentials v or u play the role of the controlled local state-parameters, provide the theoretical framework for the electron-following perspective on molecular displacements. It emphasizes the primary role attributed in this BO-type approach to perturbative shifts in the nuclear positions (molecular geometry), which induce the subsequent electron redistribution in the molecular system under consideration. In this description the displacements in the system geometrical parameters define “perturbations”, which induce subsequent equilibrium responses in the molecular electronic structure.

However, for the complete theoretical framework, capable of tackling all issues in chemical reactivity, one additionally requires the complementary development within the chemical-hardness representation, in which the roles of the nuclear and electronic local state-variables are reversed. In such a description one is interested in the Taylor expansions in powers of displacements in the ground-state electron density, which represent independent perturbations of the molecular system, and are regarded as preceding the subsequent movement of the nuclei. In the EP-perspective the local values of the electronic density $\rho(\mathbf{r})$ constitute the controlled state-parameters, to which the nuclear (geometrical) factors respond. Such an attitude is close to the chemical thinking on how to manipulate molecules in order to induce desirable changes in the molecular geometry. Indeed, chemists often successfully modify the pattern of the chemical bonds by judiciously designing the crucial electronic perturbation of the system, which induces the coupled movement of nuclei in the desired direction. This approach is also in the spirit of DFT, which considers the system ground-state electron density as the complete specification of the molecular electronic structure [1,18,22,24]. We shall summarize the elements of such a description in the next section.

2.2. Chemical-hardness representation

Displacements of the electron density, $\Delta\rho(\mathbf{r})$, define the system perturbations in the chemical-hardness representation of the EP-perspective on molecular structure. They generate forces driving responses in nuclear positions, giving rise to the adjusted external potential v (or u). This is in the spirit of the Hellmann–Feynman theorem, since in the EP-description the electronic structure is seen as the primary cause of the observed geometrical structures of molecular systems. This way of viewing and, ultimately, manipulating molecular changes dominates the speculative chemical thinking about molecules and reactants.

The chemical-hardness representation of closed or open molecular systems is thus obtained, when the ground-state electron density replaces the external potential in the list of the system state-parameters [2–4,6,38,51]. This is accomplished through the appropriate $v \rightarrow \rho$ Legendre transformation. The relevant “thermodynamic” potentials of the hardness representation, which determine the molecular equilibria in the externally closed and open systems, respectively, are thus given by the following Legendre transforms of $E[N, v]$ (for the N -controlled equilibria) or $\Omega[\mu, v]$ (for the μ -controlled equilibria):

$$\begin{aligned}\mathcal{F}[N, \rho] &= E - \int \left(\frac{\partial E[N, v]}{\partial v(\mathbf{r})} \right)_N v(\mathbf{r}) d\mathbf{r} \\ &= E - \int \rho(\mathbf{r}) v(\mathbf{r}) d\mathbf{r} = F[\rho],\end{aligned}\tag{47}$$

$$\begin{aligned}
\mathcal{R}[\mu, \rho] &= \Omega - \int \left(\frac{\partial \Omega[\mu, v]}{\partial v(\mathbf{r})} \right)_{\mu} v(\mathbf{r}) d\mathbf{r} \\
&= \Omega - \int \rho(\mathbf{r}) v(\mathbf{r}) d\mathbf{r} = F[\rho] - \mu N[\rho] = R_{\mu}[\rho].
\end{aligned} \tag{48}$$

They give rise to the corresponding first differentials:

$$d\mathcal{F}[N, \rho] = \mu dN - \int v(\mathbf{r}) d\rho(\mathbf{r}) d\mathbf{r} = - \int u(\mathbf{r}) d\rho(\mathbf{r}) d\mathbf{r}, \tag{49}$$

$$d\mathcal{R}[\mu, \rho] = -N d\mu - \int v(\mathbf{r}) d\rho(\mathbf{r}) d\mathbf{r}. \tag{50}$$

Therefore, in these chemical-hardness representations, within the EP-perspective on the closed and open molecular systems, respectively, the electronic energy component $E_v[\rho] = E[N, v]$ of the EF-perspective, in the chemical-softness representation, is replaced by the universal (v -independent) functional $F[\rho]$ for the expectation value of the sum of the electron repulsion and kinetic energies. As seen in the two preceding equations, these additional “thermodynamic” potentials have been expressed as corresponding density functionals: $\mathcal{F}[N, \rho] = F[\rho] \equiv F_{\rho}[u[\rho]]$ and $\mathcal{R}[\mu, \rho] \equiv R_{\rho}[v; \mu]$. The notation $F_{\rho}[u]$ and $R_{\rho}[v; \mu]$ stresses the dependent role of the nuclear state-variables u and v , and the independent character of the electronic state-parameter ρ in these chemical-hardness representations. For the equilibrium (ground-state) density the thermodynamic potential $\mathcal{F}[N, \rho] = F[\rho]$ defines the repulsive, universal part of the Hohenberg–Kohn density functional for the system electronic energy, while the free- F potential $\mathcal{R}[\mu, \rho] = R_{\rho}[v[\rho]; \mu]$ represents its open system analog.

It should be observed that the $\mathcal{R}[\mu, \rho]$ potential represents the *complete* Legendre transform of the system electronic energy, in which all principal parameters (N, v) of the electronic Hamiltonian have been replaced by their energy-conjugates (μ, ρ), respectively. Contrary to the ordinary thermodynamics [62], where such complete transformation gives rise to the identically vanishing potential due to the Euler equation for the homogeneous first-order function of the system internal energy, the molecular potential $\mathcal{R}[\mu, \rho]$ does not vanish. This is because the molecular electronic energy is not the homogeneous function of degree-1 in its principal parameters of state. Another manifestation of this fact is the non-vanishing character of the molecular analog of the familiar Gibbs–Duhem equation of ordinary thermodynamics [62]:

$$-d\mathcal{R}[\mu, \rho] = N d\mu + \int v(\mathbf{r}) d\rho(\mathbf{r}) d\mathbf{r} \neq 0. \tag{51}$$

In the closed (N -controlled) molecular systems, for which the thermodynamic potential is given by the Legendre-transform $\mathcal{F}[N, \rho] = F[\rho]$, the ground-state density constitutes the only independent parameter of state. In accordance with the basic theorems of DFT, it uniquely identifies the electronic Hamiltonian and thus completely specifies the molecular properties. The conjugate variable of the Euler equation (1), the relative external potential $u = u[\rho]$, now plays the role of the dependent (nuclear) variable. Therefore, the thermodynamic potential (47) can be also interpreted as the functional of the relative external potential $u[\rho]$, which is the equilibrium-matched to the specified electron density:

$$\mathcal{F}[N, \rho] = F[u[\rho]; \rho] = F[\rho]. \tag{52}$$

This notation emphasizes the dependent role of the state-variable u and the independent character of the electronic state-parameter ρ .

For a trial (variational) external potential u' , which does not match through equation (1) the specified (v -representable) density ρ , $F[u'; \rho] \neq F[\rho]$. Therefore, the density-functional notation $F[\rho]$ is less general than the above two-argument notation $F[u'; \rho]$. It covers only the equilibrium case, when the external potential identifies the specified density as its ground-state density: $F[\rho] = F[u[\rho]; \rho]$. It cannot account for the variational, non-equilibrium situation $F[u'; \rho]$, when u' does not match the given ρ as its ground-state conjugate.

In fact, the equilibrium potential $\mathcal{F}[N, \rho] = F[\rho]$ can be constructed via the density-constrained search for the optimum external potential [2,51,63],

$$\mathcal{F}[N, \rho] = \max_{v'} \left\{ E_{v'}[\rho] - \int v'(\mathbf{r}) \rho(\mathbf{r}) d\mathbf{r} \right\} \equiv \max_{v'} \mathcal{F}[v'; \rho] = F[\rho]. \quad (53)$$

It yields the external potential $v = v[\rho]$ matching the specified (v -representable) electron density ρ .

Since the ground-state density is uniquely determined by the relative external potential u , $\rho = \rho[u]$, the equilibrium functional $F[\rho]$ can be also regarded as the composite functional of u :

$$F[\rho] = F[\rho[u]] = \tilde{F}[u]. \quad (54)$$

The Euler equation (1) then identifies the F -conjugate of the ground-state density ρ , *i.e.*, the local “intensity” defined by the functional derivative of $F[\rho]$, as the negative relative external potential, $-u$, while the corresponding kernel of the second functional derivatives is given by the hardness kernel $\eta(\mathbf{r}, \mathbf{r}')$ of equation (23). Together these functional derivatives define in this EP-perspective the second-order (“horizontal”) Taylor expansion of $F[\rho]$ in powers of displacements of the controlling state-parameter ρ :

$$\Delta^{(1+2)} F[\rho] = - \int u(\mathbf{r}) \Delta \rho(\mathbf{r}) d\mathbf{r} + \frac{1}{2} \iint \Delta \rho(\mathbf{r}) \eta(\mathbf{r}, \mathbf{r}') \Delta \rho(\mathbf{r}') d\mathbf{r} d\mathbf{r}'. \quad (55)$$

One could also examine the equivalent expansion of the composite functional $\tilde{F}[u]$ (see (54)) in powers of displacements $\Delta u(\mathbf{r})$ of the equilibrium relative-potential $u = u[\rho]$ for the displaced electron density $\rho(\mathbf{r})$. Using the functional chain-rule transformations one then finds the following functional derivatives of $\tilde{F}[u]$:

$$\frac{\delta \tilde{F}[u]}{\delta u(\mathbf{r})} = \int \frac{\delta F[\rho]}{\delta \rho(\mathbf{r}')} \frac{\delta \rho(\mathbf{r}')}{\delta u(\mathbf{r})} d\mathbf{r}' \equiv \int \sigma(\mathbf{r}, \mathbf{r}') u(\mathbf{r}') d\mathbf{r}', \quad (56)$$

$$\begin{aligned} \frac{\delta^2 \tilde{F}[u]}{\delta u(\mathbf{r}) \delta u(\mathbf{r}')} &= \iint \frac{\delta \rho(\mathbf{r}''')}{\delta u(\mathbf{r})} \frac{\delta^2 F[\rho]}{\delta \rho(\mathbf{r}''') \delta \rho(\mathbf{r}'')} \frac{\delta \rho(\mathbf{r}'')}{\delta u(\mathbf{r}')} d\mathbf{r}'' d\mathbf{r}''' \\ &= \iint \sigma(\mathbf{r}, \mathbf{r}''') \eta(\mathbf{r}''', \mathbf{r}'') d\mathbf{r}''' \sigma(\mathbf{r}', \mathbf{r}'') d\mathbf{r}'' \\ &= \int \delta(\mathbf{r} - \mathbf{r}'') \sigma(\mathbf{r}', \mathbf{r}'') d\mathbf{r}'' = \sigma(\mathbf{r}', \mathbf{r}). \end{aligned} \quad (57)$$

In the second and third lines of the last equation we have used the inverse property of the softness and hardness kernels (see (32)).

Hence, the quadratic Taylor expansion of the composite functional $\tilde{F}[u]$, in the spirit of the EF-perspective of the chemical-softness representation, reads:

$$\Delta^{(1+2)}\tilde{F}[u] = \int \left[\Delta u(\mathbf{r}) \int \sigma(\mathbf{r}, \mathbf{r}') d\mathbf{r}' \right] u(\mathbf{r}') d\mathbf{r}' + \frac{1}{2} \iint \Delta u(\mathbf{r}) \sigma(\mathbf{r}, \mathbf{r}') \Delta u(\mathbf{r}') d\mathbf{r} d\mathbf{r}'. \quad (58)$$

One can easily verify the equivalence of expansions (55) and (58). For example, the square bracket of the first-order contribution in the preceding equation generates, via the chain-rule transformation, $-\Delta\rho[\Delta u]$, so that the resulting first-order change reproduces the first differential in equations (49) and (55). It should be stressed, that both these Taylor series are “horizontal” in character, since a given electronic perturbation $\Delta\rho$ implies the equilibrium displacement in the conjugate nuclear quantity, $\Delta u = \Delta u[\Delta\rho]$, and *vice versa*, a given shift in the relative potential due to the nuclei, Δu , results in the concomitant change in its electron density, $\Delta\rho = \Delta\rho[\Delta u]$.

The linear-response parts of these functional relations thus read:

$$\begin{aligned} \Delta u(\mathbf{r}) &= - \int \Delta\rho(\mathbf{r}') \eta(\mathbf{r}', \mathbf{r}) d\mathbf{r}' = \Delta u[\Delta\rho; \mathbf{r}], \\ \Delta\rho(\mathbf{r}) &= - \int \Delta u(\mathbf{r}') \sigma(\mathbf{r}', \mathbf{r}) d\mathbf{r}' = \Delta\rho[\Delta u; \mathbf{r}]. \end{aligned} \quad (59)$$

In terms of these coupled shifts in the complementary state-variables the second-order terms in equations (55) and (58) have now a common physical interpretation:

$$\begin{aligned} \Delta^{(2)}F[\rho] &= -\frac{1}{2} \int \Delta\rho(\mathbf{r}) \Delta u[\Delta\rho; \mathbf{r}] d\mathbf{r} \\ &= \Delta^{(2)}\tilde{F}[u] = -\frac{1}{2} \int \Delta u(\mathbf{r}) \Delta\rho[\Delta u; \mathbf{r}] d\mathbf{r}. \end{aligned} \quad (60)$$

Next, let us separate the internal system polarization, for the fixed overall number of electrons N , *i.e.*, $\Delta N = 0$, from changes in the electron distribution induced by the external CT, due to the finite inflow/outflow of electrons, $\Delta N \neq 0$, to/from the molecular system under consideration. This is accomplished by expressing the electron density as the product of its overall normalization N and the unity-normalized shape (probability) factor $p(\mathbf{r})$:

$$\rho(\mathbf{r}) = Np(\mathbf{r}), \quad \int p(\mathbf{r}) d\mathbf{r} = 1 \quad \text{or} \quad \int \delta p(\mathbf{r}) d\mathbf{r} = 0. \quad (61)$$

Hence,

$$\left(\frac{\partial \rho(\mathbf{r})}{\partial N} \right)_p = p(\mathbf{r}) \quad \text{and} \quad \left(\frac{\partial \rho(\mathbf{r}')}{\partial p(\mathbf{r})} \right)_N = N\delta(\mathbf{r} - \mathbf{r}'). \quad (62)$$

This factorization gives

$$\Delta\rho(\mathbf{r}) = N\Delta p(\mathbf{r}) + p(\mathbf{r})\Delta N = [\Delta\rho(\mathbf{r})]_N + [\Delta\rho(\mathbf{r})]_p, \quad (63)$$

where the first term originates from the polarizational changes in the density shape-factor, while the second contribution combines the first-order effect due to the external-CT. It

should be observed that the CT-induced density polarization, reflected by a change in the equilibrium polarization of the $(N + \Delta N)$ -electron system relative to that of the N -electron system, is the second-order effect and as such it is not present in the first differential of equation (63). It also follows from the separation of equation (61) that the fixed-density constraint introduces an implicit dependence between the infinitesimal displacements of the local shape factor $p(\mathbf{r})$ and the density normalization N :

$$d\rho(\mathbf{r}) = N dp(\mathbf{r}) + p(\mathbf{r}) dN \equiv [d\rho(\mathbf{r})]_N + [d\rho(\mathbf{r})]_p = 0. \quad (64)$$

It is reflected by the associated implicit derivatives:

$$\left(\frac{\partial p(\mathbf{r})}{\partial N} \right)_p = \left(\frac{\partial N}{\partial p(\mathbf{r})} \right)_p^{-1} = -\frac{p(\mathbf{r})}{N}. \quad (65)$$

Consider now the first partials of $\mathcal{F}[Np] \equiv F[\rho]$. Using the Euler equation (1) and equation (62) gives

$$\begin{aligned} \left(\frac{\partial \mathcal{F}[Np]}{\partial N} \right)_p &= \int \left(\frac{\delta F}{\delta \rho(\mathbf{r})} \right) \left(\frac{\partial \rho(\mathbf{r})}{\partial N} \right)_p d\mathbf{r} = - \int u(\mathbf{r}) p(\mathbf{r}) d\mathbf{r} \equiv -\bar{u} \\ &= \mu - \int v(\mathbf{r}) p(\mathbf{r}) d\mathbf{r} \equiv \mu - \bar{v}, \\ \left(\frac{\partial \mathcal{F}[Np]}{\partial p(\mathbf{r})} \right)_N &= \left(\frac{\delta F}{\delta \rho(\mathbf{r})} \right) \left(\frac{\partial \rho(\mathbf{r})}{\partial p(\mathbf{r})} \right)_N = -Nu(\mathbf{r}) \equiv -\tilde{u}(\mathbf{r}). \end{aligned} \quad (66)$$

It can be straightforwardly verified that these partial derivatives indeed reproduce the first differential of equation (49):

$$dF[\rho] = - \int u(\mathbf{r}) d\rho(\mathbf{r}) d\mathbf{r} = -\bar{u} dN - N \int u(\mathbf{r}) dp(\mathbf{r}) d\mathbf{r} = d\mathcal{F}[Np]. \quad (67)$$

Let us examine next the second partials of $\mathcal{F}[Np]$. The “diagonal” derivative with respect to N results from the following chain-rule transformation of $F[\rho]$:

$$\begin{aligned} \left(\frac{\partial^2 \mathcal{F}[Np]}{\partial N^2} \right)_p &= - \left(\frac{\partial \bar{u}}{\partial N} \right)_p \\ &= \int \int \left(\frac{\partial \rho(\mathbf{r})}{\partial N} \right)_p \left(\frac{\partial^2 F[\rho]}{\partial \rho(\mathbf{r}) \partial \rho(\mathbf{r}')} \right) \left(\frac{\partial \rho(\mathbf{r}')}{\partial N} \right)_p d\mathbf{r} d\mathbf{r}' \\ &= \int \int p(\mathbf{r}) \eta(\mathbf{r}, \mathbf{r}') p(\mathbf{r}') d\mathbf{r} d\mathbf{r}' \equiv \bar{\eta}. \end{aligned} \quad (68)$$

This derivative represents the shape-factor averaged hardness kernel defining the mean global hardness $\bar{\eta}$. A similar transformation of the other “diagonal” derivative, with respect to the local shape-factor, gives alternative measure of the internal hardness kernel, of the closed molecular system (for constant N):

$$\begin{aligned} \left(\frac{\partial^2 \mathcal{F}[Np]}{\partial p(\mathbf{r}) \partial p(\mathbf{r}')} \right)_N &= - \left(\frac{\partial \tilde{u}(\mathbf{r})}{\partial p(\mathbf{r}')} \right)_N = -N \left(\frac{\delta u(\mathbf{r}')}{\delta \rho(\mathbf{r})} \right) \left(\frac{\partial \rho(\mathbf{r})}{\partial p(\mathbf{r})} \right)_N \\ &= N^2 \eta(\mathbf{r}, \mathbf{r}'). \end{aligned} \quad (69)$$

It thus represents the renormalized hardness kernel. Finally, for the mixed derivative of $\mathcal{F}[Np]$ one finds

$$\begin{aligned}
 \left(\frac{\partial}{\partial N} \left(\frac{\partial \mathcal{F}[Np]}{\partial p(\mathbf{r})} \right) \right)_N \Big|_p &= - \left(\frac{\partial \tilde{u}}{\partial p(\mathbf{r})} \right)_N \\
 &= - \left(\frac{\partial \tilde{u}(\mathbf{r})}{\partial N} \right)_p \\
 &= \iint \left(\frac{\partial \rho(\mathbf{r}'')}{\partial N} \right)_p \left(\frac{\partial^2 F[\rho]}{\partial \rho(\mathbf{r}'') \partial \rho(\mathbf{r}')} \right) \left(\frac{\partial \rho(\mathbf{r}')}{\partial p(\mathbf{r})} \right)_N d\mathbf{r}'' d\mathbf{r}' \\
 &= N \iint p(\mathbf{r}'') \eta(\mathbf{r}'', \mathbf{r}') \delta(\mathbf{r}' - \mathbf{r}) d\mathbf{r}'' d\mathbf{r}' \\
 &= N \bar{\eta}(\mathbf{r}),
 \end{aligned} \tag{70}$$

where the p -averaged (non-equalized) local hardness $\bar{\eta}(\mathbf{r}) = \int p(\mathbf{r}') \eta(\mathbf{r}', \mathbf{r}) d\mathbf{r}'$. These shape-factor resolved derivatives give rise to the following expression for $d^2 \mathcal{F}[Np] = d^2 F[\rho]$:

$$\begin{aligned}
 d^2 \mathcal{F}[Np] &= \frac{1}{2} \left[\bar{\eta} (dN)^2 + 2N dN \int \bar{\eta}(\mathbf{r}) dp(\mathbf{r}) d\mathbf{r} \right. \\
 &\quad \left. + N^2 \iint dp(\mathbf{r}) \eta(\mathbf{r}, \mathbf{r}') d\mathbf{r} d\mathbf{r}' \right].
 \end{aligned} \tag{71}$$

It can be directly verified that this expansion is equivalent to the second differential implied by the quadratic forms of equations (55) and (58).

Finally, let us briefly explore the EP-description of the externally-open (μ -controlled) molecular systems. The thermodynamic potential, which determines the equilibrium state of the molecular equilibrium state specified by the system/reservoir chemical potential μ and the ensemble-average electron density $\rho(\mathbf{r})$ is given by the Legendre transform $\mathcal{R}[\mu, \rho]$ of equation (48). Its first differential (equation (50)) identifies the corresponding partial derivatives with respect to these state-parameters:

$$\left(\frac{\partial \mathcal{R}}{\partial \mu} \right)_\rho = -N, \quad \left(\frac{\partial \mathcal{R}}{\partial \rho(\mathbf{r})} \right)_\mu = -v(\mathbf{r}). \tag{72}$$

The external potential due to the nuclei is thus the only dependent (unconstrained) variable, since N is uniquely determined by the system electron density.

It should be observed, that the chemical-hardness representation $\mathcal{R}[\mu, \rho] \equiv R_\rho[v; \mu]$ can be regarded as the “inverse” description relative to the chemical-softness representation $E[N, v] \equiv E_v[\rho]$. In the same spirit one could regard the $\mathcal{F}[N, \rho] \equiv F_\rho[u[\rho]]$ and $\Omega[\mu, v] \equiv \Omega_u[\rho[u]]$ representations as the mutually “inverse” descriptions of equilibrium states in molecular systems. The notation $R_\rho[v; \mu]$ again stresses the dependent role of v in determining the equilibrium state defined by μ and ρ . Indeed, the equilibrium value of the Legendre transform (48) follows from the following maximum- v principle [2,3]:

$$\begin{aligned}
 \mathcal{R}[\mu, \rho] &= \max_{v'} \left\{ \Omega[\mu, v'] - \int v'(\mathbf{r}) \rho(\mathbf{r}) d\mathbf{r} \right\} \\
 &\equiv \max_{v'} \mathcal{R}[v'; \mu, \rho] = R_\rho[v[\rho]; \mu].
 \end{aligned} \tag{73}$$

The second partials of $\mathcal{R}[\mu, \rho]$ read:

$$\begin{aligned} \left(\frac{\partial^2 \mathcal{R}}{\partial \mu^2} \right)_\rho &= - \left(\frac{\partial N}{\partial \mu} \right)_\rho = 0, \\ \left(\frac{\partial^2 \mathcal{R}}{\partial \rho(\mathbf{r}') \partial \rho(\mathbf{r})} \right)_\mu &= - \left(\frac{\partial v(\mathbf{r})}{\partial \rho(\mathbf{r}') \partial \mu} \right)_\mu = - \left(\frac{\partial u(\mathbf{r})}{\partial \rho(\mathbf{r}') \partial \mu} \right)_\mu = \eta(\mathbf{r}', \mathbf{r}), \\ \frac{\partial^2 \mathcal{R}}{\partial \rho(\mathbf{r}') \partial \mu} &= - \left(\frac{\partial N}{\partial \rho(\mathbf{r}') \partial \mu} \right)_\mu = - \left(\frac{\partial v(\mathbf{r})}{\partial \mu} \right)_\rho = -1. \end{aligned} \quad (74)$$

The last equation expresses the fact, that the ground-state density determines the external potential to the additive constant μ . The derivatives of equations (72) and (74) give the following “horizontal” expansion of $\mathcal{R}[\mu, \rho]$, in terms of displacements $(\Delta\mu, \Delta\rho)$ in the representation independent state-parameters:

$$\begin{aligned} \Delta^{(1+2)} \mathcal{R}[\mu, \rho] &= -N \Delta\mu - \int v(\mathbf{r}) \Delta\rho(\mathbf{r}) d\mathbf{r} - \Delta\mu \Delta N \\ &\quad + \frac{1}{2} \iint \Delta\rho(\mathbf{r}) \eta(\mathbf{r}, \mathbf{r}') \Delta\rho(\mathbf{r}') d\mathbf{r} d\mathbf{r}', \end{aligned} \quad (75)$$

where $\Delta N = \int \Delta\rho d\mathbf{r}$.

Since $\rho = \rho[u]$ this “thermodynamic” potential can be also regarded as the composite functional of the relative external potential u : $\mathcal{R}[\mu, \rho] = \mathcal{R}[\mu, \rho[u]] \equiv \tilde{R}_\mu[u]$. Its functional derivatives for the fixed chemical potential of the reservoir, *i.e.*, for the density functional $\mathcal{R}[\mu, \rho] \equiv R_\mu[\rho]$, then read:

$$\frac{\delta \tilde{R}_\mu}{\delta u(\mathbf{r})} = \int \frac{\delta \rho(\mathbf{r}')}{\delta u(\mathbf{r})} \frac{\delta R_\mu}{\delta \rho(\mathbf{r}')} d\mathbf{r}' = \int \sigma(\mathbf{r}, \mathbf{r}') v(\mathbf{r}') d\mathbf{r}', \quad (76)$$

$$\frac{\delta^2 \tilde{R}_\mu}{\delta u(\mathbf{r}) \delta u(\mathbf{r}')} = \int \frac{\delta \rho(\mathbf{r}'')}{\delta u(\mathbf{r})} \frac{\delta^2 R_\mu}{\delta \rho(\mathbf{r}'') \delta \rho(\mathbf{r}''')} \frac{\delta \rho(\mathbf{r}''')}{\delta u(\mathbf{r}')} d\mathbf{r}'' d\mathbf{r}''' = \sigma(\mathbf{r}, \mathbf{r}'). \quad (77)$$

These functional derivatives give the following variational (“vertical”) Taylor expansion:

$$\begin{aligned} \Delta^{(1+2)} \tilde{R}_\mu[u] &= \iint \sigma(\mathbf{r}, \mathbf{r}') v(\mathbf{r}') d\mathbf{r}' \Delta u(\mathbf{r}) d\mathbf{r} \\ &\quad + \frac{1}{2} \iint \Delta u(\mathbf{r}) \sigma(\mathbf{r}, \mathbf{r}') \Delta u(\mathbf{r}') d\mathbf{r} d\mathbf{r}'. \end{aligned} \quad (78)$$

2.3. Transformations between perturbations and responses

The linear responses of the system unconstrained (dependent) state-variables can be expressed as transformations of the corresponding perturbations, given by the specified displacements in the representation independent state-parameters [2–4,6].

In the $E[N, v]$ -representation, within the EF-perspective, the displacements $(\Delta N, \Delta v)$ of the independent state-parameters generate the following equilibrium linear responses of the respective (dependent) energy-conjugates:

$$\Delta\mu = \left(\frac{\partial \mu}{\partial N} \right)_v \Delta N + \int \left(\frac{\partial \mu}{\partial v(\mathbf{r})} \right)_v \Delta v(\mathbf{r}) d\mathbf{r} = \eta \Delta N + \int f(\mathbf{r}) \Delta v(\mathbf{r}) d\mathbf{r}, \quad (79)$$

$$\begin{aligned}\Delta\rho(\mathbf{r}) &= \left(\frac{\partial\rho(\mathbf{r})}{\partial N}\right)_v \Delta N + \int \left(\frac{\partial\rho(\mathbf{r})}{\partial v(\mathbf{r}')}\right)_N \Delta v(\mathbf{r}') d\mathbf{r}' \\ &= f(\mathbf{r})\Delta N + \int \Delta v(\mathbf{r}')\beta(\mathbf{r}', \mathbf{r}) d\mathbf{r}'.\end{aligned}\quad (80)$$

These two relations can be jointly combined into the following matrix transformation:

$$[\Delta\mu, \Delta\rho(\mathbf{r})] = \left[\Delta N, \int d\mathbf{r}' \Delta v(\mathbf{r}')\right] \begin{bmatrix} \eta & f(\mathbf{r}) \\ f(\mathbf{r}') & \beta(\mathbf{r}', \mathbf{r}) \end{bmatrix}. \quad (81)$$

In the “inverse”, $\mathcal{R}[\mu, \rho]$ -representation of the EP-perspective, the independent perturbations $(\Delta\mu, \Delta\rho)$ determine the coupled linear responses in the conjugate unconstrained variables $\Delta N = \int \Delta\rho(\mathbf{r}) d\mathbf{r}$ and

$$\begin{aligned}\Delta v(\mathbf{r}) &= \left(\frac{\partial v(\mathbf{r})}{\partial\mu}\right)_\rho \Delta\mu + \int \left(\frac{\partial v(\mathbf{r})}{\partial\rho(\mathbf{r}')}\right)_\mu \Delta\rho(\mathbf{r}') d\mathbf{r}' \\ &= \Delta\mu - \int \Delta\rho(\mathbf{r}')\eta(\mathbf{r}', \mathbf{r}) d\mathbf{r}'.\end{aligned}\quad (82)$$

These linear transformations can be combined into the associated matrix relation:

$$[\Delta N, \Delta v(\mathbf{r})] = \left[\Delta\mu, \int d\mathbf{r}' \Delta\rho(\mathbf{r}')\right] \begin{bmatrix} 0 & 1 \\ 1 & -\eta(\mathbf{r}', \mathbf{r}) \end{bmatrix}. \quad (83)$$

The corresponding transformations in the $F[\rho]$ - and $\Omega[u]$ -representations are summarized in equation (59). They can be further resolved in terms of the corresponding partial derivatives. Consider for example the transformation of perturbations $(\Delta\mu, \Delta v)$ in the $\Omega[\mu, v]$ -representation into the conjugate responses $(\Delta N, \Delta\rho)$:

$$\Delta N = \left(\frac{\partial N}{\partial\mu}\right)_v \Delta\mu + \int \left(\frac{\partial N}{\partial v(\mathbf{r})}\right)_\mu \Delta v(\mathbf{r}) d\mathbf{r} = S\Delta\mu - \int s(\mathbf{r})\Delta v(\mathbf{r}) d\mathbf{r}, \quad (84)$$

$$\begin{aligned}\Delta\rho(\mathbf{r}) &= \left(\frac{\partial\rho(\mathbf{r})}{\partial\mu}\right)_v \Delta\mu + \int \left(\frac{\partial\rho(\mathbf{r})}{\partial v(\mathbf{r}')}\right)_\mu \Delta v(\mathbf{r}') d\mathbf{r}' \\ &= s(\mathbf{r})\Delta\mu - \int \Delta v(\mathbf{r}')\sigma(\mathbf{r}', \mathbf{r}) d\mathbf{r}'.\end{aligned}\quad (85)$$

Combining these partial relations into the joint, matrix form gives

$$[\Delta N, \Delta\rho(\mathbf{r})] = \left[\Delta\mu, \int d\mathbf{r}' \Delta v(\mathbf{r}')\right] \begin{bmatrix} S & s(\mathbf{r}) \\ -s(\mathbf{r}') & -\sigma(\mathbf{r}', \mathbf{r}) \end{bmatrix}. \quad (86)$$

In the $F[\rho] = \mathcal{F}[N, \rho]$ -representation the resolution of the polarization (P) and charge-transfer (CT) components is not unique. For example, the Hilbert-space, “geometric” interpretation of charge rearrangements in molecules [3,64,65] can also be used to separate these components of a general displacement in the system electron density. This approach uses the projector operators acting in the vector (Hilbert) space spanned by the independent modes of density displacements, and gives rise to the (P, CT)-resolution of the hardness and softness kernels. The geometric partition allows one to view the overall relations of equation (59) in terms of the separate P- and CT-effects, as well as contributions reflecting the coupling between these two components of the density reconstruction in molecular systems.

Alternative separation comes from the shape-factor approach of equations (61)–(71). More specifically, equation (66) identifies the conjugates of (N, p) , represented by the average and scaled relative-potential quantities $(-\bar{u}, -\tilde{u})$. The linear responses $(\Delta\bar{u}, \Delta\tilde{u})$ to displacements $(\Delta N, \Delta p)$ are then defined by the second partials of equations (68)–(70):

$$\begin{aligned}\Delta\bar{u} &= \left(\frac{\partial\bar{u}}{\partial N}\right)_p \Delta N + \int \left(\frac{\partial\bar{u}}{\partial p(\mathbf{r})}\right)_N \Delta p(\mathbf{r}) d\mathbf{r} \\ &= -\bar{\eta} \Delta N - N \int \bar{\eta}(\mathbf{r}) \Delta p(\mathbf{r}) d\mathbf{r},\end{aligned}\quad (87)$$

$$\begin{aligned}\Delta\tilde{u}(\mathbf{r}) &= \left(\frac{\partial\tilde{u}(\mathbf{r})}{\partial N}\right)_p \Delta N + \int \left(\frac{\partial\tilde{u}(\mathbf{r})}{\partial p(\mathbf{r}')}\right)_N \Delta p(\mathbf{r}') d\mathbf{r}' \\ &= -N\bar{\eta}(\mathbf{r}) \Delta N - N^2 \int \Delta p(\mathbf{r}') \eta(\mathbf{r}', \mathbf{r}) d\mathbf{r}'.\end{aligned}\quad (88)$$

These relations can be combined into the following matrix transformation:

$$[\Delta\bar{u}, \Delta\tilde{u}(\mathbf{r})] = \left[\Delta N, \int d\mathbf{r}' \Delta p(\mathbf{r}') \right] \begin{bmatrix} -\bar{\eta} & -N\bar{\eta}(\mathbf{r}) \\ -N\bar{\eta}(\mathbf{r}') & -N^2\eta(\mathbf{r}', \mathbf{r}) \end{bmatrix}. \quad (89)$$

3. ELECTRONIC AND NUCLEAR SENSITIVITIES IN GEOMETRIC REPRESENTATIONS

3.1. Principal representation and its derivative quantities

The direct coupling relations between the electron density $\rho(\mathbf{r})$ and nuclear coordinates \mathbf{R} in the principal representation defined by the system total electronic energy $W[N, v(\mathbf{R})] \equiv W(N, \mathbf{R})$ (see (11)) is obtained by replacing the implicit dependence on \mathbf{R} through the external potential $v(\mathbf{r}; \mathbf{R})$ by the explicit dependence on nuclear coordinates. To facilitate a compact vector notation we arrange the nuclear coordinates $\mathbf{R} = \{\mathbf{R}_\alpha\} = \{X_{\alpha,s}\}$, where index α denotes the nucleus and $s = (x, y, z)$ labels its Cartesian coordinates, in the row vector

$$\begin{aligned}\mathbf{R} &= [\dots, (X_{\alpha,x}, X_{\alpha,y}, X_{\alpha,z}), (X_{\alpha+1,x}, X_{\alpha+1,y}, X_{\alpha+1,z}), \dots] \\ &= (\dots, \mathbf{R}_\alpha, \mathbf{R}_{\alpha+1}, \dots) = \{X_k\}.\end{aligned}\quad (90)$$

The corresponding components of the generalized gradient of the scalar field $g(\mathbf{R})$, $\partial g(\mathbf{R})/\partial \mathbf{R} \equiv \partial g(\mathbf{R})/\partial \mathbf{R}$, will be similarly arranged in the row vector

$$\begin{aligned}\frac{\partial g(\mathbf{R})}{\partial \mathbf{R}} &= \left[\dots, \left(\frac{\partial g}{\partial X_{\alpha,x}}, \frac{\partial g}{\partial X_{\alpha,y}}, \frac{\partial g}{\partial X_{\alpha,z}} \right), \left(\frac{\partial g}{\partial X_{\alpha+1,x}}, \frac{\partial g}{\partial X_{\alpha+1,y}}, \frac{\partial g}{\partial X_{\alpha+1,z}} \right), \dots \right] \\ &= \left\{ \frac{\partial g}{\partial X_k} \right\}.\end{aligned}\quad (91)$$

We have already referred to this principal geometric representation in equation (13), in which the key geometric kernel $[\partial v(\mathbf{r}; \mathbf{R})/\partial \mathbf{R}]^T \equiv \{\partial v(\mathbf{r})/\partial X_k\} = \mathbf{G}(\mathbf{r}; \mathbf{R}) = (\dots, \mathbf{G}_\alpha(\mathbf{r}; \mathbf{R}), \mathbf{G}_{\alpha+1}(\mathbf{r}, \mathbf{R}), \dots)$ (row vector) effecting this $[N, v] \rightarrow [N, \mathbf{R}]$ transformation has been introduced. It constitutes the row-vector transcription of the $\mathbf{G}(\mathbf{r}; \mathbf{R})$ matrix of

Section 1. We have shown there that the NFF $\boldsymbol{\varphi}$, arranged as the corresponding row vector $\boldsymbol{\varphi} = (\dots, \varphi_\alpha, \varphi_{\alpha+1}, \dots)$, is just the \mathbf{G} -transform of the electronic FF of equation (9):

$$\begin{aligned}\boldsymbol{\varphi}(N, \mathbf{R}) &= \frac{\partial \mathbf{F}(N, \mathbf{R})}{\partial N} = -\left(\frac{\partial \mu(N, \mathbf{R})}{\partial \mathbf{R}}\right)^T \equiv -\int f(\mathbf{r}) \mathbf{G}(\mathbf{r}; \mathbf{R}) d\mathbf{r} \\ &= \{\boldsymbol{\varphi}_\alpha(N, \mathbf{R})\}.\end{aligned}\quad (92)$$

It measures a direct coupling between the overall number of electrons N , reflecting the molecular net-charge (oxidation state), and the forces acting on the system nuclei. By the cross-differentiation (Maxwell) identity of equation (92) they also reflect the effect of the nuclear displacements on the molecular chemical potential.

In this geometric representation the row vector of forces acting on the system nuclei reads:

$$\begin{aligned}\mathbf{F}(\mathbf{R}) &= -\left(\frac{\partial W(N, \mathbf{R})}{\partial \mathbf{R}}\right)^T \\ &= -\left(\frac{\partial V_{nn}(\mathbf{R})}{\partial \mathbf{R}}\right)^T - \int \left(\frac{\delta E[N, v]}{\delta v(\mathbf{r})}\right)_N \left(\frac{\partial v(\mathbf{r}; \mathbf{R})}{\partial \mathbf{R}}\right)^T d\mathbf{r} \\ &\equiv \mathbf{F}_n(\mathbf{R}) - \int \rho(\mathbf{r}) \mathbf{G}(\mathbf{r}; \mathbf{R}) d\mathbf{r} = \left\{ \mathbf{F}_\alpha(\mathbf{R}) = -\left(\frac{\partial W(N, \mathbf{R})}{\partial \mathbf{R}_\alpha}\right)^T \right\}.\end{aligned}\quad (93)$$

A reference to this Hellmann–Feynman formula shows that these forces include the trivial contribution $\mathbf{F}_n(\mathbf{R})$ due to the repulsion between the system nuclei and the \mathbf{G} -transform of the electronic density.

Let us now examine the remaining second-order derivatives of this principal geometric representation. The geometric Hessian of nuclear force-constants can be also expressed as the nuclear-repulsion term $\mathbf{H}_n(\mathbf{R}, \mathbf{R}')$ and the *full* \mathbf{G} -transform of the LR-function of equation (18):

$$\begin{aligned}\mathbf{H} &= \frac{\partial^2 W(N, \mathbf{R})}{\partial \mathbf{R} \partial \mathbf{R}} = -\frac{\partial \mathbf{F}(N, \mathbf{R})}{\partial \mathbf{R}} \\ &= \frac{\partial^2 V_{nn}(\mathbf{R})}{\partial \mathbf{R} \partial \mathbf{R}} + \iint \left(\frac{\partial v(\mathbf{r}; \mathbf{R})}{\partial \mathbf{R}}\right) \left(\frac{\delta^2 E[N, v]}{\delta v(\mathbf{r}) \delta v(\mathbf{r}')} \right)_N \left(\frac{\partial v(\mathbf{r}'; \mathbf{R})}{\partial \mathbf{R}}\right)^T d\mathbf{r} d\mathbf{r}' \\ &\equiv \mathbf{H}_n + \iint \mathbf{G}^T(\mathbf{r}; \mathbf{R}) \beta(\mathbf{r}, \mathbf{r}') \mathbf{G}(\mathbf{r}'; \mathbf{R}) d\mathbf{r} d\mathbf{r}'.\end{aligned}\quad (94)$$

Of interest also is the partial-transform of this kernel,

$$\mathbf{B}(\mathbf{r}; \mathbf{R}) \equiv \int \beta(\mathbf{r}, \mathbf{r}') \mathbf{G}(\mathbf{r}'; \mathbf{R}) d\mathbf{r}' = \left(\frac{\partial \rho[\mathbf{r}; v(\mathbf{R})]}{\partial \mathbf{R}}\right)_N^T, \quad (95)$$

which reflects the direct effect of nuclear displacements on electron density: $\rho(\mathbf{r}) = \rho[\mathbf{r}; v(\mathbf{R})] \equiv \rho(\mathbf{r}; N, \mathbf{R})$. It represents in the (N, \mathbf{R}) -representation the nuclear (geometric) equivalent of the “softness”-kernel in the closed molecule.

A similar transformation of the electronic softness-kernel of the open molecular system (31) generates its nuclear analog:

$$\mathbf{S}(\mathbf{r}; \mathbf{R}) \equiv \int \sigma(\mathbf{r}, \mathbf{r}') \mathbf{G}(\mathbf{r}'; \mathbf{R}) d\mathbf{r}' = \left(\frac{\partial \rho[\mathbf{r}; v(\mathbf{R})]}{\partial \mathbf{R}}\right)_\mu^T. \quad (96)$$

Therefore, by multiplying both sides of equation (40) by $\mathbf{G}(\mathbf{r}'; \mathbf{R})$ and integrating over \mathbf{r}' gives the Berkowitz–Parr relation in the associated, geometric-representation form [39]:

$$\mathbf{S}(\mathbf{r}; \mathbf{R}) = -\mathbf{B}(\mathbf{r}; \mathbf{R}) - \boldsymbol{\varphi}(\mathbf{R})s(\mathbf{r}) = -\mathbf{B}(\mathbf{r}; \mathbf{R}) - \boldsymbol{\varphi}(\mathbf{R})Sf(\mathbf{r}). \quad (97)$$

The independent displacements $(\Delta N, \Delta \mathbf{R})$ (perturbations) of this principal geometric representation give rise to the first differential of its thermodynamic potential $W(N, \mathbf{R})$:

$$\begin{aligned} dW(N, \mathbf{R}) &= \left(\frac{\partial W}{\partial N} \right)_{\mathbf{R}} \Delta N + \left(\frac{\partial W}{\partial \mathbf{R}} \right)_N^T \Delta \mathbf{R}^T \\ &= \mu \Delta N - \mathbf{F} \Delta \mathbf{R}^T \equiv \mu \Delta N - \sum_{\alpha} \mathbf{F}_{\alpha} \Delta \mathbf{R}_{\alpha}^T, \end{aligned} \quad (98)$$

where the row vector $\mathbf{R}_{\alpha} = \{X_{\alpha,s}\}$ and $\mathbf{F}_{\alpha} = \{F_{\alpha,s}\}$ group the coordinates and force components of atom α , respectively. Therefore, the generalized Hessian \mathcal{H} transforming the perturbations $(\Delta N, \Delta \mathbf{R})$ into the liner-responses of the conjugate variables $(\Delta \mu, -\Delta \mathbf{F})$,

$$(\Delta \mu, -\Delta \mathbf{F}) = (\Delta N, \Delta \mathbf{R}) \mathcal{H}, \quad (99)$$

includes the following matrix elements:

$$\mathcal{H} = \begin{bmatrix} \eta & -\boldsymbol{\varphi} \\ -\boldsymbol{\varphi}^T & \mathbf{H} \end{bmatrix} = \{\mathcal{H}_{x,y}\}, \quad x, y \in \{N, \mathbf{R}\}, \quad (100)$$

where η stands for the rigid-geometry measure of the global hardness (16). The matrix transformation (99) summarizes the two ground-state relations:

$$\Delta \mu = \Delta N \eta - \Delta \mathbf{R} \boldsymbol{\varphi}^T \quad \text{and} \quad -\Delta \mathbf{F} = -\Delta N \boldsymbol{\varphi} + \Delta \mathbf{R} \mathbf{H}. \quad (101)$$

3.2. Legendre-transformed representations

The inverse of \mathcal{H} determines the geometric compliance matrix describing the open system in the (μ, \mathbf{F}) -representation. Setting $\mathbf{F} = \mathbf{0}$ then identifies properties for the equilibrium (relaxed) molecular geometry. The relevant thermodynamic potential is defined by the Legendre transform of the system total electronic energy replacing (N, \mathbf{R}) with (μ, \mathbf{F}) , respectively:

$$\Sigma(\mu, \mathbf{F}) = W - N \left(\frac{\partial W}{\partial N} \right)_{\mathbf{R}} - \mathbf{R} \left(\frac{\partial W}{\partial \mathbf{R}} \right)_N^T = W - N\mu + \mathbf{R} \mathbf{F}^T, \quad (102)$$

$$d\Sigma = -N d\mu + \mathbf{R} d\mathbf{F}^T \quad \text{or} \quad -N = \left(\frac{\partial \Sigma}{\partial \mu} \right)_{\mathbf{F}} \quad \text{and} \quad \mathbf{R} = \left(\frac{\partial \Sigma}{\partial \mathbf{F}} \right)_{\mu}^T. \quad (103)$$

This representation thus constitutes a geometric analog of the chemical hardness representation $\mathcal{R}[\mu, \rho]$. The above mentioned compliance matrix [2,8,10,56,66–71]

$$\mathcal{S} = \mathcal{H}^{-1} = \begin{bmatrix} -(\frac{\partial N}{\partial \mu})_{\mathbf{F}} & (\frac{\partial \mathbf{R}}{\partial \mu})_{\mathbf{F}} \\ -(\frac{\partial N}{\partial \mathbf{F}})_{\mu} & (\frac{\partial \mathbf{R}}{\partial \mathbf{F}})_{\mu} \end{bmatrix} = \{\mathcal{S}_{x,y}\}, \quad x, y \in \{\mu, \mathbf{F}\}, \quad (104)$$

relates displacements of the representation independent variables $(\Delta \mu, \Delta \mathbf{F})$ with the conjugate responses $(-\Delta N, \Delta \mathbf{R})$:

$$(-\Delta N, \Delta \mathbf{R}) = (\Delta \mu, \Delta \mathbf{F}) \mathcal{S}. \quad (105)$$

It thus summarizes the individual responses in the system (negative) average number of electrons and its geometry:

$$-\Delta N = \Delta\mu\mathcal{S}_{\mu,\mu} + \Delta\mathbf{F}\mathcal{S}_{\mathbf{F},\mu}, \quad \Delta\mathbf{R} = \Delta\mu\mathcal{S}_{\mu,\mathbf{F}} + \Delta\mathbf{F}\mathcal{S}_{\mathbf{F},\mathbf{F}}. \quad (106)$$

A reference to equation (104) shows that the diagonal element $\mathcal{S}_{\mu,\mu}$ represents the relaxed-geometry analog of the negative global softness (compare equation (17)).

It follows from the second equation (106) that a change in the open system chemical potential induces an extra relaxation of the molecular frame. This geometric “softness” is measured by derivatives $\mathcal{S}_{\mu,\mathbf{F}} = \mathcal{S}_{\mathbf{F},\mu}^T$. One can directly express this matrix in terms of the elements of the principal charge sensitivities defining the generalized geometric “hardness” matrix of equation (100), by eliminating ΔN and $\Delta\mathbf{R}$ from (101):

$$\begin{aligned} -\Delta N &= -\Delta\mu(\eta - B)^{-1} + \Delta\mathbf{F}\mathbf{H}^{-1}\boldsymbol{\varphi}^T(\eta - B)^{-1}, \quad B = \boldsymbol{\varphi}\mathbf{H}^{-1}\boldsymbol{\varphi}^T; \\ \Delta\mathbf{R} &= \Delta\mu\boldsymbol{\varphi}\mathbf{H}^{-1}\mathbf{C} - \Delta\mathbf{F}\mathbf{H}^{-1}\mathbf{C}\eta, \quad \mathbf{C} = (\eta\mathbf{I} - \boldsymbol{\varphi}^T\boldsymbol{\varphi}\mathbf{H}^{-1})^{-1}; \end{aligned} \quad (107)$$

or in the combined, matrix form of equation (104):

$$\mathcal{S} = \begin{bmatrix} -(\frac{\partial N}{\partial \mu})_{\mathbf{F}} = -(\eta - B)^{-1} & (\frac{\partial \mathbf{R}}{\partial \mu})_{\mathbf{F}} = \boldsymbol{\varphi}\mathbf{H}^{-1}\mathbf{C} \\ -(\frac{\partial N}{\partial \mathbf{F}})_{\mu} = \mathbf{H}^{-1}\boldsymbol{\varphi}^T(\eta - B)^{-1} & (\frac{\partial \mathbf{R}}{\partial \mathbf{F}})_{\mu} = -\mathbf{H}^{-1}\mathbf{C}\eta \end{bmatrix}. \quad (108)$$

Let us now turn to the mixed (N, \mathbf{F}) -representation, which provides the geometric analog of the hardness representation $\mathcal{F}[N, \rho] = F[\rho]$ for closed molecular systems. The relevant thermodynamic potential is defined by the $\mathbf{R} \rightarrow \mathbf{F}$ Legendre transformation of $W(N, \mathbf{R})$:

$$\Theta(N, \mathbf{F}) = W - \mathbf{R} \left(\frac{\partial W}{\partial \mathbf{R}} \right)_N = W + \mathbf{R}\mathbf{F}^T, \quad d\Theta = \mu dN + \mathbf{R}d\mathbf{F}^T; \quad (109)$$

$$\mu = \left(\frac{\partial \Theta}{\partial N} \right)_{\mathbf{F}} \quad \text{and} \quad \mathbf{R} = \left(\frac{\partial \Theta}{\partial \mathbf{F}} \right)_N^T. \quad (110)$$

Eliminating $\Delta\mu$ from the first equation (106) and inserting it into the second equation (106) then gives the following transformation of the representation independent displacements $(\Delta N, \Delta\mathbf{F})$ into the linear responses of their conjugates $(\Delta\mu, \Delta\mathbf{R})$,

$$(\Delta\mu, \Delta\mathbf{R}) = (\Delta N, \Delta\mathbf{F})\mathbf{V}, \quad (111)$$

expressed in terms of the principal compliance coefficients of equations (104) and (108):

$$\begin{aligned} \mathbf{V} &= \begin{bmatrix} (\frac{\partial \mu}{\partial N})_{\mathbf{F}} & (\frac{\partial \mathbf{R}}{\partial N})_{\mathbf{F}} \\ (\frac{\partial \mu}{\partial \mathbf{F}})_{\mathbf{N}} & (\frac{\partial \mathbf{R}}{\partial \mathbf{F}})_{\mathbf{N}} \end{bmatrix} = \begin{bmatrix} -\mathcal{S}_{\mu,\mu}^{-1} & -\mathcal{S}_{\mu,\mathbf{F}}\mathcal{S}_{\mu,\mu}^{-1} \\ -\mathcal{S}_{\mathbf{F},\mu}\mathcal{S}_{\mu,\mu}^{-1} & \mathcal{S}_{\mathbf{F},\mathbf{F}} - \mathcal{S}_{\mathbf{F},\mu}\mathcal{S}_{\mu,\mathbf{F}}\mathcal{S}_{\mu,\mu}^{-1} \end{bmatrix} \\ &= \{V_{x,y}\}, \quad x, y \in \{N, \mathbf{F}\}. \end{aligned} \quad (112)$$

Again, a comparison with equation (16) indicates that the diagonal element $V_{N,N}$ represents the molecular hardness for the relaxed geometry of the molecule.

The two partial relations combined in equation (111),

$$\Delta\mu = \Delta N V_{N,N} + \Delta\mathbf{F}V_{\mathbf{F},N} \quad \text{and} \quad \Delta\mathbf{R} = \Delta N V_{N,\mathbf{F}} + \Delta\mathbf{F}V_{\mathbf{F},\mathbf{F}}, \quad (113)$$

again imply that there is an additional geometry relaxation due to the finite CT, $\Delta N \neq 0$, between the molecule and the electron reservoir/catalyst, besides the usual term due to the

forces acting on the system nuclei for constant N . This extra relaxation of the molecular frame is described by the coupling blocks $V_{N,F} = V_{F,N}^T$.

The matrix elements $\{V_{x,y}\}$ can be directly expressed in terms of the principal geometric derivatives defining the generalized Hessian of equation (100). This can be accomplished by first expressing $\Delta \mathbf{R}$ as function of ΔN and $\Delta \mathbf{F}$, using the second equation (101), and then inserting this relation into the first equation (101):

$$\Delta \mu = \Delta N(\eta - B) + \Delta \mathbf{F} \mathbf{H}^{-1} \boldsymbol{\varphi}^T \quad \text{and} \quad \Delta \mathbf{R} = \Delta N \boldsymbol{\varphi} \mathbf{H}^{-1} - \Delta \mathbf{F} \mathbf{H}^{-1}. \quad (114)$$

A comparison between equations (113) and (114) then gives

$$\mathbf{V} = \begin{bmatrix} (\frac{\partial \mu}{\partial N})_F = \eta - B & (\frac{\partial \mathbf{R}}{\partial N})_F = \boldsymbol{\varphi} \mathbf{H}^{-1} \\ (\frac{\partial \mu}{\partial \mathbf{F}})_N = \mathbf{H}^{-1} \boldsymbol{\varphi}^T & (\frac{\partial \mathbf{R}}{\partial \mathbf{F}})_N = -\mathbf{H}^{-1} \end{bmatrix}. \quad (115)$$

Finally, let us examine the perturbation-response transformations in the (μ, \mathbf{R}) representation, the geometric analog of the chemical-softness representation $Q(\mu, v)$ of the EF perspective. The relevant $N \rightarrow \mu$ Legendre transform of the total electronic energy defines the following thermodynamic potential for this selection of the state-parameters in an open molecular system:

$$\mathcal{E}(\mu, \mathbf{R}) = W - N \left(\frac{\partial W}{\partial N} \right)_{\mathbf{R}} = W - N\mu, \quad d\mathcal{E} = -N d\mu - \mathbf{F} d\mathbf{R}^T; \quad (116)$$

$$-N = \left(\frac{\partial \mathcal{E}}{\partial \mu} \right)_{\mathbf{R}} \quad \text{and} \quad -\mathbf{F} = \left(\frac{\partial \mathcal{E}}{\partial \mathbf{R}} \right)_{\mu}^T. \quad (117)$$

Eliminating $d\mathbf{F}$ from the second equation (106) and inserting the result into the first of these two equations give the following transformation of the representation independent perturbations $(\Delta \mu, \Delta \mathbf{R})$ into the linear responses of their conjugates $(-\Delta N, -\Delta \mathbf{F})$, expressed in terms of the matrix elements of the generalized compliance matrix \mathcal{J} (see (104) and (108)):

$$(-\Delta N, -\Delta \mathbf{F}) = (\Delta \mu, \Delta \mathbf{R}) \mathcal{J}, \quad (118)$$

$$\mathcal{J} = \begin{bmatrix} -(\frac{\partial N}{\partial \mu})_{\mathbf{R}} & -(\frac{\partial \mathbf{F}}{\partial \mu})_{\mathbf{R}} \\ -(\frac{\partial N}{\partial \mathbf{R}})_{\mu} & -(\frac{\partial \mathbf{F}}{\partial \mathbf{R}})_{\mu} \end{bmatrix} = \begin{bmatrix} \mathcal{S}_{\mu,\mu} - \mathcal{S}_{\mu,\mathbf{F}} \mathcal{S}_{\mathbf{F},\mathbf{F}}^{-1} \mathcal{S}_{\mathbf{F},\mu} & \mathcal{S}_{\mu,\mathbf{F}} \mathcal{S}_{\mathbf{F},\mathbf{F}}^{-1} \\ \mathcal{S}_{\mathbf{F},\mathbf{F}}^{-1} \mathcal{S}_{\mathbf{F},\mu} & -\mathcal{S}_{\mathbf{F},\mathbf{F}}^{-1} \end{bmatrix} \\ = \{\mathcal{I}_{x,y}\}, \quad x, y \in \{\mu, \mathbf{R}\}. \quad (119)$$

The above matrix transformation combines the following partial relations:

$$-\Delta N = \Delta \mu \mathcal{I}_{\mu,\mu} + \Delta \mathbf{R} \mathcal{I}_{\mathbf{R},\mu} \quad \text{and} \quad -\Delta \mathbf{F} = \Delta \mu \mathcal{I}_{\mu,\mathbf{R}} + \Delta \mathbf{R} \mathcal{I}_{\mathbf{R},\mathbf{R}}. \quad (120)$$

The elements of this mapping-relation, from the combined electronic/geometric perturbation $(\Delta \mu, \Delta \mathbf{R})$ of an open molecular system into the linear responses in their \mathcal{E} -conjugates $(-\Delta N, -\Delta \mathbf{F})$, can be also expressed in terms of the generalized Hessian (see (100)), by eliminating ΔN from the first equation (101) and by subsequent insertion of the resulting expression into the second of these equations:

$$-\Delta N = -\Delta \mu \eta^{-1} - \Delta \mathbf{R} \boldsymbol{\varphi}^T \eta^{-1} \equiv -\Delta \mu S - \Delta \mathbf{R} \boldsymbol{\mathfrak{s}}^T, \\ -\Delta \mathbf{F} = -\Delta \mu \boldsymbol{\mathfrak{s}} + \Delta \mathbf{R} (\mathbf{H} - \boldsymbol{\varphi}^T S \boldsymbol{\varphi}) = -\Delta \mu \boldsymbol{\mathfrak{s}} + \Delta \mathbf{R} (\mathbf{H} - \boldsymbol{\varphi}^T \boldsymbol{\mathfrak{s}}). \quad (121)$$

Here S is the electronic rigid-geometry measure of the global softness (17) and the geometric “softnesses” \mathfrak{z} are defined as products of the global softness and NFF (see (10)):

$$\mathfrak{z} = S\varphi = \left(\frac{\partial \mathbf{F}}{\partial \mu}\right)_{\mathbf{R}} = \left(\frac{\partial N}{\partial \mathbf{R}}\right)_{\mu}^{\mathrm{T}}. \quad (122)$$

A reference to the second equation (121) shows that the effective geometrical Hessian of an open molecular system differs from that for the closed system (see (94)) by the CT-contribution involving the geometrical softnesses and NFF. Finally, one identifies the corresponding blocks of $\mathbf{J} = \{\mathcal{I}_{x,y}\}$ by comparing the general relations of equation (120) with the explicit transformations of equation (121):

$$\mathbf{J} = \begin{bmatrix} -(\frac{\partial N}{\partial \mu})_{\mathbf{R}} = -S & -(\frac{\partial \mathbf{F}}{\partial \mu})_{\mathbf{R}} = -\mathfrak{z} \\ -(\frac{\partial N}{\partial \mathbf{F}})_{\mu} = -\mathfrak{z}^{\mathrm{T}} & -(\frac{\partial \mathbf{F}}{\partial \mathbf{R}})_{\mu} = \mathbf{H} - \varphi^{\mathrm{T}}\mathfrak{z} \end{bmatrix}. \quad (123)$$

Several geometrical quantities introduced in this section provide natural descriptors measuring a coupling between the molecular electronic and geometrical structures. Consider, for example, the canonical geometrical representation $W(N, \mathbf{R})$, in which the generalized Hessian \mathcal{H} is defined (see (100)). In this matrix the diagonal blocks, the system rigid-geometry hardness, η , and the matrix of force-constants, \mathbf{H} , describe the *decoupled* aspects of the electronic and geometric structures, respectively. As we have already observed above, the NFF φ , defining the off-diagonal blocks in \mathcal{H} , reflects the coupling between the electronic and nuclear aspects of the molecular structure. They describe the effect of a geometrical displacement in the closed-system on the chemical potential, or the influence of an external CT on the system forces on nuclei. As we have indicated in equation (122) the geometrical softnesses $\mathfrak{z} = \{\mathfrak{z}_{\alpha}\}$ reflect similar couplings in the externally-open molecular systems. It should be stressed, however, that in the geometric compliance matrix of equation (104) the coupling between these two facets of molecular structure enters also the diagonal blocks, as we have explicitly shown in equations (107) and (108). A similar diagonal coupling effect is seen in the transformation matrices of equations (115) and (123).

There are two types of the geometrical constraints, which can be imposed on the molecule: that of the rigid geometry \mathbf{R} and the condition of the equilibrium geometry, i.e., of the vanishing forces, $\mathbf{F} = \mathbf{0}$, reflecting the equilibrium positions of the system nuclei. The latter description amounts to the compliant formalism of nuclear motions [2,8,10,56,66–71], in which one allows the system to relax all its remaining (electronic and/or nuclear) degrees-of-freedom in response to the probing displacement in the position of an AIM or the system number of electrons. The $\Theta(N, \mathbf{F})$ and $\Sigma(\mu, \mathbf{F})$ representations correspond to such a nuclear-compliant treatment of the molecular geometrical structure, while the $W(N, \mathbf{R})$ and $\Xi(\mu, \mathbf{R})$ representations adopt the rigid-geometry approach. The above Legendre-transformed approach to geometric representations of molecular states provides the complete set of quantities, which can be used to monitor or index the electronic–geometric couplings in molecular systems in both these approaches, covering the externally-open and externally-closed molecular systems.

It should be also realized, that the geometric softness matrix of equations (104) and (108) also represents the compliant treatment of the electronic “coordinate” N coupled to the system geometric relaxations. Indeed, the relaxed-geometry global softness of the geometrical

representation,

$$\begin{aligned} -S_{\mu,\mu} &= \left(\frac{\partial N}{\partial \mu} \right)_{\mathbf{F}} = (\eta - B)^{-1} = (\eta - \boldsymbol{\varphi} \mathbf{H}^{-1} \boldsymbol{\varphi}^T)^{-1} \\ &\neq \eta^{-1} = S = \left(\frac{\partial N}{\partial \mu} \right)_{\mathbf{R}}, \end{aligned} \quad (124)$$

differs from the conventional definition of the electronic global softness S (see (17)), which invokes the rigid-geometry constraint. The geometric-hardness term B effectively softens the electronic distribution via the relaxation of nuclei, as reflected by the negative purely-geometric compliant \mathbf{H}^{-1} and the “weighting” factors provided by the NFF $\boldsymbol{\varphi}$ measuring the geometric softness of the molecule. The other diagonal block of the generalized geometrical compliants, which reflect the electronic–nuclear couplings,

$$\begin{aligned} S_{\mathbf{F},\mathbf{F}} &= \left(\frac{\partial \mathbf{R}}{\partial \mathbf{F}} \right)_{\mu} = -\mathbf{H}^{-1} \mathbf{C} \eta = -\mathbf{H}^{-1} (\eta \mathbf{I} - \boldsymbol{\varphi}^T \boldsymbol{\varphi} \mathbf{H}^{-1})^{-1} \eta \\ &\neq -\mathbf{H}^{-1} = V_{\mathbf{F},\mathbf{F}}, \end{aligned} \quad (125)$$

is also seen to differ from the purely-geometrical compliant $V_{\mathbf{F},\mathbf{F}}$ by the additional factor of both the electronic and nuclear origins. The mixture of the electronic and nuclear inputs is also seen to determine the off-diagonal blocks of the geometric compliant matrix, respectively measuring the effect of the chemical potential on the relaxed nuclear positions ($S_{\mu,\mathbf{F}}$) or the influence of the forces on nuclei on the effective oxidation state of an open molecule coupled to the external electron reservoir.

Let us now examine selected compliant constants in the externally-closed systems within the $\Theta(N, \mathbf{F})$ representation, defined by the corresponding blocks of the geometric charge-sensitivities $\mathbf{V} = \{V_{x,y}\}$ (see (115)). Again, the first diagonal derivative in this matrix, $V_{N,N} = (\partial \mu / \partial N)_{\mathbf{F}} = \eta - B$ allows the geometry of the system to relax, after an addition/removal of an electron, until the forces on nuclei exactly vanish: $\mathbf{F} = \mathbf{0}$. The electronic–geometric interaction is also detected in the coupling blocks $V_{N,\mathbf{F}} = (\partial \mathbf{R} / \partial N)_{\mathbf{F}}$ and $V_{\mathbf{F},N} = (\partial \mu / \partial \mathbf{F})_N$, which are determined by the nuclear compliants $V_{\mathbf{F},\mathbf{F}}$ (geometrical aspect of molecular structure) and NFF, which expresses the electronic FF in the geometric representation.

The electronic–nuclear coupling in molecules is also evident in the other partial Legendre-transformed representation $\mathcal{E}(\mu, \mathbf{R})$, in which the Hessian $\mathcal{J} = \{\mathcal{I}_{x,y}\}$ of equation (119) is defined. Its first diagonal derivative,

$$\mathcal{I}_{\mu,\mu} = - \left(\frac{\partial N}{\partial \mu} \right)_{\mathbf{R}} = - \left(\frac{\partial N}{\partial \mu} \right)_v = -S, \quad (126)$$

represents the purely-electronic, global compliant reflecting the negative (rigid-geometry) global softness of the system electron distribution (17). The off-diagonal blocks $\mathcal{I}_{\mu,\mathbf{R}} = -(\partial \mathbf{F} / \partial \mu)_{\mathbf{R}} = -(\partial N / \partial \mathbf{F})_{\mu}^T$, represent geometric softnesses of equation (122). They measure the effect, for the rigid nuclear frame, of the system chemical potential on forces on nuclei. In the alternative physical interpretation of these quantities they reflect the influence of forces, which accompany the conformation changes, on the open system net charge. Since in this representation the molecular system is externally open one detects the influence of the external CT, triggered by nuclear displacements, in the geometrical

Hessian of this representation:

$$\mathcal{I}_{\mathbf{R},\mathbf{R}} = -\left(\frac{\partial \mathbf{F}}{\partial \mathbf{R}}\right)_{\mu} = \mathbf{H} - \boldsymbol{\varphi}^T \boldsymbol{\mathcal{A}} = \mathbf{H} - \boldsymbol{\varphi}^T S \boldsymbol{\varphi} \neq \mathbf{H} = -\left(\frac{\partial \mathbf{F}}{\partial \mathbf{R}}\right)_N. \quad (127)$$

4. MINIMUM-ENERGY COORDINATES IN COMPLIANCE FORMALISM

In this section we shall explore several concepts of the compliant description of the combined electronic–nuclear degrees-of-freedom of molecular systems [2,8,10,56,70,71]. This development is in spirit of the earlier minimum-energy derivatives, for the vanishing forces acting on nuclei, which determine the compliance approach to nuclear motions [66–69].

In this compliance perspective the inverse of the force-constant matrix \mathbf{H} of equation (94),

$$\mathbf{H} = \left\{ \left(\frac{\partial W(N, \mathbf{R})}{\partial X_k \partial X_l} \right) = -\left(\frac{\partial F_l(N, \mathbf{R})}{\partial X_k} \right)_{X_i \neq k} \right\}, \quad (128)$$

determines the nuclear (purely geometric) compliance matrix:

$$\begin{aligned} \mathbf{C}(\mathbf{F}, \mathbf{F}) &= \frac{\partial^2 \Theta(N, \mathbf{F})}{\partial \mathbf{F} \partial \mathbf{F}} \\ &= -\mathbf{H}^{-1} = \left\{ \left(\frac{\partial^2 \Theta(N, \mathbf{F})}{\partial F_k \partial F_l} \right) = \left(\frac{\partial X_l(N, \mathbf{F})}{\partial F_k} \right)_{F_i \neq k} \right\}. \end{aligned} \quad (129)$$

Here $\Theta(N, \mathbf{F})$ stands for the Legendre-transform of the total potential-energy surface $W(N, \mathbf{R})$, which replaces the nuclear-position coordinates $\mathbf{R} = \{X_k\}$ by the corresponding forces $\mathbf{F} = \{F_k\}$ in the list of the ground-state parameters of the geometric representation (see (109)). Hence, for the fixed number of electrons N ,

$$[d\Theta(N, \mathbf{F})]_N = \mathbf{R} d\mathbf{F}^T \quad \text{and} \quad \left[\frac{\partial^2 \Theta(N, \mathbf{F})}{\partial F_k \partial F_l} \right]_N = \left(\frac{\partial X_l}{\partial F_k} \right)_{N, \mathbf{F}'}. \quad (130)$$

The constraint of $\mathbf{F}' = \{F_{l \neq k} = 0\}$ in these derivatives implies that the nuclear frame is free to relax atomic positions until the forces associated with the remaining geometrical degrees of freedom vanish, thus marking the minimum of the system energy with respect to $\{X_{l \neq k}\}$.

The ratio of the elements in k th row of \mathbf{C} , $\mathbf{C}_k = \{C_{k,l}, l = 1, 2, \dots\}$, to the diagonal element $C_{k,k}$ determines k th vector of nuclear interaction-constants [66,67]:

$$(l)_k = \frac{C_{k,l}}{C_{k,k}} = \left(\frac{\partial X_l}{\partial F_k} \right)_{F_{l \neq k}} \left(\frac{\partial X_k}{\partial F_k} \right)_{F_{l \neq k}}^{-1} = \left(\frac{\partial X_l}{\partial X_k} \right)_{F_{l \neq k}}, \quad l = 1, 2, \dots \quad (131)$$

These indices describe the minimum-energy responses, for $\{F_{l \neq k} = 0\}$, of the remaining nuclear-position variables $\{X_{l \neq k}\}$ per unit displacement of k th nuclear coordinate. They determine the k th (nuclear) minimum-energy coordinate [66,67]. These concepts can be used to predict the equilibrium responses of the system geometric structure to a given displacement (perturbation) of the k th nuclear coordinate, ΔX_k , from the initial, equilibrium

geometry of the molecule, which reflect couplings between the nuclear-position coordinates:

$$d\mathbf{R}(\Delta X_k)|_{\mathbf{F}=\mathbf{0}} = \{(l)_k \Delta X_k\}. \quad (132)$$

Similar concepts can be introduced in the combined electron–nuclear treatment of the geometric representation of the molecular structure [2,8,10,56,70,71]. Consider, *e.g.*, the generalized interaction constants defined by the geometric-softness matrix of equation (104). The ratios of the matrix elements in $\mathcal{S}_{\mu,\mathbf{F}} = \{\mathcal{S}_{\mu,l}\}$ to $\mathcal{S}_{\mu,\mu}$ define the following interaction constants between the nuclear coordinates and the system average number of electrons:

$$(l)_\mu = \frac{\mathcal{S}_{\mu,l}}{\mathcal{S}_{\mu,\mu}} = \left(\frac{\partial X_l}{\partial \mu} \right)_{\mathbf{F}=\mathbf{0}} / \left(\frac{\partial N}{\partial \mu} \right)_{\mathbf{F}=\mathbf{0}} = \left(\frac{\partial X_l}{\partial N} \right)_{\mathbf{F}=\mathbf{0}}. \quad (133)$$

They reflect the minimum-energy responses of the system geometrical coordinates to unit displacement in the system number of electrons. The row vector $\ell = \{(l)_\mu\}$ can be also interpreted as an alternative set the geometric (nuclear) Fukui-function indices, which diagnose the normalized effect of changing the oxidation-state of the molecular system as a whole on its geometry. These indices define the following minimum energy coordinate,

$$d\mathbf{R}(\Delta N)|_{\mu,\mathbf{F}=\mathbf{0}} = \{(l)_\mu \Delta N\}, \quad (134)$$

grouping responses in nuclear coordinates due to a finite inflow/outflow of electrons, $\Delta N \neq 0$. The remaining interaction constants defined in this representation are given by the ratios

$$\begin{aligned} (N)_{k,\mu} &= \frac{\mathcal{S}_{\mu,k}}{\mathcal{S}_{k,k}} = \left(\frac{\partial N}{\partial X_k} \right)_{\mu,\mathbf{F}'=\mathbf{0}} \quad \text{and} \\ (l)_{k,\mu} &= \frac{\mathcal{S}_{k,l}}{\mathcal{S}_{k,k}} = \left\{ \left(\frac{\partial X_l}{\partial X_k} \right)_{\mu,\mathbf{F}'=\mathbf{0}} \right\}, \end{aligned} \quad (135)$$

where again $\mathbf{F}' = (\dots, F_{k-1}, F_{k+1}, \dots)$. In the molecular system coupled to an external electron reservoir, which fixes the system chemical potential, they combine the minimum-energy responses in the system number of electrons and the remaining nuclear coordinates to a unit displacement of X_k . These minimum-energy coordinates

$$dN(\Delta X_k)|_{\mathbf{F}'=\mathbf{0}} = (N)_{k,\mu} \Delta X_k \quad \text{and} \quad d\mathbf{R}(\Delta X_k)|_{\mu,\mathbf{F}'=\mathbf{0}} = \{(l)_{k,\mu} \Delta X_k\}, \quad (136)$$

add to a variety of descriptors of the electronic and geometric structures of molecular systems. They can be used to probe the structural consequences of the hypothetical nuclear-position perturbations of the molecule, thus facilitating a search for the most effective geometric manipulations of the molecular system in question.

The partial-compliant matrix \mathbf{V} (see (112)) of the $\Theta(N, \mathbf{F})$ representation defines analogous interaction constants for the N -controlled (externally-closed) molecules:

$$(l)_N = \frac{V_{N,l}}{V_{N,N}} = \left(\frac{\partial X_l}{\partial N} \right)_{\mathbf{F}=\mathbf{0}} / \left(\frac{\partial \mu}{\partial N} \right)_{\mathbf{F}=\mathbf{0}} = \left(\frac{\partial X_l}{\partial \mu} \right)_{\mathbf{F}=\mathbf{0}}, \quad (137)$$

where $\{V_{N,l}\} = V_{N,F}$, and

$$(\mu)_k = \frac{V_{k,\mu}}{V_{k,k}} = \left(\frac{\partial \mu}{\partial X_k} \right)_{N,F'=0} \quad \text{and} \quad (l)_k = \frac{V_{l,k}}{V_{k,k}} = \left(\frac{\partial X_l}{\partial X_k} \right)_{N,F'=0} / \left(\frac{\partial X_k}{\partial F_k} \right)_{N,F'=0} = \left(\frac{\partial X_l}{\partial X_k} \right)_{N,F'=0}, \quad (138)$$

with $\{V_{k,\mu}\} = V_{F,N}$. The corresponding minimum-energy coordinates

$$d\mathbf{R}(\Delta\mu)|_{N,F=0} = \{(l)_N \Delta\mu\}, \quad d\mu(\Delta X_k)|_{N,F'=0} = \{(\mu)_k \Delta X_k\} \quad \text{and} \quad d\mathbf{R}(\Delta X_k)|_{N,F'=0} = \{(l)_k \Delta X_k\}, \quad (139)$$

measure the equilibrium responses in the system chemical potential and geometrical coordinates to the unit shift in the system chemical potential (see (134)) or in the selected k th geometrical coordinate.

5. COMPLIANT INDICES OF ATOMS-IN-MOLECULES

We shall now examine the related compliance properties in the atomic resolution $N = \{N_\alpha = \int \rho_\alpha d\mathbf{r}\}$ of the electronic global state-variable $N = \sum_\alpha N_\alpha$, and the underlying division of the molecular electron density, $\rho = \sum_\alpha \rho_\alpha$ (see, e.g., [2–4,7,8]). The total electronic energy in the canonical geometric representation of closed AIM now depends upon the independently controlled atomic electron populations N , $W^{\text{AIM}}(N, \mathbf{R})$, while the “reverse”, open-atom representation involves the independently controlled chemical potentials $\boldsymbol{\mu} = \{\mu_\alpha = (\partial W^{\text{AIM}} / \partial N_\alpha)_\mathbf{R}\} = (\partial W^{\text{AIM}} / \partial N)_\mathbf{R}^\text{T}$ of the separate AIM reservoirs. The atomic discretization is derived from the molecular ground-state density ρ , for which all AIM charge sensitivities are calculated. This implies the initial equalization of atomic chemical potentials $\boldsymbol{\mu} = \{\mu_\alpha\} = \mu[\rho]\mathbf{I}$.

The principal second derivatives in the energy representation then involve the following N -derivatives, for the rigid geometry of the molecule, of electrons in bonded atoms (see, e.g., [2–4,6–10]):

(i) hardness matrix, for the “frozen” molecular geometry:

$$\mathbf{h}^{\text{AIM}} = \left(\frac{\partial^2 W^{\text{AIM}}}{\partial N \partial N} \right)_\mathbf{R} = \left(\frac{\partial \boldsymbol{\mu}}{\partial N} \right)_\mathbf{R} = \left\{ \eta_{\alpha,\beta} = \left(\frac{\partial \mu_\beta}{\partial N_\alpha} \right)_\mathbf{R} \right\}; \quad (140)$$

(ii) geometrical FF (NFF) matrix, for the rigid molecular geometry:

$$\begin{aligned} \boldsymbol{\varphi}^{\text{AIM}}(N, \mathbf{R}) &= \left(\frac{\partial F(N, \mathbf{R})}{\partial N} \right)_\mathbf{R} = - \left(\frac{\partial \boldsymbol{\mu}(N, \mathbf{R})}{\partial \mathbf{R}} \right)_N \\ &\equiv - \int \mathbf{f}^{\text{AIM}}(\mathbf{r})^\text{T} \mathbf{G}(\mathbf{r}; \mathbf{R}) d\mathbf{r} \\ &= \left\{ \left(\frac{\partial F_l}{\partial N_\alpha} \right)_\mathbf{R} \right\} = - \left\{ \left(\frac{\partial \mu_\beta}{\partial X_k} \right)_{\{X_l \neq k\}} \right\}. \end{aligned} \quad (141)$$

Here the row vector of the electronic FF of AIM is defined by the mixed partial derivatives:

$$\mathbf{f}^{\text{AIM}}(\mathbf{r}) = \left[\frac{\partial^2 W^{\text{AIM}}}{\partial N \partial v(\mathbf{r})} \right]^\text{T} = \left[\frac{\partial \boldsymbol{\mu}}{\partial v(\mathbf{r})} \right]_N = \left[\frac{\partial \rho(\mathbf{r})}{\partial N} \right]_v^\text{T} = \{f_\alpha(\mathbf{r})\}. \quad (142)$$

Together with the nuclear force-constants $\mathbf{H} = (\partial^2 W^{\text{AIM}} / \partial \mathbf{R} \partial \mathbf{R})_N$ these derivatives define the AIM-resolved, combined electronic–nuclear Hessian of equation (100):

$$\mathcal{H}^{\text{AIM}} = \begin{bmatrix} \mathbf{h}^{\text{AIM}} & -\boldsymbol{\varphi}^{\text{AIM}} \\ -\boldsymbol{\varphi}^{\text{AIM},\text{T}} & \mathbf{H} \end{bmatrix} = \{\mathbf{H}_{x,y}^{\text{AIM}}\}, \quad x, y \in \{N, \mathbf{R}\}, \quad (143)$$

which transforms the representation principal perturbations $(\Delta N, \Delta \mathbf{R})$ into the linear responses in the conjugate variables $(\Delta \boldsymbol{\mu}, -\Delta \mathbf{F})$:

$$\begin{aligned} (\Delta \boldsymbol{\mu}, -\Delta \mathbf{F}) &= (\Delta N, \Delta \mathbf{R}) \mathcal{H}^{\text{AIM}} \quad \text{or} \\ \Delta \boldsymbol{\mu} &= \Delta N \mathbf{h}^{\text{AIM}} - \Delta \mathbf{R} \boldsymbol{\varphi}^{\text{AIM},\text{T}} \quad \text{and} \quad -\Delta \mathbf{F} = -\Delta N \boldsymbol{\varphi}^{\text{AIM}} + \Delta \mathbf{R} \mathbf{H}. \end{aligned} \quad (144)$$

The corresponding differential of $W^{\text{AIM}}(N, \mathbf{R})$ thus reads:

$$dW^{\text{AIM}}(N, \mathbf{R}) = \boldsymbol{\mu} dN^{\text{T}} - \mathbf{F} d\mathbf{R}^{\text{T}}. \quad (145)$$

The inverse representation $\Sigma^{\text{AIM}}(\boldsymbol{\mu}, \mathbf{F})$ corresponds to the thermodynamic potential:

$$\begin{aligned} \Sigma^{\text{AIM}}(\boldsymbol{\mu}, \mathbf{F}) &= W^{\text{AIM}} - N \left(\frac{\partial W^{\text{AIM}}}{\partial N} \right)_{\mathbf{R}} - \mathbf{R} \left(\frac{\partial W}{\partial \mathbf{R}} \right)_N \\ &= W - N \boldsymbol{\mu}^{\text{T}} + \mathbf{R} \mathbf{F}^{\text{T}}, \end{aligned} \quad (146)$$

$$\begin{aligned} d\Sigma^{\text{AIM}} &= -N d\boldsymbol{\mu}^{\text{T}} + \mathbf{R} d\mathbf{F}^{\text{T}} \quad \text{or} \\ -N &= \left(\frac{\partial \Sigma^{\text{AIM}}}{\partial \boldsymbol{\mu}} \right)_{\mathbf{F}} \quad \text{and} \quad \mathbf{R} = \left(\frac{\partial \Sigma^{\text{AIM}}}{\partial \mathbf{F}} \right)_{\boldsymbol{\mu}}^{\text{T}}. \end{aligned} \quad (147)$$

The corresponding blocks of the geometric compliance matrix in AIM resolution,

$$\mathcal{S}^{\text{AIM}} = (\mathcal{H}^{\text{AIM}})^{-1} = \begin{bmatrix} -(\frac{\partial N}{\partial \boldsymbol{\mu}})_{\mathbf{F}} & (\frac{\partial \mathbf{R}}{\partial \boldsymbol{\mu}})_{\mathbf{F}} \\ -(\frac{\partial N}{\partial \mathbf{F}})_{\boldsymbol{\mu}} & (\frac{\partial \mathbf{R}}{\partial \mathbf{F}})_{\boldsymbol{\mu}} \end{bmatrix} = \{\mathbf{S}_{x,y}^{\text{AIM}}\}, \quad x, y \in \{\boldsymbol{\mu}, \mathbf{F}\}, \quad (148)$$

transform the representation perturbations $(\Delta \boldsymbol{\mu}, \Delta \mathbf{F})$ into the conjugate responses $(-\Delta N, \Delta \mathbf{R})$:

$$\begin{aligned} (-\Delta N, \Delta \mathbf{R}) &= (\Delta \boldsymbol{\mu}, \Delta \mathbf{F}) \mathcal{S}^{\text{AIM}} \quad \text{or} \\ -\Delta N &= \Delta \boldsymbol{\mu} \mathbf{S}_{\boldsymbol{\mu},\boldsymbol{\mu}}^{\text{AIM}} + \Delta \mathbf{F} \mathbf{S}_{\mathbf{F},\boldsymbol{\mu}}^{\text{AIM}} \quad \text{and} \quad \Delta \mathbf{R} = \Delta \boldsymbol{\mu} \mathbf{S}_{\boldsymbol{\mu},\mathbf{F}}^{\text{AIM}} + \Delta \mathbf{F} \mathbf{S}_{\mathbf{F},\mathbf{F}}^{\text{AIM}}. \end{aligned} \quad (149)$$

Again a straightforward elimination process allows one to express the compliant matrix of equation (148) in terms of blocks defining the Hessian of equation (143):

$$\begin{aligned} \mathcal{S}^{\text{AIM}} &= \begin{bmatrix} -\mathbf{K}^{-1} & \mathbf{K}^{-1} \boldsymbol{\varphi}^{\text{AIM}} \mathbf{H}^{-1} \\ \mathbf{H}^{-1} \boldsymbol{\varphi}^{\text{AIM},\text{T}} \mathbf{K}^{-1} & -\mathbf{H}^{-1} (\mathbf{I} + \boldsymbol{\varphi}^{\text{AIM},\text{T}} \mathbf{K}^{-1} \boldsymbol{\varphi}^{\text{AIM}} \mathbf{H}^{-1}) \end{bmatrix}, \\ \mathbf{K} &= \mathbf{h}^{\text{AIM}} - \boldsymbol{\varphi}^{\text{AIM}} \mathbf{H}^{-1} \boldsymbol{\varphi}^{\text{AIM},\text{T}}, \end{aligned} \quad (150)$$

or

$$\begin{aligned} \mathcal{S}^{\text{AIM}} &= \begin{bmatrix} -\mathbf{s}^{\text{AIM}} (\mathbf{I}^{\text{AIM}} + \boldsymbol{\varphi}^{\text{AIM}} \mathbf{D}^{-1} \boldsymbol{\varphi}^{\text{AIM},\text{T}} \mathbf{s}^{\text{AIM}}) & \mathbf{s}^{\text{AIM}} \boldsymbol{\varphi}^{\text{AIM}} \mathbf{D}^{-1} \\ \mathbf{D}^{-1} \boldsymbol{\varphi}^{\text{AIM},\text{T}} \mathbf{s}^{\text{AIM}} & -\mathbf{D}^{-1} \end{bmatrix}, \\ \mathbf{D} &= \mathbf{H} + \boldsymbol{\varphi}^{\text{AIM},\text{T}} \mathbf{s}^{\text{AIM}} \boldsymbol{\varphi}^{\text{AIM}}. \end{aligned} \quad (151)$$

In the preceding equation the electronic softness matrix for the “frozen” nuclear frame is

the inverse of the AIM hardness matrix for the rigid molecular geometry (see (140)):

$$\mathbf{s}^{\text{AIM}} = \left\{ s_{\alpha,\beta} = \left(\frac{\partial N_\beta}{\partial \mu_\alpha} \right)_{\mathbf{R}} \right\} = \left(\frac{\partial \mathbf{N}}{\partial \boldsymbol{\mu}} \right)_{\mathbf{R}} = (\mathbf{h}^{\text{AIM}})^{-1}. \quad (152)$$

It differs from the geometrically-relaxed softness matrix in AIM resolution,

$$\boldsymbol{\sigma}^{\text{AIM}} = -\mathbf{S}_{\boldsymbol{\mu},\boldsymbol{\mu}}^{\text{AIM}} = \left(\frac{\partial \mathbf{N}}{\partial \boldsymbol{\mu}} \right)_{\mathbf{F}} = \left\{ \sigma_{\alpha,\beta} = \left(\frac{\partial N_\beta}{\partial \mu_\alpha} \right)_{\mathbf{F}} \right\} \equiv (\boldsymbol{\eta}^{\text{AIM}})^{-1}, \quad (153)$$

which in turn defines its inverse, the geometrically-relaxed hardness matrix of AIM, $\boldsymbol{\eta}^{\text{AIM}} = (\partial \boldsymbol{\mu} / \partial \mathbf{N})_{\mathbf{F}}$.

Consider next the partially-transformed representation $\Theta^{\text{AIM}}(\mathbf{N}, \mathbf{F})$ for the AIM-resolved thermodynamic potential

$$\Theta^{\text{AIM}}(\mathbf{N}, \mathbf{F}) = W^{\text{AIM}} - \mathbf{R} \left(\frac{\partial W^{\text{AIM}}}{\partial \mathbf{R}} \right)_{\mathbf{N}} = W^{\text{AIM}} + \mathbf{R} \mathbf{F}^{\text{T}}, \quad (154)$$

$$\begin{aligned} d\Theta^{\text{AIM}} &= \boldsymbol{\mu} d\mathbf{N}^{\text{T}} + \mathbf{R} d\mathbf{F}^{\text{T}} \quad \text{or} \\ \boldsymbol{\mu} &= \left(\frac{\partial \Theta^{\text{AIM}}}{\partial \mathbf{N}} \right)_{\mathbf{F}}^{\text{T}} \quad \text{and} \quad \mathbf{R} = \left(\frac{\partial \Theta^{\text{AIM}}}{\partial \mathbf{F}} \right)_{\mathbf{N}}^{\text{T}}. \end{aligned} \quad (155)$$

The transformation matrix of the representation independent perturbations $(\Delta \mathbf{N}, \Delta \mathbf{F})$ into the linear responses of their conjugates $(\Delta \boldsymbol{\mu}, \Delta \mathbf{R})$,

$$(\Delta \boldsymbol{\mu}, \Delta \mathbf{R}) = (\Delta \mathbf{N}, d\mathbf{F}) \mathbf{V}^{\text{AIM}}, \quad (156)$$

is provided by the AIM-resolved analog of matrix \mathbf{V} (see (112) and (115)):

$$\begin{aligned} \mathbf{V}^{\text{AIM}} &= \begin{bmatrix} \left(\frac{\partial \boldsymbol{\mu}}{\partial \mathbf{N}} \right)_{\mathbf{F}} = \boldsymbol{\eta}^{\text{AIM}} = \mathbf{K} & \left(\frac{\partial \mathbf{R}}{\partial \mathbf{N}} \right)_{\mathbf{F}} = \boldsymbol{\varphi}^{\text{AIM}} \mathbf{H}^{-1} \\ \left(\frac{\partial \boldsymbol{\mu}}{\partial \mathbf{F}} \right)_{\mathbf{N}} = \mathbf{H}^{-1} \boldsymbol{\varphi}^{\text{AIM,T}} & \left(\frac{\partial \mathbf{R}}{\partial \mathbf{F}} \right)_{\mathbf{N}} = -\mathbf{H}^{-1} \end{bmatrix} \\ &= \{ \mathbf{V}_{x,y}^{\text{AIM}} \}, \quad x, y \in \{ \mathbf{N}, \mathbf{F} \}. \end{aligned} \quad (157)$$

Above we have identified its first diagonal block as the geometry-relaxed hardness matrix of equation (150).

In the $\mathcal{E}^{\text{AIM}}(\boldsymbol{\mu}, \mathbf{R})$ representation the thermodynamic potential reads:

$$\mathcal{E}^{\text{AIM}}(\boldsymbol{\mu}, \mathbf{R}) = W^{\text{AIM}} - \mathbf{N} \frac{\partial W^{\text{AIM}}}{\partial \mathbf{N}} = W^{\text{AIM}} - \mathbf{N} \boldsymbol{\mu}^{\text{T}}, \quad (158)$$

and hence,

$$\begin{aligned} d\mathcal{E}^{\text{AIM}} &= -\mathbf{N} d\boldsymbol{\mu}^{\text{T}} - \mathbf{F} d\mathbf{R}^{\text{T}} \quad \text{or} \\ -\mathbf{N} &= \left(\frac{\partial \mathcal{E}^{\text{AIM}}}{\partial \boldsymbol{\mu}} \right)_{\mathbf{R}}^{\text{T}} \quad \text{and} \quad -\mathbf{F} = \left(\frac{\partial \mathcal{E}^{\text{AIM}}}{\partial \mathbf{R}} \right)_{\boldsymbol{\mu}}^{\text{T}}. \end{aligned} \quad (159)$$

One then determines the transformation of independent displacements $(\Delta \boldsymbol{\mu}, \Delta \mathbf{R})$ into the linear responses of their conjugates $(-\Delta \mathbf{N}, -\Delta \mathbf{F})$ [compare equations (118)–(123)]:

$$(-\Delta \mathbf{N}, -\Delta \mathbf{F}) = (\Delta \boldsymbol{\mu}, \Delta \mathbf{R}) \mathcal{J}^{\text{AIM}}, \quad (160)$$

$$\begin{aligned} \mathcal{J}^{\text{AIM}} &= \begin{bmatrix} -\left(\frac{\partial \mathbf{N}}{\partial \boldsymbol{\mu}} \right)_{\mathbf{R}} = -\mathbf{s}^{\text{AIM}} & -\left(\frac{\partial \mathbf{F}}{\partial \boldsymbol{\mu}} \right)_{\mathbf{R}} = -\mathbf{s}^{\text{AIM}} \boldsymbol{\varphi}^{\text{AIM}} \\ -\left(\frac{\partial \mathbf{N}}{\partial \mathbf{R}} \right)_{\boldsymbol{\mu}} = -\boldsymbol{\varphi}^{\text{AIM,T}} \mathbf{s}^{\text{AIM}} & -\left(\frac{\partial \mathbf{F}}{\partial \mathbf{R}} \right)_{\boldsymbol{\mu}} = \mathbf{H} - \boldsymbol{\varphi}^{\text{AIM,T}} \mathbf{s}^{\text{AIM}} \boldsymbol{\varphi}^{\text{AIM}} \end{bmatrix} \\ &= \{ \mathcal{J}_{x,y}^{\text{AIM}} \}, \quad x, y \in \{ \boldsymbol{\mu}, \mathbf{R} \}. \end{aligned} \quad (161)$$

The AIM-softness matrix of equation (152) represents the purely-electronic compliant matrix for the relaxed molecular geometry, *i.e.*, $\mathbf{F} = \mathbf{0}$. It determines the corresponding coupling-constants $\{(\beta)_{\alpha, \mathbf{F}}\}$ of AIM,

$$(\beta)_{\alpha, \mathbf{F}} = \frac{\sigma_{\alpha, \beta}}{\sigma_{\alpha, \alpha}} = \left(\frac{\partial N_{\beta}}{\partial \mu_{\alpha}} \right)_{\mathbf{F}} / \left(\frac{\partial N_{\alpha}}{\partial \mu_{\alpha}} \right)_{\mathbf{F}} = \left(\frac{\partial N_{\beta}}{\partial N_{\alpha}} \right)_{\mathbf{F}}, \quad \beta = 1, 2, \dots, m, \quad (162)$$

defining the α th (geometrically-relaxed) minimum-energy coordinate of atomic populations,

$$dN(\Delta N_{\alpha})|_{\mathbf{F}=\mathbf{0}} = \{(\beta)_{\alpha, \mathbf{F}=\mathbf{0}} \Delta N_{\alpha}\}. \quad (163)$$

It reflects the equilibrium displacements in atomic populations per unit shift in the electron population of atom α , when the nuclear coordinates are free to relax to their corresponding equilibrium values. Therefore, these complaints allow one to diagnose the effect of the CT on one of the constituent atoms, *e.g.*, that resulting from electrophilic ($\Delta N_{\alpha} < 0$) or nucleophilic ($\Delta N_{\alpha} > 0$) attacks, on the electron populations (effective charges) of remaining atoms.

Similarly, the AIM-softness matrix of equation (152), for the rigid molecular geometry, determines the corresponding interaction-constants $\{(\beta)_{\alpha, \mathbf{R}}\}$ between atomic electron populations:

$$(\beta)_{\alpha, \mathbf{R}} = \frac{s_{\alpha, \beta}}{s_{\alpha, \alpha}} = \left(\frac{\partial N_{\beta}}{\partial \mu_{\alpha}} \right)_{\mathbf{R}} / \left(\frac{\partial N_{\alpha}}{\partial \mu_{\alpha}} \right)_{\mathbf{R}} = \left(\frac{\partial N_{\beta}}{\partial N_{\alpha}} \right)_{\mathbf{R}}, \quad \beta = 1, 2, \dots, m. \quad (164)$$

They define the α th populational (geometrically-rigid) minimum-energy coordinate,

$$dN(\Delta N_{\alpha})|_{\mathbf{R}} = \{(\beta)_{\alpha, \mathbf{R}} \Delta N_{\alpha}\}, \quad (165)$$

which reflects displacements in atomic populations generated by ΔN_{α} shift in N_{α} , when the nuclear coordinates are held in their “frozen” initial positions. These couplings between the atomic electron populations, estimated for the rigid molecular geometry (fixed external potential), complement the purely-nuclear coupling constants of equation (131) and the nuclear minimum-energy coordinates defined by them. They are useful in several reactivity issues, *e.g.*, in determining how an electrophilic/nucleophilic approach to the specified atom affects the electron populations on remaining constituent atoms, when geometry of the attacked molecular system is held “frozen”.

The present electron–nuclear development, however, also allows one to explicitly include the couplings between these two facets of the molecular structure, which are neglected in the separate electronic and nuclear developments. We have already identified such joint-compliants in the global resolution of the preceding section. The matrix blocks in equations (148)–(151), (157), and (161) contain all the required data for defining such generalized minimum-energy coordinates, which reflect the electron–nuclear coupling. For example, the diagonal block $\mathbf{S}_{\mu, \mu}^{\text{AIM}} \equiv \{S_{\alpha, \beta} = -(\partial N_{\beta} / \partial \mu_{\alpha})_{\mathbf{F}}\}$, again gives rise to interaction constants of equation (162) for the equilibrium molecular structure, identified by $\mathbf{F} = \mathbf{0}$,

$$(\beta)_{\alpha, \mathbf{F}=\mathbf{0}} = \frac{S_{\alpha, \beta}}{S_{\alpha, \alpha}} = \left(\frac{\partial N_{\beta}}{\partial \mu_{\alpha}} \right)_{\mathbf{F}=\mathbf{0}} / \left(\frac{\partial N_{\alpha}}{\partial \mu_{\alpha}} \right)_{\mathbf{F}=\mathbf{0}} = \left(\frac{\partial N_{\beta}}{\partial N_{\alpha}} \right)_{\mathbf{F}=\mathbf{0}}, \quad \beta = 1, 2, \dots, m, \quad (166)$$

and determines the geometrically-relaxed electronic minimum-energy coordinate, in which

the coupling between electron populations of AIM are taken into account for the fully minimized geometry of the populationally displaced system, when $\Delta N_\alpha \neq 0$.

Next, let us examine the interaction constants resulting from the off-diagonal block $\mathbf{S}_{\mu,F}^{\text{AIM}} \equiv \{S_{\alpha,j} = (\partial X_j / \partial \mu_\alpha)_F\}$. The ratios

$$(l)_{\alpha,F=0} = -\frac{S_{\alpha,l}}{S_{\alpha,\alpha}} = \left(\frac{\partial X_l}{\partial \mu_\alpha} \right)_{F=0} / \left(\frac{\partial N_\alpha}{\partial \mu_\alpha} \right)_{F=0} = \left(\frac{\partial X_l}{\partial N_\alpha} \right)_{F=0},$$

$$l = 1, 2, \dots, \quad (167)$$

determine the equilibrium effect of a unit displacement in the population of atom α on the system nuclear coordinates.

One can similarly combine the elements of the other off-diagonal block, $\mathbf{S}_{F,\mu}^{\text{AIM}} \equiv \{S_{k,\beta} = (\partial N_\beta / \partial F_k)_\mu\}$, with the second diagonal block, $\mathbf{S}_{F,F}^{\text{AIM}} \equiv \{S_{l,k} = (\partial X_l / \partial F_k)_{\mu,F'=0}\}$,

$$(\beta)_{k,\mu} = -\frac{S_{k,\beta}}{S_{k,k}} = \left(\frac{\partial N_\beta}{\partial F_k} \right)_{\mu,F'=0} / \left(\frac{\partial X_k}{\partial F_k} \right)_{\mu,F'=0} = \left(\frac{\partial N_\beta}{\partial X_k} \right)_{\mu,F'=0},$$

$$\beta = 1, 2, \dots, m. \quad (168)$$

These interaction constants monitor the equilibrium responses in the atomic electron populations per unit shift in the k th nuclear coordinate, for the fixed (equalized) chemical potentials of the separate atomic external reservoirs, $\mu = \mu[\rho]\mathbf{I}$, and the relaxed values of the remaining geometrical coordinates.

Finally, one can similarly define the interaction constants between the geometrical coordinates, for the fixed chemical potentials of AIM (see (6.6)), by taking ratios of matrix elements in the diagonal block $\mathbf{S}_{F,F}^{\text{AIM}}$:

$$(l)_{k,\mu} = \frac{S_{l,k}}{S_{k,k}} = \left(\frac{\partial X_l}{\partial F_k} \right)_{\mu,F'=0} / \left(\frac{\partial X_k}{\partial F_k} \right)_{\mu,F'=0} = \left(\frac{\partial X_l}{\partial X_k} \right)_{\mu,F'=0},$$

$$l = 1, 2, \dots \quad (169)$$

The interaction constants and the associated minimum-energy coordinates can be also derived from the partly-transformed compliant matrices in atomic resolution (see (151) and (161)). The electronic (diagonal) block $\mathbf{V}_{N,N}^{\text{AIM}} = \{V_{\alpha,\beta} = (\partial \mu_\beta / \partial N_\alpha)_{F=0}\}$ represents the geometrically-relaxed hardness matrix of bonded atoms: $\mathbf{V}_{N,N}^{\text{AIM}} = \boldsymbol{\eta}^{\text{AIM}}$ (see (153)). The ratios

$$(\beta)_{\alpha,F=0} = \frac{V_{\alpha,\beta}}{V_{\alpha,\alpha}} = \left(\frac{\partial \mu_\beta}{\partial N_\alpha} \right)_{F=0} / \left(\frac{\partial \mu_\alpha}{\partial N_\alpha} \right)_{F=0} = \left(\frac{\partial \mu_\beta}{\partial \mu_\alpha} \right)_{F=0},$$

$$\beta = 1, 2, \dots, m, \quad (170)$$

then reflect the interaction between AIM chemical potentials when the geometrical frame of the molecule is fully relaxed, until the forces on atoms identically vanish.

By similarly combining the derivatives of $\mathbf{V}_{N,F}^{\text{AIM}} = \{V_{\alpha,j} = (\partial X_j / \partial N_\alpha)_{F=0}\}$ with the diagonal derivatives $\{V_{\alpha,\alpha}\}$ one determines the effects of AIM chemical potentials on the relaxed nuclear coordinates, as measured by the interaction constants:

$$(l)_{\alpha,F=0} = \frac{V_{\alpha,l}}{V_{\alpha,\alpha}} = \left(\frac{\partial X_l}{\partial N_\alpha} \right)_{F=0} / \left(\frac{\partial \mu_\alpha}{\partial N_\alpha} \right)_{F=0} = \left(\frac{\partial X_l}{\partial \mu_\alpha} \right)_{F=0},$$

$$l = 1, 2, \dots \quad (171)$$

Within the nuclear diagonal block $\mathbf{V}_{F,F}^{\text{AIM}} = \{V_{k,l} = (\partial X_l / \partial F_k)_N\}$ one establishes the following geometrical (minimum-energy) interaction constants of the externally-closed AIM (compare equation (169)):

$$(l)_{k,N} = \frac{V_{k,l}}{V_{k,k}} = \left(\frac{\partial X_l}{\partial F_k} \right)_N / \left(\frac{\partial X_k}{\partial F_k} \right)_N = \left(\frac{\partial X_l}{\partial X_k} \right)_N, \quad l = 1, 2, \dots \quad (172)$$

These interaction indices between nuclear coordinates reflect the equilibrium responses in the remaining geometrical coordinates per unit displacement in the specified coordinate X_k , when the average numbers of electrons on constituent atoms are fixed.

Finally, by combining the diagonal derivatives $\{V_{k,k}\}$ with the off-diagonal derivatives $\mathbf{V}_{F,N}^{\text{AIM}} = \{V_{k,\beta} = (\partial \mu_\beta / \partial F_k)_N\}$ in the ratios

$$(\beta)_{k,N} = \frac{V_{k,\beta}}{V_{k,k}} = \left(\frac{\partial \mu_\beta}{\partial F_k} \right)_N / \left(\frac{\partial X_k}{\partial F_k} \right)_N = \left(\frac{\partial \mu_\beta}{\partial X_k} \right)_N, \quad \beta = 1, 2, \dots, m, \quad (173)$$

one generates the interaction constants measuring a coupling between the geometrical coordinates and the chemical potentials of AIM.

Next we examine the set of interaction constants constructed from the matrix elements of the compliant matrix of equation (161). As we have already observed before, its electronic diagonal block $\mathcal{I}_{\mu,\mu}^{\text{AIM}} = \{\mathcal{I}_{\alpha,\beta} = -(\partial N_\beta / \partial \mu_\alpha)_R\}$ represents the geometrically-rigid chemical softnesses of constituent atoms. The ratios

$$(\beta)_{\alpha,R} = \frac{\mathcal{I}_{\alpha,\beta}}{\mathcal{I}_{\alpha,\alpha}} = \left(\frac{\partial N_\beta}{\partial \mu_\alpha} \right)_R / \left(\frac{\partial N_\alpha}{\partial \mu_\alpha} \right)_R = \left(\frac{\partial N_\beta}{\partial N_\alpha} \right)_R, \quad \beta = 1, 2, \dots, m, \quad (174)$$

define components of the populational minimum-energy coordinate for the “frozen” molecular geometry. They represent the geometrically non-relaxed analogs of the electronic minimum-energy coordinates of equation (166). Similarly, combining the diagonal derivatives $\{\mathcal{I}_{\alpha,\alpha}\}$ with the off-diagonal derivatives $\mathcal{I}_{\mu,R}^{\text{AIM}} = \{\mathcal{I}_{\alpha,l} = -(\partial F_l / \partial \mu_\alpha)_R\}$ determines the atomic NFF:

$$(l)_{\alpha,R} = \frac{\mathcal{I}_{\alpha,l}}{\mathcal{I}_{\alpha,\alpha}} = \left(\frac{\partial F_l}{\partial \mu_\alpha} \right)_R / \left(\frac{\partial N_\alpha}{\partial \mu_\alpha} \right)_R = \left(\frac{\partial F_l}{\partial N_\alpha} \right)_R, \quad l = 1, 2, \dots \quad (175)$$

Indeed, these interaction-constants measure responses in geometrical forces per unit displacement in the electron population of atom α , for the frozen molecular geometry. Finally, the nuclear diagonal block $\mathcal{I}_{R,R}^{\text{AIM}} = \{\mathcal{I}_{k,l} = -(\partial F_l / \partial X_k)_\mu\}$ and the corresponding off-diagonal block $\mathcal{I}_{R,\mu}^{\text{AIM}} = \{\mathcal{I}_{k,\beta} = -(\partial N_\beta / \partial X_k)_\mu\}$ give rise to the following interaction-constants:

$$(l)_{k,\mu} = \frac{\mathcal{I}_{k,l}}{\mathcal{I}_{k,k}} = \left(\frac{\partial F_l}{\partial X_k} \right)_\mu / \left(\frac{\partial F_k}{\partial X_k} \right)_\mu = \left(\frac{\partial F_l}{\partial F_k} \right)_\mu, \quad j = 1, 2, \dots, \quad (176)$$

$$(\beta)_{k,\mu} = \frac{\mathcal{I}_{k,\beta}}{\mathcal{I}_{k,k}} = \left(\frac{\partial N_\beta}{\partial X_k} \right)_\mu / \left(\frac{\partial F_k}{\partial X_k} \right)_\mu = \left(\frac{\partial N_\beta}{\partial F_k} \right)_\mu, \quad \beta = 1, 2, \dots, m. \quad (177)$$

These indices thus measure the effect of displacements in one force component on the remaining force components and AIM electron populations for the fixed chemical potentials of the external reservoirs, to which the bonded atoms are coupled.

6. ATOMIC RESOLUTION—A REAPPRAISAL

In the condensed (coarse-grained) AIM outlook on molecular electronic structure within the Electron-Preceding Perspective, in which the hardness matrices in atomic resolution are defined for either the relaxed or rigid geometry of the molecule, the electron populations $N = \{N_\alpha\}$ of constituent atoms are regarded as independent electronic degrees-of-freedom, to which the nuclei respond. In the reverse Electron-Following Perspective, in which the corresponding softness matrices of AIM are defined, the nuclear degrees of freedom determine the primary perturbation of the molecular system, to which the atomic electron populations adjust themselves to regain the global equilibrium in the whole molecular system.

The equilibrium distribution of electrons implies the mutually-open AIM for the specified global number of electrons $N = \sum_\alpha N_\alpha = N\mathbf{I}^T$ and the given external potential $v(\mathbf{r})$. These state-parameters represent the independent degrees-of-freedom in the canonical representation $E^{\text{AIM}}[N(N, v), v] = E[N, v]$. It implies the equalization of atomic chemical potentials at the global chemical potential level: $\mu = \mu\mathbf{I}$. In this approach the atomic electron populations are functions of the overall number of electrons, $N = N(N)$, as reflected by the electronic FF indices of AIM:

$$f^{\text{AIM}} = \left(\frac{\partial N}{\partial N} \right)_v = \left\{ f_\alpha = \left(\frac{\partial N_\alpha}{\partial N} \right)_v \right\}, \quad \sum_\alpha f_\alpha = f^{\text{AIM}}\mathbf{I}^T = 1. \quad (178)$$

It is the main purpose of this section to summarize the basic relations of the Legendre-transformed representations of molecular states, in which both the electronic and nuclear parameters of state are represented by the appropriate AIM-discretized quantities [2,6,8,10]. As we have already indicated in Section 5, the basis for the AIM-discretization is provided by the exhaustive division of the molecular electron density into effective atomic distributions of electrons $\rho(\mathbf{r}) = \{\rho_\alpha(\mathbf{r}) = N_\alpha p_\alpha(\mathbf{r})\}$, $\rho(\mathbf{r}) = \sum_\alpha \rho_\alpha(\mathbf{r})$, which also determines the associated probability distributions (shape factors) of individual atoms, $p(\mathbf{r}) = \{p_\alpha(\mathbf{r}) = \rho_\alpha(\mathbf{r})/N_\alpha\}$, where $N_\alpha = \int \rho_\alpha(\mathbf{r}) d\mathbf{r}$ and hence $\int p_\alpha(\mathbf{r}) d\mathbf{r} = 1$. For example, the local Hirshfeld [72] division can be carried out to generate the localized pieces of the molecular density, which represent the so-called “stockholder” AIM [3,72–74].

In order to transform the integral transformations involving $v(\mathbf{r})$ into the corresponding matrix equations in atomic resolution, one introduces the additional AIM-discretization of the external potential “variable”. This can be carried out using the normalized atomic shape factors, $p(\mathbf{r}) = \{p_\alpha(\mathbf{r}) = \rho_\alpha(\mathbf{r})/N_\alpha\}$, in the adopted partitioning scheme of the molecular electron density. The relevant external potential indices $\mathbf{V} = \{V_\alpha\}$ can then be chosen to measure the atomic nuclear-attraction energy per electron:

$$V_\alpha = \int \left[\frac{\rho_\alpha(\mathbf{r})}{N_\alpha} \right] v(\mathbf{r}) d\mathbf{r} \equiv \frac{V_{n\alpha}}{N_\alpha} \equiv \int p_\alpha(\mathbf{r}) v(\mathbf{r}) d\mathbf{r}, \quad \alpha = 1, 2, \dots, m. \quad (179)$$

Hence, the nuclear attraction energy by the system nuclei can be expressed as the following product of the electronic and nuclear vector-quantities in atomic resolution:

$$V_{\text{ne}}[\rho] = \int \rho(\mathbf{r}) v(\mathbf{r}) d\mathbf{r} = N\mathbf{V}^T = \sum_\alpha N_\alpha V_\alpha. \quad (180)$$

One can similarly define the condensed index of the molecular attraction energy per electron for the system as a whole,

$$V = \int \left[\frac{\rho(\mathbf{r})}{N} \right] v(\mathbf{r}) d\mathbf{r} \equiv \int p(\mathbf{r}) v(\mathbf{r}) d\mathbf{r}, \quad N = \int \rho(\mathbf{r}) d\mathbf{r},$$

$$V_{\text{ne}}[\rho] = NV, \quad (181)$$

with $p(\mathbf{r})$ now standing for the shape factor of the molecular electron distribution.

The first differential of the total electronic energy in the $E^{\text{AIM}}(N, \mathbf{V})$ representation of the global equilibrium of the mutually open AIM, where $E^{\text{AIM}}(N, \mathbf{V}) \equiv E[N, v] \equiv E^{\text{AIM}}(N(N), \mathbf{V})$, then reads:

$$dE^{\text{AIM}}(N, \mathbf{V}) = \mu dN + N d\mathbf{V}^T = \mu \mathbf{I} dN^T + N d\mathbf{V}^T = \boldsymbol{\mu} dN^T + N d\mathbf{V}^T, \quad (182)$$

where $\boldsymbol{\mu} = \mu \mathbf{I}$ groups the equalized chemical potentials of AIM. Indeed, the differential of the electronic energy $E_v[\rho] = E[N, v]$ can be straightforwardly transformed into the above AIM-discretized form:

$$dE[N, v] = \mu dN + \int \rho(\mathbf{r}) dv(\mathbf{r}) d\mathbf{r} = \mu dN + \sum_{\alpha} N_{\alpha} \int p_{\alpha}(\mathbf{r}) dv(\mathbf{r}) d\mathbf{r}$$

$$= \mu dN + \sum_{\alpha} N_{\alpha} dV_{\alpha} \equiv dE^{\text{AIM}}(N, \mathbf{V}), \quad (183)$$

and hence,

$$\left(\frac{\partial E^{\text{AIM}}(N, \mathbf{V})}{\partial N} \right)_{\mathbf{V}} = \mu, \quad \left(\frac{\partial E^{\text{AIM}}(N, \mathbf{V})}{\partial \mathbf{V}} \right)_{\mathbf{N}}^T = N. \quad (184)$$

One similarly arrives at the AIM-expression for the second differential of $E^{\text{AIM}}(N, \mathbf{V})$,

$$d^2 E[N, v]$$

$$= \frac{1}{2} \left[\eta (dN)^2 + 2 dN \int f(\mathbf{r}) dv(\mathbf{r}) d\mathbf{r} + \iint dv(\mathbf{r}) \beta(\mathbf{r}, \mathbf{r}') dv(\mathbf{r}') d\mathbf{r} d\mathbf{r}' \right]$$

$$= \frac{1}{2} [\eta (dN)^2 + 2 dN \mathbf{f}^{\text{AIM}} d\mathbf{V}^T + d\mathbf{V} \boldsymbol{\beta}^{\text{AIM}} d\mathbf{V}^T], \quad (185)$$

where η is the system global hardness (16), while the AIM electronic FF vector \mathbf{f}^{AIM} and the linear-response matrix $\boldsymbol{\beta}^{\text{AIM}}$ are now defined by the following partial derivatives in this double atomic resolution:

$$\frac{\partial^2 E^{\text{AIM}}(N, \mathbf{V})}{\partial N \partial \mathbf{V}} = \left(\frac{\partial N}{\partial N} \right)_{\mathbf{V}} = \left(\frac{\partial \mu}{\partial \mathbf{V}} \right)_{\mathbf{N}}^T = \mathbf{f}^{\text{AIM}}, \quad (186)$$

$$\left(\frac{\partial^2 E^{\text{AIM}}(N, \mathbf{V})}{\partial \mathbf{V} \partial \mathbf{V}} \right)_{\mathbf{N}} = \left(\frac{\partial N}{\partial \mathbf{V}} \right)_{\mathbf{N}} = \boldsymbol{\beta}^{\text{AIM}}. \quad (187)$$

Hence, the responses $(\Delta\mu, \Delta N)$ in the representation unconstrained variables can be expressed in terms of the independent perturbations $(\Delta N, \Delta \mathbf{V})$:

$$\Delta\mu = \Delta N \eta + \Delta \mathbf{V} \mathbf{f}^{\text{AIM},T} \quad \text{and} \quad \Delta N = \Delta N \mathbf{f}^{\text{AIM}} + \Delta \mathbf{V} \boldsymbol{\beta}^{\text{AIM}}. \quad (188)$$

They can be combined in the joint matrix transformation (compare equation (81)):

$$[\Delta\mu, \Delta N] = [\Delta N, \Delta V] \begin{bmatrix} \eta & f^{\text{AIM}} \\ f^{\text{AIM},T} & \beta^{\text{AIM}} \end{bmatrix}. \quad (189)$$

In the $Q^{\text{AIM}}(\mu, V)$ representation,

$$Q^{\text{AIM}}(\mu, V) = E^{\text{AIM}}(N, V) - \left(\frac{\partial E^{\text{AIM}}}{\partial N} \right)_V N = E^{\text{AIM}} - \mu N, \quad (190)$$

in which μ has replaced N as the system global parameter of state, one similarly finds:

$$\begin{aligned} dQ^{\text{AIM}}(\mu, V) &= -N d\mu + \sum_{\alpha} N_{\alpha} dV_{\alpha} = \sum_{\alpha} N_{\alpha} d(V_{\alpha} - \mu) \\ &\equiv \sum_{\alpha} N_{\alpha} dU_{\alpha} = N dU^T, \end{aligned} \quad (191)$$

and hence,

$$\begin{aligned} \left(\frac{\partial Q^{\text{AIM}}(\mu, V)}{\partial \mu} \right)_V &= -N, \\ \left(\frac{\partial Q^{\text{AIM}}(\mu, V)}{\partial V} \right)_{\mu}^T &= \left(\frac{\partial Q^{\text{AIM}}(U)}{\partial U} \right)^T = N. \end{aligned} \quad (192)$$

The AIM-discretized Euler equation is obtained upon the multiplication of equation (1) by the atomic shape-factor and the subsequent integration over the physical space:

$$\begin{aligned} \int p_{\alpha}(\mathbf{r}) u(\mathbf{r}) d\mathbf{r} &\equiv U_{\alpha} = \int p_{\alpha}(\mathbf{r}) v(\mathbf{r}) d\mathbf{r} - \mu \\ &\equiv V_{\alpha} - \mu = - \int p_{\alpha}(\mathbf{r}) \left\{ \frac{\delta F[\rho]}{\delta \rho(\mathbf{r})} \right\} d\mathbf{r} \\ &= - \int \left\{ \frac{\partial \rho(\mathbf{r})}{\partial N_{\alpha}} \right\} \left\{ \frac{\delta F[\rho]}{\delta \rho(\mathbf{r})} \right\} d\mathbf{r} \\ &\equiv - \frac{\partial F^{\text{AIM}}(N[\rho])}{\partial N_{\alpha}}, \quad \alpha = 1, 2, \dots, m. \end{aligned} \quad (193)$$

In equations (191)–(193) we have introduced the row vector $U = V - \mu I = \{U_{\alpha} = V_{\alpha} - \mu = \int p_{\alpha}(\mathbf{r}) u(\mathbf{r}) d\mathbf{r}\}$, representing in the AIM discretization the atomic attraction energy per electron due to the relative external potential $u(\mathbf{r})$.

Let us formally express these energies as functions of atomic electron-populations,

$$\begin{aligned} E^{\text{AIM}}(N, V) &= N(N) V^T + F(N(N)) \\ &\equiv E^{\text{AIM}}(N(N), V) \equiv E^{\text{AIM}}(N; V) \quad \text{and} \\ Q^{\text{AIM}}(\mu, V) &= N(V - \mu I)^T + F^{\text{AIM}}(N) = N(U) U^T + F^{\text{AIM}}(N(U)) \\ &\equiv Q^{\text{AIM}}(U) \equiv Q^{\text{AIM}}(N; U), \end{aligned} \quad (194)$$

where the semicolon separates the dependent variables (atomic electron populations) from the representation discrete external-potential data. The Euler equations (193) for the optimum electron populations N ,

$$\frac{\partial Q^{\text{AIM}}(N; U)}{\partial N} = U + \frac{\partial F^{\text{AIM}}(N)}{\partial N} = 0, \quad (195)$$

follow from the AIM-resolved variational principle for the system energy (compare equation (2)):

$$\delta[E^{\text{AIM}}(N; \mathbf{V}) - \mu \mathbf{I} N^T] = 0. \quad (196)$$

The AIM-resolved expression for the second differential of the thermodynamic potential $Q^{\text{AIM}}(\mu, \mathbf{V}) = Q^{\text{AIM}}(\mathbf{U}) = Q^{\text{AIM}}(N; \mathbf{U})$,

$$\begin{aligned} d^2 Q^{\text{AIM}}(\mu, \mathbf{V}) &= \frac{1}{2} [-S(d\mu)^2 + 2 d\mu \mathbf{s}^{\text{AIM}} d\mathbf{V}^T - d\mathbf{V} \mathbf{s}^{\text{AIM}} d\mathbf{V}^T] \\ &= -\frac{1}{2} d\mathbf{U} \mathbf{s}^{\text{AIM}} d\mathbf{U}^T = d^2 Q^{\text{AIM}}(\mathbf{U}). \end{aligned} \quad (197)$$

Here S denotes the global softness (see (17), (29), (42)), $\mathbf{s}^{\text{AIM}} = \mathbf{I} \mathbf{s}^{\text{AIM}}$ groups the rigid-geometry electronic softnesses of bonded atoms, and \mathbf{s}^{AIM} represents the related softness matrix in atomic resolution (see (152)). They are defined by the following partial derivatives in the $Q^{\text{AIM}}(\mu, \mathbf{V})$ representation:

$$\begin{aligned} \left(\frac{\partial^2 Q^{\text{AIM}}(\mu, \mathbf{V})}{\partial \mu^2} \right)_{\mathbf{V}} &= - \left(\frac{\partial N}{\partial \mu} \right)_{\mathbf{V}} = -S, \\ \frac{\partial^2 Q^{\text{AIM}}(\mu, \mathbf{V})}{\partial \mu \partial \mathbf{V}} &= \left(\frac{\partial N}{\partial \mu} \right)_{\mathbf{V}} = - \left(\frac{\partial N}{\partial \mathbf{V}} \right)_{\mu}^T = \mathbf{s}^{\text{AIM}}, \\ \left(\frac{\partial^2 Q^{\text{AIM}}(\mu, \mathbf{V})}{\partial \mathbf{V} \partial \mathbf{V}} \right)_{\mu} &= \left(\frac{\partial N}{\partial \mathbf{V}} \right)_{\mu} = \frac{\partial^2 Q^{\text{AIM}}(\mathbf{U})}{\partial \mathbf{U} \partial \mathbf{U}} = \frac{\partial N}{\partial \mathbf{U}} = -\mathbf{s}^{\text{AIM}}. \end{aligned} \quad (198)$$

The linear responses in unconstrained variables ΔN and $\Delta N = \mathbf{I} \Delta N^T$ of this representation can then be expressed in terms of its natural perturbations $(\Delta \mu, \Delta \mathbf{V})$ or $\Delta \mathbf{U}$ through the following transformations:

$$\begin{aligned} -\Delta N &= -\Delta \mu S + \Delta \mathbf{V} \mathbf{s}^{\text{AIM},T}, & \Delta N &= \Delta \mu \mathbf{s}^{\text{AIM}} - \Delta \mathbf{V} \mathbf{s}^{\text{AIM}}, \quad \text{or} \\ \Delta N &= -\Delta \mathbf{U} \mathbf{s}^{\text{AIM}}. \end{aligned} \quad (199)$$

In the combined matrix notation (compare equation (86)) this transformation reads:

$$[-\Delta N, \Delta N] = [\Delta \mu, \Delta \mathbf{V}] \begin{bmatrix} -S & \mathbf{s}^{\text{AIM}} \\ \mathbf{s}^{\text{AIM},T} & -\mathbf{s}^{\text{AIM}} \end{bmatrix}. \quad (200)$$

Again, these matrix elements can be expressed in terms of the principal energy derivatives defined in the $E^{\text{AIM}}(N, \mathbf{V})$ representation. The relevant elimination of variables in equation (188) then gives

$$[-\Delta N, \Delta N] = [\Delta \mu, \Delta \mathbf{V}] \begin{bmatrix} -\eta^{-1} & \eta^{-1} \mathbf{f}^{\text{AIM}} \\ \eta^{-1} \mathbf{f}^{\text{AIM},T} & \boldsymbol{\beta}^{\text{AIM}} - \eta^{-1} \mathbf{f}^{\text{AIM},T} \mathbf{f}^{\text{AIM}} \end{bmatrix}. \quad (201)$$

In the foregoing equation the lower diagonal element of the transformation matrix expresses the Berkowitz–Parr relation (equation (40)) in atomic resolution:

$$\begin{aligned} \mathbf{s}^{\text{AIM}} &= -\boldsymbol{\beta}^{\text{AIM}} + \mathbf{f}^{\text{AIM},T} S \mathbf{f}^{\text{AIM}} = -\boldsymbol{\beta}^{\text{AIM}} + \mathbf{s}^{\text{AIM},T} \mathbf{f}^{\text{AIM}} \\ &= -\boldsymbol{\beta}^{\text{AIM},T} + \mathbf{f}^{\text{AIM},T} \mathbf{s}^{\text{AIM}} = -\boldsymbol{\beta}^{\text{AIM}} + \mathbf{f}^{\text{AIM},T} \eta^{-1} \mathbf{f}^{\text{AIM}}. \end{aligned} \quad (202)$$

Consider next the Legendre-transformed representation $\mathcal{F}^{\text{AIM}}(N(N), N) = F^{\text{AIM}}(N) = F[\rho]$ in the adopted atomic resolution,

$$\begin{aligned}\mathcal{F}^{\text{AIM}}(N, N) &= E^{\text{AIM}}(N, \mathbf{V}) - \mathbf{V} \left(\frac{\partial E^{\text{AIM}}}{\partial \mathbf{V}} \right)_N \\ &= E^{\text{AIM}} - \mathbf{V} \mathbf{N}^T = F^{\text{AIM}}(N),\end{aligned}\quad (203)$$

in which N has replaced \mathbf{V} in the list of the system AIM parameters of state. Its first differential reads:

$$\begin{aligned}d\mathcal{F}^{\text{AIM}}(N, N) &= \mu dN - \sum_{\alpha} V_{\alpha} dN_{\alpha} = - \sum_{\alpha} [V_{\alpha} - \mu] dN_{\alpha} = - \sum_{\alpha} U_{\alpha} dN_{\alpha} \\ &= -\mathbf{U} d\mathbf{N}^T \equiv dF^{\text{AIM}}(N),\end{aligned}\quad (204)$$

and hence,

$$\left(\frac{\partial F^{\text{AIM}}(N)}{\partial N} \right)^T = -\mathbf{U}. \quad (205)$$

The AIM-resolved expression for the second differential of this thermodynamic potential is then given by the quadratic form,

$$d^2 F^{\text{AIM}}(N) = \frac{1}{2} dN \mathbf{s}^{\text{AIM}, -1} dN^T = \frac{1}{2} dN \mathbf{h}^{\text{AIM}} dN^T, \quad (206)$$

where the hardness matrix \mathbf{h}^{AIM} for the rigid molecular geometry is defined by the partial derivative (see also equations (31), (40), and (152)):

$$\frac{\partial^2 F^{\text{AIM}}(N)}{\partial N \partial N} = -\frac{\partial \mathbf{U}}{\partial N} = \mathbf{s}^{\text{AIM}, -1} = \mathbf{h}^{\text{AIM}}. \quad (207)$$

Hence, the linear responses $(\Delta\mu, \Delta\mathbf{V})$ of the unconstrained variables in this representation, or equivalently $\Delta\mathbf{U} = \Delta\mathbf{V} - \Delta\mu\mathbf{I}$, can be expressed in terms of perturbations $[\Delta N(\Delta N), \Delta\mathbf{N}]$ or ΔN through the transformation:

$$(\Delta\mu, \Delta\mathbf{V}) = [\Delta N, \Delta\mathbf{N}] \begin{bmatrix} \eta - \mathbf{f}^{\text{AIM}}(\boldsymbol{\beta}^{\text{AIM}})^{-1} \mathbf{f}^{\text{AIM}, T} & -\mathbf{f}^{\text{AIM}}(\boldsymbol{\beta}^{\text{AIM}})^{-1} \\ (\boldsymbol{\beta}^{\text{AIM}})^{-1} \mathbf{f}^{\text{AIM}, T} & (\boldsymbol{\beta}^{\text{AIM}})^{-1} \end{bmatrix} \quad (208)$$

or

$$-d\mathbf{U} = dN \mathbf{h}^{\text{AIM}}. \quad (209)$$

Finally, let us briefly summarize the $\mathcal{R}^{\text{AIM}}(\mu, N)$ representation,

$$\begin{aligned}\mathcal{R}^{\text{AIM}}(\mu, N) &= E^{\text{AIM}} - \mathbf{V} \left(\frac{\partial E^{\text{AIM}}}{\partial \mathbf{V}} \right)_N - N \left(\frac{\partial E^{\text{AIM}}}{\partial N} \right)_V \\ &= E^{\text{AIM}} - \mathbf{V} \mathbf{N}^T - \mu N = F^{\text{AIM}}(N) - \mathbf{V} \mathbf{N}^T,\end{aligned}\quad (210)$$

in which the system chemical potential, equal to that of the external reservoir of electrons, and the AIM electron populations define the system independent state-parameters. Its first differential

$$d\mathcal{R}^{\text{AIM}}[\mu, N] = -N d\mu - dN \mathbf{V}^T, \quad (211)$$

identifies the following partial derivatives:

$$\left(\frac{\partial \mathcal{R}^{\text{AIM}}(\mu, N)}{\partial \mu} \right)_N = -N, \quad \left(\frac{\partial \mathcal{R}^{\text{AIM}}(\mu, N)}{\partial N} \right)_\mu^T = -V. \quad (212)$$

The linear responses of these dependent variables, due to perturbations of the representation independent state-parameters, can thus be expressed in terms of charge sensitivities of equation (189). A proper elimination of variables from equation (188) then gives the transformation matrix

$$\begin{aligned} & (-\Delta N, -\Delta V) \\ &= [\Delta \mu, \Delta N] \\ &\quad \times \begin{bmatrix} -L^{-1} & L^{-1} f^{\text{AIM}}(\beta^{\text{AIM}})^{-1} \\ L^{-1}(\beta^{\text{AIM}})^{-1} f^{\text{AIM},T} & -(\beta^{\text{AIM}})^{-1} - L^{-1}(\beta^{\text{AIM}})^{-1} f^{\text{AIM},T} f^{\text{AIM}}(\beta^{\text{AIM}})^{-1} \end{bmatrix}, \\ &L = \eta - f^{\text{AIM}}(\beta^{\text{AIM}})^{-1} f^{\text{AIM},T}. \end{aligned}$$

Alternatively, one can express the elements of this transformation in terms of the AIM softness quantities of equation (200). The relevant elimination of variables in equation (199) then gives

$$\begin{aligned} & (-\Delta N, -\Delta V) \\ &= [\Delta \mu, \Delta N] \begin{bmatrix} s^{\text{AIM}}(s^{\text{AIM}})^{-1} s^{\text{AIM},T} - S & -s^{\text{AIM}}(s^{\text{AIM}})^{-1} \\ - (s^{\text{AIM}})^{-1} s^{\text{AIM},T} & (s^{\text{AIM}})^{-1} \end{bmatrix}. \end{aligned}$$

To summarize, the AIM-discretized quantities of this section are related by the equations which are isomorphic with the corresponding equations in terms of density functionals, which correspond to the fine-grained description of DFT. This opens the AIM-resolved theory of generalized molecular responses (polarizabilities) to a semi-empirical modeling, which has been widely used in the theory of chemical reactivity [2,8–10].

7. COLLECTIVE CHARGE DISPLACEMENTS AND MAPPING RELATIONS

Changes in atomic electron populations, $\Delta N = \{\Delta N_\alpha\}$, are strongly coupled through the off-diagonal elements of the hardness matrices \mathbf{h}^{AIM} or $\boldsymbol{\eta}^{\text{AIM}}$. Indeed, the given displacement ΔN affects chemical potentials of all constituent atoms. In the “geometric” representation of charge redistribution in molecular systems [2,8–10] the electron populations of atoms are regarded as coordinates of the system overall population vector $n = \sum_\alpha N_\alpha \mathbf{e}_\alpha$, defined in the Euclidean vector space spanned by the unit basis vectors $\{\mathbf{e}_\alpha\}$: $\mathbf{e}_\alpha \bullet \mathbf{e}_\beta = \delta_{\alpha,\beta}$. In other words, in this interpretation the AIM populations reflect projections of n onto the atomic population axes, provided by the scalar products $\{N_\alpha = \mathbf{e}_\alpha \bullet n\}$.

A compact description of the system electronic structure is obtained using the decoupled reference frames of collective shifts in the atomic electron densities (or populations), which generally involve displacements on all constituent atoms [2,7–10,35,52,56,64,65,70,71,76–83]. In the local description they constitute the eigenvectors $\boldsymbol{\chi}(\mathbf{r}) = \{\chi_k(\mathbf{r})\}$ of the hardness kernel or its inverse, the softness kernel:

$$\int \eta(\mathbf{r}, \mathbf{r}') \chi_k(\mathbf{r}') d\mathbf{r}' = \eta_k \chi_k(\mathbf{r}) \quad \text{and} \quad \int \sigma(\mathbf{r}, \mathbf{r}') \chi_k(\mathbf{r}') d\mathbf{r}' = \sigma_k \chi_k(\mathbf{r}),$$

$$\int \chi_k^*(\mathbf{r}) \chi_l(\mathbf{r}) d\mathbf{r} = \delta_{k,l}, \quad (213)$$

where the eigenvalues $\boldsymbol{\eta} = \{\eta_k\}$ and $\boldsymbol{\sigma} = \{\sigma_k = \eta_k^{-1}\}$ represent the system principal hardnesses and softnesses, respectively. These eigenvalue problems also generate the spectral-resolutions of the underlying hardness and softness kernels and operators [35,64,65,75], *e.g.*,

$$\eta(\mathbf{r}, \mathbf{r}') = \sum_k \chi_k(\mathbf{r}) \eta_k \chi_k^*(\mathbf{r}') \quad \text{and} \quad \sigma(\mathbf{r}, \mathbf{r}') = \sum_k \chi_k(\mathbf{r}) \sigma_k \chi_k^*(\mathbf{r}'). \quad (214)$$

In the externally-closed molecular systems the eigenvectors of the linear-response kernel $\beta(\mathbf{r}, \mathbf{r}')$ similarly define their principal polarizational normal modes [2,3,8,64,65,75,76]:

$$\begin{aligned} -\int \beta^{-1}(\mathbf{r}, \mathbf{r}') \phi_i(\mathbf{r}') d\mathbf{r}' &= \eta_i^{\text{int}} \phi_i(\mathbf{r}) \quad \text{and} \quad -\int \beta(\mathbf{r}, \mathbf{r}') \phi_i(\mathbf{r}') d\mathbf{r}' = \beta_i \phi_i(\mathbf{r}), \\ \int \phi_j(\mathbf{r}) d\mathbf{r} &= 0, \quad \int \phi_i^*(\mathbf{r}) \phi_j(\mathbf{r}) d\mathbf{r} = \delta_{i,j}, \quad -\beta(\mathbf{r}, \mathbf{r}') = \sum_i \phi_i(\mathbf{r}) \beta_i \phi_i^*(\mathbf{r}'), \end{aligned} \quad (215)$$

where $\boldsymbol{\eta}^{\text{int}} = \{\eta_i^{\text{int}} = -\beta_i^{-1}\}$ and $\boldsymbol{\sigma}^{\text{int}} = \{\sigma_i^{\text{int}} = -\beta_i\}$ group the system principal internal hardnesses and softnesses, respectively.

In atomic resolution the Populational Normal Modes (PNM) represent the eigenvectors of atomic hardness and softness matrices [2,7–10,35,43,52,70,71,75–81]. Therefore, in this representation both these matrices are diagonal. For example, for the rigid molecular geometry these populational modes of AIM are defined by the eigenvectors of \mathbf{h}^{AIM} and $\mathbf{s}^{\text{AIM}} = (\mathbf{h}^{\text{AIM}})^{-1}$,

$$\mathbf{h}^{\text{AIM}} \mathbf{T}_a^{\text{T}} = h_a \mathbf{T}_a^{\text{T}} \quad \text{and} \quad \mathbf{s}^{\text{AIM}} \mathbf{T}_a^{\text{T}} = s_a \mathbf{T}_a^{\text{T}}, \quad a = 1, 2, \dots, m, \quad (216a)$$

represented by column vectors $\{\mathbf{T}_a^{\text{T}} = (T_{\alpha,a}, \alpha = 1, 2, \dots, m)\}$ in $\mathbf{T} = (\mathbf{T}_1^{\text{T}}, \mathbf{T}_2^{\text{T}}, \dots, \mathbf{T}_m^{\text{T}})$, which diagonalizes these matrices in the similarity transformation:

$$\begin{aligned} \mathbf{T}^\dagger \mathbf{h}^{\text{AIM}} \mathbf{T} &= \mathbf{h}^{\text{PNM}} = \{h_a \delta_{a,b}\}, \\ \mathbf{T}^\dagger \mathbf{s}^{\text{AIM}} \mathbf{T} &= \mathbf{s}^{\text{PNM}} = \{s_a \delta_{a,b} = h_a^{-1} \delta_{a,b}\}, \quad \mathbf{T}^\dagger \mathbf{T} = \mathbf{I}. \end{aligned} \quad (216b)$$

In the externally-closed molecular systems the independent modes of the molecular electronic structure are similarly reflected by the corresponding eigenvectors of the linear-response matrix in atomic resolution, represented by columns $\{\mathbf{t}_c^{\text{T}} = \{t_{\alpha,c}, \alpha = 1, 2, \dots, m\}, c = 1, 2, \dots, m\}$ of the overall transformation matrix $\mathbf{t} = (\mathbf{t}_1^{\text{T}}, \mathbf{t}_2^{\text{T}}, \dots, \mathbf{t}_m^{\text{T}})$, $\mathbf{t}^\dagger \mathbf{t} = \mathbf{I}$:

$$\begin{aligned} -\mathbf{t}^\dagger (\boldsymbol{\beta}^{\text{AIM}})^{-1} \mathbf{t} &= \mathbf{H}^{\text{PNM}} = \{H_c \delta_{c,d}\} \quad \text{and} \\ -\mathbf{t}^\dagger \boldsymbol{\beta}^{\text{AIM}} \mathbf{t} &= \mathbf{S}^{\text{PNM}} = \{S_c \delta_{c,d} = (H_c)^{-1} \delta_{c,d}\}. \end{aligned} \quad (217a)$$

Here the diagonal matrices \mathbf{h}^{PNM} and \mathbf{H}^{PNM} group the principal hardnesses of the externally open and closed molecular systems, respectively, while the diagonal matrices \mathbf{s}^{PNM} and \mathbf{S}^{PNM} combine their corresponding inverses representing the principal softnesses in atomic resolution. These eigenvectors satisfy the corresponding eigenvalue problems:

$$-\boldsymbol{\beta}^{\text{AIM},-1} \mathbf{t}_c^{\text{T}} = H_c \mathbf{t}_c^{\text{T}} \quad \text{and} \quad -\boldsymbol{\beta}^{\text{AIM}} \mathbf{t}_c^{\text{T}} = S_c \mathbf{t}_c^{\text{T}}. \quad (217b)$$

The (geometrically) Relaxed Populational Modes (RPM) in open molecular systems are similarly defined by the eigenvectors $\boldsymbol{\tau} = \{\boldsymbol{\tau}_a^T\}$, $\boldsymbol{\tau}^\dagger \boldsymbol{\tau} = \mathbf{I}$, of the geometrically relaxed hardness and softness matrices in atomic resolution $\boldsymbol{\eta}^{\text{AIM}}$ and $\boldsymbol{\sigma}^{\text{AIM}} = (\boldsymbol{\eta}^{\text{AIM}})^{-1}$:

$$\boldsymbol{\eta}^{\text{AIM}} \boldsymbol{\tau}_a^T = \eta_a \boldsymbol{\tau}_a^T \quad \text{and} \quad \boldsymbol{\sigma}^{\text{AIM}} \boldsymbol{\tau}_a^T = \sigma_a \boldsymbol{\tau}_a^T, \quad a = 1, 2, \dots, m, \\ \boldsymbol{\tau}^\dagger \boldsymbol{\eta}^{\text{AIM}} \boldsymbol{\tau} = \boldsymbol{\eta}^{\text{RPM}} = \{\eta_a \delta_{a,b}\} \quad \text{and} \quad \boldsymbol{\tau}^\dagger \boldsymbol{\sigma}^{\text{AIM}} \boldsymbol{\tau} = \boldsymbol{\sigma}^{\text{RPM}} = \{\sigma_a \delta_{a,b}\}. \quad (218)$$

The PNM concept has been extended into fragments of reactive systems [2,7–10,81]. Both the internally (intra-subsystem) and externally (inter-subsystem) decoupled collective modes of reactants have been widely used to probe the reactivity preferences of chemisorption systems [2,8,70,82,83].

We also recall that the nuclear normal coordinates $\mathbf{Q} = (\mathbf{Q}_1^T, \mathbf{Q}_2^T, \dots)$ diagonalize the system geometric Hessian $\mathbf{H} = [\partial^2 W(N, \mathbf{R}) / \partial \mathbf{R} \partial \mathbf{R}]_N$ (see (94)), which contains the force-constants for the adopted system of geometric coordinates $\mathbf{R} = \{X_k\}$:

$$\mathbf{Q}^\dagger \mathbf{H} \mathbf{Q} = \mathbf{K} = \{K_p \delta_{r,p}\} \quad \text{or} \quad \mathbf{H} \mathbf{Q}_p^T = K_p \mathbf{Q}_p^T, \quad \mathbf{Q}^\dagger \mathbf{Q} = \mathbf{I}, \quad (219)$$

with the principal force-constants $\mathbf{K} = \{K_p\}$ of the diagonal matrix $\mathbf{K} = \{K_p \delta_{r,p}\}$ reflecting the “curvatures” of the Born–Oppenheimer potential energy surface $W(N, \mathbf{Q})$ for the cross-sections along these nuclear normal-modes (NNM).

The ground-state relation between the geometric and electronic structure quantities provides a mapping between the nuclear-position and electronic (populational) degrees of freedom in molecular systems. In the past an understanding of a subtle interplay between these state-parameters has been a major goal of theoretical chemistry. It has recently been demonstrated [2,8,10,38–41,43] that the AIM-resolved CSA provides a theoretical framework for constructing explicit mapping relations between the atomic (or collective) electron-population “coordinates” and the corresponding nuclear (or collective, normal) displacement modes.

It should be recalled that the above decoupling of nuclear motions (see (219)) can be interpreted as the “rotation” of the nuclear-position reference-frame to the principal axes of the symmetric tensor \mathbf{H} of the system geometric force-constants, defined by the vibrational normal modes \mathbf{Q} . One similarly interprets the PNM in atomic resolution, which represent independent (decoupled) modes of collective displacements in the atomic electron populations. They define the principal-axes $\mathbf{d} = \mathbf{e}^T \mathbf{T}$ of the hardness/softness tensors in the populational vector space spanned by the atomic (unit) vectors $\mathbf{e} = \{\mathbf{e}_\alpha\}$ [2,8]. The corresponding electron populations associated with these normal modes are then given by the transformed AIM populations, $\mathbf{n} = \mathbf{N} \mathbf{T}$. Therefore, the transformation matrix \mathbf{T} can be interpreted as combining the following derivatives:

$$\mathbf{T} = \left(\frac{\partial \mathbf{n}}{\partial N} \right)_\mu \quad \text{and} \quad \mathbf{T}^{-1} = \mathbf{T}^\dagger = \left(\frac{\partial N}{\partial \mathbf{n}} \right)_\mu. \quad (220)$$

This derivative interpretation allows one to use \mathbf{T} in the relevant chain-rule transformations, to determine the mapping transformations between the electronic and geometrical structures of the externally open molecular systems.

Similarly, the electron population quantities associated with the polarizational normal modes in the externally-closed molecules, $(\mathbf{n})_N = \mathbf{N} \mathbf{t}$, allow one to interpret the transformation matrix \mathbf{t} and its inverse $\mathbf{t}^{-1} = \mathbf{t}^\dagger$ as the following derivatives:

$$\mathbf{t} = \left(\frac{\partial \mathbf{n}}{\partial N} \right)_N \quad \text{and} \quad \mathbf{t}^{-1} = \left(\frac{\partial N}{\partial \mathbf{n}} \right)_N. \quad (221)$$

Accordingly, the normal coordinates of the system nuclei, $\mathbf{q} = \mathbf{R}\mathbf{Q}$, representing their \mathbf{Q} -transformed Cartesian coordinates \mathbf{R} , allow one to interpret the principal-axes “rotation” transformation as grouping the corresponding geometric derivatives:

$$\mathbf{Q} = \frac{\partial \mathbf{q}}{\partial \mathbf{R}} \quad \text{and} \quad \mathbf{Q}^{-1} = \mathbf{Q}^\dagger = \frac{\partial \mathbf{R}}{\partial \mathbf{q}}. \quad (222)$$

Let $\mathbf{R} = \{X_k\}$ denote the complete space of Cartesian coordinates, which uniquely specify the geometric structure of the molecule under consideration. The AIM-population displacements for constant N are then linked with the corresponding geometrical displacements via the following chain-rule transformation:

$$\begin{aligned} (\Delta N)_N &= \Delta \mathbf{R} \left(\frac{\partial V}{\partial \mathbf{R}} \right) \left(\frac{\partial N}{\partial V} \right)_N = \Delta \mathbf{R} \left(\frac{\partial N}{\partial \mathbf{R}} \right)_N \\ &= \Delta \mathbf{R} \mathbf{G}^{\text{AIM}} \boldsymbol{\beta}^{\text{AIM}} \equiv \Delta \mathbf{R} \mathbf{T}[\mathbf{R} \rightarrow N]_N. \end{aligned} \quad (223)$$

Here the linear-response matrix in atomic resolution $\boldsymbol{\beta}^{\text{AIM}}$ is defined in equation (187) and the geometric matrix in atomic resolution,

$$\mathbf{G}^{\text{AIM}} = \frac{\partial V}{\partial \mathbf{R}} = \left\{ G_{k,\alpha} = \frac{\partial V_\alpha}{\partial X_k} = \int p_\alpha(\mathbf{r}) \left[\frac{\partial v(\mathbf{r})}{\partial X_k} \right]_N d\mathbf{r} = \int p_\alpha(\mathbf{r}) G_k(\mathbf{r}; \mathbf{R}) d\mathbf{r} \right\}, \quad (224)$$

represents the AIM-representation of the local geometric transformation of equation (13).

The overall transformation matrix $\mathbf{T}[\mathbf{R} \rightarrow N]_N$ in equation (223) provides the explicit electron-following (EF) “translator” of the given displacements of the system nuclei $\Delta \mathbf{R}$ into the conjugate linear-response in atomic electron populations $(\Delta N)_N$. This EF-mapping between the electronic and geometrical “coordinates” can be straightforwardly generalized to provide the transformations involving the populational and/or nuclear normal modes in both the externally open and closed molecular systems, $\mathbf{T}[\mathbf{Q} \rightarrow N]_N$, $\mathbf{T}[\mathbf{R} \rightarrow \mathbf{n}]_N$, $\mathbf{T}[\mathbf{Q} \rightarrow \mathbf{n}]_N$, *etc.* For example,

$$\begin{aligned} (\Delta \mathbf{n})_N &= \Delta \mathbf{R} \left(\frac{\partial V}{\partial \mathbf{R}} \right) \left(\frac{\partial \mathbf{n}}{\partial V} \right)_N = \Delta \mathbf{R} \left(\frac{\partial \mathbf{n}}{\partial \mathbf{R}} \right)_N \\ &= \Delta \mathbf{R} \mathbf{G}^{\text{AIM}} \boldsymbol{\beta}^{\text{AIM}} \mathbf{t} \equiv \Delta \mathbf{R} \mathbf{T}[\mathbf{R} \rightarrow \mathbf{n}]_N, \end{aligned} \quad (225)$$

where we have used the chain-rule

$$\left(\frac{\partial \mathbf{n}}{\partial V} \right)_N = \left(\frac{\partial N}{\partial V} \right)_N \left(\frac{\partial \mathbf{n}}{\partial N} \right)_N = \boldsymbol{\beta}^{\text{AIM}} \mathbf{t}. \quad (226)$$

The corresponding EF-mapping transformations for the externally open molecules are similarly defined by the system softness matrix in atomic resolution, $\mathbf{s}^{\text{AIM}} = -\partial N / \partial U = (\partial N / \partial V)_\mu$:

$$\begin{aligned} \Delta N &= \Delta \mathbf{R} \left(\frac{\partial V}{\partial \mathbf{R}} \right)_N \left(\frac{\partial N}{\partial V} \right)_\mu = \Delta \mathbf{R} \left(\frac{\partial N}{\partial \mathbf{R}} \right)_\mu \\ &= -\Delta \mathbf{R} \mathbf{G}^{\text{AIM}} \mathbf{s}^{\text{AIM}} \equiv \Delta \mathbf{R} \mathbf{T}[\mathbf{R} \rightarrow N]_\mu, \end{aligned} \quad (227)$$

$$\begin{aligned} \Delta \mathbf{n} &= \Delta \mathbf{R} \left(\frac{\partial V}{\partial \mathbf{R}} \right)_\mu \left(\frac{\partial \mathbf{n}}{\partial V} \right)_\mu = \Delta \mathbf{R} \left(\frac{\partial \mathbf{n}}{\partial \mathbf{R}} \right)_\mu \\ &= -\Delta \mathbf{R} \mathbf{G}^{\text{AIM}} \mathbf{s}^{\text{AIM}} \mathbf{t} \equiv \Delta \mathbf{R} \mathbf{T}[\mathbf{R} \rightarrow \mathbf{n}]_\mu, \end{aligned} \quad (228)$$

since

$$\left(\frac{\partial \mathbf{n}}{\partial \mathbf{V}}\right)_\mu = \left(\frac{\partial \mathbf{N}}{\partial \mathbf{V}}\right)_\mu \left(\frac{\partial \mathbf{n}}{\partial \mathbf{N}}\right)_\mu = -\mathbf{s}^{\text{AIM}}_{\mathbf{t}}. \quad (229)$$

The relevant electron-preceding (EP) relations are also directly available from CSA in atomic resolution. Consider as an illustrative example the NFF matrix of equation (141), $\boldsymbol{\varphi}^{\text{AIM}}(\mathbf{N}, \mathbf{R}) = \partial \mathbf{F} / \partial \mathbf{N}$, which can be combined with the geometric block $\mathbf{V}_{\mathbf{F}, \mathbf{F}} = (\partial \mathbf{R} / \partial \mathbf{F})_{\mathbf{N}} = -\mathbf{H}^{-1}$ of the closed-system compliance matrix of equation (115). The chain-rule transformation generating the linear responses in nuclear coordinates from the known displacements in atomic electron populations then reads:

$$\begin{aligned} (\Delta \mathbf{R})_{\mathbf{F}'=\mathbf{0}, \mathbf{N}} &= (\Delta \mathbf{N})_{\mathbf{N}} \left(\frac{\partial \mathbf{F}}{\partial \mathbf{N}}\right)_{\mathbf{N}} \left(\frac{\partial \mathbf{R}}{\partial \mathbf{F}}\right)_{\mathbf{N}} = (\Delta \mathbf{N})_{\mathbf{N}} \left(\frac{\partial \mathbf{R}}{\partial \mathbf{N}}\right)_{\mathbf{F}'=\mathbf{0}, \mathbf{N}} \\ &= -(\Delta \mathbf{N})_{\mathbf{N}} \boldsymbol{\varphi}^{\text{AIM}} \mathbf{H}^{-1} \equiv (\Delta \mathbf{N})_{\mathbf{N}} \mathbf{T}[\mathbf{N} \rightarrow \mathbf{R}]_{\mathbf{N}}. \end{aligned} \quad (230)$$

It should be observed that the geometric compliance matrix $(\partial \mathbf{R} / \partial \mathbf{F})_{\mathbf{N}} = \{(\partial \mathbf{R} / \partial F_k)_{\mathbf{F}'=\mathbf{0}', \mathbf{N}}\}$ implies the vanishing forces $\mathbf{F}' = \mathbf{0}'$ in all remaining geometrical degrees of freedom, so that the coordinates generated by this relation reflect the geometry relaxation following the given displacement $(\Delta \mathbf{N})_{\mathbf{N}}$ in the system electronic structure. A comparison of the resulting mapping transformation with the $\mathbf{V}_{\mathbf{N}, \mathbf{F}}$ block of the compliant matrix \mathbf{V}^{AIM} of equation (157) identifies

$$\mathbf{T}[\mathbf{N} \rightarrow \mathbf{R}]_{\mathbf{N}} = -\mathbf{V}_{\mathbf{N}, \mathbf{F}}. \quad (231)$$

Subsequent multiplication of equation (230), from the right, by the transformation matrix $\mathbf{Q} = \partial \mathbf{q} / \partial \mathbf{R}$ gives rise to the associated $\Delta \mathbf{N} \rightarrow \Delta \mathbf{q}$ mapping:

$$\begin{aligned} (\Delta \mathbf{q})_{\mathbf{N}} &= (\Delta \mathbf{N})_{\mathbf{N}} \left(\frac{\partial \mathbf{F}}{\partial \mathbf{N}}\right)_{\mathbf{N}} \left(\frac{\partial \mathbf{R}}{\partial \mathbf{F}}\right)_{\mathbf{N}} \left(\frac{\partial \mathbf{q}}{\partial \mathbf{R}}\right)_{\mathbf{N}} = (\Delta \mathbf{N})_{\mathbf{N}} \left(\frac{\partial \mathbf{q}}{\partial \mathbf{N}}\right)_{\mathbf{N}} \\ &= -(\Delta \mathbf{N})_{\mathbf{N}} \boldsymbol{\varphi}^{\text{AIM}} \mathbf{H}^{-1} \mathbf{Q} \equiv (\Delta \mathbf{N})_{\mathbf{N}} \mathbf{T}[\mathbf{N} \rightarrow \mathbf{q}]_{\mathbf{N}}. \end{aligned} \quad (232)$$

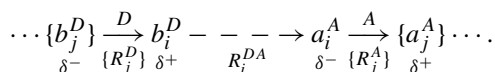
The corresponding translators between normal modes of the electronic and geometric structures of molecular systems similarly follow from the corresponding chain-rule transformations of the above mapping relations. For example, inserting the identity matrix $\mathbf{I} = \mathbf{Q}\mathbf{Q}^\dagger$ into equation (225) gives

$$\begin{aligned} (\Delta \mathbf{n})_{\mathbf{N}} &= (\Delta \mathbf{R}\mathbf{Q}) \left[\mathbf{Q}^\dagger \left(\frac{\partial \mathbf{n}}{\partial \mathbf{R}}\right)_{\mathbf{N}} \right] = \left[\Delta \mathbf{R} \left(\frac{\partial \mathbf{q}}{\partial \mathbf{R}}\right) \right] \left[\left(\frac{\partial \mathbf{R}}{\partial \mathbf{q}}\right) \left(\frac{\partial \mathbf{n}}{\partial \mathbf{R}}\right)_{\mathbf{N}} \right] \\ &= \Delta \mathbf{q} \left(\frac{\partial \mathbf{n}}{\partial \mathbf{q}}\right)_{\mathbf{N}} \equiv \Delta \mathbf{q} \mathbf{T}[\mathbf{q} \rightarrow \mathbf{n}]_{\mathbf{N}}. \end{aligned} \quad (233)$$

Illustrative “translators” for these mapping relations have been reported elsewhere [2,8,10,38,39,41,43,84]. The electronegativity-equalization principle of Sanderson [25] has also been used to derive explicit transformations for illustrative molecular systems. They provide semi-quantitative indicators of the system charge reorganization accompanying the given conformational or electronic changes, both in a single molecule and in reactants forming the bimolecular complex. They represent an important part of the CSA conceptual basis, by providing means to diagnose in the EF-perspective the charge displacement patterns accompanying nuclear displacements, and to predict in the EP-approach the geometrical implications of the hypothetical manipulations of the system distribution of electrons.

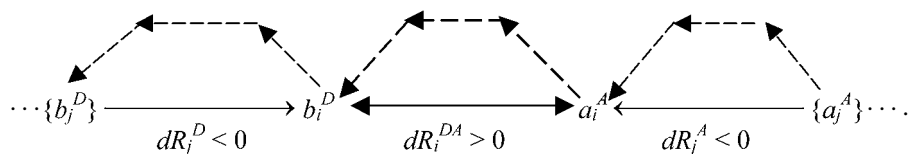
The EP-mappings between the atomic (or collective) displacements in the electron-population space and the atomic (or collective) shifts in the nuclear-position space can be used to quickly assess the feasibility of alternative reaction mechanisms. Various populational displacements in a molecule or reactive system can be directly translated into the conjugate changes in the system geometric structure. They allow one to predict whether the specified trial electronic displacements “translate” into the desired bond-breaking–bond-forming changes in the molecule. For example, these semi-quantitative relations from the CSA calculations can be used as a tool for a judicious manipulation of the catalyst surface in a systematic search for the specific electronic conditions in the catalyst, which bring about the desired charge redistribution in the adsorbate. The EF-mappings similarly predict main trends in charge responses to nuclear displacements, *e.g.*, the effect of a decreasing polarity of the elongated ionic bond. Of great interest in qualitative predictions of molecular charge-responses also are the indirect bond polarizations induced by the specified conformational changes. They are readily available from the relevant AIM or collective mapping translators.

The above mapping relations have been shown to provide a semi-quantitative basis for the intuitive, qualitative bond-length variation rules of Gutmann [44]. Consider the donor–acceptor system $D \rightarrow A \equiv [DA]$ bonded through the coordinating atoms $b_i^D \in D$ and $a_i^A \in A$, as shown in the diagram



Let atoms $\{b_j^D\}$ and $\{a_j^A\}$ describe the other atoms of both reactants, which are bonded to their respective coordinating atoms in the [DA] complex. These atoms typically exhibit the alternating extra charge-shifts $\{\delta^q\}$ due to the $b_i^D \rightarrow a_i^A$ coordination, which are schematically displayed at the bottom of the diagram. They reflect the intuitively expected inductive polarizations of the intra- and inter-reactant bonds in this bimolecular complex.

The intuitively expected electron redistributions, which accompany a hypothetical lengthening of the inter-reactant bond b_i^D – a_i^A are shown in the next diagram, where the straight (solid) arrows represent the relative movement of the nuclei and the bent (broken) arrows reflect the induced flows of electrons. This diagram takes into account the decreased CT component of the bond being stretched (the directly coupled electronic response) and the induced polarizations of the remaining bonds involving the coordinating atoms, inside the two reactants (indirectly coupled responses). The latter moderate the effects of the primary charge shift, in the spirit of the Le Châtelier–Braun principle of thermodynamics [62]:



These charge responses are well reflected by the mapping relations [2,8,10,38,39,41,43,84]. Paraphrasing the first bond-length variation rule of Gutmann [44], the larger the distance R_i^{DA} between the coordinating atoms of two reactants, the lower polarization of the bond being stretched and the greater coordination (shorter lengths) of other bonds $\{R_j^D\}$ and $\{R_j^A\}$ inside the two reactants, which involve the two coordinating atoms of the [DA]

system. As also emphasized by Gutmann, the structures of molecules are not rigid, but rather they are adaptable to their environment. The mapping relations from the CSA model allow one to view this relationship between the electronic and geometric structures of molecules and their complexes from many chemically interesting perspectives. Changes in the charge density pattern are reflected by trends in geometrical displacements, which in turn may lead to new reactivity preferences. By modifying the molecular environment, *e.g.*, using the catalyst, one can induce the desired electronic conditions for “activating” bonds of interest.

One could also use the mapping relations to identify the vibrational modes associated with a given normal or local charge polarizations in the molecule. This is also of great importance for catalysis, since the electronic “promotion” of the chemisorbed molecule by an active site of the catalyst can then be “translated” into the conjugate bond-stretches, possibly those leading to bond cleavages. One could also use these maps in a search for the optimum matching of two reactants towards achieving the desired bond polarizations, ultimately leading to the expected chemical transformation in a concerted mechanism, which takes into account the accompanying intra-reactant geometry and/or electron density relaxation in the bimolecular reactive system.

8. CONCEPTS FOR REACTING MOLECULES

8.1. Equilibrium states and charge sensitivities of reactants

In the theory of chemical reactivity the most important division of a bimolecular reactive system is the reactant partitioning $R = A-B$, with A and B denoting the *acidic* (electron-acceptor) and *basic* (electron-donor) partners in the [DA] complex, respectively [2,7–10, 33–35,52,56–58]. This A or B classification of interacting species can be carried out by examining the chemical potentials (negative electronegativities) of the separate (infinitely distant) reactants, in the dissociation limit $R^0(\infty) = A^0 + B^0$, with the chemical potentials $\mu_R^0 = (\mu_A^0, \mu_B^0)$ of these free reactants satisfying the inequality: $\mu_A^0 < \mu_B^0$.

The electron densities of the geometrically and electronically “frozen” free subsystems, $\rho_R^0 = (\rho_A^0, \rho_B^0)$, when shifted to their finite separation and the mutual orientation specified by the nuclear coordinates \mathbf{R}_{AB} , determine the “promolecular” distribution $\rho_R^0 = \rho_A^0 + \rho_B^0$ of the bimolecular complex. Against this reference $R^0(\mathbf{R}_{AB}) = (A^0|B^0)$, consisting of the mutually-closed (non-bonded) reactants, one extracts the effects due to the chemical bonds between the two interacting molecular fragments.

It is an accepted convention in the reactivity theory to view the interaction between reactants in two stages. At the intermediate, Polarization (P) stage of a chemical reaction the mutually-closed subsystems in $R^P(\mathbf{R}_{AB}) = (A^+|B^+)$ modify their electron distributions to $\rho_R^P = (\rho_A^+, \rho_B^+)$ due to the presence of the other reactant, thus determining the associated overall density distribution of the polarized reactants $\rho_R^P = \rho_A^+ + \rho_B^+$. The subsequent internal Charge-Transfer (CT) between the mutually-open reactants in $R^{CT}(\mathbf{R}_{AB}) = (A^*|B^*)$, which preserves the overall number of electrons $N_R = N_A^* + N_B^*$ in R as a whole, then establishes the final equilibrium electron distributions of both subsystems, $\rho_R^{CT} = (\rho_A^*, \rho_B^*)$, in such an externally closed reactive system, which give rise to the overall density $\rho_R^{CT} = \rho_A^* + \rho_B^*$.

The final CT-stage of the interaction gives rise to the equilibrium distribution of electrons ρ_R^{CT} in the molecular complex $R^{\text{CT}}(\mathbf{R}_{AB}) = (A^*|B^*)$, for its specified external potential

$$v_R(\mathbf{r}; \mathbf{R}_{AB}) = v_A(\mathbf{r}; \mathbf{R}_{AB}) + v_B(\mathbf{r}; \mathbf{R}_{AB}),$$

where $v_\alpha(\mathbf{r}; \mathbf{R}_{AB})$ denotes the external potential due to the nuclei of subsystem α . We shall often combine the subsystem external potentials into the row vector $\mathbf{v}_{\mathfrak{R}}^{\text{P}}(\mathbf{r}; \mathbf{R}_{AB}) = [v_A(\mathbf{r}; \mathbf{R}_{AB}), v_B(\mathbf{r}; \mathbf{R}_{AB})] \equiv [v_A(\mathbf{r}), v_B(\mathbf{r})] \equiv \mathbf{v}_{\mathfrak{R}}^{\text{P}}(\mathbf{r})$. In the reactive system one can separately modify geometries of individual reactants, thus independently changing their contributions to the external potential of the whole system. Therefore, these two components can be regarded as independent nuclear (geometric) degrees-of-freedom of the reactive system.

The bonded, mutually-open reactants in R^{CT} reach their equilibrium distributions $\rho_R^* = (\rho_A^*, \rho_B^*)$ for the CT-displaced average numbers of electrons preserving the overall number of electrons N_R . Of interest also are, *e.g.*, in chemisorption systems, the externally-open bimolecular systems $\mathfrak{R}^{\text{CT}}(\mathbf{R}_{AB}) = (\mathcal{R}|A^*|B^*)$ and $\mathfrak{R}^{\text{P}}(\mathbf{R}_{AB}) = (\mathcal{R}_A|A^+|B^+|\mathcal{R}_B)$, consisting of the externally open reactants coupled in \mathfrak{R}^{CT} to a common electron reservoir \mathcal{R} , and, in \mathfrak{R}^{P} , to the separate reservoirs \mathcal{R}_A and \mathcal{R}_B , respectively. In the former case the system global average number of electrons N_R determines a single populational parameter of state, as reflected by the global Fukui functions (FF) of both subsystems combined in the row vector

$$\begin{aligned} f_{\mathfrak{R}}^{\text{CT}}(\mathbf{r}) &= \left(\frac{\partial \rho_{\mathfrak{R}}^{\text{CT}}(\mathbf{r})}{\partial N_R} \right)_{v_R} = \left\{ \left(\frac{\partial \rho_A^*(\mathbf{r})}{\partial N_R} \right)_{v_R}, \left(\frac{\partial \rho_B^*(\mathbf{r})}{\partial N_R} \right)_{v_R} \right\} \\ &\equiv \{ f_A^{\text{CT}}(\mathbf{r}), f_B^{\text{CT}}(\mathbf{r}) \}. \end{aligned} \quad (234)$$

In the latter case the overall electron populations of both reactants, $\mathbf{N}_{\mathfrak{R}}^{\text{P}} = (N_A^+, N_B^+) = N_{\mathfrak{R}}^{\text{P}}[\rho_{\mathfrak{R}}^{\text{P}}]$, can be independently varied by exchanges (external CT) with their separate reservoirs. This gives rise to the FF matrix for reactants in \mathfrak{R}^{P} :

$$\mathbf{f}_{\mathfrak{R}}^{\text{P}}(\mathbf{r}) = \left(\frac{\partial \rho_{\mathfrak{R}}^{\text{P}}(\mathbf{r})}{\partial N_{\mathfrak{R}}^{\text{P}}} \right)_{v_R} = \begin{bmatrix} \left(\frac{\partial \rho_A^+(\mathbf{r})}{\partial N_A} \right)_{v_R, N_B} & \left(\frac{\partial \rho_B^+(\mathbf{r})}{\partial N_A} \right)_{v_R, N_B} \\ \left(\frac{\partial \rho_A^+(\mathbf{r})}{\partial N_B} \right)_{v_R, N_A} & \left(\frac{\partial \rho_B^+(\mathbf{r})}{\partial N_B} \right)_{v_R, N_A} \end{bmatrix} \equiv \{ f_{\alpha, \beta}(\mathbf{r}) \}. \quad (235)$$

The ground-state electron density of R^{CT} in \mathfrak{R}^{CT} , $\rho_{\mathfrak{R}}^{\text{CT}} = \rho_A^* + \rho_B^*$, and the associated energy $E_{v_R}[\rho_{\mathfrak{R}}^{\text{CT}}]$ are uniquely determined by the system external potential v_R and the average overall number of electrons N_R :

$$\rho_{\mathfrak{R}}^{\text{CT}} = \rho_{\mathfrak{R}}^{\text{CT}}[N_R, v_R], \quad E_{v_R}[\rho_{\mathfrak{R}}^{\text{CT}}] \equiv E_{\mathfrak{R}}^{\text{CT}}[N_R, v_R]. \quad (236)$$

The corresponding functional relations for the open-reactants of R^{P} in \mathfrak{R}^{P} read:

$$\rho_{\mathfrak{R}}^{\text{P}} = \rho_{\mathfrak{R}}^{\text{P}}[\mathbf{N}_{\mathfrak{R}}^{\text{P}}, v_R], \quad \tilde{E}_{v_R}[\rho_{\mathfrak{R}}^{\text{P}}] \equiv \tilde{E}_{\mathfrak{R}}^{\text{P}}[\mathbf{N}_{\mathfrak{R}}^{\text{P}}, v_R], \quad (237)$$

where the row vectors of electron densities of the polarized, externally-open reactants $\rho_{\mathfrak{R}}^{\text{P}} = (\rho_A^+, \rho_B^+)$ and $\mathbf{N}_{\mathfrak{R}}^{\text{P}} = (N_A^+, N_B^+) = N_{\mathfrak{R}}^{\text{P}}[\rho_{\mathfrak{R}}^{\text{P}}]$.

The populational partial derivative of $E_{v_R}[\rho_{\mathfrak{R}}^{\text{CT}}] \equiv E_{\mathfrak{R}}^{\text{CT}}[N_R, v_R]$ determines the system global chemical potential, equal to that of the reservoir,

$$\mu_{\mathfrak{R}}^{\text{CT}} = \left(\frac{\partial E_{v_R}[\rho_{\mathfrak{R}}^{\text{CT}}]}{\partial \rho_{\mathfrak{R}}^{\text{CT}}(\mathbf{r})} \right)_{v_R} = \left(\frac{\partial E_{\mathfrak{R}}^{\text{CT}}[N_R, v_R]}{\partial N_R} \right)_{v_R}, \quad (238)$$

which is equalized throughout the space, while the functional derivative with respect to v_R gives, by the Hellmann–Feynman theorem, the system overall electron density:

$$\rho_{\mathfrak{R}}^{\text{CT}}(\mathbf{r}) = \left(\frac{\partial E_{\mathfrak{R}}^{\text{CT}}[N_R, v_R]}{\partial v_R(\mathbf{r})} \right)_{N_R}. \quad (239)$$

These derivatives determine the corresponding first differential of $E_{\mathfrak{R}}^{\text{CT}}[N_R, v_R]$:

$$dE_{\mathfrak{R}}^{\text{CT}}[N_R, v_R] = \mu_{\mathfrak{R}}^{\text{CT}} dN_R + \int \rho_{\mathfrak{R}}^{\text{CT}}(\mathbf{r}) dv_R(\mathbf{r}) d\mathbf{r}. \quad (240)$$

The second partial derivatives of this energy functional define the following charge sensitivities of the externally open reactive system R^{CT} in \mathfrak{R}^{CT} :

hardness:

$$\eta_{\mathfrak{R}}^{\text{CT}} = \left(\frac{\partial^2 E_{\mathfrak{R}}^{\text{CT}}[N_R, v_R]}{\partial N_R^2} \right)_{v_R} = \left(\frac{\partial \mu_{\mathfrak{R}}^{\text{CT}}[N_R, v_R]}{\partial N_R^2} \right)_{v_R}; \quad (241)$$

Fukui function:

$$\begin{aligned} f_{\mathfrak{R}}^{\text{CT}}(\mathbf{r}) &= \frac{\partial^2 E_{\mathfrak{R}}^{\text{CT}}[N_R, v_R]}{\partial N_R \partial v_R(\mathbf{r})} = \left(\frac{\partial \rho_{\mathfrak{R}}^{\text{CT}}(\mathbf{r})}{\partial N_R} \right)_{v_R} = \left(\frac{\partial \mu_{\mathfrak{R}}^{\text{CT}}}{\partial v_R(\mathbf{r})} \right)_{N_R} \\ &= f_A^{\text{CT}}(\mathbf{r}) + f_B^{\text{CT}}(\mathbf{r}); \end{aligned} \quad (242)$$

density response kernel:

$$\begin{aligned} \beta_{\mathfrak{R}}^{\text{CT}}(\mathbf{r}, \mathbf{r}') &= \left(\frac{\partial^2 E_{\mathfrak{R}}^{\text{CT}}[N_R, v_R]}{\partial v_R(\mathbf{r}) \partial v_R(\mathbf{r}')} \right)_{N_R} = \left(\frac{\partial \rho_{\mathfrak{R}}^{\text{CT}}(\mathbf{r}')}{\partial v_R(\mathbf{r})} \right)_{N_R} \\ &= \beta_{\mathfrak{R}}^{\text{CT}}(\mathbf{r}', \mathbf{r}), \end{aligned} \quad (243)$$

where the closure relation implies: $\int \beta_{\mathfrak{R}}^{\text{CT}}(\mathbf{r}, \mathbf{r}') d\mathbf{r}' = [\partial N_R / \partial v_R(\mathbf{r})]_{N_R} = 0$. These charge sensitivities determine the second differential of $E_{\mathfrak{R}}^{\text{CT}}[N_R, v_R]$:

$$\begin{aligned} d^2 E_{\mathfrak{R}}^{\text{CT}}[N_R, v_R] &= \frac{1}{2} \left\{ \eta_{\mathfrak{R}}^{\text{CT}} (dN_R)^2 + 2 dN_R \int f_{\mathfrak{R}}^{\text{CT}}(\mathbf{r}) dv_R(\mathbf{r}) d\mathbf{r} \right. \\ &\quad \left. + \iint dv_R(\mathbf{r}) \beta_{\mathfrak{R}}^{\text{CT}}(\mathbf{r}, \mathbf{r}') dv_R(\mathbf{r}') d\mathbf{r} d\mathbf{r}' \right\}. \end{aligned} \quad (244)$$

The corresponding relations for R^{P} in \mathfrak{R}^{P} , which define the first differential of $\tilde{E}_{v_R}[\rho_{\mathfrak{R}}^{\text{P}}] \equiv \tilde{E}_{\mathfrak{R}}^{\text{P}}[N_{\mathfrak{R}}^{\text{P}}, v_R]$ read:

$$\mu_{\mathfrak{R}}^{\text{P}} = \left(\frac{\partial \tilde{E}_{v_R}[\rho_{\mathfrak{R}}^{\text{P}}]}{\partial \rho_{\mathfrak{R}}^{\text{P}}(\mathbf{r})} \right)_{v_R}^{\text{T}} = \left(\frac{\partial \tilde{E}[N_{\mathfrak{R}}^{\text{P}}, v_R]}{\partial N_{\mathfrak{R}}^{\text{P}}} \right)_{v_R}^{\text{T}} = (\mu_A^+, \mu_B^+), \quad (245)$$

$$\rho_{\mathfrak{R}}^{\text{P}}(\mathbf{r}) = \left(\frac{\partial \tilde{E}[N_{\mathfrak{R}}^{\text{P}}, v_R]}{\partial v_R(\mathbf{r})} \right)_{N_{\mathfrak{R}}^{\text{P}}} = \rho_A^+(\mathbf{r}) + \rho_B^+(\mathbf{r}), \quad (246)$$

$$dE_{\mathfrak{R}}^{\text{P}}[N_{\mathfrak{R}}^{\text{P}}, v_R] = \mu_{\mathfrak{R}}^{\text{P}} dN_{\mathfrak{R}}^{\text{P,T}} + \int \rho_{\mathfrak{R}}^{\text{P}}(\mathbf{r}) dv_R(\mathbf{r}) d\mathbf{r}. \quad (247)$$

The second derivatives of this electronic energy define the following charge sensitivities of the mutually-closed but externally-open reactants in \mathfrak{R}^{P} :

hardnesses:

$$\eta_{\mathfrak{R}}^{\text{P}} = \left(\frac{\partial^2 \tilde{E}[N_{\mathfrak{R}}^{\text{P}}, v_R]}{\partial N_{\mathfrak{R}}^{\text{P}} \partial N_{\mathfrak{R}}^{\text{P}}} \right)_{v_R} = \left(\frac{\partial \mu_{\mathfrak{R}}^{\text{P}}}{\partial N_{\mathfrak{R}}^{\text{P}}} \right)_{v_R} = \{\eta_{\alpha, \beta}\}; \quad (248)$$

Fukui functions:

$$f_{\mathfrak{R}}^{\text{P}}(\mathbf{r}) = \frac{\partial^2 \tilde{E}[N_{\mathfrak{R}}^{\text{P}}, v_R]}{\partial N_{\mathfrak{R}}^{\text{P}} \partial v_R(\mathbf{r})} = \left(\frac{\partial \rho_{\mathfrak{R}}^{\text{P}}(\mathbf{r})}{\partial N_{\mathfrak{R}}^{\text{P}}} \right)_{v_R}^{\text{T}} = \left(\frac{\partial \mu_{\mathfrak{R}}^{\text{P}}}{\partial v_R(\mathbf{r})} \right)_{N_{\mathfrak{R}}^{\text{P}}} = \{f_{\alpha}^{\text{P}}(\mathbf{r})\}; \quad (249)$$

density response kernel:

$$\beta_{\mathfrak{R}}^{\text{P}}(\mathbf{r}, \mathbf{r}') = \left(\frac{\partial^2 \tilde{E}^{\text{P}}[N_{\mathfrak{R}}^{\text{P}}, v_R]}{\partial v_R(\mathbf{r}) \partial v_R(\mathbf{r}')} \right)_{N_{\mathfrak{R}}^{\text{P}}} = \left(\frac{\partial \rho_{\mathfrak{R}}^{\text{P}}(\mathbf{r}')}{\partial v_R(\mathbf{r})} \right)_{N_{\mathfrak{R}}^{\text{P}}} = \beta_{\mathfrak{R}}^{\text{P}}(\mathbf{r}', \mathbf{r}). \quad (250)$$

Since $dv_R(\mathbf{r}) = [dv_A(\mathbf{r})]_{v_B} = [dv_B(\mathbf{r})]_{v_A}$ one could also define the corresponding linear response matrix in reactant resolution:

$$\begin{aligned} \beta_{\mathfrak{R}}^{\text{P}}(\mathbf{r}, \mathbf{r}') &= \left(\frac{\partial^2 \tilde{E}^{\text{P}}[N_{\mathfrak{R}}^{\text{P}}, v_{\mathfrak{R}}^{\text{P}}]}{\partial v_{\mathfrak{R}}^{\text{P}}(\mathbf{r}) \partial v_{\mathfrak{R}}^{\text{P}}(\mathbf{r}')} \right)_{N_{\mathfrak{R}}^{\text{P}}} = \left(\frac{\partial \rho_{\mathfrak{R}}^{\text{P}}(\mathbf{r}')}{\partial v_{\mathfrak{R}}^{\text{P}}(\mathbf{r})} \right)_{N_{\mathfrak{R}}^{\text{P}}} \mathbf{I} = \mathbf{I}^{\text{T}} \left(\frac{\partial \rho_{\mathfrak{R}}^{\text{P}}(\mathbf{r}')}{\partial v_R(\mathbf{r})} \right)_{N_{\mathfrak{R}}^{\text{P}}} \mathbf{I} \\ &= \mathbf{I}^{\text{T}} \beta_{\mathfrak{R}}^{\text{P}}(\mathbf{r}', \mathbf{r}) \mathbf{I} = \{\beta_{\alpha, \beta}^{\text{P}}(\mathbf{r}', \mathbf{r}) = \beta_{\mathfrak{R}}^{\text{P}}(\mathbf{r}', \mathbf{r})\}, \end{aligned} \quad (251)$$

where $\tilde{E}_{\mathfrak{R}}^{\text{P}}[N_{\mathfrak{R}}^{\text{P}}, v_{\mathfrak{R}}^{\text{P}}] = \tilde{E}_{\mathfrak{R}}^{\text{P}}[N_{\mathfrak{R}}^{\text{P}}, v_R]$. Again, by the external closure relations

$$\begin{aligned} \int \beta_{\mathfrak{R}}^{\text{P}}(\mathbf{r}, \mathbf{r}') d\mathbf{r}' &= \left[\frac{\partial N_{\mathfrak{R}}^{\text{P}}}{\partial v_R(\mathbf{r})} \right]_{N_{\mathfrak{R}}^{\text{P}}} \\ &= \int \beta_{\alpha, \beta}^{\text{P}}(\mathbf{r}, \mathbf{r}') d\mathbf{r}' = \left[\frac{\partial N_{\beta}^{+}}{\partial v_{\alpha}(\mathbf{r})} \right]_{N_{\beta}^{+}} = 0, \end{aligned} \quad (252)$$

where $N_{\beta}^{+} = \int \rho_{\beta}^{+}(\mathbf{r}) d\mathbf{r}$, $\beta = A, B$.

The FF indices of equation (249) can be expressed in terms of the corresponding descriptors of equation (235) using the following chain-rule transformation:

$$\begin{aligned} f_{\alpha}^{\text{P}}(\mathbf{r}) &= \left(\frac{\partial \rho_{\mathfrak{R}}^{\text{P}}(\mathbf{r})}{\partial N_{\alpha}} \right)_{v_R} = \sum_{\beta} \sum_{\gamma} \left(\frac{\partial \rho_{\beta}^{+}(\mathbf{r})}{\partial N_{\gamma}} \right)_{v_R} \left(\frac{\partial N_{\gamma}}{\partial N_{\alpha}} \right)_{v_R} \\ &= \sum_{\beta} \sum_{\gamma} f_{\gamma, \beta} \delta_{\gamma, \alpha} = \sum_{\beta} f_{\alpha, \beta}. \end{aligned} \quad (253)$$

The derivatives of equations (248)–(251) define the associated second differential of $\tilde{E}_{\mathfrak{R}}^{\text{P}}[N_{\mathfrak{R}}^{\text{P}}, v_R]$:

$$\begin{aligned} d^2 \tilde{E}_{\mathfrak{R}}^{\text{P}}[N_{\mathfrak{R}}^{\text{P}}, v_R] &= \frac{1}{2} \left\{ dN_{\mathfrak{R}}^{\text{P}} \eta_{\mathfrak{R}}^{\text{P}} dN_{\mathfrak{R}}^{\text{P}, \text{T}} + 2 dN_{\mathfrak{R}}^{\text{P}} \int f_{\mathfrak{R}}^{\text{P}}(\mathbf{r})^{\text{T}} dv_R(\mathbf{r}) d\mathbf{r} \right. \\ &\quad \left. + \int \int dv_R(\mathbf{r}) \beta_{\mathfrak{R}}^{\text{P}}(\mathbf{r}, \mathbf{r}') dv_R(\mathbf{r}') d\mathbf{r} d\mathbf{r}' \right\}. \end{aligned} \quad (254)$$

Integration of the local FF indices of reactants (equations (234) and (235)) gives rise the corresponding condensed indices in the reactant resolution, measuring responses in the

overall number of electrons in each subsystem:

$$\mathbf{F}_{\mathfrak{R}}^{\text{CT}} = \int \mathbf{f}_{\mathfrak{R}}^{\text{CT}}(\mathbf{r}) d\mathbf{r} = \left(\frac{\partial N_{\mathfrak{R}}^{\text{CT}}}{\partial N_R} \right)_{v_R} = \left\{ \left(\frac{\partial N_A}{\partial N_R} \right)_{v_R}, \left(\frac{\partial N_B}{\partial N_R} \right)_{v_R} \right\} \equiv \{F_A, F_B\}, \quad (255)$$

$$\mathbf{F}_{\mathfrak{R}}^{\text{P}} = \int \mathbf{f}_{\mathfrak{R}}^{\text{P}}(\mathbf{r}) d\mathbf{r} = \left\{ \left(\frac{\partial N_{\beta}}{\partial N_{\alpha}} \right)_{v_R} = \delta_{\alpha,\beta} \right\}, \quad \alpha, \beta \in \{A, B\}. \quad (256)$$

The FF of the whole bimolecular system, reflected by the normalized responses of the overall density $\rho_R = \rho_A + \rho_B$ per unit shift in the global number of electrons N_R , are then given by the relevant combinations of these elementary responses of the externally open subsystems:

$$f_{\mathfrak{R}}^{\text{CT}}(\mathbf{r}) = \left(\frac{\partial \rho_{\mathfrak{R}}^{\text{CT}}(\mathbf{r})}{\partial N_R} \right)_{v_R} = f_A^{\text{CT}}(\mathbf{r}) + f_B^{\text{CT}}(\mathbf{r}), \quad (257)$$

$$f_{\mathfrak{R}}^{\text{P}}(\mathbf{r}) = \left(\frac{\partial \rho_{\mathfrak{R}}^{\text{P}}(\mathbf{r})}{\partial N_R} \right)_{v_R} = \sum_{\alpha,\beta} f_{\alpha,\beta}(\mathbf{r}) \\ = [f_{A,A}(\mathbf{r}) + f_{B,A}(\mathbf{r})] + [f_{A,B}(\mathbf{r}) + f_{B,B}(\mathbf{r})] \equiv f_A^{\text{P}}(\mathbf{r}) + f_B^{\text{P}}(\mathbf{r}), \quad (258)$$

where $\rho_{\mathfrak{R}}^{\text{CT}}$ and $\rho_{\mathfrak{R}}^{\text{P}}$ denote the overall electron densities of reactants in the externally-open systems \mathfrak{R}^{CT} and \mathfrak{R}^{P} , respectively. The $f_{\mathfrak{R}}^{\text{CT}}$ and f_{α}^{P} (or $f_{\alpha,\alpha}$) FF satisfy the familiar unity “normalization”:

$$\int f_{\mathfrak{R}}^{\text{CT}}(\mathbf{r}) d\mathbf{r} = \left(\frac{\partial N_R}{\partial N_R} \right)_{v_R} = 1, \\ \int f_{\alpha}^{\text{P}}(\mathbf{r}) d\mathbf{r} = \int f_{\alpha,\alpha}(\mathbf{r}) d\mathbf{r} = \left(\frac{\partial N_{\alpha}}{\partial N_{\alpha}} \right)_{v_R} = 1, \quad (259)$$

while the “off-diagonal” FF terms in subsystem resolution, reflecting the polarization of the closed reactant induced by the unit CT to/from the other reactant, must integrate to zero, *e.g.*,

$$\int f_{A,B}(\mathbf{r}) d\mathbf{r} = \left(\frac{\partial N_B}{\partial N_A} \right)_{v_R, N_B} = 0. \quad (260)$$

The reactant partitioning of the system overall electron density implies the two-component approach to reactive systems. The electrons of the mutually-open reactants in \mathfrak{R}^{CT} exhibit identical chemical potentials, equalized at the common reservoir level, $\mu_A^* = \mu_B^* = \mu_{\mathcal{R}}$, or in the equivalent matrix notation $\boldsymbol{\mu}_{\mathfrak{R}}^{\text{P}} = (\mu_A^*, \mu_B^*) = \mu_{\mathcal{R}} \mathbf{I}$, where $\mathbf{I} = (1, 1)$. In \mathfrak{R}^{P} the mutually-closed subsystems exhibit different chemical potentials: $\mu_{\mathcal{R}_A} = \mu_A^+ \neq \mu_B^+ = \mu_{\mathcal{R}_B}$, reflecting the populational derivatives of the two-component density-functional for the system electronic energy (equation (237)):

$$E_{v_R}[\rho_{\mathfrak{R}}^{\text{P}}] \equiv \tilde{E}_{v_R}[\boldsymbol{\rho}_{\mathfrak{R}}^{\text{P}}] = \int \rho_{\mathfrak{R}}^{\text{P}}(\mathbf{r}) v_R(\mathbf{r}) d\mathbf{r} + \tilde{F}[\boldsymbol{\rho}_{\mathfrak{R}}^{\text{P}}], \quad (261)$$

with the repulsive (universal, v_R -independent) part $\tilde{F}[\boldsymbol{\rho}_{\mathfrak{R}}^{\text{P}}]$ generating the sum of the electron kinetic and repulsion energies of the mutually-closed reactants. It is defined by the

Levy-type constrained-search construction [85]:

$$\tilde{F}[\rho_{\mathfrak{R}}^{\text{P}}] = \inf_{\Psi_A \rightarrow \rho_A^+, \Psi_B \rightarrow \rho_B^+} \langle \Psi_{\mathfrak{R}}^+ | \hat{T}_{\text{e}} + \hat{V}_{\text{ee}} | \Psi_{\mathfrak{R}}^+ \rangle, \quad \Psi_{\mathfrak{R}}^+ \in \{\mathcal{A}(\Psi_A \Psi_B)\}, \quad (262)$$

where the search is over all antisymmetrized products $\Psi_{\mathfrak{R}}^+$ of the subsystem wave functions Ψ_A and Ψ_B , which integrate to the prescribed densities of the mutually-closed, polarized reactants in \mathfrak{R}^{P} .

From the variational principle for the optimum (ground-state) densities of both reactants,

$$\delta \{ \tilde{E}_{v_R}[\rho_{\mathfrak{R}}^{\text{P}}] - \mu_{\mathfrak{R}}^{\text{P}} \mathbf{N}_{\mathfrak{R}}^{\text{P}}[\rho_{\mathfrak{R}}^{\text{P}}]^{\text{T}} \} = 0, \quad (263)$$

one derives the following Euler equations:

$$v_R(\mathbf{r}) - \mu_{\alpha}^+ \equiv u_{\alpha}^+(\mathbf{r}) = -\frac{\partial \tilde{F}[\rho_{\mathfrak{R}}^{\text{P}}]}{\partial \rho_{\alpha}^+(\mathbf{r})}, \quad \alpha = A, B. \quad (264)$$

Therefore, the relative external potentials of reactants, $\mathbf{u}_{\mathfrak{R}}^{\text{P}}(\mathbf{r}) = \mathbf{v}_{\mathfrak{R}}^{\text{P}}(\mathbf{r}) - \mu_{\mathfrak{R}}^{\text{P}} = \{u_A^{\text{P}}(\mathbf{r}), u_B^{\text{P}}(\mathbf{r})\}$, $\mathbf{v}_{\mathfrak{R}}^{\text{P}}(\mathbf{r}) = \{v_A^{\text{P}}(\mathbf{r}), v_B^{\text{P}}(\mathbf{r})\} \equiv v_R(\mathbf{r})\mathbf{I}$, are functionals of the subsystem densities: $\mathbf{u}_{\mathfrak{R}}^{\text{P}} = \mathbf{u}_{\mathfrak{R}}^{\text{P}}[\rho_{\mathfrak{R}}^{\text{P}}]$. This functional dependence defines the hardness representation in the reactant resolution. It also follows from equations (264) that in the complementary, softness representation the reactant densities can be regarded as functionals of the fragment relative external potentials: $\rho_{\mathfrak{R}}^{\text{P}} = \rho_{\mathfrak{R}}^{\text{P}}[\mathbf{u}_{\mathfrak{R}}^{\text{P}}]$. This defines the softness representation of the reactive system.

In the hardness representation one obtains the following expression for the first differential of $\mathbf{u}_{\mathfrak{R}}^{\text{P}}[\rho_{\mathfrak{R}}^{\text{P}}]$ in terms of the relevant hardness kernels of the reactant resolution:

$$\begin{aligned} du_{\alpha}^+(\mathbf{r}) &= dv_R(\mathbf{r}) - d\mu_{\alpha}^+ = -\sum_{\beta} \int d\rho_{\beta}^+(\mathbf{r}') \frac{\partial^2 \tilde{F}[\rho_{\mathfrak{R}}^{\text{P}}]}{\partial \rho_{\beta}^+(\mathbf{r}') \partial \rho_{\alpha}^+(\mathbf{r})} d\mathbf{r}' \\ &= \sum_{\beta} \int d\rho_{\beta}^+(\mathbf{r}') \frac{\delta u_{\alpha}^+(\mathbf{r}')}{\delta \rho_{\beta}^+(\mathbf{r}')} d\mathbf{r}' \equiv -\sum_{\beta} \int d\rho_{\beta}^+(\mathbf{r}') \eta_{\beta, \alpha}(\mathbf{r}', \mathbf{r}) d\mathbf{r}', \\ \alpha &= (A, B), \quad \text{or} \\ \Delta \mathbf{u}_{\mathfrak{R}}^{\text{P}}(\mathbf{r}) &= -\int \Delta \rho_{\mathfrak{R}}^{\text{P}}(\mathbf{r}') \boldsymbol{\eta}_{\mathfrak{R}}^{\text{P}}(\mathbf{r}', \mathbf{r}) d\mathbf{r}'. \end{aligned} \quad (265)$$

Here the elements of the square matrix of the hardness kernels in reactant resolution, $\boldsymbol{\eta}_{\mathfrak{R}}^{\text{P}}(\mathbf{r}', \mathbf{r}) = \{\eta_{\alpha, \beta}(\mathbf{r}', \mathbf{r})\}$, measure the negative responses of the relative external potential of subsystem β , per unit shift in the electron density of subsystem α . They transform displacements in the reactant electron densities $\Delta \rho_{\mathfrak{R}}^{\text{P}}$ into the concomitant responses $\Delta \mathbf{u}_{\mathfrak{R}}^{\text{P}}$ of the reactant effective relative potentials. Its inverse defines the square matrix of the corresponding softness kernels of these complementary molecular fragments, in the softness representation of this two-component reactive system:

$$\sigma_{\mathfrak{R}}^{\text{P}}(\mathbf{r}, \mathbf{r}') = -\frac{\delta \rho_{\mathfrak{R}}^{\text{P}}(\mathbf{r}')}{\delta \mathbf{u}_{\mathfrak{R}}^{\text{P}}(\mathbf{r})} = \left\{ \sigma_{\alpha, \beta}(\mathbf{r}, \mathbf{r}') = -\frac{\delta \rho_{\beta}^+(\mathbf{r}')}{\delta u_{\alpha}^+(\mathbf{r})} \right\} = \boldsymbol{\eta}_{\mathfrak{R}}^{\text{P}}(\mathbf{r}, \mathbf{r}')^{-1}. \quad (266)$$

It satisfies the following reciprocity relation:

$$\int \sigma_{\mathfrak{R}}^{\text{P}}(\mathbf{r}, \mathbf{r}') \boldsymbol{\eta}_{\mathfrak{R}}^{\text{P}}(\mathbf{r}', \mathbf{r}'') d\mathbf{r}'' = \delta(\mathbf{r} - \mathbf{r}'') \mathbf{I}^R, \quad (267)$$

where the 2×2 identity matrix $\mathbf{I}^R = \{\delta_{\alpha,\beta}\}$. These softness kernels transform displacements $\Delta \mathbf{u}_{\mathfrak{R}}^P$ of external potentials into the conjugate shifts $\Delta \boldsymbol{\rho}_{\mathfrak{R}}^P$ of electron densities:

$$\begin{aligned} d\rho_{\beta}^{+}(\mathbf{r}') &= - \sum_{\alpha} \int d\mathbf{u}_{\alpha}^{+}(\mathbf{r}) \sigma_{\alpha,\beta}(\mathbf{r}, \mathbf{r}') d\mathbf{r}, \quad \alpha = (A, B), \quad \text{or} \\ \Delta \boldsymbol{\rho}_{\mathfrak{R}}^P(\mathbf{r}') &= - \int \Delta \mathbf{u}_{\mathfrak{R}}^P(\mathbf{r}) \boldsymbol{\sigma}_{\mathfrak{R}}^P(\mathbf{r}, \mathbf{r}') d\mathbf{r} \\ &= - \int \Delta v_{\mathfrak{R}}^P(\mathbf{r}) \sigma_{\mathfrak{R}}^P(\mathbf{r}, \mathbf{r}') d\mathbf{r} + \Delta \mu_{\mathfrak{R}}^P \int \sigma_{\mathfrak{R}}^P(\mathbf{r}, \mathbf{r}') d\mathbf{r} \\ &\equiv - \int \Delta v_{\mathfrak{R}}^P(\mathbf{r}) \sigma_{\mathfrak{R}}^P(\mathbf{r}, \mathbf{r}') d\mathbf{r} + \Delta \mu_{\mathfrak{R}}^P \mathbf{s}_{\mathfrak{R}}^P(\mathbf{r}'), \end{aligned} \quad (268)$$

where the local softness matrix in subsystem resolution

$$\mathbf{s}_{\mathfrak{R}}^P(\mathbf{r}) = \left(\frac{\partial \boldsymbol{\rho}_{\mathfrak{R}}^P(\mathbf{r})}{\partial \mu_{\mathfrak{R}}^P} \right)_{v_R} = \int \boldsymbol{\sigma}_{\mathfrak{R}}^P(\mathbf{r}', \mathbf{r}) d\mathbf{r}' = \left\{ s_{\alpha,\beta}(\mathbf{r}) = \left(\frac{\partial \rho_{\beta}^{+}(\mathbf{r})}{\partial \mu_{\alpha}^{+}} \right)_{v_R} \right\}. \quad (269)$$

Writing $d\mu_{\mathfrak{R}}^P$ (of $d\mathbf{u}_{\mathfrak{R}}^P(\mathbf{r})$) as differential $d\tilde{\mu}_{\mathfrak{R}}^P[N_{\mathfrak{R}}^P, v_R]$ also gives (see equations (248) and (249)):

$$d\tilde{\mu}_{\mathfrak{R}}^P[N_{\mathfrak{R}}^P, v_R] = dN_{\mathfrak{R}}^P \boldsymbol{\eta}_{\mathfrak{R}}^P + \int dv_R(\mathbf{r}) f_{\mathfrak{R}}^P(\mathbf{r}) d\mathbf{r}. \quad (270)$$

It should be observed that the condensed hardness matrix $\boldsymbol{\eta}_{\mathfrak{R}}^P$ in this equation can be expressed in terms of the hardness kernels $\boldsymbol{\eta}_{\mathfrak{R}}^P(\mathbf{r}', \mathbf{r})$ of equation (265) using the relevant chain-rule transformation:

$$\begin{aligned} \boldsymbol{\eta}_{\mathfrak{R}}^P &= \iint \left(\frac{\partial \boldsymbol{\rho}_{\mathfrak{R}}^P(\mathbf{r}')}{\partial N_{\mathfrak{R}}^P} \right)_{v_R} \frac{\partial^2 \tilde{F}[\boldsymbol{\rho}_{\mathfrak{R}}^P]}{\partial \boldsymbol{\rho}_{\mathfrak{R}}^P(\mathbf{r}') \partial \boldsymbol{\rho}_{\mathfrak{R}}^P(\mathbf{r})} \left(\frac{\partial \boldsymbol{\rho}_{\mathfrak{R}}^P(\mathbf{r})}{\partial N_{\mathfrak{R}}^P} \right)_{v_R} d\mathbf{r} d\mathbf{r}' \\ &= \iint \mathbf{f}_{\mathfrak{R}}^P(\mathbf{r}') \boldsymbol{\eta}_{\mathfrak{R}}^P(\mathbf{r}', \mathbf{r}) \mathbf{f}_{\mathfrak{R}}^P(\mathbf{r})^T d\mathbf{r} d\mathbf{r}'. \end{aligned} \quad (271)$$

Combining equations (268) and (270) then gives

$$\begin{aligned} d\boldsymbol{\rho}_{\mathfrak{R}}^P(\mathbf{r}) &= dN_{\mathfrak{R}}^P \boldsymbol{\eta}_{\mathfrak{R}}^P \mathbf{s}_{\mathfrak{R}}^P(\mathbf{r}) - \int dv_{\mathfrak{R}}^P(\mathbf{r}') \boldsymbol{\sigma}_{\mathfrak{R}}^P(\mathbf{r}', \mathbf{r}) d\mathbf{r}' \\ &\quad + \left[\int dv_{\mathfrak{R}}^P(\mathbf{r}') \mathbf{f}_{\mathfrak{R}}^P(\mathbf{r}')^T d\mathbf{r}' \right] \mathbf{s}_{\mathfrak{R}}^P(\mathbf{r}). \end{aligned} \quad (272)$$

One can independently write this differential using the alternative functional dependence $\boldsymbol{\rho}_{\mathfrak{R}}^P[\mathbf{u}_{\mathfrak{R}}^P] = \boldsymbol{\rho}_{\mathfrak{R}}^P[N_{\mathfrak{R}}^P, v_R]$ (see equations (249)–(252)):

$$\begin{aligned} d\boldsymbol{\rho}_{\mathfrak{R}}^P(\mathbf{r}) &= dN_{\mathfrak{R}}^P \mathbf{f}_{\mathfrak{R}}^P(\mathbf{r}) + \int dv_{\mathfrak{R}}^P(\mathbf{r}') \boldsymbol{\beta}_{\mathfrak{R}}^P(\mathbf{r}', \mathbf{r}) d\mathbf{r}' \\ &= dN_{\mathfrak{R}}^P \mathbf{f}_{\mathfrak{R}}^P(\mathbf{r}) + \int dv_{\mathfrak{R}}^P(\mathbf{r}') \boldsymbol{\beta}_{\mathfrak{R}}^P(\mathbf{r}', \mathbf{r}) d\mathbf{r}'. \end{aligned} \quad (273)$$

A subsequent comparison between the preceding two equations gives the reactant-resolved generalization of the Berkowitz–Parr relation:

$$\mathbf{f}_{\mathfrak{R}}^P(\mathbf{r}) = \boldsymbol{\eta}_{\mathfrak{R}}^P \mathbf{s}_{\mathfrak{R}}^P(\mathbf{r}) \quad \text{or} \quad \mathbf{s}_{\mathfrak{R}}^P(\mathbf{r}) = \mathbf{S}_{\mathfrak{R}}^P \mathbf{f}_{\mathfrak{R}}^P(\mathbf{r}), \quad (274)$$

$$\begin{aligned}\beta_{\mathfrak{R}}^{\mathbf{P}}(\mathbf{r}', \mathbf{r}) &= -\sigma_{\mathfrak{R}}^{\mathbf{P}}(\mathbf{r}', \mathbf{r}) + \mathbf{f}_{\mathfrak{R}}^{\mathbf{P}}(\mathbf{r}')^{\mathbf{T}} \mathbf{S}_{\mathfrak{R}}^{\mathbf{P}}(\mathbf{r}) \\ &= -\sigma_{\mathfrak{R}}^{\mathbf{P}}(\mathbf{r}', \mathbf{r}) + \mathbf{f}_{\mathfrak{R}}^{\mathbf{P}}(\mathbf{r}')^{\mathbf{T}} \mathbf{S}_{\mathfrak{R}}^{\mathbf{P}} \mathbf{f}_{\mathfrak{R}}^{\mathbf{P}}(\mathbf{r}),\end{aligned}\quad (275)$$

where the condensed softness matrix is the inverse of the hardness matrix of equation (248):

$$\mathbf{S}_{\mathfrak{R}}^{\mathbf{P}} = (\boldsymbol{\eta}_{\mathfrak{R}}^{\mathbf{P}})^{-1} = \left\{ S_{\alpha, \beta} = \left(\frac{\partial N_{\beta}^{+}}{\partial \mu_{\alpha}^{+}} \right)_{v_R} \right\}. \quad (276)$$

The explicit transformation of “perturbations” $[\Delta N_{\mathfrak{R}}^{\mathbf{P}}, \Delta \mathbf{v}_{\mathfrak{R}}^{\mathbf{P}}(\mathbf{r}')]]$ into the ground-state conjugate responses $[\Delta \boldsymbol{\mu}_{\mathfrak{R}}^{\mathbf{P}}, \Delta \boldsymbol{\rho}_{\mathfrak{R}}^{\mathbf{P}}(\mathbf{r})]$ in the chemical softness representation can be summarized in the following matrix equation:

$$[\Delta \boldsymbol{\mu}_{\mathfrak{R}}^{\mathbf{P}}, \Delta \boldsymbol{\rho}_{\mathfrak{R}}^{\mathbf{P}}(\mathbf{r})] = \left[\Delta N_{\mathfrak{R}}^{\mathbf{P}}, \int d\mathbf{r}' \Delta \mathbf{v}_{\mathfrak{R}}^{\mathbf{P}}(\mathbf{r}') \right] \begin{bmatrix} \boldsymbol{\eta}_{\mathfrak{R}}^{\mathbf{P}} & \mathbf{f}_{\mathfrak{R}}^{\mathbf{P}}(\mathbf{r}) \\ \mathbf{f}_{\mathfrak{R}}^{\mathbf{P}}(\mathbf{r}')^{\mathbf{T}} & \beta_{\mathfrak{R}}^{\mathbf{P}}(\mathbf{r}', \mathbf{r}) \end{bmatrix}. \quad (277)$$

The inverse transformation, in the chemical hardness representation, reads

$$[\Delta N_{\mathfrak{R}}^{\mathbf{P}}, \Delta \mathbf{v}_{\mathfrak{R}}^{\mathbf{P}}(\mathbf{r})] = \left[\Delta \boldsymbol{\mu}_{\mathfrak{R}}^{\mathbf{P}}, \int d\mathbf{r}' \Delta \boldsymbol{\rho}_{\mathfrak{R}}^{\mathbf{P}}(\mathbf{r}') \right] \begin{bmatrix} \mathbf{0} & \mathbf{I} \\ \mathbf{I} & -\boldsymbol{\eta}_{\mathfrak{R}}^{\mathbf{P}}(\mathbf{r}', \mathbf{r}) \end{bmatrix}, \quad (278)$$

where $\mathbf{0}$ denotes the zero (2×2) square matrix.

To conclude this section we summarize the explicit expressions for the condensed charge sensitivities in reactant resolution [86] in terms of the canonical matrix of the subsystem hardnesses (248):

$$\boldsymbol{\eta}_{\mathfrak{R}}^{\mathbf{P}} = \begin{bmatrix} \eta_{A,A} & \eta_{A,B} \\ \eta_{B,A} & \eta_{B,B} \end{bmatrix}, \quad (279)$$

where by the Maxwell (cross-differentiation) identity $\eta_{A,B} = \eta_{B,A}$. The associated softness matrix is provided by the inverse of $\boldsymbol{\eta}_{\mathfrak{R}}^{\mathbf{P}}$:

$$\sigma_{\mathfrak{R}}^{\mathbf{P}} = (\boldsymbol{\eta}_{\mathfrak{R}}^{\mathbf{P}})^{-1} = \begin{bmatrix} \eta_{B,B}/D & -\eta_{A,B}/D \\ -\eta_{A,B}/D & \eta_{A,A}/D \end{bmatrix}, \quad (280)$$

where the determinant $D = \det \boldsymbol{\eta}_{\mathfrak{R}}^{\mathbf{P}} = \eta_{A,A}\eta_{B,B} - (\eta_{A,B})^2$. This matrix subsequently determines the respective fragment and global softnesses,

$$\begin{aligned}S_{\mathfrak{R}}^{\text{CT}} &= \left(S_A = \frac{\eta_B^R}{D}, S_B = \frac{\eta_A^R}{D} \right), \quad S_{\mathfrak{R}}^{\text{CT}} = \frac{1}{\eta_{\mathfrak{R}}^{\text{CT}}} = S_A + S_B, \\ \eta_A^R &= \eta_{A,A} - \eta_{A,B}, \quad \eta_B^R = \eta_{B,B} - \eta_{A,B},\end{aligned}\quad (281)$$

and hence the condensed Fukui functions of equation (255):

$$\mathbf{F}_{\mathfrak{R}}^{\text{CT}} = \left\{ F_A = S_A \eta_{\mathfrak{R}}^{\text{CT}} = \frac{\eta_B^R}{\eta_A^R + \eta_B^R}, F_B = S_B \eta_{\mathfrak{R}}^{\text{CT}} = \frac{\eta_A^R}{\eta_A^R + \eta_B^R} \right\}. \quad (282)$$

In atomic resolution, the functions and kernels of the local description are replaced by the corresponding vectors and square matrices of the AIM-condensed quantities, respectively, the dimensions of which are determined by the number of constituent atoms in each reactant. For the corresponding AIM development within the two-reactant approach the reader is referred to [2,4,6–8].

8.2. *In situ* quantities in donor–acceptor systems

In this section we shall examine selected *in situ* derivatives characterizing the internal (N_R -restricted) $B \rightarrow A$ CT process in the donor–acceptor (DA) reactive system $R = A-B \equiv (A^*|B^*)$, from the basic reactant B to its acidic partner A , for the fixed external potential $v_R(\mathbf{r}) = v_A(\mathbf{r}) + v_B(\mathbf{r})$ due to the nuclei of the constituent atoms of both reactants, *i.e.*, for the “frozen” geometry of the reactive system. Here, the vertical broken line symbolizes the freedom of the bonded, mutually-open but externally-closed reactants to exchange electrons. For simplicity we shall further assume, that the geometries of the isolated reactants A^0 and B^0 are held frozen in the DA complex R , so that there exists the unique “promolecular” reference of a reactive system, $R^0 \equiv (A^0|B^0)$, consisting of the free, “frozen”-geometry reactants shifted to their mutual orientation and separation in R . Above, the vertical solid line separating the non-bonded reactants in R^0 implies that they are both mutually and externally closed. For such an internal electron-transfer in R , for which the overall number of electrons $N_A + N_B = N_R$ is held fixed, the overall electron populations on reactants, $N_R = (N_A, N_B)$, which result from the integration of the subsystem densities $\rho_R = (\rho_A, \rho_B)$, $N_\alpha = \int \rho_\alpha(\mathbf{r}) d\mathbf{r}$, $\alpha = A, B$, determine the current amount of the internal (inter-reactant) CT in R :

$$\begin{aligned} N_{CT} &= N_A - N_A^0 = N_B^0 - N_B > 0 \quad \text{or} \\ N_R(N_{CT}) &= (N_A^0 + N_{CT}, N_B^0 - N_{CT}) \equiv N_R^0 + \Delta N_R(N_{CT}). \end{aligned} \quad (283)$$

The row vector $N_R^0 = (N_A^0, N_B^0)$ in the preceding equation groups the reference electron populations of the separate (free) reactants defining the promolecular system R^0 .

The amount of such an internal CT represents the independent “reaction coordinate” for the intra- R (inter-reactant) displacement of the system electronic structure. It should be observed, that for the equilibrium geometries of the isolated reactants, which determine the fragment (fixed) external potentials, the electron densities of the separated reactants are functions of their overall electron populations, $\rho_R^0 = \{\rho_\alpha^0(N_\alpha^0)\}$, since N_α^0 and $v_\alpha(\mathbf{r})$ uniquely identify the electronic Hamiltonian of the separated reactant α . A similar N_R -dependence characterizes the electron densities of the bonded reactants in R , $\rho_R = \{\rho_\alpha[N_R(N_{CT})] = \rho_\alpha(N_{CT})\}$, and the system electronic energy in the reactant resolution, $E_R = E_R[N_R(N_{CT})] = E_R(N_{CT})$, for the given amount of CT.

The *in situ* electron population derivatives [2,8,87,88] involve the differentiation with respect to the amount of internal CT. Equation (235) then implies the following internal, FF-like, populational derivatives along the internal CT-coordinate:

$$f_A = \left(\frac{dN_A}{dN_{CT}} \right)_{N_R} = 1 \quad \text{and} \quad f_B = \left(\frac{dN_B}{dN_{CT}} \right)_{N_R} = -1, \quad (284)$$

which enter the chain-rule expressions for the reactant *in situ* derivatives. For example, the energy conjugate of N_{CT} ,

$$\mu_{CT}(N_{CT}) = \frac{\partial E_R(N_{CT})}{\partial N_{CT}} = \frac{\partial E_R}{\partial N_A} f_A + \frac{\partial E_R}{\partial N_B} f_B = \mu_A(N_{CT}) - \mu_B(N_{CT}), \quad (285)$$

measures the relative chemical potential of two subsystems in R . The condition of the vanishing CT-gradient, $\mu_{CT}(N_{CT}^*) = 0$, then yields the equilibrium value of $N_{CT} = N_{CT}^*$, for which the chemical potentials of reactants in R are equalized: $\mu_A^*(N_{CT}^*) = \mu_B^*(N_{CT}^*)$. It represents the global equilibrium criterion for the DA reactive system.

One similarly obtains the following expression for the *in situ* hardness of the DA system:

$$\begin{aligned}
 \eta_{\text{CT}} &= \frac{\partial^2 E_R(N_{\text{CT}})}{\partial N_{\text{CT}}^2} = \frac{\partial \mu_{\text{CT}}}{\partial N_{\text{CT}}} = \frac{\partial \mu_A}{\partial N_A} f_A + \frac{\partial \mu_A}{\partial N_B} f_B - \frac{\partial \mu_B}{\partial N_A} f_A - \frac{\partial \mu_B}{\partial N_B} f_B \\
 &= (\eta_{A,A} - \eta_{B,A}) - (\eta_{A,B} - \eta_{B,B}) \equiv \eta_A^R + \eta_B^R \\
 &= \eta_{A,A} + \eta_{B,B} - 2\eta_{A,B},
 \end{aligned} \tag{286}$$

where η_α^R stands for the *in situ* hardness of reactant α in R (see also equation (281)). It should be emphasized, that the chemically interacting reactants at a finite mutual separation include the diagonal hardness, $\eta_{\alpha,\alpha} = \partial^2 E_R / \partial N_\alpha^2 = \partial \mu_\alpha / \partial N_\alpha \cong \eta_\alpha^0 = \partial^2 E_\alpha^0 / (\partial N_\alpha^0)^2 = \partial \mu_\alpha^0 / \partial N_\alpha^0$, modified by the finite coupling hardness, $\eta_{\beta,\alpha} = \partial^2 E_R / \partial N_\beta \partial N_\alpha = \partial \mu_\alpha / \partial N_\beta$, $\beta \neq \alpha$, due to the system complementary subsystem (a finite electron “reservoir”), which effectively softens the fragment α in R . This hardness coupling term vanishes at large separations between reactants, when $\eta_{\text{CT}}^0 = \eta_A^0 + \eta_B^0$.

Let us next consider the *in situ* softness quantities and the related FF indices of reactants in R . One first observes that the derivatives of equation (284) represent the condensed *in situ* FF indices of reactants. Their vanishing sum, $f_A + f_B = (\partial N_R / \partial N_{\text{CT}})_{N_R} = 0$, reflects the conservation of the overall number of electrons in the externally closed R . The relevant FF of reactants in R then follow from the following chain rules (see (235)):

$$f_A^{\text{CT}}(\mathbf{r}) = \frac{\partial \rho_A(\mathbf{r})}{\partial N_{\text{CT}}} = \frac{\partial \rho_A(\mathbf{r})}{\partial N_A} f_A + \frac{\partial \rho_A(\mathbf{r})}{\partial N_B} f_B = f_{A,A}(\mathbf{r}) - f_{B,A}(\mathbf{r}), \tag{287}$$

$$f_B^{\text{CT}}(\mathbf{r}) = \frac{\partial \rho_B(\mathbf{r})}{\partial N_{\text{CT}}} = \frac{\partial \rho_B(\mathbf{r})}{\partial N_A} f_A + \frac{\partial \rho_B(\mathbf{r})}{\partial N_B} f_B = f_{A,B}(\mathbf{r}) - f_{B,B}(\mathbf{r}). \tag{288}$$

They give rise to the overall *in situ* FF of R as a whole:

$$f_{\text{CT}}(\mathbf{r}) = \frac{\partial \rho_R(\mathbf{r})}{\partial N_{\text{CT}}} = f_A^{\text{CT}}(\mathbf{r}) + f_B^{\text{CT}}(\mathbf{r}). \tag{289}$$

The global CT softness is defined by the inverse of CT hardness of equation (286):

$$\begin{aligned}
 S_{\text{CT}} &= \frac{1}{\eta_{\text{CT}}} = \frac{\partial N_{\text{CT}}}{\partial \mu_{\text{CT}}} = \left(\frac{\partial N_A}{\partial \mu_{\text{CT}}} \right)_N = - \left(\frac{\partial N_B}{\partial \mu_{\text{CT}}} \right)_N \\
 &= (\eta_{A,A} + \eta_{B,B} - 2\eta_{A,B})^{-1}.
 \end{aligned} \tag{290}$$

The explicit expressions for $\eta_{\text{CT}} = \eta_{\text{RT}}^{\text{CT}}$ and $S_{\text{CT}} = S_{\text{RT}}^{\text{CT}}$ in terms of condensed hardnesses in reactant resolution, reported in equations (286) and (290), also directly follow from equation (281). Finally, by multiplying the subsystem FF of equations (287) and (288) by S_{CT} gives the *in situ* local softnesses of reactants in R :

$$s_{\text{CT}}(\mathbf{r}) = \{s_\alpha^{\text{CT}}(\mathbf{r}) = f_\alpha^{\text{CT}}(\mathbf{r}) S_{\text{CT}}\}. \tag{291}$$

The *in situ* charge sensitivities can be also defined in the partially condensed, atomic resolution of both reactants. These internal-CT derivatives can be also used to define the corresponding compliant and minimum-energy concepts for reactive systems [2,8,88].

8.3. Implications of equilibrium and stability criteria

The equalization of the reactant chemical potentials, $\mu_{\text{CT}} = 0$, constitutes the equilibrium criterion for the DA reactive system. The driving force for the inter-reactant CT is the initial *in situ* chemical potential of the ground-state electron distributions of the mutually closed, polarized reactants in \mathfrak{R}^{P} (see (245)):

$$\mu_{\text{CT}}^+ = \mu_{\text{CT}}(N_{\text{CT}} = 0) = \mu_A^+ - \mu_B^+ < 0. \quad (292)$$

The equalization of the reactant chemical potentials in \mathfrak{R}^{CT} (see (285)),

$$\begin{aligned} \mu_{\text{CT}}^*(N_{\text{CT}}^*) &= \mu_A^*(N_{\text{CT}}^*) - \mu_B^*(N_{\text{CT}}^*) = (\mu_A^+ + \eta_A^R N_{\text{CT}}^*) - (\mu_B^+ - \eta_B^R N_{\text{CT}}^*) \\ &= \mu_{\text{CT}}^+ + \eta_{\text{CT}} N_{\text{CT}}^* = 0, \end{aligned} \quad (293)$$

then gives the following two-reactant expression for the equilibrium amount of CT:

$$N_{\text{CT}}^*(\mu_{\text{CT}}^+) = -\frac{\mu_{\text{CT}}^+}{\eta_{\text{CT}}} = -\mu_{\text{CT}}^+ S_{\text{CT}}. \quad (294)$$

It should be emphasized, that both the initial chemical potential difference (292) and the effective *in situ* hardness (286) include the “embedding” terms due to the presence of the other reactant. Only at the very early stage of a reaction, at large inter-reactant separation, when there is little charge-coupling between the two species, can they be approximated by the separate-reactant quantities:

$$\mu_{\text{CT}}^+ \cong \mu_{\text{CT}}^0 = \mu_A^0 - \mu_B^0, \quad \eta_{\text{CT}} \cong \eta_{\text{CT}}^0 = \eta_A^0 + \eta_B^0, \quad (295)$$

where η_{α}^0 stands for the chemical hardness of the free reactant α . The coupling hardnesses $\eta_{A,B} = \eta_{B,A}$ were shown to be crucial for a realistic two-reactant description of the chemical reactivity trends in both the gas-phase and chemisorption processes [2,8,33,70,82,90].

The related *in situ* expression for the sum of the first- and second-order CT-energy terms reads:

$$E_{\text{CT}}^* = \mu_{\text{CT}}^+ N_{\text{CT}}^* + \frac{1}{2} \eta_{\text{CT}} (N_{\text{CT}}^*)^2 = \frac{1}{2} \mu_{\text{CT}}^+ N_{\text{CT}}^* (\mu_{\text{CT}}^+) = -\frac{1}{2} (\mu_{\text{CT}}^+)^2 S_{\text{CT}}. \quad (296)$$

It is proportional to the chemical potential difference for the polarized and initially mutually-closed reactants, marking the initial *in situ* chemical potential of R , and the amount of CT taking place, when the barrier for the flow of electrons between these two subsystems is removed. The last term of the preceding equation indicates that the overall dependence of the magnitude of the CT stabilization energy on the chemical potential difference is quadratic, with the *in situ* softness determining the proportionality constant.

Next, let us briefly summarize the stability requirements for molecular and reactive systems [2,8,89]. For simplicity we envisage a general partitioning of the system under consideration into two complementary subsystems A and B , *e.g.*, the two reactants of the DA reactive complex. There are two, *external* and *internal*, perspectives on the charge-stability in the bimolecular reactive system $\mathfrak{R}^{\text{CT}} = (\mathcal{R}^{\dagger} A^* | B^*)$ and its externally closed analog $R^* = (A^* | B^*)$, respectively.

We first assume the initial internal-equilibrium in R^* , marked by the equalized chemical potentials of both subsystems: $\mu_A^* = \mu_B^*$. The internal stability refers to hypothetical internal electronic displacements in R^* , $\delta N^*(\Delta) = (\delta N_A^*, \delta N_B^*) = (\Delta, -\Delta)$, reflected by the population-shift Δ , relative to the initial (equilibrium) electron popu-

lations $N^* = (N_A^*, N_B^*)$, which automatically preserve the overall number of electrons $N_R = N_A + N_B$. The charge distribution in R^* is stable, when any finite $\delta N^*(\Delta)$ implies an increase in the system electronic energy:

$$\delta E_{CT}(\Delta) = \frac{1}{2}\eta_{CT}\Delta^2 > 0 \quad \text{or} \quad \eta_{CT} > 0. \quad (297)$$

It then follows from equation (286), that this stability criterion can be transcribed into the following inequality in terms of the condensed hardnesses of reactants:

$$a \equiv \frac{\eta_{A,A} + \eta_{B,B}}{2} > \eta_{A,B} > 0. \quad (298)$$

Hence, the charge distribution of the reactive system is internally stable, when the arithmetic average a of the diagonal hardnesses $\{\eta_{\alpha,\alpha} > 0\}$ of both subsystems exceeds the magnitude of the coupling (off-diagonal) hardness between these two complementary fragments in R^* .

Next we assume the initial equilibrium between R^* and an external electron reservoir \mathcal{R} in $\mathfrak{R}^{CT} = (\mathcal{R}|A^*|B^*)$, *e.g.*, the surface of the heterogeneous catalyst. It implies the chemical potential equalization $\mu_A^* = \mu_B^* = \mu_{\mathcal{R}}$ and thus the vanishing first-order change in the system electronic energy due to the hypothetical electron exchange between the reactive system R^* and its reservoir \mathcal{R} . In order to diagnose the external stability, of the reactive system relative to its reservoir, one examines a virtual flow of electrons between these two subsystems, which generates the second-order change in the electronic energy of \mathfrak{R}^{CT} :

$$\delta E_{CT}(\delta N_R) = \frac{1}{2}\eta_R(\delta N_R)^2 > 0, \quad (299)$$

where $\eta_R = \partial^2 E_R[N_R, v_R]/\partial N_R^2 = \partial \mu_R[N_R, v_R]/\partial N_R$ denotes the chemical hardness of R^* as a whole. We have indicated above that in the externally-stable reactive system this charge displacement must increase the energy of the combined system \mathfrak{R}^{CT} . Expressing η_R in terms of the condensed hardnesses of reactants (248),

$$\eta_R = \frac{\eta_{A,A}\eta_{B,B} - (\eta_{A,B})^2}{\eta_{CT}}, \quad (300)$$

allows one to transcribe the external stability requirement in terms of the geometric average g of the diagonal hardnesses of both reactants:

$$g \equiv (\eta_{A,A}\eta_{B,B})^{1/2} > \eta_{A,B} > 0. \quad (301)$$

Therefore, for a reactive system to be externally stable the geometric average of the diagonal hardnesses of the mutually closed, polarized reactants must be higher than the coupling (off-diagonal) hardness.

In examining the stability regimes as functions of $\eta_{A,B} > 0$ one recalls that $g = [4a^2 - (\eta_{A,A} - \eta_{B,B})^2]^{1/2} < a$. In a typical region of the coupling hardness between the two reactants, $0 < \eta_{A,B} < \eta_{A,A}$, where we have recognized the acidic fragment as the electronically harder subsystem, $\eta_{A,A} > \eta_{B,B}$, one therefore obtains the following stability predictions for the externally open reactive system R^* :

$$\begin{aligned} 0 < \eta_{A,B} < g, & \quad \text{internally and externally stable;} \\ g \leq \eta_{A,B} < a, & \quad \text{internally stable and externally unstable;} \\ a \leq \eta_{A,B} < \eta_{A,A}, & \quad \text{internally unstable and externally stable.} \end{aligned}$$

Thus, the system exhibits both the internal and external stability in the weakly coupled reactants, when $\eta_{A,B} < g$. With an increase of the charge coupling between the two molecular subsystems, as measured by the inter-subsystem hardness, one first observes the onset of the external instability of R^* , relative to the electron reservoir, when the off-diagonal hardness reaches the critical value $\eta_{A,B} = g$. The second critical point for the stability prediction is $\eta_{A,B} = a$, above which the internal instability sets in, while the system regains the external stability. This precedence of the external instability before the internal one, when coupling between the two reactant increases, has qualitative implications for catalysis [2,8,89]. Indeed, one requires a smaller coupling between reactants to effect the charge instability involving the catalyst (external electron reservoir), compared to the inter-reactant coupling required to generate the internal instability in the gas phase. This subsequently triggers a reaction between the chemisorbed reactants. Specific examples of using the stability analysis in exploring reactivity trends of model chemisorption complexes and oxide clusters have been reported elsewhere [2,8,56,88,89].

8.4. Entropic charge sensitivities of reactants

It has been recently demonstrated that the Information Theory (IT) [91–93] can be successfully applied to extract an interpretation of molecular electron distributions in terms of bonded atoms [3,6,73,74,94,95] and chemical bonds [3,96–105]. The IT approach gives rise to a thermodynamic-like interpretation of electron densities of molecules and their fragments [3,106–110]. The promolecule-referenced partition of the molecular electron density into distributions of the molecular fragments can be carried out in the most unbiased manner by using an appropriate entropy-deficiency (information-distance) principle, which enforces the relevant molecular-distribution constraints. For example, such a division of the molecular electron density yields the Hirshfeld (stockholder) bonded atoms [72] or subsystems in the bimolecular reactive system, which preserve the maximum of the information contained in the distribution of the free (separate) fragments. Such entropic measures of the information similarity between the stockholder reactants and the corresponding reactants or products of chemical reactions have recently been used [111] to quantify the familiar (qualitative) Hammond postulate [112] in the theory of chemical reactivity. The electron localization function of DFT [113] has also been given an IT interpretation [114].

The information-theoretic approach to molecular subsystems generates the entropy-deficiency (information-distance, relative-entropy) representation, in which the molecular subsystems satisfy the thermodynamic-like variational principles [3,106–110]. The derivatives of these cross-entropy descriptors of molecular fragments influence the reactivity indices of reacting species [115]. In this section we shall introduce the charge-affinity concept for molecular subsystems, *e.g.*, reactants in $R^P = (A^+|B^+)$, which combine the derivative quantities defined in the complementary energy and entropy representations of molecules and their fragments.

As we have already remarked above, the entropy-equilibrium densities $\rho_R^P = \rho_R^P(N_R^0) = (\rho_A^+, \rho_B^+)$ of the polarized, mutually-closed reactants in the externally-closed reactive system R^P , for $N_R^P = N_R^0 = (N_A^0, N_B^0)$, can be obtained from the relevant minimum entropy-deficiency principle of IT [3,116]. For the fixed value of $N_R^+ = N_A^+ + N_B^+ = N_A^0 + N_B^0 = N_R^0$, only one global Lagrange multiplier, say for A^+ , $N_A^+ = N_A^0$, is required

to simultaneously enforce the specified number of electrons on the other reactant in a search for the optimum densities of both reactants, which yield the given molecular distribution of electrons. Indeed, the requirement of an exhaustive local division of the given overall density, that the optimum subsystem densities reproduce at each point in space the given density of R^P as a whole, $\sum_{\alpha=A,B} \rho_{\alpha}^+(\mathbf{r}) = \rho_R^P(\mathbf{r})$, already enforces the global constraint of the specified number of electrons in the system as a whole:

$$\int \rho_R^P(\mathbf{r}) d\mathbf{r} = N_R^P = N_A^+ + N_B^+ = N_R^0. \quad (302)$$

This is indeed the case in the Hirshfeld division scheme. Hence, it is sufficient to satisfy the global subsidiary condition on one reactant, say $\int \rho_A^+(\mathbf{r}) d\mathbf{r} = N_A^+ = N_A^0$, to simultaneously guarantee the closure constraint of the other reactant: $\int \rho_B^+(\mathbf{r}) d\mathbf{r} = N_B^+ = N_B^0$.

To enforce the local constraint of the exhaustive division, one has to use the appropriate Lagrange multiplier function $\lambda(\mathbf{r})$ in the variational principle for the minimum of the entropy-deficiency in the reactant resolution,

$$\Delta S[\rho_R | \rho_R^0] = \sum_{\alpha=A,B} \int \rho_{\alpha}(\mathbf{r}) \ln \frac{\rho_{\alpha}(\mathbf{r})}{\rho_{\alpha}^0(\mathbf{r})} d\mathbf{r}, \quad (303)$$

subject to the appropriate local and global constraints. The optimum densities ρ_R^P correspond to the stationary point of the auxiliary functional

$$\begin{aligned} & \delta \mathcal{L}[\rho_R^P | N_A^0, \rho_R^0, \rho_R^P] \\ & \equiv \delta \left\{ \Delta S[\rho_R^P | \rho_R^0] - \int \lambda(\mathbf{r}) [\rho_A^+(\mathbf{r}) + \rho_B^+(\mathbf{r})] d\mathbf{r} - \lambda_A \int \rho_A^+(\mathbf{r}) d\mathbf{r} \right\} = 0. \end{aligned} \quad (304)$$

Above, the auxiliary information-distance $\mathcal{L}[\rho_R^P | N_A^0, \rho_R^0, \rho_R^P]$ depends upon the two “variable” functions $\rho_R^P = (\rho_A, \rho_B)$ and involves the free-reactant references ρ_R^0 and the constraint-terms corresponding to the fixed local and global “parameters”, $\rho_R^P(\mathbf{r}) = \rho_R(\mathbf{r})$ and $N_A^+ = N_A^0$, respectively. Its first term represents the information “penalty” for the optimum subsystem densities deviating from their free-reactant distributions, while the remaining terms enforce the local and global constraints through the Lagrange multipliers $\lambda(\mathbf{r})$ and λ_A .

The minimum of the entropy deficiency between the polarized densities of subsystems ρ_R^P and the reference densities ρ_R^0 of the separated reactants of the same (“frozen”) internal geometry as in R^P , implies the maximum information “similarity” between the equilibrium subsystem densities and the corresponding electron distributions of the separate reactants. The second term in equation (304) enforces the local constraint of the conserved density of R^P as a whole, while the last term guarantees the prescribed overall number of electrons in the internally polarized A^+ . As we have argued above, these two subsidiary conditions automatically guarantee the complementary number of electrons in B^+ .

The resulting Euler equations for the optimum densities $\rho_R^P = (\rho_A^+, \rho_B^+)$ of the polarized-reactants are generated by the vanishing functional derivatives:

$$\begin{aligned} \left. \frac{\delta \mathcal{L}}{\delta \rho_A(\mathbf{r})} \right|_{\rho_{\text{gr}}^P} &= \ln \frac{\rho_A^+(\mathbf{r})}{\rho_A^0(\mathbf{r})} + 1 - \lambda(\mathbf{r}) - \lambda_A \equiv \ln \frac{\rho_A^+(\mathbf{r})}{\rho_A^0(\mathbf{r}) C_A(\mathbf{r})} = 0, \\ \left. \frac{\delta \mathcal{L}}{\delta \rho_B(\mathbf{r})} \right|_{\rho_{\text{gr}}^P} &= \ln \frac{\rho_B^+(\mathbf{r})}{\rho_B^0(\mathbf{r})} + 1 - \lambda(\mathbf{r}) \equiv \ln \frac{\rho_B^+(\mathbf{r})}{\rho_B^0(\mathbf{r}) C_B(\mathbf{r})} = 0, \end{aligned} \quad (305)$$

where $C_B(\mathbf{r}) \equiv \exp[\lambda(\mathbf{r}) - 1]$ and $C_A(\mathbf{r}) = \exp(\lambda_A)C_B(\mathbf{r}) \equiv CC_B(\mathbf{r})$. Hence,

$$\rho_A^+(\mathbf{r}) = \rho_A^0(\mathbf{r})C_A(\mathbf{r}) \quad \text{and} \quad \rho_B^+(\mathbf{r}) = \rho_B^0(\mathbf{r})C_B(\mathbf{r}). \quad (306)$$

The local constraint then gives the following expression for $C_B(\mathbf{r})$ in terms of C ,

$$C_B(\mathbf{r}) = \frac{\rho_R^P(\mathbf{r})}{C\rho_A^0(\mathbf{r}) + \rho_B^0(\mathbf{r})}, \quad (307)$$

while the global constraint generates the integral equation for determining C :

$$N_A^+ = N_A^0 = C \int \frac{\rho_A^0(\mathbf{r})\rho_R^P(\mathbf{r})}{C\rho_A^0(\mathbf{r}) + \rho_B^0(\mathbf{r})} d\mathbf{r}. \quad (308)$$

It can be straightforwardly verified, that one recovers the stockholder solutions for $\lambda_A = 0$ ($C = 1$), when the global constraint in equation (304) is absent, so that both subsystems can freely exchange electrons in $R^{\text{CT}} = (A^*|B^*)$.

Clearly, one can enforce in this way any admissible value of the average electron populations of subsystems, $N_A \neq N_A^0$ and the associated value of $N_B = N_R - N_A \neq N_B^0$, defining the population vector $\mathbf{N}_R = (N_A, N_B)$ and determining the associated densities $\rho_R = \rho_R(\mathbf{N}_R)$. The entropic variational principle (304) also applies to the externally open reactive system $\mathfrak{R}^P = (\mathcal{R}_A|A^+|B^+|\mathcal{R}_B)$, when $N_R = \int \rho_R^P(\mathbf{r}) d\mathbf{r} = N_A^+ + N_B^+ \neq N_R^0$. Again, no separate global Lagrange multipliers are required to guarantee the prescribed average numbers of electrons on both reactants, since the local constraint enforces the right average number of electrons in the system as a whole.

In other words, this minimum entropy-deficiency rule allows one to determine the equilibrium reactant densities, which at the same time reproduce the exact density of the reactive system as a whole, thus conserving the number of electrons in the whole reactive complex, and carry the prescribed average electron populations on both reactants. This principle introduces a unique dependence of the subsystem densities on their average numbers of electrons in R : $\rho_R = \rho_R(\mathbf{N}_R)$. This feature allows one to uniquely define the subsystem FF descriptors of equation (235). It also establishes the entropy-deficiency functional as the function of the global electron populations of both reactants:

$$\Delta S[\rho_R(\mathbf{N}_R)|\rho_R^0] \equiv \Delta \tilde{S}(\mathbf{N}_R). \quad (309)$$

Let us define the row vector of the entropy-deficiency conjugates of electron populations \mathbf{N}_R , $\Phi_R = \partial \Delta \tilde{S}(\mathbf{N}_R)/\partial \mathbf{N}_R = \{\Phi_A, \Phi_B\}$. Using the functional chain-rule gives

$$\begin{aligned} \Phi_\alpha &= \frac{\partial \Delta S[\rho_R(\mathbf{N}_R)|\rho_R^0]}{\partial N_\alpha} \\ &= \sum_\beta \int \frac{\partial \Delta S[\rho_R(\mathbf{N}_R)|\rho_R^0]}{\partial \rho_\beta(\mathbf{r})} \frac{\partial \rho_\beta(\mathbf{r})}{\partial N_\alpha} d\mathbf{r} \\ &\equiv \sum_\beta \int S_\beta(\mathbf{r}) f_{\alpha,\beta}(\mathbf{r}) d\mathbf{r}, \quad \alpha = A, B, \end{aligned} \quad (310)$$

or in the compact matrix form:

$$\Phi_R = \int S_R(\mathbf{r}) \mathbf{f}_{\mathfrak{R}}^P(\mathbf{r})^T d\mathbf{r}. \quad (311)$$

Here the row vector $\mathbf{S}_R(\mathbf{r}) = [S_A(\mathbf{r}), S_B(\mathbf{r})]$ groups the entropy-deficiency conjugates of the reactant densities:

$$\mathbf{S}_R(\mathbf{r}) = \frac{\partial \Delta S[\rho_R(N_R)|\rho_R^0]}{\partial \rho_R(\mathbf{r})} = \left\{ \ln \frac{\rho_A(\mathbf{r})}{\rho_A^0(\mathbf{r})} + 1, \ln \frac{\rho_B(\mathbf{r})}{\rho_B^0(\mathbf{r})} + 1 \right\} \quad (312)$$

and the FF-matrix $\mathbf{f}_{\mathfrak{R}}^P(\mathbf{r})$ is defined in equation (235). It should be observed that the first-order expansion of the logarithms in the preceding equation gives,

$$S_\alpha(\mathbf{r}) = \ln \frac{\rho_\alpha^0(\mathbf{r}) + \Delta \rho_\alpha(\mathbf{r})}{\rho_\alpha^0(\mathbf{r})} + 1 \cong \frac{\Delta \rho_\alpha(\mathbf{r})}{\rho_\alpha^0(\mathbf{r})} + 1 = \frac{\rho_\alpha(\mathbf{r})}{\rho_\alpha^0(\mathbf{r})}, \quad (313)$$

where $\rho_\alpha(\mathbf{r}) \equiv \rho_\alpha^0(\mathbf{r}) + \Delta \rho_\alpha(\mathbf{r}) \cong \rho_\alpha^0(\mathbf{r})$ and hence $|\Delta \rho_\alpha(\mathbf{r})/\rho_\alpha^0(\mathbf{r})| \ll 1$.

The FF-type quantities in the entropy-deficiency representation (see (310) and (311)), define the CT affinities (CTA) of reactants [3,6,115], which represent generalized derivative (“force”) indices of reactants measuring the “intensities” associated with the “extensive” electron population variables N_R . They combine the entropy ($\mathbf{S}_R(\mathbf{r})$) and energy ($\mathbf{f}_{\mathfrak{R}}^P(\mathbf{r})$) derivatives, providing more adequate CT indices, which recognize the information-distance dependence of charge sensitivities of molecular subsystems. A presence of the cross-entropy factors in CTA should not come as a surprise, since the unique, unbiased definition of molecular fragments indeed requires the entropy-deficiency representation.

It should be stressed that the equilibrium condition in the *energy* representation alone, represented by the equalization of the subsystem chemical potentials (electronegativities), is insufficient to define the equilibrium partitioning of the electron density of the whole molecular system into the densities of the reactant subsystems. For their unique, unbiased definition the minimum principle of the promolecule-referenced entropy deficiency is thus required [3]. The generalized, entropic FF-type indices of equation (311) reflect the effect of the information-theoretic origin of molecular stockholder subsystems upon the charge affinities of reactants in this entropy representation.

A reference to equation (283) shows that electron populations in R^P , $N_R = (N_A = N_A^0 + N_{CT}, N_B = N_B^0 - N_{CT}) \equiv N_R(N_{CT})$ are linear functions of the amount of the internal CT in R^P , N_{CT} , which represents the independent variable measuring the progress of such internal $B \rightarrow A$ charge flow. Therefore, of interest in the theory of chemical reactivity is also the *in situ* derivative of the entropy deficiency with respect to this relative electronic “reaction coordinate” [2,8]:

$$\begin{aligned} \Phi_{CT} &= \frac{\partial \Delta S[\rho_R(N_R(N_{CT}))|\rho_R^0]}{\partial N_{CT}} = \sum_{\alpha} \left(\frac{\partial \Delta S[\rho_R(N_R(N_{CT}))|\rho_R^0]}{\partial N_{\alpha}} \right) \left(\frac{\partial N_{\alpha}}{\partial N_{CT}} \right)_{N_R} \\ &= \Phi_A - \Phi_B \\ &= \int \{ [f_{A,A}(\mathbf{r}) - f_{B,A}(\mathbf{r})] S_A(\mathbf{r}) + [f_{A,B}(\mathbf{r}) - f_{B,B}(\mathbf{r})] S_B(\mathbf{r}) \} d\mathbf{r} \\ &\equiv \int \{ f_A^{CT}(\mathbf{r}) S_A(\mathbf{r}) + f_B^{CT}(\mathbf{r}) S_B(\mathbf{r}) \} d\mathbf{r}, \end{aligned} \quad (314)$$

where the reactant *in situ* FF of reactants, $\mathbf{f}_{CT}(\mathbf{r}) = [f_A^{CT}(\mathbf{r}), f_B^{CT}(\mathbf{r})]$ (see (287) and (288)) group the subsystem partial derivatives for the frozen external potential $v_R(\mathbf{r})$:

$$\mathbf{f}_{CT}(\mathbf{r}) = \frac{\partial \rho_R(\mathbf{r})}{\partial N_{CT}}. \quad (315)$$

As indicated in the second line of equation (314), the *in situ* CTA Φ_{CT} of the donor–acceptor system, representing the FF-type derivative in the entropy-deficiency representation with respect to the amount of CT between reactants, is measured by the difference between the CT-affinities of the acidic and basic subsystems.

In the ρ_R^{CT} -constrained (“vertical”) CT problem one determines the equilibrium entropy-deficiency partition of the fixed density $\rho_R(\mathbf{r})$ of the reactive system R^{CT} among the two reactant subsystems, when the barrier preventing the inter-reactant CT is lifted. This implies $\lambda_A = 0$ in the information principle (304) and gives rise to the Hirshfeld reactant densities, $\rho_R^H(\mathbf{r}) = [\rho_A^H(\mathbf{r}), \rho_B^H(\mathbf{r})]$, and the associated electron populations $N_R^H = \{N_\alpha^H = \int \rho_\alpha^H d\mathbf{r}\}$. For this equilibrium division between the mutually-open subsystems in the externally-closed reactive system, $\rho_R(\mathbf{r}) = \rho_A^H(\mathbf{r}) + \rho_B^H(\mathbf{r})$, the subsystem entropic intensities of equation (312) are equalized at the global value describing the reactive complex as a whole:

$$S_A^H(\mathbf{r}) = S_B^H(\mathbf{r}) = S_R(\mathbf{r}) = \ln \frac{\rho_R(\mathbf{r})}{\rho_R^0(\mathbf{r})} + 1 \equiv \ln w_R(\mathbf{r}) + 1, \quad (316)$$

where $\rho_R^0(\mathbf{r}) = \rho_A^0(\mathbf{r}) + \rho_B^0(\mathbf{r})$ denotes the electron density of the promolecular reference R^0 .

Since $\sum_\beta f_{\alpha,\beta}(\mathbf{r}) = \partial \rho_R(\mathbf{r}) / \partial N_\alpha$ (see (253)), the preceding equation gives rise to the vanishing subsystem CTA for the ρ_R -constrained (“vertical”) CT between reactants in R^{CT} (identified by the subscript ρ),

$$\begin{aligned} (\Phi_\alpha^H)_\rho &= \int S_R(\mathbf{r}) \sum_\beta f_{\alpha,\beta}(\mathbf{r}) d\mathbf{r} \\ &= \int S_R(\mathbf{r}) \left[\frac{\partial \rho_R(\mathbf{r})}{\partial N_\alpha} \right]_\rho d\mathbf{r} = 0, \quad \alpha = A, B, \end{aligned} \quad (317)$$

thus confirming the entropy-equilibrium character of the Hirshfeld densities of reactants. Using equation (314) also gives

$$(\Phi_{CT}[\rho_R^H])_\rho = (\Phi_A^H)_\rho - (\Phi_B^H)_\rho = 0. \quad (318)$$

To summarize, the Hirshfeld reactants in the donor–acceptor reactive system $R^{CT} = (A^H|B^H)$ do indeed correspond to the equilibrium amount of the vertical-CT. We have explicitly demonstrated that the internal CTAs, *i.e.*, “forces” behind the charge flow between reactants combining the entropy deficiency intensities and the FFs of reactants, identically vanish for the Hirshfeld acidic and basic subsystems.

One similarly defines in the reactant resolution the corresponding second-order population derivatives of the entropy deficiency, which define the information-stiffnesses of the two subsystems. First, we introduce the square matrix of the populational derivatives of CTA in the linear-response approximation:

$$\begin{aligned} \Lambda_R &= \frac{\partial \Phi_R}{\partial N_R} = \left\{ \Lambda_{\alpha,\beta} = \frac{\partial \Phi_\beta}{\partial N_\alpha} \right\} \\ &= \int \frac{\partial S_R(\mathbf{r})}{\partial N_R} \mathbf{f}_{\mathfrak{N}}^P(\mathbf{r})^T d\mathbf{r} \equiv \int \Theta_R(\mathbf{r}) \mathbf{f}_{\mathfrak{N}}^P(\mathbf{r})^T d\mathbf{r}, \end{aligned} \quad (319)$$

where the square matrix of the local entropic sensitivities

$$\Theta_R(\mathbf{r}) = \left\{ \Theta_{\alpha,\beta}(\mathbf{r}) = \frac{\partial S_\beta(\mathbf{r})}{\partial N_\alpha} = \frac{\partial^2 \Delta S[\rho_R(N_R)|\rho_R^0]}{\partial \rho_\beta(\mathbf{r}) \partial N_\alpha} = \frac{f_{\alpha,\beta}(\mathbf{r})}{\rho_\beta(\mathbf{r})} \right\}. \quad (320)$$

It thus follows from the preceding two equations that

$$\Lambda_{\alpha,\beta} = \sum_{\gamma} \int f_{\alpha,\gamma}(\mathbf{r}) \rho_{\gamma}(\mathbf{r})^{-1} f_{\beta,\gamma}(\mathbf{r}) d\mathbf{r}, \quad (321)$$

or in the matrix form

$$\mathbf{\Lambda}_R = \int \mathbf{f}_{\mathcal{R}}^{\mathbf{P}}(\mathbf{r}) \mathbf{g}(\mathbf{r}) \mathbf{f}_{\mathcal{R}}^{\mathbf{P}}(\mathbf{r})^T d\mathbf{r}, \quad \mathbf{g}(\mathbf{r}) \equiv \{\rho_{\beta}(\mathbf{r})^{-1} \delta_{\alpha,\beta}\}. \quad (322)$$

The corresponding *in situ* information-stiffnesses of reactants are similarly defined as derivatives with respect to the amount of the internal CT:

$$\Lambda_R^{\text{CT}} = \frac{\partial \Phi_R}{\partial N_{\text{CT}}} = \{\Lambda_A^{\text{CT}} = \Lambda_{A,A} - \Lambda_{B,A}, \Lambda_B^{\text{CT}} = \Lambda_{A,B} - \Lambda_{B,B}\}. \quad (323)$$

They in turn determine the *in situ* information-stiffness of the whole reactive system:

$$\Lambda_{\text{CT}} = \frac{\partial \Phi_{\text{CT}}}{\partial N_{\text{CT}}} = \Lambda_A^{\text{CT}} - \Lambda_B^{\text{CT}} = \Lambda_{A,A} + \Lambda_{B,B} - 2\Lambda_{A,B}. \quad (324)$$

9. CONCLUSION

In this survey we have examined alternative quantities describing molecular responses to both electronic and nuclear perturbations, within the electron-preceding and electron-following perspectives on molecular structure. Basic quantities and relations of CSA have been summarized for both the externally closed and open molecular systems, and transformations between the system perturbations, displacements of independent state-parameters, and the linear-responses in their conjugate (unconstrained) state-variables have been examined in alternative Legendre-transformed representations. A special emphasis has been placed upon the so-called geometrical representations, in which the nuclear coordinates replace the external potential due to nuclei in the list of the system state-parameters. Specific quantities reflecting the coupling between the geometrical and electronic structures of molecular systems have also been identified and discussed.

All chemical or conformational changes involve both nuclear displacements and the concomitant electron redistributions. By the Hohenberg–Kohn theorem of DFT the non-degenerate ground-state electron density of a molecule is in one-to-one correspondence with the underlying external potential due to the system nuclei. In a given stage of the system displacement, depending on what is considered as “perturbation” and what the equilibrium “response” to it, the electron-following or the electron-preceding approaches can be adopted. The mapping relations of CSA in the atomic resolution provide an explicit and transparent framework for discussing these ground-state relations between the Electron Population Space (EPS) and Nuclear-Position Space (NPS) characteristics of molecular systems. The nature of the atomic discretization of the electronic and nuclear state-variables has been examined. It has been stressed, that a division of the molecular electron distribution among constituent fragments can be facilitated using the unbiased principle of the minimum of the promolecule-referenced entropy-deficiency of IT. The resulting shape-factors of molecular fragments can then be used to discretize the molecular external potential.

In examining the electronic–geometric coupling in molecular systems one is interested in adequately “translating” the reaction-coordinate representations in both the EPS and NPS, one into the other. The relevant mapping relations in atomic resolution generate a useful framework for relating the minimum-energy-paths in these alternative reference-frames. They have profound implications for catalysis and the theory of chemical reactivity in general. More specifically, a desired geometrical (bond-stretch) NPS-displacement can be translated into the associated EPS-shift, and *vice versa*. One can thus transform the selected EPS-channels of the electron redistribution, *e.g.*, the electronic minimum-energy coordinates (MEC) of the nuclear and/or electronic compliant formalisms, the population normal modes (PNM) or the system internal normal modes (INM), into their respective NPS-conjugates. The numerical data for a variety of illustrative molecular and reactive systems have amply demonstrated in the past the physical significance of the PNM reference frame. The latter are almost indistinguishable from the INM, having only an additional channel, the hardest pure-CT mode, having practically identical displacements of electron populations on all constituent AIM. The softest PNM or INM is most relevant for diagnosing the chemical reactivity phenomena, since it is energetically most accessible, requiring the least activation (promotion) energy.

The vibrational normal modes (VNM) of the system nuclei are known to have physical meaning at low energies (amplitudes). These “natural”, independent vibrations were shown to uniquely “translate” in simple polyatomics into the corresponding “natural” polarizations represented by the system softest PNM (or INM). The system geometrical/electronic structure relaxations were also shown to take place along a very few MEC and normal modes, in both the NPS and EPS representations. The one-to-one character of some normal mappings is important for both the interpretative and predictive purposes. The successful applications of the PNM reactivity criteria can be thus given a more conventional, NPS rationalization, when the [collective–collective]-translators are dominated by the one-to-one correspondences between NPS and EPS modes. Indeed, electrons in such systems relax along a single INM/PNM in response to a geometrical distortion along the conjugated VNM.

The qualitative trends in variations of the molecular geometry due to charge displacements in the donor–acceptor systems can be also predicted using the empirical Gutmann rules of structural chemistry. The mapping concepts of the DFT/CSA approach, which provide them a sound theoretical basis, should facilitate a better understanding of the physical origins of these rules. The semiquantitative EP-rules in reactant resolution should be useful in establishing the best complementary matching of reactants, and in facilitating an understanding of the hierarchy of the direct and induced flows of electrons in elementary chemical reactions.

Specific concepts for reactive systems have also been outlined, for both the externally-closed and open reactants. The corresponding charge sensitivities in reactant resolution have been introduced, and the so-called *in situ* derivative descriptors of the Donor–Acceptor complexes have been discussed in a more detail. The implications of the electronic stability criteria of reactants have been established and their implications for the chemical reactivity, *e.g.*, in catalysis, have been briefly discussed. Finally, the novel descriptors of molecular fragments, which unite their energetic and entropic response quantities, have been proposed. Such generalized charge-affinities and stiffness moduli from DFT and IT represent attractive tools for indexing and diagnosing molecular reactivity phenomena.

REFERENCES

- [1] R.G. Parr, W. Yang, *Density-Functional Theory of Atoms and Molecules*, Oxford Univ. Press, New York, 1989.
- [2] R.F. Nalewajski, J. Korchowiec, *Charge Sensitivity Approach to Electronic Structure and Chemical Reactivity*, World Scientific, Singapore, 1997.
- [3] R.F. Nalewajski, *Information Theory of Molecular Systems*, Elsevier, Amsterdam, 2006.
- [4] R.F. Nalewajski, Charge sensitivities of molecules and their fragments, in: K.D. Sen (Ed.), *Reviews of Modern Quantum Chemistry: A Celebration of the Contributions of Robert G. Parr*, vol. II, World Scientific, Singapore, 2002, pp. 1071–1105.
- [5] P. Geerlings, F. De Proft, W. Langenaeker, Conceptual density functional theory, *Chem. Rev.* **103** (2003) 1793–1873.
- [6] R.F. Nalewajski, Electronic structure and chemical reactivity: Density functional and information theoretic perspectives, *Adv. Quantum Chem.* **43** (2003) 119–184.
- [7] R.F. Nalewajski, Consistent two-reactant approach to chemisorption complexes in charge sensitivity analysis, in: W.M. Mortier, R.A. Schoonheydt (Eds.), *Developments in the Theory of Chemical Reactivity and Heterogeneous Catalysis*, Research Signpost, Trivandrum, 1997, pp. 135–196.
- [8] R.F. Nalewajski, J. Korchowiec, A. Michalak, Reactivity criteria in charge sensitivity analysis, *Topics in Current Chemistry* **183** (1996) 25–141.
- [9] R.F. Nalewajski, The hardness based molecular charge sensitivities and their use in the theory of chemical reactivity, *Structure and Bonding* **80** (1993) 115–186.
- [10] R.F. Nalewajski, Charge sensitivity analysis as diagnostic tool for predicting trends in chemical reactivity, in: E.K.U. Gross, R.M. Dreizler (Eds.), *Proceedings of the NATO ASI on Density Functional Theory*, Plenum, New York, 1995, pp. 339–389.
- [11] P.K. Chattaraj, R.G. Parr, Density functional theory of chemical hardness, in: K.D. Sen (Ed.), *Chemical Hardness, Structure and Bonding*, vol. 80, Springer-Verlag, Berlin, 1993, pp. 11–25.
- [12] M. Berkowitz, R.G. Parr, Molecular hardness and softness, local hardness and softness, hardness and softness kernels, and relations among these quantities, *J. Chem. Phys.* **88** (1988) 2554–2557.
- [13] J.L. Gázquez, Hardness and softness in density functional theory, in: K.D. Sen (Ed.), *Chemical Hardness, Structure and Bonding*, vol. 80, Springer-Verlag, Berlin, 1993, pp. 27–43.
- [14] J.L. Gázquez, A. Vela, M. Galván, Fukui function, electronegativity and hardness in the Kohn–Sham theory, in: K.D. Sen, C.K. Jørgensen (Eds.), *Electronegativity, Structure and Bonding*, vol. 66, Springer-Verlag, Berlin, 1987, pp. 79–97.
- [15] B.G. Baekelandt, W.J. Mortier, R.A. Schoonheydt, The EEM approach to chemical hardness in molecules and solids: Fundamentals and applications, in: K.D. Sen (Ed.), *Chemical Hardness, Structure and Bonding*, vol. 80, Springer-Verlag, Berlin, 1993, pp. 187–227.
- [16] W.M. Mortier, R.A. Schoonheydt (Eds.), *Developments in the Theory of Chemical Reactivity and Heterogeneous Catalysis*, Research Signpost, Trivandrum, 1997.
- [17] R.F. Nalewajski, J. Korchowiec, Basic concepts and illustrative applications of the sensitivity analysis of molecular charge distribution, *J. Mol. Catal.* **54** (1989) 324–342.
- [18] P. Hohenberg, W. Kohn, Inhomogeneous electron gas, *Phys. Rev. B* **136** (1964) 864–871.
- [19] H. Nakatsuji, Electrostatic force theory for a molecule and interacting molecules. I. Concept and illustrative applications, *J. Am. Chem. Soc.* **95** (1973) 345–354.
- [20] H. Nakatsuji, Common natures of the electron cloud of the system undergoing change in nuclear configuration, *J. Am. Chem. Soc.* **96** (1974) 24–30.
- [21] H. Nakatsuji, Electron-cloud following and preceding and the shapes of molecules, *J. Am. Chem. Soc.* **96** (1974) 30–37.
- [22] W. Kohn, L.J. Sham, Self-consistent equations including exchange and correlation effects, *Phys. Rev. A* **140** (1965) 1133–1138.
- [23] R.M. Dreizler, E.K.U. Gross, *Density Functional Theory: An Approach to the Quantum Many-Body Problem*, Springer-Verlag, Berlin, 1990.
- [24] R.F. Nalewajski (Ed.), *Density Functional Theory, vols. I–IV, Topics in Current Chemistry*, vol. 180–183, Springer-Verlag, Berlin, 1996.
- [25] R.T. Sanderson, An Interpretation of bond lengths and a classification of bond, *Science* **114** (1951) 670–672;
R.T. Sanderson, *Chemical Bonds and Bond Energy*, second ed., Academic Press, New York, 1976.

- [26] K. Fukui, *Theory of Orientation and Stereoselection*, Springer-Verlag, Berlin, 1975.
- [27] K. Fukui, Role of frontier orbitals in chemical reactions, *Science* **218** (1987) 747–754.
- [28] H. Fujimoto, K. Fukui, Intermolecular interactions and chemical reactivity, in: G. Klopman (Ed.), *Chemical Reactivity and Reaction Paths*, Wiley-Interscience, New York, 1974, pp. 23–54.
- [29] R.G. Parr, W. Yang, Density functional approach to the frontier-electron theory of chemical reactivity, *J. Am. Chem. Soc.* **106** (1984) 4049–4050.
- [30] W. Yang, R.G. Parr, Hardness, softness, and the Fukui function in the electronic theory of metals and catalysis, *Proc. Natl. Acad. Sci. USA* **82** (1985) 6723–6726.
- [31] W. Yang, R.G. Parr, R. Pucci, Electron density, Kohn–Sham frontier orbitals, and Fukui functions, *J. Chem. Phys.* **81** (1984) 2862–2863.
- [32] A. Michalak, F. De Proft, P. Geerlings, R.F. Nalewajski, Fukui functions from the relaxed Kohn–Sham orbitals, *J. Phys. Chem. A* **103** (1999) 762–771.
- [33] J. Korchowiec, T. Uchimaru, The charge transfer Fukui function: Extension of the finite-difference approach to reactive systems, *J. Phys. Chem. A* **102** (1998) 10167–10172.
- [34] P.W. Ayers, M. Levy, Perspective on “Density functional approach to the frontier-electron theory of chemical reactivity” [Parr, R.G. and Yang, W. (1984). *J. Am. Chem. Soc.* **106**: 4049–4050]. *Theor. Chem. Acc.* **103** (2000) 353–360.
- [35] M.H. Cohen, Strengthening the foundations of chemical reactivity theory, in: R.F. Nalewajski (Ed.), *Density Functional Theory IV: Theory of Chemical Reactivity, Topics in Current Chemistry*, vol. 183, Springer-Verlag, Berlin, 1996, pp. 143–184.
- [36] M.H. Cohen, M.V. Ganguglia-Pirovano, J. Kurnovský, Electronic and nuclear chemical reactivity, *J. Chem. Phys.* **101** (1994) 8988–8997.
- [37] M.H. Cohen, M.V. Ganguglia-Pirovano, J. Kurnovský, Reactivity kernels, the normal modes of chemical reactivity, and the hardness and softness spectra, *J. Chem. Phys.* **103** (1995) 3543–3551.
- [38] R.F. Nalewajski, A coupling between the equilibrium state variables of open molecular and reactive systems, *Phys. Chem. Chem. Phys.* **1** (1999) 1037–1049.
- [39] R.F. Nalewajski, Coupling relations between molecular electronic and geometrical degrees of freedom in density functional theory and charge sensitivity analysis, *Computers Chem.* **24** (2000) 243–257.
- [40] R.F. Nalewajski, Studies of the nonadditive kinetic energy functional and the coupling between electronic and geometrical structures, in: V. Barone, A. Bencini, P. Fantucci (Eds.), *Recent Advances in Density Functional Methods, Part III*, World Scientific, Singapore, 2002, pp. 257–277.
- [41] R.F. Nalewajski, O. Sikora, Electron-following mapping transformations from the electronegativity equalization principle, *J. Phys. Chem. A* **104** (2000) 5638–5646.
- [42] P.W. Ayers, R.G. Parr, Variational principles for describing chemical reactions: Reactivity indices based on the external potential, *J. Am. Chem. Soc.* **123** (2001) 2007–2017.
- [43] B.G. Baekelandt, G.O.A. Janssens, H. Toufar, W.J. Mortier, R.A. Schoonheydt, R.F. Nalewajski, Mapping between electron population and vibrational modes within the charge sensitivity analysis, *J. Phys. Chem.* **99** (1995) 9784–9794.
- [44] V. Gutmann, *The Donor–Acceptor Approach to Molecular Interactions*, Plenum, New York, 1978.
- [45] R.G. Parr, R.A. Donnelly, M. Levy, W.E. Palke, Electronegativity: The density functional viewpoint, *J. Chem. Phys.* **69** (1978) 4431–4439.
- [46] J.P. Perdew, R.G. Parr, M. Levy, J.L. Balduz, Density functional theory for fractional particle number: Derivative discontinuities of the energy, *Phys. Rev. Lett.* **49** (1982) 1691–1694.
- [47] J.P. Perdew, M.R. Norman, Electron removal energies in Kohn–Sham density functional theory, *Phys. Rev. B* **26** (1982) 5445–5450.
- [48] J.P. Perdew, M. Levy, Physical content of the exact Kohn–Sham orbital energies: Band gaps and derivative discontinuities, *Phys. Rev. Lett.* **51** (1983) 1884–1887.
- [49] J.P. Perdew, What do the Kohn–Sham orbital energies mean? How do atoms dissociate?, in: R.M. Dreizler, J. da Providencia (Eds.), *Density Functional Methods in Physics*, Plenum, New York, 1985, pp. 265–308.
- [50] R.G. Parr, R.G. Pearson, Absolute hardness: Companion parameter to absolute electronegativity, *J. Am. Chem. Soc.* **105** (1983) 7512–7516.
- [51] R.F. Nalewajski, R.G. Parr, Legendre transforms and Maxwell relations in density functional theory, *J. Chem. Phys.* **77** (1982) 399–407, the extremum principle in Eqs. (69) and (70) of this paper is the maximum principle.
- [52] R.F. Nalewajski, Charge response criteria of chemical reactivity: Fukui function indices and populational reference frames reflecting the inter-reactant charge coupling, *Int. J. Quantum Chem.* **61** (1997) 181–196.

- [53] R.F. Nalewajski, Electrostatic effects in interactions between hard (soft) acids and bases, *J. Am. Chem. Soc.* **106** (1984) 944–945.
- [54] R.F. Nalewajski, A study of electronegativity equalization, *J. Phys. Chem.* **89** (1985) 2831–2837.
- [55] R.F. Nalewajski, On the chemical potential/electronegativity equalization in density functional theory, *Polish J. Chem.* **72** (1998) 1763–1778.
- [56] R.F. Nalewajski, Chemical reactivity concepts in charge sensitivity analysis, *Int. J. Quantum Chem.* **56** (1995) 453–476.
- [57] R.F. Nalewajski, Kohn–Sham description of equilibria and charge transfer in reactive systems, *Int. J. Quantum Chem.* **69** (1998) 591–605.
- [58] R.F. Nalewajski, Charge sensitivities of the externally interacting open reactants, *Int. J. Quantum Chem.* **78** (2000) 168–178.
- [59] P.W. Ayers, R.G. Parr, Variational principles for site selectivity in chemical reactivity: The Fukui function and chemical hardness revisited, *J. Am. Chem. Soc.* **122** (2000) 2010–2018.
- [60] G. Klopman, Chemical reactivity and the concept of charge and frontier-controlled reactions, *J. Am. Chem. Soc.* **90** (1968) 223–234.
- [61] G. Klopman, The generalized perturbational theory of chemical reactivity and its applications, in: G. Klopman (Ed.), *Chemical Reactivity and Reaction Paths*, Wiley-Interscience, New York, 1974, pp. 55–165.
- [62] H.B. Callen, *Thermodynamics: An Introduction to the Physical Theories of Equilibrium Thermodynamics and Irreversible Thermodynamics*, Wiley, New York, 1962.
- [63] F. Colonna, A. Savin, Correlation energies for some two- and four-electron systems along the adiabatic connection in density functional theory, *J. Chem. Phys.* **110** (1999) 2828–2835.
- [64] R.F. Nalewajski, Geometric separation of the polarization and charge transfer components of charge sensitivities of open molecular systems, *Chem. Phys. Lett.* **353** (2002) 143–153.
- [65] R.F. Nalewajski, Geometric interpretation of density displacements and charge sensitivities, *J. Chem. Sci.* **117** (2005) 455–466.
- [66] J.C. Decius, Compliance matrix and molecular vibrations, *J. Chem. Phys.* **38** (1963) 241–248.
- [67] L.H. Jones, R.R. Ryan, Interaction coordinates and compliance constants, *J. Chem. Phys.* **52** (1970) 2003–2004.
- [68] B.I. Swanson, Minimum energy coordinates. A relationship between molecular vibrations and reaction coordinates, *J. Am. Chem. Soc.* **98** (1976) 3067–3071.
- [69] B.I. Swanson, S.K. Satija, Molecular vibrations and reaction pathways. Minimum energy coordinates and compliance constants for some tetrahedral and octahedral complexes, *J. Am. Chem. Soc.* **99** (1977) 987–991.
- [70] R.F. Nalewajski, A. Michalak, Use of charge sensitivity analysis in diagnosing chemisorption clusters: Minimum energy coordinate and Fukui function study of model Toluene-[V₂O₅] systems, *Int. J. Quantum Chem.* **56** (1995) 603–613.
- [71] R.F. Nalewajski, J. Korchowiec, Use of charge sensitivity analysis in testing adequacy of cluster representations of catalytic active sites, *Computers Chem.* **19** (1995) 217–230.
- [72] F.L. Hirshfeld, Bonded-atom fragments for describing molecular charge densities, *Theor. Chim. Acta (Berl.)* **44** (1977) 129–138.
- [73] R.F. Nalewajski, R.G. Parr, Information theory, atoms in molecules, and molecular similarity, *Proc. Natl. Acad. Sci. USA* **97** (2000) 8879–8882.
- [74] R.F. Nalewajski, Hirshfeld analysis of molecular densities: Subsystem probabilities and charge sensitivities, *Phys. Chem. Chem. Phys.* **4** (2002) 1710–1721.
- [75] R.F. Nalewajski, M. Koniński, Density polarization and chemical reactivity, *Z. Naturforsch* **42a** (1987) 451–462.
- [76] R.F. Nalewajski, J. Korchowiec, Z. Zhou, Molecular hardness and softness parameters and their use in chemistry, *Int. J. Quantum Chem. Symp.* **22** (1988) 349–366.
- [77] R.F. Nalewajski, Normal (decoupled) representation of electronegativity equalization equations in a molecule, *Int. J. Quantum Chem.* **40** (1991) 265–285; Errata: *ibid Int. J. Quantum Chem.* **43** (1992) 443.
- [78] R.F. Nalewajski, On geometric concepts in sensitivity analysis of molecular charge distribution, *Int. J. Quantum Chem.* **42** (1992) 243–265.
- [79] R.F. Nalewajski, A.M. Köster, T. Bredow, K. Jug, Charge sensitivity analysis of oxide catalysts: TiO₂(110, 100) clusters and H₂O adsorption/dissociation on TiO₂(110), *J. Mol. Catal.* **82** (1993) 407–423.
- [80] R.F. Nalewajski, J. Korchowiec, Charge sensitivity analysis of oxide catalysts: Oxidation state dependence of normal-mode description of surface V₂O₅ clusters, *J. Mol. Catal.* **82** (1993) 383–405.

- [81] R.F. Nalewajski, J. Korchowiec, A. Michalak, Intermediate hardness decoupling schemes for chemical reactivity, *Proc. Indian Acad. Sci. (Chemical Sci.)* **106** (1994) 353–378.
- [82] R.F. Nalewajski, A. Michalak, Charge sensitivity and bond-order analysis of reactivity trends in Allyl-[MoO₃] systems: Two-reactant approach, *J. Phys. Chem.* **100** (1996) 20076–20088.
- [83] R.F. Nalewajski, A. Michalak, Charge sensitivity/bond-order analysis of reactivity trends in Allyl-[MoO₃] chemisorption systems: A comparison between (010)- and (100)-surfaces, *J. Phys. Chem. A* **102** (1998) 636–640.
- [84] G.O.A. Janssens, W.J. Mortier, R.A. Schoonheydt, The mapping relations between electronic and geometric structure, in: W.M. Mortier, R.A. Schoonheydt (Eds.), *Developments in the Theory of Chemical Reactivity and Heterogeneous Catalysis*, Research Signpost, Trivandrum, 1997, pp. 81–134.
- [85] M. Levy, Universal variational functionals of electron densities, first-order density matrices, and natural spin-orbitals and solution of the *v*-representability problem, *Proc. Natl. Acad. Sci. USA* **76** (1979) 6062–6065;
see also R.F. Nalewajski, Coupling constant integration analysis of density functionals for subsystems, *Adv. Quant. Chem.* **38** (2000) 217–277.
- [86] R.F. Nalewajski, Rigid and relaxed hardness parameters of molecular fragments, *Acta Phys. Polon. A* **77** (1990) 817–832.
- [87] J. Ciosłowski, S.T. Mixon, Electronegativities *in situ*, bond hardnesses, and charge-transfer components of bond energies from the topological theory of atoms in molecules, *J. Am. Chem. Soc.* **115** (1993) 1084–1088.
- [88] R.F. Nalewajski, Sensitivity analysis of charge transfer systems: *In situ* quantities, intersecting state model and its implications, *Int. J. Quantum Chem.* **49** (1994) 675–703.
- [89] R.F. Nalewajski, Qualitative charge stability and Fukui function analysis of a model system with implications for chemical reactivity, *J. Mol. Catal.* **82** (1993) 371–381.
- [90] A.K. Chandra, A. Michalak, M.T. Nguyen, R.F. Nalewajski, Regional matching of atomic softnesses in chemical reactions: A two-reactant charge sensitivity study, *J. Phys. Chem. A* **102** (1998) 10182–10188.
- [91] R.A. Fisher, On the mathematical foundations of theoretical statistics, *Philos. Trans. R. Soc. Lond. Ser. A* **222** (1922) 309–368;
R.A. Fisher, Theory of statistical estimation, *Proc. Cambridge Phil. Soc.* **22** (1925) 700–725;
R.A. Fisher, *Statistical Methods and Scientific Inference*, second ed., Oliver & Boyd, London, 1959;
see also B.R. Frieden, *Physics from the Fisher Information—A Unification*, Cambridge University, Cambridge, 2000.
- [92] C.E. Shannon, The mathematical theory of communication, *Bell System Tech. J.* **27** (1948) 379–493, 623–656;
C.E. Shannon, W. Weaver, *The Mathematical Theory of Communication*, University of Illinois, Urbana, 1949.
- [93] S. Kullback, R.A. Leibler, On information and sufficiency, *Ann. Math. Stat.* **22** (1951) 79–86;
S. Kullback, *Information Theory and Statistics*, Wiley, New York, 1959.
- [94] R.F. Nalewajski, E. Świtka, A. Michalak, Information distance analysis of molecular electron densities, *Int. J. Quantum Chem.* **87** (2002) 198–213;
R.F. Nalewajski, E. Broniatowska, Entropy displacement and information distance analysis of electron distributions in molecules and their Hirshfeld atoms, *J. Phys. Chem. A* **107** (2003) 6270–6280;
R.F. Nalewajski, E. Broniatowska, Atoms-in-molecules from the stockholder partition of the molecular two-electron distribution, *Theor. Chem. Acc.*, in press.
- [95] R.F. Nalewajski, Information principles in the theory of electronic structure, *Chem. Phys. Lett.* **372** (2003) 28–34.
- [96] R.F. Nalewajski, Entropic measures of bond multiplicity from the information theory, *J. Phys. Chem. A* **104** (2000) 11940–11951.
- [97] R.F. Nalewajski, Entropic and difference bond multiplicities from the two-electron probabilities in orbital resolution, *Chem. Phys. Lett.* **386** (2004) 265–271.
- [98] R.F. Nalewajski, Entropy descriptors of the chemical bond in information theory: I. Basic concepts and relations, *Mol. Phys.* **102** (2004) 531–546.
- [99] R.F. Nalewajski, Entropy descriptors of the chemical bond in information theory: II. Applications to simple orbital models, *Mol. Phys.* **102** (2004) 547–566.
- [100] R.F. Nalewajski, Communication theory approach to the chemical bond, *Structural Chemistry* **15** (2004) 395–407.
- [101] R.F. Nalewajski, Reduced communication channels of molecular fragments and their entropy/information bond indices, *Theor. Chem. Acc.* **114** (2005) 4–18.

- [102] R.F. Nalewajski, Partial communication channels of molecular fragments and their entropy/information indices, *Mol. Phys.* **103** (2005) 451–470.
- [103] R.F. Nalewajski, Entropy/information bond indices of molecular fragments, *J. Math. Chem.* **38** (2005) 43–66.
- [104] R.F. Nalewajski, Comparison between the valence-bond and communication theories of the chemical bond in H_2 , *Mol. Phys.* **104** (2006) 365–375.
- [105] R.F. Nalewajski, Atomic resolution of bond descriptors in the two-orbital model, *Mol. Phys.* **104** (2006) 493–501.
- [106] R.F. Nalewajski, R.G. Parr, Information theoretic thermodynamics of molecules and their Hirshfeld fragments, *J. Phys. Chem. A* **105** (2001) 7391–7400.
- [107] R.F. Nalewajski, Information theoretic approach to fluctuations and electron flows between molecular fragments, *J. Phys. Chem. A* **107** (2003) 3792–3802.
- [108] R.F. Nalewajski, Local information-distance thermodynamics of molecular fragments, *Ann. Phys. (Leipzig)* **13** (2004) 201–222.
- [109] R.F. Nalewajski, Electronic chemical potential as information temperature, *Mol. Phys.* **104** (2005) 255–261.
- [110] R.F. Nalewajski, Orbital resolution of molecular information channels and stockholder atoms, *Mol. Phys.* **104** (2006) 2533–2543.
- [111] R.F. Nalewajski, E. Broniatowska, Information distance approach to Hammond postulate, *Chem. Phys. Lett.* **376** (2003) 33–39.
- [112] G.S. Hammond, A correlation of reaction rates, *J. Am. Chem. Soc.* **77** (1955) 334–338.
- [113] A.D. Becke, K.E. Edgecombe, A simple measure of electron localization in atomic and molecular systems, *J. Chem. Phys.* **92** (1990) 5397–5403.
- [114] R.F. Nalewajski, A.M. Köster, S. Escalante, Electron localization function as information measure, *J. Phys. Chem. A* **109** (2005) 10038–10043.
- [115] R.F. Nalewajski, E. Świtka, Information theoretic approach to molecular and reactive systems, *Phys. Chem. Chem. Phys.* **4** (2002) 4952–4958.
- [116] R.F. Nalewajski, R. Loska, Bonded atoms in sodium chloride—The information-theoretic approach, *Theor. Chem. Acc.* **105** (2001) 374–382.

This page intentionally left blank

Subject Index

$1j$ -symbol, 102
 $1jm$ -symbol
 – definition, 69
 – diagram, 80, 81
 2D MRS, 168
 $3j$ -symbol, 79, 102
 $3jm$ -symbol diagrams, 83–87, 118, 119
 $3nj$ -symbols higher ($n > 3$), 113
 $6j$ -symbol
 – definition, 104
 – equation, 106–110
 – properties, 106
 $9j$ -symbol
 – definition, 105
 – equation, 110
 – properties, 110–113
 Δ^2 -process, 227

A

absolute values of the amplitudes, 180
 absorption
 – component shape spectra, 215
 – envelope spectra, 197, 209
 – spectra, 171
 – spectrum, 170
 – total shape spectra, 197, 200, 202
 – total shape spectrum, 167, 189
 abundance, 158
 acceleration, 165
 accelerators, 160
 accuracy, 231
 acidic/basic subsystems *see*
 donor–acceptor systems,
 reactants-in-molecules
 acquisition times, 159

ad hoc, 177
 – guesses, 161
 adjustable parameters, 164
 admixture, 164
 Aitken extrapolation, 165, 227
 Ala (alanine), 189
 algebra, 126
 algebraic
 – algorithms, 165
 – condition, 165, 191
 – structure, 185
 algorithmic instabilities, 231
 AMARES (advanced method for
 accurate, robust and efficient spectral
 fitting), 163
 ambivalency (of group class), 61
 amplitude, 161
 amplitudes, 159, 174, 222, 224
 analytic function, 171
 analytical
 – continuation, 160, 186, 229
 – formula, 226
 – results, 179
 – information, 158, 161, 224
 angular momentum
 – coupling, 60
 – – scheme, 81
 – diagrams, 60
 – operators, 60
 – quantum theory of, 61
 – Schwinger’s representation, 64
 annihilation operator, 5, 44
 anti-causal Padé- z transform, 159
 antisymmetrizer, 11
 antiunitary operator, 70

apparent information, 163
 approximate Fourier coefficients, 162
 atomic charges, 140
 atoms-in-molecules (AIM), 237, 239,
 265–282
 – discretization, 265–282
 – electron densities, 265, 271
 – shape factors, 271
 attenuated complex exponentials, 174
 auto-correlation
 – function, 173, 174
 – functions, 167, 176
 average density, 166

B

background, 169, 170, 176
 – contribution, 177
 – polynomial, 177, 178
 backgrounds, 177
 backward prediction coefficients, 179
 bandwidth, 159, 160, 162, 166, 167, 197
 basic
 – ambiguities, 189
 – defect of fitting, 166
 – functions, 172
 – set, 177
 – – double zeta, 24
 – – minimum, 13, 51
 – – STO-3G, 13
 BECCD, 13
 biochemical and physical functionality,
 161
 biochemical information, 158, 161, 222,
 224, 228
 bond breaking, 2–4, 13, 16–26, 34, 35,
 37, 40, 42
 Born–Oppenheimer (BO) approximation,
 238
 boundary condition, 166
 branch cuts, 171
 branching indices, 130
 broad resonances, 170

C

cancer diagnostics, 222
 Cauchy, 160
 – analytical continuation principle, 165,
 181, 198, 229
 – distribution, 171
 – residue, 180, 230
 – – formula, 175
 – residues, 181, 182, 226
 causal Padé z -transform (PzT), 159, 165
 CCD, 13–15
 – generalized (GCCD), 45, 46
 CCSD, 2, 3, 13–42, 52
 – generalized (GCCSD), 45, 46
 CCSDT, 3, 13, 24, 25, 27, 39–42, 52
 CCSDTQ, 3, 27, 52
 CCSDTQP, 3, 27
 CCSD[T], 2, 3
 CCSD(T), 2, 3, 24, 25, 39, 41, 42
 CCSD(TQ_f), 2, 3, 24, 25, 39, 41, 42
 CCSDT- n , 3
 CCSDTQ-1, 3
 CCSDT[Q], 3
 CCSDT(Q_f), 3, 24, 39, 40, 42
 characteristic
 – equation, 174, 226
 – equations, 179
 – polynomials, 182
 charge sensitivities, 237–263, *see also*
 charge transfer (CT), chemical
 hardness, chemical softness, Fukui
 function (FF)
 – AIM of, 265–280
 – chemical-hardness representation in,
 248–254
 – chemical-softness representation in,
 141–248
 – energy Legendre transforms of,
 243–245, 248–256, 258–263,
 266–270, 273–276
 – entropic, 294–299
 – geometric representations in, 256–270
 – geometrically rigid/relaxed *see*
 compliance analysis,

- global, 241, 244, 247, 252, 258–262, 291–293, 295–299
- *in situ*, 280–293, 297–299 *see also* charge transfer (CT)
- principal, 241–243, 256–258, 265, 266, 272, 283–293
- reactants of, 283–299
- shape-factor averaged, 252, 256, 271–276
- charge sensitivity analysis (CSA) *see* charge sensitivities
- charge stability considerations, 236, 292–294
- implications for catalysis, 294
- charge transfer (CT), 236, 242, 246–252, 282, 292–294, 297–299
- affinities (CTA), 297–299
- external, 246, 252
- internal, 242, 246–248, 251, 252, 282
- sensitivities *see* charge sensitivities *in situ*
- systems *see* donor–acceptor systems
- chemical
 - hardness, *see also* charge sensitivities
 - – average, 252
 - – global, 241, 247, 255, 226
 - – internal, 246
 - – kernel, 243, 244, 246, 247, 250, 251, 255, 256
 - – local, 247, 253, 256
 - – – equalization of, 247
 - – representation, 248–254
 - shift imaging (CSI), 158
 - shifts, 187, 201, 215, 224, 228
 - softness, *see also* charge sensitivities
 - – global, 241, 246, 255, 256
 - – internal, 242, 246
 - – kernel, 244, 246, 250, 251, 255, 256
 - – local, 244, 247, 255
 - – representation, 241–248
- Cho (choline), 189
- CISD, 52, 53
- CISDT, 52, 53
- CISDTQ, 52–54
- Clebsch–Gordan
 - definition of coefficients, 72
 - diagrams, 74, 77
 - generalized coefficients, 81, 82
 - series, 71–73
 - symmetry of coefficients, 72–80
 - theorem, 72
 - transition to $3jm$ -symbols, 87–89
- clinical
 - diagnostics, 186
 - oncology, 167, 231
 - scanner, 167
 - scanners, 222
- closed/open systems, 237, 241–256
- cluster amplitudes, 5, 7, 13, 27
 - doubly excited, 8, 9, 27
 - singly excited, 8, 9, 27
- cluster operator, 5, 6, 45
 - many-body component of, 5, 45
 - one-body component of, 7
 - two-body component of, 7, 45
- clusters
 - doubly excited (T_2), 7–12, 14, 15, 16, 19, 20, 24–39, 42, 45
 - quadruply excited (T_4), 3, 14, 16
 - singly excited (T_1), 7–13, 15, 16, 19, 20, 24–39, 42, 45
 - triply excited (T_3), 3, 13, 15, 28, 30
- coincident (confluent) fundamental frequencies, 182
- coincident peaks, 189
- completely renormalized coupled-cluster (CR-CC) methods, 30, 31
- completeness, 173
- complex, 224
 - amplitudes, 172, 180, 188, 191
 - damped exponentials, 164, 174
 - energies, 172
 - energy, 169
 - – plane, 169, 171
 - frequencies, 172, 187, 188, 191, 215, 219, 226
 - fundamental frequencies, 186, 216
 - harmonic variable, 159
 - spectra, 170, 182

- compliance analysis, 258–270, 278–282
 - in atomic resolution, 265–270
 - compliance matrices, 258, 259, 263, 266, 280
 - ground-state coupling between state-variables, 258–263, 265–267
 - minimum-energy coordinates, 263–265, 268–270
 - in molecular resolution, 258–265
 - component shape spectra, 163, 209, 213
 - compound
 - nucleus, 168
 - system, 169
 - concentration, 187
 - concentrations, 158, 159, 163, 222, 224, 227
 - Condon and Shortley phase convention, 71
 - configuration of the poles, 215
 - configurations, 214, 217
 - confluent
 - harmonics, 182
 - resonances, 182
 - congested peaks, 162
 - conjugate domain, 162
 - conjugated molecule, 127
 - connectivity index, 130
 - consecutive
 - difference spectra, 203, 206
 - systems, 173
 - constancy, 166, 183, 184
 - constrained relationship, 167
 - constraint, 166
 - constructive and destructive interference
 - of all the individual resonances, 163
 - continued fraction, 172
 - contraction
 - basis vectors of, 67
 - lines in diagrams of, 75–77
 - contrastandard
 - basis, 68
 - representation, 67–69
 - converged envelope spectrum, 203
 - convergence, 160, 216, 218, 219
 - absolute values of amplitudes of, 220
 - accelerator, 160
 - rate, 184, 206
 - rates, 185, 189, 201
 - regions, 200
 - convolution, 171
 - convolution (folding), 171
 - correlated dynamics, 173
 - correlations, 173
 - Coulson integral formula, 128
 - coupled-cluster (CC) (theory, method, approach), 1–4, 26–28, 45
 - coupling scheme, 81
 - Yamanouchi–Kotani, 114
 - Cr (creatine), 189
 - CR-CCSD(T), 30, 31, 34–37, 39–42
 - CR-CCSD(TQ), 30, 31, 34–40, 42
 - CR-CC(2,3), 31
 - creation operator, 5, 44
 - cross validation, 160
 - cross checking, 180
 - cross-correlation plots, 168
 - cross-disciplinary research, 161
 - cross fertilisation, 224
 - cross-section, 171
 - cross-sections, 168, 169
 - cross-validation, 167, 175, 181, 185
 - CT (computerised tomography), 225
- D**
- damped
 - complex, 161, 163
 - – exponentials, 184, 188, 226, 228
 - fundamental harmonics, 228
 - oscillations, 171, 226
 - – harmonic, 160
 - data matrix, 164, 165
 - decay, 168, 169
 - time, 169
 - – constants, 187
 - deexcitation
 - amplitudes, 5, 8, 9
 - operator, 5, 6
 - – “lambda”, 6
 - – one-body, 8
 - – two-body, 8

decaying states, 169
degeneracies, 183
degenerate
– and non-degenerate fundamental frequencies, 182
– frequency, 182
– Lorentzian resonance, 228
degrees, 176, 180
denominator
– polynomial, 166, 170, 176
– polynomials, 179
density functional theory (DFT),
237–239, 243, 245–247, 249, 287,
294, 299, 300
destructively, 162
determined, 181
– system, 165
determinism of quantum mechanics, 173
diagnostic
– information, 222
– methods, 225
– tools, 225
diagonal, 177, 178
diagonalisation, 164, 172
diagrammatic
– diagrams building blocks, 74, 75
– rules *see* rules
diagrams
– angular momentum, 74–121
– building blocks, 74, 75
– closed, 101
– irreducible, 101–113
– many-body perturbation theory, 114
– reducible, 101
direct quantification problem, 173
discrete
– Dirichlet problem, 149
– states, 169
diseased, 159
dispersion
– formula, 169
– functions, 171
– of light, 169
– spectrum, 170

distinct
– roots, 175
– strategies, 181
distributions, 222
– complex frequencies of, 219
– poles of, 212
divergent
– sequence, 160
– series, 181
Doppler broadening, 171
donor–acceptor systems, 236, 282–300
doubly-transformed Hamiltonian, 4, 8, 9
downhill simplex method, 51
dwell time, 162

E

ECCD, 13–16
ECCSD, 7–26, 31, 33, 34–39, 42
– Arponen–Bishop, 9–12, 22–26, 35,
37–42
– bi-linear (BECCSD), 9, 13, 14, 16–21,
24–26
– linear (LECCSD), 9, 10, 14, 16, 18
– Piecuch–Bartlett, 8, 9, 13–22, 24, 26
– quadratic (QECCSD), 9, 11–13, 16–26,
34–42
ECCSD(T), 34–38, 41, 42
ECCSD(TQ), 34–38, 42
echo
– time, 167, 186, 188
– times, 224
eigenenergies, 184
eigenfrequencies, 172
eigenfunctions, 172
eigenspectrum, 166
eigenvalue problem, 172
electron density
– as basic variable, 237, 238, 248–256,
see also density functional theory
(DFT)
– Hellmann–Feynman theorem
expressions, 238, 239, 244, 262
– partition of, 237, 238, *see also*
atoms-in-molecules (AIM)
– shape factor, 251–253

- electron localization function, 294
- electronegativity, 142
 - equalization principle of, 149, 237, 239, 245, 265, 269, 280
 - relaxation, 142
- electronic energy
 - density functionals, 237, 238, 243–248
 - DFT in, 237, 283
 - Legendre transforms of, 248–254, *see also* grand potential
 - Taylor expansions, 242, 243, 284, 285, 292, 293
- electronic structure interpretations
 - horizontal/vertical (variational) displacements, 242, 243, 245, 250, 251, 254
 - information theory (IT) from, 294–299
 - perspectives, 239–256
 - – electron following (EF), 239, 241–248, 254, 255
 - – electron preceding (EP), 248–256
- encoding, 159, 161, 162, 167, 224
- energy
 - functional, 4, 7, 50
 - operator, 172
- entry data, 167
- envelope
 - spectra, 167, 185, 213, 225
 - spectrum, 163, 164, 222, 229
- EOMCCSD, 53
- EOMCCSDT, 53
- EOMCCSDTQ, 53, 54
- equation of motion coupled-cluster (EOMCC), 54
- equivalence, 174
- equivalent variants, 175
- error, 164
 - analysis, 167, 206
 - function, 172
 - spectra, 201, 206
- ersatz spectrum, 180
- Euler equations
 - atomic resolution in, 273
 - DFT in, 237, 238
 - information theory in, 295, 296
- Euler–Rodrigues parametrization, 63
- evolution
 - matrix, 164
 - operator, 167, 172–174
- excitation operator, 5
 - double, 8
 - single, 8
- excitations, 168
- excited
 - determinant, 8, 27–29
 - state, 168
- expectation value, 15, 19, 20, 47, 48
- exponential
 - convergence, 195
 - – rates, 160
 - form of SU(2) element, 62, 63
- exponentially
 - attenuated, 171
 - damped envelopes, 159
- $\exp(X)$ conjecture, 45–50
 - extension of to excited states, 49, 50
- extended
 - accuracy, 194, 196
 - convergence regions, 165
 - coupled-cluster (ECC) theory, 4–7, 31
 - – Arponen-Bishop, 6, 7, 38–42
 - – bi-variational, 7, 9
 - – Piecuch-Bartlett, 5, 6, 7
- external
 - magnetic fields, 222
 - perturbation, 159
 - perturbations, 168, 175
 - potential
 - – as state-parameter, 238, 239, 241–248, 254, 255
 - – atomic resolution in, 271, 273
 - – embedding correction for subsystems, 238
- extraneous
 - peaks or dips, 162
 - poles, 193
- extrapolation, 168, 224, 227

F

- factorization rules, 92–97
- fast Fourier transform (FFT), 159
- fast Padé transform, 214
- finite-rank Green function, 175, 176, 184
- finite-rank Hamiltonian matrix, 184
- fittings, 161, 163, 225, 229
- forced
 - excitations, 171
 - to converge, 160
- forces on nuclei, 240, 257–270, *see also*
 - compliant analysis, nuclear Fukui function (NFF)
- forward, 179
- Fourier
 - analysis, 230
 - dichotomy, 160
 - grid, 163
 - – frequencies, 162
 - integral, 230
 - sequences, 165
 - uncertainty principle, 163
- free
 - adjustable parameters, 166
 - induction decay (FID), 158
 - parameters, 164
- frequency
 - content, 162
 - domain, 162, 165, 175, 183, 225
 - resolution, 159
 - spectrum, 230
- Froissart doublets, 161, 183, 191, 232
- Froissart-cleaned spectrum, 193
- frontier electron theory, 239
- Fukui function
 - electronic (FF), 236, 239–242, 246, 247, 254, 255, 257, 258
 - condensed,
 - – AIM of, 265
 - – reactants of, 283–286, 288–291, 296–299
 - nuclear (NFF), 240, 241, 257–263
 - – AIM of, 265–267

full

- configuration interaction (CI), 6, 13–15, 17–25, 43, 44, 47, 51–53
- convergence, 191, 193, 194, 206, 212, 219, 222
- information, 174
- functionality, 160
- fundamental
 - complex
 - – frequencies, 179, 180, 214, 218, 224
 - – frequencies and amplitudes, 167
 - drawback—the lack of extrapolation features, 163
 - frequencies, 161, 229
 - frequencies and amplitudes, 160
 - harmonics, 159, 229

G

- Gauss, 171
- Gaussian broadenings, 172
- Gaussians, 163
- genealogy, 81
- generators of general linear group, 66
- generic spectrum, 175
- genuine, 164
 - and spurious resonances, 192
 - metabolites, 225
 - resonance, 162
 - resonances, 161, 183, 186, 193
 - roots, 179
- geometric series, 175
- giant water resonance, 161
- Gibbs
 - oscillations, 162, 163
 - ringing, 159
- Gibbs–Duhem equation, 249
- Gln (glutamate), 189
- global (or at least the local) completeness relation, 173
- Glu (glutamine), 189
- gold standard, 185
- gradient magnetic fields, 159

grand potential, 243–245
 – derivatives, 244–247
 – Taylor expansion, 245
 graph
 – eigenvalues, 127
 – energy, 127, 128
 – theory, 126
 – – algebraic, 132
 – – chemical, 125
 – – spectral, 132
 graphical method of spin algebras, 74
 Green
 – function, 159, 176, 227, 229
 – operators, 173
 Green–Padé, 179
 – functions, 176, 181, 183, 226
 group theoretical characteristics of states,
 74
 Gutmann rules, 241, 281, 282

H

H8 (model, system), 51–54
 Hammond postulate, 294
 Hankel
 – (data) matrix, 164
 – determinant, 227
 – determinants, 165, 183
 – matrix, 165
 Hankel–Lanczos Singular Value
 Decomposition (HLSVD), 164
 hardness matrix, 142
 harmonic
 – analysis, 224
 – inversion, 225
 – – problem, 167
 – oscillations, 171
 – oscillator, 64
 – variable, 214, 215
 Hazi–Taylor stabilisation method, 184
 Heaviside partial
 – fraction, 180
 – – expansions, 185
 – fractions, 175, 181, 199

Hellmann–Feynman theorem, 238, 239,
 244, 248, 262, *see also* electronic
 structure interpretations
 Hessenberg matrix, 230
 high-resolution
 – signal processors, 224
 – spectral analysis, 231
 – spectrum, 167
 Hohenberg–Kohn theorems *see* density
 functional theory (DFT)
 Horn–Weinstein formula, 46–48
 Hückel molecular orbital, 127, 132
 hydrogen atoms, 13, 51

I

ill-conditioned task, 186
 imaginary
 – frequencies, 187, 215, 224
 – frequency, 222
 impediment, 159
 improvement, 159
 incoming
 – boundary conditions, 159
 – wave, 169
 infinite length, 162
 infinitely long FIDs, 162
 information stiffness, 299
 – *in situ*, 299
 information theory, 294–299
 inhomogeneities, 161
 inhomogeneity, 172
 initial, 166
 – convergence
 – – range, 165
 – – regions, 197, 198
 – estimates, 203
 input
 – data, 161
 – information, 203
 Ins (inositol), 189
 intensity, 159, 172
 interdisciplinary
 – fields, 231
 – research, 170

interfere constructively, 162
 intermolecular forces, 114
 internal structure, 163
 inverse
 – Fourier integral, 172
 – problem, 158, 167, 225
 ion cyclotron resonance mass
 spectroscopy (ICRMS), 184
 irreducible diagrams, 101–113
 isolated, 189, 228
 isolated, overlapped, tightly overlapped,
 nearly degenerate, or degenerate
 (confluent), 224
 isolated resonance, 212
 iterations, 164

K

Kekulé structures, 133
 kernel, 172
 Kramer–Rao, 164
 – bounds, 164
 Krylov, 166
 – state space, 166

L

Lanczos basis set functions, 166
 Laplacian matrix, 142
 Larmor
 – frequency, 228
 – precession frequency, 187
 least square (LS), 163
 Levenberg–Marquardt, 164
 Levi–Civita tensor, 62
 Levy construction, 287
 lifetime, 169
 line-shapes, 163, 171, 172, 180–182
 linear combination of model (LCModel),
 163
 linear
 – equations, 164
 – external, 90
 – free, 90
 – internal, 90

– predictor, 230
 lipid (Lip), 189
 Lorentzian, 171
 – line-shapes, 164
 – (non-degenerate) spectra, 166
 Lorentzians, 163

M

machine
 – accuracy, 172
 – accurate convergence, 198
 Maclaurin, 180
 – development, 229
 – expansion, 175
 – series, 176, 230
 – sum, 186
 macromolecules, 177, 178
 magnetic field
 – shimming, 162
 – strength, 185, 186
 magnetic resonance (MR), 161
 – imaging (MRI), 158
 – spectroscopic imaging (MRSI), 158
 – spectroscopy (MRS), 158
 mapping relations, 279–282
 Markov chain, 150
 mathematical
 – ill-conditioning, 226
 – methods, 225
 – model, 226, 231
 – processing, 224
 Matlab, 179, 230
 maximum probability, 173
 McClelland inequalities, 128
 medical
 – diagnostics, 167
 – physics, 161
 medicine, 167, 224, 225
 meromorphic functions, 179
 metabolic information, 160
 metabolites, 158–160, 162, 163, 211, 224,
 227, 228
 metastable, 169
 – state, 169

method of moments of coupled-cluster equations (MMCC), 26–35, 37, 40–42

- CI-corrected, 30
- generalized (GMMCC), 4, 31–35, 37–39
- multireference MBPT-corrected, 30
- quadratic, 30
- quasi-variational, 30

metric tensor

- diagram, 80, 81
- (of $SU(2)$), definition, 68

minimal frequency, 163

molecular equilibria *see* electronegativity equalization principle, Euler equations

- in reactive systems, 282–299

molecular stability *see* charge stability considerations

molecular structure, 162

moment problem, 225

moments of coupled-cluster (CC) equations, 28–32, 34, 35, 37, 41

multi-level

- Breit–Wigner, 168
- BW formulae, 170

multiple

- roots, 166, 175, 182
- voxels, 158, 224

multiplicities, 179, 182, 183

N

N_2 (molecule), 13, 16–26, 34, 37–42

NAA (nitrogen acetyl aspartate), 188

Nakatsuji density equation, 46

near-degeneracy, 189

nearly, 228

- degenerate resonances, 189, 212

NMR, 224

noise, 159, 163, 167, 168, 184

noise-free, 184

noiseless, 184

- FIDs, 186

non-degeneracy, 180, 182

non-degenerate, 175

- resonances, 180
- spectrum, 181

non-diagonal, 165

non-Hermitean, 172

non-invasive

- diagnostic method, 158
- methods, 160

non-Lorentzian (degenerate) spectra, 166

non-Lorentzians, 164

non-orthogonal expansion

- functions, 226
- sets, 164

non-parametric

- estimations, 228
- processing, 160
- processors, 163

non-stationary

- amplitudes, 167, 227
- polynomial-type, 174

non-unique, 161

non-uniqueness, 189, 225, 226

normal coordinates

- electronic, 276, 277
- nuclear, 278
- populational normal modes (PNM), 277, 278

nuclear

- magnetic resonance (NMR), 184
- transmutations, 168

number, 160

- of resonances, 160, 167

numerator, 176

numerator

- and denominator polynomial, 183
- and denominator polynomials, 181
- polynomial, 170
- algorithms, 165
- analysis, 165
- values, 185, 186, 189, 190, 193, 196, 203

Nyquist

- frequency, 162
- interval, 228
- range, 166

O

observables, 173, 174
 off-diagonal, 176, 177
 one polynomial, 160
 one-dimensional (1D) MRS, 168
 operator
 – amplitudes, 174
 – Padé approximant, 159
 optimal
 – estimator, 174
 – performance, 186
 – response, 175
 – stability, 231
 – suitability, 175, 184
 oscillator, 171
 out-performance of the FFT by the FPT,
 185
 out-performance of the FFT by the
 FPT⁽⁻⁾, 203
 outgoing boundary conditions, 159
 outside and inside the unit circle, 165
 outside the unit circle, 159, 200
 over-determined system of linear
 equations, 181
 over-estimating, 161
 over-fitting, 161, 225
 overlap, 20, 21, 51–53
 overlapped, 189, 212, 228
 – resonances, 224
 overlapping resonances, 162, 164

P

Padé
 – analysis, 231
 – approximant (PA), 165, 229–230
 – approximations, 176
 – methodology, 176, 183, 227, 229
 – poles, 215
 – polynomial quotient, 230
 – reconstructions, 180
 – spectral analysis, 180, 230
 Padé-based MRS, 231

Padé-based quantification, 161
 Padé-reconstructed resonance profiles,
 201
 para-diagonal, 165, 174, 177, 178, 180
 parametric, 228
 – estimation, 160, 167
 – estimators, 163
 partial
 – fractions, 230
 – signal, 192, 194, 203, 206
 – lengths, 186, 196
 – sum, 175, 176
 – sums, 165
 particle
 – flux, 169
 – fluxes, 171
 – scatterings, 169
 Pauli spin matrix, 62
 peak
 – areas, 159, 187, 224, 226, 227
 – height, 224
 – heights, 214
 – parameters (position, width, height,
 phase), 180
 – position, 224
 – positions, 163
 – width, 224
 perfect matchings, 133
 perturbation, 171
 PET (positron emission tomography), 225
 phase, 159, 188
 phases, 187
 physical, 161, 179, 228
 – information, 184
 – poles, 186
 – resonances, 163, 167, 185, 201
 pole-zero
 – cancellation, 190, 191, 232
 – cancellations, 161, 183
 poles, 165, 171, 179, 191, 215
 polynomial
 – expansion coefficients, 179
 – quotient, 174, 185, 192
 – quotients, 182

positions, 172
 – moment problem, 167
 – series, 175
 potential energy curve, 14–18, 22–25, 37, 40, 41
 prior information, 164, 166, 226
 probability
 – densities, 173
 – function or the w -function, 172
 projection operator, 173
 proper mathematical modelling, 174

Q

QECCD, 13
 QECCSD(T), 34–42
 QECCSD(TQ), 34–42
 quadratic convergence, 160
 qualitative
 – description, 162
 – information, 163, 225
 quantification, 158, 163, 224, 225
 – problem, 161, 167, 184, 189, 190, 196, 225, 228, 231
 – problems, 232
 quantifications, 185, 226, 229
 quantitative information, 162, 163, 225, 230
 quantum
 – graph, 142
 – mechanics, 172, 174, 227
 – scattering theory, 169
 quantum-mechanical, 159
 – concept of resonances, 168, 171
 – spectral analysis, 164, 166, 231
 quotient, 159, 160, 165
 – of two polynomials, 171

R

radiative de-excitations, 168
 radio-frequency
 – photons, 172
 – pulses, 159

random
 – Gaussian noise, 184
 – walk, 150
 rank, 165
 rational
 – analytical functions, 229
 – function, 171
 – functions, 165, 168, 197
 – polynomial, 174
 – polynomials, 165
 – response function, 166
 raw FID, 164
 Rayleigh
 – bound, 163
 – limit, 166
 reactivity criteria *see* charge sensitivities
 reconstructed
 – data, 168
 – spectral parameters, 189, 190
 reconstruction, 184, 185, 228
 – problems, 184
 – true number K of resonances of, 190
 reconstructions, 167, 209
 recoupling (of angular momenta), 102–106
 – coefficients, 104, 105
 reduced
 – matrix element, 92
 – resolution, 159
 redundant input information, 165
 reference metabolite, 188
 Regge symmetry, 108
 relaxation
 – formalism, 159
 – time, 159, 163, 169
 – times, 158, 224
 reliability, 161, 164, 212, 231
 representation (group or diagram)
 – contragredient, 67
 – contrastandard, 67
 – simply reducible, 61
 – standard, 67
 – symmetric group, 114
 – unitary, 61

- residual
 - or error spectra, 201, 212
 - spectra, 203
 - water metabolite, 189
 - residues, 163
 - resolution enhancement, 159, 160, 166
 - resolvent, 159
 - operator, 173
 - resolving power, 184
 - resonance, 159, 162
 - data, 170
 - effect, 169
 - energy, 169
 - formula, 169
 - frequencies, 212
 - frequency, 187
 - peak, 180
 - phenomenon, 170
 - position, 180
 - profiles, 171
 - width, 169
 - resonances, 216, 224, 229, 230
 - resonant
 - frequency, 159, 201
 - maximum, 169
 - nuclear scattering, 168
 - scattering theory, 184
 - function, 159, 168, 171
 - functions, 176
 - robust
 - quantification, 162
 - signal processor, 167
 - robustness, 231
 - rooting the characteristic polynomial, 164
 - roots, 179
 - round-off errors, 230
 - rules (for diagram manipulation), 89–101, 115–121
- S**
- S4 (model, system), 13–16
 - S-matrix, 171
 - sampling rate, 162, 197
 - scalar or inner product, 173
 - scattering
 - matrix, 171
 - wave function, 169
 - Schrödinger
 - eigenproblem, 166
 - eigenspectrum, 166
 - eigenstate, 166
 - eigenvalue problem, 164, 172
 - equation, 5, 6, 172, 226
 - – adjoint form of, 6
 - – bra counterpart of, 6
 - – connected cluster form of, 6
 - Schwinger
 - representation, 63–67
 - states, 66
 - variational principles, 227
 - second-quantized representation of
 - angular momentum theory, 63–67
 - secular
 - equation, 164, 179, 226
 - polynomial, 230
 - separation rules, 97–101
 - series in powers, 160
 - Shanks
 - algorithm, 175
 - transform, 165, 183, 227
 - shape estimations, 160
 - shieldings, 228
 - shimming, 161, 189
 - shortening the FID, 160
 - side lobes, 162
 - signal
 - length, 162, 167, 190, 202, 206
 - processing, 159, 161, 162, 174, 225
 - processor, 160
 - processors, 168, 227
 - signal-to-noise ratio (SNR), 163
 - signature of the resonance effect, 169
 - similarity-transformed Hamiltonian, 4, 8, 27
 - simple, 182
 - simply reducible group, 61
 - sinc side lobes, 162
 - sinc-interpolation, 162

- single
 - peak, 189
 - resonance, 189
 - voxel, 158, 222
 - single-level
 - Breit–Wigner, 168
 - BW formulae, 170
 - singular
 - eigenvalues, 165
 - points (poles), 160, 198
 - value decomposition (SVD), 165
 - singularities, 165, 169, 171
 - slowly convergent series, 181
 - SNR, 185
 - SO(3)
 - group, 61
 - Lie algebra, 61
 - SPECT (single photon emission computerised tomography), 225
 - spectral
 - analysis, 159, 224, 231
 - convergence, 160, 195
 - decomposition, 160, 162, 228
 - deformations, 159, 162, 163
 - information, 159, 167, 222
 - parameters, 159, 167, 173, 180, 184, 188, 197, 201, 214, 216, 224, 227, 229
 - pattern, 158, 222
 - quality, 159
 - representation, 174
 - shapes, 163
 - structures, 162
 - spectroscopic information, 201
 - spectroscopy, 159, 170
 - spectrum, 159, 162, 165, 224, 228
 - of metabolites, 162
 - spurious, 164
 - metabolites, 225
 - poles, 184, 186
 - resonances, 161
 - zeros, 184
 - stabilisation, 192
 - stability, 184
 - stable, 184
 - estimation, 222
 - static magnetic
 - field, 159
 - fields, 172
 - stationary
 - amplitudes, 167, 174, 184
 - conditions, 6
 - stick structure, 162
 - striking differences, 201
 - structure, 159, 160
 - stunning reliability, 231
 - SU(2)
 - irreducible representation, 67
 - Lie algebra, 61
 - SU(3) groups, 61
 - subjective, 161
 - sufficient condition, 212
 - sum rule, 109
 - suppression, 161
 - synthesised, 159, 162, 167, 184
 - FID, 161
 - time
 - – signal, 187
 - – signals, 185
 - system
 - function, 175
 - of linear equations, 178
 - operator, 172, 173
 - response function, 181
 - systems of linear equations, 178, 179
- T**
- tabular data, 187
 - the Froissart doublets, 190
 - theory
 - of approximations, 165
 - of chemical reactivity in electron
 - – following (EF) representation, 238–240, 241–248
 - – preceding (EP) representation, 239, 240, 248–254
 - tightly overlapped, 189

time, 175, 183
 – and frequency, 162
 – – domain, 230
 – domain, 162, 163, 175, 179, 183
 – evolution operator, 173
 – frequency domain, 165
 – reversal, 69–71
 – signal, 174, 176, 178, 188
 – signals, 158, 231
 time-dependent Schrödinger equation,
 173
 tissue, 158, 161, 163, 222, 228
 – content, 161
 – metabolites, 222
 tissues, 159
 total
 – acquisition
 – – time, 162
 – – times, 224
 – duration
 – – of the FID, 162
 – – time, 197
 – energy, 127
 – – π -electron, 127
 – shape spectrum, 163, 209
 transient, 159
 triangular delta, 79
 truncation
 – artefacts, 162
 – error, 163
 – errors, 162
 – number, 206
 two unique polynomial, 160
 two-dimensional (2D) MRS, 168

U

unambiguous quantification, 162
 under-estimating, 161
 under-fitting, 161, 225
 unique
 – capability, 161
 – quantification, 174
 – rational polynomials, 176
 unit circle, 215

unitary group approach, 114
 unity operator, 174
 unstable transients, 184
 US (ultrasound), 225

V

VAPRO, AMARES, LCModel, 189
 VAPRO (variable projection), 163
 variational principle, 47
 Voigt, 171
 – convolution integral, 172
 – frequency profile, 171, 172
 – time profile, 172

W

water, 159, 187, 201
 – and/or fat suppression, 162
 – suppression, 189
 wave
 – function, 171, 173
 – functions, 173
 – packet, 169
 weighted sum, 164
 Weisskopf–Wigner theory, 169
 Weyl’s formula, 43
 whole information, 173
 wide variations, 166
 widths, 172
 widths, heights, and phases of, 163
 Wiener index, 130, 133
 Wigner–Eckart
 – proof, 92
 – theorem analogy of diagram
 factorization, 95
 window, 165
 – size, 159
 Wynn
 – ε -algorithm, 165, 183, 227
 – ε -non-linear recursion, 165
 – algorithm, 165
 – recursion, 183

Z

z -transform, 176

zero

– filling, 162, 168

– padding, 162

zeros, 179